ISSN 1520-295X

Design of Reinforced Concrete Panels for Wind-borne Missile Impact

by
Brian Terranova, Andrew S. Whittaker and Len Schwer

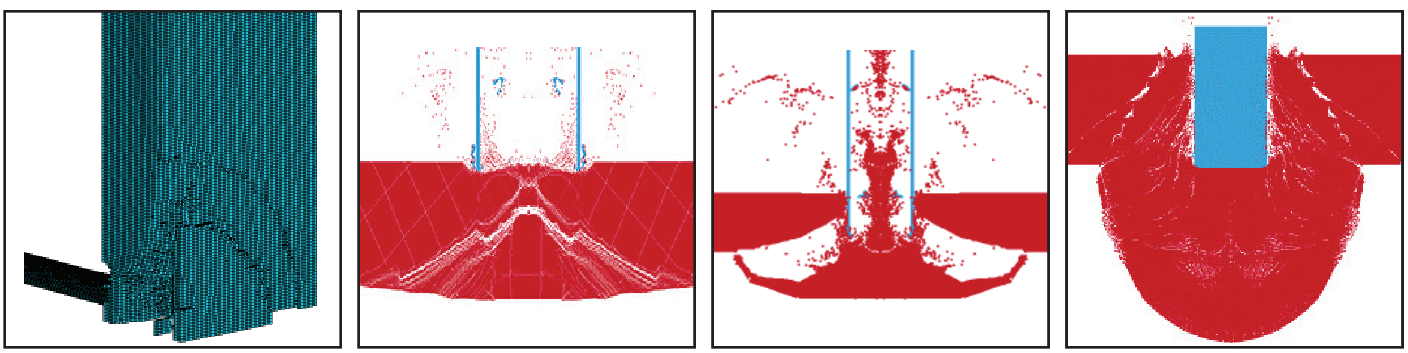

Technical Report MCEER-17-0004

July 18, 2017

This research was conducted at the University at Buffalo, State University of New York, and was supported primarily by MCEER.

NOTICE

Design of Reinforced Concrete Panels for Wind-borne Missile Impact

by

Brian Terranova,[1] Andrew S. Whittaker[2] and Len Schwer[3]

Publication Date: July 18, 2017
Submittal Date: June 16, 2017

Technical Report MCEER-17-0004

1 Research Engineer and former Graduate Student, Department of Civil, Structural and Environmental Engineering, University at Buffalo, State University of New York
2 Professor and MCEER Director, Department of Civil, Structural and Environmental Engineering, University at Buffalo, State University of New York
3 Schwer Engineering & Consulting Services, Windsor, California

MCEER
University at Buffalo, State University of New York
212 Ketter Hall, Buffalo, NY 14260
E-mail: *mceer@buffalo.edu*; Website: *http://mceer.buffalo.edu*

Preface

MCEER is a national center of excellence dedicated to the discovery and development of new knowledge, tools and technologies that equip communities to become more disaster resilient in the face of earthquakes and other extreme events. MCEER accomplishes this through a system of multidisciplinary, multi-hazard research, in tandem with complimentary education and outreach initiatives.

Headquartered at the University at Buffalo, The State University of New York, MCEER was originally established by the National Science Foundation in 1986, as the first National Center for Earthquake Engineering Research (NCEER). In 1998, it became known as the Multidisciplinary Center for Earthquake Engineering Research (MCEER), from which the current name, MCEER, evolved.

Comprising a consortium of researchers and industry partners from numerous disciplines and institutions throughout the United States, MCEER's mission has expanded from its original focus on earthquake engineering to one which addresses the technical and socio-economic impacts of a variety of hazards, both natural and man-made, on critical infrastructure, facilities, and society.

The Center derives support from several Federal agencies, including the National Science Foundation, Federal Highway Administration, Department of Energy, Nuclear Regulatory Commission, and the State of New York, foreign governments and private industry.

The overarching goal of the research project was to validate a numerical model for the analysis of reinforced concrete panels impacted by wind-borne missiles. Experiments from the 1970s were used for the validation exercise. The Lagrangian and Smooth Particle Hydrodynamics (SPH) algorithms in LS-DYNA were used for numerical analysis. Challenges with the use of Lagrangian elements for impact simulations prompted study of the SPH method. The axisymmetric formulation was adopted for the SPH-based impact simulations. The partially validated numerical model was used in a parametric study to investigate the effects of panel thickness, Schedule 40 pipe size, pipe velocity, and concrete uniaxial compressive and tensile strength on panel response. Impact by annular and solid missiles was investigated. Results of the parametric study were used to draft design guidance.

ABSTRACT

United States Nuclear Regulatory Commission Regulatory Guide (RG) 1.76, *Design-Basis Tornado and Tornado Missiles for Nuclear Power Plants*, and RG 1.221, *Design-Basis Hurricane and Hurricane Missiles for Nuclear Power Plants*, identify a set of missiles and impact velocities to be considered in the design of nuclear power plants. Empirical formulae are used to calculate local behavior (scabbing, penetration, perforation) of reinforced concrete walls and slabs impacted by tornado- and hurricane-borne missiles. An evaluation of these empirical formulae using results from impact tests conducted by EPRI and Calspan at Sandia Laboratory in the 1970s showed that these formulae are not of the accuracy required for analysis of nuclear power plant structures. Shortcomings with the empirical equations, and a lack of knowledge regarding those parameters that most affect impact resistance against soft and hard missiles, prompted an effort to validate a numerical model in LS-DYNA for impact analysis of reinforced concrete panels. Four EPRI tests were chosen for the validation exercise. The Lagrangian and Smooth Particle Hydrodynamics (SPH) algorithms in LS-DYNA were used for numerical analysis. Challenges with the use of Lagrangian elements for impact simulations (e.g., element distortion and negative volume errors) prompted study of the SPH method. The axisymmetric formulation was adopted for the SPH-based impact simulations. The axisymmetric model predicted the results of the EPRI experiments with reasonable accuracy using the MAT072R3 concrete material model but the lack of metadata from the EPRI experiments make it impossible to formally validate the numerical model. The partially validated numerical model was used in a parametric study to investigate the effects of panel thickness, Schedule 40 pipe size (mass and diameter), pipe velocity, and concrete uniaxial compressive and tensile strength on panel response. Results showed that all of these parameters affect the impact resistance of reinforced concrete panels, and so should be considered in design and in future development of empirical formulae. Results of the parametric study were used to draft design guidance for reinforced concrete panels impacted by wind-borne missiles. Minimum panel thicknesses of 15 in (381 mm) and 18 in (460 mm) are required to prevent scabbing and perforation if normally impacted by a 6 in (152 mm) diameter Schedule 40 pipe at velocities of 1575 in/sec (40 m/s) and 3937 in/sec (100 m/s), respectively, for concrete compressive and tensile strengths greater than or equal to 4351 psi (30 MPa) and 435 psi (3 MPa), respectively. Impact of solid missiles was also simulated and shown to be more damaging than annular missiles of the same mass.

ACKNOWLEDGEMENTS

The authors thank Mr. Michael Hessheimer of Sandia National Laboratory for providing background documents on the experiments performed in the 1970s and for his insights into performing impact experiments on reinforced concrete panels.

TABLE OF CONTENTS

TABLE OF CONTENTS (CONTD.)

TABLE OF CONTENTS (CONTD.)

TABLE OF CONTENTS (CONTD.)

TABLE OF CONTENTS (CONTD.)

LIST OF FIGURES

LIST OF FIGURES (CONTD.)

LIST OF FIGURES (CONTD.)

LIST OF FIGURES (CONTD.)

LIST OF FIGURES (CONTD.)

LIST OF FIGURES (CONTD.)

LIST OF TABLES

LIST OF TABLES (CONTD.)

LIST OF TABLES (CONTD.)

SECTION 1
INTRODUCTION

1.1 Introduction

Nuclear power plants are designed for a wide range of natural and man-made hazards, and risk assessment is performed to judge whether target performance goals (e.g. mean annual frequency of core melt) are achieved. Two of the natural hazards that must be considered for design are a) impact of wind-borne missiles, and b) earthquake shaking. This report addresses the impact of wind-borne missiles (e.g., steel pipe, timber poles) on the exterior of reinforced concrete buildings that house nuclear reactors.

1.2 Organization of this Report

In this report, reinforced concrete walls and slabs are grouped together as panels. Reinforced concrete panels in nuclear structures, vertical, horizontal or inclined, must be designed to resist the impact of steel, timber, automobile, and solid spherical projectiles borne by extreme winds such as tornadoes and hurricanes. A goal of design against these impact loadings is to prevent the loss of either backface (non-impact face) concrete or the projectile into containment, where it is impossible to predict the consequences of such outcomes. Normal impact of the projectile on panel is assumed, because the likelihood of negative consequences is reduced by oblique impact. Although the likelihood of normal impact is very small, given all possible angles of attack, there is no technical basis for assuming oblique impact of an arbitrary orientation. This report is presented in six chapters, as described below.

Chapter 2 introduces impact loading and describes past experimental and numerical studies.

Chapter 3 examines existing empirical formulae for impact assessment and compares predictions of these formulae with results from tests performed at Sandia National Laboratory in the 1970s.

Chapter 4 discusses modeling of test components (e.g., Schedule 40 pipe and reinforced concrete panels) using Lagrangian finite elements in the commercial finite element code LS-DYNA (LSTC, 2012). Three-dimensional quarter models, contact algorithms, boundary conditions, strain-rate parameters, and material models are described. The results of impact simulations are presented, and then are compared with the measurements from the experiments to validate, in part, the numerical models. The advantages, disadvantages, and shortcomings of the Lagrangian formulation are identified.

Chapter 5 describes modeling techniques in LS-DYNA using the axisymmetric SPH formulation. Contact, boundary conditions, material models, and equations of state are introduced. The results of axisymmetric Schedule 40 pipe impact simulations are presented. The SPH model is validated to the degree possible using the Sandia data.

Chapter 6 presents the results of a parametric study that investigates the effects of a number of design parameters on the impact resistance of reinforced concrete panels. Results of these studies are used to provide draft technical guidance for the performance assessment of reinforced concrete panels impacted by wind-borne missiles.

Chapter 7 summarizes the studies presented in Chapters 3 through 6, and provides the key conclusions and findings. References are presented in Chapter 8.

SECTION 2
IMPACT LOADING: AN INTRODUCTION

2.1 Introduction

Nuclear power plants (NPPs) are an essential part of the world's energy infrastructure, generating electricity and process heat. Containment structures are an integral part of NPPs, providing a pressure vessel and radiation shield in the event of damage to the reactor core (Russell, 1962). Figure 2-1 is a photograph of two containment vessels at the Diablo Canyon Nuclear Generating Station. Such containment structures are designed to remain intact under very rare earthquake shaking and for the effects of severe meteorological events, including tornado and/or hurricane winds and missiles borne by those winds.

Figure 2-1: Diablo Canyon Nuclear Generating Station (Britannica, 2014)

Wind-borne objects can pose a serious threat to nuclear power plant walls because these objects may penetrate or even perforate wall and floor panels, causing damage to the reactor and its safety systems. Missile impact testing of reinforced concrete panels in the 1970's by Sandia Laboratory (Stephenson, 1977) indicated that the damage is local and not global. Local damage is characterized by penetration of the panel, which is sometimes accompanied by scabbing (ejection of fragments of concrete) of the concrete on the back (non-impact) face and perforation if the panel is thin. Perforation is the complete penetration of the missile through the panel.

Regulatory Guide 1.76 *Design-Basis Tornado and Tornado Missiles For Nuclear Power Plants* (Regulatory Guide 1.76, 2007) promulgated by the United States Nuclear Regulatory Commission (U.S. NRC) provides a set of missiles to be used for the design of exterior, above grade, walls and slabs, in nuclear power plants. The design-basis missiles for nuclear power plants should include at least a massive high-kinetic energy missile that deforms on impact, a rigid missile that tests penetration resistance, and a small rigid missile of a size sufficient to pass through openings in protective barriers. The impact speeds vary as a function of the region (I, II, III) of the United States in which the plant is located, where Region I corresponds to the highest wind speeds and velocities for tornado-borne missiles. The three design missiles for Region I are listed below: missile type, size, weight and impact velocity.

- Automobile: 16.4 ft. × 6.6 ft. × 4.3 ft., 4000 lbs., 135 ft. /sec.
- Steel Pipe: 6 in. diameter × 15 ft. long Schedule 40 pipe, 287 lbs., 135 ft. /sec.
- Solid Steel Sphere: 1 in. diameter, 0.147 lbs., 26 ft. /sec.

The Schedule 40 pipe and the automobile are used as the penetrating and massive high-kinetic energy missiles, respectively. The solid sphere is assumed capable of passing through openings in protective barriers. Of these missiles, the focus here is on the Schedule 40 pipes due its higher probability of penetrating concrete panels and scabbing concrete. Regulatory Guide 1.221 *Design-Basis Hurricane and Hurricane Missiles for Nuclear Power Plants* (Regulatory Guide 1.221, 2011) identifies the same missiles and specifications described above. However, for a hurricane wind speed of 336 mph (the max velocity considered), the horizontal missile velocity for the automobile, steel pipe, and sphere are specified to be 372, 309, and 278 ft./sec., respectively: much greater than the corresponding velocities specified in RG 1.76 for tornado-borne missiles.

Empirical formulae for normal (90º) impact have traditionally been used in the design of nuclear facilities against the effects of hurricane and tornado-borne missiles. The reliability of these empirical equations is questionable because they were formulated from high-speed (500-2000 ft./sec) impact tests of non-deformable missiles designed for penetration (Kennedy, 1975). Design velocities for missile impact on nuclear facilities are substantially lower, as noted in the bulleted list above, and these missiles are typically both blunt ended and deformable. Such missiles are expected to absorb some of the energy of the impact, reducing the local damage.

Since the empirical formulae were developed for rigid missiles, they should, if accurate, overestimate local damage caused by deformable missiles.

In the 1970s, when many of today's operating nuclear plants were designed and constructed, the most commonly used empirical equations for tornado-borne missile impact were the Modified Petry (MP) and the Modified National Defense Research Committee (NDRC) formulae (Stephenson, 1977). Both were derived by empirical or semi-empirical means from military tests of non-deformable projectiles impacting very thick walls. These two equations and the seven others listed below are evaluated herein. These formulae categorize response by 1) missile penetration depth, 2) wall panel thickness required to prevent scabbing, and 3) wall panel thickness to prevent perforation. Source materials for the formulae are identified in the last pair of brackets in the list below.

- Modified Petry (MP) (Kennedy, 1975)
- Army Corps of Engineers (ACE) (Kennedy, 1975)
- Modified National Defense Research Committee (NDRC) (Kennedy, 1975)
- Amman and Whitney (AW) (Kennedy, 1975)
- Ballistic Research Laboratory (BRL) (Kennedy, 1975)
- Bechtel (B) (Kennedy, 1975)
- CEA-EDF (CEA-EDF) (DOE, 2006)
- CRIEPI (CRIEPI) (DOE, 2006)
- Chang (CF) (DOE, 2006)

Other empirical formulae have been proposed but will not be discussed here, including Whiffen, Kar, UKAEA, Stone and Webster, Haldar and Hamieh, Adeli and Amin, Hughes, Healey and Weissman, IRS, and the UMIST (see Rahman et al., 2010). Table 2-1 identifies the reported capabilities of the bulleted empirical methods with the symbol "✓".

Table 2-1: Capabilities of empirical methods

	Penetration depth, X	Scabbing thickness, s	Perforation thickness, e
MP	✓[1]	✓	✓
ACE	✓	✓	✓
NDRC	✓	✓	✓
CEA-EDF			✓
CRIEPI		✓	✓
CF		✓	✓
AW	✓		
BRL		✓	✓
B		✓	

1. denotes local impact phenomenon computed by empirical formulae

2.2 Code Requirements for Impact Loading on Reinforced Concrete Nuclear Structures: ACI 349-13

Appendix F of ACI 349-13 *Code Requirements for Nuclear Safety-Related Concrete Structures and Commentary* (ACI, 2013) requires consideration of local and global responses to impact loadings on nuclear structures. Global responses are permitted to be calculated using equivalent Single Degree of Freedom (SDOF) models. Local responses are calculated using empirical formulae such as those introduced previously.

For global analysis using SDOF models, the properties of the equivalent system are based on load and mass transformation factors, which can be traced to the seminal work of Biggs and his co-workers (e.g., Biggs, 1964). These factors enable a calculation of equivalent mass, stiffness and load but require the analyst to define a shape function. For two-way slabs and walls in the elastic range of response, the deflected shape is generally taken as either the fundamental mode shape or the deformed shape calculated by applying the dynamic load statically. In the inelastic range of response, the deflected shape can be taken as the collapse mechanism.

Although the equivalent SDOF system is mathematically straightforward for global analysis, it must be used with caution for analysis of near-field blast and impact loadings. Impact loadings typically produce local deformations with effects experienced within a few multiples of the panel thickness from the point of impact, and the displaced shape of the impacted panel is likely very different from the fundamental mode shape or the elastic displaced shape or (global) collapse mechanism of the panel if the impacting force is applied quasi-statically. Further, a resistance function derived for SDOF analysis of a panel will generally assume an intact cross section, which will not be the case if it sustains damage. Impactive loadings on reinforced concrete panels can generate high strain rates. Traditional analysis and design for blast and impact loadings makes use of dynamic increase factors (DIFs) to increase the mechanical properties of reinforcement and concrete in tension and compression, and concrete in shear.

Table 2-2 presents DIFs for three grades of reinforcement and for concrete, where $\dot{\varepsilon}$ is the strain rate. More current information is presented in Dusenberry (2010). Unresolved challenges with the use of DIFs include a) the temporal and spatial variation of strain rate over the impacted component, and b) predictions of spalling, scabbing, penetration and perforation. The only reliable means of predicting the response of reinforced concrete panels to missile impact are by either testing or numerical simulation using verified and validated numerical tools, which are discussed in Section 2.9 and in later sections of this report.

Table 2-2: Dynamic increase factors (ACI, 2013)

Material	Dynamic Increase Factor (DIF)
Reinforcing steel	
Grade 40	$1.1 + 0.0723(\log \dot{\varepsilon} + 3.3) \leq 1.2$
Grade 50	$1.05 + 0.08(\log \dot{\varepsilon} + 3) \leq 1.15$
Grade 60	$1.0 + 0.02625(\log \dot{\varepsilon} + 5.9) \leq 1.1$
Concrete	
Axial and flexural compression	$0.9 + 0.1(\log \dot{\varepsilon} + 5) \leq 1.25$
Shear	$\left[0.9 + 0.1(\log \dot{\varepsilon} + 5)\right]^{1/2} \leq 1.1$

Appendix F provides guidance on formulae to be used for local response calculations but notes the shortcomings with the use of empirical equations: 1) for rigid missiles, the NDRC, Bechtel and Stone and Webster formulae provide reasonable calculations of perforation and scabbing thicknesses, 2) for rigid missiles, the Modified Petry and BRF formulae should not be used, and 3) for highly deformable missiles, the empirical formulae tend to be conservative.

2.3 Concrete Material Models for Impact Simulations

LS-DYNA (LSTC, 2012) includes three concrete material models for use with Lagrangian and Smoothed Particle Hydrodynamics (SPH) simulations of impact: Pseudo_Tensor (MAT016), Concrete_Damage (MAT072R3), and CSCM (MAT159). Each of these models is introduced below because they are used in the simulations that follow in Chapters 4, 5, and 6. These three models each generate a set a parameters describing the elastic and inelastic response of the concrete using only the uniaxial concrete compressive strength as input.

The Pseudo_Tensor (MAT016) model was developed to analyze buried reinforced concrete structures subjected to impulsive loadings. MAT016 was written for the Lagrangian finite element code DYNA3D (Malvar et al., 1997), which was developed by Lawrence Livermore National Laboratory. Volumetric and deviatoric responses are decoupled in MAT016. Malvar et al. (1997) describe MAT016 as follows:

> "…An equation of state gives the current pressure as a function of current and previous minimum (most compressive) volumetric strain. Once the pressure is known, a moveable surface-herein denominated a yield or failure surface--limits the second invariant of the deviatoric stress tensor. The volumetric response is easily captured using a tabulated input for the equation of state…"

Karagozian and Case (K&C), a consultancy in Los Angeles, California developed the Concrete_Damage (MAT072) material model for analysis of reinforced concrete components subjected to blast and impact loadings. The original K&C model was an updated version of MAT016 in which the volumetric and deviatoric responses are coupled. Malvar et al. (1997) provides a detailed description of the first implementation of MAT072 in DYNA3D (Whirley et al., 1993). MAT072 is based on three independent strength surfaces (e.g., maximum, yield, and residual), which are defined using nine user-input parameters that are calibrated to experimental data. Wu et al. note "…the failure surface is interpolated between the maximum strength surface and either the yield strength surface or the residual strength surface." A scale factor that is dependent on the 3rd invariant of the deviatoric stress tensor enables a smooth transition between brittle (low confinement) and ductile (high confinement) behavior. Plastic flow can be non-associative, fully associative, or partially associative. MAT072 was exported to the LS-DYNA platform in the mid-2000s (Wu et al., 2012). MAT072R3 (e.g., Magallanes et al., 2010) is the current version of the K&C model available in LS-DYNA.

The Continuous Surface Cap Model (CSCM), MAT159 in LS-DYNA, was developed by Murray et al. (2007a; 2007b) to predict the response of concrete structures used in roadside safety structures to impact loadings. Similar to MAT072R3, volumetric and deviatoric behaviors are coupled by combining the shear failure surface and a hardening compaction surface. MAT159 includes a fracture-energy based damage function used to model both softening and post-peak stress-modulus reduction. The model and its validation are described in Murray et al. (2007a; 2007b). Wu et al. (2012) compare the performance of MAT072, MAT159, and other concrete models available in LS-DYNA.

2.4 Experimental Testing Related to Wind-borne Missile Impact

Limited data from a small number of physical tests involving wooden utility poles, steel pipes and rods are available to establish the accuracy of the empirical formulae and validate numerical tools. These data are introduced below. There are no data for wind-borne automobile impact on reinforced concrete panels.

2.4.1 Sandia Laboratory

Tests were conducted at Sandia Laboratory by the Electric Power Research Institute (EPRI) in the 1970s (Stephenson, 1977). Wooden utility poles, steel pipes, and steel rods were propelled into reinforced concrete panels with thicknesses typical of walls and roofs of auxiliary buildings in nuclear power plants. The panels tested at Sandia were 17 × 17 ft. overall, spanning 15 × 15 ft., with thickness of 12, 18, and 24 inches. The test panels were constructed with 3000 psi concrete and 0.31%, 0.28%, and 0.27% reinforcing steel ratio, each way, each face, for the 12-, 18-, and 24-inch panels, respectively. The Grade 60 reinforcement was spaced at 12 inches on center. Figure 2-2 shows the experimental test setup that includes the missile launcher, the reinforced concrete wall panel, and a fixture for the support of the test panel. The desired speed at impact was achieved by selecting a launch position on the rail and the number of rockets (up to four) mounted to the sled.

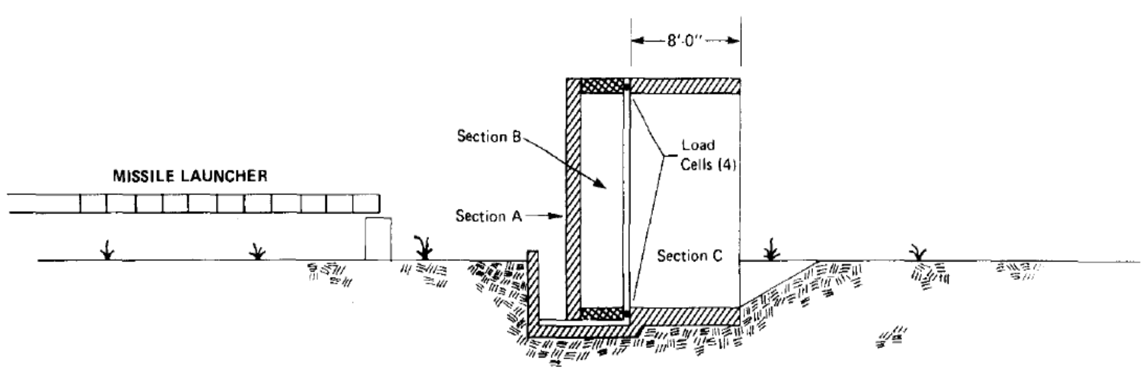

Figure 2-2: Experimental impact test setup (Stephenson, 1977)

Load cells were installed at all four corners of the wall to determine the reactions. There are no metadata for the load cells. These load cells are identified in Figure 2-2. Records from high-speed film provided the velocity histories for the impacting missiles. The acceleration history of a missile was obtained by differentiating the velocity history. The inertial force at impact was calculated as the product of the missile mass and the acceleration at impact. The displacements of the wall panels were not recorded for the impacts of the wooden utility poles but crack patterns were photographed and these can be used to indirectly measure the level of damage to the panel. Information on the effects of the impacting steel pipes and rods and wooden utility poles, including penetration depth, conical plug dimensions caused by the impact, rebound velocity, and photographs of local damage to the specimen was documented. Chapter 4 provides information on these tests.

Thirteen normal-impact tests were conducted using a 12-inch diameter Schedule 40 pipe as the wind-borne missile. One 3-inch Schedule 40 pipe was also used for testing. The data were used to judge the utility of empirical equations with an emphasis on the MF and Modified NDRC formulas, Stephenson (1977) concluded that

- The formulae predict several inches of penetration for the wooden utility pole but the pole did not penetrate at all, and so should not be used for impacting wooden utility poles
- The NDRC formula predicted the measured penetration depth of the Schedule 40 pipes reasonably accurately using the outer diameter of the missile in the calculations
- The MP formula did not accurately recover the penetration depth for the Schedule 40 pipes
- The MP formula did not recover scabbing thickness
- The NDRC equation over-predicted the panel thickness required to prevent scabbing
- Scabbing thickness was predicted reasonably well as 3 times the penetration depth computed by the NDRC formula for the 12-inch diameter Schedule 40 pipe.

One impact test (Test #19 per Table 1-1 in Stephenson (1977)) was performed on an 18-inch thick panel to judge the influence of oblique impact. A 12-inch diameter Schedule 40 pipe, with a weight equal to 765 lbs., impacted the panel at an angle of 45° at a velocity of 222 fps. The reported uniaxial compressive strength of the concrete in the panel was 3900 psi. Damage was compared to that of a nearly identical test (Test # 3 per Table 1-1 in Stephenson (1977)) with normal impact. The normal-impact test scabbed concrete from the panel. The oblique-impact test produced less damage than the normal-impact test, namely, only cracking on the back face. (This is an expected result because the travel path through the panel for oblique impact is greater than that for normal impact.)

2.4.2 Calspan

Missile impact tests were performed on 9 ft. × 9 ft. reinforced concrete panels by Calspan in 1975 for Bechtel Power Corporation (Vassallo, 1975). The panels were 12, 18, and 24 inches thick and cast with 3500 to 4500 psi concrete. The Grade 60 reinforcement was spaced at 12 inches on center; the reinforcement ratios ranged between 0.4% and 0.6% each way, each face. The impacting missiles were 8-inch diameter Schedule 40 pipes, wooden utility poles and solid steel slugs.

The test setup included a missile launcher, a reaction fixture for support of the test panels, and instrumentation for recording data (Vassallo, 1975). High-speed photography was used to capture the velocity of the missile at impact. The displacement of the back face of the panels was measured using a custom fabricated scratch gage.

Calspan did not compare and contrast the results of the tests and predictions using the empirical equations. An empirical equation, Bechtel, was developed using data from the Calspan tests to predict the panel thickness required to prevent scabbing for 8-inch diameter Schedule 40 pipes (Vassallo, 1975). This formula was calibrated for 8-inch Schedule 40 pipes, Vassallo cautioned against its use for other pipe diameters and wall thicknesses.

2.5 Kennedy Study of Empirical Methods

Kennedy (1975) evaluated empirical formulae including the MP, ACE, NDRC, AW, and BRL and observed significant differences in predictions of local damage. His study focused on the 8-inch diameter Schedule 40 pipe, wooden utility pole, and the 8- inch diameter steel slugs used in the Calspan tests. He used an effective diameter for the analysis of the pipe, taken as the diameter of a solid cylinder with the same initial contact area as the actual 8-inch diameter Schedule 40 pipe (=8.40 in^2). Kennedy drew the following conclusions:

- Empirical formulae are not applicable for impact analysis of wooden poles

- Only the NDRC formula was capable of accurately predicting the perforation and scabbing thicknesses over the range of missile diameters (up to 16 inches), caliber densities (0.2 – 6.0 lb. /in^3), and missile velocities (100-3000 ft. /sec) for which test data were available.

2.6 Other Experimental Testing Related to Missile Impact

2.6.1 Full Scale Aircraft Impact Experiments

Full-scale aircraft impact tests were conducted at Sandia Laboratory in 1993. The purpose of the test was to determine the impact force history caused by the normal impact of a F4 Phantom jet onto a massive rigid reinforced concrete target at a velocity of 215 m/s (Sugano, 1993a). Other objectives included the evaluation of the crushing behavior of the aircraft, probability of engine detachment, and dispersal of fuel after the impact. A flyable F4 Phantom jet was acquired by Sandia Laboratory for the experiment and the fuel tanks were filled with water to provide proper mass distribution and evaluate fuel dispersal after impact. The jet was propelled into the reinforced concrete target using a sled and a two stage rocket system. The target consisted of a 7 $\times$ 7 m reinforced concrete block that was 3.66 m thick; the block weighed 469 tonnes. The target was placed on air bearings, which allowed the structure to move after impact. The experimental results showed that the aircraft was completely crushed upon impact, and the local damage caused by the fuselage was insignificant compared to the local damage caused by the engines (Sugano, 1993a). The damage to the target was relatively minor, which indicates that most of the impact energy was absorbed in moving the target and aircraft deformation.

2.6.2 Aircraft Engine Impact Experiments

In 1993, a number of experiments were conducted that involved the normal impact of aircraft engines, and simplified models thereof, onto reinforced concrete panels. Small-, intermediate-, and full-scale tests were carried out using the General Electric (GE) J-79 turbojet engine as the impacting missile (Sugano, 1993b). The purpose of these experiments was to gain insight into aircraft impact, investigate the appropriateness of using similarity laws to scale the tests, and modeling the engine as a deformable missile. The small- and intermediate-scale tests used simplified rigid and deformable missiles representing the J-79 turbojet engine to determine the reduction in damage caused by missile deformability. The full-scale tests used the actual J-79 turbojet engine and a deformable-missile representation of the engine. The reinforced concrete panels for the small-, intermediate-, and full-scale tests were 1.5 m, 2.5 m, and 7 m square, with thicknesses of 60-350, 300-600, and 900-1600 mm, respectively. Reinforcement ratios ranging from 0.2 to 0.6% each way, each face, were used for the small- and intermediate-scale tests; 0.4% was used for the full-scale tests. The use of a steel liner (or scab plate) on the back face of the reinforced concrete panel in the intermediate- and full-scale tests was also explored. The tests resulted in significant local damage to the panels including penetration, perforation, and scabbing. The application of the steel liner prevented concrete scabbing on the back face of the panel. A significant reduction in local damage was observed in the tests using the deformable missiles. The similarity and scaling rules used to scale the small- and intermediate-tests were validated.

2.6.3 Experimental Tests of RC Barriers against Aircraft Impact

In 1999, three 1/7.5 scale model impact tests were performed to explore the use of two consecutive reinforced concrete barriers to mitigate the effects of aircraft impact. This concept allowed an aircraft to perforate the first wall and strike the second wall at a much reduced velocity (Tsubota et al., 1999). The goals of these experiments were to 1) assess damage to the outer panel, 2) measure the residual velocity of the impactor after perforation of the first panel, and 3) determine the impact load on the second panel. The outer panels in the three experiments were 1.5 × 1.5 m in plan with thicknesses of 60, 80, and 100 mm, and rebar spacing of 25, 85, and 68 mm, respectively. The reinforcement ratio for all three tests was 0.47% each way, each face. The inner panel was a 2 × 2 m in plan and 350 mm thick and was suspended as a pendulum behind the outer panel. A simplified model of the aircraft missile was designed according the axial strength and mass distribution of the actual aircraft used in the full-scale aircraft impact tests conducted at Sandia Laboratory in 1993 by Sugano (1993a). Perforation of the outer panel occurred in two of the three experiments and the missile impacted the inner panel. There was a drastic decrease in the impact load to the second panel with an increase in the thickness of the outer panel (Tsubota et al., 1999).

2.6.4 Experimental Tests of SC Composite Shear Walls against Aircraft Impact

Mizuno et al. (2005) conducted five 1/7.5 scale model tests to investigate the behavior of SC composite shear walls against aircraft impact. To understand the benefits of the added steel plates, the tests of Tsubota et al. (1999) were repeated. Two types of 1.7 × 1.7 m SC panels were tested 1) Full SC–steel face plates on both faces of the panel and no traditional reinforcement, and 2) Half SC–steel face plate on the back face and traditional reinforcement on the front face. The panel and steel plate thicknesses ranged from 60 to 120 mm, and 0.8 to 1.6 mm, respectively. The missile was designed using the axial strength and mass distribution of the aircraft used in the full-scale impact tests conducted at Sandia Laboratory in 1993 (see Sugano, 1993a). The tests indicated that the steel faceplates, especially the rear faceplate played a significant role in limiting the scabbing on the back face of the panel. The panel thickness required to prevent perforation could be greatly reduced if the conventional reinforcement was replaced by steel faceplates (Mizuno et al., 2005).

2.6.5 Experimental Tests of High Strength Concrete against Projectile Impact

Dancygier et al. (2007) conducted experiments to study the response of high performance concrete (HPC) plates impacted by non-deformable steel projectiles. The goal was to understand the influence of the concrete mix design and amount and type of reinforcement on the performance of HSC panels (Dancygier et al., 2007). The variables examined were aggregate (type and size), addition of micro-silica (MS) and steel fibers, and reinforcement details. The 800 × 800 × 200 mm concrete specimens were impacted by a 1.5 kg, 50 mm diameter, 200 mm long solid cylinder with a sharp conical nose of hardened steel, at velocities of up to 315 m/s. The projectiles were accelerated to their desired velocities using a gas gun. A total of 39 concrete specimens were tested.

Normal strength concrete (NSC) control specimens with a nominal compressive strength of 30 MPa were constructed with coarse crushed dolomite aggregate of 22 mm maximum size. The reinforcement of these specimens consisted of 400 MPa yield strength bars with a nominal diameter of 8 mm, spaced at 200 mm on the front face, and 100 mm on the rear face, corresponding to reinforcement ratios of 0.14% and 0.28%, respectively. The clear cover on both faces was 15 mm.

The influence of the following HSC mixture ingredients on the performance of the NSC control specimens under impact were examined; addition of MS, 30 mm and 60 mm hooked-end steel fibers, aggregate type and maximum size including basalt, flint, and dolomite ranging from 12 to 50 mm in diameter. Compression and tension reinforcement ratios and the effect of transverse reinforcement were also examined. All HSC mixtures were designed with trial strength of approximately 100 MPa. In all 39 specimens, the perpendicular reinforcement did not intersect at the center of the plate and projectiles did not contact any of the rebar.

Dancygier et al. (2007) also evaluated perforation velocity (the velocity at which the panel just prevents perforation) for the panels using the NDRC and Barr formulae. The formulae for penetration depth were manipulated to determine a perforation velocity for a specific panel thickness. The study used perforation limit and front- and rear-face-crater diameter to quantify damage to the specimens. Based on the test data, Dancygier et al. (2007) concluded

- All HSC specimens had a higher perforation limit than the NSC specimens
- Addition of MS and steel fibers had a limited effect on the perforation limit of the panels; the main contribution of the fibers was to reduce the damaged area on the front and rear faces
- A greater front face reinforcement ratio and multiple curtains of reinforcement increased perforation resistance but did not decrease front face damage
- The larger and harder (i.e., basalt and flint) the aggregate, the greater the perforation resistance. Larger aggregate resulted in a greater rear face crater diameter due to a low tensile strength caused by a small aggregate-matrix area in the concrete
- The smaller aggregates reduced the diameter of the rear face crater due to increased tensile strength caused by a greater aggregate-matrix area
- The formulae (NDRC and Barr) predicted the perforation limit for the NSC specimens with reasonable accuracy, but significantly overestimated the perforation limit for HSC specimens. The empirical formulae calibrated for the NSC impact tests were not suitable for predicting perforation limits for HSC.

2.6.6 Drop Tests on Reinforced Concrete Slabs

Zineddin et al. (2007) conducted impact experiments to study the effect of reinforcement on the dynamic response of reinforced concrete slabs. Three 90 × 1524 × 3353 mm concrete slabs with different reinforcement configurations were tested: 1) 152 × 152 mm mesh of welded steel wire located 25 mm below the surface of the concrete on both faces, 2) 152 × 152 mm mesh of #3 steel bars at the mid thickness of the slab, and 3) 152 × 152 mm mesh of #3 steel bars 25 mm below the surface of the concrete on both faces of the slab. The compressive strength of the concrete was not documented. The slabs were laid flat and bolted on all four sides to a steel frame as illustrated in Figure 2-3, creating an unsupported slab area of 914 × 2743 mm.

The impact tests were performed using a drop hammer with a mass of 2608 kg. The drop was on the center of the slabs. The diameter of the drop hammer was not documented. The three reinforcement arrangements were evaluated at drop heights of 152, 305, and 610 mm. Impact mass acceleration, slab accelerations, peak load and duration, slab deflection, steel frame accelerations, reinforcing steel strains, and high speed videos were recorded.

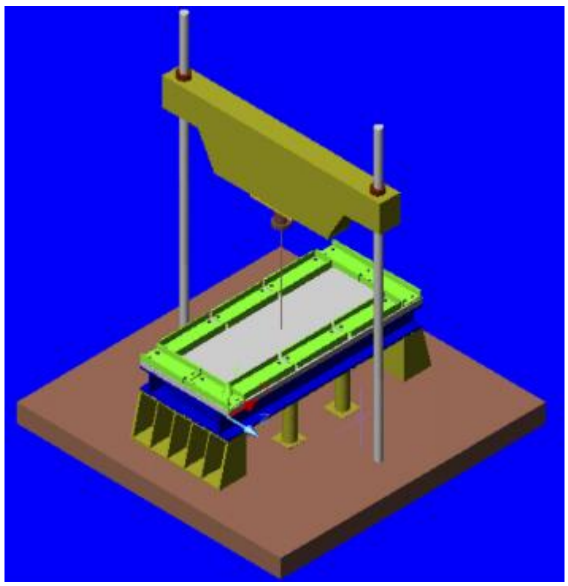

Figure 2-3: Impact testing system (Zineddin et al., 2007)

Based on the impact tests, Zineddin et al. (2007) observed

- Peak displacement of the plate occurred after peak load was reached. The damage to the panels was local and not global
- The maximum displacement at the center of the plate for all three drop heights occurred for the plates reinforced with welded steel mesh on both faces; the wire mesh failed in all three tests
- The reinforcement yielded in the impact zone in all six tests involving #3 bars; a longitudinal bar ruptured in one of the tests at a drop height of 610 mm
- Punching shear failure and scabbing on the back (non-impact) face in all three tests at a drop height of 610 mm; the plate reinforced with one layer of #3 bars at the center had the largest rear face crater diameter

2.7 Numerical Simulation of Impact Tests

2.7.1 Tornado Borne Missile Impact of Reinforced Concrete Panels

Tu and Murray (1977) used the finite element method to examine impact of tornado-borne missiles on reinforced concrete panels. Data from the Sandia and Calspan tests were used to determine the utility of the NDRC formula. They concluded that the NDRC formula would predict the local impact effects of the Schedule 40 pipe if the effective diameter of the pipe (as defined in Section 2.5) was used in the calculations. The study did not identify the diameter of the pipes examined or provide data for re-evaluation. The NDRC formula did not predict the penetration of steel slugs but calculated scabbing thickness for the steel slugs reasonably well.

The finite element program HONDO was used for the impact simulations. HONDO is an explicit finite element code designed to calculate the large deformation, elastic and inelastic response of plane or axis-symmetric bodies of arbitrary shape and composition (Tu and Murray, 1977). The finite element simulations focused on an 8-inch diameter steel slug used in the Calspan tests. The steel slug was 14 inches in length and weighed 214 pounds. The models of the concrete near the back (rear) face of the panel were strengthened to account for the presence of reinforcement (no actual reinforcement was modeled). Three sets of numerical simulations were conducted with the following objectives:

- Compare the simulated impact interaction of the missile and target models with test results
- Assess progression of damage for two target thickness as a function of missile velocity
- Examine the loading history for deformable missile impacting a reinforced concrete panel

One simulation was run for a deformable missile but the results were not validated and no information was provided on the modeling of the missile in HONDO. Insufficient information was reported to enable a detailed review of the numerical models and solution algorithms. Tu and Murray validated their models using scabbing data. Predicted values for penetration depth and conical plug size were not reported.

2.7.2 Soft Missile Impact of Reinforced Concrete Panels

Oliveira et al. (2009) developed a numerical model in LS-DYNA to predict the response of a reinforced concrete wall subjected to impact by a “soft” missile. The numerical model was based on experimental tests conducted by the VTT Technical Research Center of Finland to examine the influence of missile type, mass, momentum and various concrete reinforcing strategies on impact resistance. The test facility consists of an apparatus capable of launching missiles of various mass and geometry at velocities on the order of hundreds of meters per second (Oliveira et al., 2009). Figure 2-4 describes the test set up. A pneumatic compressor is used to increase the air pressure inside the accumulator. The accumulator and the acceleration tube are separated by a thin steel disk termed the explosion sheathing in Figure 2-4, which is designed to rupture at a pressure corresponding to a desired impact velocity. The rupture of the steel disk sends the compressed air through the tube, which accelerates the piston and the externally attached missile on a set of guide rails towards the concrete panel. The piston is stopped at the end of the rails, allowing only the missile to impact the target. The reinforced concrete panel is mounted within a frame that is bolted to a support structure comprised of I-beams and back pipes that connect to surrounding rock (Oliveira et al., 2009).

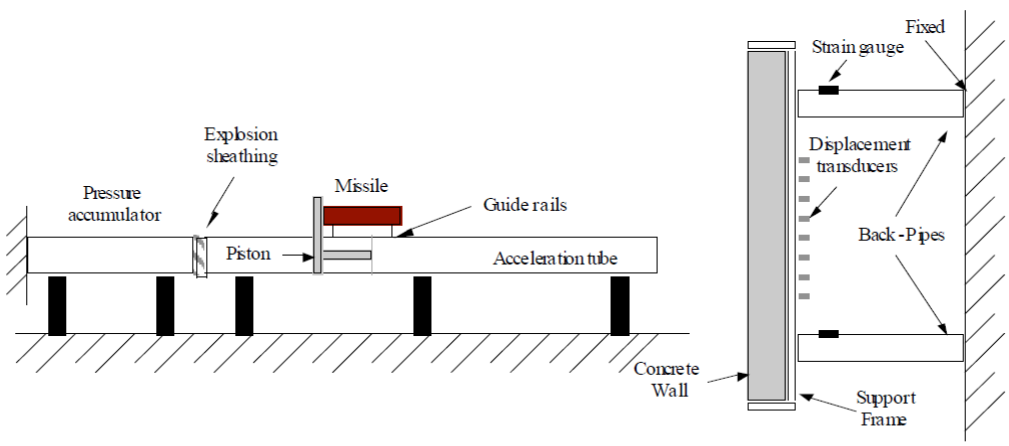

Figure 2-4: VTT experimental test setup (Oliveira et al., 2009)

The target consisted of a 2300 × 2000 × 150 mm reinforced concrete panel. The target was reinforced with A500HW longitudinal and shear reinforcement with nominal diameters of 8 mm and 6 mm, respectively. The longitudinal rebar was equally spaced at 50 mm on center with 15 mm cover on both faces of the panel. The unconfined compressive strength of the concrete was 59.5 MPa, as determined by compression tests on cubes of concrete.

The impacting missile was a solid, flat-nosed projectile fabricated from EN AW6060 T66 aluminum. An “additional mass” pipe of low-carbon steel was fitted over the back end of the missile to allow the mass to be varied for different tests. In the experiment, the missile was 1800 mm long, had a diameter of 250 mm and a total mass of 51.3 kg, and an initial velocity of 127 m/sec. Guides were bolted to the missile for stabilization during the acceleration phase. The impact load from the experiments was determined using data from the strain gages installed on the back pipes (identified in Figure 2-4). The deflection of the panel was measured using displacement transducers installed on the back (non-impact) face. Strain gauge data from the rebar were also recorded. The damage to the panel was not documented.

The numerical model was developed using LS-DYNA. MAT072R3 was used to model the concrete in the panel. The strain-rate parameters of Malvar and Ross (1998) for compression and tension were used. The PLASTIC_KINEMATIC material model (MAT003) was used for the reinforcement in the panel. The dynamic increase factors for the rebar were determined based on the empirical relation proposed by Malvar and Crawford (Oliveira et al., 2009). The reinforcement was coupled to the concrete using the CONSTRAINED_LAGRANGE_IN_SOLID formulation. The material model PIECEWISE_LINEAR_PLASTICITY (MAT024) was used for the aluminum missile.

Beam elements were used for the reinforcement. Eight-node solid elements were used to model the concrete and shell elements were used for the missile. The concrete was modelled with 20 $\times$ 20 $\times$ 21.5 mm elements. The missile was modeled with 5 $\times$ 5 mm shells. The constant stress formulation and Belytschko-Lin-Tsay formulation were used for solid and shell elements, respectively. One-dimensional truss elements were used for the reinforcement. Damage formulations were not included in this study; the damage to the panel in the numerical simulations was not reported.

Oliveira et al. (2009) compared the results of the numerical simulation and the experimental test data and observed

- The measured and predicted deflection at the center of the slab were in good agreement
- There were significant differences in the measured and predicted rebar strains at the center of the panel; the differences could have been due to the slightly off-center impact of the missile.

Insufficient information was reported to enable a detailed comparison of the numerical simulation and the experimental results. Although Oliveira et al. (2009) stated that the numerical model could predict the non-linear response of reinforced concrete panels impacted by missiles, no rigorous validation was performed.

2.7.3 Missile Impact on SC Composite Shear Walls

Bruhl et al. (2015) developed a three-step method for designing steel plate composite (SC) walls subjected to missile impact. The study discusses the development and benchmarking of 3D finite elements models for predicting the behavior and local failure of SC walls subjected to missile impact. The finite element models were used to conduct parametric studies for further verification of the design method.

The 3D finite element models were benchmarked in LS-DYNA using tests conducted by Tsubota et al., which included 50 specimens (combination of SC and RC shear walls) with dimensions of 23.6 × 23.6 inches and thicknesses between 1.97 and 6.3 inches (Bruhl et al., 2015). The 0.24-inch diameter Grade 60 reinforcement was spaced at 3.94 inches on center. The compressive strength of the concrete was 3550 psi with a maximum aggregate diameter of 0.25 inch. The simulations utilized a Lagrangian formulation. Reduced integration solid elements were used to model the concrete and steel plates. Beam elements were used to model the rebar and shear studs. The bi-linear kinematic hardening model *MAT_003-PLASTIC_KINEMATIC was used for the rebar, shear studs, and steel plates. Dynamic increase factors for the steel were taken from *Methodology for Performing Aircraft Impact Assessment for New Plant Designs* (NEI 07-13, 2009). The missiles from the Tsubota et al. tests were constructed with solid mild steel and had a very high axial compressive strength (value not disclosed). These missiles were modeled as rigid cylinders: 1.38 inches in diameter and 2.36 inches long (Bruhl et al., 2015).

The Winfrith (MAT084/085) model in LS-DYNA was used for concrete. The formulation utilizes a smeared crack model and a bilinear curve to capture the tension-softening behavior using crack-width constants ($c_1 = 0.71$, and $c_2 = 5.14$) developed by Broadhouse and Attwood (1993) as seen in Figure 2-5. Using these constants, two crack widths (w_1, w_2) can be estimated using Equations (2-1) and (2-2), where G_F is the fracture energy of the concrete and f_t' is the tensile strength of the concrete. The card *MAT_ADD_EROSION was activated using a maximum strain, $MXEPS$, corresponding to the crack width at zero residual tensile stress using Equation (2-3), where L_{eff} is the effective length of a cubic solid concrete element in the impact zone and can be estimated using Equation (2-4), where $V_{element}$ is the volume of the element.

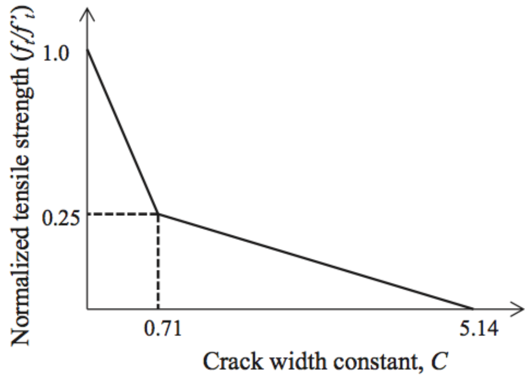

Figure 2-5: Bi-linear tension softening model of Winfrith model (Bruhl et al., 2015)

$$w_1 = c_1\left(\frac{G_F}{f'_t}\right) \tag{2-1}$$

$$w_2 = c_2\left(\frac{G_F}{f'_t}\right) \tag{2-2}$$

$$MXEPS = \frac{w_2}{L_{eff}} \tag{2-3}$$

$$L_{eff} = \sqrt[3]{V_{element}} \tag{2-4}$$

where all terms are defined above.

Based on Table 2.1.4 of CEB-FIP Model Code 90 (CEB, 1993), the fracture energy for 3550 psi compressive strength concrete with a maximum aggregate diameter of 0.25 inch is 0.3283 lb-in/in^2. The predictions of fracture energy, and MXEPS based on the CEB formulation and the study conducted by Bruhl et al. (Table 3) (2015) are shown in Table 2-3. The values used in Bruhl et al. (2015) correspond to a compressive strength of almost 10,000 psi with an aggregate diameter of 1.3 inches and are much greater than the values corresponding to the concrete used in the numerical simulations.

Table 2-3: Fracture energy and MXEPS values from CEB and Bruhl et al.

	CEB (1993)	Bruhl et al. (2015)
G_F (lb-in/in^2)	0.328	0.832
$MXEPS$ (in./in.)	0.057	0.144

The LS-DYNA models utilized two different mesh densities (0.125 inch in the impact region, 0.5 inch outside the impact region) for the steel plates and concrete. A penalty-based contact was used to define the contact between the rigid missile and the components of the SC wall. Rebar elements were embedded into the concrete using a penalty coupling method that assumes perfect bond with the concrete. According to Bruhl et al. (2015) the results of the LS-DYNA simulations matched the experimental results well for front crater diameter, penetration depth, rear bulge diameter and depth, and damage mode.

2.7.4 IRIS Benchmark Study for Missile Impact

The Integrity and Ageing of Components and Structures Working Group (WGIAGE) conducted a study called IRIS_2010 "Improving Robustness assessment of structures Impacted by missiles". The objective was to conduct a benchmark study to validate the evaluation techniques used in the assessment of structures impacted by missiles (NEA/CSNI, 2011). The organization selected 28 teams consisting of universities, companies, and laboratories to conduct finite element simulations for three widely known and accepted experimental tests. The specifications of the tests are bulleted below.

- Meppen II-4: 6 × 6 × 0.7 m RC slab impacted at its center by a 1000 kg soft missile at 250 m/s
- VTT with bending mode failure: 2 × 2 × 0.25 m RC slab impacted by a 50 kg hard missile at 130 m/s
- VTT with punching mode failure: 2 × 2 × 0.25 m RC slab impacted by a 50 kg hard missile at 130 m/s.

The teams used a wide range of finite element codes and modeling techniques including constitutive material models, strain rate parameters, erosion criteria, and mesh sizes. The variability of these modeling techniques led to a wide scatter for the simulation results. Critiques of the IRIS document by outside professionals recommended that the analysts take part in a design of experiments to determine which physical parameters are most important for their simulations mainly in the evaluation of various constitutive models for concrete and strain rate parameters (NEA/CNSI, 2011). Modeling strain rate effects in high impact simulations was determined to be important; inclusion/omission of strain rate effects could introduce differences of up to 30% in the results.

The study also discussed the use of erosion criteria in penetration and perforation problems to combat issues with high deformations in Lagrangian elements. Concern was expressed that there was no correlation between erosion criteria and physically observed damage. Calibration of finite element models based on erosion criteria to match experimental results is not useful in terms of expanding the size of an experimental dataset by numerical simulations. On this basis, the use of erosion criteria may not be the best approach for problems with severe local non-linear behavior involving fragmentation of concrete elements (NEA/CNSI, 2011). The document urged the exploration of "particle based" formulations including Smooth Particle Hydrodynamics (SPH), and the discrete element method, neither of which involve erosion and are likely better suited for impact problems.

The IRIS_2010 study was a useful step towards understanding the difficulties involved with modeling highly nonlinear experiments with finite element methods. The study uncovered significant shortcomings in the methods being used to develop numerical tools for assessing missile impact including quantifying physical damage with erosion criteria, correct use of strain rate parameters for high rates of loading, and constitutive properties of materials.

2.7.5 Simulation of Concrete Cylinder Perforation

Schwer (2009b) studied impact on concrete using SPH, a Multi-Material Arbitrary Lagrange Eulerian (MM-ALE) method, and a Lagrangian method utilizing material erosion. The goals of his numerical study were to: 1) compare the methods, and 2) evaluate the SPH method as an alternative numerical technique for ballistics problems. The cylindrical concrete target was eight inches in diameter and four inches long. The cylinders were impacted by steel projectiles one inch in diameter and three inches in length. The targets were secured by steel ring fixtures at the front and back. The impact was normal to the base of the concrete target at a contact velocity of 685 ft/sec (209 m/s). Three concrete models were used in this study: Pseudo_Tensor (MAT016), Concrete_Damage (MAT072R3), and CSCM (MAT159) (see Section 2.3).

The SPH model consisted of four parts: 1) inner SPH particles representing the concrete that interacted with the penetrator, 2) a Lagrange steel projectile, 3) a cylinder of concrete consisting of Lagrange elements, which creates the outer portion of the concrete target, and 4) two rings of rigid material made with Lagrange solids to simulate the fixtures. A quarter of the numerical model was developed and two planes of symmetry were used to preserve the displacement and rotational boundary conditions. Particle spacings of 0.063 inch (1.6 mm) and 0.0393 inch (1 mm) were used to determine how spacing affected the results. The exit velocities were relatively insensitive to the changes in particle spacing for all three concrete models. Figure 2-6 shows a cutaway view of the SPH model.

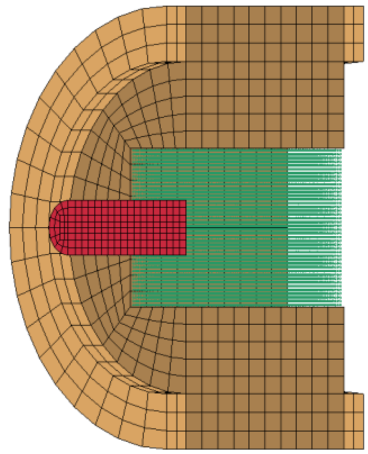

Figure 2-6: Cutaway view of SPH model (Schwer, 2009b)

The MM-ALE model consisted of four parts; 1) inner cylinder of MM-ALE cells representing the concrete that interacted with the penetrator (the outer annulus of the concrete was also constructed with MM-ALE cells), 2) a Lagrange steel projectile, 3) two rings of rigid material of Lagrange solids to simulate the fixtures, and 4) MM-ALE solid elements to represent the air surrounding the target. The core of the concrete target used 0.117 inch (2.98 mm) cells along the length and a cell size of 0.078 inch (1.99 mm) in the direction perpendicular to impact. The outer annulus of the concrete cylinder used fewer cells in the radial direction with a geometric progression of cell size from the core to the rings (Schwer, 2009b). Figure 2-7 shows a cutaway view of the MM-ALE model: the surrounding MM-ALE air (green), the MM-ALE concrete target (dark brown), the Lagrange fixture rings (tan), and the Lagrange steel projectile (red).

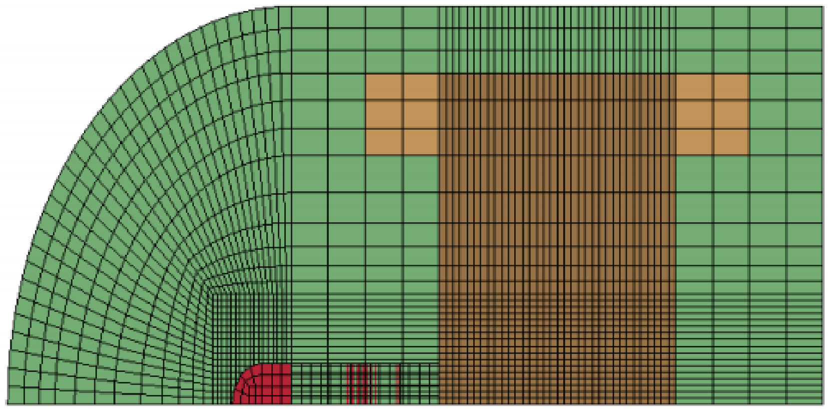

Figure 2-7: Cutaway view of MM-ALE model (Schwer, 2009b)

The Lagrange model was identical to the SPH model, except that Lagrange solids were used to represent the inner cylinder of the concrete that interacted with the penetrator. Material erosion was activated to avoid severe element distortion and negative volume errors in the impact zone. Four meshes for the inner cylinder were studied to determine how mesh size affected the results. The Lagrangian solids along the length of the target and perpendicular to the projectile ranged from 0.22 to 0.06 inch, and from 0.155 to 0.043 inch, respectively.

A comparative analysis of projectile exit velocities for the SPH and MM-ALE models was conducted for MAT016 and MAT072R3. The MM-ALE and SPH projectile exit velocities for MAT016 were identical. The MM-ALE exit velocity was 24% greater than the SPH-calculated velocity for MAT072R3. The difference in results was due to the accumulation of errors in interdependent history variables during volume-fraction averaging in MM-ALE advection (transfer of matter by flow of a fluid) (Schwer, 2015). The MAT072R3 material model is no longer available for use with the MM-ALE solver.

To develop a comparable Lagrangian model using material erosion, an erosion-criteria convergence study and a mesh convergence study were conducted. These studies were performed using MAT016. The Lagrange model with erosion produced the greatest exit velocity (= 434 fps). The SPH model using MAT016 produced a lower exit velocity of 385 fps, which is comparable to the MM-ALE exit velocity of 375 fps, also calculated using MAT016.

Schwer (2009b) concluded that the SPH method is a suitable technique for ballistics problems and allows the user to avoid shortcomings related to the MM-ALE and Lagrangian formulations.

2.7.6 Aircraft Engine Impact Simulations using the Discrete Element Method

Sawamoto et al. (1998) proposed the use of a Discrete Element Method (DEM) for assessing local damage to reinforced concrete structures subjected to impact loadings. The study discusses the validation of DEM parameters and validation of a numerical model for impact analyses using the experiments conducted by Sugano et al. (1993b).

The DEM idealizes a structure as an assemblage of rigid circular elements connected to each other by non-linear springs and dashpots, in which every particle satisfies equilibrium conditions and equations of motion (Sawamoto et al., 1998). Interaction between two elements is illustrated in Figure 2-8, where (Δv_i, Δu_i, $\Delta\phi_i$, Δv_j, Δu_j, $\Delta\phi_j$), and (r_i, r_j) are degrees of freedom and radii for particles i and j, respectively; (k_n, k_s) and (η_n, η_s) are spring constants and damping coefficients for the normal and shear directions, respectively; and (Δu_n, Δu_s) are gap displacements in the normal and shear direction, respectively. Two states are defined for interaction forces between the particles; 1) state one – initial state - compression, tension, and shear, 2) state two – re-contact of particles - compression and shear. If these forces exceed the defined tension failure point, the interaction changes from the first to the second state. The second state defines the interaction once the separated particles come into contact again.

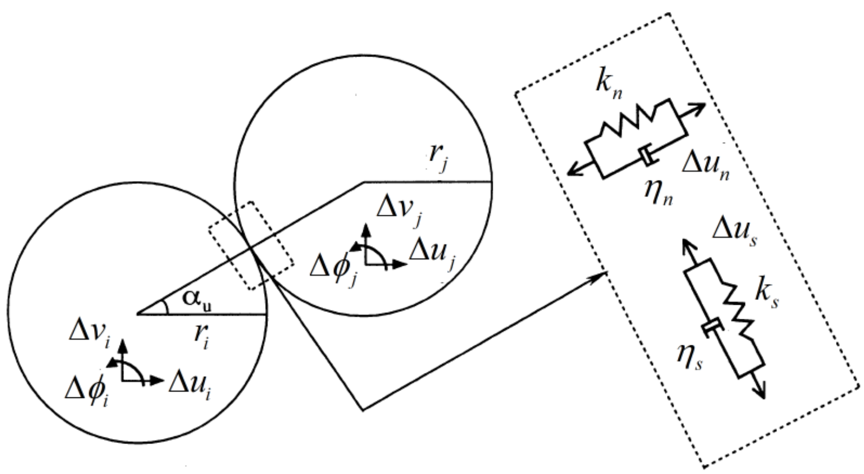

Figure 2-8: DEM model (Sawamoto et al., 1998)

Sawamoto et al. (1998) simulated concrete material tests (uniaxial compression and tensile splitting tests) to determine appropriate analytical parameters for the DEM, including material constants, failure criteria, and dynamic increase factors (DIFs) for strain rate. The spring constants in the normal and shear directions define the material constants and failure criteria;

these constants can be derived by substituting a discrete element model in a linear elastic continuum body (Sawamoto et al., 1998). The DIFs for concrete in tension and compression were calculated using empirical formula proposed by Fujimoto (Sawamoto et al., 1998). The dynamic increase factor for cohesive strength, DIF_s, is defined in Equation (2-5), where DIF_c and DIF_t are dynamic increase factors in compression and tension, respectively. According to Sawamoto et al. (1998), the failure mechanisms observed in the simulations corresponded well with the experiments and the process used to parametrize the particles for the material tests was repeated for the impact simulations.

$$DIF_s = \sqrt{DIF_c \times DIF_t} \tag{2-5}$$

Sawamoto et al. (1998) simulated the small and full scale impact tests conducted by Sugano et al. (1993b) that were discussed in Section 2.6.2. Four simulations of the small scale tests were conducted: 1) T180R: 18 cm thick panel using a rigid missile, 2) T180D: 18 cm thick panel using a deformable missile, 3) T300R: 30 cm thick panel using a rigid missile, and 4) T120D: 12 cm thick panel using a deformable missile. Figure 2-9 presents a drawing of the rigid and deformable missiles from the experiments (top row) and their corresponding models using the DEM (bottom row). The aluminum component of the rigid missile was not included in the DEM model.

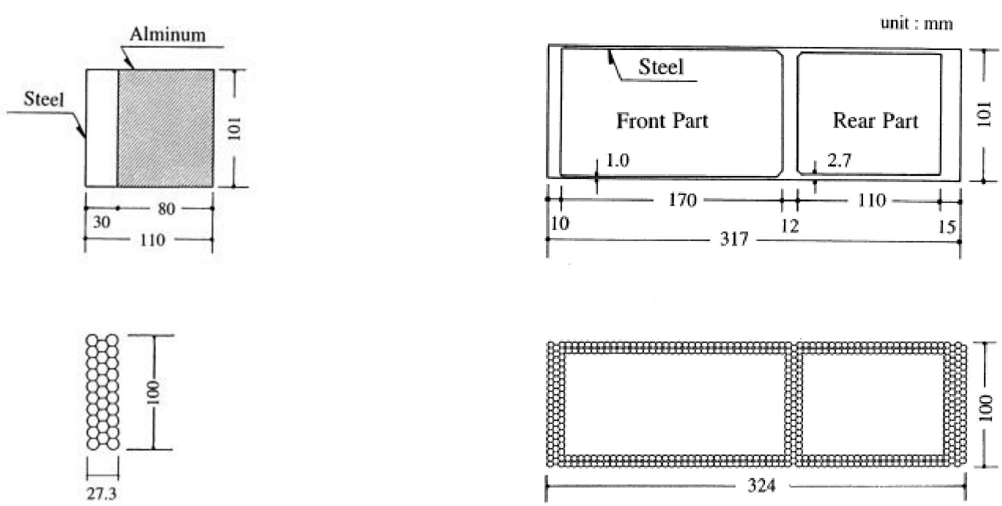

(a) Rigid missile (b) Deformable missile

Figure 2-9: Analytical models of a missile (Sawamoto et al., 1998)

An axisymmetric model of the concrete panel and the missile was created using the DEM. The spring constants, mass, failure strength for individual particles, and DIFs for strain rate were calibrated using data from material tests (e.g., uniaxial compression and split-tension tests). Reinforcement was modeled using a single column of circular particles and linear springs were used to connect them to surrounding elements (Sawamoto et al., 1998). Figure 2-10 presents impact simulation results for T300R and T180D at 1.5 and 2.0 msec, respectively. Based on the numerical simulations of the small scale tests, Sawamoto et al. (1998) reported

- The experimental and analytical penetration depths were 39 (27) and 42 (24) mm, respectively for test T300R (T180D). The numerical results were in good agreement with the experimental data.
- The panel was perforated in both the numerical simulation and the experiment for test T120D.
- The simulated buckling of the deformable missile was in good agreement with the observed damage.
- For the rigid missiles, the numerically calculated crater diameters were slightly smaller on the front face and larger on the back face than the measured values. For the deformable missiles, the numerically calculated values were in good agreement with the measured values on the front face but were smaller on the back face.

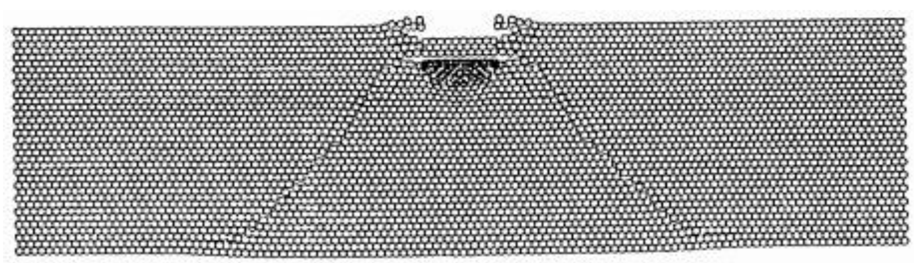

(a) T300R at 1.5 msec

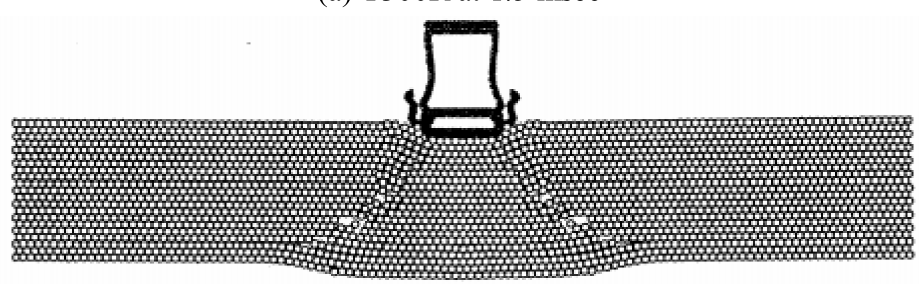

(b) T180D at 2.0 msec

Figure 2-10: Numerical simulation results (Sawamoto et al., 1998)

Two simulations of Sugano's full scale tests were conducted: 1) 115 cm thick reinforced concrete panel with a 2.4 mm-thick steel liner attached to the back face, and 2) 115 cm thick reinforced concrete panel. An axisymmetric model of the concrete panel and missile was developed using the DEM. The missile was a simplified model of the J-79 jet engine used in the experiments; the actual engine was too complicated to model explicitly using the DEM. The reinforcement was modeled using the approach described above for the small scale simulations. The steel plate was represented using a single layer of uniform size particles with a stiffness equivalent to that of the steel plate. A fixed boundary condition was imposed around the panel. Based on the results of these numerical simulations, Sawamoto et al. (1998) observed

- For the RC panel (no liner), the simulations were in good agreement with the experiments; both showed buckling of the engine and the formation of a conical plug. The numerical model was unable to capture scabbing of the concrete on the back face of the panel observed in the experiment.
- For the lined panel, the simulations were in good agreement with the experiments; the residual deformation of the steel liner in the numerical simulation and the experiment were 20 and 25 cm, respectively
- The steel liner prevented concrete scabbing in both the experiments and numerical simulations.

2.7.7 Aircraft Impact Simulations using the Discrete Element Method

Morikawa et al. (1999) simulated the experimental tests presented in Section 2.6.3 using the DEM to a) investigate the effectiveness of consecutive reinforced concrete barriers to mitigate the effects of aircraft impact, and b) examine its utility for impact analysis. Outer panel thicknesses of 6, 8, and 10 cm were considered in the impact simulations.

The aircraft, reinforced concrete panel, and pendulum were created using the axisymmetric formulation of the DEM. The aircraft model was based on the simplified aircraft missile used in the experiments. Particles of equal diameter were arranged in two columns for the thin-walled tubular section and fuselage to enable buckling of the missile (Morikawa et al., 1999). The steel outer shell of the engine, and fiberglass skin and shell of the fuselage were also modeled with particles of equal diameter. Material properties can be found in Tsubota et al. (1999). Morikawa el al. refers to the numerical study conducted by Sawamoto et al. (1998) for formulations regarding the calculation of spring constants between interacting particles. Figure 2-11a presents the DEM model of the aircraft including part labels and dimensions.

The outer reinforced concrete panel was modeled as a disk fixed along its perimeter. The radius of the disk was determined such that its natural period was identical to that of the 1.5 m square panel used in the experiments. The concrete was modeled with circular particles of equal diameter, with at least 13 layers throughout its thickness; the number of layers increased as the panel thickness increased. Concrete material tests were used to determine appropriate analytical parameters for the DEM including material constants, failure criteria, and DIFs for strain rate. Reinforcing bars were modeled as bi-linear axial springs connected to the concrete elements; fracture of the reinforcement occurred when it reached the tensile fracture strain. The inner concrete panel was modeled as a rigid plate positioned 75 cm from the impact surface of the first panel (Morikawa et al., 1999). Figure 2-11b presents the axisymmetric model including the aircraft, concrete panel, and the rigid plate.

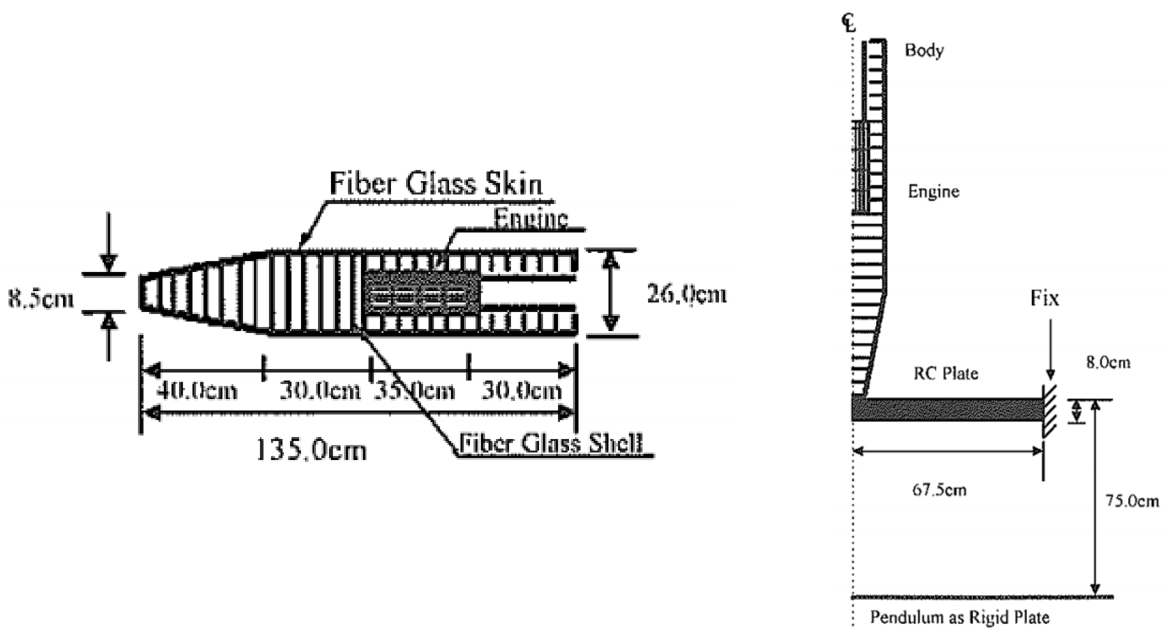

(a) Aircraft (b) 2D axisymmetric model

Figure 2-11: DEM model for aircraft impact (Morikawa et al., 1999)

Figure 2-12 presents the simulation results of the aircraft missile perforating the 8 cm thick outer concrete wall then impacting the inner panel; results are shown at 3, 5, and 25 msec after impact on the outer wall, respectively. Only the outer wall is shown in panels (a) and (b) of the figure. Morikawa et al. (1999) compared the damage to the outer panel, velocity histories of the missile (and engine), and impact loads on the inner panel from the simulation and the experiments and observed

- The missile perforated the 6 and 8 cm thick outer panels in the simulations and experiments. The rear face crater diameters for the 6 and 8 cm thick panels in the simulations were 45 and 50 cm, respectively; these values are identical to the crater diameters observed in the experimental tests.
- The missile penetrated the 10 cm thick outer panel in the simulation and the experiment. No perforation of the panel occurred in the simulation or the experiment; the penetration depths were not documented. Twenty (19) cm of the engine was crushed in the experiment (numerical simulation).
- The velocity histories of the missile (and engine) during impact correlate well with those from the experiments
- The experimental and numerical values of maximum impact load on the inner panel using the 6 (8) cm thick outer panel were 550 (270) and 430 (300) kN, respectively.

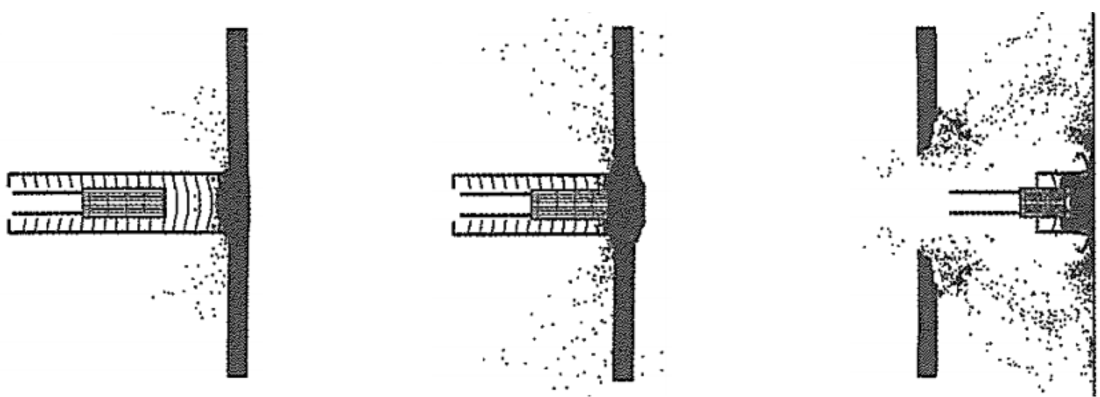

(a) 3 msec (b) 5 msec (c) 25 msec

Figure 2-12: Aircraft impact simulation results (Morikawa et al., 1999)

2.7.8 Impact Simulations using the Karagozian & Case Mesh-Free Method

Wu et al. (2013) developed a method to simulate penetration and perforation that combined a mesh-free formulation and traditional finite elements (e.g., Lagrangian): KC-FEMFRE. The mesh-free formulation uses a reproducing kernel particle method (RKPM) that incorporates the same physics-based constitutive models as traditional finite elements. Similarly, to the SPH formulation, the RKPM method divides the domain into a set of discrete particles over which their properties are smoothed by a kernel function. The contribution of each particle to a property is weighted according to its distance from the particle of interest.

A model is constructed using Lagrangian elements in the KC-FEMFRE method. During a simulation, if an element meets the user-specified criterion for mesh conversion (e.g., deformation criteria) or the damage limit is reached, its nodes are replaced with particles using the RKPM algorithm. The failure surface interpolation parameter, η, is used to determine a dynamically evolving failure surface (i.e., maximum strength, $\hat{\sigma}_m$; yield strength, $\hat{\sigma}_y$; residual strength, $\hat{\sigma}_r$) depending on the current value of the internal damage parameter, λ. This is achieved by interpolating between the $\hat{\sigma}_y$ and $\hat{\sigma}_m$ surfaces using values of η from 0.0 to 1.0 if $\lambda \leq \lambda_m$ (hardening) and between the $\hat{\sigma}_m$ and $\hat{\sigma}_r$ surfaces using values of η from 1.0 to 0.0 if $\lambda \geq \lambda_m$ (softening). The interpolation function, $\eta(\lambda)$, shown in Figure 2-13 and calculated using Equation (2-6), provides a means to compute a value of the interpolation parameter, η, which changes monotonically as a function of the damage parameter, λ. The damage parameter is a state variable and a function of effective plastic strain (Wu et al., 2015). The variable α is an index on the (λ, η) input pairs such that $\lambda \in [\lambda^{\alpha}, \lambda^{\alpha+1}]$.

$$\eta(\lambda) = \eta^{\alpha} + \frac{\eta^{\alpha+1} - \eta^{\alpha}}{\lambda^{\alpha+1} - \lambda^{\alpha}}(\lambda - \lambda^{\alpha}) \tag{2-6}$$

A normalized form of the internal damage parameter, called a damage index, δ, can be computed using Equation (2-7). Once the damage index reaches a value of approximately 2.0, conversion of the element to the RKPM formulation will occur. Element erosion and hourglass control that are often utilized for the Lagrangian formulation for impact simulations are not required if the KC-FEMFRE formulation is adopted.

In the Lagrangian formulation, the field variables (e.g., displacement and velocity) and state variables (e.g., stress and strain) are defined at the nodes and integration points (typically at the center), respectively. In KC-FEMFRE, both formulations (Lagrangian & RKPM) use nodal integration, which allows the state variables to be computed at the nodes to avoid mapping state variables from one set of material points to another during the transformation process from Lagrangian to RKPM (Wu et al., 2013).

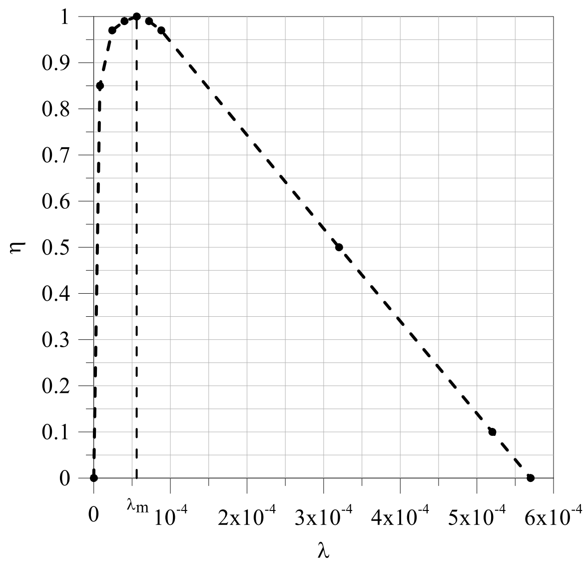

Figure 2-13: Failure surface interpolation function, $\eta(\lambda)$

$$\delta = \frac{2\lambda}{\lambda + \lambda_m} \tag{2-7}$$

Simulations including an implosion test of a concrete cylinder, and unconfined uni-axial compression (cube) and tension (cylinder) tests were performed by Wu et al. (2013) in an effort to benchmark the KC-FEMFRE formulation. The simulation results (e.g., implosion pressure and predicted crack locations) were in good agreement with test data. Simulations of a high velocity penetration test were also performed. Two 9.2 kg fragments (geometry not documented), traveling at 50 m/s (lower fragment seen in Figure 2-14a) and 1000 m/s (upper fragment seen in Figure 2-14a) impacted a 762 × 457.2 × 101.6 mm concrete slab. The damage index in the K&C concrete model (defined above in Equation (2-7)) was used as the criterion for converting solid elements to RKPM formulation. The results of the simulation at different times are shown in Figure 2-14. The color fringes represent the damage level (0.0 = no damage; 2.0 = severe damage). A full model was used in the simulation; half of the model is shown to better illustrate the level of damage through the cross section. The Lagrangian to RKPM conversion is observed at 0.296 msec (Figure 2-14f). The simulation terminated at 0.296 msec due to instabilities caused by concrete softening at large deformations. The simulations were not benchmarked using test data.

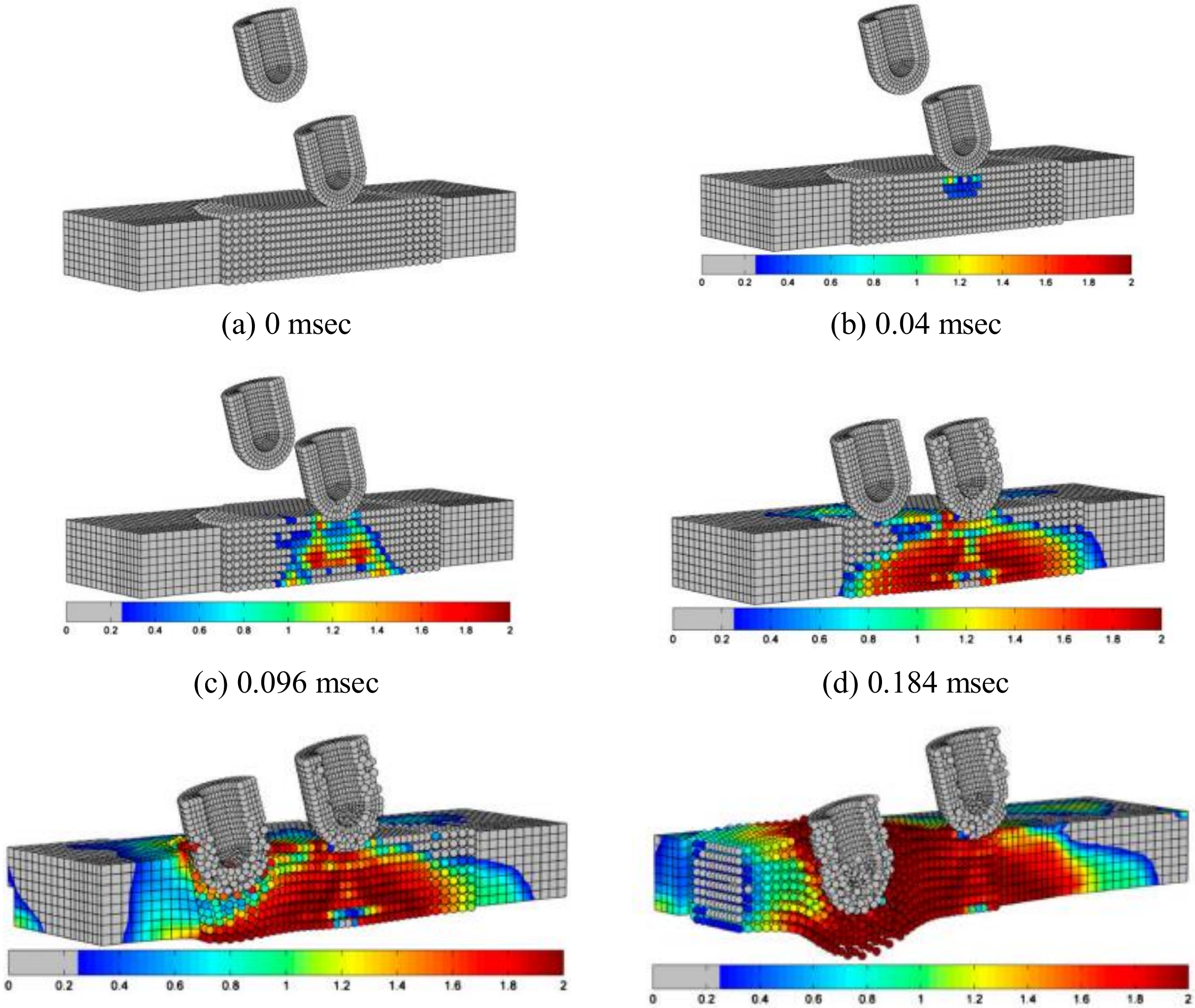

(a) 0 msec (b) 0.04 msec

(c) 0.096 msec (d) 0.184 msec

(e) 0.24 msec (f) 0.296 msec

Figure 2-14: High velocity penetration simulation (Wu et al., 2013)

2.7.9 Hypervelocity Impact Experiments and Numerical Simulations

O'Toole et al. (2015) conducted hypervelocity impact experiments using a gas gun to examine plastic deformation of steel plates. Cylindrical rods (i.e., Lexan projectiles) with a diameter of 5.58 mm and length of 8.61 mm impacted ASTM A36 steel plates with dimensions of 152.4 × 152.4 × 12.7 mm. The thickness of the target plates was chosen to ensure that perforation would not occur. The impact velocities of the Lexan projectiles ranged from 4.5 to 6 km/s. In all five experiments, the projectiles disintegrated upon impact with the target surface. Craters and bulges were observed on the impact and non-impact faces of the targets, respectively, as shown in Figure 2-15. Spall cracks were also observed in the targets between the crater and the bulge (also seen in Figure 2-15). Penetration depths, crater- and bulge-diameters, and spall crack sizes were documented after each experiment. Additionally, free surface velocities on the back face were monitored during the experiments.

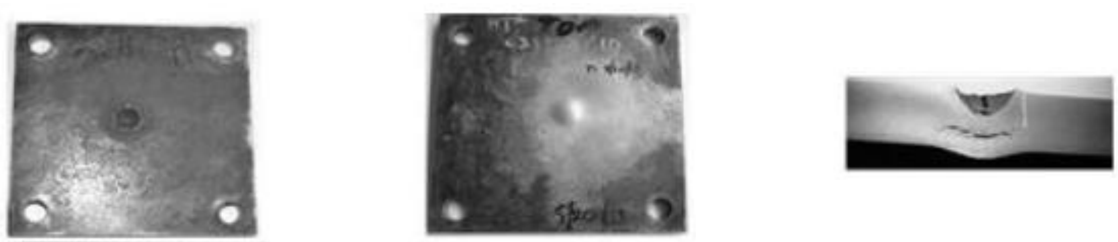

(a) Crater (b) bulge (c) Spall

Figure 2-15: Damage to target plates after impact (O'Toole et al., 2015)

Numerical simulations of the impact experiments were carried out using two different methods and codes: 1) the smooth particle hydrodynamics (SPH) method in LS-DYNA, and 2) the Eulerian method in the Eulerian hydrocode CTH[1]. The SPH and Eulerian based models are presented below in Figure 2-16a and Figure 2-16b, respectively. The axisymmetric formulation was utilized in both methods. In the SPH model, the SPH particle spacing in the target was 0.05 mm – the particle spacing in the projectile was selected by matching the SPH particle mass of the projectile to the SPH particle mass of the target. In the Eulerian model, cell sizes of 0.05 × 0.05 mm were chosen for the projectile and target. Tracer particles were placed on the back face of the target to monitor the target velocities. The Johnson-Cook material model was used to represent the Lexan projectiles and the A36 steel targets in the SPH and Eulerian simulations.

[1] CTH is an Eulerian hydrodynamics computer code developed and maintained by Sandia National Laboratories (O'Toole et al., 2015).

The Mie-Gruneisen Equation of State was used to represent the thermodynamic behaviors of the projectiles and steel targets. No boundary conditions were applied to either model because the impact is localized.

(a) SPH model (b) Eulerian model

Figure 2-16: Axisymmetric models of impact simulations

The plate penetration depths and the crater and bulge diameters of the experiment and numerical simulations are presented in Table 2-4, for a projectile impact velocity of 4.763 km/s. The results of the impact simulations were in good agreement with the experiments (O'Toole et al., 2015). The velocity profile on the back face of the target in the SPH and CTH simulations were compared to the velocities captured in the experiment. Both models were able to recover major features (e.g., velocity magnitudes and target oscillatory behavior) observed in the experiments with reasonable accuracy (O'Toole et al., 2015).

Table 2-4: Results summary (O'Toole et al., 2015)

	Experiment	SPH model	CTH model
Penetration depth (in.)	4.83	4.44	4.50
Crater diameter (in.)	15.37	16.20	16.20
Bulge diameter (in.)	1.42	1.39	1.40

2.8 Disaggregating the Effects of Strain Rate and Confinement on Concrete Strength

Much has been written in the literature regarding the effect of strain rate on the compressive and tensile strength of concrete. Chapter 4 of Dusenberry (2010) identifies sources of information on the subject, including Bischoff and Perry (1991), CEB (1993), Schuler et al. (2006), and Zhou and Hao (2008). Each of these documents provides data in support of a relationship between strain rate and uniaxial compressive and/or tensile strength of concrete. Most of the data were generated from tests using a Split Hopkinson Pressure Bar (SHPB). Little/no data are provided in the summaries on the specimens tested, noting that a specimen less than 3 inches in diameter is not likely representative of concrete used in the field.

Of interest here are the effects of both strain rate and lateral confinement on the compressive and tensile strength of concrete. Takeda et al. (1974) conducted uniaxial compressive and tensile tests on concrete cylinders at a) strain rates ranging from 2×10^{-7} s^{-1} to 2 s^{-1}, and b) static confining pressures between 0 and 30 MPa (4.35 ksi). Figure 2-17a, from Takeda et al., presents uniaxial axial compressive stress-strain curves for three ranges of strain rate: S (0.2 to 2)$\times10^{-6}$ s^{-1}, III (0.2 to 2)$\times10^{-2}$ s^{-1}, and I (0.2 to 2) s^{-1}. The values reported in Figure 2-17a (i.e., 67) are the lateral confining pressures applied to the specimens. The results clearly show that the uniaxial compressive strength of the concrete increases for increasing 1) levels of confinement, and 2) strain rate. Similar plots are presented in Takeda et al. (1974) for confined concrete in tension. The shear failure surfaces (i.e., axial stress as a function of lateral confining pressure) generated by Takeda in compression and tension are shown in Figure 2-17b (compression above the origin, tension below the origin). The shear failure surfaces expand with increasing strain rate. (The data for tension are difficult to interpret from the available figure.) Figure 2-17c presents octahedral shear (deviatoric) stress versus octahedral normal (hydrostatic) pressure for tension and compression. In this figure, the deviatoric and normal stresses are normalized by the unconfined uniaxial strength of the concrete at the corresponding strain rate. The shear failure surface from the dynamic tests (i.e., ranges I and III) lie on top of the surface generated from the static tests (i.e., S), which suggest that strain rate effects in both concrete in compression and tension are independent of the level of lateral confinement.

Yamaguchi et al. (1989) tested 10-cm diameter, 20-cm tall cylinders in compression, at strain rates between 10^{-5} s^{-1} and 10^{-1} s^{-1}, and at lateral confining pressures between 0 MPa and 90 MPa (13.0 ksi). Figures in that paper present data that show a) uniaxial compressive strength increases with strain rate, and b) uniaxial compressive strength increases with lateral confining pressure. Data at failure, collected from cylinder tests at combinations of strain rate and confining pressure, were normalized by static uniaxial compressive strength. The normalized data (Figure 7 of Yamaguchi et al.) supported the conclusion of Takeda et al., namely, the effects of strain rate and lateral confinement can be uncoupled.

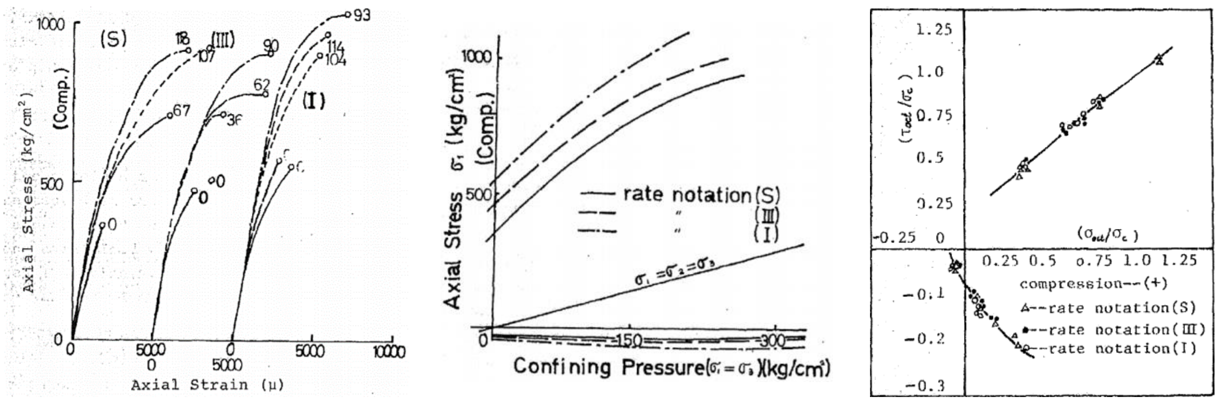

(a) Compressive stress-strain curves

(b) Axial stress as a function of confining pressure

(c) Octahedral shear stress as a function of octahedral normal stress

Figure 2-17: Compression and tension test results (Takeda et al., 1974)

Gran et al. (1989) conducted compression tests of nine 100 MPa concrete cylinders at strain rates ranging from 1 s^{-1} to 5 s^{-1}. The lateral confining pressures ranged from 10 MPa (1.45 ksi) to 124 MPa (18.0 ksi). Failure of specimens was recorded for combinations of strain rate and lateral confining pressure: (1.3 s^{-1}, 10 MPa), (2.0 s^{-1}, 10 MPa), (2.9 s^{-1}, 41 MPa), and (5.0 s^{-1}, 97 MPa). These four data points were used to develop an approximate shear failure surface for a strain rate equal to 2 s^{-1}. The resultant failure surface was compared to one developed using a strain rate of 10^{-4} s^{-1} (assumed to represent quasi-static behavior). The four order-of-magnitude increase in strain rate expanded the quasi-static shear failure surface by 30% to 40%.

Li and Meng (2003) summarized past SHPB experiments on concrete in compression and performed numerical simulations of selected experiments to determine contributions to uniaxial strength enhancement. At strain rates of the order of 1 s^{-1}, the dynamic increase factor was approximately 1.1. At strain rates of the order of 100 s^{-1}, where the CEB model code (CEB, 1993) suggests a value of the dynamic increase factor of approximately 2, Li and Meng noted the increase in axial strength is "…strongly influenced by the hydrostatic stress effect due to the lateral inertial confinement…" and that this effect had been "…wrongly interpreted as strain-rate effect…". Zhang et al. (2009) drew a similar conclusion based on SHPB experiments and concluded the dynamic increase factor of "…concrete-like materials may be greatly enhanced by the inertial-induced radial confinement, which may be unavoidable in many SHPB tests on brittle materials [such as concrete]".

Schwer (2009c) observed that the percentage increase in deviatoric stresses measured by Gran et al. for a strain rate of 2 s^{-1} was consistent with the corresponding dynamic increase factor (=1.3) calculated using the CEB equations (CEB, 1993). He too suggested that strain rate effects in concrete were independent of the degree of confinement, stating "…the limited strain rate data on dynamic compression tests, i.e., up to 2/s, indicates the shear failure surface is shifted (increased) by about the same factor (DIF) as found in the unconfined compression tests." Schwer also noted "…No data is presently available to extend this conclusion much beyond strain rates of 2/s, which is much lower than the range of interest for practical applications", which may be between 10 s^{-1} and 100 s^{-1}.

The tests described above used an active lateral confining pressure, typically provided in a triaxial compression cell. Passive confinement in reinforced concrete is provided by two sources a) transverse reinforcement (used for increasing the deformation capacity of components resisting earthquake and blast effects), and b) presence of adjacent, unloaded concrete, which prevents the unrestricted expansion of the loaded concrete. If the loading in an unconfined compression test is quasi-static, the concrete will expand radially due to Poisson's effect. If the same test is performed dynamically, there will be a delay in the radial expansion of the perimeter concrete in the cylinder, as this material must first be accelerated in that direction. This delay in the radial expansion of the surface concrete effectively provides a passive confining pressure, leading to a momentary increase in uniaxial compressive strength: *inertial confinement*.

Schwer (2009c) studied the effect of strain rate on uniaxial compressive strength, with a focus on inertial confinement. He simulated the behavior of unconfined and confined concrete cylinders across a range of strain rates using MAT016 in LS-DYNA. The cylinder is shown in Figure 2-18: a diameter and height of 400 mm, and an unconfined uniaxial compressive strength of 45.6 MPa. Strain rate multipliers (or dynamic increase factors) were set aside, allowing a focus on inertial confinement.

The simulations of the unconfined cylinders were performed at quasi-static (0.1 s^{-1}) and dynamic (1, 10 and 100 s^{-1}) rates of strain. Simulations were validated using SHPB data reported by Li et al. (2003). Axial stress, defined as the total force at the bottom of the cylinder divided by its cross-sectional area, was used to gauge the increase in strength associated with strain rate. The maximum numerical axial stresses for the four selected strain rates of 0.1, 1, 10, and 100 s^{-1} were

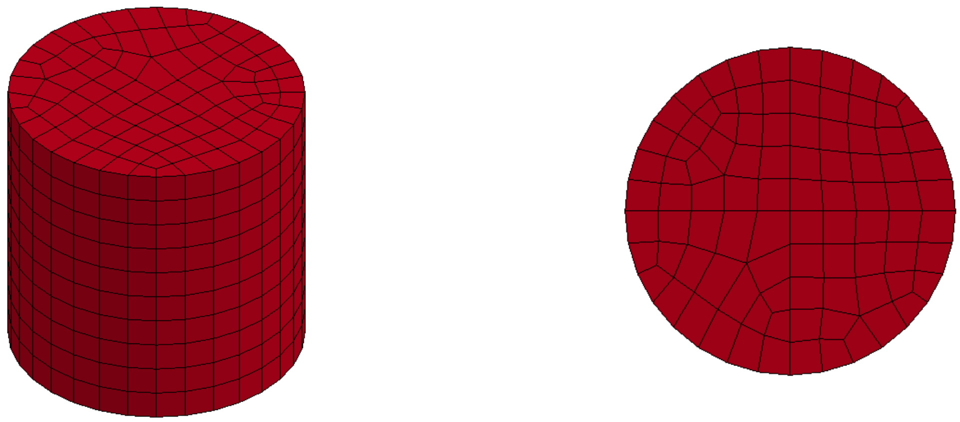

(a) Isometric view (b) Top view

Figure 2-18: Concrete cylinder simulated by Schwer (2009c)

45.6, 46.2, 52.2, and 74.9 MPa, respectively, indicating an increase in concrete strength with an increase in strain rate. The simulated deformation of the cylinder was not uniform at strain rates of 100 s^{-1} and greater. Schwer (2009c) noted a) this non-uniformity of behavior had been observed in experiments, and b) non-uniform deformation should disqualify the data for use in model validation.

Simulations of confined concrete cylinders were performed using the numerical model of Figure 2-18: repeating the numerical experiments of Schwer. The specimen was loaded hydrostatically (top, bottom, and perimeter) with confining pressures of 5, 10, 20, and 40 MPa and then the top surface was subjected to strain rates of 0.1, 1, 10, and 100 s^{-1}. The axial stress was used to gauge the increase in strength due to strain rate. Figure 2-19a presents axial stress histories of the concrete cylinder for strain rates of 0.1, 1, 10 and 100 s^{-1} at a confinement pressure of 40 MPa. The confinement pressure of 40 MPa was reached at 4 msec. At 5 msec, a velocity corresponding to the target strain rate was applied to all nodes at the top of the cylinder. At a strain rate of 0.1 s^{-1}, assumed by Schwer to represent quasi-static behavior, an axial stress of approximately 133 MPa was reached at 45 msec. The axial stress histories of Figure 2-19a are replotted in Figure 2-19b, with a truncated range on time to highlight the behavior of the cylinder (peaks and oscillatory behavior) at the higher strain rates (e.g., 10 and 100 s^{-1}). The simulations involving strain rates of 10 and 100 s^{-1} showed an instantaneous rise to peak stress (used to compute the dynamic increase factor) and then oscillated back towards a value close to the confined strength of the concrete. The initial increase in strength at 5 msec is due to inertial confinement of the inner core of the concrete cylinder. This behavior is further illustrated in Figure 2-20 which presents the vertical stress field (in psi) in the cylinder at the instant the axial pressure is applied at a strain rate of 100 s^{-1}, for a lateral confinement pressure of 40 MPa. The stress in the core of the cylinder is greater than that near the circumference, indicating a momentary increase in strength caused by inertial confinement. The stress field shown in Figure 2-20 is not uniform.

Table 2-5 (adapted from Schwer, 2009c) summarizes the dynamic increase factors (maximum *recorded* axial stress at high strain rate divided by maximum axial stress under static loading) calculated from the results of the simulations of the response of confined cylinders. The factor of approximately 1.1 for a strain rate of 10 s^{-1} (for a range of confining pressures from 5 MPa to 40 MPa) is consistent with the value predicted using the equations of Tedesco and Ross (1998), Grote et al. (2001), and Li and Meng (2003). Schwer notes that the large values of the factor at a strain rate of 100 s^{-1}, which range between 1.30 and 1.78, are "…associated with non-homogenous deformation of the specimen": similar to that seen below in Figure 2-20. He concluded that if the mean value of the long duration stress is used to calculate the dynamic increase factor, then the factor would be less than 1.10 for strain rates between 1 and 100 s^{-1}.

2.9 Finite Element Formulations for Impact Analysis

Finite element analysis is a well-established numerical technique for calculating the response of components and systems to mechanical and thermal loadings. Explicit time integration analysis is used for the solution of blast and impact problems. Formulations used for impact analysis include Lagrangian, Smooth Particle Hydrodynamics (SPH), Element Free Galerkin (EFG), Discrete Elements, and KC-FEMFRE. The EFG formulation was originally developed to solve crack propagation problems but has been shown capable of addressing large deformations, material distortion, and moving discontinuities (Hu et al., 2010). Typical applications for the EFG formulation include manufacturing (e.g., metal extrusion, cutting, and forging), crashworthiness (e.g., car seats, barriers, human dummies, and windshields), and fracture (e.g., crack propagation). Nothing has been published on the use of the EFG formulation for penetration and perforation simulations.

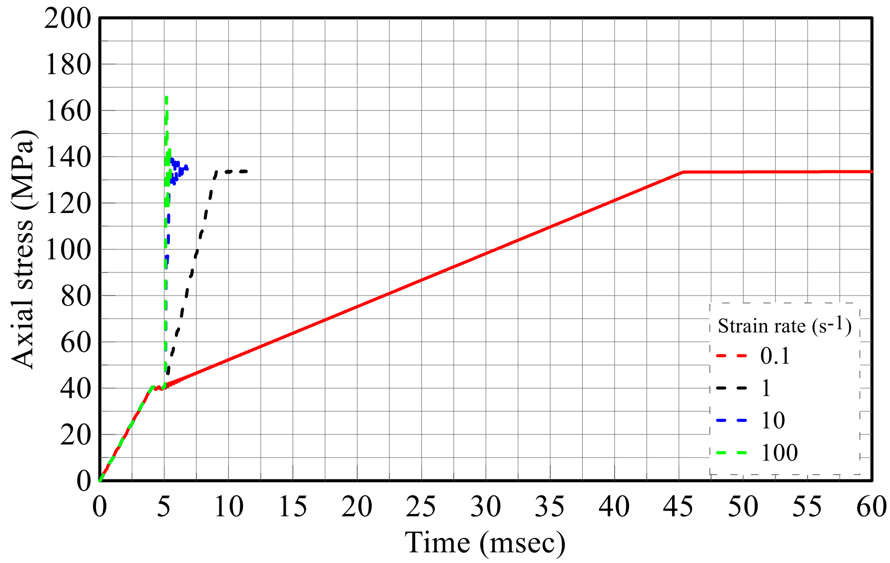

(a) 60 msec time range

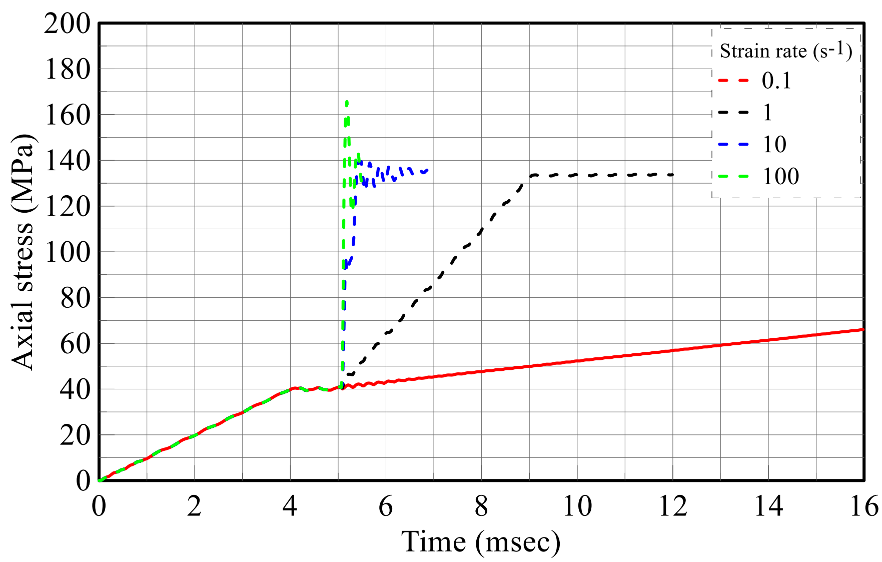

(b) truncated time range

Figure 2-19: Axial stress histories, 40 MPa lateral confinement, multiple strain rates

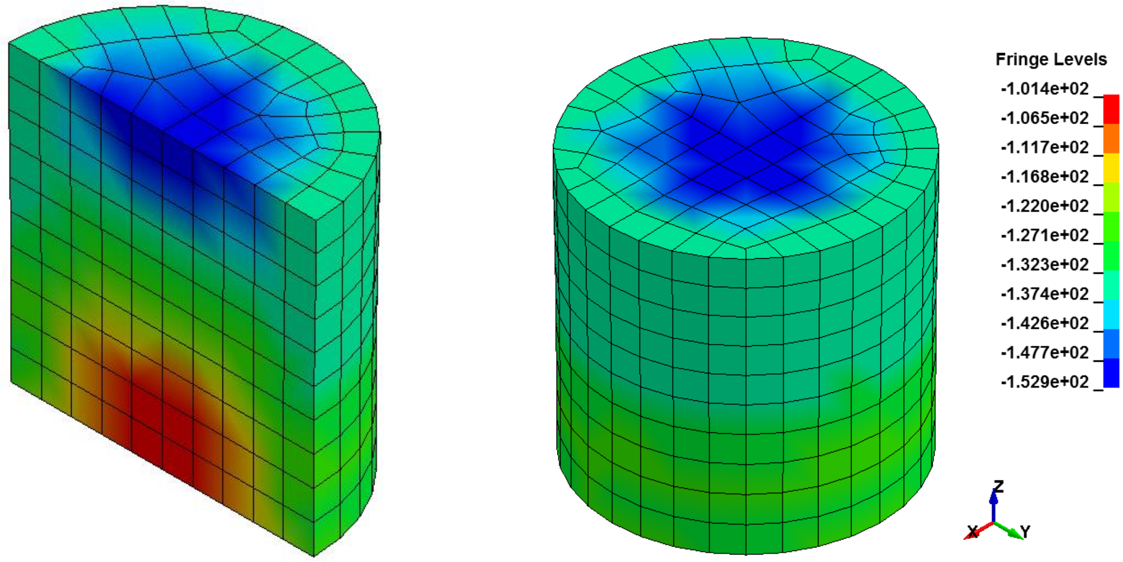

Figure 2-20: Axial stress field in a concrete cylinder at the time instant the upper pressure is applied at a strain rate of 100 s-1, 40 MPa lateral confinement, units of psi

Table 2-5: Dynamic increase factors calculated from cylinder simulations (Schwer, 2009c)

Confinement pressure, MPa (psi)	Static axial stress, MPa (psi)	Dynamic increase factor		
		1 s^{-1}	10 s^{-1}	100 s^{-1}
5 (725)	64.8 (9398)	1.00	1.08	1.48
10 (1451)	78.7 (11414)	1.00	1.09	1.78
20 (2901)	100 (14504)	1.00	1.10	1.31
40 (5802)	128 (18565)	1.05	1.09	1.30

The two analysis methods investigated in this report for tornado- and hurricane-borne missile impact are Lagrangian and Smooth Particle Hydrodynamics. The code used for the analysis is LS-DYNA (LSTC, 2012). The Lagrangian method utilizes solid, shell, beam, and discrete elements (springs) to solve equilibrium equations describing the conservation of mass, momentum, and energy in the analyzed system. In Lagrangian impact simulations, the shortcomings are associated with the deformation and distortion of the solid elements; these limitations may cause a finite element simulation to terminate. Solid elements are typically used to model large uniform bodies (e.g., the target) and are defined using four to eight nodes, depending on whether 2D or 3D systems are being analyzed. The standard elements are based on linear shape functions and use one integration (Gauss) point at the center of the element. A limitation of solid and shell elements with a single integration point is the presence of hourglass modes, which are nonphysical, zero-energy modes of deformation that produce zero strain and zero stress (e.g., LSTC, 2012). In LS-DYNA, the keyword *CONTROL_HOURGLASS can be activated to inhibit hourglass modes by applying an artificial stiffness or artificial viscosity to the affected element. The LS-DYNA Keyword User's Manual recommends the use of artificial stiffness and artificial viscosity for static/quasistatic and dynamic/high velocity impact simulations, respectively. Full integration solid elements are also available to combat zero-energy modes but these are computationally expensive.

In the Lagrangian formulation, a one-to-one mapping between the solid elements of the physical space (actual geometry) and solid elements of the iso-parametric space is created by the Jacobian matrix $[J]$. Illustrations of a four-noded solid element with eight degrees of freedom in the physical (X, Y) and iso-parametric (r, s) space are shown in Figure 2-21a and Figure 2-21b, respectively. The element in the iso-parametric space is severely distorted; this phenomenon often happens in impact simulations using a Lagrangian mesh. In the case where the element is highly distorted or folds back on itself (as shown in Figure 2-21b), the unique relationship between the coordinate systems (physical and iso-parametric) no longer exists, causing the determinant of the Jacobian to be negative, leading to a negative volume error and termination of the finite element program (e.g., Bathe, 1996). The determinant of the Jacobian for the distorted element shown in Figure 2-21b is evaluated in Appendix A and compared with the determinant of the Jacobian for the non-distorted element (shown in Figure 2-21a). The determinant of the non-distorted element remains positive at all locations within the element, while the determinant for the distorted element is negative in the top half of the element resulting in termination of the analysis as discussed above. The stiffness matrices for the distorted and non-distorted elements are evaluated and presented in Appendix A.

Element erosion is used to help combat issues related to large mesh deformations and termination of LS-DYNA (and similar) simulations. The distorted elements are removed from the analysis once a user-specified failure criterion is met. If the analyst chooses to use failure criteria, they can be applied using the *MAT_ADD_EROSION keyword in LS-DYNA. Analysts use effective plastic strain (EPS), minimum time step, and stress- and strain-based erosion criteria in impact and blast loading simulations. However, each criterion has limitations.

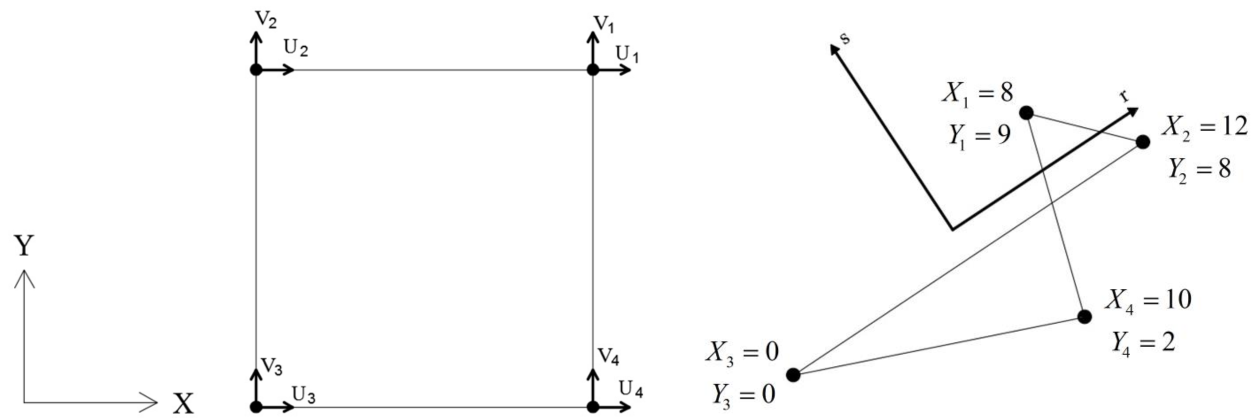

(a) Physical space, non-distorted element (b) Iso-parametric space, distorted element

Figure 2-21: 2D solid element

The most common criterion used for element erosion is EPS and is defined as the unrecoverable portion of strain beyond the yield limit. Parameters such as EPS are well suited to characterize isotropic materials like metals (e.g., steel, copper, and iron) but have no physical basis for anisotropic materials such as concrete (e.g., Shin et al., 2014). The use of EPS as an erosion criterion in penetration simulations involving concrete panels will result in incorrect characterization and accumulation of damage in the concrete elements, leading to the erroneous removal of elements.

Material erosion can also be initiated by a limiting value of time step. A local time step is computed for each element in a model as a fraction of the time required for the passage of the dilatational wave across the minimum element dimension (e.g., Shin et al., 2014). The global time step of the simulation is taken as the minimum value of the local time steps. If elements are highly distorted, the minimum dimension of all distorted elements can be very small, which greatly decreases the time step. To combat this, a user defined minimum time step can be used to remove these highly distorted elements from the simulation. However, in some instances, the material strength of the element may be drastically reduced but the pressure-volume response of the material is maintained, which leads to a highly deformed element maintaining a nearly constant volume, and thus a nearly constant, stable time step (Schwer, 2009b).

Stress-based erosion criteria are also used as the basis for removal of concrete elements, but the challenge is to select an appropriate value, which is heavily dependent on the co-existing hydrostatic (confining) pressure. Strain-based erosion criteria are preferred to stress-based criteria, but the analyst must a) conduct a convergence study to obtain a reasonable value for the erosion criterion, and b) perform a mesh convergence study once the value is chosen (Schwer, 2009b). Shin et al. (2015) conducted a series of single element simulations to characterize erosion strain as a function of variables such as concrete strength, rate of traction loading, maximum traction loading, and element size. The values of erosion strain were then used to characterize damage in finite element simulations of a reinforced concrete column subjected to blast loading. Based on that study, significant effort is needed to produce reasonable results using strain-based erosion criteria.

Some material models (including MAT159 and MAT072R3) include a damage function, which is typically used to model both strain softening and modulus reduction. A damage function can also be used in lieu of erosion criteria such that the elements are deleted once the damage parameter reaches a specific value (for MAT159, the damage parameter ranges from zero for no damage to one for complete damage). The use of a material model that incorporates a damage model will reduce the computational effort required because erosion-related convergence studies are not needed. In LS-DYNA, the keyword *MAT_NONLOCAL can be activated to minimize the mesh dependency of the criterion by averaging failure values of neighboring elements. Although the use of erosion in finite elements seems intuitive, it is a numerical work around that does not have a physical basis and could lead to a loss of mass and momentum in the system. In LS-DYNA, the ENMASS parameter in the *CONTROL_CONTACT keyword gives the user the option to remove the nodes of eroded elements or allow these nodes to remain active in the simulation. The removal of the eroded nodes makes the calculation more stable, however in problems where erosion is important the reduction of mass will lead to incorrect results (LSTC, 2012).

The size of a finite element mesh for an impact simulation is governed by the required accuracy of the solution and contact of the bodies to avoid penetration of interacting elements. Element penetration in impact simulations causes an erroneous transfer of energy between the missile and the target. Smaller elements allow for a more accurate solution and for the contact algorithm to search for nearby nodes to create the desired interaction between the missile and the target. Impact problems require a relatively small mesh for the contact algorithm, which greatly reduces the time step in the simulation. The initial time step, Δt, of the simulation can be predicted using equation (2-8) where l is the discrete length or mesh size of the finite element, v is the velocity at which the compression wave (P-wave) travels through the material as defined in equation

(2-9), κ is the bulk modulus, λ and μ are Lame constants (μ=0 (shear) for gas and liquids) and ρ is the density of the material. The time step decreases as the mesh size (l) decreases: the Courant condition (Bathe, 1996).

$$\Delta t = \frac{l}{v} \tag{2-8}$$

$$v = \sqrt{\frac{\kappa}{\rho}} = \sqrt{\frac{\lambda + 2\mu}{\rho}} \tag{2-9}$$

The SPH formulation is an effective way to combat the problems associated with Lagrangian solutions to impact simulations. SPH particles divide a domain into a set of discrete elements. These particles have a spatial distance (known as a "smoothing length"), over which their properties are smoothed by a kernel function (LSTC, 2014). The contribution of each particle to a property is weighted according to its distance from the particle of interest, usually with a Gaussian function. This action saves computational time by not including relatively minor contributions from distant particles (LSTC, 2014). A key difference between SPH particles and standard Lagrangian finite elements is the interpolation algorithm to determine strain. In Lagrangian finite elements, constant stress and fully integrated solid elements are available. A constant stress solid element has one integration point at the center where the values are computed. For a fully integrated solid element, the strains are calculated at all integration points and the average is taken at the center. Alternatively, in the SPH formulation there is no node-to-element connectivity matrix and the algorithm must search for neighboring particles, which can change at each time step. The neighboring particles that are within the domain of influence of the SPH particle of interest are used to establish the displacement field, and the spatial derivative of that displacement field is evaluated at the particle to provide the strain at that particular particle (Schwer, 2008b). This allows for very large distortions of the SPH mesh (groups of particles) without convergence problems and permits particles to move apart and no longer interact. This behavior is not possible in Lagrangian formulations.

The SPH formulation is more computationally expensive than Lagrangian finite elements. An alternative numerical approach to reduce computational demand is to use SPH particles in the impact zone where high deformations and nonlinearities are expected and Lagrangian elements for the remainder of the structure. However, the mesh density requirements in particle-based methods are normally more demanding of a finer mesh for good accuracy than Lagrangian meshes. According to Schwer (2009a), using SPH particles for impact ballistic assessment requires a spacing of one to three millimeters to obtain reasonable results. To obtain this spacing between SPH particles for one of the 12-inch panels tested at Sandia, upwards of 6 million particles are needed in the impact zones, requiring significant computational power. The use of a quarter model with symmetric boundary conditions does not necessarily reduce computational demand significantly. Symmetry planes must be utilized to inform the algorithm that interaction from particles on the other side of the symmetry planes is expected. The algorithm reflects the SPH particles over the planes and sets up a matrix of ghost nodes. These nodes have a comparable computational demand to the SPH particles in the quarter model. One numerical technique that is widely used for impact simulations to limit the number of particles is the axisymmetric model, which represents a slice of a 3D model. If rotated around the reference Cartesian coordinate system, the axisymmetric model would recover the 3D structure. This enables the use of a small particle spacing but limits the computational expense.

3D Lagrangian and axisymmetric SPH models are investigated in this report for wind-borne missile impact.

2.10 Objectives of this Report

A relatively small number of tests have been performed to judge the impact resistance of reinforced concrete panels and to develop empirical equations for design. To the knowledge of the authors, only Tu and Murray (1977) have performed detailed numerical simulations of wind-borne missile impact on reinforced concrete panels, and these simulations were limited in scope.

Finite element codes such as LS-DYNA (LSTC, 2012) and ABAQUS (SIMULIA, 2012), once verified and validated for impact analysis, can enable the development of robust empirical equations for impact design of reinforced concrete panels. Accordingly, the main objectives of this part of this report are

- Examine the empirical methods used to evaluate reinforced concrete panels for impacting wind-borne missiles
- Compare predictions using the empirical methods with experimental results obtained at Calspan and Sandia Laboratory for Schedule 40 pipes

- Discuss how the use of the outer or effective diameter of the missile affects various empirical formulae
- Develop and validate models of reinforced concrete panels in LS-DYNA for impact analysis of steel pipes
- Discuss strategies for modeling impact using the Lagrangian and Smooth Particle Hydrodynamics formulations
- Design a family of numerical experiments and execute the experiments in LS-DYNA to develop design guidance for impact analysis and design

"This Page Intentionally Left Blank"

SECTION 3
EMPIRICAL FORMULAE FOR IMPACT ASSESSMENT

3.1 Introduction

Although a number of empirical formulae have been developed for the assessment of reinforced concrete panels subjected to missile impact, their applicability for wind-borne projectiles is unknown. This chapter examines these formulae for wind-borne missile impact using data from tests conducted at Sandia Laboratory by the Electric Power Research Institute (EPRI) and Calspan. The U.S. NRC Regulatory Guides 1.76 (NRC, 2007) and 1.221 (NRC, 2011) recommend the use of a Schedule 40 pipe as a design-basis projectile due to its high probability of penetrating concrete panels and scabbing concrete, and so it is the focus of this assessment. Section 3.2 introduces the terminology and symbols used in this chapter. Sections 3.3 through 3.12 present the empirical formulae introduced in Chapter 2. The predictive equations for penetration depth, scabbing thickness, and perforation thickness are compared in Section 3.13. The utility of the formulae are assessed using data from the Sandia tests in Section 3.14. A summary is provided in Section 3.15.

3.2 Terminology and Symbols

The following terminology and symbols are used in this chapter of the report.

A	=	cross sectional area of the projectile (ft.^{2})
d	=	projectile diameter (in.)
D	=	W / d^3, caliber density of the projectile (lb. /in.^{3})
e	=	perforation thickness (in.), the minimum thickness of the target for a missile with a given impact velocity will completely penetrate the panel
e_{eff}	=	perforation thickness computed from the empirical formulae using the effective diameter of the missile
e_{out}	=	perforation thickness computed from the empirical formulae using the outer diameter of the missile
f_c'	=	compressive strength of concrete (psi)

g	=	acceleration due to gravity (32.2 ft. / sec^2)
K	=	$180/\sqrt{f_c'}$, concrete penetrability factor, providing the resistance of the concrete to penetration
K_p	=	penetration coefficient (unit less)
N	=	projectile shape factor; (0.72 for flat nosed bodies; 0.84 blunt nosed bodies; 1.00 for average bullet nose; and 1.14 for very sharp nose)
s	=	scabbing thickness (in.); the thickness required to prevent back face scabbing for a missile with a given impact velocity
s_{eff}	=	scabbing thickness computed from the empirical formulae using the effective diameter of the missile
s_{out}	=	scabbing thickness computed from the empirical formulae using the outer diameter of the missile
$t_{\exp}$	=	thickness of the reinforced concrete panel
U	=	200 ft./sec; reference velocity used in CRIEPI and CF formulas
V	=	impact velocity of the missile (ft. /sec)
W	=	weight of the missile (lb.)
X	=	penetration depth (in.) in which a missile will penetrate into an infinitely thick target
X_{eff}	=	penetration depth computed from the empirical formulae using the effective diameter of the missile
X_{out}	=	penetration depth computed from the empirical formulae using the outer diameter of the missile
$X_{\exp}$	=	measured penetration depth

3.3 Modified Petry Formulae

The Modified Petry (MP) formulae was developed in 1910 to predict the local effects of hard missile impact (Kennedy, 1975). Appendix F of ACI 349-13 (2013) cautions against the use of these formulae for predicting the local effects of wind-borne missiles, but they are included here for completeness. Equation (3-1) predicts penetration depth; all variables are defined in Section 3.2. The penetration coefficient, K_p, is unitless and is set equal to 0.00799 for mass concrete, 0.00426 for normal reinforced concrete, and 0.00284 for specially reinforced concrete (with ties), and is independent of concrete strength (Kennedy, 1975). In 1950, Amirikian revised K_p to account for concrete strength between 2000 and 7000 psi; values are presented in Figure 3-1 (Kennedy, 1975). These values were developed for reinforced concrete, where the front and rear face rebar curtains were connected with ties. The values of K_p proposed by Amirikian are also commonly used for normal reinforced concrete because they are a function of concrete compressive strength and are expected to yield better predictions of penetration depth (Kennedy, 1975). Figure 3-1 is used in Section 3.14 for the evaluation of the MP formulae for wind-borne missiles although the front and rear rebar in the Sandia tests were not tied together. The scabbing thickness and perforation thickness were defined as multiples of the predicted penetration depth; see equations (3-2) and (3-3), respectively.

$$X = 12k_p\left(\frac{W}{A}\right)\log_{10}\left(1+\frac{V^2}{215000}\right) \tag{3-1}$$

$$s = 2.2X \tag{3-2}$$

$$e = 2X \tag{3-3}$$

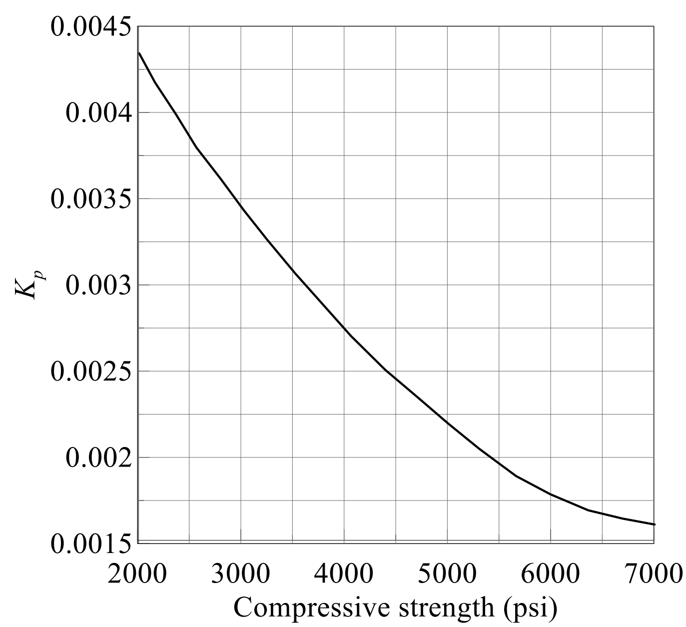

Figure 3-1: Penetration coefficient K_p as a function of concrete compressive strength (Kennedy, 1975)

3.4 Army Corps of Engineers Formulae

The Army Corps of Engineers (ACE) formulae were developed in 1946 and were based on penetration tests conducted in 1943 for 37 mm[2], 75 mm[3], and 155 mm[4] uncapped, explosive projectiles (Kennedy, 1975). A total of 9 to 15 rounds were fired into each of the 39 slabs tested. The velocities of the projectiles were not disclosed, but ranged from lowest practical velocity to above the perforation limit of the slabs (NRCCFD, 1944). Regression analysis of the test results led to equations for penetration depth (3-4), scabbing thickness (3-5), and perforation thickness (3-6). Since these formulae were calibrated for a specific data set, usage outside these applicable ratios of s/d and e/d can lead to unreasonable results (Kennedy, 1975).

$$\frac{X}{d} = \frac{282Dd^{0.215}}{\sqrt{f_c'}}\left(\frac{V}{1000}\right)^{1.5} + 0.5 \qquad (3\text{-}4)$$

$$\frac{s}{d} = 2.12 + 1.36\left(\frac{X}{d}\right) \qquad \text{for } 3 \le \frac{s}{d} \le 18 \qquad (3\text{-}5)$$

$$\frac{e}{d} = 1.32 + 1.24\left(\frac{X}{d}\right) \qquad \text{for } 3 \le \frac{e}{d} \le 18 \qquad (3\text{-}6)$$

3.5 Modified National Defense Research Committee Formulae

In 1946, the National Defense Research Committee (NDRC) proposed equations for rigid projectiles penetrating an infinitely thick concrete target (Kennedy, 1975). The impact pressure (force per unit contact area), P_i, at any time, t_i, is a function of both the depth of penetration, x_i, and the projectile velocity, v_i (Kennedy, 1975). Equations (3-7) and (3-8) present the penetration depth for values of $X/d \le 2$ and $X/d > 2$, respectively. All variables are defined in Section 3.2.

The penetrability factor, K, in these equations was calibrated to a set of available test data, namely, the ACE impact tests involving 37- and 155-mm projectiles, and it ranges between 2 and 5, depending on the concrete strength (Beth, 1946). This factor was not fully developed due to limited research on the penetration of concrete slabs after World War 2 (Kennedy, 1975). In

[2] The 37 mm shell is an armor piercing round from an anti-tank gun.
[3] The 75 mm shell is fired by a tank gun, first introduced in World War II.
[4] The 155 mm shell is a high explosive shell from a Howitzer.

1966, and based on theoretical and experimental considerations, it was suggested that K be proportional to the square root of the concrete compressive strength, as defined above in Section 3.2 (Kennedy, 1975).

For ratios of required slab thickness to projectile diameter greater than 3, equations (3-7) and (3-8) can be used with equations (3-5) and (3-6) to predict scabbing and perforation thickness (Kennedy, 1975). For many impact problems, the ratio is much less than 3. A curve fit extrapolation of equations (3-5) and (3-6) for ratios less than 3 was proposed, which led to equations to predict scabbing thickness (3-9) and perforation thickness (3-10) (Kennedy, 1975).

$$X = \sqrt{4KNWd\left(\frac{V}{1000d}\right)^{1.8}} \qquad \text{for } X/d \le 2 \tag{3-7}$$

$$X = KNW\left(\frac{V}{1000d}\right)^{1.8} + d \qquad \text{for } X/d > 2 \tag{3-8}$$

$$\frac{s}{d} = 7.91\left(\frac{X}{d}\right) - 5.06\left(\frac{X}{d}\right)^2 \qquad \text{for } X/d \le 0.65 \tag{3-9}$$

$$\frac{e}{d} = 3.19\left(\frac{X}{d}\right) - 0.718\left(\frac{X}{d}\right)^2 \qquad \text{for } X/d \le 1.35 \tag{3-10}$$

Since equations (3-9) and (3-10) are extensions of equations (3-5) and (3-6), respectively, the latter equations can be used for values of the ratio of penetration depth to projectile diameter of 0.65 and 1.35 for scabbing and perforation, respectively (Kennedy, 1975).

3.6 Atomic Energy and Alternative Energies Commission – Electricity of France Formula

The Atomic Energy and Alternative Energies Commission (CEA) – Electricity of France (EDF) empirical formula was proposed in 1977. It was based on regression analysis of 52 impact tests on reinforced concrete slabs using solid, flat-nosed cylindrical missiles. The missile velocities and masses ranged from 25 to 450 m/s and 20 to 300 kg, respectively. The ratio of missile diameter to slab thickness ranged from 0.24 to 2.9; slab dimensions were 1.5 × 1.5 m and 5 × 5 m (Berriaud et al., 1978). The slab reinforcement ratios were not documented. Equation (3-11) is the CEA-EDF empirical formula to predict the thickness required to prevent perforation.

$$e = 0.765\left(f_c'\right)^{-\frac{3}{8}}\left(\frac{W}{d}\right)^{\frac{1}{2}}\left(V\right)^{\frac{3}{4}} \tag{3-11}$$

3.7 Central Research Institute of the Electric Power Industry Formulae

In 1985, the Central Research Institute of the Electric Power Industry (CRIEPI) of Japan performed impact experiments involving low velocity missiles, and developed empirical equations to predict scabbing and perforation thicknesses. The experiments consisted of 18 beams and 30 slabs impacted by a steel striking hammer with a diameter of 9.8 cm (3.9 in.) and a weight of 687 N (154.3 lbs.) at velocities up to 50 m/s (164 ft/sec) (Ohnuma et al., 1985). The beams ranged in depth from 20 to 50 cm (7.9 to 19.7 in.) and were doubly reinforced (1% compression and tension reinforcement). The slabs ranged in thickness from 10 to 30 cm (4 to 11.8 in.) with 1% reinforcement each way, each face. The compressive strength of the concrete in the beams and slabs was 23.4 MPa (3400 psi), although it is unclear if this was the strength on the day of testing. Equations (3-12) and (3-13) predict the wall thickness required to prevent scabbing and perforation, respectively. All of the units in equations (3-12) and (3-13) are specified in Section 3.2, except that d, e, and s are in feet, and f_c' is in psf.

$$s = 1.75\left(\frac{U}{V}\right)^{0.13}\frac{\left(\frac{W}{g}V^2\right)^{0.4}}{d^{0.2}\left(f_c'\right)^{0.4}} \tag{3-12}$$

$$e = 0.90\left(\frac{U}{V}\right)^{0.25}\left(\frac{\frac{W}{g}V^2}{df_c'}\right)^{0.5} \tag{3-13}$$

3.8 Chang Formulae

In 1981, Chang (CF) proposed an empirical formulae based on a set of published test data (Alderson et al., 1977; Gupta et al., 1975; Sliter, 1979) to predict the thickness required to prevent scabbing and perforation of reinforced concrete panels impacted by a rigid cylindrical steel missile (DOE, 2006). The test data includes missile velocities ranging from 55 fps (16.7 m/s) to 1023 fps (311.8 m/s), missile weights from 0.24 lbs. (1 N) to 756 lbs. (3363 N), missile diameters from 0.79 in (2 cm) to 12 in (30.5 cm), concrete strengths from 3300 psi (23 MPa) to

6600 psi (46 MPa), slabs with thickness from 2 in (5.1 cm) to 24 in (61 cm), and reinforcement ratios ranging from 0.3% to 1.5% each way, each face (Chang, 1981). Equations (3-14) and (3-15) predict the panel thickness required to prevent scabbing and perforation, respectively. All units used in equations (3-14) and (3-15) are specified in Section 3.2, except that d, e, and s are in feet, and f_c' is in psf.

$$s = 1.84\left(\frac{U}{V}\right)^{0.13} \frac{\left(\frac{W}{g}V^2\right)^{0.4}}{d^{0.2}\left(f_c'\right)^{0.4}} \tag{3-14}$$

$$e = \left(\frac{U}{V}\right)^{0.25} \left(\frac{\frac{W}{g}V^2}{df_c'}\right)^{0.5} \tag{3-15}$$

3.9 Amman and Whitney Formula

Amman and Whitney (AW) proposed equation (3-16) to predict the penetration depth of small explosively generated fragments traveling over 1000 ft. /sec (305 m/s). The formula was not intended for lower velocity missiles, such as those generated by wind (Kennedy, 1975).

$$\frac{X}{d} = \frac{282NDd^{0.2}}{\sqrt{f_c'}}\left(\frac{V}{1000}\right)^{1.8} \tag{3-16}$$

3.10 Ballistic Research Laboratory Formulae

Equations (3-17) and (3-18) present equations for perforation and scabbing thickness, respectively, proposed by the Ballistic Research Laboratory (BRL). The scabbing thickness is defined as a multiple of the predicted perforation thickness. Appendix F of ACI 349-13 (2013) cautions against the use of these formulae for predicting the local effects of wind-borne missiles, but they are included here for completeness.

$$\frac{e}{d} = \frac{427Dd^{0.2}}{\sqrt{f_c'}}\left(\frac{V}{1000}\right)^{1.33} \tag{3-17}$$

$$s = 2e \tag{3-18}$$

3.11 Bechtel Formula

Equation (3-19) is the Bechtel (B) formula prediction for scabbing thickness derived from the Calspan tests conducted at Sandia Laboratory (Rotz, 1975). The formula is based on impact tests using an 8-inch diameter Schedule 40 pipe.

$$s = 5.42 \frac{W^{0.4} V^{0.65}}{\sqrt{f_c'} d^{0.2}} \tag{3-19}$$

3.12 EPRI – Modified National Defense Research Committee Formula

EPRI increased the NDRC prediction for penetration depth (equations (3-7), (3-8)) by a factor of two to predict a thickness required to prevent scabbing (EPRI-NDRC) (Stephenson, 1977). The predictions fit the test data for scabbing thickness reasonably well for the 12-inch diameter Schedule 40 pipes. The EPRI document notes this prediction may be inappropriate for either pipes of other diameters or solid missiles (Stephenson, 1977).

3.13 A Comparison of Predictive Formulae for Local Impact Effects

3.13.1 Predictions Plotted as a Function of Velocity

The penetration depth, scabbing thickness, and perforation thickness, as available, are plotted as a function of velocity (in fps) to illustrate the differences in the formulae used to predict local impact effects. Table 3-1 presents the values of weight, W, diameter, d, projectile shape factor, N, concrete compressive strength, f_c', and caliber density, D, used to develop the figures. The outer diameter of the Schedule 40 pipe was used for the predictions.

Table 3-1: Empirical formulae parameters

W (lbs.)	100
d (in.)	6
N	1
f_c' (psi)	3000
D (lb./in^3)	0.463

Figure 3-2, Figure 3-3, and Figure 3-4 present the predicted penetration depth, scabbing thickness, and perforation thickness as a function of velocity, respectively. Significant differences are observed in each figure. These differences can be attributed, in part, to the wide range of test data used to develop and calibrate each formula.

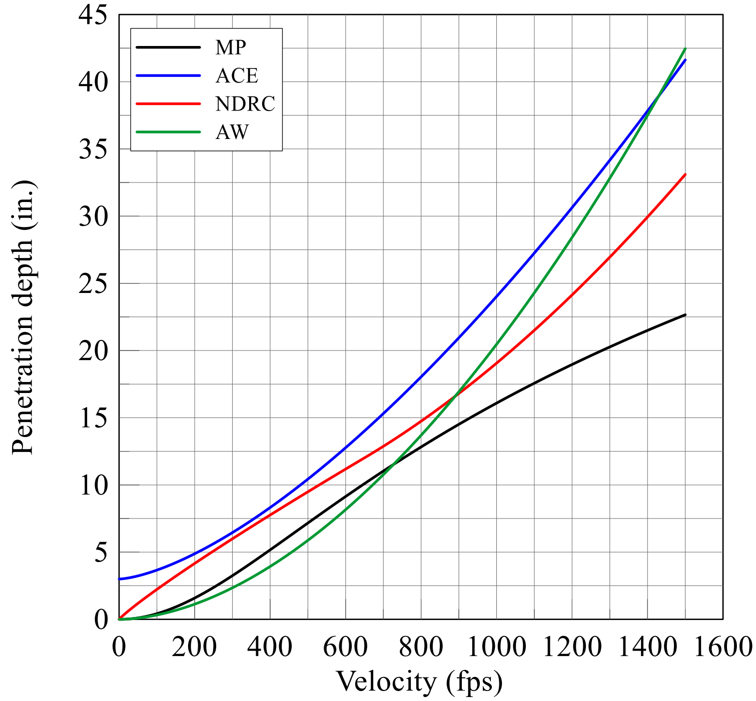

Figure 3-2: Penetration depth as a function of impact velocity

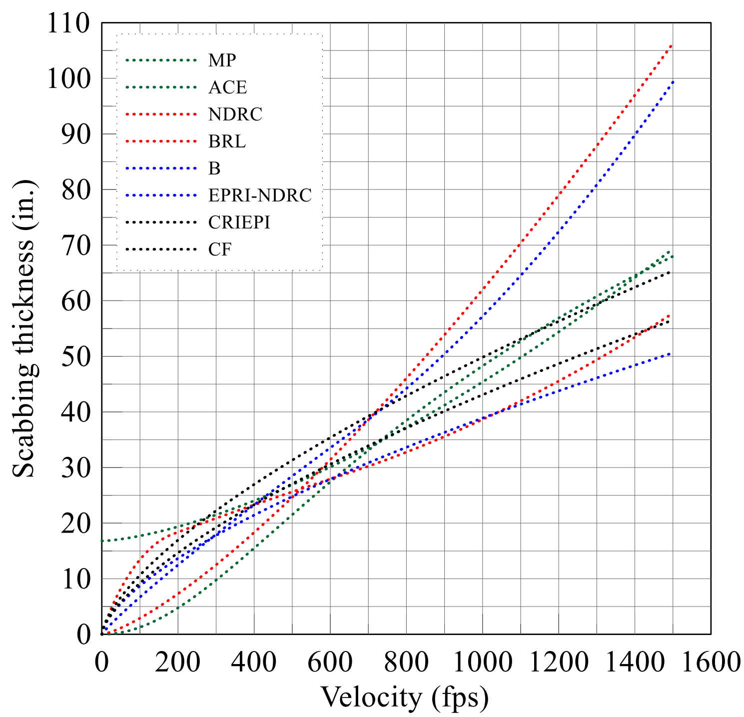

Figure 3-3: Scabbing thickness as a function of impact velocity

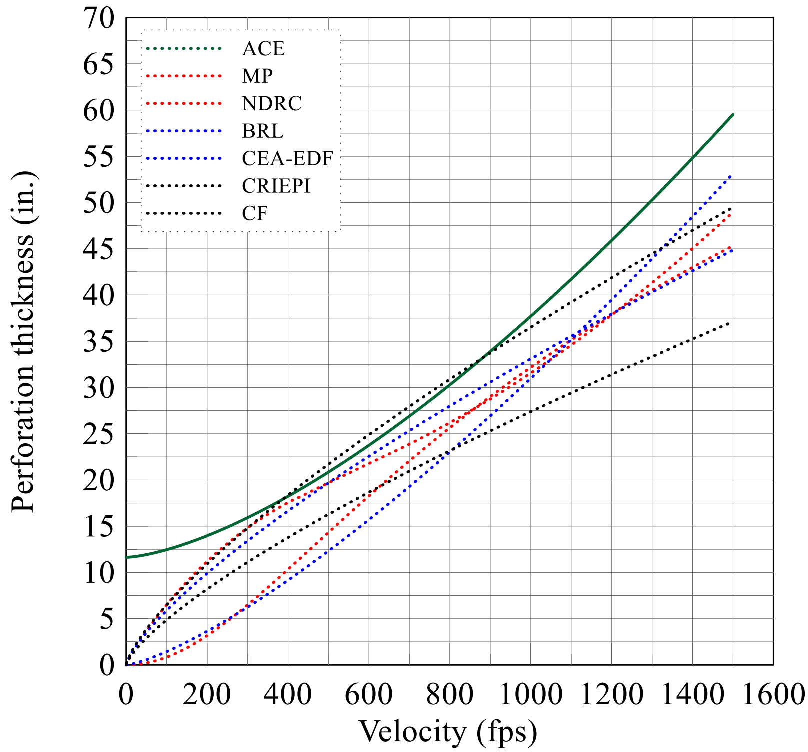

Figure 3-4: Perforation thickness as a function of impact velocity

3.13.2 Effect of Diameter Definition on Predictions

The outer and effective diameters of Schedule 40 pipe have been used to compare empirical predictions with experimental data (Kennedy, 1975; Stephenson, 1977). The effective diameter is defined as the diameter of a solid cylinder of the same cross sectional area, as illustrated in Figure 3-5. Kennedy (1975) compared the Sandia data with the empirical predictions using the effective diameter of Schedule 40 pipe. EPRI (Stephenson, 1977) also evaluated formulae but used the outer diameter of the pipe. Since Kennedy (1975) and Stephenson (1977) used different definitions of diameter, it is unclear, which diameter, if either, should be used in the predictions. To better understand the differences in the predictions using the effective and outer diameters, the MP and NDRC predictions are plotted as function of velocity for five Schedule 40 pipes (outer diameters of 3, 6, 8, 12, and 16 inches). Table 3-2 and Table 3-3 present the weight of the pipe, penetration coefficient, area of the pipe, missile shape factor, concrete penetrability factor, concrete compressive strength, and caliber density of the pipe for the outer and effective diameters, respectively. All variables are defined in Section 3.2. The areas computed for each pipe size in Table 3-2 are based on a solid cross section. The effective area, A_{eff}, and effective diameter, d_{eff}, in Table 3-3 are computed using Equations (3-20) and (3-21), respectively.

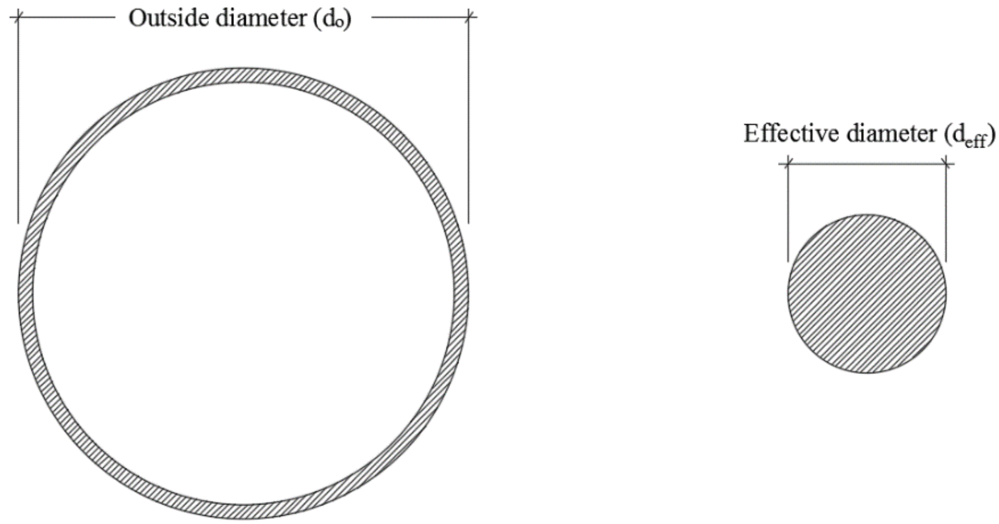

Figure 3-5: Effective diameter calculation

$$A_{eff} = \frac{\pi d_o^2}{4} - \frac{\pi d_i^2}{4} = \pi d_o t \tag{3-20}$$

$$d_{eff} = \sqrt{\frac{4A_{eff}}{\pi}} = 2\sqrt{d_o t} \tag{3-21}$$

where d_i and d_o are inner and outer diameter, respectively, and t is wall thickness, of the Schedule 40 pipe. The length of each Schedule 40 pipe is 10 feet.

Table 3-2: Empirical formulae parameters based on outer diameter

	d_o = 3 in	d_o = 6 in	d_o = 8 in	d_o = 12 in	d_o = 16 in
t (in)	0.216	0.280	0.322	0.406	0.500
W (lb.)	75.8	190	286	536	780
K_p	0.0035	0.0035	0.0035	0.0035	0.0035
A (ft^2)	0.049	0.196	0.349	0.785	1.40
N	0.84	0.84	0.84	0.84	0.84
K	3.29	3.29	3.29	3.29	3.29
f_c' (psi)	3000	3000	3000	3000	3000
D (lb./in^3)	2.81	0.878	0.558	0.310	0.190

Table 3-3: Empirical formulae parameters based on effective diameter

	$d_o = 3$ in	$d_o = 6$ in	$d_o = 8$ in	$d_o = 12$ in	$d_o = 16$ in
t (in)	0.216	0.280	0.322	0.406	0.500
W (lb.)	75.8	189.7	285.5	536	780
K_p	0.0035	0.0035	0.0035	0.0035	0.0035
A_{eff} (ft^2)	0.015	0.039	0.059	0.109	0.169
d_{eff} (ft.)	0.140	0.222	0.274	0.373	0.464
N	0.84	0.84	0.84	0.84	0.84
K	3.29	3.29	3.29	3.29	3.29
f_c' (psi)	3000	3000	3000	3000	3000
D (lb./in^3)	15.96	10.00	8.05	5.99	4.52

Figure 3-6a and Figure 3-6b present the MP penetration-depth predictions as a function of impact velocity, using the outer and effective diameters of the pipe, respectively. The 3-inch and 16-inch diameter pipes predict the largest and smallest penetration depths, respectively, using the outer diameter (see Figure 3-6a). The depth of penetration (ultimately perforation) is strongly dependent on the geometry of the shear failure surface, which varies as a function of panel thickness, pipe diameter, impact velocity, and concrete compressive and tensile strength. The effects of these parameters on impact resistance (i.e., penetration and perforation) are presented in Chapter 6.

Figure 3-6b shows the predictions of penetration depth for all five pipes to be virtually identical for all impact velocities, if effective diameter is used for the calculations. The effective diameter is based on the contact area of the projectile and is significantly less than the outer diameter of the pipe. The penetration depths are much greater if effective diameter is used. The MP predictions of minimum thickness required to prevent scabbing and perforation are multiples of the penetration depth and show the same trends seen in Figure 3-6. They are not presented here.

As observed in Figure 3-6a and Figure 3-6b, the predicted penetration depths are significantly different for outer and effective diameter. The effect of missile geometry (i.e., annular vs. solid) on panel response is investigated numerically in Chapter 5.

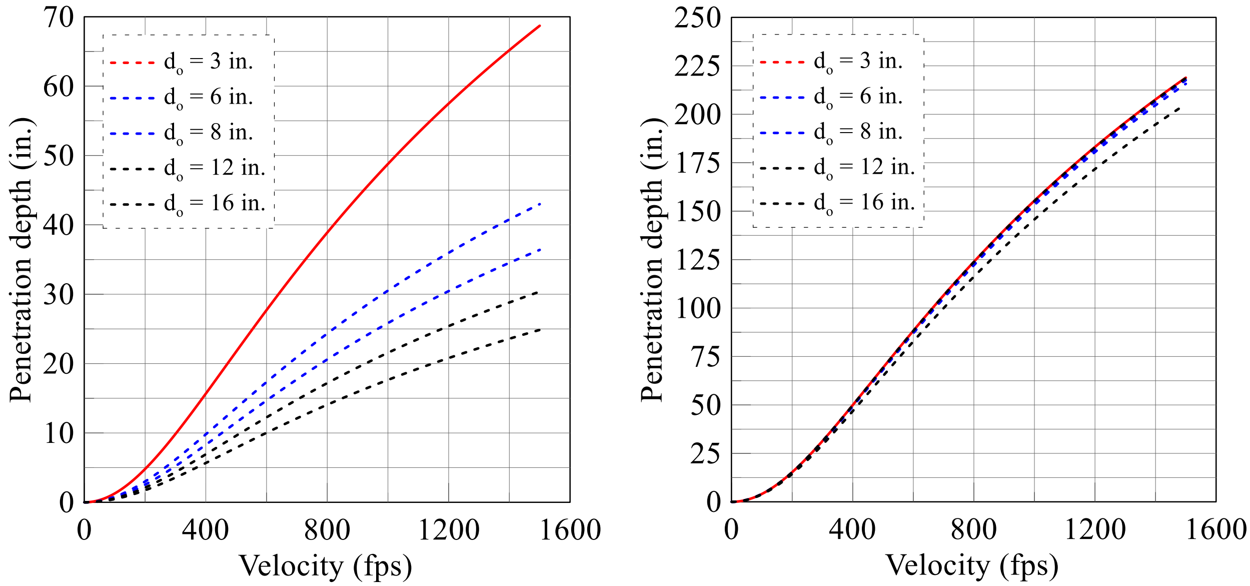

(a) Outer diameter (b) Effective diameter

Figure 3-6: MP penetration depth as a function of impact velocity

Figure 3-7a and Figure 3-7b present the NDRC predictions of penetration depth as a function of velocity, using outer and effective diameters, respectively. There are significant differences in the predictions: the use of the outer (effective) diameter yields a penetration depth of approximately 6 (11) inches for a 12-inch diameter pipe with an impact velocity of 200 fps. Stephenson (1977) documented a penetration depth of approximately 7 inches for a 12-inch diameter pipe with an impact velocity of 200 fps. The use of the outer diameter in the equations better predicts penetration depths at velocities typical of wind-borne missiles (i.e., 40 to 100 m/s).

Figure 3-8a and Figure 3-8b present the NDRC predictions of minimum thickness to prevent scabbing using outer and effective diameters of the pipe, respectively. There are differences in the predictions: the use of the outer (effective) diameter predict a thickness required to prevent scabbing of 35 (25) inches for a 12-inch diameter pipe with an impact velocity of 200 fps. Stephenson (1977) observed no scabbing on the 24-inch panel when impacted by a 12-inch diameter pipe at 200 fps. In this case, the effective diameter better predicts the thickness required to prevent scabbing.

The optimal definition of diameter to be used for impact calculations, if one is possible, for predictions of scabbing, penetration, and perforation is unclear at this time because none of the empirical formulae were developed using data from pipe impact tests. Nonetheless, outer and effective diameters of the pipe are used in Section 3.14 to compare empirical predictions and experimental results.

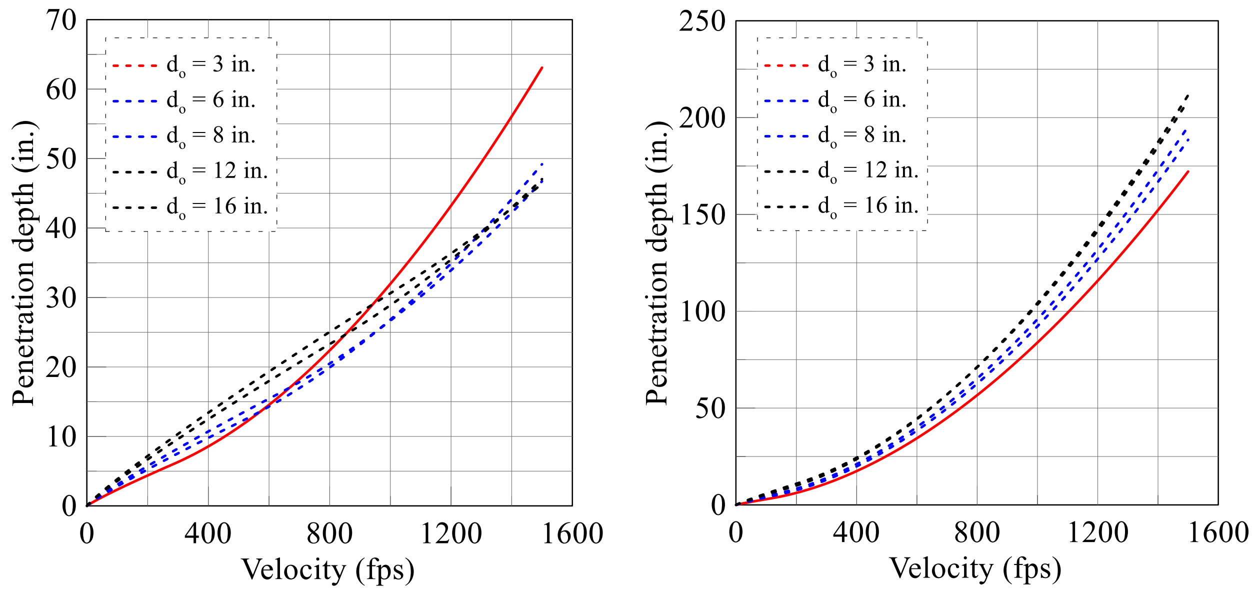

(a) Outer diameter (b) Effective diameter

Figure 3-7: NDRC penetration depth as a function of impact velocity

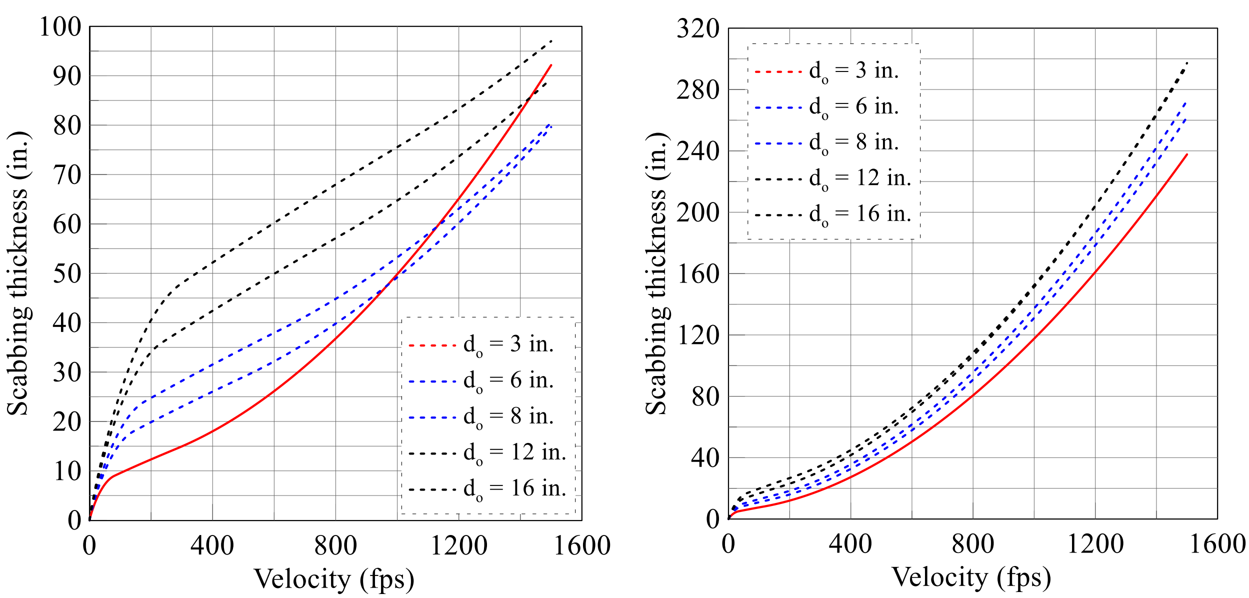

(a) Outer diameter (b) Effective diameter

Figure 3-8: NDRC scabbing thickness as a function of impact velocity

3.14 Comparison of Empirical Predictions and Experimental Results

Results from six of the EPRI experiments (Test #5, 8, 3, 12, 10, 11, and 11) and four of the Calspan experiments (Test # 15F, 16F, 5F, and 6F), with the Schedule 40 pipe as the impacting projectile, are used to evaluate the empirical equations. The numbers given in parentheses above are the test numbers from the source documents. Table 3-4 and Table 3-5 show the EPRI and Calspan test specifications, respectively, including the test number, diameter and weight of the missile, concrete panel wall thickness, velocity of the missile, and the compressive strength of the concrete. The penetration depth, scabbing thickness, and perforation thickness are computed using the nine empirical formulae and the predictions are compared with experimental results. The results of the empirical formulae have either the subscript *out* or *eff* indicating the use of the outer or effective diameter of the pipe in the predictions, respectively.

Table 3-4: EPRI test specifications (Stephenson, 1977)

Test	d , in (mm)	W , lbs. (N)	Panel t , in (mm)	V , ft/sec (m/s)	f_c' , psi (MPa)
5	3 (76)	78 (347)	12 (305)	212 (64.6)	3340 (23.0)
8	12 (305)	743 (3305)	24 (610)	202 (61.6)	3795 (26.2)
3	12 (305)	743 (3305)	18 (457)	202 (61.6)	3350 (23.1)
12	12 (305)	743 (3305)	18 (457)	203 (61.9)	4535 (31.3)
10	12 (305)	743 (3305)	12 (305)	143 (43.6)	3690 (25.4)
11	12 (305)	743 (3305)	12 (305)	98 (29.9)	3595 (24.8)

Table 3-5: Calspan test specifications (Vassallo, 1975)

Test	d , in (mm)	W , lbs. (N)	Panel t , in (mm)	V , ft/sec (m/s)	f_c' , psi (MPa)
15F	8 (203)	202 (899)	12 (305)	135 (41.1)	5210 (35.9)
16F	8 (203)	202 (899)	12 (305)	209 (63.7)	5770 (39.8)
5F	8 (203)	205 (912)	18 (457)	210 (64.0)	5210 (35.9)
6F	8 (203)	209 (930)	18 (457)	319 (97.2)	5210 (35.9)

Table 3-6 presents the ratio of the penetration depth predicted by an empirical formula (X_{out} and X_{eff}) to the penetration depth measured in the experiment ($X_{\exp}$). The penetration depth is overestimated when the effective diameter is used. In Test 10, the ratio is low for all predictions because the panel was perforated in the experiment and the penetration depth was reported as the panel thickness (=12 inches). Based on these results, the NDRC formula predicts penetration depth for Schedule 40 pipes within 20 percent if the outer diameter is used. The MP and AW formulae underestimate, and the ACE formula overestimates, penetration depth if the outer diameter is used.

Kennedy (1975) evaluated the empirical formulae by taking the ratio of the predicted thickness, s, required to prevent scabbing to the thickness of tested panels, $t_{\exp}$. An alternate approach is used here: the appropriateness of a predictive equation is judged by whether scabbing was predicted and whether scabbing was observed after the experiment or not. Table 3-7 presents results. None of the empirical formulae are perfect. The NDRC formula using the effective diameter scores the best using this criterion, with 9 correct answers out of 10. However, the predicted thickness required to prevent scabbing cannot be fully evaluated without knowing the actual thickness required to prevent scabbing.

Table 3-6: Ratios of predictions and experimental results for penetration depth

		Empirical formula							
		MP		NDRC		ACE		AW	
Test	$X_{\exp}$ (in.)	$\frac{X_{eff}}{X_{\exp}}$	$\frac{X_{out}}{X_{\exp}}$	$\frac{X_{eff}}{X_{\exp}}$	$\frac{X_{out}}{X_{\exp}}$	$\frac{X_{eff}}{X_{\exp}}$	$\frac{X_{out}}{X_{\exp}}$	$\frac{X_{eff}}{X_{\exp}}$	$\frac{X_{out}}{X_{\exp}}$
5	4.6	3.5	0.80	1.4	0.93	3.4	1.2	1.7	0.45
8	6.8	2.6	0.32	1.7	1.1	3.5	1.4	1.6	0.24
3	7	2.8	0.345	1.7	1.1	3.6	1.4	1.7	0.25
12	7.5	2.1	0.26	1.5	0.94	2.9	1.3	1.3	0.20
10	12	0.8	0.10	0.68	0.45	1.3	0.70	0.49	0.08
11	4.5	1.1	0.13	1.3	0.86	2.1	1.7	0.67	0.10
15F	2.5	1.3	0.19	1.6	1.1	2.5	2.1	0.73	0.13
16F	4	1.5	0.22	1.4	0.96	2.6	1.5	0.95	0.17
5F	4.5	1.7	0.24	1.3	0.88	2.4	1.3	0.91	0.16
6F	7.4	2.1	0.31	1.2	0.79	2.6	1.0	1.2	0.21

The thickness of the panel required to prevent perforation, e, was evaluated using the same *yes* or *no* criterion. Table 3-8 evaluates the ability of the empirical formulae to predict perforation. Perforation was observed in only one test: Test 10. The MP, BRL, and CRIEPI formulae using outer diameter predict correctly in 9 out of 10 tests but importantly did not predict perforation in Test 10. The CF formula using outer diameter also predicted correctly 9 times out of 10 and predicted perforation in Test 10. Results using the other formula and definitions of diameter performed were poorer. None of the formulae inspire the level of confidence expected for the analysis of a nuclear structure.

Table 3-7: Predictions of thickness required to prevent scabbing

			Empirical formulae															
			MP		NDRC		EPRI-NDRC		ACE		B		BRL		CRIEPI		CF	
Test	t_{exp} (in.)	Scabbing	s_{out}	s_{eff}	s_{out}	s_{eff}	s_{out}	s_{eff}	s_{out}	s_{eff}	s_{out}	s_{eff}	s_{out}	s_{eff}	s_{out}	s_{eff}	s_{out}	s_{eff}
5	12	No	✓[1]	×	×	✓	×	×	×	×	×	×	×	×	×	×	×	×
8	24	No	✓	×	×	✓	✓	×	×	×	✓	×	✓	×	×	×	×	×
3	18	Yes	×	✓	✓	✓	✓	✓	✓	✓	✓	✓	×	✓	✓	✓	✓	✓
12	18	Yes	×	✓	✓	✓	✓	✓	✓	✓	✓	✓	×	✓	✓	✓	✓	✓
10	12	Yes	×	✓	✓	✓	✓	✓	✓	✓	✓	✓	×	✓	✓	✓	✓	✓
11	12	Yes	×	✓	✓	✓	×	✓	✓	✓	✓	✓	×	✓	✓	✓	✓	✓
15F	12	No	✓	✓	×	✓	✓	✓	×	×	✓	×	✓	×	✓	×	×	×
16F	12	Yes	×	✓	✓	✓	×	✓	✓	✓	×	✓	×	✓	✓	✓	✓	✓
5F	18	No	✓	×	×	✓	✓	✓	×	×	✓	✓	✓	×	✓	✓	✓	×
6F	18	No	✓	×	×	×	✓	×	×	×	✓	×	✓	×	×	×	×	×

1. ✓ = formula predicted scabbing and it occurred in experiment or formula did not predict scabbing and it not occur in experiment; × = formula did not predict scabbing but it occurred in experiment or formula predicted scabbing but it did not occur in the experiment

Table 3-8: Predictions of thickness required to prevent perforation

		Empirical formula													
		MP		NDRC		ACE		BRL		CEA-EDF		CRIEPI		CF	
Test	Perforation	e_{out}	e_{eff}	e_{out}	e_{eff}	e_{out}	e_{eff}	e_{out}	e_{eff}	e_{out}	e_{eff}	e_{out}	e_{eff}	e_{out}	e_{eff}
5	No	✓[1]	×	✓	✓	✓	×	✓	×	✓	×	✓	×	✓	×
8	No	✓	×	✓	✓	×	×	✓	×	✓	×	✓	✓	✓	×
3	No	✓	×	×	×	×	×	✓	×	✓	×	✓	×	×	×
12	No	✓	×	×	×	×	×	✓	×	✓	×	✓	×	✓	×
10	Yes	×	✓	✓	✓	✓	✓	×	✓	✓	✓	×	✓	✓	✓
11	No	✓	✓	✓	×	×	×	✓	×	✓	×	✓	×	✓	×
15F	No	✓	✓	✓	✓	×	✓	✓	✓	✓	✓	✓	✓	✓	✓
16F	No	✓	✓	✓	✓	×	×	✓	×	✓	×	✓	✓	✓	×
5F	No	✓	✓	✓	✓	✓	✓	✓	✓	✓	✓	✓	✓	✓	✓
6F	No	✓	×	✓	✓	×	×	✓	×	✓	×	✓	✓	✓	×

1. ✓ = formula predicted perforation and it occurred in experiment or formula did not predict perforation and it not occur in experiment; × = formula did not predict perforation but it occurred in experiment or formula predicted perforation but it did not occur in the experiment

3.15 Conclusions

Results from six of the EPRI experiments and four of the Calspan experiments using a Schedule 40 pipe as the impacting projectile, were used to evaluate the empirical equations. The shortcomings with the predictive equations, and the lack of knowledge regarding those parameters that most affect impact resistance against soft and hard missiles, prompted the authors to begin an effort to formally validate a numerical tool for impact analysis of reinforced concrete panels. The development of these numerical tools and results are discussed in the following chapters.

“This Page Intentionally Left Blank”

SECTION 4
LAGRANGIAN IMPACT SIMULATIONS

4.1 Introduction

Finite element analysis is a well-established numerical technique for calculating the response of components and systems to mechanical and thermal loadings. One of the most well-known formulations for impact loading is the Lagrangian method, which utilizes solid, shell, beam, and discrete elements (springs) to solve equilibrium equations describing the conservation of mass, momentum, and energy in the analyzed system. In this chapter, the Lagrangian formulation is used to validate, in part, a numerical model in LS-DYNA for impact analysis using available data from the EPRI tests.

Table 4-1 summarizes the experiments simulated in this chapter, including test number, concrete compressive strength, f_c', panel thickness, t, projectile velocity, v, and observed local damage. These tests involved 12-inch (305 mm) to 24-inch (610 mm) thick reinforced concrete panels impacted by a 12-inch (305 mm) diameter Schedule 40 pipe with impact velocities ranging from 98 fps (30 m/s) to 202 fps (62 m/s). Section 4.2 discusses modeling of test components in LS-DYNA for impact simulations using a Lagrangian finite element model; contact algorithms, boundary conditions, material models, element formulations, and strain rate effects. The results of the Schedule 40 pipe impact simulations and partial validation of the numerical models are presented in Section 4.3. Section 4.4 summarizes the chapter and presents the key conclusions.

Table 4-1: Summary of simulated experiments, Lagrangian formulation

Test	Panel t, mm (in)	v, m/s (fps)	f_c', MPa (psi)	Projectile	Panel damage per Stephenson (1977)
11	305 (12)	30 (98)	24.8 (3600)	Schedule 40 pipe	Pipe penetrated panel , scabbing on the back face
10	305 (12)	44 (143)	25.5 (3700)	Schedule 40 pipe	Pipe perforated panel, scabbing on the back face
3	457 (18)	62 (202)	23.4 (3400)	Schedule 40 pipe	Pipe penetrated panel, scabbing on back face
8	610 (24)	62 (202)	26.2 (3800)	Schedule 40 pipe	Pipe penetrated panel, radial cracking on back face

4.2 Modeling Techniques in LS-DYNA for Lagrangian Impact Simulations

4.2.1 Introduction

This section discusses the modeling of the tested components in LS-DYNA: material models, element formulations, contact algorithms, mesh sizes, material models, boundary conditions, and strain-rate parameters are described. The simulations will focus on the experiments presented in Table 4-1: the normal (90°) impact of 12-, 18-, and 24-inch thick reinforced concrete panels by 12-inch diameter Schedule 40 pipes.

4.2.2 12-inch Panels (Tests 10 and 11)

The Lagrangian model of the 12-inch thick panel and pipe are shown in Figure 4-1; a quarter model of the pipe and panel was used to reduce the computational demand. The simulation results were effectively identical to those of a half-symmetry model, confirming the use of a quarter model in the simulations. The upper left hand corner of the panel was modeled as shown in Figure 4-2. The displacement vector component perpendicular to the plane and the rotational vector components parallel to the plane were set to zero on the right side (RS) and bottom (B) of the panel (see Figure 4-2) to simulate the symmetric boundary conditions. One column of nodes constrained displacement in the X-direction on the left side (LS) and top of the panel (T) to simulate the pinned boundary condition imposed in the experiments.

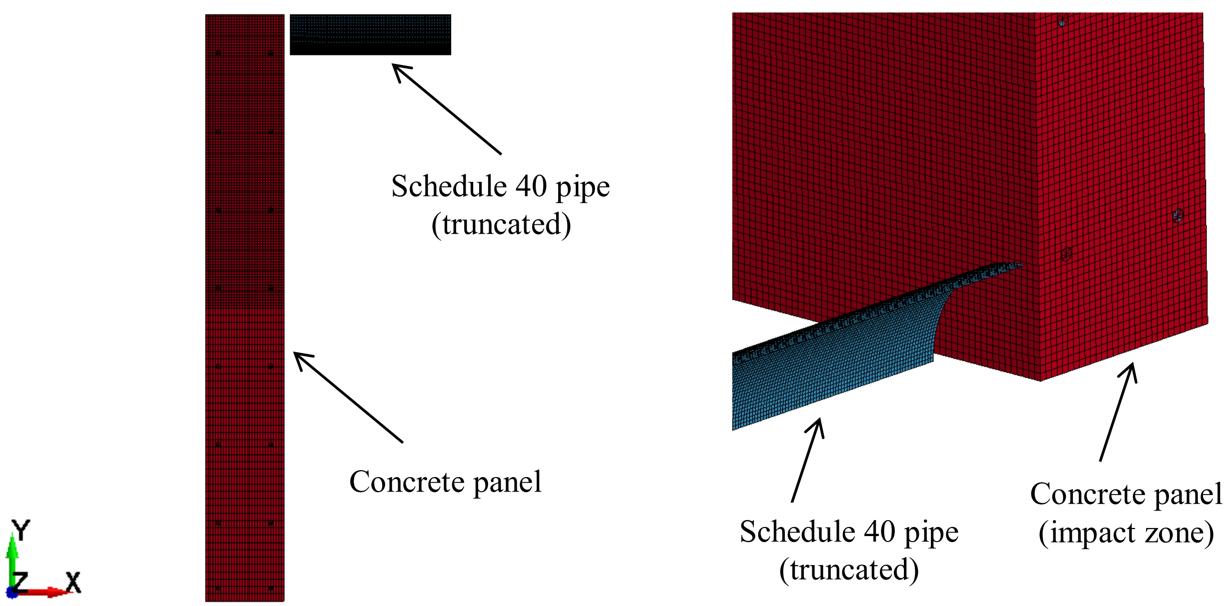

(a) Top view (b) View of impact zone, pipe and panel

Figure 4-1: Lagrangian model, 12-inch thick panel

The layout of the longitudinal reinforcement in the panel is presented in Figure 4-3. The same boundary conditions applied to concrete panel were applied to the reinforcement. Symmetric boundary conditions were also applied to the edges of the pipe along its total length (=165 inches).

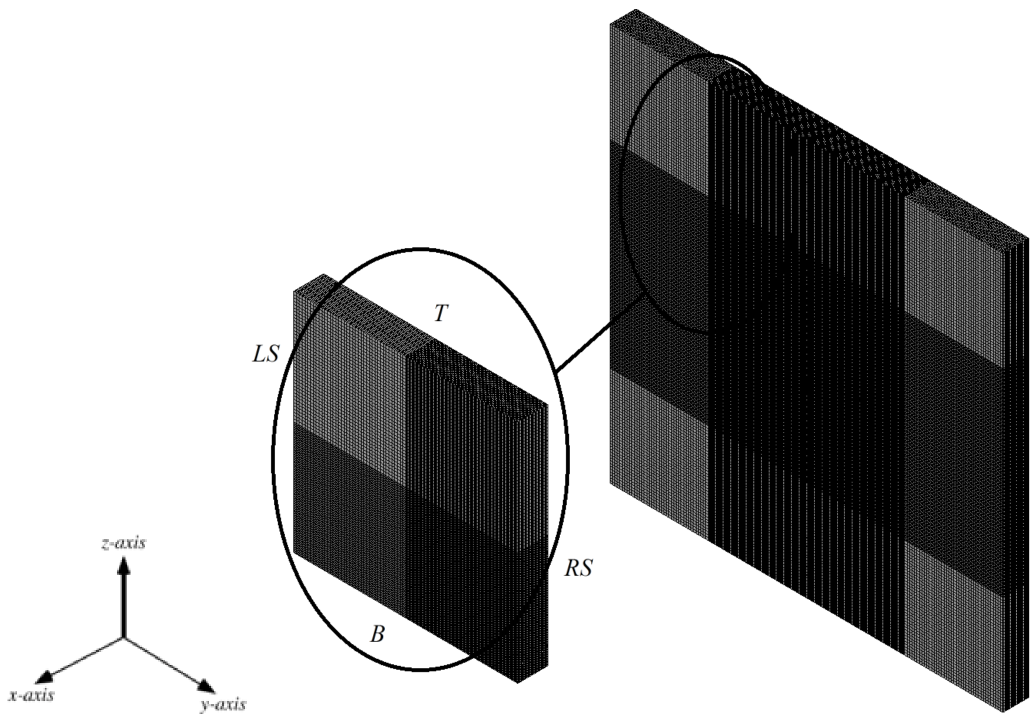

Figure 4-2: Quarter model of 12-inch panel in LS-DYNA

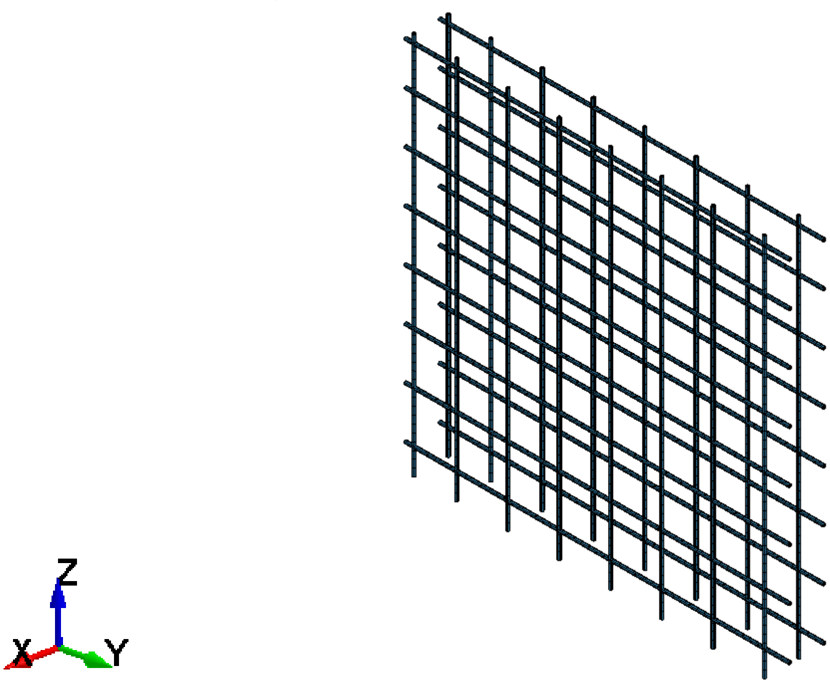

Figure 4-3: Rebar layout, 12-inch panel, Lagrangian model

The CSCM material model (MAT159) was used to model concrete (see Section 2.3). Table 4-2 presents values of the parameters of the CSCM model for EPRI Test 11 (f_c'=3600 psi). The variables used in Table 4-2 are shear modulus, G; bulk modulus, K; tri-axial compression surface constant, α; tri-axial compressive surface linear constant, θ; tri-axial compression surface nonlinear constant, λ; tri-axial compression surface exponent, β; torsion surface constant, α_1; torsion surface linear constant, θ_1; torsion surface nonlinear constant, λ_1; torsion surface exponent, β_1; tri-axial extension surface constant, α_2; tri-axial extension surface linear constant, θ_2; tri-axial extension surface nonlinear constant, λ_2; tri-axial extension surface exponent, β_2; cap aspect ratio, R; cap initial location, X_o; maximum plastic volume compaction, W_p; linear shape parameter, D_1; quadratic shape factor, D_2; ductile shape softening parameter, B_d; fracture energy in uniaxial stress, G_{FC}; brittle shape softening parameter, D_b; fracture energy in uniaxial tension, G_{FT}; fracture energy in pure shear stress, G_{FS}; shear-to-compression transition parameter, $PWRC$; shear to tension transition parameter, $PWRT$; rate effects parameter for uniaxial compressive stress, η_{oc}; rate effects power for uniaxial compressive stress, η_c; rate effects parameter for uniaxial tensile stress, η_{ot}; rate effects power for uniaxial tensile stress, η_t; maximum overstress allowed in compression, $Overc$; maximum overstress allowed in tension, $Overt$; ratio of effective shear stress to tensile stress fluidity parameters, $Srate$; and power to increase fracture energy with rate effects, $REPOW$. The CSCM model parameters for Tests 10, 3, and 8 are presented in Tables B-1, B-2, and B-3 of Appendix B, respectively.

Murray et al. (2007b) formulated a set of equations to calculate the dynamic increase factors (DIF) as a function of strain rate in compression $C(\dot{\varepsilon})$, and tension $T(\dot{\varepsilon})$. These equations are defined in terms of the parameters used to characterize the CSCM model and are presented in equations (4-1) and (4-2), respectively (Murray et al., 2007b). The CSCM model can be fit to any formulation of $C(\dot{\varepsilon})$ and $T(\dot{\varepsilon})$ the analyst chooses.

$$C(\dot{\varepsilon}) = 1 + \frac{E_{Tc}\dot{\varepsilon}\eta_{oc}}{f_c'(\dot{\varepsilon})^{\eta_c}} \tag{4-1}$$

$$T(\dot{\varepsilon}) = 1 + \frac{E_{Tc}\dot{\varepsilon}\eta_{ot}}{f_t'(\dot{\varepsilon})^{\eta_t}} \tag{4-2}$$

where $\dot{\varepsilon}$ is the strain rate and E_{Tc} is Young's modulus. All other variables were defined previously.

Table 4-2: CSCM concrete model inputs, EPRI Test 11

G (psi)	1.49E+06	D_1 (psi)	1.72E-06
K (psi)	1.63E+06	D_2 (psi^2)	1.66E-11
α (psi)	1989.6723	B_d	100
β (psi^{-1})	1.33E-04	D_b	0.1
λ (psi)	1522.8963	G_{FT} (psi-in)	0.4677
θ	2.80E-01	G_{FC} (psi-in)	46.77
α_1	0.74735	G_{FS} (psi-in)	0.4677
β_1 (psi^{-1})	5.18E-04	$PWRC$	5
λ_1	0.17	$PWRT$	1
θ_1 (psi^{-1})	9.05E-06	η_t	0.77
α_2	0.66	η_{ot}	1.40E-04
β_2 (psi^{-1})	5.25E-04	η_c	0.69
λ_2	0.16	η_{oc}	3.90E-04
θ_2 (psi^{-1})	1.06E-05	$Srate$	1
R	5	$Overc$ (psi)	2866.1
X_o (psi)	1.28E+04	$Overt$ (psi)	2866.1
W_p	0.05	$REPOW$	1

The Dynamic Increase Factors (DIFs) for concrete follow the CEB formulation in compression and the Hao and Zhou formulation in tension (Dusenberry, 2010). Figure 4-4 shows the CEB formulation in compression as a function of strain rate and the best curve fit using equation (4-1) in log-space. The curve fit targeted the high strain rates expected in the impact simulations. The values of η_{oc} and η_c used to fit the CEB formulation for Test 11 are presented in Table 4-2.

Figure 4-5 presents the Hao and Zhou formulation as a function of strain rate and the best curve fit calculated using equation (4-2) in log-space. The values of η_{ot} and η_t used to fit the Hao and Zhou formulation for Test 11 are presented in Table 4-2. The curve fits to the CEB and Hao and Zhou formulations for Tests 10, 3, and 8 are presented in Figures B-1, B-2, and B-3 of Appendix B, respectively.

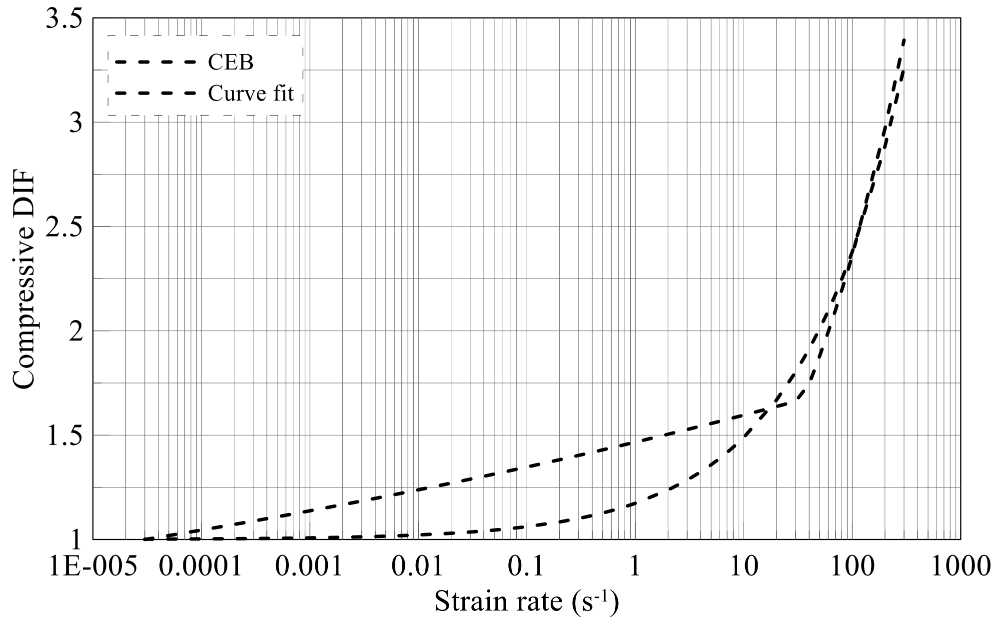

Figure 4-4: CEB formulation in compression and best fit line, Test 11

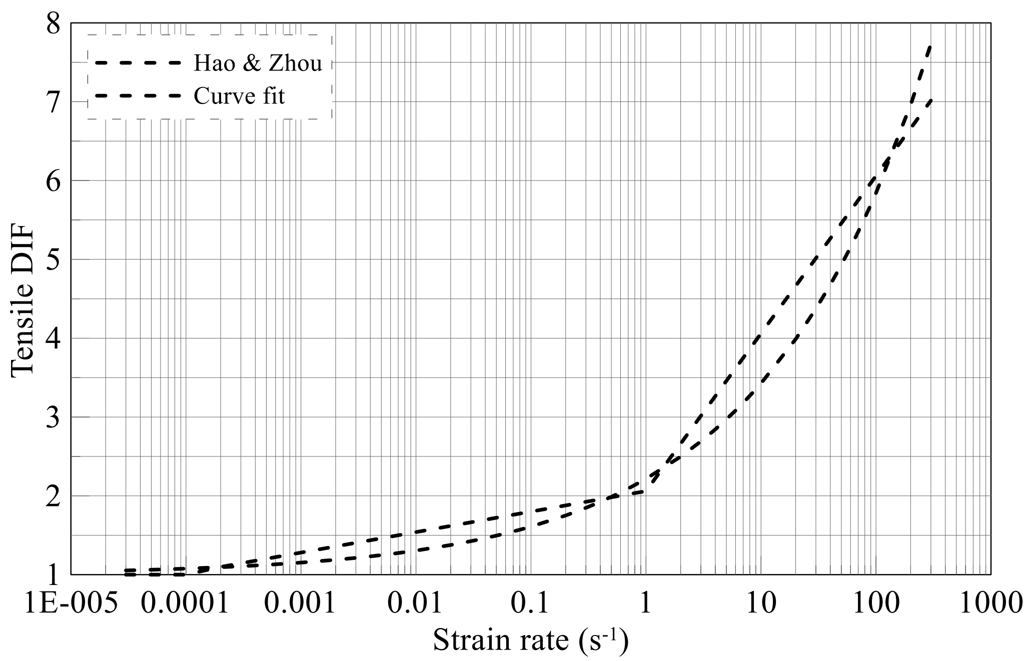

Figure 4-5: Hao and Zhou formulation and best fit line, Test 11

To help combat issues related to large mesh deformations and simulation termination, erosion was activated in the CSCM material model using the damage function: elements are deleted once the damage parameter reaches a value of 1.00 (total loss of stiffness and strength in the element) and the user-specified maximum principal strain is exceeded. The user-specified maximum principal strain is implemented in the material model using the ERODE parameter (i.e., ERODE=1.05 corresponds to a maximum principal strain of 5%). If the maximum principal strain is set to a value of 1.00 in LS-DYNA (i.e., ERODE=1), element erosion is independent of maximum principal strain and the element will erode once the damage parameter reaches a value of 1.00. A numerical study by Murray et al. (2007a) that investigated the applicability of the CSCM material model for analysis of a motor vehicle hitting a roadside safety structure (e.g., bridge rails and barriers) recommended a maximum principal strain of 5% to 10% based on calibration studies. An ERODE value of 1.05 was used for the impact simulations presented in this chapter.

The simplified Johnson-Cook (JC) material model (MAT098) was used for the Grade 60 reinforcement. This model is widely used to describe material behavior at large strains, high strain rates, and high temperatures and is known for its use in impact and penetration related problems (Banerjee et al., 2015). The Johnson-Cook formulation (Davidson, 1996) is presented in equation (4-3); values of the constants for the rebar are presented in Table 4-3.

$$\bar{\sigma} = \left[A + B\left(\bar{\varepsilon}^{p}\right)^{n} \right]\left[1 + C \ln \dot{\varepsilon}^{*}\right]\left[1 - \left(T^{*}\right)^{m}\right] \tag{4-3}$$

$$T^{*} = \frac{T - T_R}{T_m - T_R} \tag{4-4}$$

where $\bar{\sigma}$ is von Mises effective flow stress, $\bar{\varepsilon}^{p}$ is equivalent plastic strain in the material, A is yield stress, B and n are hardening coefficients, C is strain rate coefficient, m is softening coefficient, $\dot{\varepsilon}^{*}$ is normalized strain rate of the material, and T^{*} is defined in equation (4-4), where T and T_M are the current and melting temperature of the material in Kelvin, respectively, and T_R is room temperature in Kelvin.

Table 4-3: Johnson-Cook material constants for 60 ksi steel (Davidson, 1996)

A (psi)	B (psi)	n	C
6.0E4	2.5E5	0.6	0.01

The MAT015 JC material model was used for the Schedule 40 pipe, with yield strength of 73 ksi. The Borvik et al. (2005) JC material parameters for 71 ksi steel were used and they are presented in Table 4-4, where $EPSO$ is a strain-rate hardening constant and $D1$ through $D5$ are fracture strain constants. All other parameters were defined previously. Values not specified below were set to the defaults.

Table 4-4: 71 ksi JC material constants (Borvik, 2005)

A (psi)	7.11E+04	$EPSO$	5.00E-04
B (psi)	1.17E+05	$D1$	0.0705
n	0.73	$D2$	1.732
C	0.0114	$D3$	-0.54
M	0.94	$D4$	-0.015
T_M (K)	1800	$D5$	0
T_R (K)	293		

Eight-noded solid elements were used to model the concrete. The mesh was finer in the impact zone (45 × 45 in) than elsewhere;. the concrete was modeled with 0.4 × 0.4 × 0.4 in. elements in the impact zone and 1.125 × 1.125 × 1.125 in. elements elsewhere. The total number of solid elements in the concrete panel was 720750. The reinforcement was meshed with a total of 1600 beam elements. The reinforcement was coupled to the concrete using the CONSTRAINED_LAGRANGE_IN_SOLID formulation. The pipe was modeled with 0.2 × 0.2 in. shell elements, with a total of 39600 elements. To ensure proper transfer of momentum from the projectile to the target, the slave elements (concrete) should be approximately twice the size of the master elements (steel pipe) to avoid penetration of interacting elements. The pipe was given an initial velocity using the INITIAL_VELOCITY_GENERATION. The CONTACT_AUTOMATIC_NODES_TO_SURFACE algorithm was used to define contact between the pipe and the panel, with the Schedule 40 pipe and the wall being the master and slave segments, respectively. This model is a one-way treatment of contact; only the user specified slave nodes are checked for penetration of the master segment. Inside the contact keyword, the card $SOFT = 1$ was activated for penalty-based contact modeling, which ensures stability when dissimilar materials come into contact. The contact card $SOFT = 2$ is recommended for impact problems but is not applicable for node-to-surface contact models. Friction between the concrete and the pipe was also considered and applied in the CONTACT_AUTOMATIC_NODES_TO_SURFACE keyword; the static coefficient of friction

FS , and dynamic coefficient of friction FD, were assigned values of 0.57 (Rabbat et al., 1985) and 0.4 (Hao et al., 2013), respectively.

The cross section integrated beam element (Hughes-Liu beam in LS-DYNA) and the constant stress formulation (ELFORM=1 in LS-DYNA) was used for the beam and solid elements, respectively. The Belytschko-Tsay formulation was used for the shell elements.

Contact between the pipe and the reinforcement was not considered in these impact simulations; the diameter of the pipe and the spacing of the rebar (=12 inches) are the same, which would allow the pipe to pass through the panel without any resistance from the rebar. The TSSFAC value was set to 0.33 in the CONTROL_TIMESTEP keyword, which allows the user to apply a penalty to the time step to increase the probability of convergence, but it increases run time significantly.

4.2.3 18- and 24-inch Panels (Tests 3 and 8)

The Lagrangian models of the 18- and 24-inch panels are shown in Figure 4-6 and Figure 4-7, respectively. The material models, strain rate effects, boundary conditions, contact algorithms, and element forms of the pipe, rebar, and the concrete panel were those described previously for the 12-inch panel. In the concrete panel, the mesh was finer in the impact zone (15 × 15 in.) than elsewhere; see Figure 4-6b and Figure 4-7b. The concrete was modeled with 0.25 × 0.25 × 0.25 in. elements in the impact zone and 1 × 1 × 1 in. elsewhere. The total number of solid elements in the 18- and 24-inch thick concrete panels were 128,625 and 165,375, respectively. In both walls, the reinforcement was meshed with a total of 1600 beam elements. The reinforcement was coupled to the concrete using the CONSTRAINED_LAGRANGE_IN_SOLID formulation. The pipe was modeled with 0.1 × 0.1 in. shell elements, with a total of 150,154 elements, in both simulations.

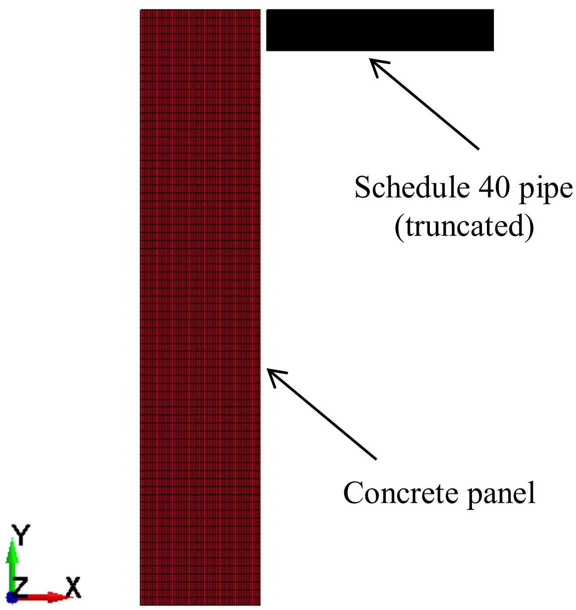

(a) Top view

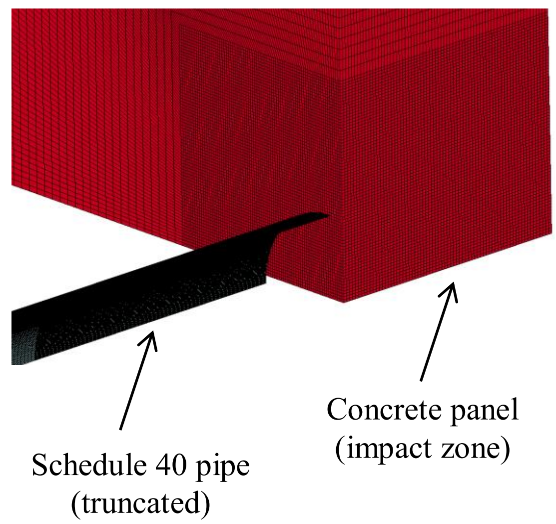

(b) View of impact zone, pipe and panel

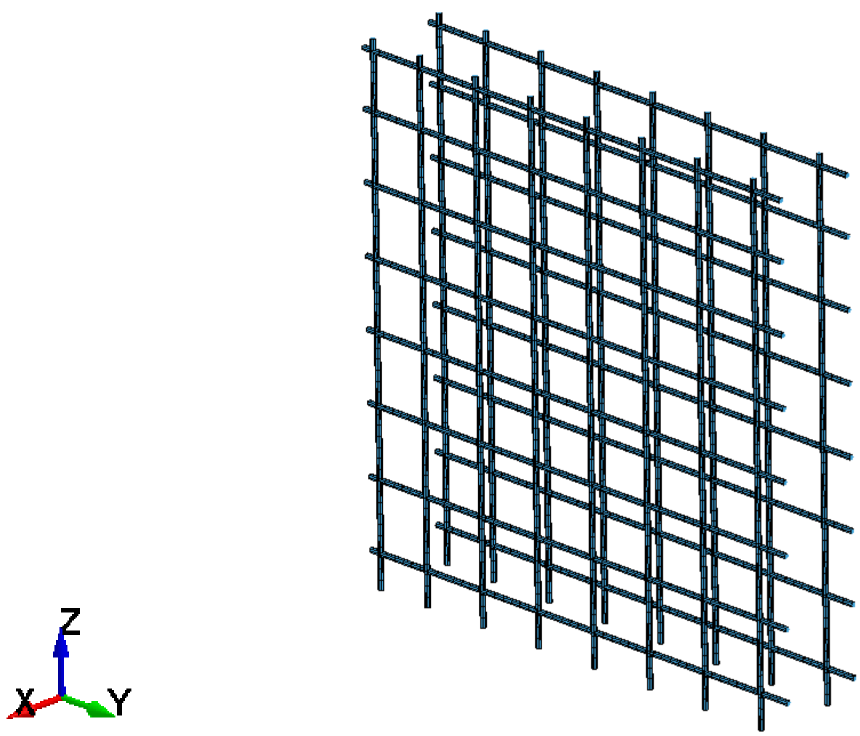

(b) Rebar layout

Figure 4-6: Lagrangian model, 18-inch thick panel

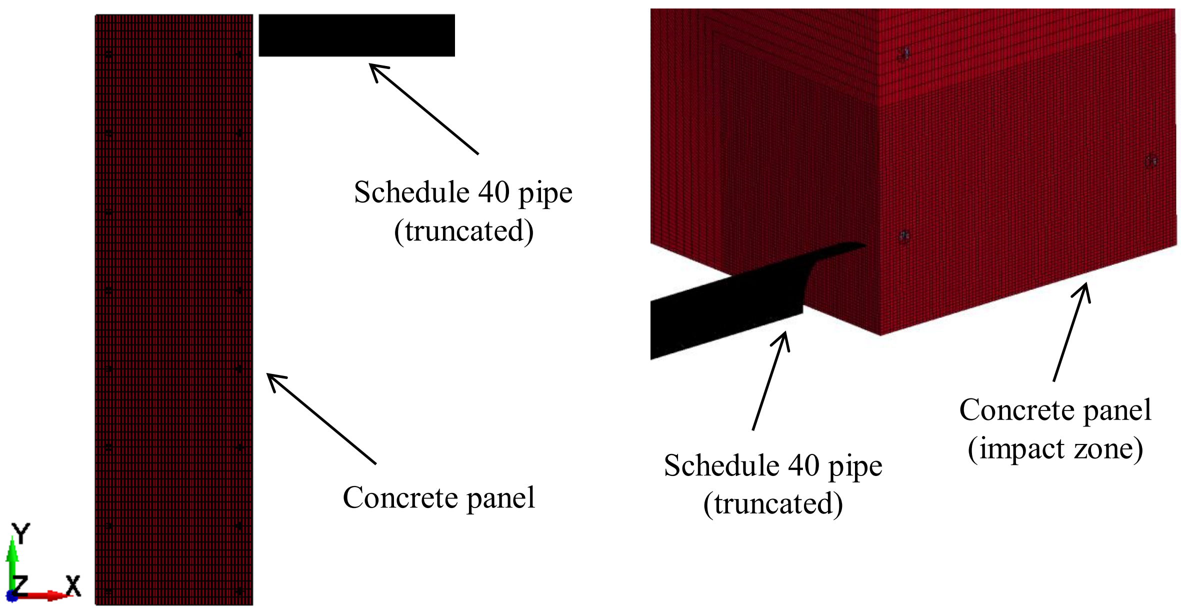

(a) Top view (b) View of impact zone, pipe and panel

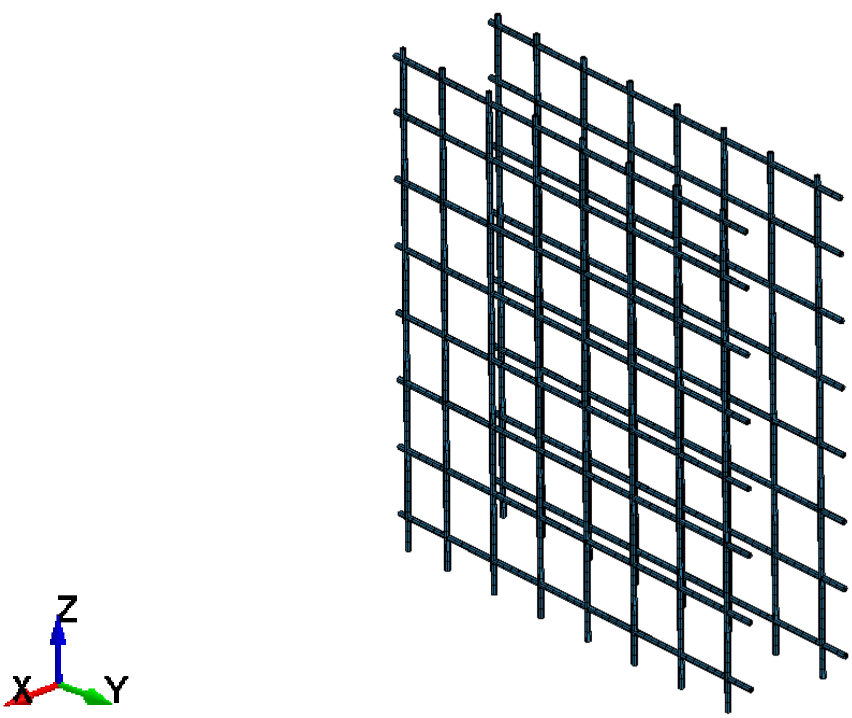

(b) Rebar layout

Figure 4-7: Lagrangian model, 24-inch thick panel

4.3 Schedule 40 Pipe Impact Simulations

4.3.1 Introduction

The following subsections present the results of the Lagrangian simulations of the EPRI impact tests for the purpose of model validation. The matrix of simulations was presented in Table 4-1. The numerically predicted local damage (i.e., front- and back-face crater diameters, scabbing, conical plug diameter, penetration depth, and perforation) is compared with the results of the experiments to aid in the validation exercise. Figure 4-8 shows the impact damage terminology used to evaluate the panels and Figure 4-9 (from Rotz, 1975) cartoons the damage to the panels observed in the Calspan experiments.

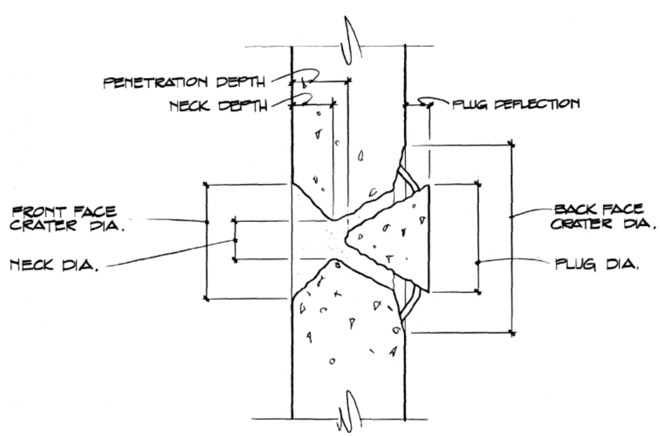

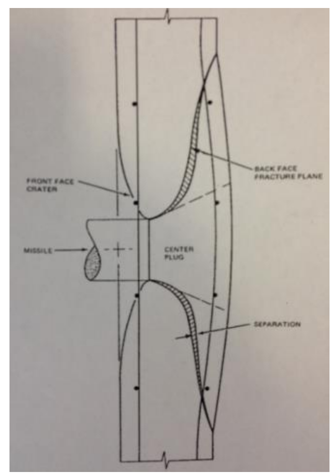

Figure 4-8: Terminology (Stephenson, 1977) Figure 4-9: Damage description (Rotz,1975)

4.3.2 Test 11

In this test, a 743 lb. Schedule 40 pipe impacted a 12-inch panel at a velocity of 98 fps. The missile penetrated the target and caused scabbing on the back (non-impact) face of the panel. Figure 4-10a and Figure 4-10b show the front and back face views, respectively, 10 msec after impact. The results show a considerable amount of scabbing on the back face of the panel.

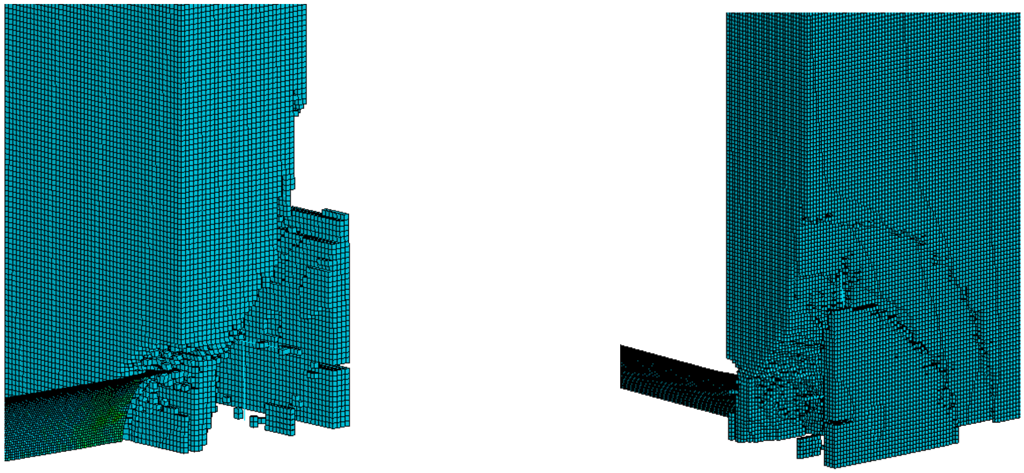

(a) Front face (b) Back face

Figure 4-10: LS-DYNA predicted damage, 10 msec, Test 11, Lagrangian simulation

The local damage on the impact face of the panel from the numerical simulation and the experiment are shown in Figure 4-11a and Figure 4-11b, respectively. The LS-DYNA quarter model was reflected over the XZ and XY planes to present an image of the whole panel. The predicted penetration depth was significantly less than that measured in the experiment.

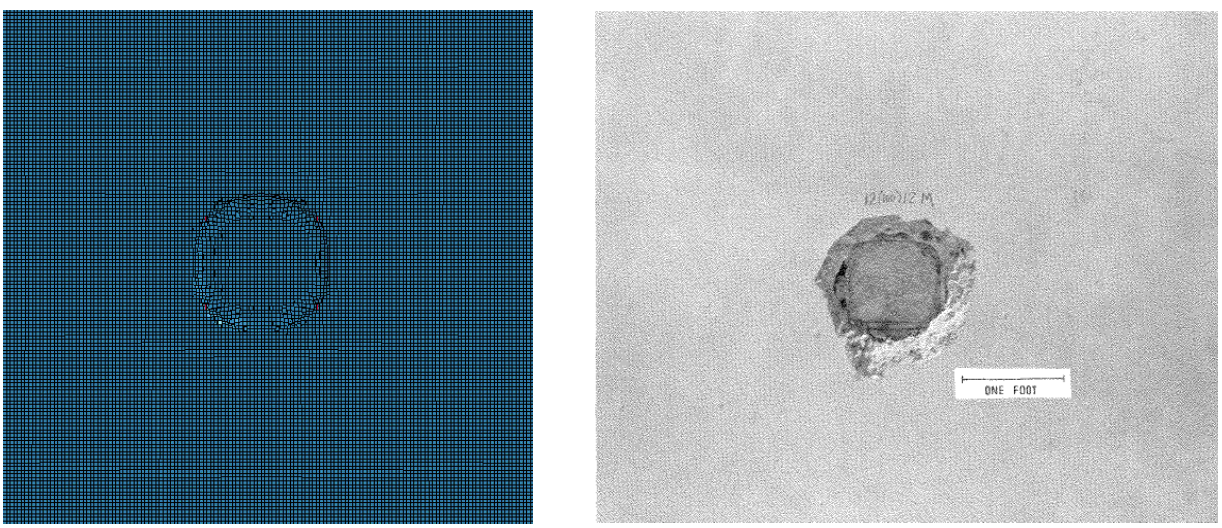

(a) LS-DYNA (b) Experiment

Figure 4-11: Damage on impact face, Test 11, Lagrangian simulation

Figure 4-12a and Figure 4-12b show the local damage to the back (non-impact face) of the panel from the numerical simulation and the experiment, respectively. Significant scabbing of the concrete on the back face was observed in the experiment and predicted well using the numerical model.

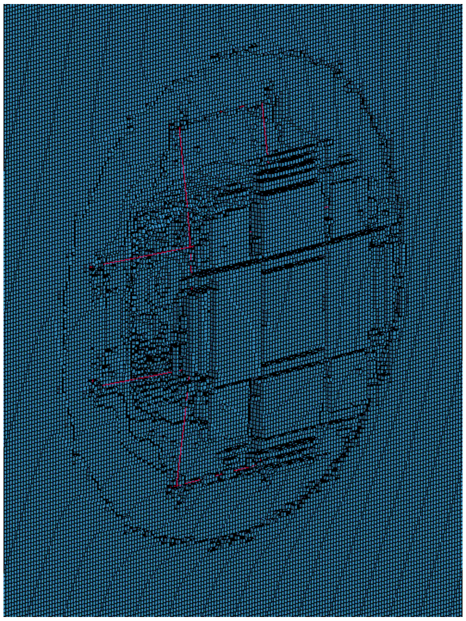

(a) LS-DYNA

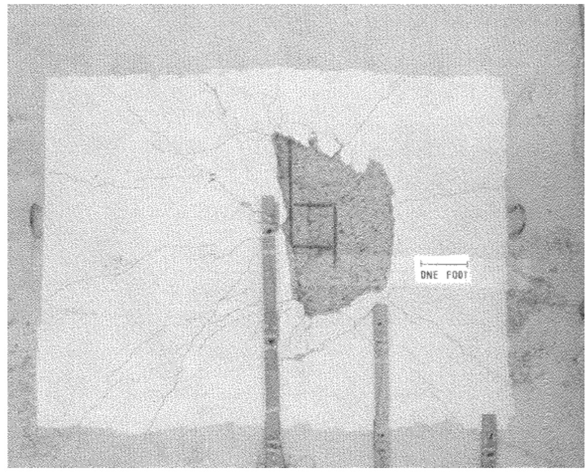

(b) Experiment

Figure 4-12: Damage on rear (non-impact) face, Test 11, Lagrangian simulation

The numerically predicted formation of the conical plug is shown in Figure 4-13a, 6 msec after impact, and is similar to the back-face fracture plane observed by Rotz in the experiments (see Figure 4-9 above). The CSCM concrete model accurately predicts the formation of this conical plug on the back face of the panel after impact. Figure 4-14 presents the impact force history from the experiment (Stephenson, 1977) and the LS-DYNA simulation. The time origin is that from which the missile was accelerated, with impact on the panel at the time shown by the open circle. After impact, (thick dashed line) the missile decelerates. Impact is simulated by imposing an initial velocity on the missile at a distance of one inch from the face of the panel; the force is also calculated as the product of the projectile mass and acceleration to enable a direct comparison of results. The peak forces in the experiment and the simulation match well: 360 kips (1601 kN) and 324 kips (1441 kN), respectively. The simulation over predicts the deceleration of the missile, which is consistent with its under prediction of the penetration.

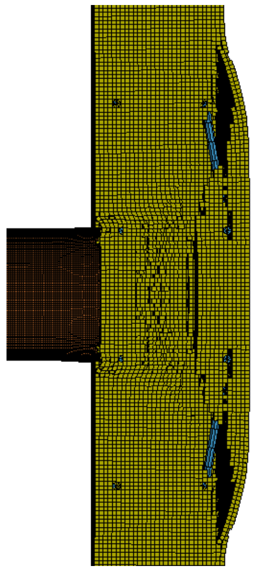

Figure 4-13: Formation of conical plug, 6 msec, Test 11

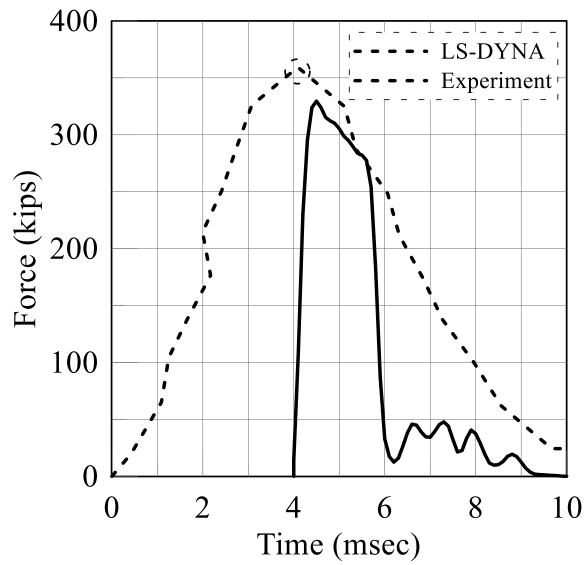

Figure 4-14: Impact force history, Test 11

Table 4-5 presents the impulse (area under the force-time curves in Figure 4-14) values from the numerical simulation and the experiment. The experimental impulse was measured from the point of impact, which is identified in Figure 4-14 by an open circle at approximately 4 msec. The impulse is 28% greater in the experiment, which is expected because the simulation over predicts the deceleration of the missile.

Table 4-5: Impulse values, Test 11, Lagrangian simulation

	Experiment	LS-DYNA
Impulse (kip-msec)	1050	755

Table 4-6 summarizes results obtained from the experiment and the simulation. The simulation results are presented for the complete panel. The simulation reasonably recovers the front and back face crater diameters, plug diameter, and impact force. Significant scabbing was observed in both the experiment and the simulation. However, the model has difficulty recovering the penetration depth of the pipe.

Table 4-6: Results summary, Test 11, Lagrangian simulation

Measurement	Experiment	LS-DYNA	Difference (%)
Front face penetration (in.)	4.5	1.1	75
Front face crater diameter (in.)	15	14	7
Back face crater diameter (in.)	51	50	2
Conical plug diameter (in.)	31	28	10
Back face damage	Scabbing	Scabbing	-
Maximum impact force, F (kips)	360	324	10

The energy histories for the Schedule 40 pipe and panel are presented in Figure 4-15; the kinetic and internal energies and their corresponding eroded energies activated by the removal of failed Lagrangian elements are presented in the figure. The initial energy in the system is the kinetic energy of the pipe $KE_{pipe,i}$ (=27,700 lb-ft or 332411.7 lb-in), and was calculated using equation (4-5) below, where m is one-fourth the mass of the Schedule 40 pipe (= 5.7675 slugs), and v is the initial velocity of the pipe during the experiment (= 98 ft/sec). The predicted values of energy per Figure 4-15 are presented in Table 4-7, where IE_{wall} is the internal energy of the wall, KE_{wall} is the kinetic energy of the wall, IE_{pipe} is the internal energy of the pipe, EE_{KE} is the eroded kinetic energy, EE_{IE} is the eroded internal energy, and E_t is the total energy in the system (also equivalent in this case to $KE_{pipe,i}$). The values of energy were documented at time $t = 20$ msec: a point in time when fluctuation in the energy histories was no longer observed. The energy balance shown in equation (4-6) can be used to ensure that the initial energy in the system is recovered. The initial energy and the total residual energy of the system are effectively identical. A significant amount of energy was eroded (41%) due to the removal of failed elements during the simulation; Figure 4-10 and Figure 4-12 give a sense of the location of the eroded elements on the back face and through the cross section of the panel.

The predicted reaction force history for the 12-inch panel is shown in Figure 4-16. The initial spike in negative force (100 kips) at approximately 1.85 msec is the arrival of the compression wave at the support caused by the pipe impact (0.85 msec for the pipe to reach the wall and 1 msec for the compressive wave to travel from the location of impact to the support). Oscillation is observed after impact, with the force dissipating by approximately 30 msec. The maximum reaction is approximately 305 kips.

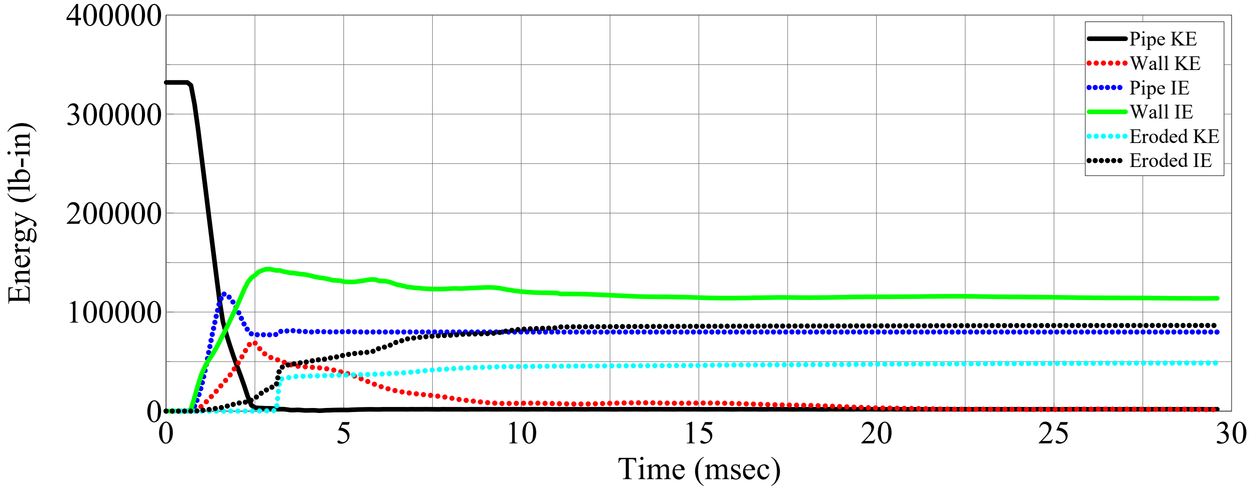

Figure 4-15: Energy plot, Test 11, Lagrangian simulation

$$KE_{pipe,i} = \frac{1}{2}mv^2 \tag{4-5}$$

$$KE_{pipe,i} = IE_{wall} + KE_{wall} + IE_{pipe} + EE_{KE} + EE_{IE} = E_t \tag{4-6}$$

Table 4-7: Summary of energies, Test 11

	$KE_{pipe,i}$	KE_{wall}	IE_{wall}	IE_{pipe}	EE_{KE}	EE_{IE}	E_t
Energy (lb-in)	332411	0	114,000	80,000	48,600	86,000	328,600

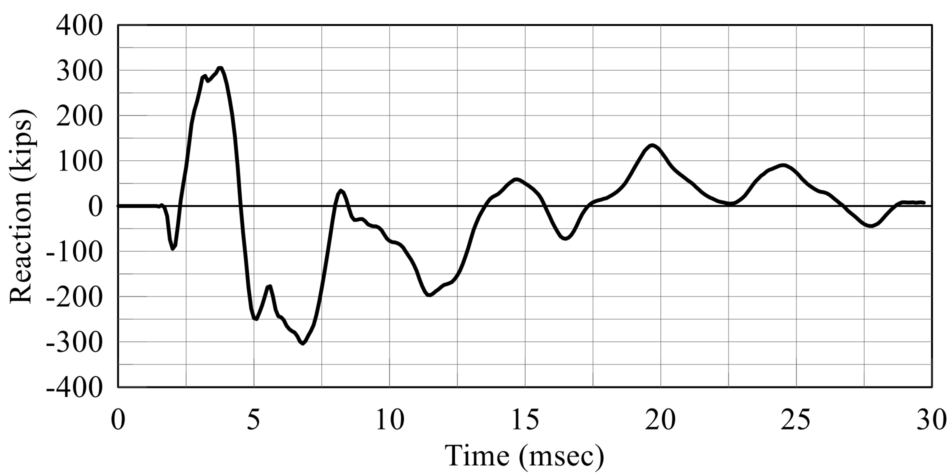

Figure 4-16: Reaction force history, Test 11, Lagrangian simulation

Figure 4-17 shows the evolution of the panel lateral displacement up to 6 msec due to concrete scabbing, which indicates only local response near the point of impact, which is an expected result.

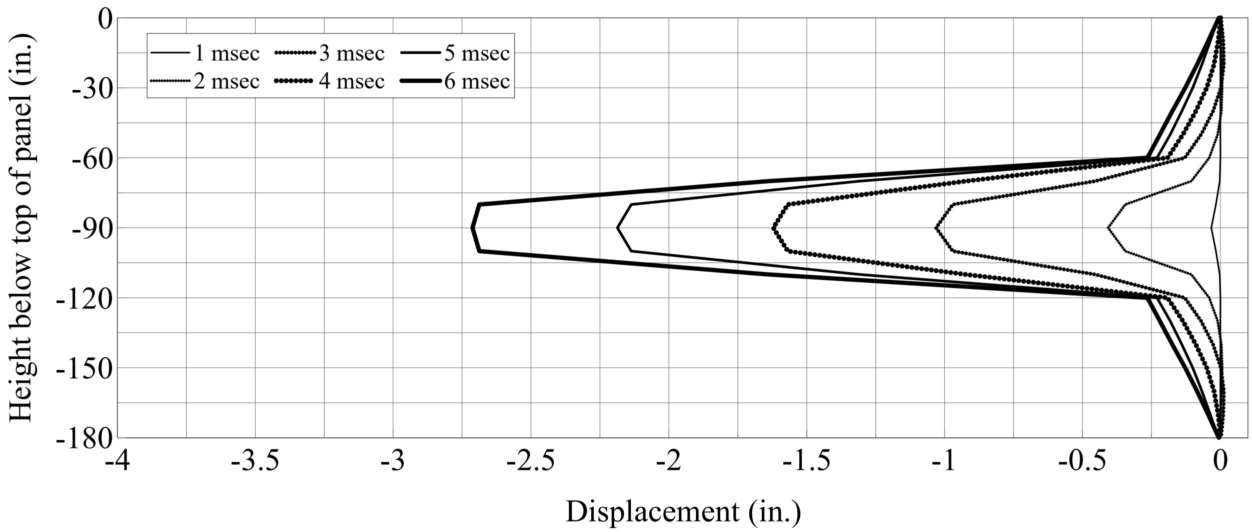

Figure 4-17: Lateral panel displacements, Test 11, Lagrangian simulation

4.3.3 Test 10

A 743 lb. Schedule 40 pipe impacted 12-inch panel wall at a velocity of 143 fps in Test 10, causing perforation of the panel and heavy scabbing on the back (non-impact) face of the wall. The exit velocity of the Schedule 40 pipe was not documented in the experiment. Results of the simulation are shown in Figure 4-18, 20 msec after impact. Figure 4-18a and Figure 4-18b show the damage to the front- and back-face of the panel, respectively; perforation of the panel and scabbing of concrete on the back face are clearly visible.

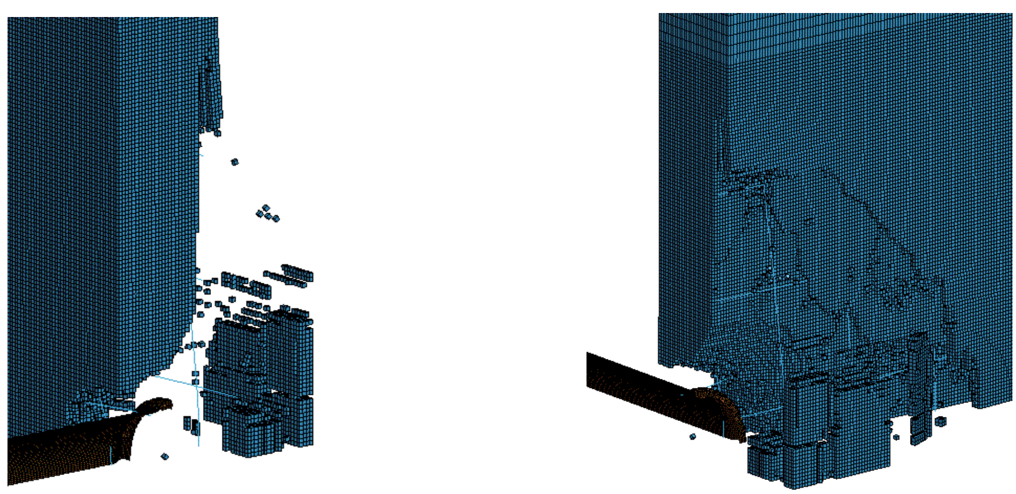

(a) Front face (b) Back face

Figure 4-18: LS-DYNA predicted damage, 20 msec, Test 10, Lagrangian simulation

The local damage to the front face of the panel from the simulation and the experiment, are shown in Figure 4-19a and Figure 4-19b, respectively. Perforation of the concrete panel was observed in the experiment and predicted using the numerical model.

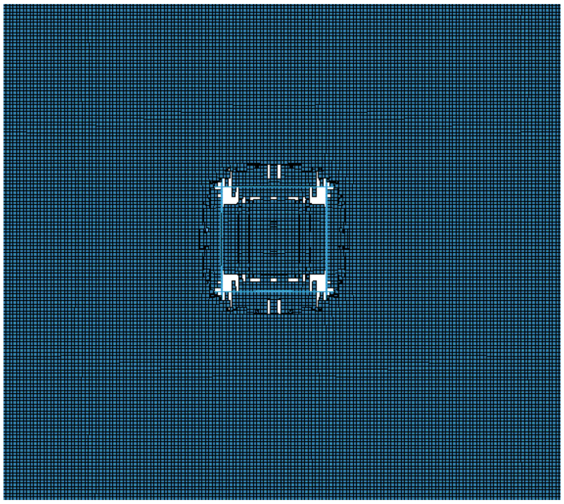

(a) LS-DYNA

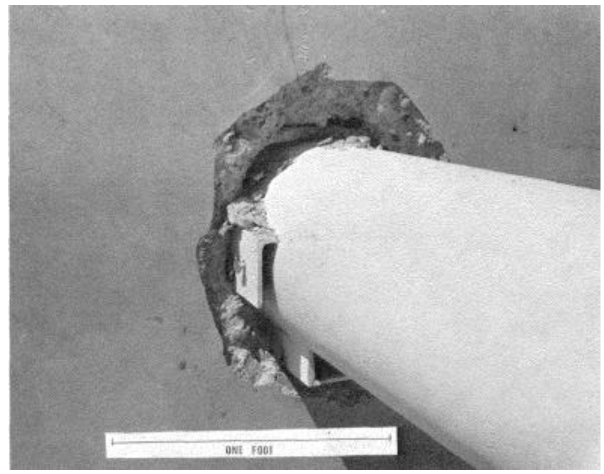

(b) Experiment (Stephenson, 1977)

Figure 4-19: Local damage on impact face, Test 10, Lagrangian simulation

Figure 4-20a and Figure 4-20b show the damage to the rear (non-impact) face of the panel from the numerical simulation and the experiment, respectively.

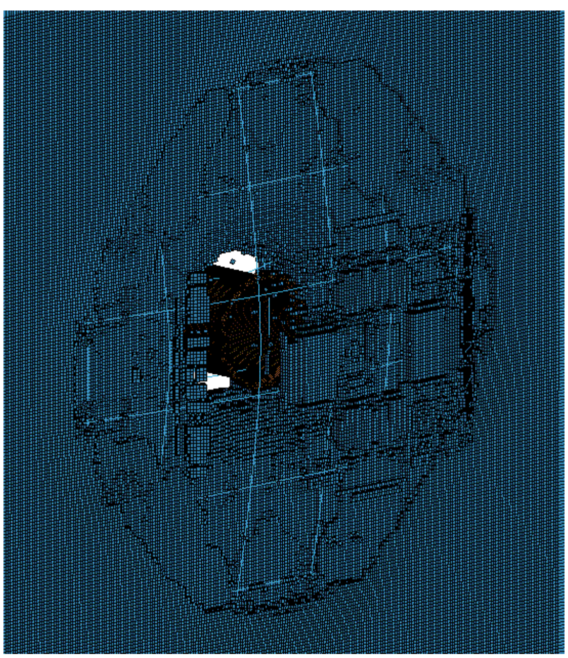

(a) LS-DYNA

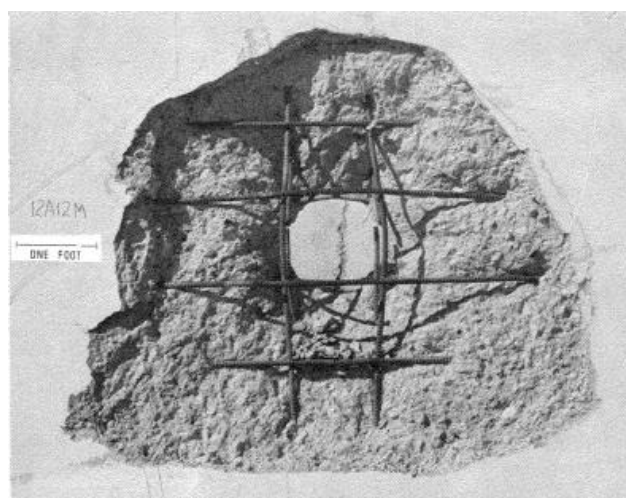

(b) Experiment (Stephenson, 1977)

Figure 4-20: Rear face damage, Test 10, Lagrangian simulation

The formation of the conical plug on the back (non-impact) face is presented in Figure 4-21, 5 msec after impact. The plug is similar in geometry to the failure plane observed by Rotz (1975) in the Calspan experiments (see Figure 4-9). The impact force history is presented in Figure 4-22; the maximum predicted impact force and impulse are approximately 358 kips and 500 kip-msec, respectively. The impact force history from the experiment was not documented.

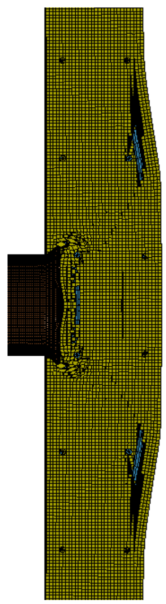

Figure 4-21: Formation of conical plug, 5 msec, Test 10

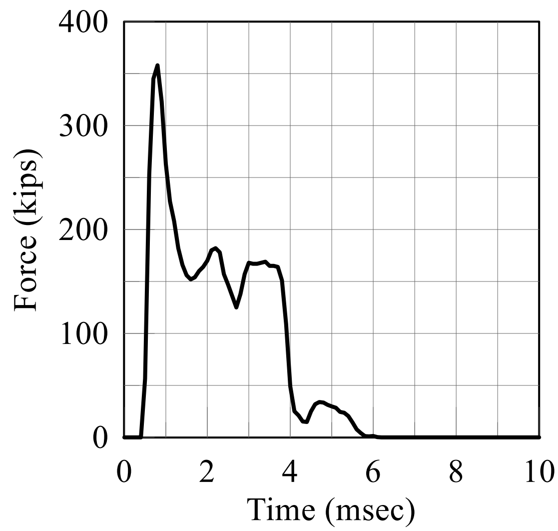

Figure 4-22: Impact force history, Test 10

A summary of results from the experiment and the simulation are presented in Table 4-8. The numerical model accurately recovered the front and back face crater diameters, and predicted perforation of the panel.

Table 4-8: Results summary, Test 10, Lagrangian simulation

Measurement	Experiment	LS-DYNA	Difference (%)
Front face crater diameter (in.)	19.5	18.5	5
Back face crater diameter (in.)	64 - 72	70	3
Back face damage	Perforation	Perforation	-
Maximum impact force, F (kips)	-	358	-

Figure 4-23 presents the energy histories of the Schedule 40 pipe, rebar, and wall panel, including kinetic and internal energies and their corresponding eroded energies activated by removal of failed Lagrangian elements. The damping and hourglass energies are also included in Figure 4-23. The initial energy introduced into the system is the kinetic energy of the pipe,

$KE_{pipe,i}$, (=58970 lb-ft or 707640 lb-in) and calculated using equation (4-5). The kinetic energy of the pipe did not reach zero, indicating a constant residual velocity as the pipe passed through the wall. Table 4-9 presents a summary of energy values taken from Figure 4-23 at 20 msec, where $KE_{pipe,f}$ is the final kinetic energy of the pipe after perforation of the panel, IE_{rebar} is the internal energy of the rebar, KE_{rebar} is the kinetic energy of the rebar, E_{HG} is the hourglass energy, E_D is the damping energy, and EE_{HG} is the eroded hourglass energy. All other variables were defined previously. The energy balance shown in equation (4-7) can be used to ensure that the initial energy in the system is recovered. The initial energy and the total residual energy of the system are effectively identical. A significant percentage of the energy (=31%) was eroded due to the removal of the failed elements during the simulation (see Figure 4-18 and Figure 4-20), which is an expected result since perforation of the panel was observed.

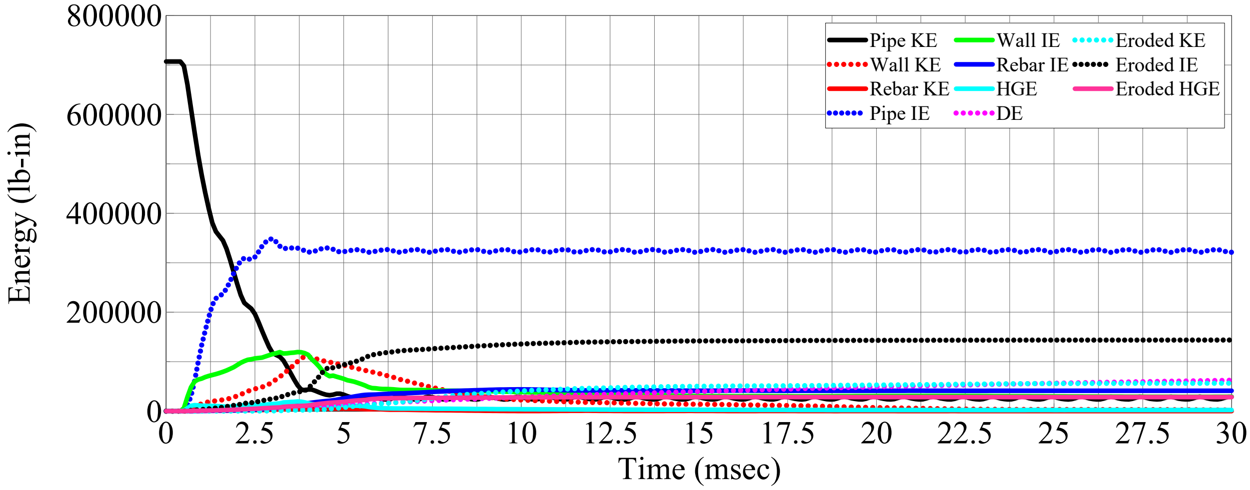

Figure 4-23: Energy plot, Test 10, Lagrangian simulation

Table 4-9: Summary of energies, Test 10

	Energy (lb-in)		Energy (lb-in)
$KE_{pipe,i}$	707640	E_D	42600
IE_{wall}	30300	EE_{KE}	50900
KE_{wall}	12600	EE_{IE}	142000
IE_{pipe}	324000	EE_{HG}	28300
IE_{rebar}	41500	$KE_{pipe,f}$	23900
KE_{rebar}	134	E_t	698734
E_{HG}	2500		

$$
\begin{aligned}
KE_{pipe,i} = IE_{wall} + KE_{wall} + IE_{pipe} + IE_{rebar} + KE_{rebar} + E_{HG} + E_D + EE_{KE} + \\
EE_{IE} + EE_{HG} + KE_{pipe,f} = E_t
\end{aligned}
\tag{4-7}
$$

The predicted reaction force history of the panel is shown in Figure 4-24. The initial spike in negative force (100 kips) at approximately 1.6 msec is the arrival of the compression wave at the support (0.6 msec for the pipe to reach the wall and 1 msec for the compressive wave to travel from the location of impact to the support). The maximum reaction is approximately 260 kips. The evolution of the panel lateral displacement is presented in Figure 4-25; significant local deformation at the midpoint of the panel is indicative of perforation.

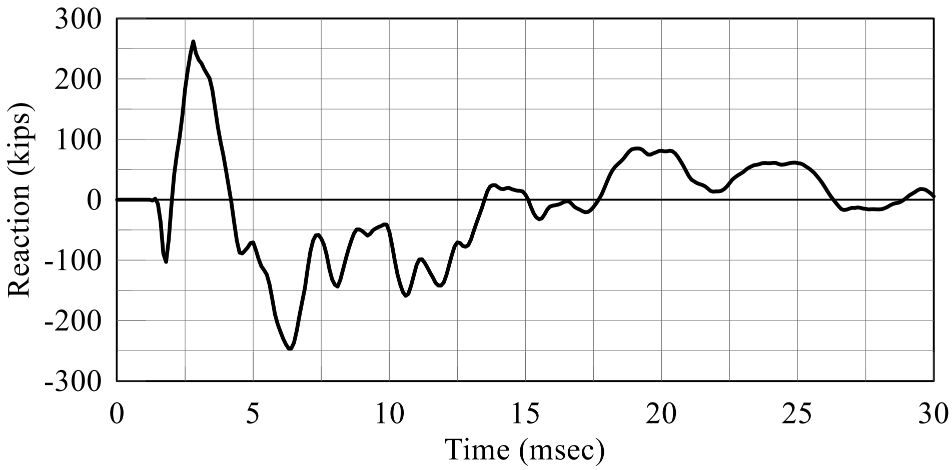

Figure 4-24: Reaction force history, Test 10

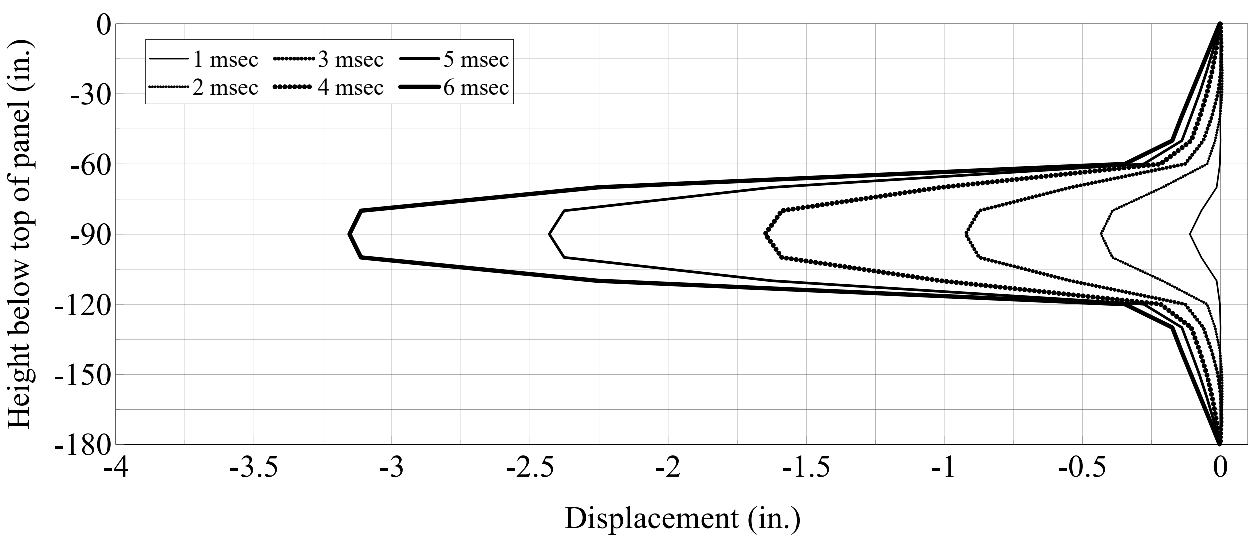

Figure 4-25: Lateral panel displacements, Test 10, Lagrangian simulation

4.3.4 Test 3

In Test 3, a 743 lb Schedule 40 pipe impacted an 18-inch thick panel wall at a velocity of 202 fps. The pipe penetrated the target causing heavy scabbing on the back (non-impact) face of the panel. Figure 4-26 shows the results of the simulation, which terminated at 0.66 msec due to a negative volume error (significant distortion of the elements in the impact zone). The distortion of the solid elements also caused a significant reduction in the time step of the simulation. As discussed in Chapter 2, a local time step is computed for each element in a model as a fraction of the time required for the passage of the dilatational wave across the minimum element dimension. The global time step of the simulation is taken as the minimum value of the local time steps. If elements are highly distorted, the minimum dimension of all distorted elements can be very small, which greatly decreases the time step of the simulation. Penetration of elements was also observed in the simulation, which results in the improper transfer of energy from the projectile to the panel. The keyword MAT000_ADD_EROSION was not activated for this simulation because the goal was to validate, and not the calibrate the numerical model.

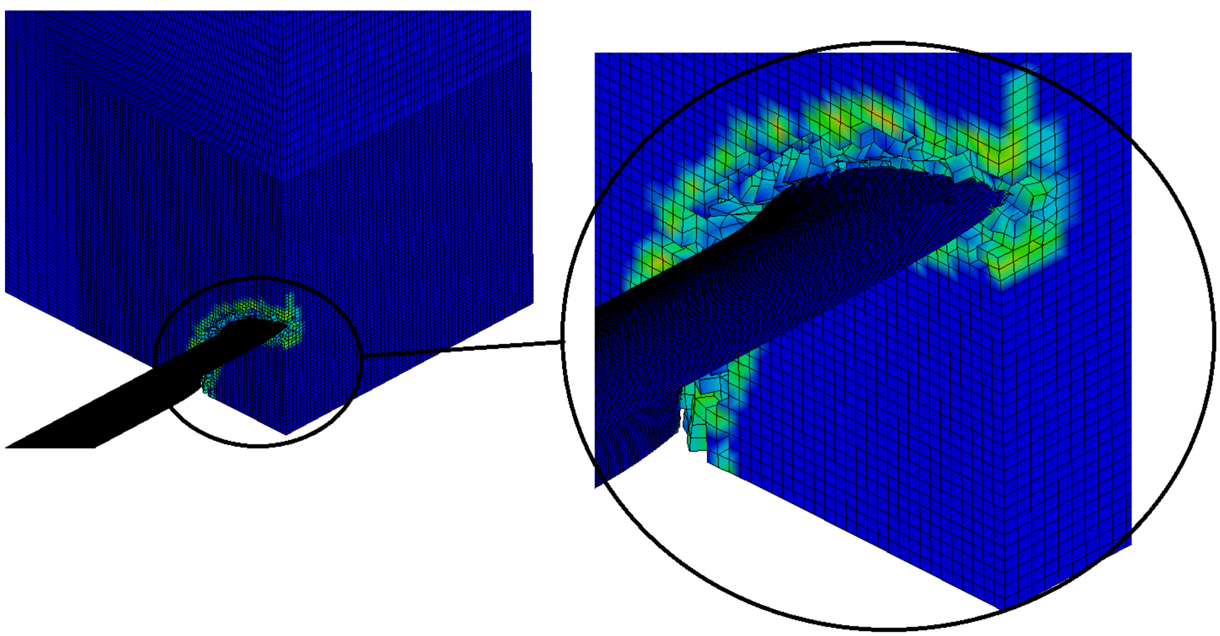

Figure 4-26: Simulation results, 18-inch panel, Test 3, Lagrangian simulation

4.3.5 Test 8

In Test 8, a 743 lb Schedule 40 pipe impact a 24-inch thick concrete panel wall at a velocity of 202 fps. The impact caused penetration of the target and radial cracking on the back (non-impact) face of the panel. The simulation results for the 24-inch panel are shown in Figure 4-27. Significant distortion of solid elements in the impact zone resulted in a diminished time step and termination of the simulation at 0.66 msec due to a negative volume error.

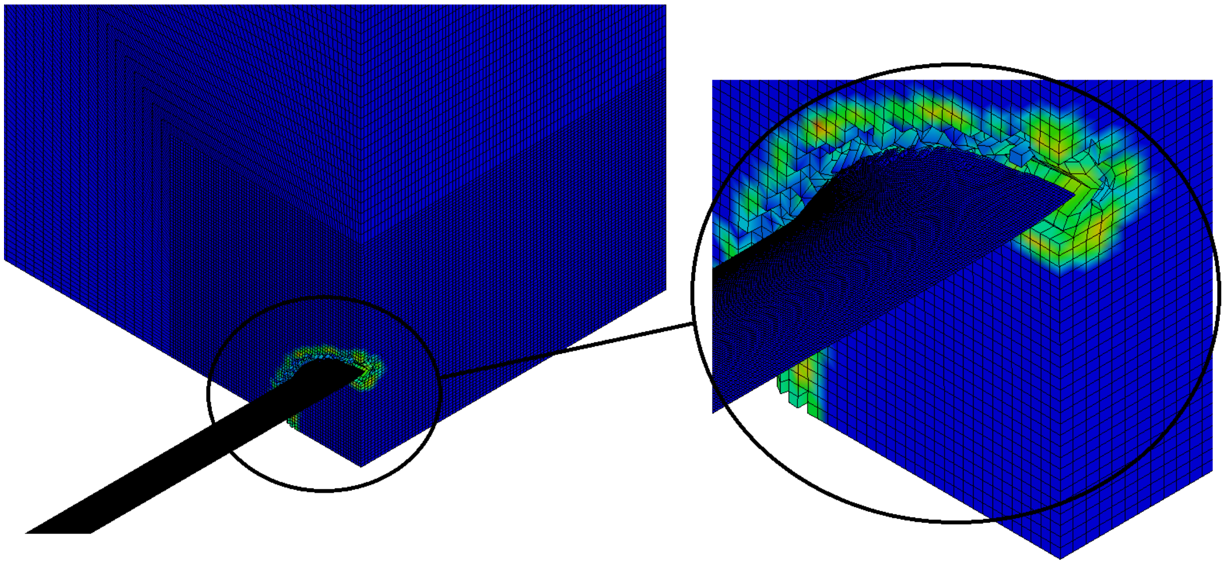

Figure 4-27: Simulation results, 24-inch panel, Test 8, Lagrangian simulation

4.4 Conclusions

Four concrete panel impact tests conducted by EPRI were used to validate, in part, a numerical model in LS-DYNA for impact analysis using the Lagrangian formulation. The analyses of the 12-inch panel (Tests 10 and 11) reasonably reproduced the front- and back-face crater diameters, and the impact force. Perforation of the panel was predicted in Test 10, but the depth of penetration was underestimated in Test 11. Although the impact simulations of the 12-inch panel seemed promising, the shortcomings of the Lagrangian formulation for impact loading (e.g., significant deformation of elements in the impact zone leading to decreased time steps and termination of the simulation due to negative volume error) became apparent in the simulations of the 18- and 24-inch thick panels (Tests 3 and 8). The difficulties in simulating the thicker panels led to exploration of particle-based methods, in particular the axisymmetric SPH formulation. Modeling of test components in LS-DYNA for impact analysis and validation of a numerical model for parametric studies using the axisymmetric SPH formulation are discussed in Chapter 5.

SECTION 5
AXISYMMETRIC SPH IMPACT SIMULATIONS

5.1 Introduction

The smooth particle hydrodynamics (SPH) method, as introduced in Chapter 2, is used here to address some of the shortcomings associated with the use of Lagrangian elements for impact simulations, namely, severe element distortion leading to reduced time step, and negative volume errors. The SPH formulation divides the domain of interest into a set of discrete mass particles that interact over a spacial distance, known as a smoothing length, over which the smoothed displacement field is computed using a kernel function. In the SPH formulation, there is no node-to-element connectivity matrix and the algorithm must search for neighboring particles, which can change at every time step. This allows for very large distortions of an SPH mesh without convergence problems and permits particles to move apart and no longer interact. Large mesh distortions are one significant advantage of the SPH formulation, but SPH simulations are more computationally expensive. One numerical technique that is widely used for impact simulations to limit the number of particles (which correlates to a reduction in computational demand) is the axisymmetric model, which represents a slice of a 3D model. If rotated around the reference Cartesian coordinate system, an axisymmetric model would recover the 3D model. This enables the use of small particle spacing and limits the computational expense. The axisymmetric SPH formulation is employed in this chapter for impact simulations.

As noted in Section 2.3, LS-DYNA (LSTC, 2012) includes three concrete material models compatible with the SPH formulation: Pseudo_Tensor (MAT016), Concrete_Damage (MAT072R3), and CSCM (MAT159). The quasi-static behavior of these material models is investigated using 3D models of a cylinder of concrete comprised of a) SPH particles, and b) Lagrangian elements. Results are presented in Section 5.2. The failure surfaces in shear for each material model and their effect on results of the impact simulations on concrete panels are discussed in Section 5.2.

Data from the EPRI experiments (Stephenson, 1977) are used here to validate, in part, a numerical model for impact analysis. Formal validation is not possible because insufficient data were collected from the experiments, as discussed later in this report. Table 5-1 summarizes the experiments simulated in this chapter, including EPRI test number, concrete uniaxial compressive strength, f_c', panel thickness, t, projectile velocity at impact, v, and observed local damage. These tests involved 12-inch (305 mm) to 24-inch (610 mm) thick reinforced concrete panels normally impacted (i.e., at 90°) by a 12-inch (305 mm) diameter Schedule 40 pipe at velocities ranging from 98 fps (30 m/s) to 202 fps (62 m/s). Section 5.3 discusses modeling techniques in LS-DYNA for impact simulations using an axisymmetric SPH finite element model, including contact, boundary conditions, element formulations, strain-rate effects, and equations of state. The Grid Convergence Index (GCI), a method used to measure discretization error in finite element simulations is used to evaluate mesh convergence in the numerical models; GCI formulae are presented in Section 5.4.

Table 5-1: Simulated experiments

Test	Panel t, mm (in)	v m/s (fps)	f_c' MPa (psi)	Projectile	Panel damage per Stephenson (1977)
11	305 (12)	30 (98)	24.8 (3600)	Schedule 40 pipe	Pipe penetrated panel , scabbing on the back face
10	305 (12)	44 (143)	25.5 (3700)	Schedule 40 pipe	Pipe perforated panel, scabbing on the back face
3	457 (18)	62 (202)	23.4 (3400)	Schedule 40 pipe	Pipe penetrated panel, scabbing on back face
8	610 (24)	62 (202)	26.2 (3800)	Schedule 40 pipe	Pipe penetrated panel, radial cracking on back face

Section 5.5 investigates wall panel behavior as a function of the three concrete models available in LS-DYNA for SPH calculations (i.e., MAT016, MAT072R3, and MAT159). Test 11 (see Table 5-1) is used for this study; the concrete compressive strength was increased to 4500 psi to accommodate the CSCM material model in the simulations, which is applicable for uniaxial concrete compressive strengths ranging from 4061 to 8412 psi (Murray et al., 2007). The uniaxial concrete compressive strength is used in all three material models as an input to internally generate parameters describing the elastic response and inelastic response including shear failure envelope, compressibility (compaction) and tensile failure.

Test 11 (see Table 5-1) was simulated using MAT016 and MAT072R3; the reported uniaxial concrete compressive strength (=3600 psi) was used for the simulations. The values for the concrete parameters describing the elastic and inelastic response of the concrete were generated internally by the material-model code using only the uniaxial concrete compressive strength as input. The two material models estimated the uniaxial tensile strength of the concrete to be approximately 10% of the uniaxial compressive strength. Results of these simulations are presented in Section 5.6. The CSCM material model was not used for these calculations because the concrete strength (=3600 psi) falls outside the bounds (4061 psi to 8412 psi) identified by Murray et al. (2007a) for parameter generation. The poor correlation of predicted and observed damage (e.g., perforation of the panel in the simulations and not in the experiment) seen in Section 5.6 prompted an investigation of the effects of concrete compressive (Section 5.7) and tensile (Section 5.8) strength on the impact resistance of reinforced concrete panels. The material and test parameters from Test 11, and MAT072R3[5] were used for these studies. The uniaxial compressive and tensile strengths of the concrete significantly affected the local response of the panel, especially the perforation resistance. Based on these findings, the Schedule 40 pipe impact simulations of Tests 11, 10, 3, and 8 (see Table 5-1) were then simulated using MAT072R3 with concrete tensile strength set equal to 15% of compressive strength (i.e., approximately 5% greater than that generated internally by the material-model codes in Section 5.6). The results of these simulations and a comparison with the EPRI test experiments are presented in Section 5.9.

The impact tests conducted by EPRI characterized the behavior of (reinforced) concrete panels impacted by deformable missiles at velocities consistent with those possible in extreme wind events such as hurricanes and tornados. Section 5.10 presents results of a study on normal impact on concrete panels by a) solid cylindrical steel missiles having the same mass as the Schedule 40 pipe, and b) rigid, solid cylindrical missiles having the same mass as the Schedule 40 pipe. EPRI tests 3, 8, 10 and 11 (see Table 5-1) provide much of the basis for these simulations. Results of the solid and rigid missile simulations are presented, and these are compared with those of the Schedule 40 annular pipes of Section 5.9.

The key findings of the chapter are identified in Section 5.11 and provide a framework for the parametric studies on wind-borne missile impact presented in Chapter 6.

5.2 Benchmarking Concrete Material Models using the SPH Formulation

5.2.1 Unconfined Cylinder Simulations

A concrete cylinder with a diameter and height of 400 mm (Figure 5-1a) was constructed in LS-DYNA using SPH particles to investigate the quasi-static behavior of different concrete material

[5] Of the three concrete material models investigated in this chapter, the MAT072R3 is the only model that allows the user to specify tensile strength.

models that are compatible with the SPH formulation. The uniaxial concrete compressive strength of the concrete was 45.6 MPa. A Lagrangian model with the same dimensions (Figure 5-1b) was created to aid in the comparison of the SPH and Lagrangian formulations for various material models under quasi-static loading. The material models considered in this study were MAT016, MAT072R3, and MAT159. The LS-DYNA input parameters are presented in Table 5-2, where ρ is density, G is shear modulus, f_c' is concrete compressive strength, f_t' is concrete tensile strength, and d_{agg} is aggregate diameter. The "-" in the cells indicates that this parameter was not a required input for the material model.

The Lagrangian cylinder (as seen in Figure 5-1b) was subjected to different rates of loading by applying a constant velocity to all nodes on the top face of the cylinder, corresponding to a specific strain rate. The axial stress in the Lagrangian cylinder was calculated by summing the nodal forces on the bottom face and dividing it by the area of the concrete cylinder. The SPH cylinder was subjected to different strain rates by applying a constant velocity to a rigid shell plate (labeled in Figure 5-1a) that contacts and compresses the concrete cylinder in the axial direction. The contact between the shell elements and SPH particles was defined using the *CONTACT_NODES_TO_SURFACE keyword. The MST option in the contact keyword, defined as the shell thickness, was set equal to the particle pitch. Simulations were conducted for SPH particle spacings of 4, 8, 16, and 25 mm to demonstrate mesh convergence. The meshes for particle spacings of 4, 8, 16, and 25 mm, are presented in Figure 5-2a through Figure 5-2d, respectively. The axial stress imposed on the cylinder by the rigid plate was calculated by summing the nodal forces on the plate and dividing it by the area of the concrete cylinder. The keyword *BOUNDARY_SPH_SYMMETRY_PLANE was used to create the boundary conditions at the bottom of the cylinder.

Figure 5-3, Figure 5-4, and Figure 5-5 show the uniaxial stress-strain behavior of the Lagrangian cylinder (see Figure 5-1b) using concrete material models MAT072R3, MAT016, and MAT159, respectively, at nominal strain rates of 0.0005/s, 0.005/s, 0.05/s, 0.25/s, and 1/s. The axial stress-strain curves are similar for strain rates of 0.0005/s, 0.005/s, 0.05/s and 0.25/s, however, dynamic behavior was observed using a strain rate of 1/s (e.g., oscillation in the stress-strain curve). Since the axial stress-strain behavior at a strain rate of 0.25/s is similar to that using a strain rate of 0.0005/s, which is representative of quasistatic loading, the strain rate of 0.25/s was used in the

SPH cylinder simulations to characterize the behavior of the material models using the SPH formulation. The use of a larger strain rate reduces the computation time.

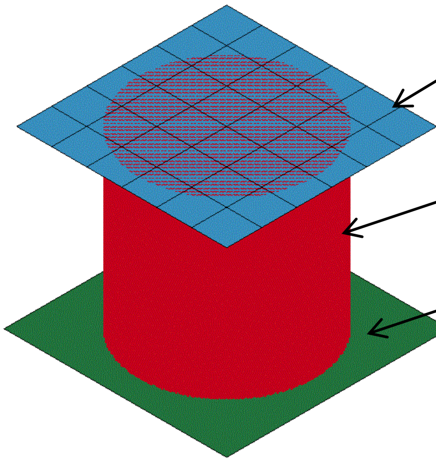

(a) SPH formulation

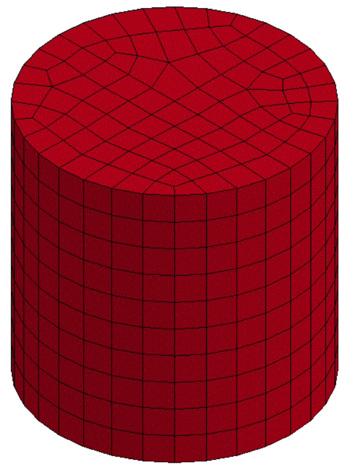

(b) Lagrangian formulation

Figure 5-1: Concrete cylinder models

Table 5-2: Concrete material inputs

	ρ (g/mm^3)	G (MPa)	ν	f_c' (MPa)	f_t' (MPa)	d_{agg} (mm)
MAT072R3	0.00217	-	0.15	45.6	4.56	-
MAT016	0.00217	4600	0.15	45.6	-	-
MAT159	0.00217	-	-	45.6	-	19

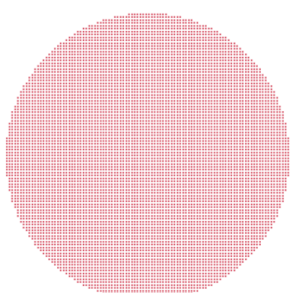

(a) 4 mm

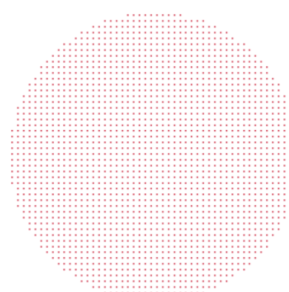

(b) 8 mm

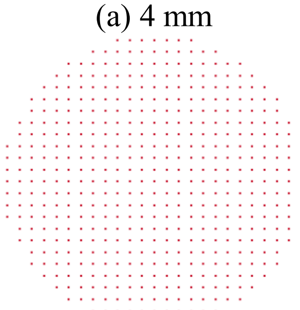

(c) 16 mm

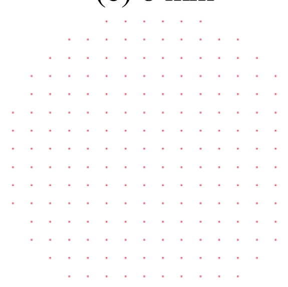

(d) 25 mm

Figure 5-2: SPH meshes of a 400-mm diameter concrete cylinder

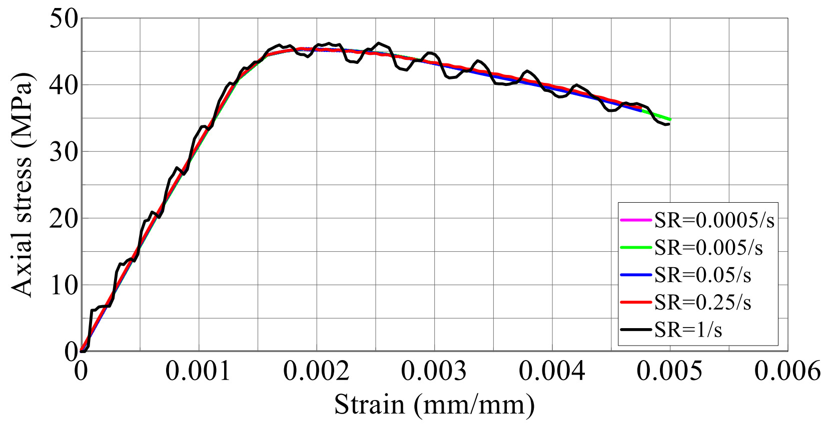

Figure 5-3: Lagrangian concrete cylinder behavior, MAT072R3

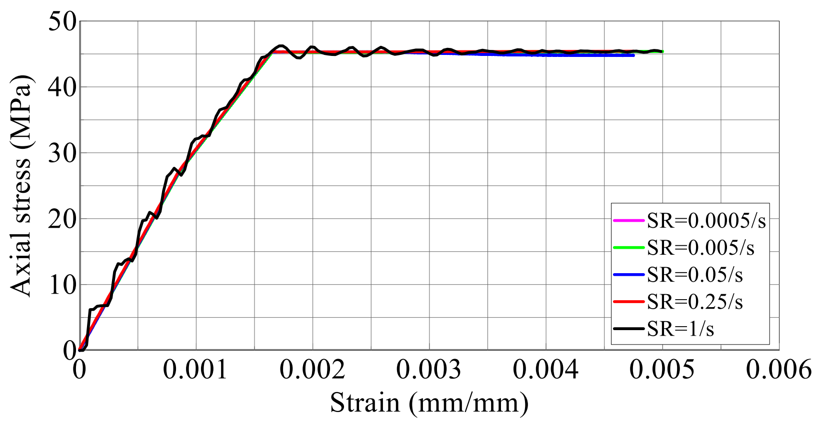

Figure 5-4:Lagrangian concrete cylinder behavior, MAT016

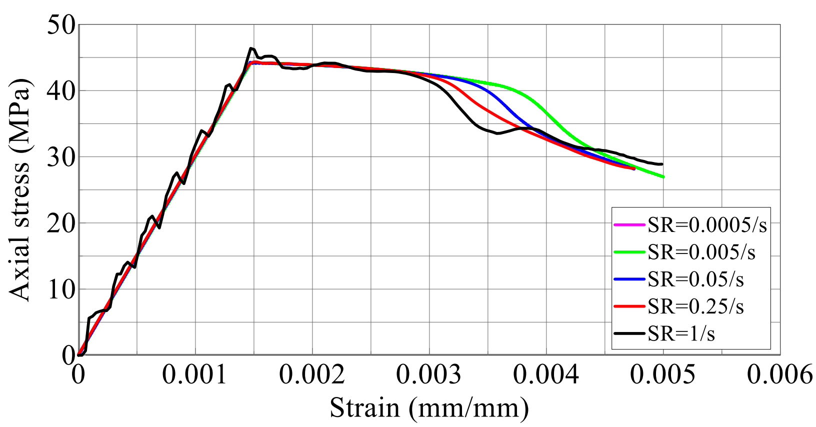

Figure 5-5: Lagrangian concrete cylinder behavior, MAT159

The uniaxial stress-strain behavior of the SPH concrete cylinder using the MAT072R3 material model is shown in Figure 5-6a, for a strain rate of 0.25/s. The curves are presented for particle spacings of 4, 8, 16, and 25 mm. Results of analysis using a particle spacing of 2 mm were identical to those of the 4 mm mesh, and so 4 mm was assumed to be a converged mesh size.

The particle spacings of 4 and 8 mm reasonably recover the compressive strength (=45.6 MPa) and elastic modulus of the concrete (=32000 MPa). The elastic moduli (concrete compressive strength) using the 16 and 25 mm mesh pitches are 20000 MPa (40 MPa) and 16666 MPa (37 MPa), respectively. The underestimation of compressive strength and elastic modulus using the coarser pitches highlight the effect of particle density on the results of the simulations and the importance of conducting mesh-refinement studies. Another important observation is that compressive strength drops immediately to zero in strain space after peak strength is reached, suggesting there is no post-peak softening of the unconfined SPH cylinder using MAT072R3. The effects of confinement on the stress-strain behavior of MAT072R3 in the SPH formulation is investigated in Section 5.2.2. The stress-strain response of an unconfined Lagrangian cylinder is also presented in Figure 5-6a for the purpose of comparison. Based on the results of the SPH cylinder with the finest mesh (=4 mm), both the SPH and Lagrangian formulations predict similar compressive strengths and elastic moduli, but post-peak softening is observed only with the Lagrangian model.

The distribution of von Mises stress in the cylinder with a mesh size of 4 mm, at time of peak strength (=6 msec), shown in Figure 5-6b, is not uniform: the inner core of the cylinder reaches the compressive strength (=45.6 MPa), the stresses in the particles in contact with the shell elements are slightly greater than the compressive strength (=48.7 MPa), and the stresses in the particles on the outer edges of the cylinder are less than the compressive strength (=39 MPa).

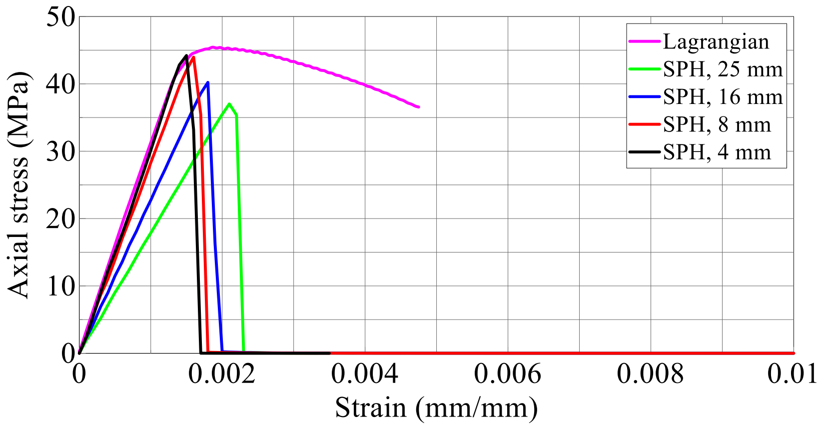

(a) Stress-strain curves

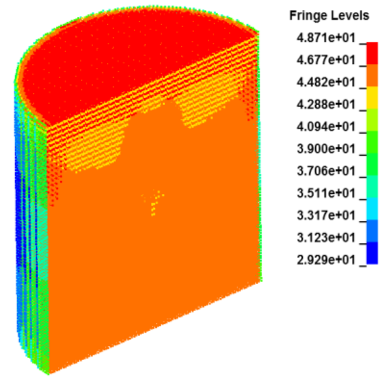

(b) Von Mises stress, 4 mm

Figure 5-6: Concrete cylinder behaviors, MAT072R3, SR=0.25/s

Figure 5-7a and Figure 5-8a present the uniaxial stress-strain curves for material models MAT016, and MAT159, respectively, at a strain rate of 0.25/s. The curves are shown for particle pitches of 4, 8, 16, and 25 mm. The simulation results using the 4 and 8 mm mesh pitches reasonably recover the concrete compressive strength (=45.6 MPa) and elastic modulus (=32000 MPa) for MAT016 and MAT159. Similarly to the simulation results using the MAT072R3 material model (see Figure 5-6a), the 16 and 25 mm mesh pitches underestimate the compressive strength and elastic modulus. The material model MAT159 exhibits post-peak softening behavior, whereas MAT016 exhibits elastic-plastic behavior, and drops to zero stress after the failure strain is reached. The failure strain of MAT016 is strongly dependent on the particle density for the unconfined cylinder. The effects of confinement on MAT016 are investigated in Section 5.2.2.

The stress-strain behavior of the Lagrangian cylinder is also presented in Figure 5-7a and Figure 5-8a for material models MAT016 and MAT159, respectively, at a strain rate of 0.25/s. The behavior of the concrete material models using the Lagrangian formulation is similar to that using the SPH formulation. The distribution of von Mises stresses in the SPH cylinders at time of peak strength is presented in Figure 5-7b and Figure 5-8b for material models MAT016 and MAT159, respectively. Similar to the behavior observed using the MAT072R3 material model, a relatively uniform distribution of von Mises stresses was observed using MAT016 and MAT159; non-uniformities exist for the particles on the outer perimeter of the cylinder and directly in contact with the rigid plate.

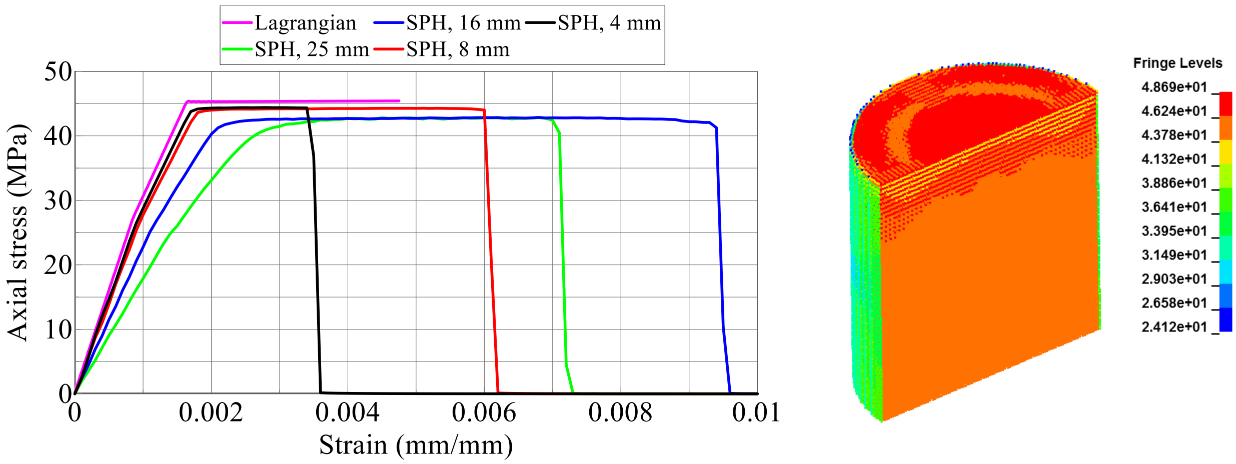

(a) Stress-strain curves

(b) Von Mises stress, 4 mm mesh

Figure 5-7: Concrete cylinder behaviors, MAT016, SR=0.25/s

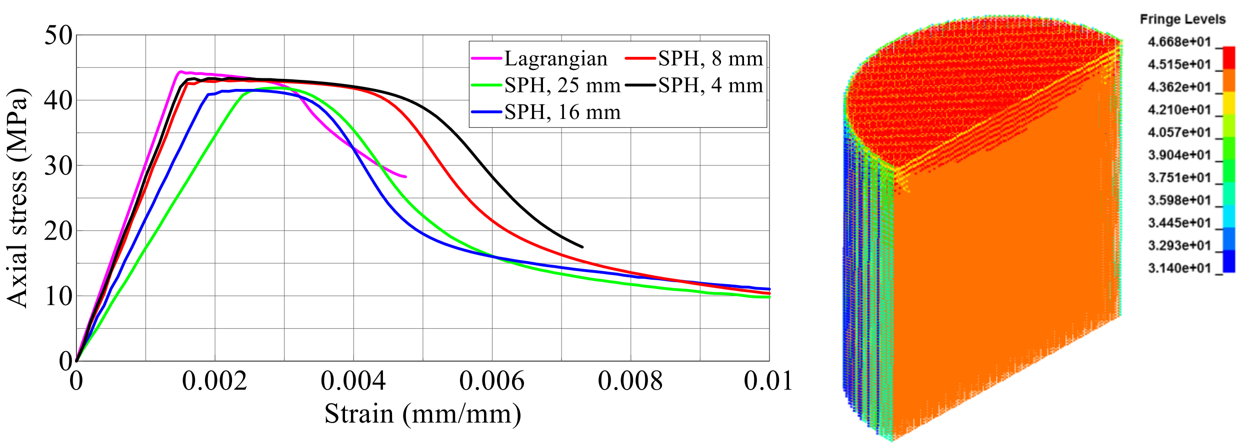

(a) Stress-strain curves

(b) Von Mises stress, 4 mm mesh

Figure 5-8: Concrete cylinder behaviors, MAT159, SR=0.25/s

The uniaxial stress-strain curve for all three material models using the SPH formulation (4 mm particle spacing) is presented in Figure 5-9. All three material models recover similar peak strengths and elastic moduli. However, the material responses are significantly different post peak: MAT159 softens, MAT072R3 drops to zero stress, and MAT016 exhibits elastic-plastic behavior. Impact simulations using all three material models are discussed later in this chapter to investigate the effects of panel response as a function of concrete material model.

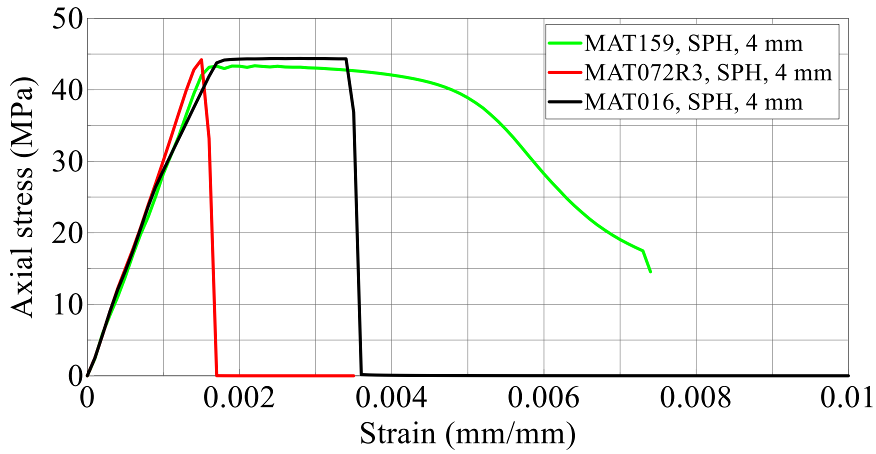

Figure 5-9: Stress-strain behavior, all concrete materials

5.2.2 Confined Cube Simulations

5.2.2.1 *Introduction*

The unconfined, quasi-static SPH cylinder simulations presented in Section 5.2.1 showed that: 1) MAT072R3 predicts an elastic modulus and compressive strength similar to that of the Lagrangian cylinder, but does not predict the post-peak softening observed in the Lagrangian simulation, and 2) the elastic-plastic behavior of MAT016 is similar to that of the Lagrangian cylinder, but the stress in the SPH cylinder drops immediately to zero after the failure strain is reached: behavior not observed in the Lagrangian simulation. The SPH formulation suffers from tensile instabilities (e.g., bunching of nodes and formation of artificial voids (Mehra et al., 2012)) and this is likely the cause of the differences in response of the SPH and Lagrangian cylinders using concrete models MAT072R3 and MAT016.

This section investigates the quasi-static behavior of MAT072R3 and MAT016 for small magnitudes of confinement (on the order of 0.2% to 2% of the concrete compressive strength (=45.6 MPa). The goal is to overcome the tensile instabilities of the SPH formulation observed in the unconfined simulations and predict stress-strain behavior similar to that of the unconfined Lagrangian cylinder without enhancing its strength due to confinement. A 400 mm × 400 mm × 400 mm concrete cube (Figure 5-10a) was constructed using SPH particles due to the ease of imposing a confining pressure on a flat surface of particles. A Lagrangian cube with the same dimensions (Figure 5-10b) was created to aid in the comparison of results using the SPH and Lagrangian formulations. The uniaxial concrete compressive strength of the concrete was 45.6 MPa; the LS-DYNA input parameters for MAT072R3 and MAT016 are those presented in Table

5-2. The methods used to load the cubes at different strain rates and the calculation of the axial stresses for the SPH and Lagrangian cubes are similar to those described in Section 5.2.1 for the unconfined simulations. The contact between the shell elements and SPH particles (see Figure 5-10a) was defined using the *CONTACT_NODES_TO_SURFACE keyword. The MST option in the contact keyword, defined as the shell thickness, was set to the particle pitch. The keyword *BOUNDARY_SPH_SYMMETRY_PLANE was used to create the boundary conditions at the bottom of the cube, as shown in Figure 5-10a. The confining pressure was imposed on the faces of SPH cube using the *LOAD_NODE_SET keyword.

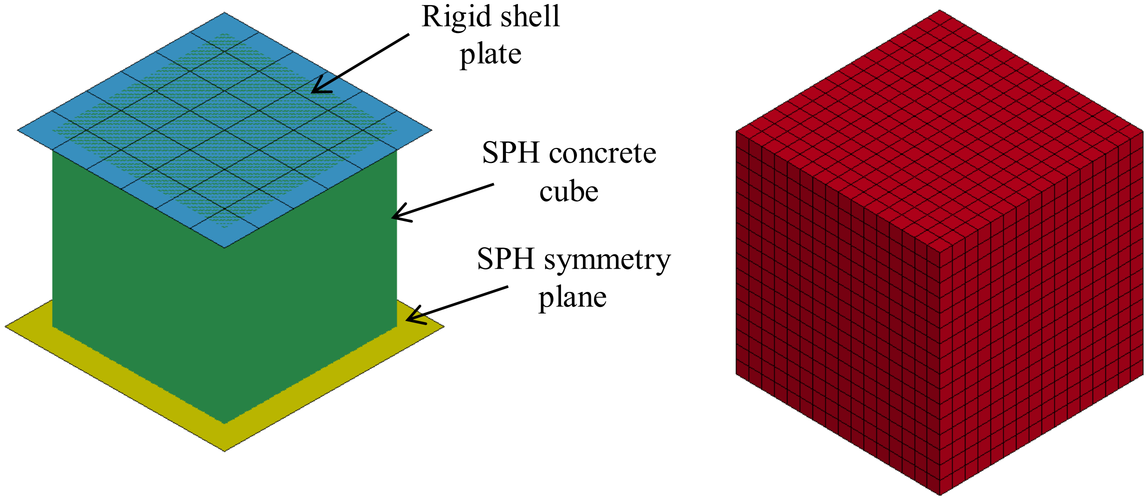

(a) SPH formulation (b) Lagrangian formulation

Figure 5-10: Concrete cube models

5.2.2.2 *Karagozian and Case (MAT072R3)*

The unconfined axial stress-strain behavior of the SPH concrete cube using the MAT072R3 material model is shown in Figure 5-11, for a strain rate of 0.25/s. The curves are presented for particle spacings of 4, 8, 16, and 25 mm to identify a converged mesh. The unconfined stress-strain behavior of the Lagrangian cube is also presented in Figure 5-11. Similar to the unconfined cylinder simulations presented in Section 5.2.1, the results using a mesh spacing of 4 and 8 mm predict an elastic modulus and compressive strength similar to that of the Lagrangian cube, but post-peak softening is not predicted.

Figure 5-12 presents the unconfined stress-strain behavior of the Lagrangian cube and the unconfined and confined stress-strain behavior of the SPH cube. Confining pressures of 0.1 MPa, 0.5 MPa, and 1 MPa were considered in this study, which correspond to 0.2%, 1%, and 2% of the concrete compressive strength. Since the 4 and 8 mm particle spacings predicted similar results in the mesh convergence study (see Figure 5-11), the cube simulations with the 8 mm particle spacing were used to generate the stress-strain curves to reduce the computational demand. The SPH cube with a confinement pressure of 0.1 MPa predicts an elastic modulus, peak strength, and post-peak strain softening similar to that of the unconfined Lagrangian cube. Confinement pressures of 0.5 MPa and 1 MPa, predict the elastic modulus with reasonable accuracy, but overestimate the compressive strength by 3% and 10%, respectively. The results indicate that small magnitudes of confinement (on the order of 0.2% of the concrete compressive strength) does not enhance the strength of the concrete and enables the SPH formulation to predict results similar to that of the Lagrangian cube simulation using MAT072R3. Schwer (2008b) stated that confining pressures on the order of 100 MPa are typically observed in penetration simulations, which is approximately 1000 times greater than the confining pressure required to recover the behavior similar to that of the Lagrangian formulation.

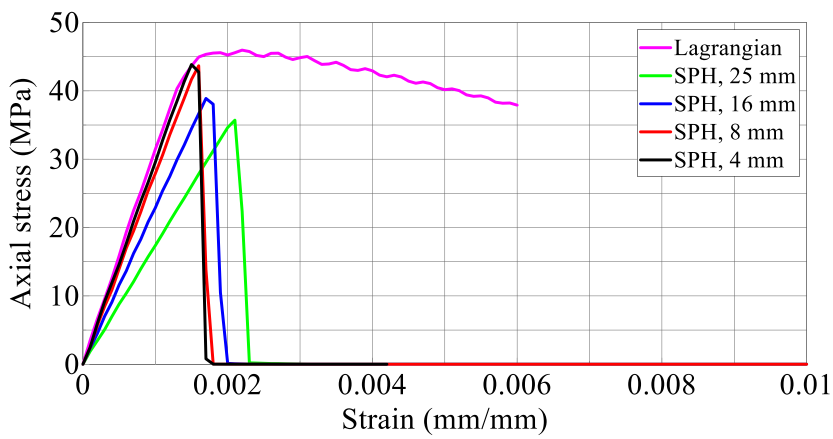

Figure 5-11: Unconfined concrete cube behavior, MAT072R3, SR=0.25/s

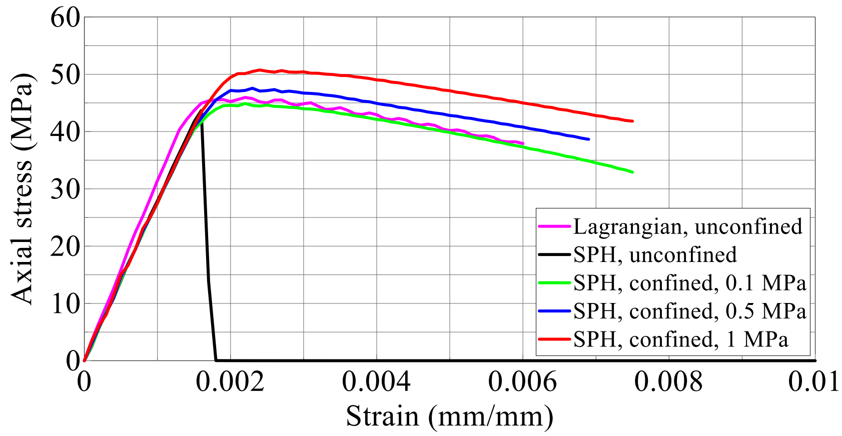

Figure 5-12: Confined concrete cube behavior, MAT072R3, SR=0.25/s

5.2.2.3 ***Pseudo Tensor (MAT016)***

Figure 5-13 shows the unconfined axial stress-strain behavior of the SPH concrete cube using MAT016, for a strain rate of 0.25/s. The results are shown for particle spacings of 4, 8, 16, and 25 mm. The stress-strain behavior of the Lagrangian cube is also presented in Figure 5-13. The 4 and 8 mm particle spacings reasonably recovered the elastic modulus and elastic-plastic behavior predicted using the Lagrangian cube, but the failure strain of the SPH cube is strongly dependent on the chosen particle spacing; similar behavior was observed in the simulations of the unconfined SPH cylinder presented in Section 5.2.1.

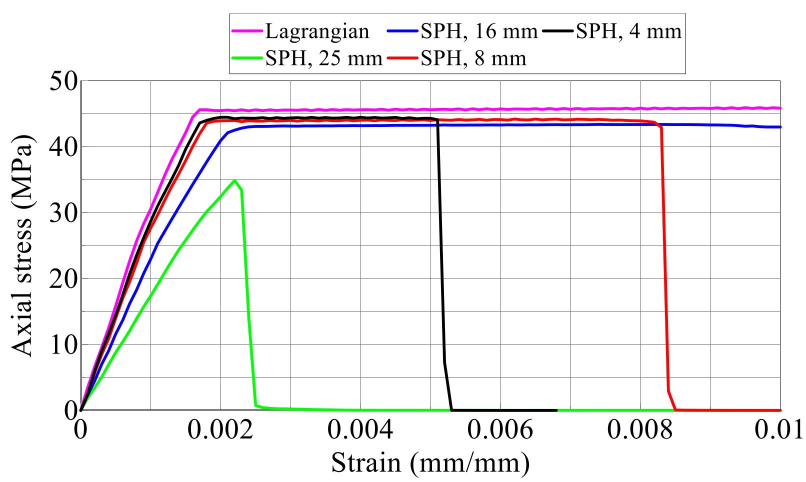

Figure 5-13:Unconfined concrete cube behavior, MAT016, SR=0.25/s

The unconfined and confined stress-strain behavior of the SPH cube are presented in Figure 5-14 for a particle spacing of 8 mm. Confinement pressures of 0.1 MPa, 0.5 MPa, and 1 MPa were considered. The unconfined behavior of the Lagrangian cube is also presented in Figure 5-14.

The failure strains of the SPH cube are 0.0086, 0.0089, 0.0093 in/in for the unconfined case, confining pressure of 0.1 MPa, and confining pressure of 0.5 MPa, respectively. As the confining pressure on the SPH cube increases, the failure strain increases and eventually achieves elastic-plastic behavior to large strains at a confining pressure of 1 MPa (2% of the compressive strength of the concrete), similar to that of the Lagrangian cube. The confinement pressure of 1 MPa results in a 6% increase in uniaxial compressive strength. According to Schwer (2008b), the confining pressures at the interface between a projectile and target during impact are of the order of 100 MPa (i.e., 100 times greater than the confining pressure required (=1 MPa) to predict behavior similar to that of the Lagrangian formulation using MAT016).

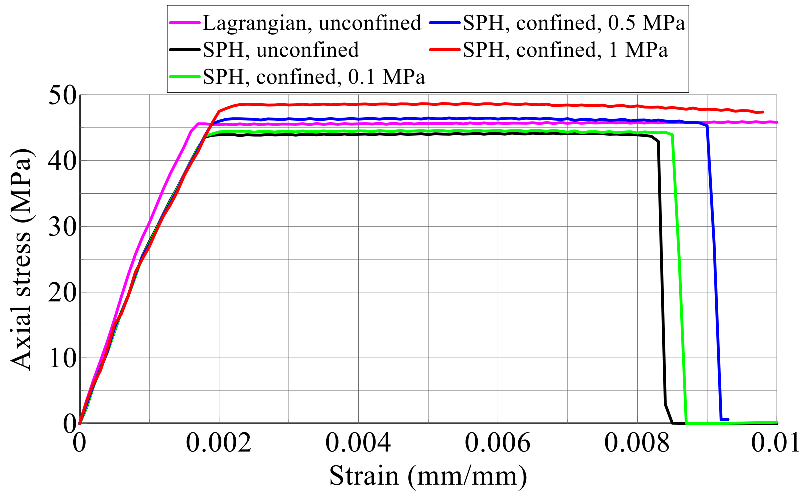

Figure 5-14: Confined concrete cube behavior, MAT016, SR=0.25/s

5.2.3 Shear Failure Surfaces for Different Concrete Material Models

The shear failure surface, defined as the variation of von Mises stress or stress difference, SD, as a function of the applied mean stress or pressure, P, can be obtained from a triaxial compression test[6], which is used to measure the compressive shear strength of concrete. The shear failure surface can be calculated using equation (5-1) for material models MAT072R3 and MAT016 (LSTC, 2012), and equation (5-2) for material model MAT159 (Murray et al., 2007a):

$$SD = a_0 + \frac{P}{a_1 + a_2 P} \tag{5-1}$$

$$SD = \alpha - \lambda \exp^{-\beta I_1} + \theta I_1 \tag{5-2}$$

[6]The test specimen is loaded hydrostatically until a desired confining pressure is attained. After that point, the lateral confining stress is held constant and the vertical stress is increased (Schwer et al., 2005).

where a_0, a_1, and a_2 are parameters determined by a regression fit of equation (5-1) to available test data, α, λ, β, and θ are parameters determined by a regression fit of equation (5-2) to available test data, and I_1 is the first invariant of the stress tensor defined as $3P$.

The values of the parameters shown above in equations (5-1) and (5-2) are internally generated by the material-model code, based on the user-specified uniaxial concrete compressive strength. The values used to define the shear failure surfaces for material models MAT072R3, MAT016, and MAT159 for a uniaxial concrete compressive strength of 45.6 MPa are presented in Table 5-3.

Table 5-3: Shear failure surface inputs, 45.6 MPa concrete

Material Model	Values of input parameters			
MAT072R3	$a_0 = 13.5$	$a_1 = 0.4463$	$a_2 = 1.77\text{e-}3$	-
MAT016	$a_0 = 11.4$	$a_1 = 0.3333$	$a_2 = 7.04\text{e-}3$	-
MAT159	$\alpha = 15.89$	$\lambda = 10.5$	$\beta = 1.93\text{e-}2$	$\theta = 0.349$

The generated shear failure surfaces for material models MAT072R3, MAT016, and MAT159 are presented in Figure 5-15. Although the surfaces intersect at a von Mises stress of 45.6 MPa (unconfined compressive strength), the models have significantly different strengths at different levels of mean stress. For a confining pressure of 100 MPa (defined by Schwer (2008b) to be a representative level of confinement in penetration simulations), the shear strengths are 108 MPa, 174 MPa, and 210 MPa for MAT016, MAT072R3, and MAT159, respectively. The responses of a concrete panel during impact loading are expected to vary as a function of the concrete model used, due to these significant differences in shear strengths. A comparison of panel responses to impact using the different material models is presented in Section 5.5.

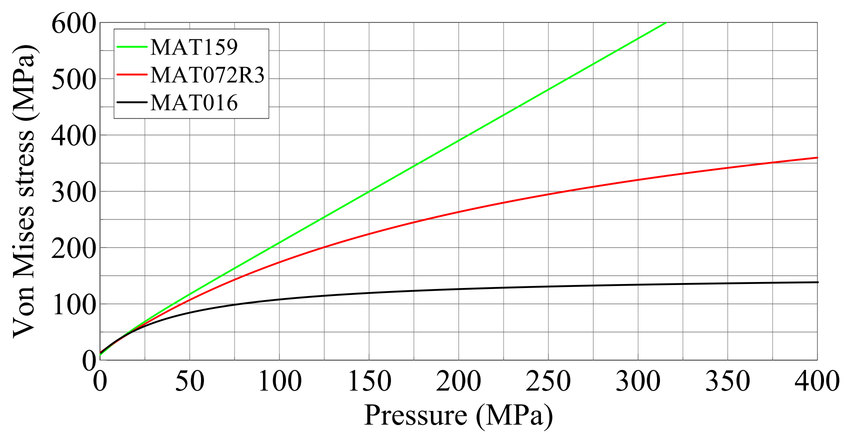

Figure 5-15: Shear failure surfaces, 45.6 MPa concrete

5.3 Modeling Impact Simulations Using Axisymmetric Elements

5.3.1 Introduction

Data from the EPRI experiments (see Table 5-1) are used in this chapter to validate, in part, a numerical model for impact analysis. Modeling of the EPRI experiments using an axisymmetric SPH-Lagrangian finite element model, including contact, boundary conditions, element formulations, strain rate effects, and equations of state for the concrete panel and steel pipe is discussed in this section. Modeling of the 12-inch (305 mm) thick, and 18-inch (457 mm) and 24-inch (610 mm) thick panels is discussed in Sections 5.3.2 and 5.3.3, respectively. The thicker panels (18- and 24-inches) are discussed separately from the 12-inch panels because different modeling techniques are employed at the boundaries (e.g., axisymmetric solid elements), with the goal of reducing the computational effort for the thicker panels.

5.3.2 12-inch panels (Test 10 and 11)

Increases in uniaxial compressive and tensile strengths due to strain rate was implemented using Dynamic Increase Factors (DIFs). The DIFs in concrete in compression follow the CEB formulation, and the Hao and Zhou formulation for concrete in tension (Dusenberry, 2010). Equations (5-3) and (5-4) present the CEB equations for concrete in compression, where $C_{CEB}\left(\dot{\varepsilon}\right)$ is the ratio of dynamic to static strength, f_{cd} is the dynamic compressive strength at strain rate $\dot{\varepsilon}$ in the range of $30\times10^{-6}\ s^{-1}$ to $300\ s^{-1}$, f_{cs} is the static compressive strength at a reference strain rate $\dot{\varepsilon}_s$ of $30\times10^{-6}\ s^{-1}$, $\log\Upsilon = 6.156\alpha-2$, $\alpha = 1/(5+9f_{cs}/f_{co})$, and $f_{co}=1450$ psi (Dusenberry, 2010).

$$C_{CEB}\left(\dot{\varepsilon}\right)=\frac{f_{cd}}{f_{cs}}=\left(\frac{\dot{\varepsilon}}{\dot{\varepsilon}_s}\right)^{1.026\alpha} \qquad \dot{\varepsilon}\le 30\ s^{-1} \tag{5-3}$$

$$C_{CEB}\left(\dot{\varepsilon}\right)=\Upsilon\left(\frac{\dot{\varepsilon}}{\dot{\varepsilon}_s}\right)^{0.33} \qquad \dot{\varepsilon}> 30\ s^{-1} \tag{5-4}$$

Equations (5-5), (5-6), and (5-7) present the Hao and Zhou equations for concrete in tension, where $T_{HZ}(\dot{\varepsilon})$ is the ratio of dynamic to static strength and $\dot{\varepsilon}$ is the strain rate in the range of $30\times10^{-6}\ s^{-1}$ to $10^{3}\ s^{-1}$ (Dusenberry, 2010).

$$T_{HZ}(\dot{\varepsilon}) = 1.0 \qquad \dot{\varepsilon} \le 10^{-4}\ s^{-1} \tag{5-5}$$

$$T_{HZ}(\dot{\varepsilon}) = 2.06 + 0.26\log(\dot{\varepsilon}) \qquad 10^{-4}\ s^{-1} \le \dot{\varepsilon} \le 1\ s^{-1} \tag{5-6}$$

$$T_{HZ}(\dot{\varepsilon}) = 2.06 + 2.0\log(\dot{\varepsilon}) \qquad 1\ s^{-1} \le \dot{\varepsilon} \le 10^{3}\ s^{-1} \tag{5-7}$$

Figure 5-16 presents the DIFs as a function of strain rate. Positive and negative strain rate indicate compression and tension, respectively. According to Bischoff et al. (1991), strain rates observed in hard impact scenarios range from 1 s^{-1} to 100 s^{-1}; a range of ± 300 s^{-1} was considered in the impact simulations, reported here.

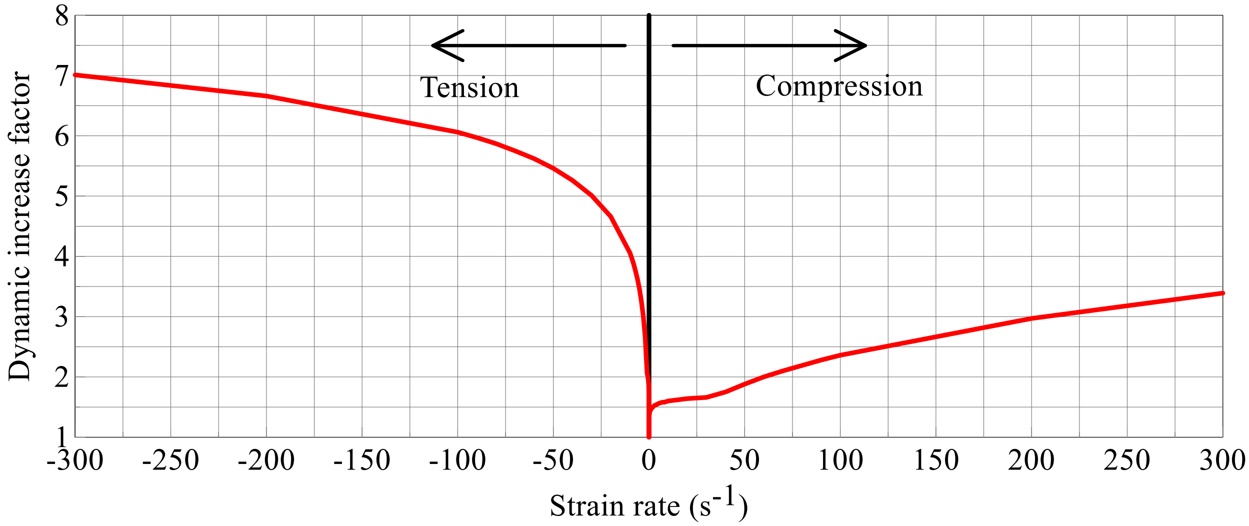

Figure 5-16: Dynamic increase factors as a function of strain rate

The Johnson-Cook (JC) material model (MAT015) was used for the Schedule 40 pipe; yield strength was set equal to 73 ksi. The Borvik et al. (2004) JC material parameters for 71 ksi steel were used because values are not available for 73 ksi steel. Values of the parameters are presented in Table 5-4, where A is yield stress, B and n are hardening coefficients, C is a strain-rate coefficient, m is a softening coefficient, $EPSO$ is a strain-rate hardening constant, TM is melting temperature in Kelvin, TR is room temperature in Kelvin, and $D1$ through $D5$ are fracture-strain constants. Although the slab reinforcement is expected to affect the global behavior of the concrete panel, it will have minimal effect on local behavior (i.e., scabbing and spalling of concrete), and so was ignored for the axisymmetric simulations. The pipe was given an initial velocity using INITIAL_VELOCITY_GENERATION.

Table 5-4: JC material constants for 71 ksi steel (adapted from Borvik et al., 2005)

A (psi)	7.11E+04	m	0.94	$D2$	1.732
B (psi)	1.17E+05	TM (K)	1800	$D3$	-0.54
n	0.73	$EPSO$	5.00E-04	$D4$	-0.015
C	0.0114	$D1$	0.0705	$D5$	0

SPH particles were used to represent the concrete panel and the pipe. The spacing of the concrete particles, h_2, is twice that of the spacing of the pipe particles, h_1, to ensure that each particle has the same mass, which provides for optimal transfer of momentum between two bodies consisting of SPH particles (i.e., concrete panel and Schedule 40 pipe) with different material densities (i.e., concrete and steel) (Schwer, 2015). The steps for determining the relationship between h_1 and h_2 are presented in equations (5-8) through (5-14) below. Setting the mass of a steel element, $m_{element,steel}$, equal to the mass of a concrete element, $m_{element,concrete}$, provides a basis for the calculations where ρ_p is density of the steel in the Schedule 40 pipe, ρ_c is the density of the concrete in the panel, $A_{concrete}$ and A_{steel} are the area of each concrete and steel element, respectively (for SPH particles, it is the particle spacing squared), and h is the height of the element, which is constant in the axisymmetric formulation. All other variables were defined previously. These calculations assume the elements have equal lengths and widths.

$$m_{element,steel} = m_{element,concrete} \tag{5-8}$$

$$\rho_p A_{steel} h = \rho_c A_{concrete} h \tag{5-9}$$

$$\rho_p A_{steel} = \rho_c A_{concrete} \tag{5-10}$$

$$A_{steel} = h_1^{\ 2} \text{ and } A_{concrete} = h_2^{\ 2} \tag{5-11}$$

$$\rho_p h_1^{\ 2} = \rho_c h_2^{\ 2} \tag{5-12}$$

$$\frac{\rho_p}{\rho_c} = \frac{h_2^{\ 2}}{h_1^{\ 2}} \tag{5-13}$$

$$\frac{h_2}{h_1} = \sqrt{\frac{\rho_p}{\rho_c}} = \sqrt{\frac{7.44e-4}{2.24e-4}} \approx 2 \tag{5-14}$$

Figure 5-17a shows the axisymmetric model of 12-inch thick concrete panel and the pipe. If the model is rotated about the axis of symmetry (labeled in Figure 5-17a), the axisymmetric model will approximately recover the panel and impacting pipe. The boundary conditions are not recovered exactly but the effect is small because response is local to the point of impact. Two columns of SPH particles constrained displacement in the Y-direction on the outer edge of the panel (also labeled in Figure 5-17a) to simulate the pinned boundary condition imposed in the experiments. Two columns were chosen to avoid stress concentrations at the boundary. The default particle approximation theory (ELFORM=0 in LS-DYNA) was used for the SPH particles. More information regarding the default particle approximation theory can be found in Lacome (2000). The equation of state keyword EOS_LINEAR_POLYNOMIAL was activated for the JC material model by setting the variable C1 equal to the bulk modulus of steel (2.3e7 psi). A full equation of state for metals is only required for modeling of hypervelocity impact or shocks to account for the sudden pressure, temperature, energy, and density changes in front of the shock wave (O'Toole et al., 2015) and so was not activated for these simulations. Monaghan-type artificial viscosity was activated by setting the variable IAVIS to zero in the *CONTROL_SPH keyword, which is required for axisymmetric simulations and variables Q1 and Q2 were set equal to one in the *CONTROL_BULK_VISCOSITY keyword per Liu et al. (2003). A close-up view of the particles at the point of impact of the panel and the pipe is presented in Figure 5-17b.

5.3.3 18- and 24-inch Panels (Test 3 and 8)

The axisymmetric models of the 18- and 24-inch thick panels are shown in Figure 5-18 and Figure 5-19, respectively. The impact zone is modeled with SPH particles. The material models, strain rate effects, particle spacing requirements (concrete particle spacing twice that of pipe spacing), and element forms of the pipe and panel in the impact zone were those described previously for the 12-inch panel (Section 5.3.2). Outside the impact zone, axisymmetric solid elements are used for the concrete panel to reduce the computational demand; see Figure 5-18 and Figure 5-19 for details. The axisymmetric solid elements are 1 × 1 in (25.4 × 25.4 mm). The 18-inch and 24-inch thick panels have 540 and 720 elements, respectively. The volume weighted element form (ELFORM=15 in LS-DYNA) was used for the axisymmetric solid elements. The area weighted element form (ELFORM=14 in LS-DYNA) is also available, but this algorithm was developed (LSTC, 2012) to solve issues in the axisymmetric and spherically symmetric formulations related to axisymmetric elements close to the line of symmetry. Considering that the axisymmetric elements are far away from the line of symmetry, both

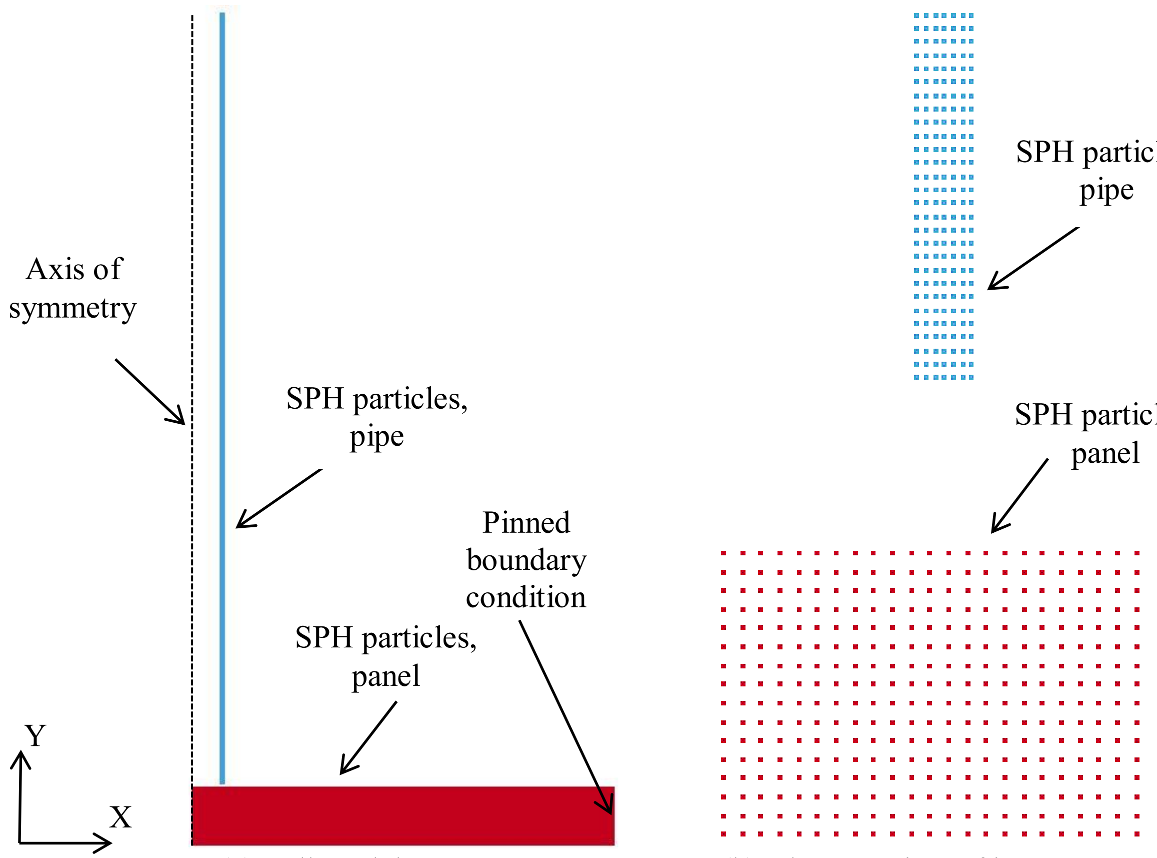

(a) Full model (b) Close up view of impact zone

Figure 5-17: Axisymmetric model, 12-inch thick panel

element forms will give the same results for the problem studied here (Schwer, 2015). A limitation of solid and shell elements with a single integration point is the presence of hourglass modes, which are nonphysical, zero-energy modes of deformation that produce zero strain and zero stress (LSTC, 2012). In LS-DYNA, the keyword *CONTROL_HOURGLASS or *CONTROL_BULK_VISCOSITY can be activated to prevent hourglass modes by applying an artificial stiffness or artificial viscosity to the affected element. The LS-DYNA Keyword User's Manual recommends the use of artificial stiffness and artificial viscosity for static/quasi-static and dynamic/high velocity impact simulations, respectively (LSTC, 2012). The *CONTROL_BULK_VISCOSITY keyword was activated and the variables Q1 and Q2 were set to values of 1.5 and 0.06 (default values), respectively, for the axisymmetric solid elements; the values of Q1 and Q2 for the SPH particles are the same as those described previously for the 12-inch panel. Five nodes constrained displacement in the Y-direction on the outer edge of the solid elements (see Figure 5-18 and Figure 5-19) to simulate the pinned boundary condition imposed in the experiments.

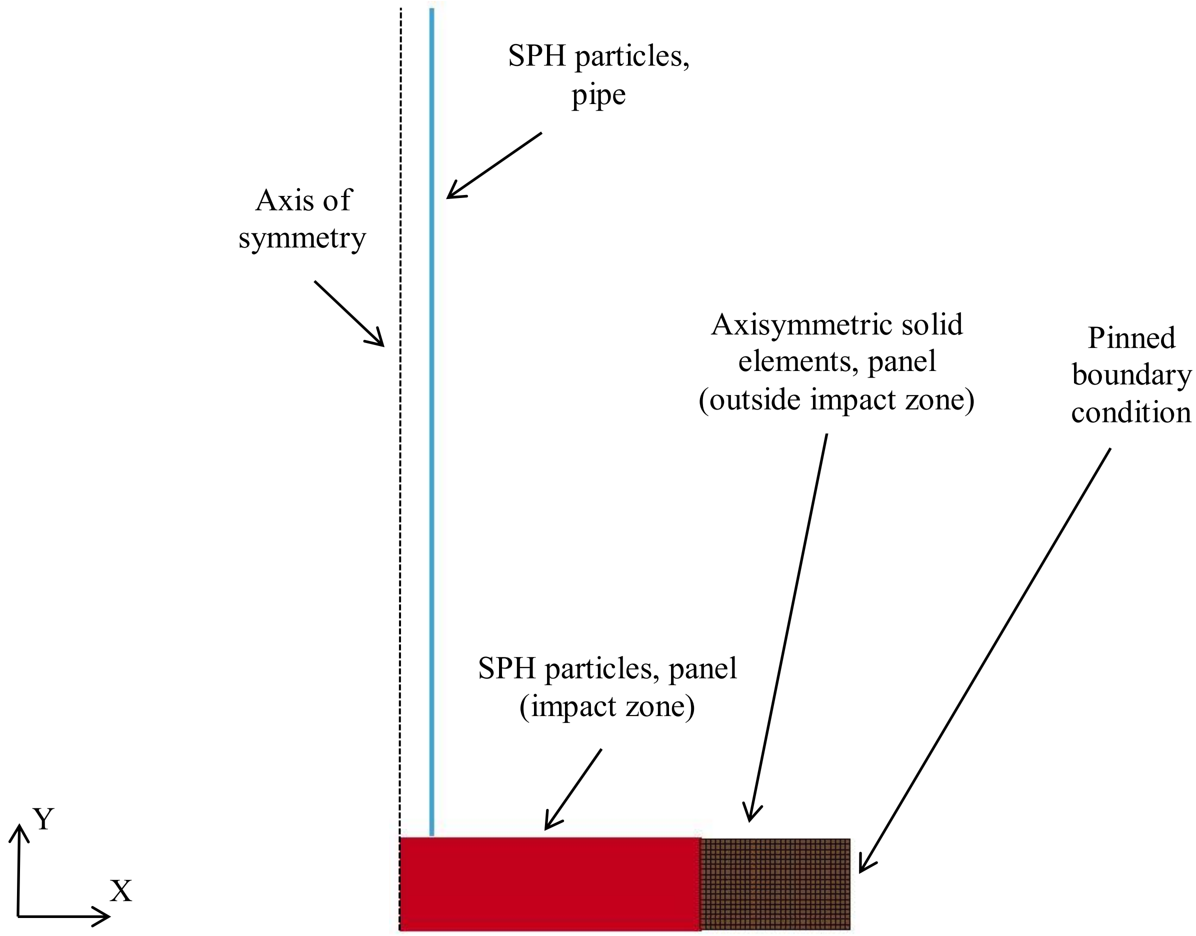

Figure 5-18: Axisymmetric model, 18-inch thick panel

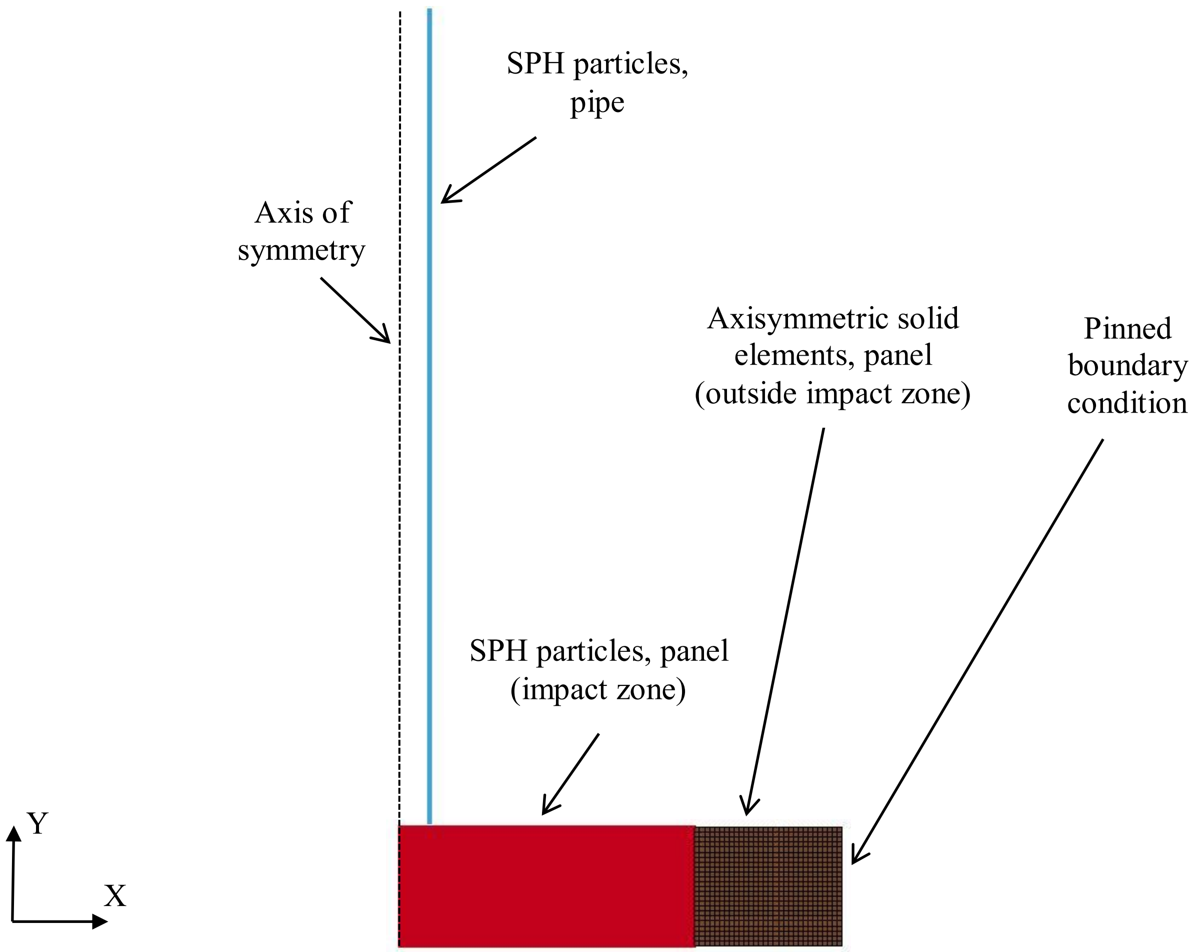

Figure 5-19: Axisymmetric model, 24-inch thick panel

One important aspect of combining SPH particles and solid Lagrangian elements into one simulation is the correct modeling of the interface between the two formulations (seen in Figure 5-20). The interface between the SPH particles and the axisymmetric solid elements in the numerical model shown in Figure 5-20 is identified as the SPH-axisymmetric solid element boundary.

A 3D beam model with a square cross section 1 × 1 in (25.4 × 25.4 mm) and a length of 39.4 in. (1000 mm) was created in LS-DYNA to investigate the behavior at a SPH-solid element boundary and confirm modeling assumptions for the impact simulations. The 3D beam model is used to investigate: 1) the propagation of compression waves (P-waves) in an elastic medium, and 2) the behavior of these waves crossing the SPH-solid element boundary. The number of SPH particles required to meet each solid element at a boundary to ensure complete transfer of the stress wave from one formulation to the other is identified and used for the subsequent impact simulations. An LS-DYNA model of the beam consisting of Lagrangian solid elements, shown in Figure 5-21a, is used first to simulate the propagation of a compression wave through an elastic material. The results of this simulation are compared to a model of the beam in which 40 mm of solid elements are replaced with SPH particles, as shown in Figure 5-21b. An elastic material model MAT001 was used for the SPH particles and the solid elements; the inputs are density (ρ=7.89×10^{-9} ton/mm^3), elastic modulus (E=2.07×10^5 MPa), and Poisson's ratio (ν=0.3). The LS-DYNA consistent units for mass, length, time, force, and stress, are ton, millimeters, seconds, Newtons, and MPa, respectively. The beam was modeled with 0.25 × 0.25 × 0.16 in. (6.35 × 6.35 × 4 mm) solid elements, with a total of 4000 elements in the full Lagrangian model (beam without SPH particles). SPH particle spacings of 6.4, 3.2, 1.6, and 1.05 mm, which correspond to 2, 3, 5, and 7 SPH particles coming into contact with each solid element at the SPH-solid element boundary, respectively, were considered in the investigation; an illustration of each boundary is presented in Figure 5-22. The constant stress formulation (ELFORM=1 in LS-DYNA) and the default particle approximation theory (ELFORM=0 in LS-DYNA) was used for the solid elements and SPH particles, respectively. The *CONTACT_TIED_NODES_TO_SURFACE keyword was used to constrain the SPH particles and the solid elements at the interface.

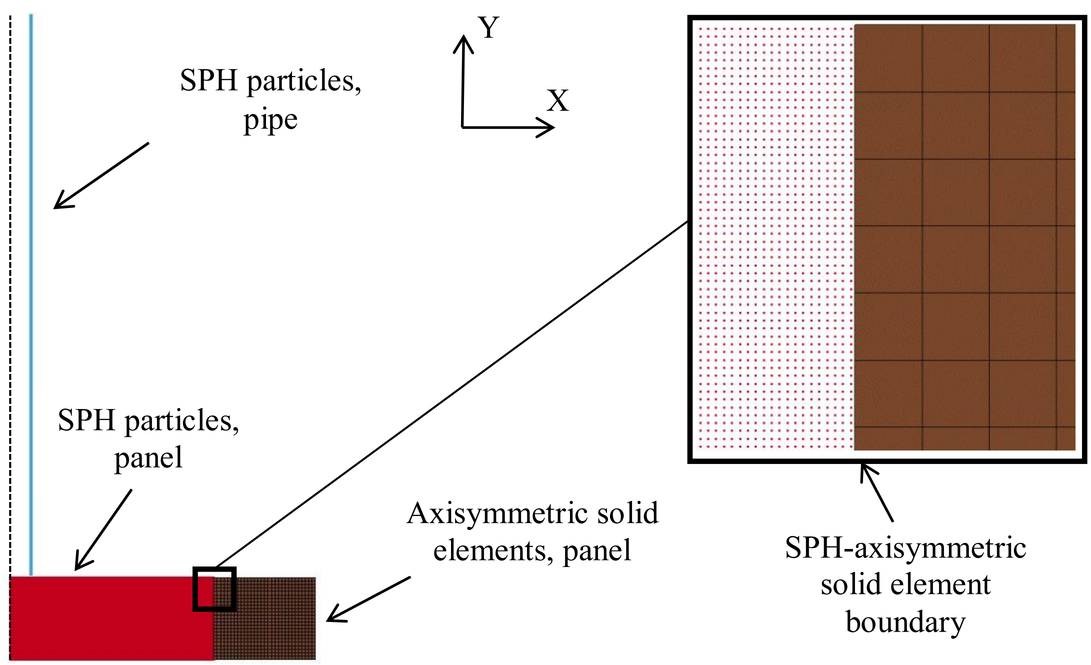

Figure 5-20: SPH-axisymmetric solid element boundary

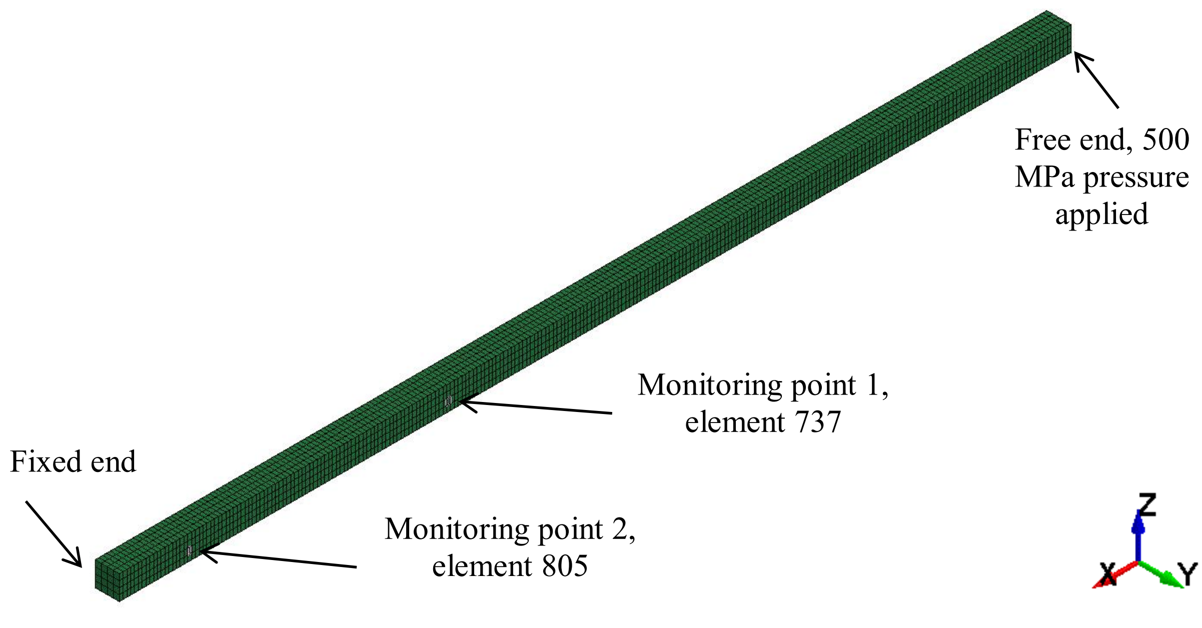

(a) Lagrangian beam model

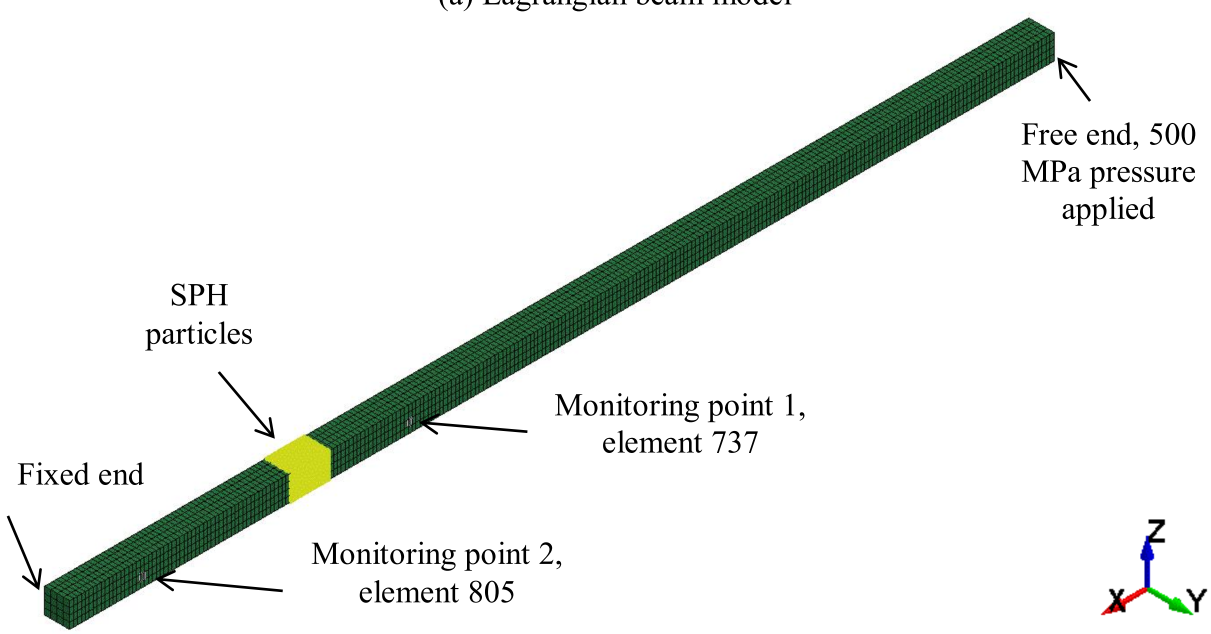

(b) Lagrangian-SPH beam model

Figure 5-21: 3D square beam model

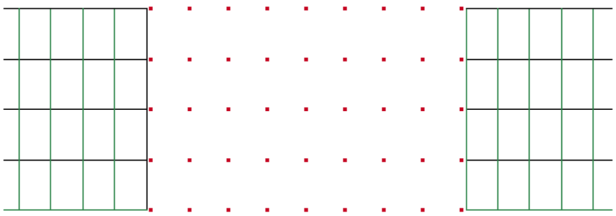

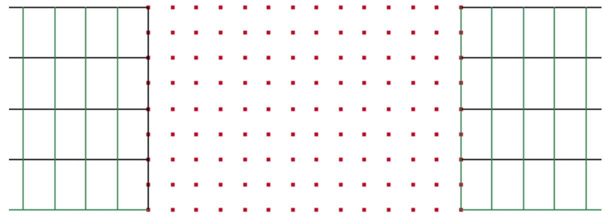

(a) 2SPH (b) 3SPH

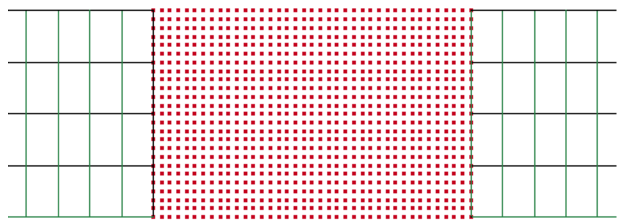

(c) 5SPH (d) 7SPH

Figure 5-22: SPH-solid element boundaries in the beam model

The left end of the beam is fixed in both models and an instantaneous pressure of 500 MPa is applied to the free end of the beam at time zero using the keyword *LOAD_SEGMENT_SET; see Figure 5-21a and Figure 5-21b. A summary of the simulations and a description of each model are presented in Table 5-5.

The movement of the stress wave was monitored at two locations along the length of the beam. Monitoring points 1 and 2 (one on each side of the boundary) were used to monitor the stress waves induced by the applied pressure, and are labeled in Figure 5-21a and Figure 5-21b. Monitoring locations 1 and 2 are 651 and 922 mm from the free end, respectively.

Table 5-5: Beam simulations for SPH-solid element boundary investigation

Simulation	Beam model	SPH particle spacing	Description
Solid	Solid only	Not applicable	Lagrangian elements used
2SPH	Solid, SPH	6.4	Two SPH particles meet each solid element at the boundary
3SPH	Solid, SPH	3.2	Three SPH particles meet each solid element at the boundary
5SPH	Solid, SPH	1.6	Five SPH particles meet each solid element at the boundary
7SPH	Solid, SPH	1.05	Seven SPH particles meet each solid element at the boundary

The axial stress histories for monitoring points 1 (element 737) and 2 (element 805) are shown in Figure 5-23a and Figure 5-23b, respectively. The compression wave arrives at monitoring points

1 and 2 at 0.13 and 0.18 msec, respectively, which are consistent with one-dimensional wave propagation theory calculations using a compression wave speed, c_o, of 5.12×10^6 mm/sec ($c_o = \sqrt{E / \rho}$) (Doyle, 1997). The amplitude of the compression wave upon arrival at the monitoring locations is equivalent to the instantaneous pressure imposed on the free end at the start of the simulation (=-500 MPa). The compression wave reaches the fixed end and is reflected back with an amplitude of -1000 MPa, which reaches monitoring points 2 and 1 at 0.21 and 0.26 msec, respectively. The compression wave then travels to the free end, and is reflected back as a tension wave with an amplitude of -500 MPa (-1000 MPa + 500 MPa = -500 MPa), which reaches monitoring points 1 and 2, at 0.52 and 0.57 msec, respectively. Finally, the tension wave travels to the fixed end and is reflected back as a tensile wave of the same amplitude (-500 MPa + 500 MPa = 0 MPa), reaching monitoring points 2 and 1, at 0.60 and 0.65 msec, respectively.

The axial stress histories in simulation 2SPH are in poor agreement with the results observed using the model with all solid elements; a significant percentage of the wave is reflected back once it reaches the boundary (see monitoring point 1 in Figure 5-23a at 0.15 msec), indicating a need to increase the number of particles contacting each solid element. The axial stress histories in simulations 3SPH, 5SPH, and 7SPH are in good agreement with the results observed using the model with all solid elements; the results improve as the number of SPH particles contacting each solid element are increased. Based on the results of this study, at least three particles should contact each solid element to ensure adequate transfer of the propagating wave over the SPH-solid element boundary.

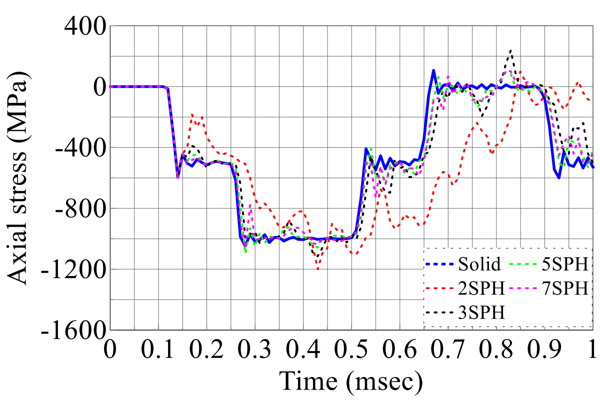

(a) Monitoring location 1, element 737

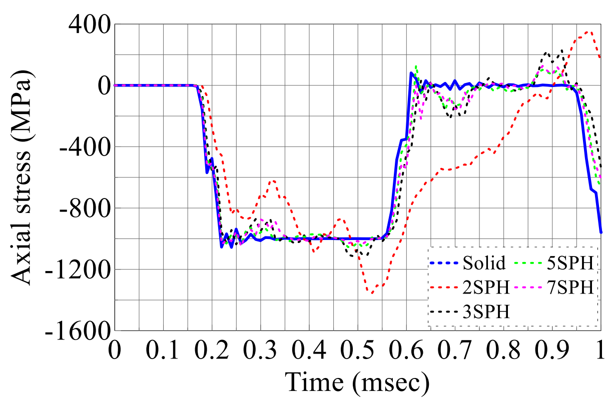

(b) Monitoring location 2, element 805

Figure 5-23: Axial stress histories for all simulations

The same methods used above in the 3D beam simulations can be applied to the axisymmetric formulation (i.e., the case where SPH particles meet axisymmetric solid elements). In the impact models (shown in Figure 5-18 and Figure 5-19), the CONTACT_2D_NODE_TO_SOLID_TIED keyword was used to constrain the SPH particles and the axisymmetric solid elements at the interface. Particle spacings in the concrete of 10, 5, 4, 3, and 2 mm were considered in the impact simulations to investigate mesh convergence, which correspond to approximately 3, 5, 6, 9 and 12 SPH particles contacting each axisymmetric solid element with dimensions of 25.4 × 25.4 mm (1 in. × 1 in.) at the boundary, respectively. The coarsest of these meshes used in the impact simulations meets the requirements of having at least three SPH particles meeting each axisymmetric solid element to ensure adequate transfer of the propagating wave.

5.4 Grid Convergence Index

Finite element analysis is a well-established numerical technique for calculating the response of components and systems to mechanical and thermal loadings. These numerical techniques solve coupled partial differential equations describing the physics of the problem by discretizing time and space variables (Schwer, 2008a). Even though a numerical solution matches the experimental results, discretization error still exists in the solution due to the choice of finite time (i.e., time step) and space resolution (i.e., mesh size). Traditional methods of estimating discretization error (i.e., Richardson Extrapolation) are available, but require the mesh to be refined by a factor of two for each iteration (Schwer, 2008a). The Grid Convergence Index, GCI, a method developed by Roache (1994) to estimate discretization error in a numerical solution, does not require the mesh to be refined by a factor of two for each iteration. This allows the user to reduce computational demand and show evidence of a converged mesh. Another advantage of using the GCI is that the analytical solution, typically unknown for complex simulations (i.e., blast and impact loading of concrete panels), is not required to estimate the discretization error (Schwer, 2008a).

A metric, f, is established first, which is representative of the damage or a response parameter being estimated (e.g., velocity, displacement, penetration depth). The value of this metric is calculated for the three finest meshes, f_1, f_2, and f_3, where f_1 represents the finest mesh and f_3 represents the coarsest mesh. Perforation velocity was chosen here as the metric; penetration depth was used when perforation did not occur. In this study, grid refinement ratios, r, defined as $r_{ji} = h_j / h_i$ and $r_{kj} = h_k / h_j$, where h_i, h_j and h_k are the i^{th}, j^{th}, and k^{th} mesh spacing ($h_i < h_j < h_k$), were not constant. The grid refinement ratios must be greater than 1.3 (e.g. $r_{21} = r_2 / r_1 > 1.3$) to obtain reasonable estimations of discretization error using the GCI (Schwer, 2008a).

The observed order of convergence, p, for the three mesh sizes is

$$p = \frac{\left| \ln \left| f_{32} / f_{21} \right| + q(p) \right|}{\ln r_{21}} \tag{5-15}$$

where $f_{ji} = f_j - f_i$ and $f_{kj} = f_k - f_j$, where f_i, f_j, and f_k are the i^{th}, j^{th}, and k^{th} metric value (Schwer, 2008a).

Equation (5-15) must be solved iteratively using a trial value for $q(p) = 0$. A value for $q(p)$ corresponding to the trial value chosen for $q(p)$ can be calculated using equations (5-16) and (5-17). If the calculated value of $q(p)$ given by equation (5-16) matches the trial value input with sufficient accuracy, the iterations have converged.

$$q(p) = \ln\left(\frac{r_{21}{}^{p} - s}{r_{32}{}^{p} - s} \right) \tag{5-16}$$

$$s = sign(f_{32} / f_{21}) \tag{5-17}$$

The estimated discretization errors GCI_{21} and GCI_{32} can be predicted using equations (5-18) and (5-19), respectively.

$$GCI_{21} = F_s \left(\frac{e_{21}}{r_{21}{}^{p} - 1} \right) \tag{5-18}$$

$$GCI_{32} = F_s \left(\frac{e_{32}}{r_{32}{}^{p} - 1} \right) \tag{5-19}$$

where e_{21} and e_{32} are the relative metric errors and are computed using equations (5-20) and (5-21), respectively. The factor, F_s, is applied to the relative error and can be thought of as representing a bound on the estimated relative error with 95% confidence (Schwer, 2008a).

Roache (1994) examined numerous CFD calculations and determined that a value of 1.25 for F_s gave the best results for 95% of the cases he examined using the GCI.

$$e_{21} = \left| \frac{f_2 - f_1}{f_1} \right| \tag{5-20}$$

$$e_{32} = \left| \frac{f_3 - f_2}{f_2} \right| \tag{5-21}$$

Based on the observed convergence rate and the results of the analysis using the two finest meshes, an estimate of the numerically converged solution, $f_{21}*$, can be computed using equation (5-22). The converged numerical solution, CI_{95}, lies in the interval given by equation (5-23) with a 95% confidence level.

$$f_{21}^* = \frac{r_{21}^p f_1 - f_2}{r_{21}^p - 1} \tag{5-22}$$

$$CI_{95} = \left[f_1(1 - GCI_{21}), f_1(1 + GCI_{21}) \right] \tag{5-23}$$

An asymptotic check value, AC, can be computed using equation (5-24) to determine the level of convergence. A value near unity indicates that the calculated results from the simulations are in the asymptotic regime.

$$AC = \frac{GCI_{32}}{r_{21}^p GCI_{21}} \tag{5-24}$$

The GCI method is used hereafter to evaluate mesh discretization error in the impact simulations.

5.5 Impact Simulations using Different Concrete Material Models

5.5.1 Introduction

EPRI Test 11 specifications (see Table 5-1 above) were used in this study to investigate wall panel behavior as a function of the three concrete models available in LS-DYNA that are compatible with the SPH formulation (i.e., MAT016, MAT072R3, and MAT159). In the Test 11 experiment, a 12-inch (305 mm) panel was impacted by a 12-inch (305 mm) diameter Schedule 40 pipe at a velocity of 98 fps (30 m/s). The compressive strength of the concrete in Test 11

(=3600 psi (24.8 MPa)) was increased to 4500 psi (31 MPa) to accommodate the CSCM material model in the simulations, which is applicable for uniaxial concrete compressive strengths ranging from 4061 to 8412 psi (28 to 58 MPa) (Murray et al., 2007a). The values for the concrete parameters describing the elastic and inelastic response of the concrete were generated internally by each material-model code using only the uniaxial concrete compressive strength as input. The shear failure surfaces for material models MAT016, MAT072R3, and MAT159 (described in more detail in Section 5.2) are shown in Figure 5-24 for a uniaxial concrete compressive strength of 4500 psi (31 MPa); the surfaces can be calculated for concrete material models MAT016 and MAT072R3 using equation (5-1) and for MAT159 using equation (5-2). The parameters used to generate the shear failure surfaces for each material model are presented in Table 5-6 (in units of psi). Based on the generated shear failure surfaces, the results of the impact simulations using the different concrete material models are expected to be different. For a confining pressure of 14500 psi (100 MPa) (defined by Schwer (2008b) to be a representative level of confinement in impact and penetration problems), the shear strengths are 11400 psi (78.6 MPa), 21900 psi (151 MPa), and 25500 psi (155 MPa) for MAT016, MAT072R3, and MAT159, respectively. The concrete material model MAT159 (MAT016) will provide the greatest (least) resistance to penetration and perforation of the panel based on shear strength.

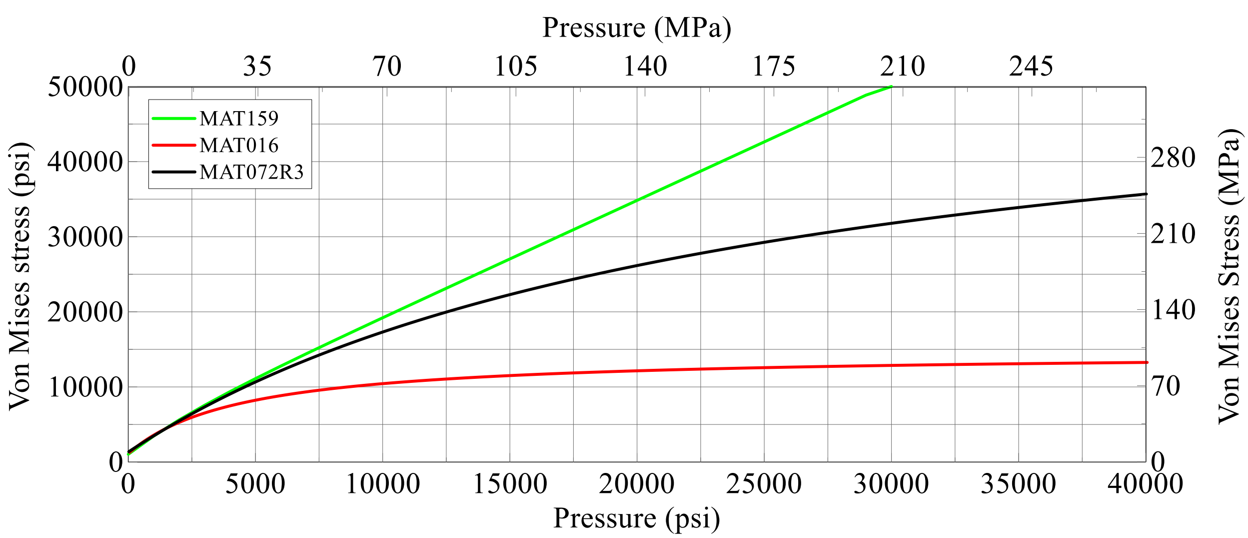

Figure 5-24: Shear failure surfaces, 4500 psi (31 MPa) concrete

Table 5-6: Shear failure surface inputs, 4500 psi (31 MPa) concrete, units of psi

Material model	Values of the input parameters			
MAT072R3	$a_0 = 1330$	$a_1 = 0.4463$	$a_2 = 1.796 \times 10^{-5}$	-
MAT016	$a_0 = 1125$	$a_1 = 0.3333$	$a_2 = 7.407 \times 10^{-5}$	-
MAT159	$\alpha = 2123$	$\lambda = 1524$	$\beta = 1.33 \times 10^{-4}$	$\theta = 0.2998$

The simulations conducted in this section are summarized in Table 5-7. For each material model, concrete particle spacings of 10, 5, 4, 3, and 2 mm were considered to achieve a converged mesh. The numerical model used in the simulations is shown in Figure 5-17.

Table 5-7: Numerical simulations, MAT072R3, MAT016, and MAT159

Simulation	Concrete mesh mm (in.)	Pipe mesh mm (in.)	Concrete model	f_c' MPa (psi)
1	10 (0.39)	5.35 (0.21)	MAT072R3	31 (4500)
2	5 (0.20)	2.67 (0.11)	MAT072R3	31 (4500)
3	4 (0.16)	2.14 (0.09)	MAT072R3	31 (4500)
4	3 (0.12)	1.6 (0.06)	MAT072R3	31 (4500)
5	2 (0.08)	1 (0.04)	MAT072R3	31 (4500)
6	10 (0.39)	5.35 (0.21)	MAT159	31 (4500)
7	5 (0.20)	2.67 (0.11)	MAT159	31 (4500)
8	4 (0.16)	2.14 (0.09)	MAT159	31 (4500)
9	3 (0.12)	1.6 (0.06)	MAT159	31 (4500)
10	2 (0.08)	1 (0.04)	MAT159	31 (4500)
11	10 (0.39)	5.35 (0.21)	MAT016	31 (4500)
12	5 (0.20)	2.67 (0.11)	MAT016	31 (4500)
13	4 (0.16)	2.14 (0.09)	MAT016	31 (4500)
14	3 (0.12)	1.6 (0.06)	MAT016	31 (4500)
15	2 (0.08)	1 (0.04)	MAT016	31 (4500)

The values of the input parameters for each material model are presented in Table 5-8 where ρ is the mass density, G is the shear modulus, ν is Poisson's ratio, and f_c' is concrete compressive strength. An "-" in a cell indicates that it is not a required input parameter for that material model.

Table 5-8: Input parameters for MAT072R3, MAT016, and MAT159

	ρ g/mm^3 (lbf-s^2/in) ($\times 10^{-3}$)	G MPa (ksi)	ν	f_c' MPa (psi)
MAT027R3	2.17 (0.22)	-	0.15	31 (4500)
MAT016	2.17 (0.22)	11462 (1662)	0.15	31 (4500)
MAT159	2.17 (0.22)	-	-	31 (4500)

For the purpose of this investigation, the tensile strength, f_t', was not specified for the MAT072R3 material model because it is not an input parameter for MAT159 and MAT016. The tensile strength will be internally generated by the concrete material model and is based on the user specified concrete compressive strength. Equations (5-25) (Schwer, 2005), (5-26) (CEB, 1993), and (5-27) (LSTC, 2012) are used to calculate the tensile strength for MAT072R3, MAT159, and MAT016, respectively. For a uniaxial compressive strength of 4500 psi (31 MPa), the calculated tensile strengths for MAT072R3, MAT159, and MAT016 are 431 psi (2.9 MPa), 432 psi (3.0 MPa), 463 psi (3.2 MPa), respectively.

$$f_t' = 1.58\left(\frac{(f_c')^2}{a_0}\right)^{1/3} \tag{5-25}$$

$$f_{ctm} = f_{ctkom}\left(\frac{f_{ck}}{f_{cko}}\right)^{2/3} \tag{5-26}$$

$$f_t' = 1.7\left(\frac{(f_c')^2}{a_0}\right)^{1/3} \tag{5-27}$$

where a_0 is a unit conversion factor: unity for f_c' measured in standard English stress units of psi, and 145 for MPa, f_{ctm} is the mean tensile strength (in MPa), f_{ctkom} is 1.40 MPa, f_{cko} is 10 MPa, and f_{ck} is the specified characteristic compressive strength (in MPa).

The results of the impact simulations using the MAT072R3, MAT159, and MAT016 material models are presented in Sections 5.5.2, 5.5.3, and 5.5.4, respectively. A comparison of panel responses using the various concrete models is presented in Section 5.5.5.

5.5.2 Karagozian and Case Material Model (MAT072R3)

Results of simulations 1 through 5 (described in Table 5-7) are presented in this section. The concrete mesh refinement study for these simulations is shown in Figure 5-25, using residual pipe velocity (also termed the exit velocity) as the convergence criterion. Results are shown for concrete particle spacings of 2, 3, 4, 5, and 10 mm; the pipe velocities begin to converge as the mesh is refined. Results of the simulation using the finest mesh (2 mm) (simulation 5 in Table 5-7), are shown in Figure 5-26, 20 msec after impact. Spalling of the concrete on the front face and perforation of the panel are shown in Figure 5-26a and Figure 5-26b, respectively.

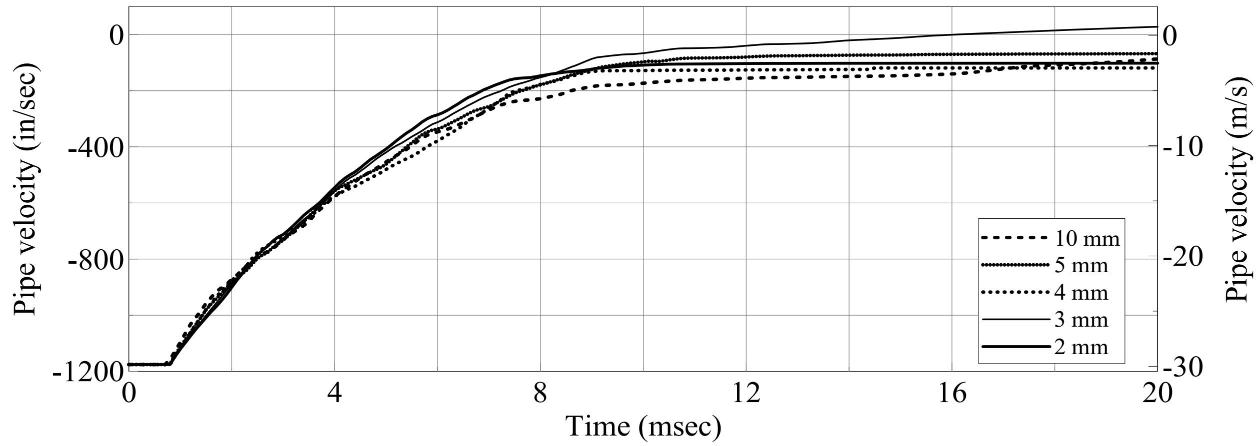

Figure 5-25: Pipe velocity histories, MAT072R3, 4500 psi (31 MPa) concrete

(a) Spalling of concrete and perforation of panel

(b) Perforation of panel

Figure 5-26: Simulation results, 20 msec, MAT072R3, 2 mm mesh, simulation 5, 4500 psi (31 MPa) concrete

The monitoring points for lateral displacement on the back face of the panel are identified in Figure 5-27 using solid black circles. The displacements are plotted every 381 mm (15 in) near the supports and every 25.4 mm (1 in) near the point of impact (see Figure 5-27); this drawing is not to scale. The lateral displacement of the back face of the panel over the duration of the simulation is presented in Figure 5-28. The displacements are shown for the finest mesh (2 mm) (i.e., simulation 5 in Table 5-7). The response is local to the point of impact, as expected.

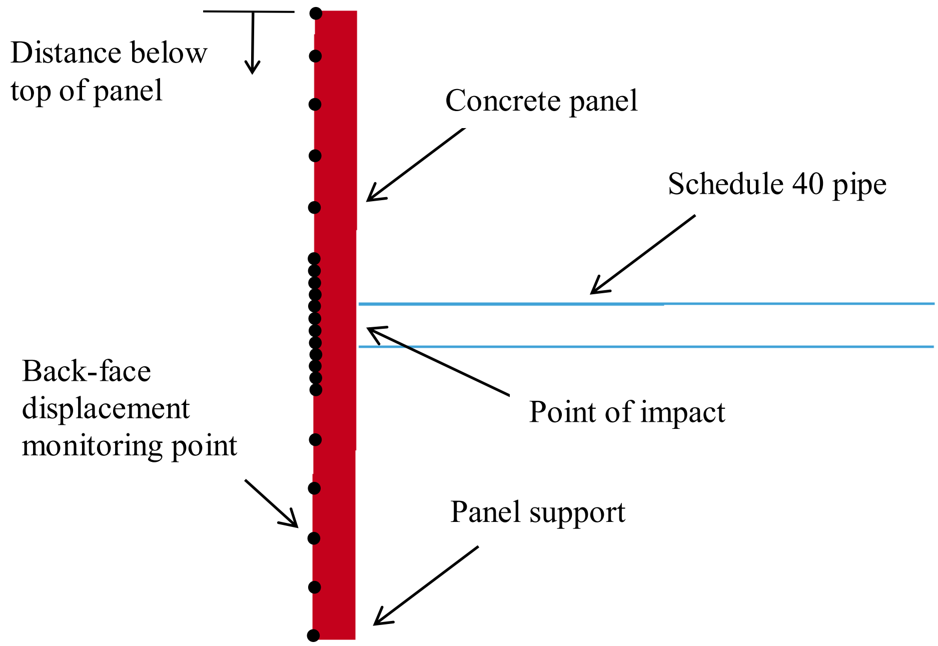

Figure 5-27: Description of panel back-face lateral displacements (not to scale)

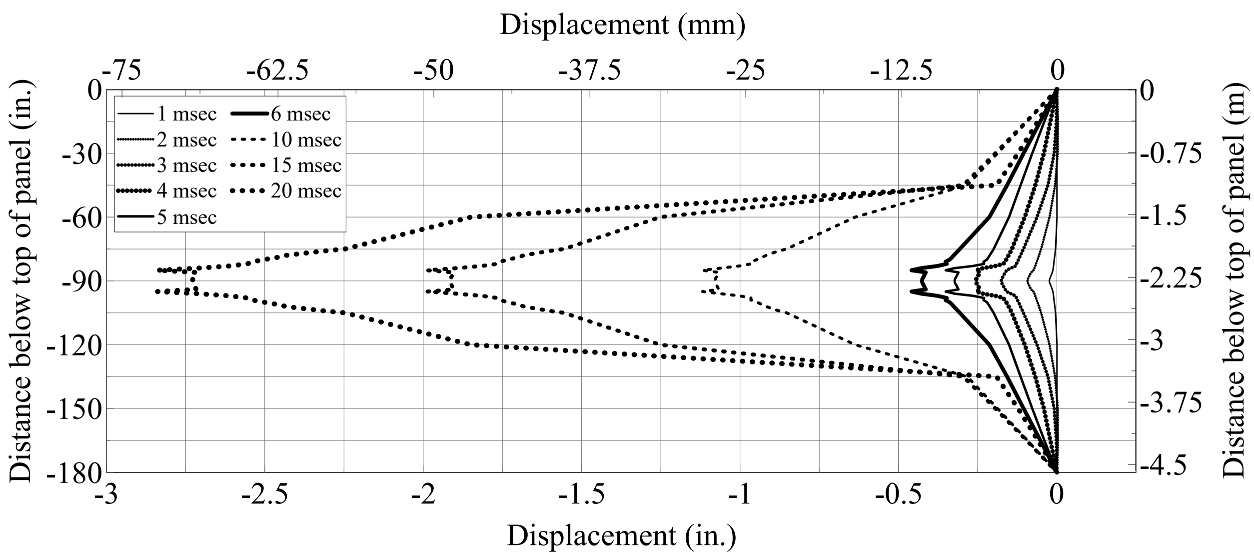

Figure 5-28: Panel back-face lateral displacement, MAT072R3, 2 mm mesh, simulation 5, 4500 psi (31 MPa) concrete

5.5.3 Continuous Surface Cap Material Model (MAT159)

Simulations 1 through 5 were re-analyzed in this section using the CSCM material model and identified as simulations 6 through 10 in Table 5-7. Figure 5-29 shows the mesh refinement study using the pipe velocity history as the convergence criterion. The results converge as the mesh is refined. Figure 5-30 shows the simulation results using the finest mesh (2 mm) (see simulation 10 in Table 5-7), 20 msec after impact. Figure 5-30a and Figure 5-30b show spalling of the concrete and perforation of the panel, respectively.

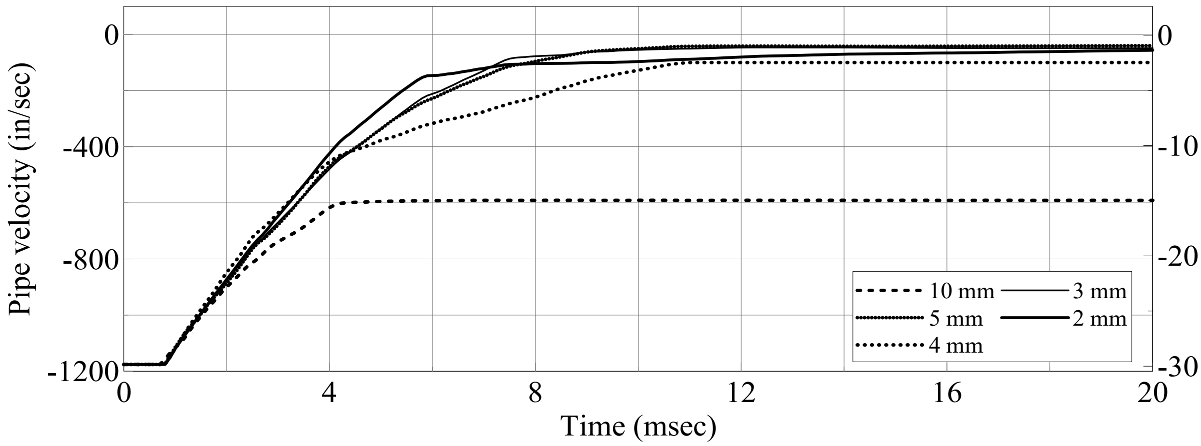

Figure 5-29: Pipe velocity histories, MAT159, 4500 psi (31 MPa) concrete

(a) Spalling of concrete and perforation of panel

(b) Perforation of panel

Figure 5-30: Simulation results, 20 msec, MAT159, 2 mm mesh, simulation 10, 4500 psi (31 MPa) concrete

Figure 5-31 shows the evolution of the panel back-face lateral displacement using the finest mesh (2 mm) (i.e., simulation 10 in Table 5-7). The results show significant deformation of the panel on the back face, opposite the point of impact.

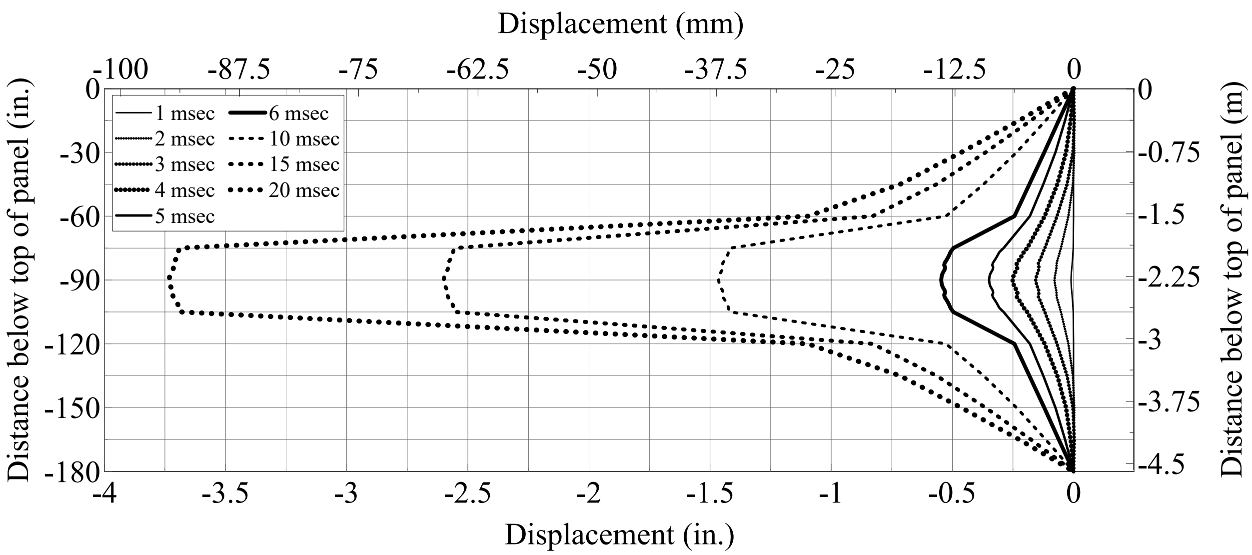

Figure 5-31: Panel back-face lateral displacement, MAT159, 2 mm mesh, simulation 10, 4500 psi (31 MPa) concrete

5.5.4 Pseudo Tensor Material Model (MAT016)

Results of simulations 11 through 15 (described in Table 5-7), are presented in this section. The mesh refinement study is presented in Figure 5-32, using the residual pipe velocity as the convergence criterion. The simulation using the finest mesh (2 mm) (i.e., simulation 15 in Table 5-7) is presented in Figure 5-33, 20 msec after impact. The full model and a close-up view of the panel perforation are presented in Figure 5-33a and Figure 5-33b, respectively. Minimal concrete spalling is seen in the simulation.

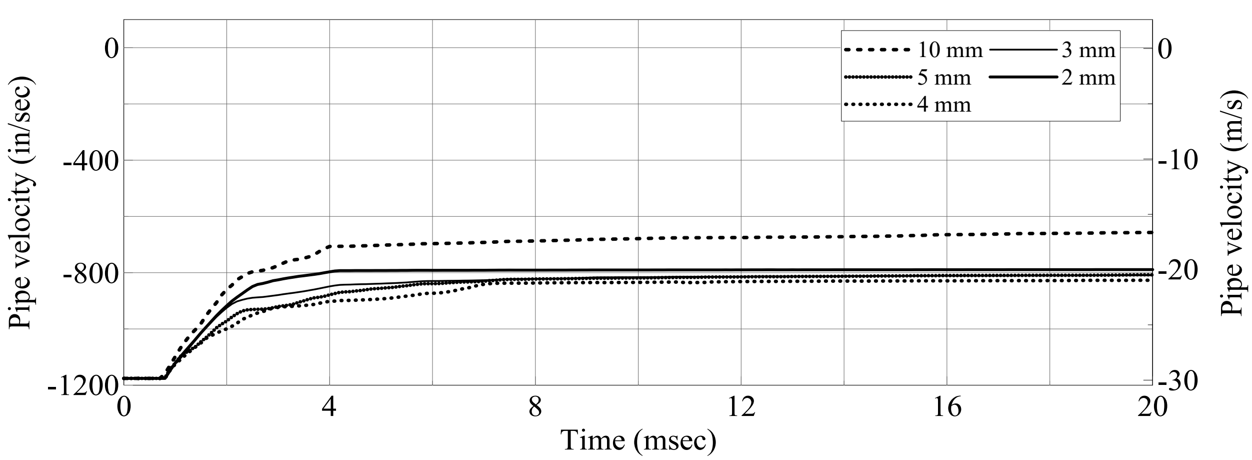

Figure 5-32: Pipe velocity histories, MAT016, 4500 psi (31 MPa) concrete

(a) Full model (b) Close up view of impact zone

Figure 5-33: Simulation results, perforation of panel, 20 msec, MAT016, 2 mm mesh, simulation 15, 4500 psi (31 MPa) concrete

The evolution of the panel back-face lateral displacement over time is presented in Figure 5-34. The results are shown for the simulation using the finest mesh (2 mm) (i.e., simulation 15 in Table 5-7). Significant deformation at the point of impact is seen.

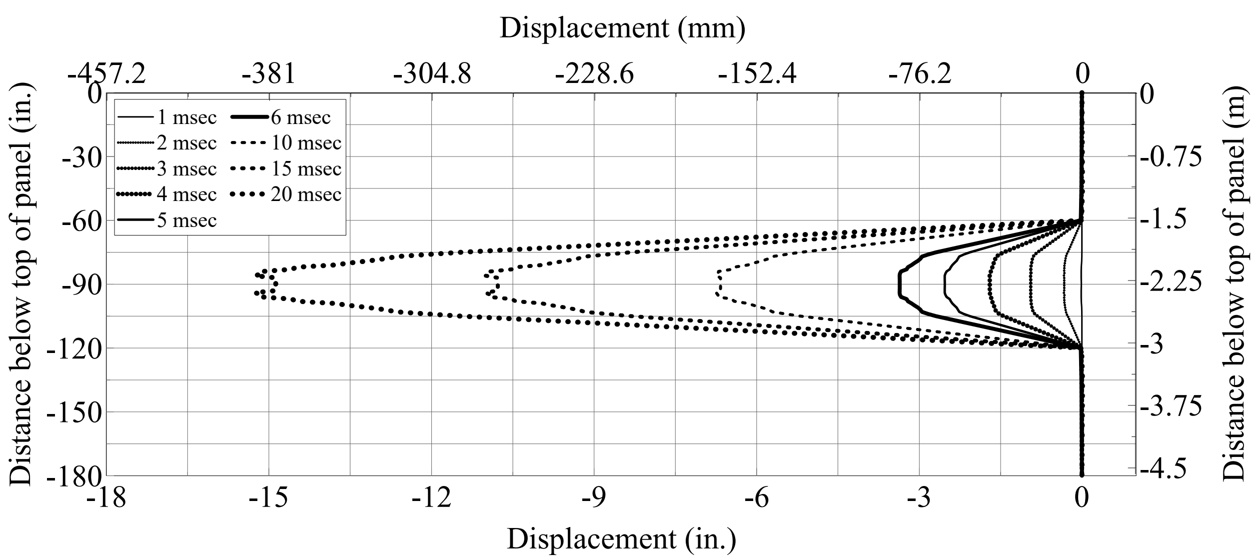

Figure 5-34: Panel back-face lateral displacement, MAT016, 2 mm mesh, simulation 15, 4500 psi (31 MPa) concrete

5.5.5 Comparison of Panel Responses using Different Material Models

The simulation results using the finest mesh (2 mm) for concrete material models MAT072R3 (simulation 5), MAT159 (simulation 10), and MAT016 (simulation 15) are compared in this section. The hydrostatic pressure fringes at the instant in time the conical plug starts to form using MAT072R3, MAT159, and MAT016 are shown in Figure 5-35, Figure 5-36, and Figure 5-37, respectively; the plug is identified by black lines in the figures. The predicted hydrostatic pressure ranges observed at the interface between the pipe and the panel are presented in Table 5-9 and are consistent with a confining pressure of 14500 psi (100 MPa), typically observed in impact and penetration problems (Schwer, 2008b).

The conical plug forms at 1.29, 5.29, and 5.49 msec using material models MAT016, MAT159, and MAT072R3, respectively. The concrete shear strength at a confinement level of 20600 psi (142 MPa) (average of the maximum confinement pressures observed in Table 5-9) are 12200 psi (84.1 MPa), 34800 psi (240 MPa), and, 26200 psi (181 MPa) using material models MAT016, MAT159, and MAT072R3, respectively. The formation of the conical plug occurs much earlier using MAT016 (=1.29 msec), which is expected, because the shear strength of MAT016 at the predicted level of confinement (=20600 psi (142 MPa)) is significantly less than that of MAT072R3 and MAT159. Since the shear strength of MAT016 is considerably less, it is expected to provides the least resistance to perforation of the three material models.

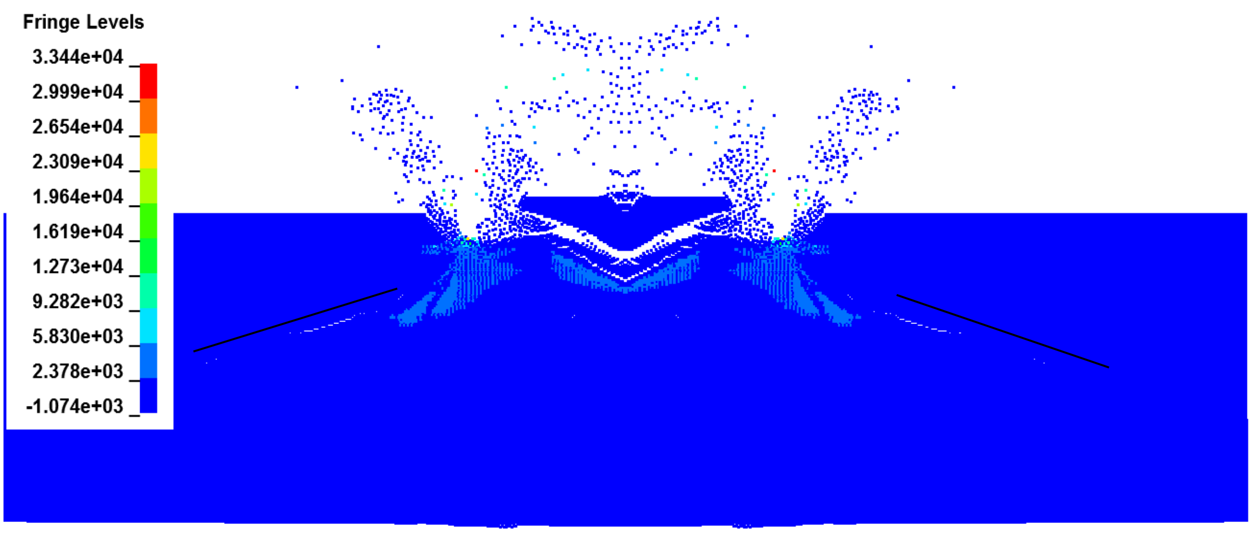

Figure 5-35: Hydrostatic pressure fringes, MAT072R3, 4500 psi concrete, 5.49 msec, units of psi (1 psi = 0.0069 MPa)

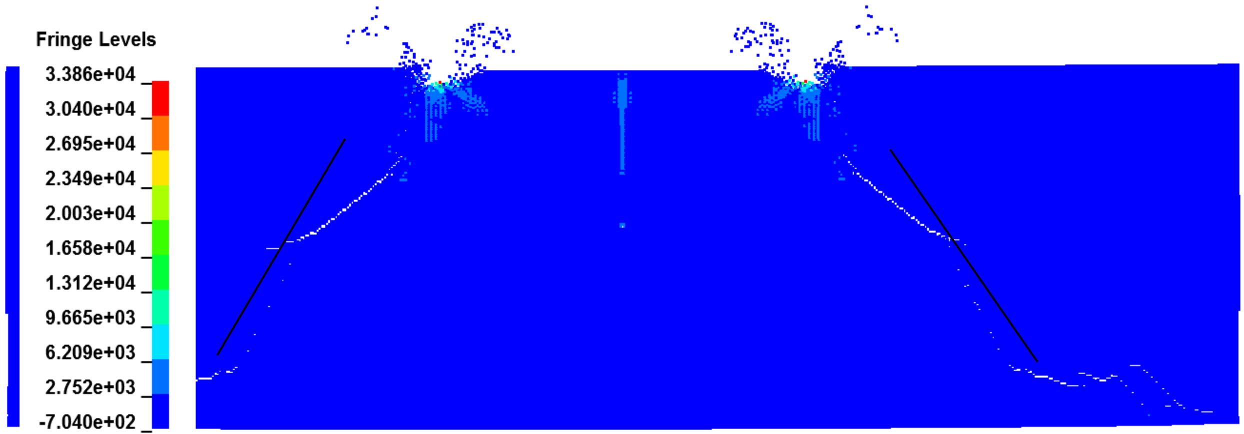

Figure 5-36: Hydrostatic pressure fringes, MAT159, 4500 psi concrete, 5.29 msec, units of psi (1 psi = 0.0069 MPa)

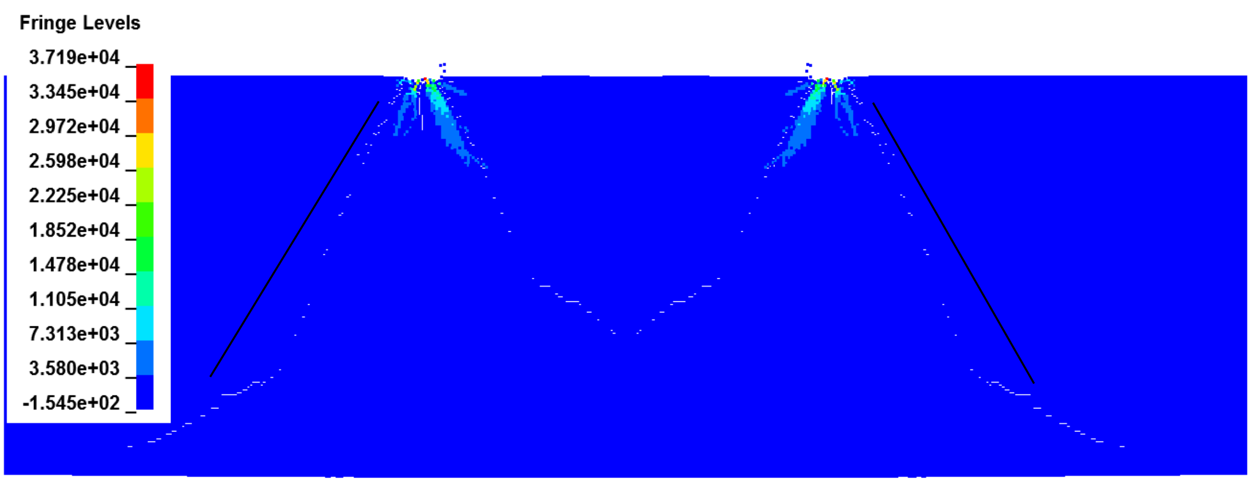

Figure 5-37: Hydrostatic pressure fringes, MAT016, 4500 psi concrete, 1.29 msec, units of psi (1 psi = 0.0069 MPa)

Table 5-9: Ranges of hydrostatic pressure during impact, 4500 psi (31 MPa) concrete

Material model	Hydrostatic pressure, psi (MPa)
MAT072R3	2300 to 19640 (15.9 to 135)
MAT159	2752 to 20000 (18.9 to 138)
MAT016	3580 to 22250 (24.7 to 153)

The pipe velocity histories are shown in Figure 5-38. The residual velocities using concrete models MAT159, MAT072R3, and MAT016 are -77 in/sec (-1.9 m/sec), -105 in/sec (-2.7 m/sec), and -785 in/sec (-19.9 m/sec), respectively. The magnitudes of the residual velocities are consistent with the predictions of perforation resistance using the generated shear failure surfaces (see Figure 5-24). The model using MAT016 provides the least resistance to perforation and achieves the greatest residual velocity of the three material models. MAT159 provides the greatest resistance to perforation and achieves the smallest residual pipe velocity. The predicted residual velocity of the pipe using the MAT072R3 model is similar to that using the MAT159 model because the concrete shear strengths at the predicted level of confinement, 26200 psi and 34800 psi, respectively, are similar.

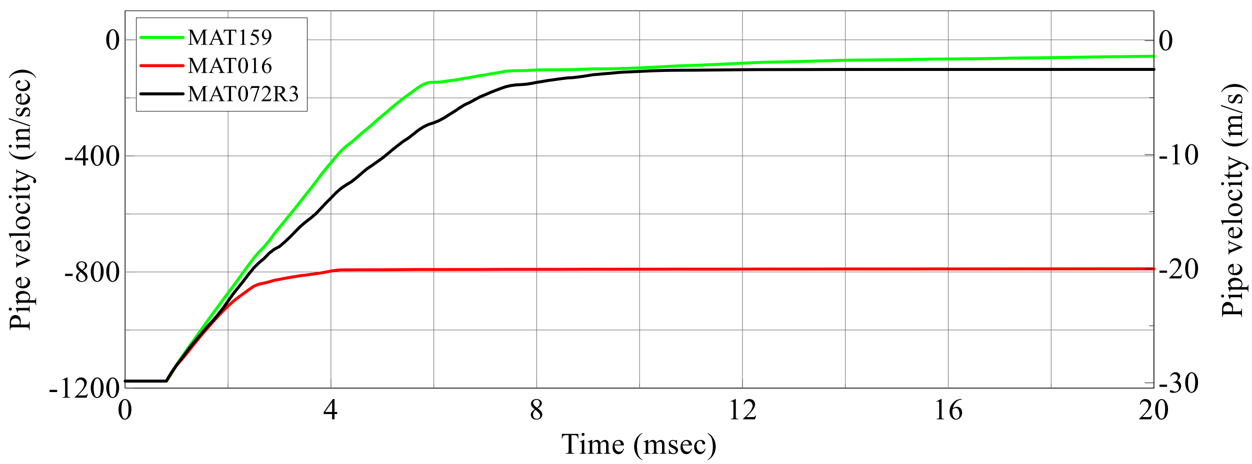

Figure 5-38: Pipe velocity histories, all material models, 2 mm mesh, 4500 psi (31 MPa) concrete

The panel back-face displacements, 20 msec after impact, using material models MAT072R3, MAT016, and MAT159 are shown in Figure 5-39. Results are presented for the finest concrete mesh used in each study (=2 mm). The predicted size of the conical plug was similar for all three material models.

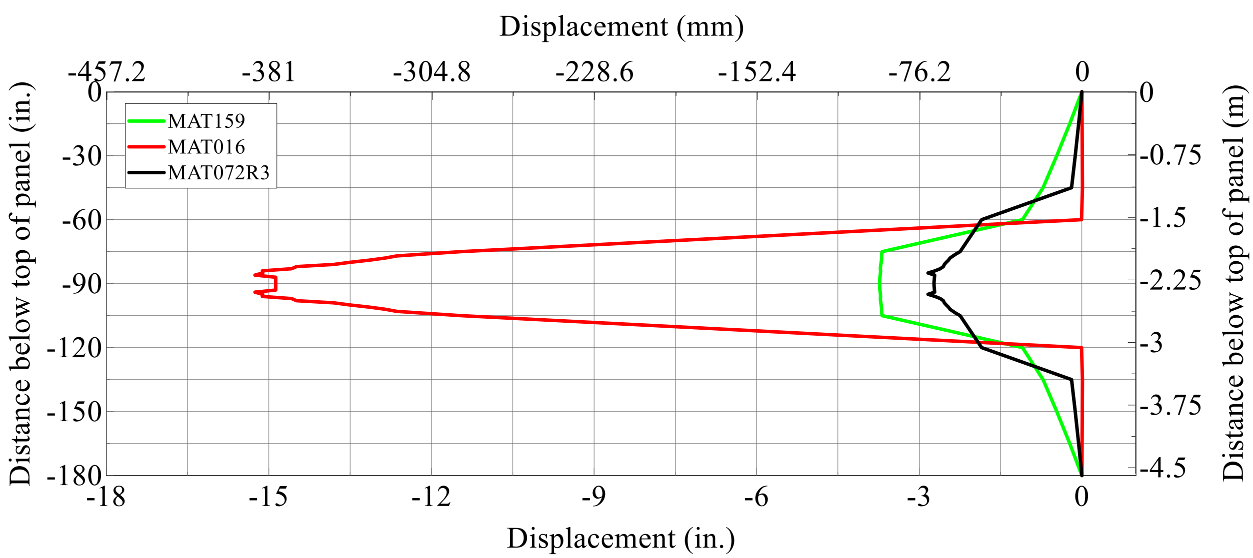

Figure 5-39: Back-face panel displacements, 2 mm mesh spacing, 4500 psi (31 MPa) concrete

5.5.6 Summary and Conclusions

EPRI Test 11 specifications (see Table 5-1) were used to investigate wall panel behavior as a function of concrete models in LS-DYNA (i.e., MAT016, MAT072R3, and MAT159); the concrete compressive was increased (=4500 psi (31 MPa)) from that specified in the physical test (=3600 psi (24.8 MPa)). The shear failure surfaces were developed and used to make predictions of panel resistance to perforation. The confining pressures at the interface between the pipe and the panel at the instant in time that the conical plug formed on the back face were estimated for all three material models. The order-of-magnitude of the pressures at the interface were consistent with the values reported in Schwer (2008b) for impact simulations. The model based on MAT016 (MAT159) provided the least (greatest) resistance to panel perforation, which is consistent with the calculated shear failure surfaces.

5.6 Comparison of EPRI Test 11 Impact Simulations using Different Concrete Material Models

5.6.1 Introduction

In this section, EPRI Test 11 (see Table 5-1) is simulated using MAT016 and MAT072R3; the reported uniaxial concrete compressive strength (=3600 psi (24.8 MPa)) was used for the simulations. The values for the concrete parameters describing the elastic and inelastic response of the concrete were generated internally by the material-model codes using only the uniaxial concrete compressive strength as input. The CSCM material model was not used for these calculations because the concrete strength (=3600 psi (24.8 MPa)) falls outside the bounds (4061 psi to 8412 psi (28 MPa to 58 MPa)) identified by Murray et al. (2007a) for parameter generation. Table 5-10 presents the simulations performed in this study. Simulations were conducted for concrete particle spacings of 3, 4, 5, and 10 mm to study mesh convergence. The numerical model used in the simulations is shown in Figure 5-17.

The values of the parameters for each material model are presented in Table 5-11, where ρ is the mass density, G is the shear modulus, ν is Poisson's ratio, and f_c' is concrete compressive strength. An "-" in a cell indicates that it is not a required input for that material model.

Table 5-10: Numerical simulations, MAT072R3 and MAT016

Simulation	Concrete mesh mm (in.)	Pipe mesh mm (in.)	Concrete model	f_c' MPa (psi)
1	10 (0.39)	5.35 (0.21)	MAT072R3	24.8 (3600)
2	5 (0.20)	2.67 (0.11)	MAT072R3	24.8 (3600)
3	4 (0.16)	2.14 (0.09)	MAT072R3	24.8 (3600)
4	3 (0.12)	1.6 (0.06)	MAT072R3	24.8 (3600)
5	10 (0.39)	5.35 (0.21)	MAT016	24.8 (3600)
6	5 (0.20)	2.67 (0.11)	MAT016	24.8 (3600)
7	4 (0.16)	2.14 (0.09)	MAT016	24.8 (3600)
8	3 (0.12)	1.6 (0.06)	MAT016	24.8 (3600)

Table 5-11: Input parameters for MAT072R3 and MAT016

	ρ g/mm^3 (lbf-s^2/in) ($\times 10^{-3}$)	G MPa (ksi)	ν	f_c' MPa (psi)
MAT027R3	2.17 (0.22)	-	0.15	24.8 (3600)
MAT016	2.17 (0.22)	4600 (667)	0.15	24.8 (3600)

The shear failure surfaces for concrete material models MAT072R3 and MAT016 are presented in Figure 5-40, calculated using equation (5-1). The input for the generation of these surfaces is presented in Table 5-12, in units of psi. The impact simulations of Section 5.5, which investigated the behavior of the panel as a function of different material models for EPRI Test 11 predicted a maximum confinement pressure on the order of 20300 psi (140 MPa) (see Table 5-9) for MAT072R3 and MAT016. For this confining pressure, Figure 5-40 predicts concrete shear strengths of 23600 psi (163 MPa) and 10100 psi (70 MPa) for MAT072R3 and MAT016, respectively. Since the concrete shear strength of MAT072R3 is approximately twice that of MAT016, the MAT072R3 material model is expected to provide greater resistance to perforation and predict a smaller residual velocity, if perforation occurs, than the MAT016 material model.

The tensile strength of concrete is generated internally by the material model and is based on the user-specified value of concrete compressive strength. For a compressive strength of 3600 psi (24.8 MPa), the tensile strengths for MAT072R3 and MAT016 are 371 psi (2.6 MPa) and 399 psi (2.8 MPa), respectively, calculated using equations (5-25) and (5-27), respectively.

Table 5-12: Shear failure surface inputs, 3600 psi (24.8 MPa) concrete, units of psi

Material model	Values of the input parameters		
MAT072R3	$a_0 = 1064$	$a_1 = 0.4463$	$a_2 = 2.24 \times 10^{-5}$
MAT016	$a_0 = 900$	$a_1 = 0.3333$	$a_2 = 9.26 \times 10^{-5}$

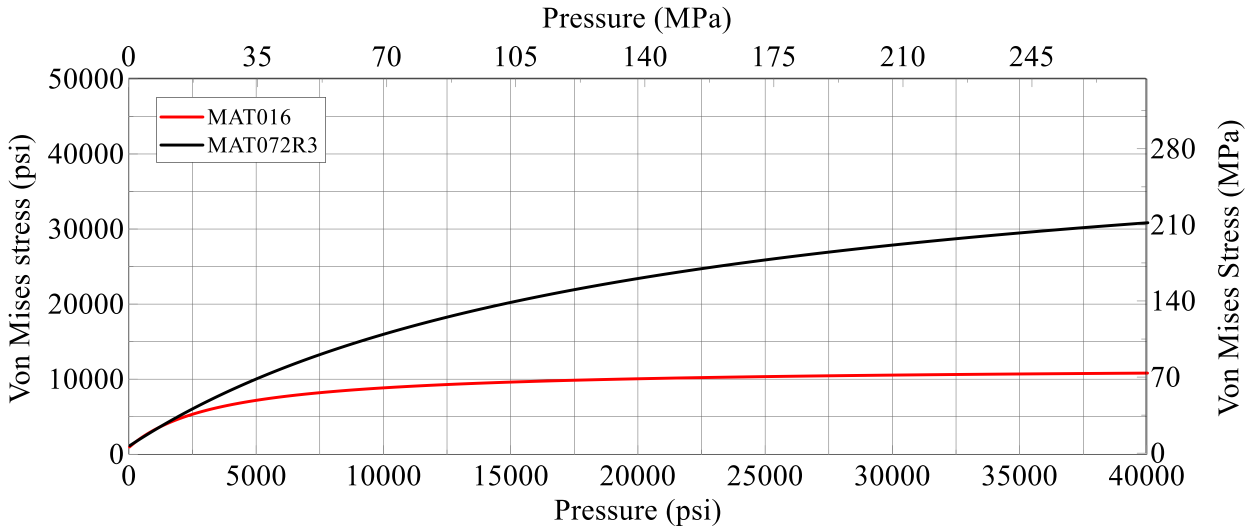

Figure 5-40: Shear failure surfaces, 3600 psi (24.8 MPa) concrete

5.6.2 Karagozian and Case Material Model (MAT072R3)

The results of simulations 1 through 4 (see Table 5-10) are presented in this section The concrete mesh refinement study for these simulations is shown in Figure 5-41. Residual pipe velocity is used as the convergence criterion. The pipe velocity begins to converge as the mesh is refined. Simulation results using the finest mesh (3 mm) are presented in Figure 5-42, 20 msec after impact. Spalling of the concrete on the front face and perforation of the panel are shown in Figure 5-42a and Figure 5-42b, respectively.

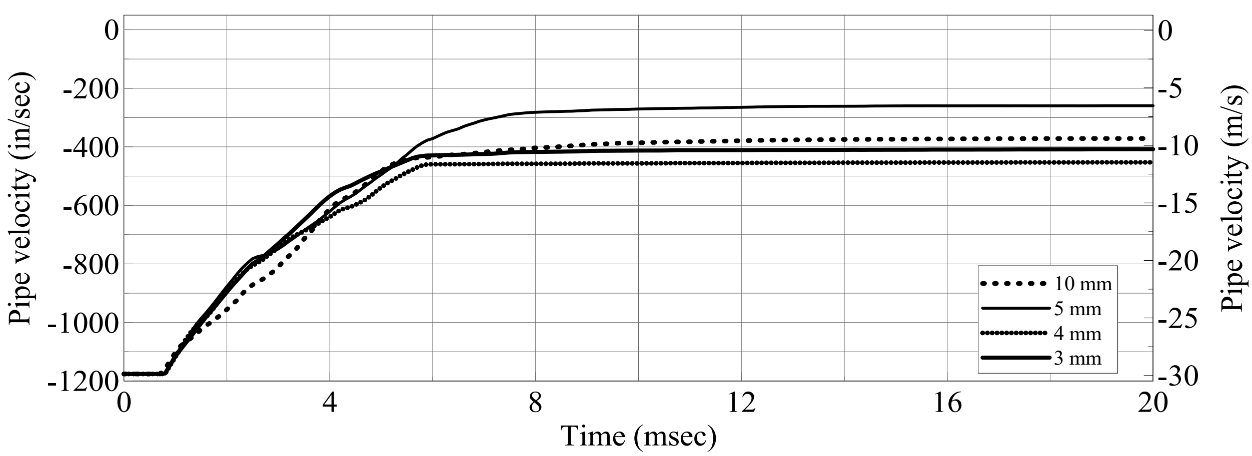

Figure 5-41: Pipe velocity histories, Test 11, MAT072R3, 3600 psi (24.8 MPa) concrete

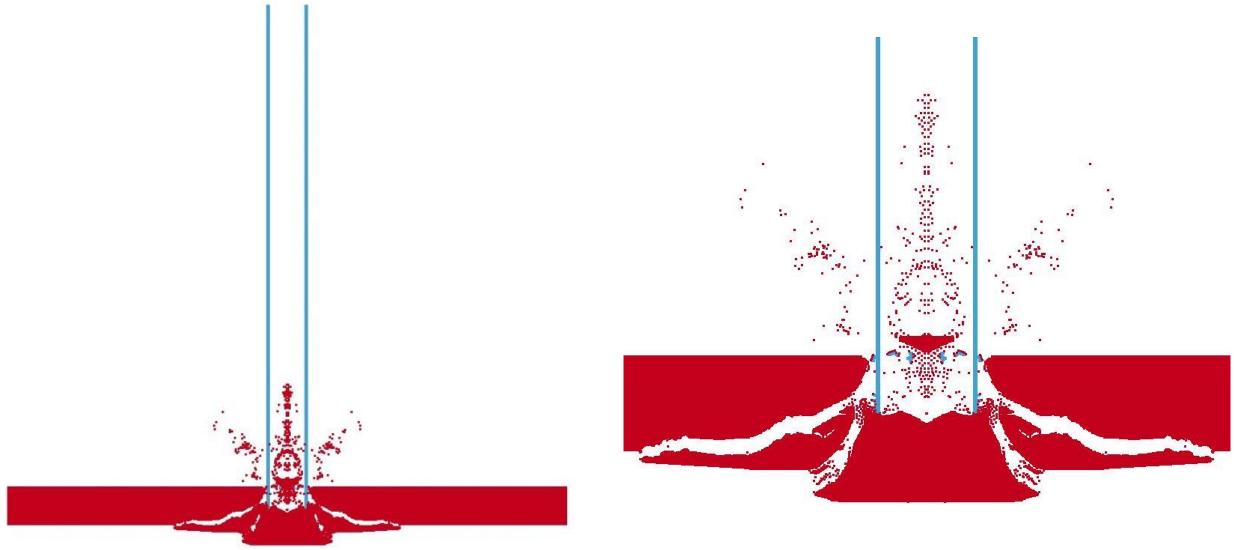

(a) Concrete spalling and perforation of panel (b) Perforation of panel

Figure 5-42: Simulation results, 20 msec, Test 11, MAT072R3, 3 mm mesh, simulation 4

Results are summarized in Table 5-13. Perforation (P) was predicted in all of the simulations but was not observed in the experiment. Based on the results of the analysis using the finest mesh (3 mm, simulation 4), the numerical model predicts the front face crater diameter reasonably well, but overpredicts the back face crater diameter by 41%. The conical plug diameter is not presented for these simulations because the panel was perforated. The evolution of panel back-face lateral displacement is presented in Figure 5-43 (simulation 4). The back-face displacement monitoring locations are presented in Figure 5-27.

Table 5-13: Summary of results, Test 11, MAT072R3

-	Concrete mesh spacing mm (in.)				
	3 (0.12)	4 (0.16)	5 (0.20)	10 (0.39)	Experiment
Penetration depth, mm (in.)	P	P	P	P	114 (4.5)
Front face crater diameter, mm (in.)	457 (18)	457 (18)	457 (18)	457 (18)	570 (18.5)
Conical plug diameter, mm (in)	-	-	-	-	787 (31)
Back face crater diameter, mm (in.)	1829 (72)	1372 (54)	1829 (72)	762 (30)	1295 (51)
Residual pipe velocity, m/s (in./sec)	-10.6 (-416)	-11.7 (-460)	-6.7 (-262)	-9.5 (-373)	-

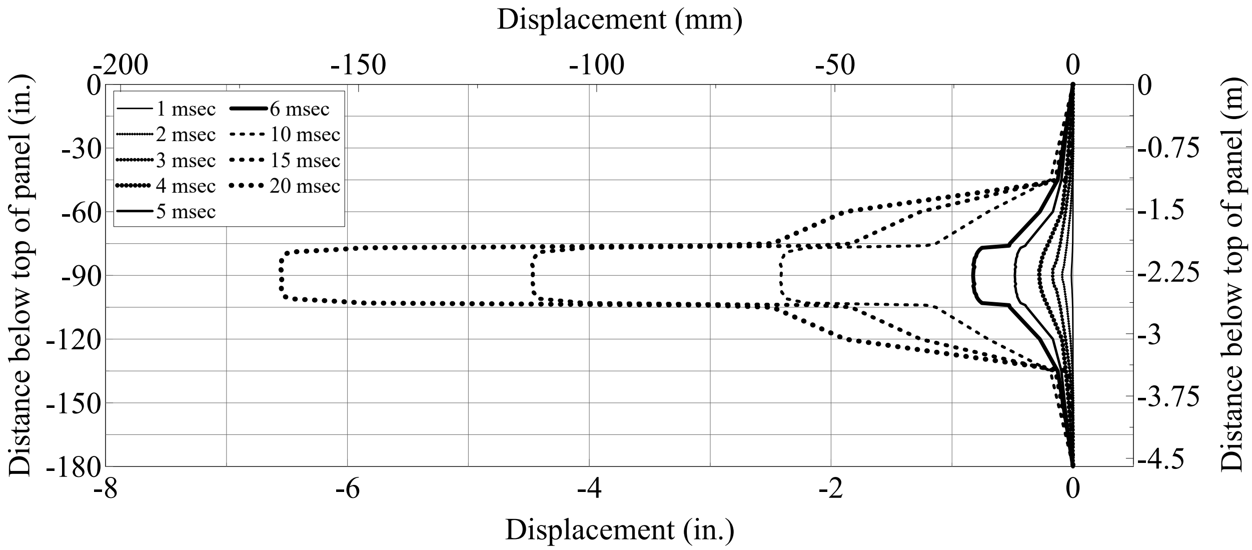

Figure 5-43: Panel back-face lateral displacement, Test 11, MAT072R3, 3 mm mesh, simulation 4

5.6.3 Pseudo Tensor Material Model (MAT016)

Simulations 1 through 4 were revisited in this section using the MAT016 material model, and are identified as simulations 5 through 8 in Table 5-10. A mesh refinement study was conducted and results are presented in Figure 5-44. The pipe velocities converge as the mesh is refined. Figure 5-45 shows results of the simulation using the finest mesh (3 mm, simulation 8), 20 msec after impact. Spalling of concrete and perforation of the panel are shown in Figure 5-45a and Figure 5-45b, respectively.

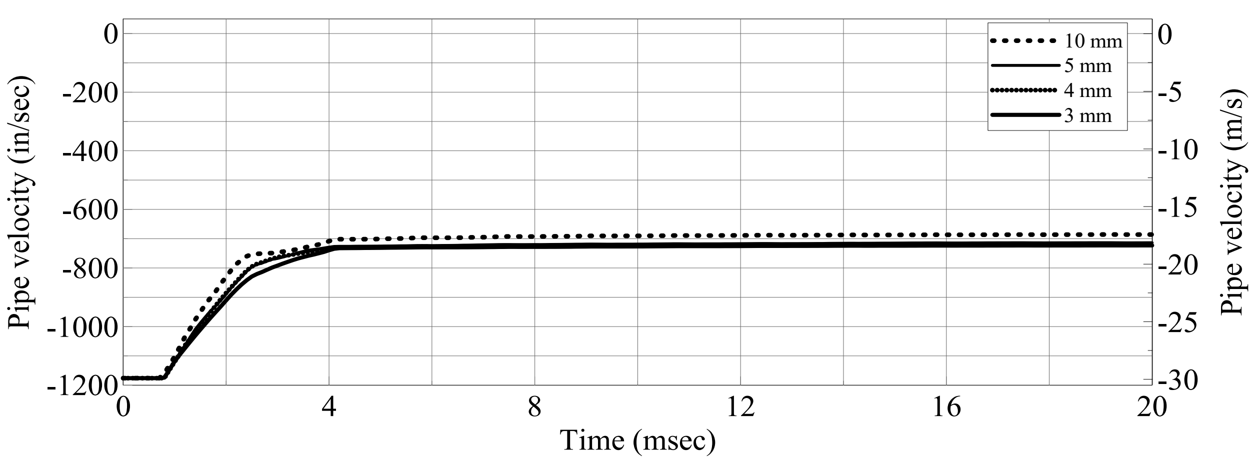

Figure 5-44: Pipe velocity histories, Test 11, MAT016, 3600 psi (24.8 MPa) concrete

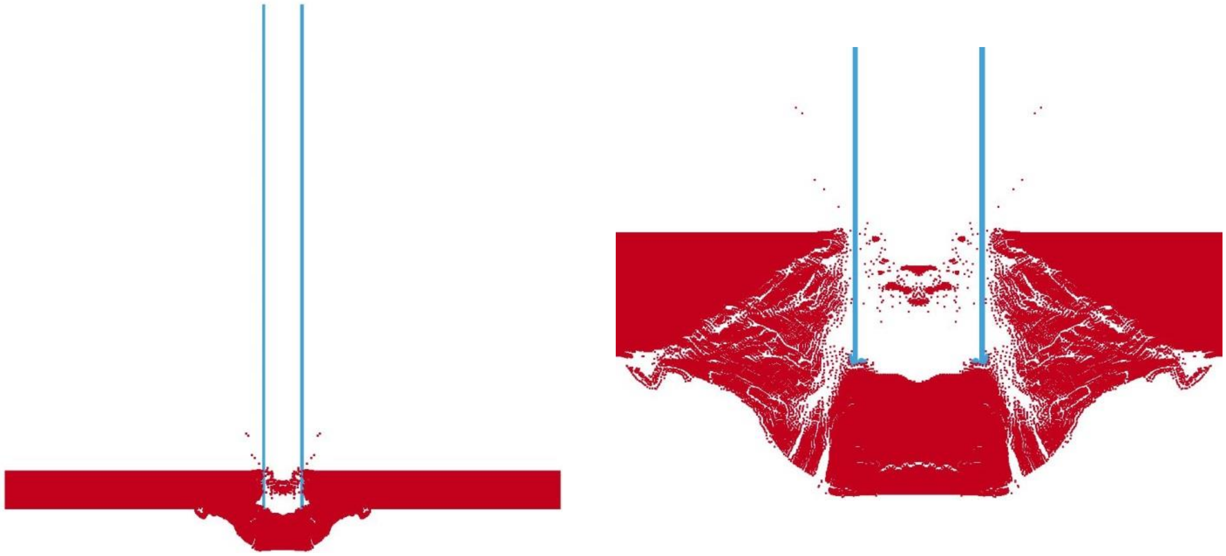

(a) Concrete spalling and perforation of panel (b) Perforation of panel

Figure 5-45: Simulation results, 20 msec, Test 11, MAT016, 3 mm mesh, simulation 8

Table 5-14 presents the results of the simulations and the experiment; perforation (P) of the panel was predicted in all four numerical simulations but was not observed in the experiment. The simulation results are presented for the complete panel. Based on the results of the finest mesh (3 mm), the front and back face crater diameters are in reasonable agreement with the results of the experiment; the conical plug diameter is not reported for the numerical simulations because the panel was perforated. Figure 5-46 shows the evolution of the panel back-face lateral displacement for the simulation using the finest mesh (3 mm, simulation 8). Significant local deformation at the point of impact is observed.

Table 5-14: Summary of results, Test 11, MAT016

	Concrete mesh spacing mm (in.)				
	3 (0.12)	4 (0.16)	5 (0.20)	10 (0.39)	Experiment
Penetration depth, mm (in.)	P	P	P	P	114 (4.5)
Front face crater diameter, mm (in.)	457 (18)	508 (20)	508 (20)	457 (18)	570 (18.5)
Conical plug diameter, mm (in)	-	-	-	-	787 (31)
Back face crater diameter, mm (in.)	1372 (54)	1270 (50)	1067 (42)	1118 (44)	1295 (51)
Residual pipe velocity, m/s (in./sec)	-17.8 (-700)	-17.8 (-700)	-17.8 (-700)	-17.8 (-700)	-

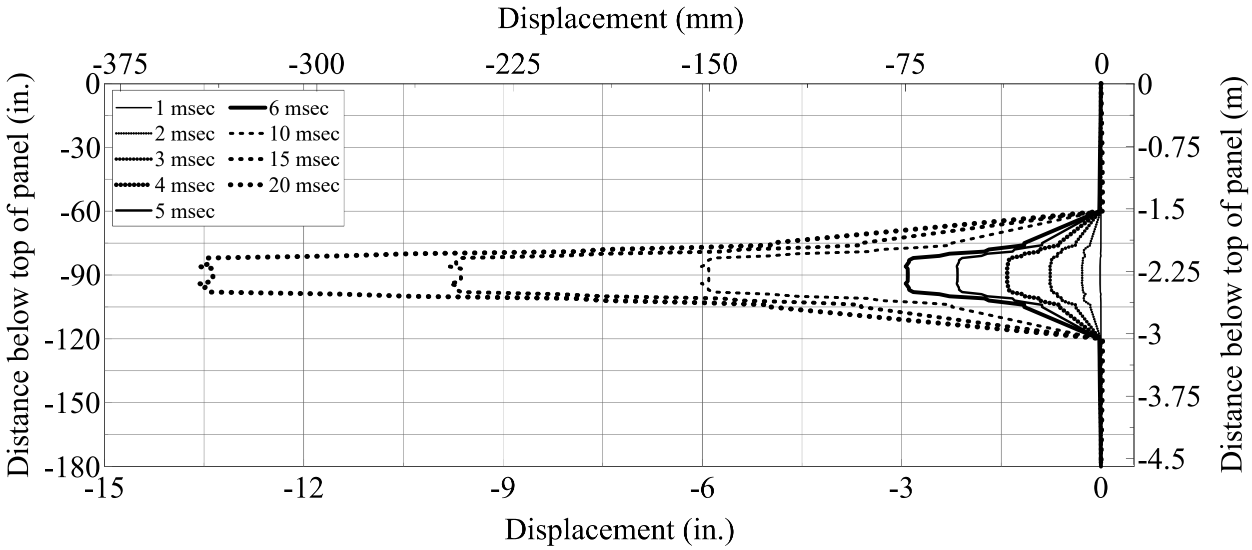

Figure 5-46: Panel back-face lateral displacement, Test 11, MAT016, 3 mm mesh, simulation 8

5.6.4 Summary and Conclusions

The EPRI Test 11 experiment was simulated in this section using the MAT072R3 and MAT016 material models. The values of the parameters used to define the elastic and inelastic response of the concrete were internally generated using the user-defined uniaxial concrete compressive strength as input. The two material models estimated the tensile strength of the concrete to be approximately 10% of the uniaxial compressive strength. Mesh refinement studies were conducted using the residual pipe velocity as the convergence criterion. Simulations using both material models predicted perforation of the panel, which was not observed in the experiment. Further, MAT072R3 did not accurately predict the damage to the back face of the panel. The poor agreement between the predicted and observed damage prompted an investigation of the effects of concrete compressive and tensile strength on the impact resistance of reinforced concrete panels, which are presented next.

5.7 Effect of Concrete Compressive Strength on Impact Resistance

A study was conducted using the MAT072R3 material model to investigate the effect of uniaxial unconfined concrete compressive strength on panel response. Test 11 (12-inch (305 mm) panel impacted by a 12-inch (305 mm) Schedule 40 pipe at a velocity of 98 fps (30 m/s) was used as the basis for the calculations. Concrete compressive strengths of 2000 psi (13.8 MPa), 3000 psi (20.7 MPa), 3500 psi (24.1 MPa), 4000 psi (27.6 MPa), 4500 psi (31.0 MPa) and 6000 psi (41.4 MPa) were considered. The tensile strength of the concrete was held constant for all analyses at

450 psi (3.1 MPa): 7.5% to 22.5% of the concrete compressive strength. A summary of the numerical simulations performed in this study is presented in Table 5-15.

The shear failure surface for these six values of unconfined compressive strength as a function of confining (hydrostatic) pressure are presented in Figure 5-47, calculated using equation (5-1). The values of the input parameters for the generation of these surfaces are presented in Table 5-16; the values are in units of psi. The application of a confining (hydrostatic) pressure substantially increases the shear strength of the concrete. For a given confining pressure, an increase in the uniaxial compressive strength (see legend in Figure 5-47) will lead to an increase in concrete shear strength. Table 5-17 presents shear strength data for a confining pressure of 19640 psi (135 MPa): the hydrostatic pressure calculated in Section 5.5.5 at the contact surface between a pipe and a reinforced concrete panel, at the instant a conical plug has formed. At this confining pressure, a three-fold increase in uniaxial compressive strength will lead to an 80% increase in shear strength. The impact resistance of a panel will improve with an increase in the uniaxial compressive strength of the concrete.

The pipe velocity history for each compressive strength is presented in Figure 5-48. Mesh convergence studies were conducted for each value of compressive strength; the pipe velocity histories for compressive strengths of 2000 psi (13.8 MPa), 3000 psi (20.7 MPa), 3500 psi (24.1 MPa), 4000 psi (27.6 MPa), 4500 psi (31.0 MPa), and 6000 psi (41.4 MPa) are presented in Figures C1 through C6 (in Appendix C), respectively. The estimated rates of convergence and values of *GCI* for each compressive strength are presented in Table C-1 in Appendix C. The results for the simulations using a concrete compressive strength of 3000 psi were discarded because the residual pipe velocities did not converge as the mesh was refined (see Figure C-2). The particle spacing of 3 mm used in the simulation with a concrete compressive strength of 4000 psi was discarded because the results were significantly different from those with other particle spacings (see Figure C-4). The converged mesh size used for each value of compressive strength is presented in the legend in Figure 5-48. The pipe did not perforate the panel for concrete compressive strengths of 4500 psi (31.0 MPa) and 6000 psi (41.4 MPa). Residual pipe velocities of -26 fps (-8 m/s), -12 fps (-3.7 m/s), and -9 fps (-2.7 m/s) were predicted for the panels with compressive strengths of 2000 psi (13.8 MPa), 3500 psi (24.1 MPa), and 4000 psi (27.6 MPa), respectively. The results of the simulations suggest that unconfined compressive strength has a significant effect on penetrability of a panel.

Table 5-15: Numerical simulations, MAT072R3, concrete compressive strength

Simulation	Concrete mesh mm (in.)	Pipe mesh mm (in.)	f_c' MPa (psi)	f_t' MPa (psi)
1	10 (0.39)	5.35 (0.21)	13.8 (2000)	3.1 (450)
2	5 (0.20)	2.67 (0.11)	13.8 (2000)	3.1 (450)
3	4 (0.16)	2.14 (0.09)	13.8 (2000)	3.1 (450)
4	3 (0.12)	1.6 (0.06)	13.8 (2000)	3.1 (450)
5	2 (0.08)	1 (0.04)	13.8 (2000)	3.1 (450)
6	10 (0.39)	5.35 (0.21)	20.7 (3000)	3.1 (450)
7	5 (0.20)	2.67 (0.11)	20.7 (3000)	3.1 (450)
8	4 (0.16)	2.14 (0.09)	20.7 (3000)	3.1 (450)
9	3 (0.12)	1.6 (0.06)	20.7 (3000)	3.1 (450)
10	2 (0.08)	1 (0.04)	20.7 (3000)	3.1 (450)
11	10 (0.39)	5.35 (0.21)	24.1 (3500)	3.1 (450)
12	5 (0.20)	2.67 (0.11)	24.1 (3500)	3.1 (450)
13	4 (0.16)	2.14 (0.09)	24.1 (3500)	3.1 (450)
14	3 (0.12)	1.6 (0.06)	24.1 (3500)	3.1 (450)
15	2 (0.08)	1 (0.04)	24.1 (3500)	3.1 (450)
16	10 (0.39)	5.35 (0.21)	27.6 (4000)	3.1 (450)
17	5 (0.20)	2.67 (0.11)	27.6 (4000)	3.1 (450)
18	4 (0.16)	2.14 (0.09)	27.6 (4000)	3.1 (450)
19	3 (0.12)	1.6 (0.06)	27.6 (4000)	3.1 (450)
20	2 (0.08)	1 (0.04)	27.6 (4000)	3.1 (450)
21	10 (0.39)	5.35 (0.21)	31.0 (4500)	3.1 (450)
22	5 (0.20)	2.67 (0.11)	31.0 (4500)	3.1 (450)
23	4 (0.16)	2.14 (0.09)	31.0 (4500)	3.1 (450)
24	3 (0.12)	1.6 (0.06)	31.0 (4500)	3.1 (450)
25	10 (0.39)	5.35 (0.21)	41.4 (6000)	3.1 (450)
26	5 (0.20)	2.67 (0.11)	41.4 (6000)	3.1 (450)
27	4 (0.16)	2.14 (0.09)	41.4 (6000)	3.1 (450)
28	3 (0.12)	1.6 (0.06)	41.4 (6000)	3.1 (450)

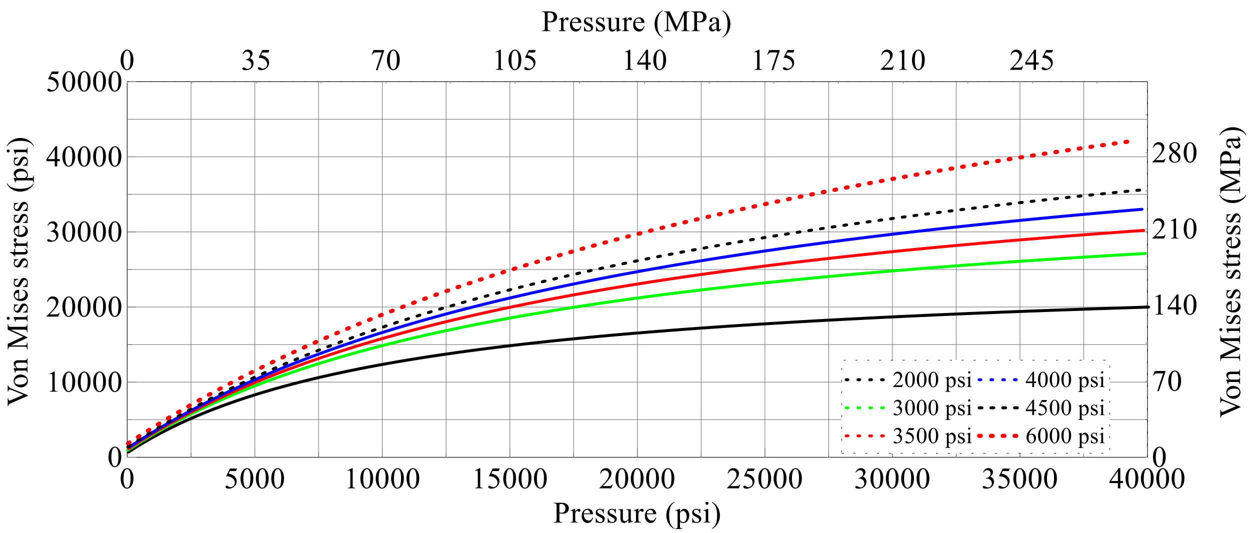

Figure 5-47: MAT072R3 shear failure surfaces for different concrete compressive strengths

Table 5-16: Shear failure surface inputs, MAT072R3, units of psi

f_c' (psi)	Values of the input parameters		
2000	$a_0 = 591$	$a_1 = 0.4463$	$a_2 = 4.04 \times 10^{-5}$
3000	$a_0 = 887$	$a_1 = 0.4463$	$a_2 = 2.69 \times 10^{-5}$
3500	$a_0 = 1040$	$a_1 = 0.4463$	$a_2 = 2.31 \times 10^{-5}$
4000	$a_0 = 1180$	$a_1 = 0.4463$	$a_2 = 2.02 \times 10^{-5}$
4500	$a_0 = 1330$	$a_1 = 0.4463$	$a_2 = 1.80 \times 10^{-5}$
6000	$a_0 = 1770$	$a_1 = 0.4463$	$a_2 = 1.35 \times 10^{-5}$

Table 5-17: Concrete shear strengths for different uniaxial unconfined concrete compressive strengths at a confining pressure of 19640 psi (135 MPa), MAT072R3

f_c', psi (MPa)	2000 (13.8)	3000 (20.7)	3500 (24.1)	4000 (27.6)	4500 (31.0)	6000 (41.4)
Concrete shear strength, psi (MPa)	16400 (113.1)	21000 (144.8)	22900 (157.9)	24500 (168.9)	25900 (178.6)	29400 (202.7)

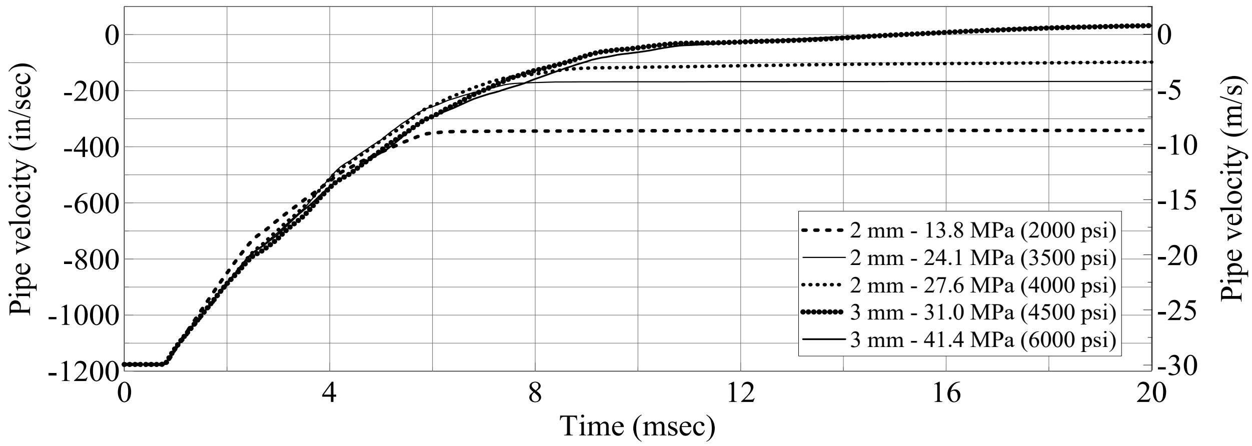

Figure 5-48: Pipe velocity histories for different concrete compressive strengths

5.8 Effect of Concrete Tensile Strength on Impact Resistance

The effect of concrete tensile strength on panel impact resistance was investigated using MAT072R3 and EPRI Test 11: 12-inch (305 mm) panel normally impacted by a 12-inch (305 mm) Schedule 40 pipe at a velocity of 98 fps (30 m/s). The concrete compressive strength was held constant for this study at a value of 3600 psi (24.8 MPa) to investigate the effect of tensile strength of concrete. Tensile strengths of 180 psi (1.24 MPa), 360 psi (2.48 MPa), 540 psi (3.72 MPa) and 720 psi (4.96 MPa) were studied, which correspond to 5%, 10%, 15%, and 20% of the concrete compressive strength, respectively, and 3, 6, 9, and 12 $\sqrt{f_c'}$, respectively. Table 5-18 lists the numerical simulations performed in this study.

The pipe velocity history for each tensile strength is presented in Figure 5-49. The mesh convergence study for each tensile strength is presented in Appendix C; the pipe velocity histories for tensile strengths of 180 psi (1.24 MPa), 360 psi (2.48 MPa), 540 psi (3.72 MPa), and 720 psi (4.96 MPa) are presented in Figures C-7, C-8, C-9, and C-10, respectively. The converged mesh size for each tensile strength is shown in the legend in Figure 5-49. The estimated rates of convergence and values of *GCI* for each tensile strength are presented in Table C-2 in Appendix C. The pipe did not perforate the panel for tensile strengths of 540 psi (3.72 MPa) and 720 psi (4.96 MPa). The residual pipe velocities for the panels with a tensile strength of 180 psi (1.24 MPa) and 360 psi (2.48 MPa) were -52 fps (-16 m/s) and -29 fps (-8.8 m/s), respectively. The results indicate that concrete tensile strength has a very significant effect on the impact resistance of concrete panels.

Table 5-18: Numerical simulations, MAT072R3, concrete tensile strength

Simulation	Concrete mesh mm (in.)	Pipe mesh mm (in.)	f_c' MPa (psi)	f_t' MPa (psi)
1	10 (0.39)	5.35 (0.21)	24.8 (3600)	1.24 (180)
2	5 (0.20)	2.67 (0.11)	24.8 (3600)	1.24 (180)
3	4 (0.16)	2.14 (0.09)	24.8 (3600)	1.24 (180)
4	3 (0.12)	1.6 (0.06)	24.8 (3600)	1.24 (180)
5	2 (0.08)	1 (0.04)	24.8 (3600)	1.24 (180)
6	10 (0.39)	5.35 (0.21)	24.8 (3600)	2.48 (360)
7	5 (0.20)	2.67 (0.11)	24.8 (3600)	2.48 (360)
8	4 (0.16)	2.14 (0.09)	24.8 (3600)	2.48 (360)
9	3 (0.12)	1.6 (0.06)	24.8 (3600)	2.48 (360)
10	2 (0.08)	1 (0.04)	24.8 (3600)	2.48 (360)
11	10 (0.39)	5.35 (0.21)	24.8 (3600)	3.72 (540)
12	5 (0.20)	2.67 (0.11)	24.8 (3600)	3.72 (540)
13	4 (0.16)	2.14 (0.09)	24.8 (3600)	3.72 (540)
14	3 (0.12)	1.6 (0.06)	24.8 (3600)	3.72 (540)
15	10 (0.39)	5.35 (0.21)	24.8 (3600)	4.96 (720)
16	5 (0.20)	2.67 (0.11)	24.8 (3600)	4.96 (720)
17	4 (0.16)	2.14 (0.09)	24.8 (3600)	4.96 (720)
18	3 (0.12)	1.6 (0.06)	24.8 (3600)	4.96 (720)

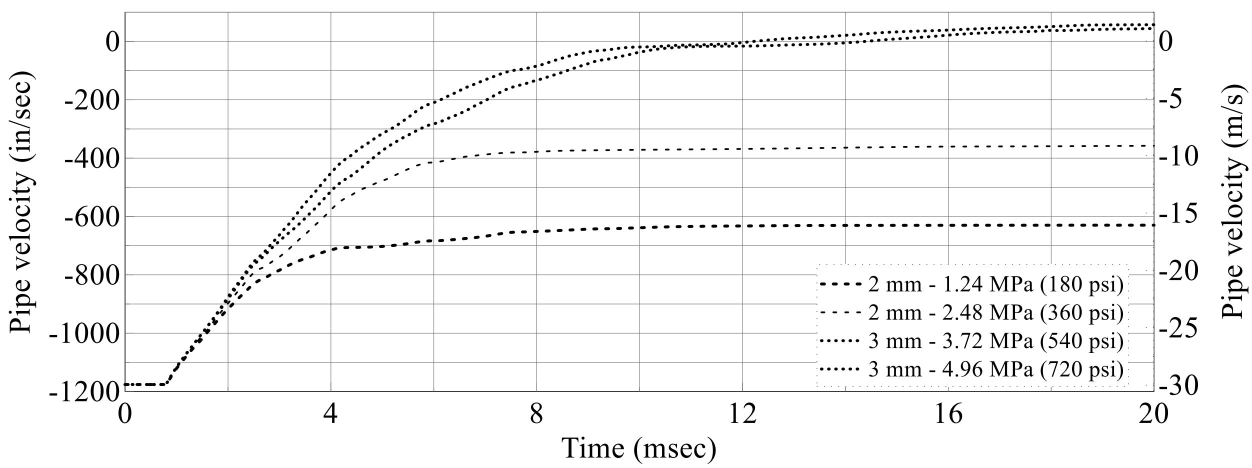

Figure 5-49: Pipe velocity histories for different concrete tensile strengths

5.9 EPRI Impact Simulations and Validation of Numerical models for Wind-borne Missile Impact

5.9.1 Introduction

The following subsections present results of axisymmetric simulations of the EPRI impact tests listed in Table 5-1. Modeling in LS-DYNA, including element formulations, strain rate effects, material models, and SPH particle spacing requirements for the pipe and panels are those presented in Section 5.3. Figure 4-8 identifies the terminology used to evaluate the performance of the panels and is used as a basis for the comparison of results from numerical predictions and experiments. Discretization error in the numerical models is evaluated using GCI. The material model MAT072R3 was used for these simulations, and the tensile strength of concrete was set equal to 15% of the unconfined uniaxial compressive strength.

5.9.2 Test 11

5.9.2.1 *Introduction*

In EPRI Test 11, a 743 lb (337 kg) Schedule 40 pipe normally impacted a 12-inch (305 mm) panel wall at a velocity of 98 fps (30 m/s). The missile penetrated the target and caused scabbing on the back (non-impact) face of the panel. Table 5-19 lists the simulations performed. Simulations were conducted for a particle spacing of 3, 4, 5, and 10 mm to study mesh convergence. The axisymmetric model used in the simulations is that described in Figure 5-17.

Table 5-19: Numerical simulations, MAT072R3, Test 11

Simulation	Concrete mesh mm (in.)	Pipe mesh mm (in.)	f_c' MPa (psi)	f_t' MPa (psi)
1	10 (0.39)	5.35 (0.21)	24.8 (3600)	3.7 (540)
2	5 (0.20)	2.67 (0.11)	24.8 (3600)	3.7 (540)
3	4 (0.16)	2.14 (0.09)	24.8 (3600)	3.7 (540)
4	3 (0.12)	1.6 (0.06)	24.8 (3600)	3.7 (540)

5.9.2.2 *Simulation Results*

Figure 5-50a shows simulation results 20 msec after impact. Results are presented for the finest mesh (3 mm), which corresponds to simulation 4 in Table 5-19. Spalling (ejecta) of the concrete on the front face and local deformation on the back face, opposite the point of impact, is apparent. Figure 5-50b through Figure 5-50d show the formation of the conical plug at 10, 15, and 20 msec after impact, respectively.

The numerically predicted damage to the panel is presented in Table 5-20 for concrete particle spacings of 3, 4, 5, and 10 mm: penetration depth, front- and back-face crater diameters, conical plug diameter, and perforation velocity (if applicable) are reported. The results of the simulation are presented for the entire panel. The damage to the panel observed in the experiment is presented in the last column of Table 5-20. Based on the results of the finest mesh (3 mm), the numerical model reasonably reproduces the front- and back-face plug diameters. The penetration depth measured in the experiment was underpredicted by a factor of three using the finest (3 mm). Since the 3 and 4 mm meshes recovered the same penetration depth (the metric used to estimate discretization error in the meshes where perforation did not occur), the numerical simulation is assumed to have converged. The GCI is not an appropriate metric in this case because the order of convergence (see equation (5-15)) is undefined: the difference between metrics, f_2 and f_1, defined as f_{21}, is zero.

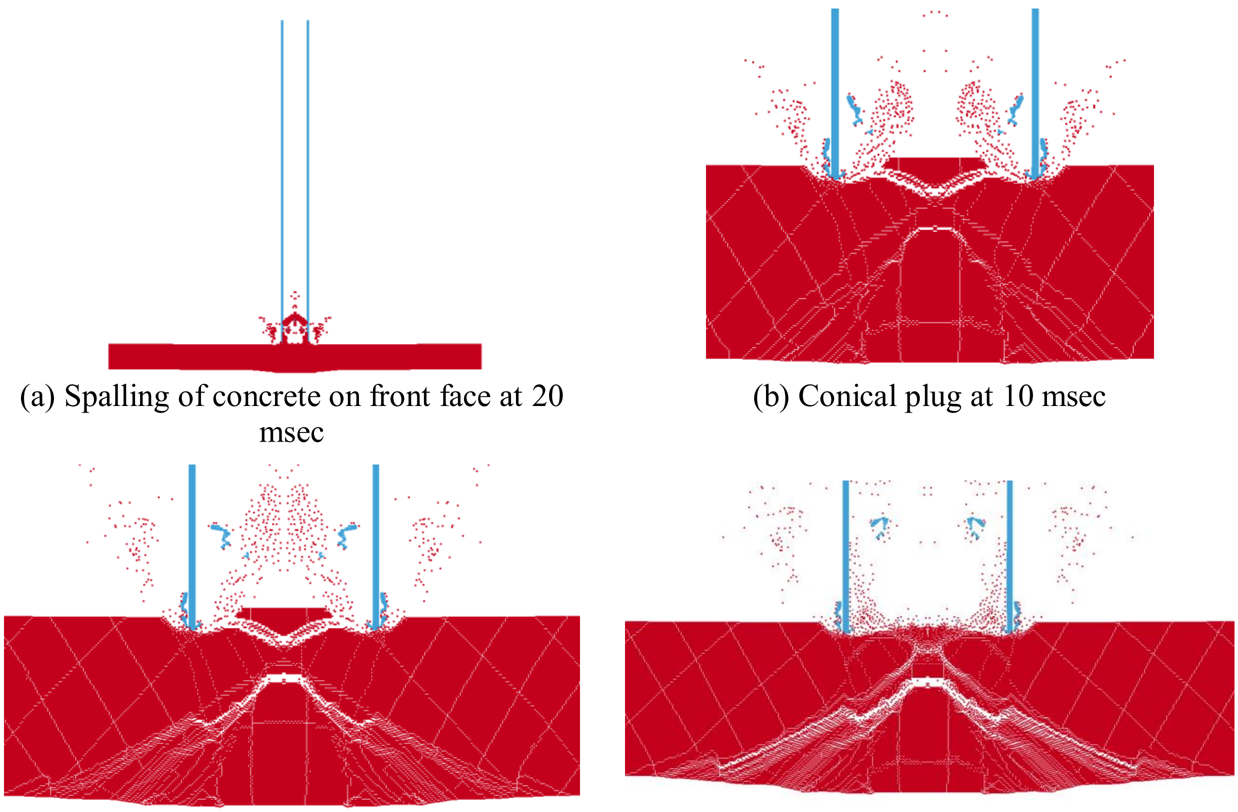

(a) Spalling of concrete on front face at 20 msec

(b) Conical plug at 10 msec

(c) Conical plug at 15 msec

(d) Conical plug at 20 msec

Figure 5-50: Simulation results, Test 11, 3 mm mesh, simulation 4

Figure 5-51 presents the pipe velocity histories for particle spacings of 3, 4, 5, and 10 mm; the results converge as the mesh is refined. The evolution of the panel back-face displacement over the duration of the simulation is shown in Figure 5-52 using a particle spacing of 3 mm (simulation 4). The panel displacement indicates local response only, near the point of impact.

Table 5-20: Results summary, Test 11

	Concrete particle spacing mm (in.)				
	3 (0.12)	4 (0.16)	5 (0.20)	10 (0.39)	Experiment
Penetration depth, mm (in.)	38.1 (1.5)	38.1 (1.5)	Perforation	Perforation	114 (4.5)
Front face crater diameter, mm (in.)	431 (17)	431 (17)	406 (16)	406 (16)	570 (18.5)
Conical plug diameter, mm (in.)	813 (32)	813 (32)	1143 (45)	1219 (48)	787 (31)
Back face crater diameter, mm (in.)	813 (32)	813 (32)	1143 (45)	1219 (48)	1295 (51)
Residual pipe velocity, m/s (in./sec)	-	-	-1.2 (-48)	-0.6 (-24)	-

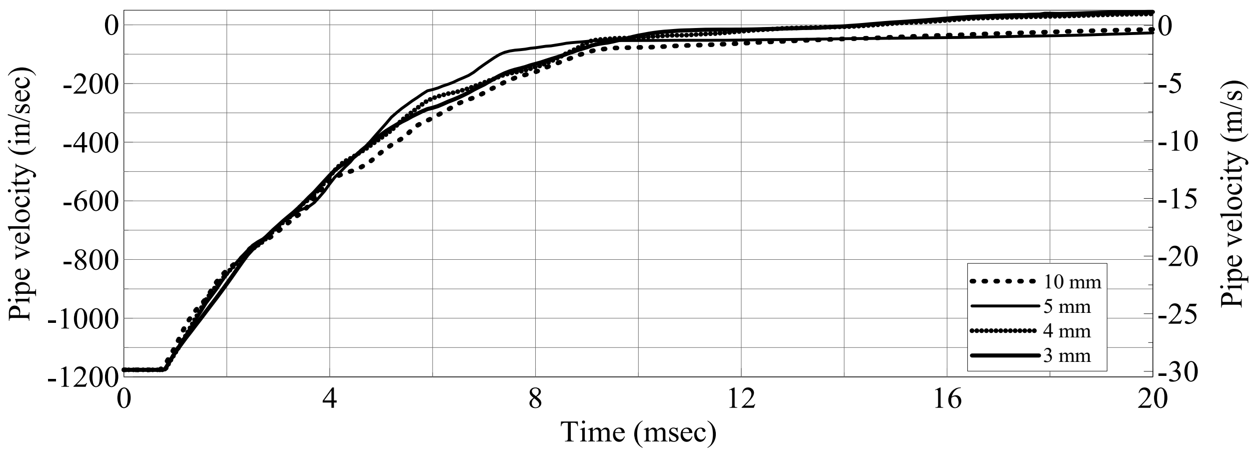

Figure 5-51: Pipe velocity histories, Test 11

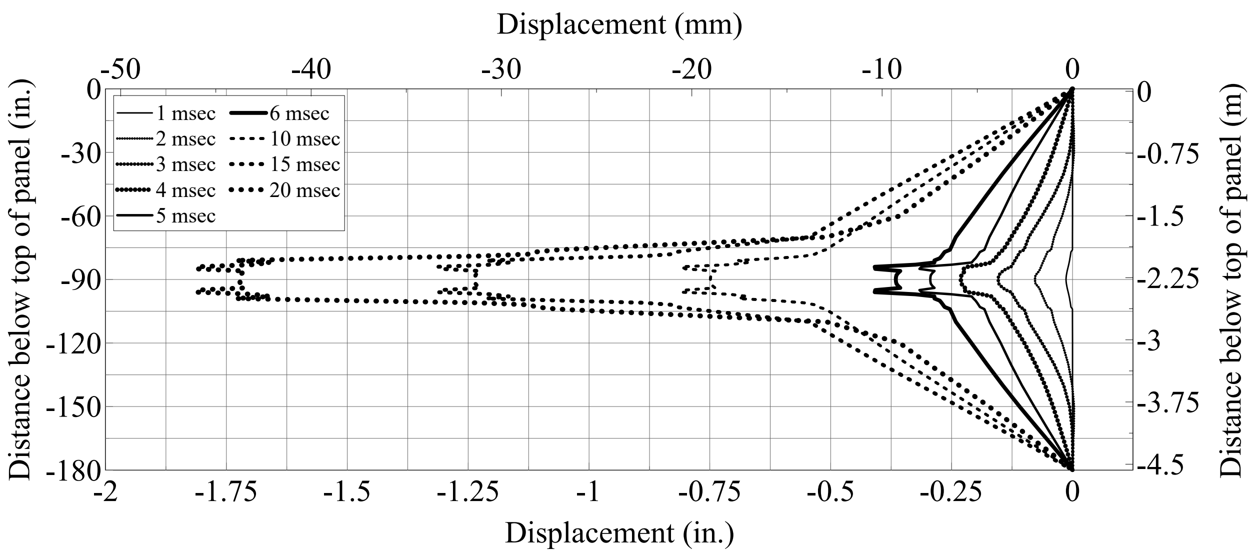

Figure 5-52: Panel back-face lateral displacement, Test 11, 3 mm mesh, simulation 4

5.9.2.3 *Impact Force and Energy Balance using the SPH Formulation*

The impact force from simulation 4 (Table 5-19) was evaluated using the SPHOUT and MATSUM options in the ASCII output files. The predicted forces were multiplied by 2π to obtain the total force.

Figure 5-53 presents the SPH impact force history from the SPHOUT output. The corresponding maximum force is 13.5 kips ($=2.15\times2\pi$ kips), which is significantly different from the experimental value of 360 kips reported in Chapter 4. The impact forces were also checked twice using MATSUM output: 1) multiplying the acceleration time history by the mass of the Schedule 40 pipe, and 2) differentiating the momentum of the concrete panel and Schedule 40 pipe. Figure 5-54 shows the rigid body acceleration history of the Schedule 40 pipe for the first 20 msec of the simulation. The maximum deceleration (=776.4g) occurs at approximately 1 msec, which is the time at which the pipe contacts the panel. Multiplying this value by the mass of the pipe in the axisymmetric simulation (=3.67 slugs), gives a maximum force of approximately 578 kips ($=92\times2\pi$ kips), which overpredicts the 360 kips calculated in the experiment.

Figure 5-55 shows the momentum history of the concrete panel and the Schedule 40 pipe. Differentiating these histories gives the impact-force history of both parts and these are shown in Figure 5-56. The maximum impact force on the panel and the Schedule 40 pipe are 1005 kips and 616 kips, respectively. The impact force predicted using the product of the mass of the pipe and the acceleration history (=578 kips) is similar to that predicted by differentiating the momentum of the Schedule 40 pipe (=616 kips).

The impact force obtained from the SPHOUT of 13.5 kips is a factor of 43 smaller than the impact force computed from the MATSUM results (=578 kips) and both predictions are significantly different from that calculated from the experimental data (=360 kips). Since, the maximum impact force predicted in the Lagrangian simulation is similar to that calculated in the experiment (see Figure 4-14), forces output from the SPH calculations are incorrect.

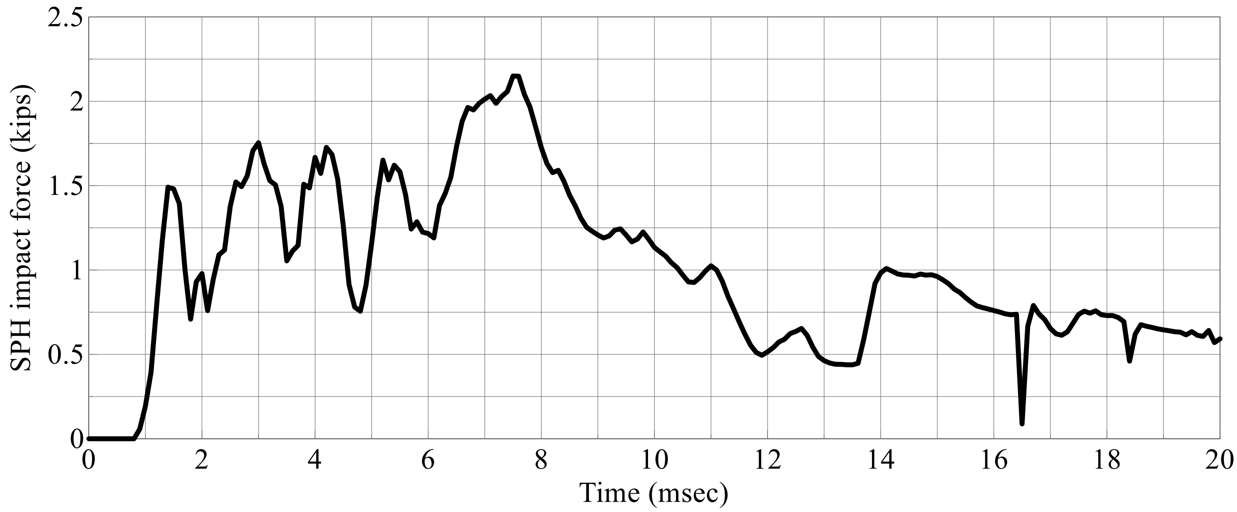

Figure 5-53: SPHOUT impact force history, Test 11, simulation 4

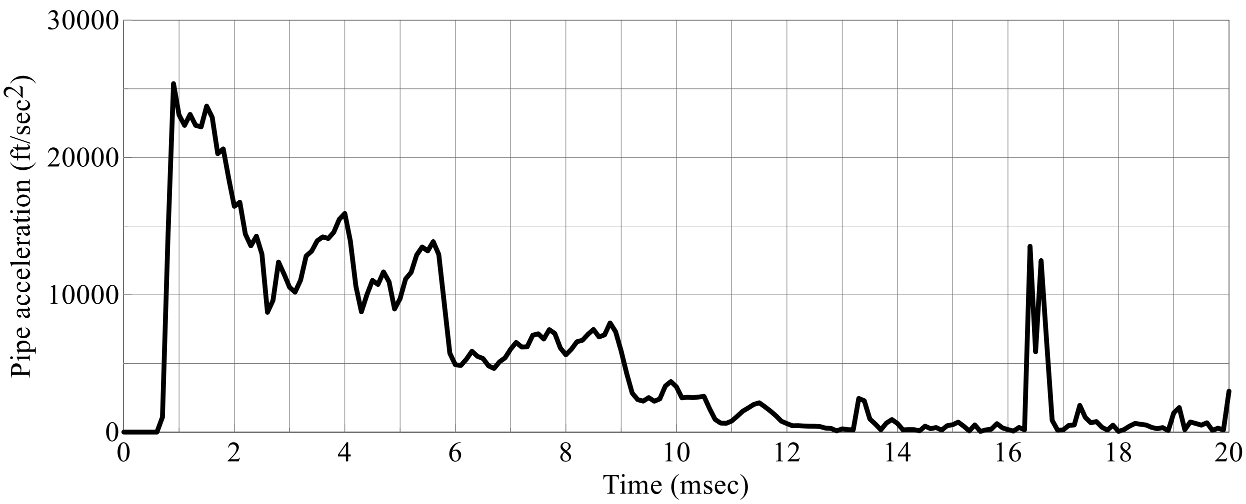

Figure 5-54: Rigid body acceleration history of Schedule 40 pipe, Test 11, simulation 4

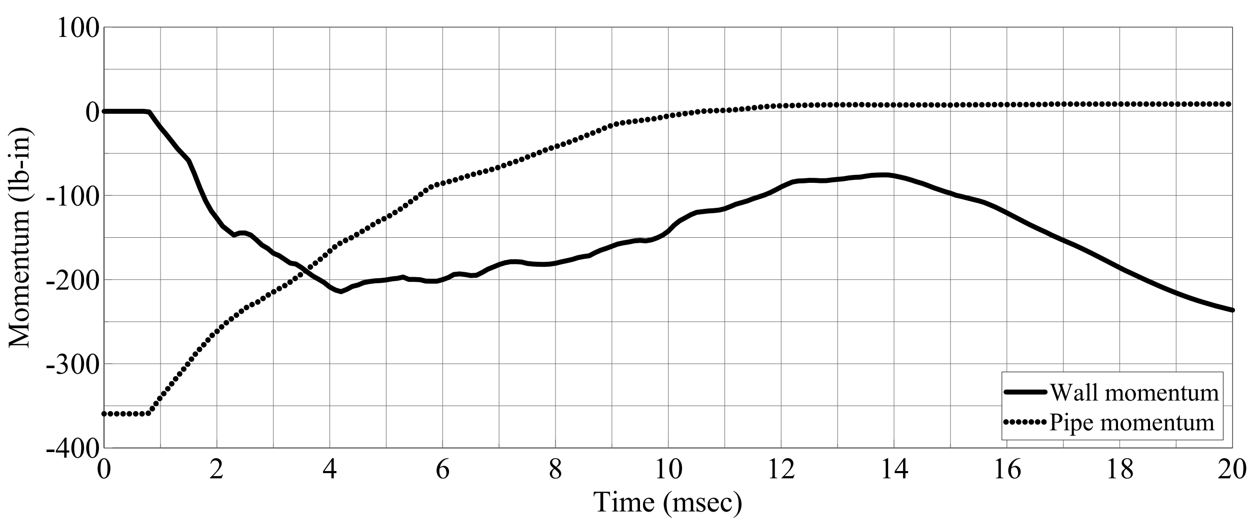

Figure 5-55: Momentum history, Test 11, simulation 4

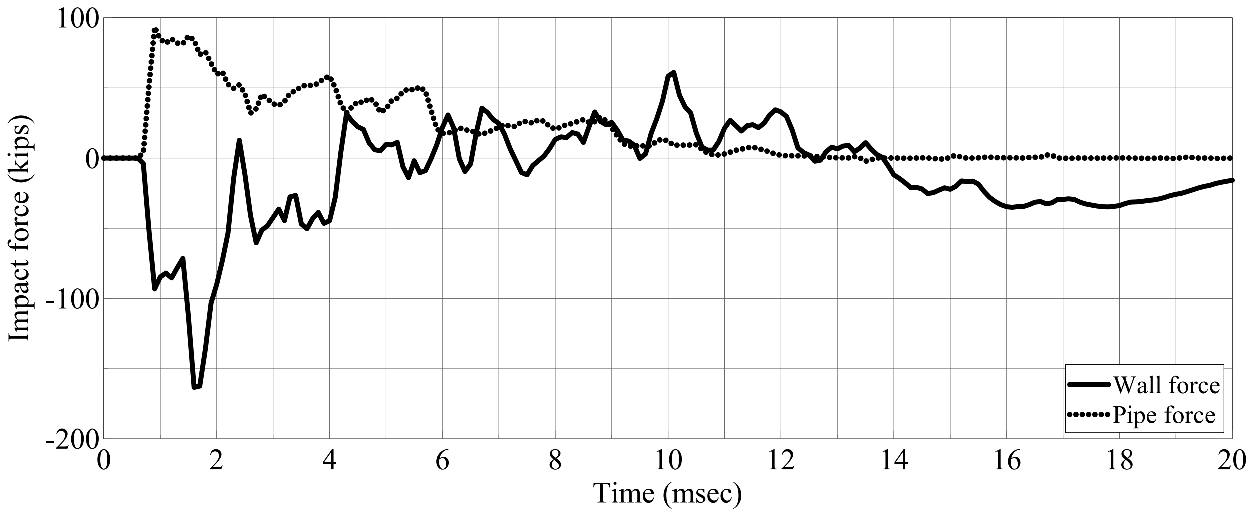

Figure 5-56: Impact force history, Test 11, simulation 4

The energy calculations from the axisymmetric simulation are presented in Figure 5-57. The kinetic and internal energies of the Schedule 40 pipe and panel are presented. The initial energy in the system is the kinetic energy of the Schedule 40 pipe ($KE_{pipe} = 0.5mv^2$). In this case, the mass, m, is 16% (57.29°/360°) of the total mass of the Schedule 40 pipe (= 22.94 slugs), and v is the velocity of the pipe at impact (= 98 ft/sec). The kinetic energy of the pipe was calculated as 17,630 lb-ft (or 211,556 lb-in per Figure 5-57).

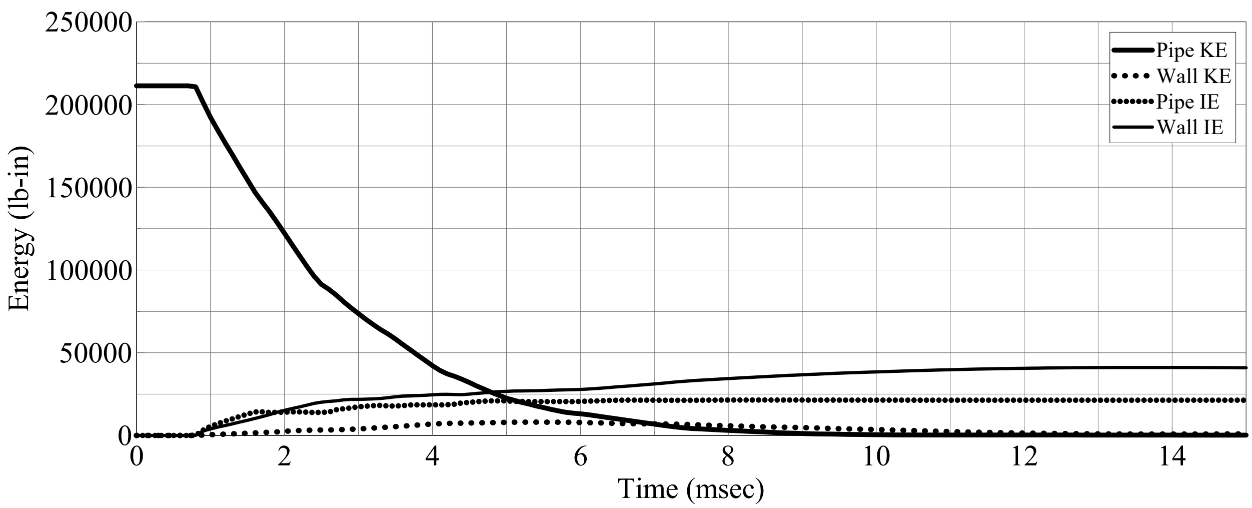

Figure 5-57: Energy plot, Test 11, simulation 4

The numerically predicted values of energy of Figure 5-57 are presented in Table 5-21, where IE_{wall} and IE_{pipe} are the internal energies of the wall and pipe, respectively. In this case, the total energy, E_t, should recover the initial kinetic energy of the pipe. The results show that 71% of the energy is unaccounted for in the SPH simulation and the energy dissipated due to bulk viscosity is not the source of the energy imbalance.

Table 5-21: Numerically predicted energy values, Test 11, simulation 4

	KE_{pipe}	IE_{wall}	IE_{pipe}	E_t
Energy (lb-in)	211,556	40,900	21,300	62,200

The SPH-based calculation of impact force and energies are clearly incorrect. In the next section, the robustness of the SPH formulation for impact simulations and predictions of damage is demonstrated using two independent analyses.

5.9.2.4 *Robustness of the SPH Formulation for Impact Analysis*

5.9.2.4.1 Introduction

The impact forces and energy histories presented in Section 5.9.2.3 for the SPH-simulation of EPRI Test 11 (see Section 5.9.2), were dramatically different from those calculated using the Lagrangian formulation (see Section 4.3.2). To demonstrate the robustness of the SPH formulation, aside from the calculations of local force and energies, results of SPH and Lagrangian analyses are presented here.

5.9.2.4.2 Elastic Impact of an Annular Pipe on a Rigid Plate

A 3D model of a 12-inch (305 mm) diameter Schedule 40 pipe and a 40 in × 40 in (1016 mm × 1016 mm) rigid plate was built to predict impact forces on a rigid plate. Simulations were performed using a) Lagrangian elements, and b) SPH particles for the Schedule 40 pipe to determine if the force histories on the rigid plate were similar. The models of the Lagrangian pipe and SPH pipe are presented in Figure 5-58 and Figure 5-59, respectively. The elastic material model MAT001 was used for the SPH particles and the solid elements in the Schedule 40 pipe; the inputs are density (ρ=7.41$\times$10^{-4} lb-sec^2/in^4 (7919 kg/m^3)), elastic modulus (E=2.9$\times$10^7 psi (2.0$\times$10^5 MPa)), and Poisson's ratio (ν=0.3). The rigid material model MAT020 was assigned to the shell elements of the rigid plate. The Schedule 40 pipe was modeled with 0.25 in × 0.25 in (6.35 mm × 6.35 mm) solid elements in the impact zone and 0.25 in × 3 in (6.35 mm × 76.2 mm) elements, elsewhere (see Figure 5-58). The plate was modeled with 2 in × 2 in (50.8 mm × 50.8 mm) shell elements. An SPH particle spacing of 0.2 in (5.08 mm) was used for the Schedule 40 pipe (see Figure 5-59). The constant stress formulation (ELFORM=1 in LS-DYNA), the default particle approximation theory (ELFORM=0 in LS-DYNA), and the Belytschko-Tsay formulation (ELFORM=2 in LS-DYNA) were used for the solid elements, SPH particles, and shell elements, respectively. The *CONTACT_AUTOMATIC_NODES_TO_SURFACE keyword was used to define contact between the Schedule 40 pipe and the rigid plate in both models. The Schedule 40 pipe had a mass of 22.94 slugs (334.8 kg) and impacted the rigid plate at a velocity of 98 fps (29.9 m/s) in both simulations.

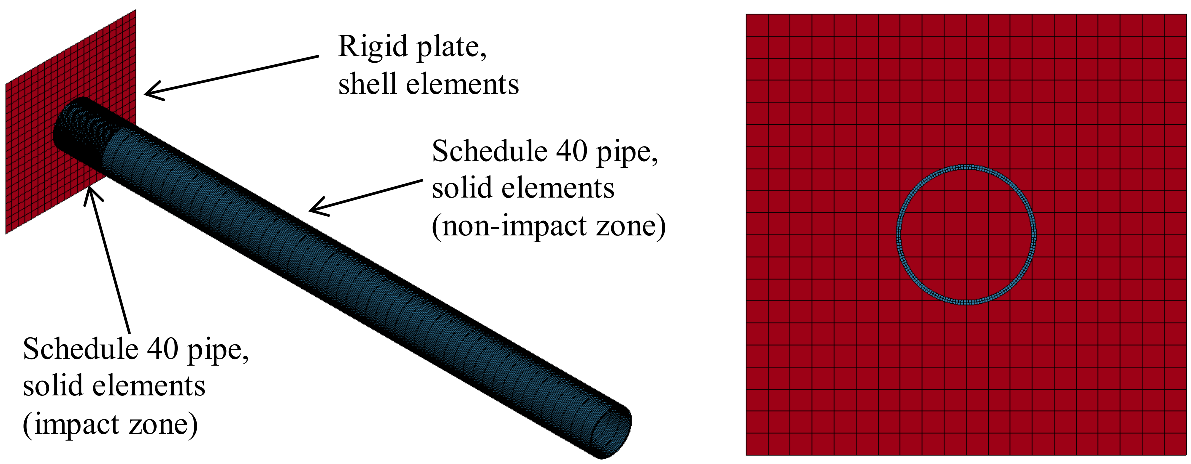

(a) Isometric view (b) Front view

Figure 5-58: 3D model of Lagrangian Schedule 40 pipe and rigid plate

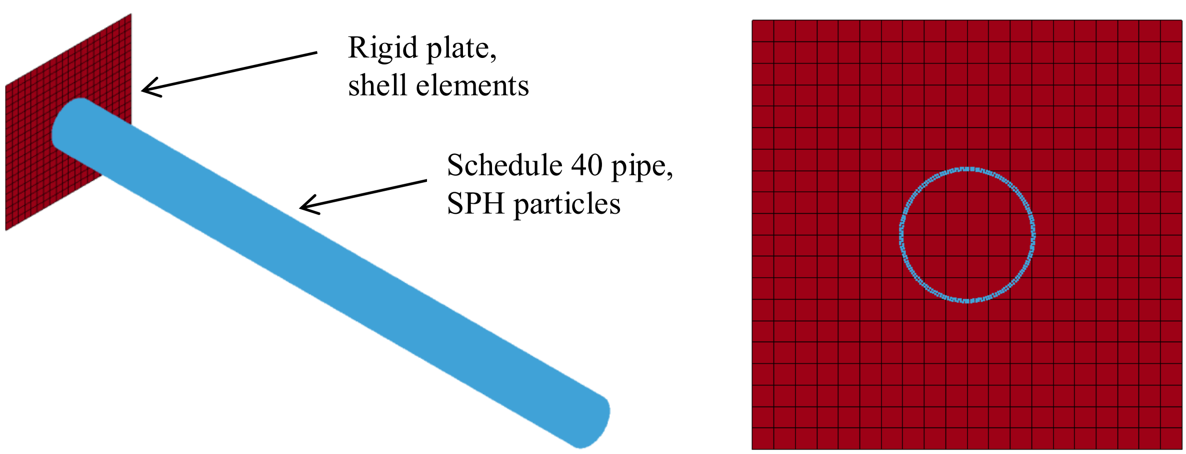

(a) Isometric view (b) Front view

Figure 5-59: 3D model of SPH Schedule 40 pipe and rigid plate

The contact force histories on the rigid plate caused by the impact of the Lagrangian and SPH Schedule 40 pipes are presented in Figure 5-60. The histories are effectively identical, making it clear that the transfer of force and energy are the same for both the Lagrangian and SPH models of the pipe.

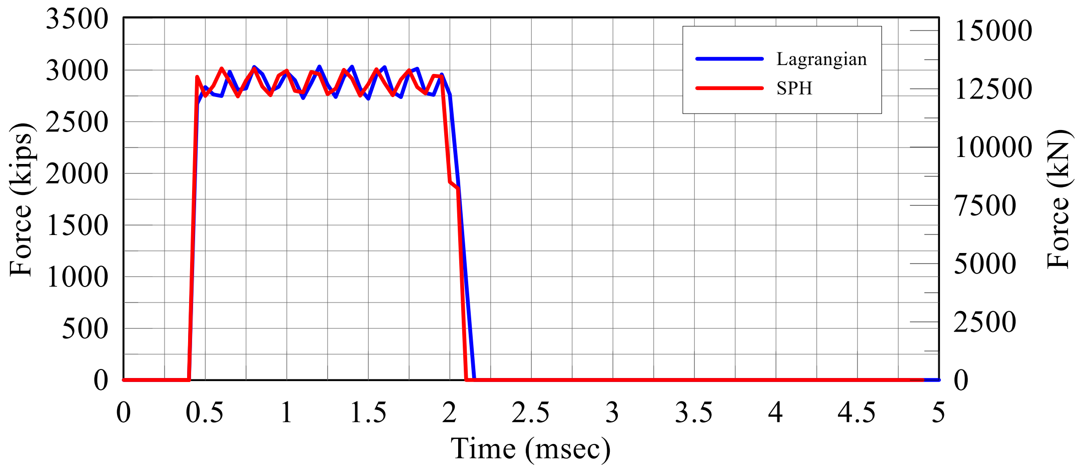

Figure 5-60: Impact force history on a rigid plate

The magnitude of the impact force is approximately 2900 kips (12900 kN) for both simulations. Since the contact between the pipe and the rigid plate is elastic (i.e., both momentum and kinetic energy are conserved), the impact force can also be predicted using equation (5-28)

$$F = \frac{\Delta p}{\Delta t} = \frac{m\Delta v}{\Delta t} \tag{5-28}$$

where F is the impact force, $\Delta p / \Delta t$ is the time rate of change of momentum, $\Delta v / \Delta t$ is the rate of change of velocity with respect to time, and m is the mass of the Schedule 40 pipe (=1.92 lb-sec^2/in (336 kg)). The time Δt is defined as the duration of contact between the Schedule 40 pipe and the rigid plate before rebound (=0.00175 sec) and calculated from the simulations to predict the impact force per equation (5-28). The computed impact force is 2655 kips (11810 kN), which is similar to that predicted in the simulations.

5.9.2.4.3 EPRI Test 11

In this section, results of the simulation of EPRI Test 11 using Lagrangian and SPH formulations, presented previously in Sections 4.3.2 and 5.9.2, respectively, are compared, with a focus on damage. Figure 5-61a and Figure 5-61b show the formation of the conical plug, 20 msec after impact, using the Lagrangian and SPH formulations, respectively. The predicted values of penetration depth, and conical plug diameter using the Lagrangian and SPH formulations are 1.1 in (27.9 mm) and 1.5 in (38.1 mm), and 28 in (711 mm) and 32 in (813 mm), respectively. The predicted values are essentially identical, providing more evidence the two formulations are delivering similar forces and energy to the reinforced concrete panel. Given that the Lagrangian output of force and energies are similar to those measured in the experiment (and described previously), the SPH formulation in LS-DYNA can be used for predictions of damage, including spalling, scabbing, conical-plug formation and perforation. Subsequent presentations of analysis results using the SPH formulation do not include force and energy histories.

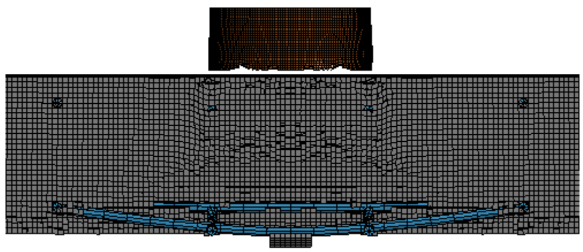

(a) Lagrangian formulation

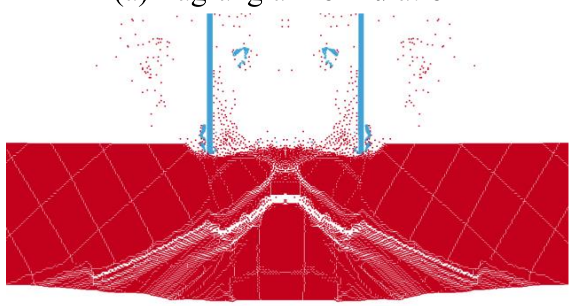

(b) SPH formulation

Figure 5-61: Formation of conical plug, EPRI Test 11, 20 msec after impact

5.9.3 Test 10

5.9.3.1 *Introduction*

In EPRI Test 10, a 743 lb (337 kg) Schedule 40 pipe normally impacted a 12-inch (305 mm) panel at a velocity of 143 fps (44 m/s), perforating the panel and causing heavy scabbing on the back face. The exit velocity of the Schedule 40 pipe was not documented. Table 5-22 presents the simulations performed in this subsection. The axisymmetric model is shown in Figure 5-17. Concrete mesh spacings of 2, 3, 4, 5, and 10 mm were considered in the study to evaluate mesh convergence.

Table 5-22: Numerical simulations, MAT072R3, Test 10

Simulation	Concrete mesh mm (in.)	Pipe mesh in. (mm)	f_c' MPa (psi)	f_t' MPa (psi)
1	10 (0.39)	5.35 (0.21)	25.5 (3700)	3.8 (555)
2	5 (0.20)	2.67 (0.11)	25.5 (3700)	3.8 (555)
3	4 (0.16)	2.14 (0.09)	25.5 (3700)	3.8 (555)
4	3 (0.12)	1.6 (0.06)	25.5 (3700)	3.8 (555)
5	2 (0.08)	1.1 (0.04)	25.5 (3700)	3.8 (555)

5.9.3.2 *Simulation Results*

Figure 5-62a and Figure 5-62b show spalling of the concrete on the front face and perforation of the panel, respectively, 20 msec after impact. The simulation results are presented for the finest mesh (i.e., 2 mm, simulation 5).

(a) Concrete spalling and perforation of panel (b) Perforation of panel

Figure 5-62: Simulation results, 20 msec, Test 10, 2 mm mesh, simulation 5

The results of the concrete mesh refinement study are presented in Figure 5-63, using residual pipe velocity as the convergence criterion. Results are shown for particle spacings of 2, 3, 4, 5, and 10 mm. The 5 mm mesh results are an outlier: the pipe velocities begin to converge as the mesh is refined. The evolution of panel back-face lateral displacement is presented in Figure 5-64; significant local deformation at the midpoint of the panel is indicative of perforation.

A summary of local damage to the panel for all five simulations and the experiment is presented in Table 5-23. Based on the results of the analysis using the finest mesh (2 mm), the results of the experiment were reproduced with reasonable accuracy (i.e., front and back face crater diameters and perforation of the panel).

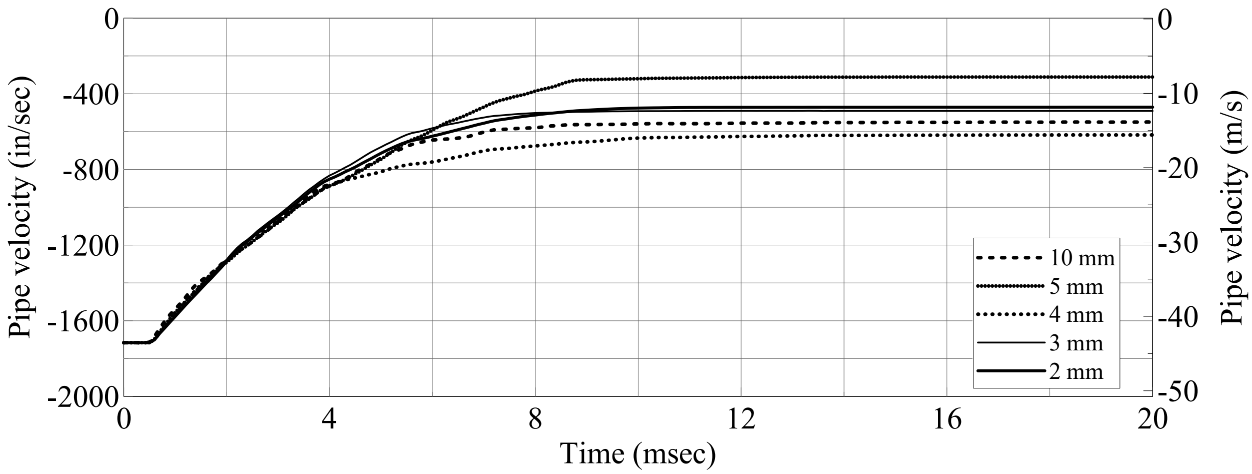

Figure 5-63: Pipe velocity histories, Test 10

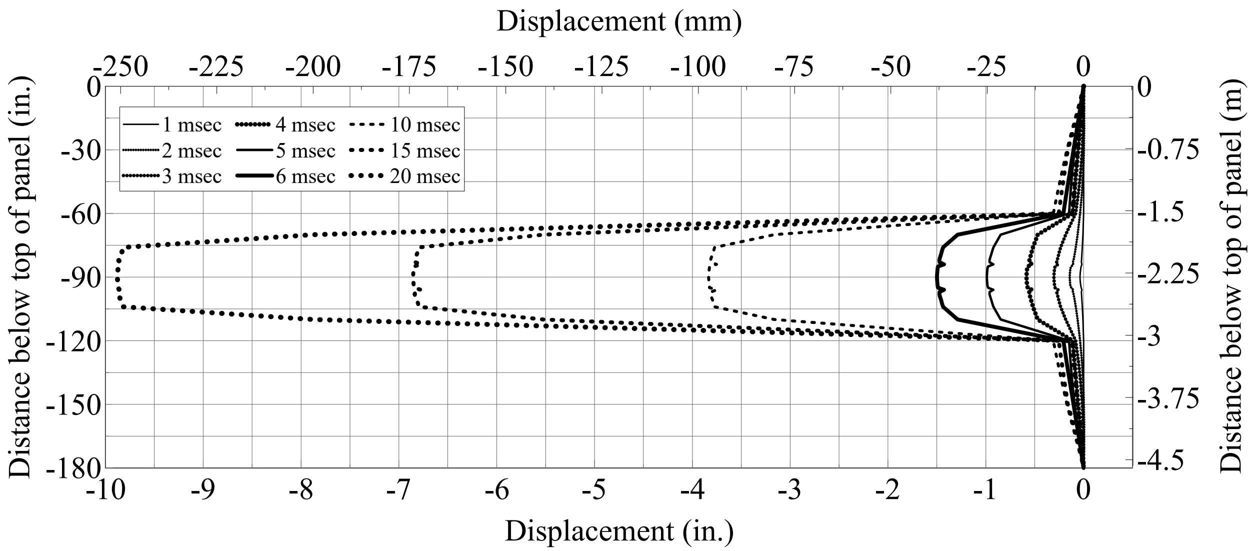

Figure 5-64: Panel back-face lateral displacement, Test 10, 2 mm mesh, simulation 5

Table 5-24 shows the estimated rates of convergence and values of the GCI for Test 10. Residual pipe velocity was used as the metric to calculate the mesh discretization error. Results of simulations using particle spacings of 2, 3, and 4 mm (shaded in Table 5-23) were used for the GCI calculations. The estimated value of the converged residual velocity, f_{21}^{*}, (=-477 in/sec) is in good agreement with the result obtained using the 2 mm mesh (=-479 in/sec). The asymptotic-check (see equation (5-24)) calculation yields a value of 0.96, indicating that the numerical results are in the asymptotic regime.

Table 5-23: Results summary, Test 10

	Concrete mesh size mm (in.)					
	2 (0.08)	3 (0.12)	4 (0.16)	5 (0.2)	10 (0.39)	Experiment
Penetration depth, mm (in.)	P	P	P	P	P	P
Front face crater diameter, mm (in.)	457 (18)	457 (18)	457 (18)	457 (18)	457 (18)	495 (19.5)
Back face crater diameter, mm (in.)	1524 (60)	1626 (64)	1372 (54)	1778 (70)	1016 (40)	1626 (64)
Residual pipe velocity, m/s (in/sec)	-12.2 (-479)	-12.7 (-500)	-15.2 (-599)	-7.6 (-298)	-12.6 (-498)	-

Table 5-24: Estimated rates of convergence and GCI, Test 10

r_{21}	1.5	p	5.77
r_{32}	1.3	GCI_{21}	0.0059
e_{21}	0.044	GCI_{32}	0.058
e_{32}	0.198	f_{21}^{*} m/s (in/sec)	-12.1 (-477)
F_s	1.25	AC	0.96
		CI_{95} m/s (in/sec)	[-12.1, -12.2] ([-476.17, -481.83])

5.9.4 Test 3

5.9.4.1 *Introduction*

In EPRI Test 3, a 743 lb (337 kg) Schedule 40 pipe normally impacted an 18-inch (457 mm) thick panel wall at a velocity of 202 fps (62 m/s). The pipe penetrated the target, causing heavy scabbing on the back face of the panel. Table 5-25 lists the simulations of Test 3. Concrete particle spacings of 1, 2, 3, 4, 5, and 10 mm were considered to study mesh convergence. The axisymmetric model is shown in Figure 5-18.

Table 5-25: Numerical simulations, MAT072R3, Test 3

Simulation	Concrete mesh mm (in.)	Pipe mesh mm (in.)	f_c' MPa (psi)	f_t' MPa (psi)
1	10 (0.39)	5.35 (0.21)	23.4 (3400)	3.5 (510)
2	5 (0.20)	2.67 (0.11)	23.4 (3400)	3.5 (510)
3	4 (0.16)	2.14 (0.09)	23.4 (3400)	3.5 (510)
4	3 (0.12)	1.6 (0.06)	23.4 (3400)	3.5 (510)
5	2 (0.08)	1.1 (0.04)	23.4 (3400)	3.5 (510)
6	1 (0.04)	0.5 (0.02)	23.4 (3400)	3.5 (510)

5.9.4.2 *Simulation Results*

Figure 5-65 shows spalling of concrete on the front (impact) face and formation of the conical plug. The panel was perforated in the simulation but not in the experiment. The results shown in Figure 5-65 are for a mesh size of 2 mm; the results of the simulation using the 1 mm particle spacing was run up to 14 msec.

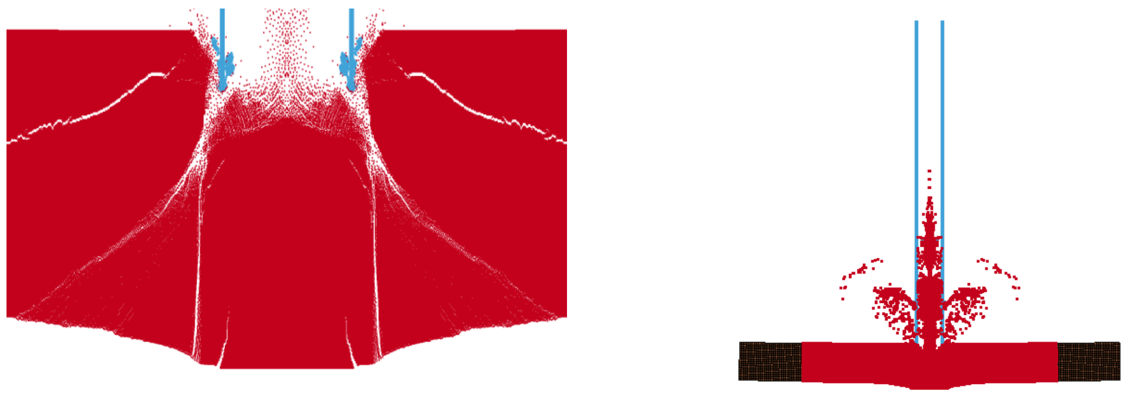

(a) Conical plug formation at 10 msec

(b) Concrete spalling on front face and formation of conical plug on back face at 20 msec

Figure 5-65: Simulation results, Test 3, 2 mm mesh, simulation 5

A summary of results is presented in Table 5-26 for all six simulations and the experiment. Although the simulation using the 2 mm mesh (simulation 5) predicted perforation of the panel (P), which was not observed in the experiment, it reproduced other observed results reasonably well (e.g., front and back face crater diameter and conical plug diameter).

Table 5-26: Summary of results, Test 3

	Concrete mesh size mm (in.)						
	1 (0.04)	2 (0.08)	3 (0.12)	4 (0.16)	5 (0.2)	10 (0.39)	Experiment
Penetration depth, mm (in.)	P	P	P	P	P	P	178 (7)
Front face crater diameter, mm (in.)	508 (20)	508 (20)	483 (19)	508 (20)	508 (20)	508 (20)	610 (24)
Conical plug diameter, mm (in.)	2134 (84)	1270 (50)	1270 (50)	1778 (70)	762 (30)	1524 (60)	1143 (45)
Back face crater diameter, mm (in.)	2134 (84)	2286 (90)	1270 (50)	1778 (70)	762 (30)	1524 (60)	2159 (85)
Residual pipe velocity, m/s (in/sec)	-9.3 (-367)	-2.8 (-117)	-11.6 (-457)	-5.3 (-207)	-0.64 (-25)	-1.9 (-73)	-

Results of the concrete mesh refinement study are presented in Figure 5-66. Results are shown for particle spacings of 1, 2, 3, 4, 5, and 10 mm. The residual velocities of the pipe in Test 3 for concrete particle spacings of 1, 2, and 3 did not converge, and so the GCI calculation was not particularly useful to estimate discretization error. The calculated values of $q(p)$ (equation (5-16)) did not converge after multiple iterations.

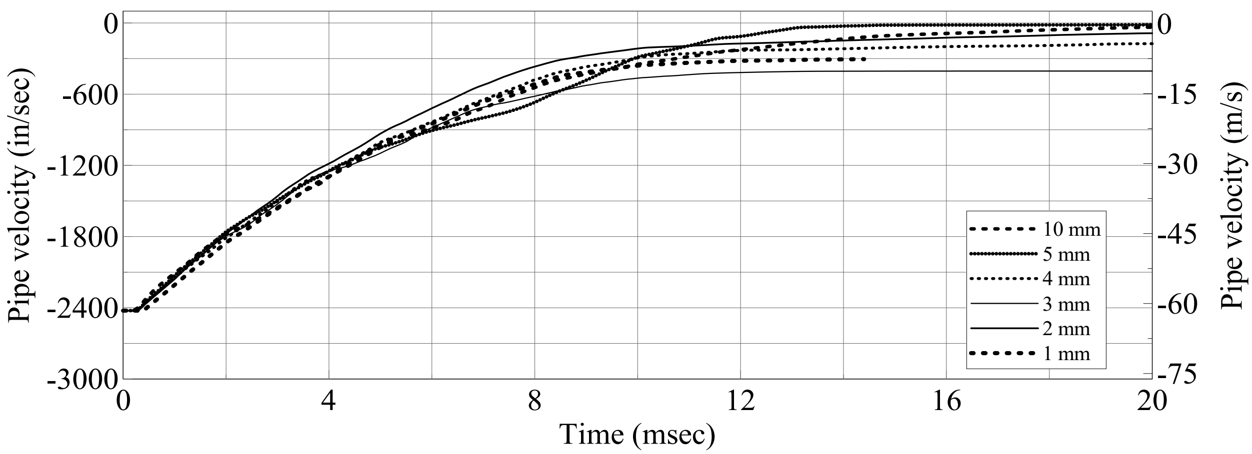

Figure 5-66: Pipe velocity histories, Test 3

The evolution of panel back-face lateral displacement is presented in Figure 5-67 for the analysis using the 2 mm mesh; significant local deformation at the midpoint of the panel is apparent, opposite the point of impact.

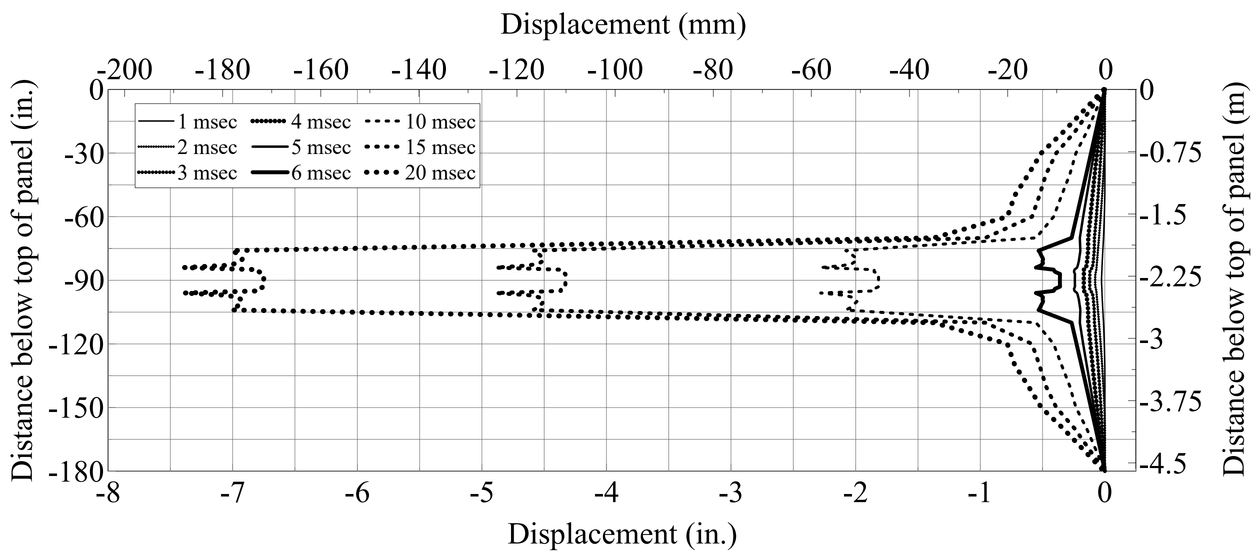

Figure 5-67: Panel back-face lateral displacement, Test 3, 2 mm mesh, simulation 5

5.9.5 Test 8

5.9.5.1 *Introduction*

In EPRI Test 8, a 743 lb (337 kg) Schedule 40 pipe normally impacted a 24-inch thick concrete panel wall at a velocity of 202 fps (62 m/s). The pipe penetrated the target and caused radial cracking on the back (non-impact) face of the panel. Table 5-27 identifies the simulations performed for this test. Concrete particle spacings of 3, 4, 5, and 10 mm were considered to investigate mesh convergence. The axisymmetric model is shown in Figure 5-19.

Table 5-27: Numerical simulations, MAT072R3, Test 8

Simulation	Concrete mesh mm (in.)	Pipe mesh mm (in.)	f_c' MPa (psi)	f_t' MPa (psi)
1	10 (0.39)	5.35 (0.21)	26.2 (3800)	3.9 (570)
2	5 (0.20)	2.67 (0.11)	26.2 (3800)	3.9 (570)
3	4 (0.16)	2.14 (0.09)	26.2 (3800)	3.9 (570)
4	3 (0.12)	1.6 (0.06)	26.2 (3800)	3.9 (570)

5.9.5.2 *Simulation Results*

Spalling of the concrete on the front face and limited scabbing on the back face of the panel are presented in Figure 5-68a and Figure 5-68b, respectively, 20 msec after impact based on the simulation using the finest mesh (3 mm). The pipe velocity histories are shown in Figure 5-69. The pipe does not perforate the panel in any of the simulations; the residual pipe velocity is zero. A summary of the penetration depths for all four simulations and the experiment is presented in Table 5-28. The penetration depth was underpredicted by a factor of three based on the analysis using the finest mesh (3 mm). Since the 3 and 4 mm meshes (shaded in Table 5-28) predict the same penetration depth (the metric used to estimate discretization error in the meshes where perforation did not occur), the numerical simulation is assumed to have converged. The GCI was not used here because the order of convergence is undefined: the difference between metrics, f_2 and f_1, defined as f_{21}, is zero.

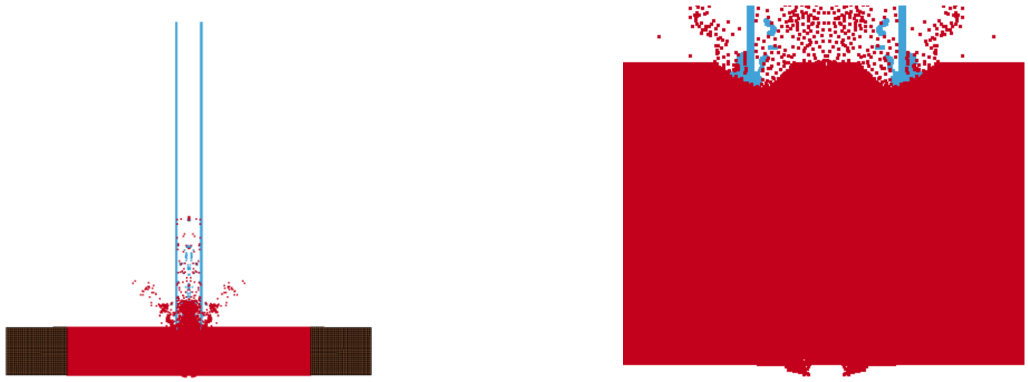

(a) Spalling of concrete on front face (b) Limited scabbing on back face

Figure 5-68: Simulation results, 20 msec, Test 8, 3 mm mesh, simulation 4

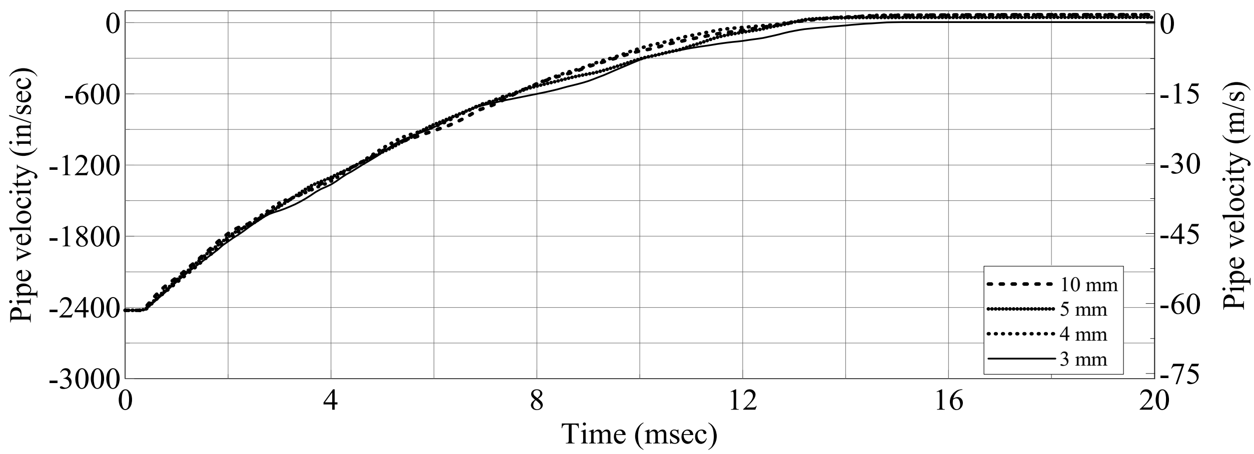

Figure 5-69: Pipe velocity history, Test 8

Table 5-28: Penetration depth, Test 8

	Concrete mesh size mm (in.)				
	3 (0.12)	4 (0.16)	5 (0.2)	10 (0.39)	Experiment
Penetration depth mm (in.)	53 (2.1)	53 (2.1)	51 (2)	51 (2)	173 (6.8)

The evolution of panel back-face displacement is presented in Figure 5-70. Global deformation of the panel dominated the response; limited local damage is observed. The panel rebounded after 7 msec and a small amount of scabbing was predicted. In the experiment, radial cracks formed on the back face of the panel, opposite the point of impact, but scabbing was not observed.

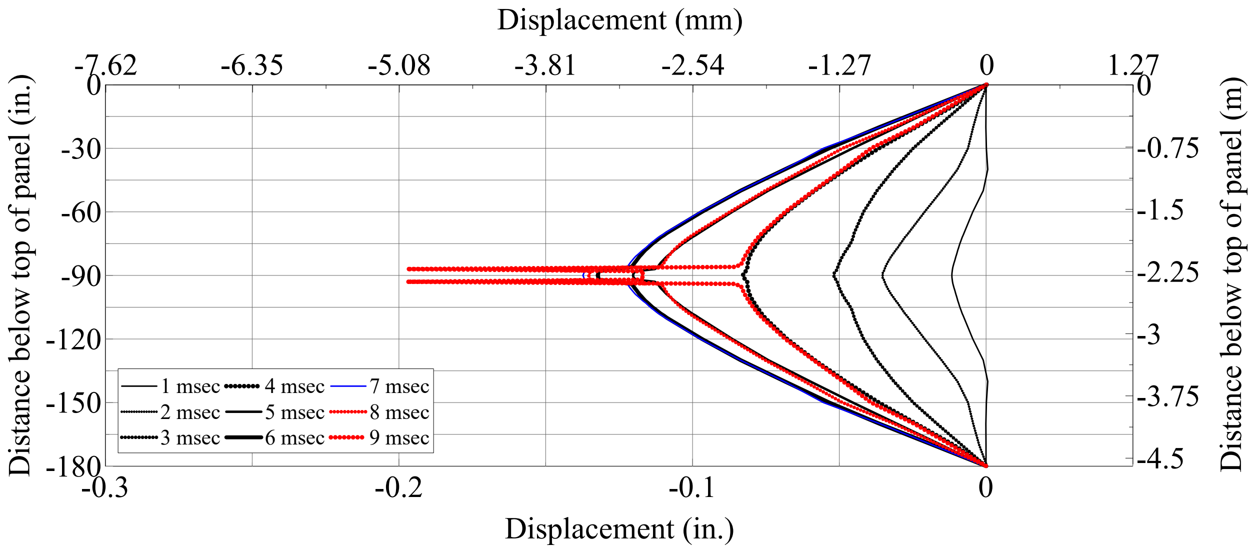

Figure 5-70: Panel back-face lateral displacement, Test 8, 3 mm mesh, simulation 4

5.9.6 Summary and Conclusions

The axisymmetric models of Section 5.3 were used to simulate four concrete panel impact tests conducted by EPRI per Table 5-1, in an effort to partially validate a numerical model for the analysis of reinforced concrete panels impacted by wind-borne missiles. Based on the results of the simulations, the numerical model:

- Reasonably reproduced the front and back face crater diameters and perforation of the panel in Test 10
- Predicted perforation of the panel in Test 3, which was not observed in the experiment but predicted the front and back face crater diameters with reasonable accuracy
- Predicted the formation and size of the conical plug on the back face and non-perforation of the panel in Test 11
- Reasonably reproduced the global response of the panel observed in Test 8
- Underpredicted the depth of penetration of the pipe by a factor of three in Tests 11 and 8.

5.10 Solid Missile Impact

5.10.1 Introduction

The response of a concrete panel impacted by a solid missile having the same mass as the Schedule 40 pipe was investigated using information from EPRI Tests 11, 10, 3, and 8 (see Table 5-1). The solid missile had a diameter and length of 12 inches (305 mm) and 24 inches (610 mm), respectively. The impact velocities identified in the EPRI tests were used in the solid missile impact simulations to ensure that the kinetic energy transferred to the panel was equal to that of the physical tests.

5.10.2 Test 11 Data, Solid Missile

The response of a concrete panel impacted by a solid missile having the same mass as a Schedule 40 pipe was investigated using data from EPRI Test 11: 12-inch (305 mm) panel impacted by a 12-inch (305 mm) diameter Schedule 40 pipe at a velocity of 98 fps (30 m/s). Figure 5-71 presents the axisymmetric model of the 12-inch (305 mm) thick concrete panel and solid missile. The material models, strain rate effects, particle spacing requirements (e.g., concrete particle spacing twice that of projectile spacing), and element formulations used here were those described in Section 5.3. Outside the impact zone, axisymmetric solid elements were used for the concrete panel to reduce computational demand; see Figure 5-71. The model had a total of 180 1 × 1 in. (25.4 × 25.4 mm) axisymmetric solid elements. In this case, the radius of the wall was modeled with 15 inches (381 mm) of axisymmetric solid elements and 75 inches (1905 mm) of SPH particles. The volume weighted element form (ELFORM=15 in LS-DYNA) was used for the axisymmetric solid elements. The *CONTROL_BULK_VISCOSITY keyword was activated and the variables Q1 and Q2 were set to values of 1.5 and 0.06 (default values), respectively. The *CONTACT_2D_NODE_TO_SOLID_TIED keyword was used to constrain the SPH particles and the axisymmetric solid elements at the interface. Five nodes constrained displacement in the Y-direction on the outer edge of the solid elements to simulate the pinned boundary condition imposed in the experiments. The location of the boundary is shown in Figure 5-71. A summary of the simulations conducted in this section is presented in Table 5-29. Concrete particle spacings of 10, 5, 4, 3, and 2 mm were used to study mesh convergence.

Table 5-29: Numerical simulations, MAT072R3, solid missile, Test 11

Simulation	Concrete mesh mm (in.)	Solid missile mesh mm (in.)	f_c' MPa (psi)	f_t' MPa (psi)
1	10 (0.39)	5.35 (0.21)	24.8 (3600)	3.72 (540)
2	5 (0.20)	2.67 (0.11)	24.8 (3600)	3.72 (540)
3	4 (0.16)	2.14 (0.09)	24.8 (3600)	3.72 (540)
4	3 (0.12)	1.6 (0.06)	24.8 (3600)	3.72 (540)
5	2 (0.08)	1 (0.04)	24.8 (3600)	3.72 (540)

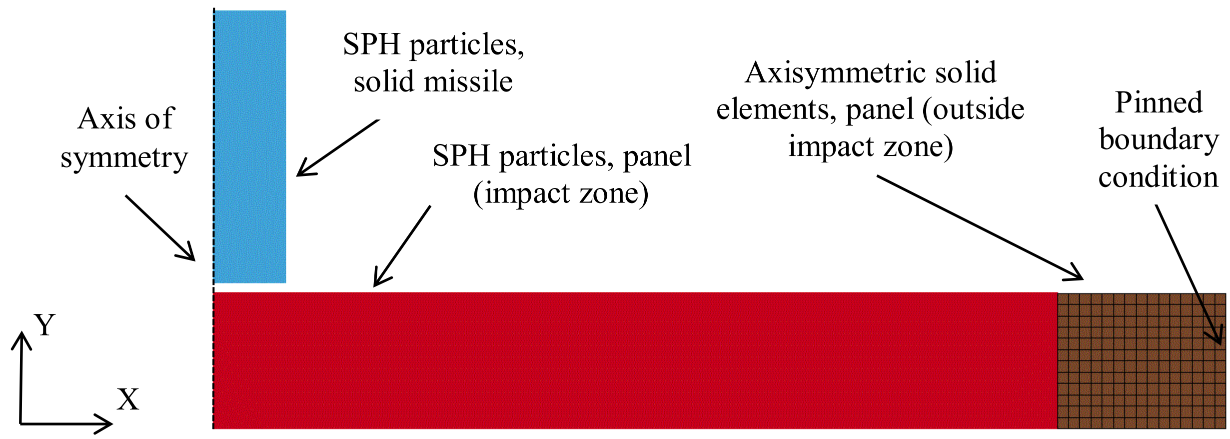

Figure 5-71: Axisymmetric model, 12 inch (305 mm) panel, solid missile, Test 11

Results of the simulation using the finest mesh (2 mm) are shown in Figure 5-72. Perforation of the panel and ejection of concrete from the back face are shown in Figure 5-72a and Figure 5-72b, respectively, 20 msec after impact.

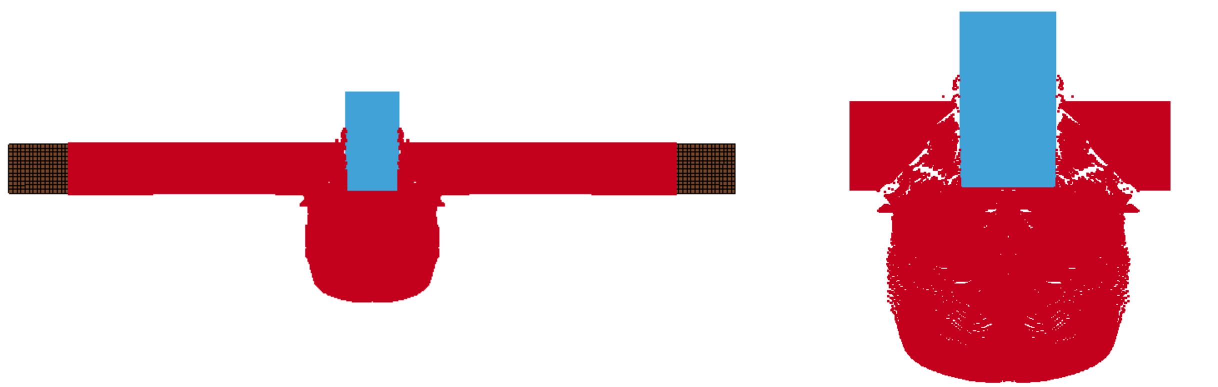
(a) Perforation of panel (b) Ejection of concrete on back face

Figure 5-72: Simulation results, 20 msec, solid missile, Test 11, 2 mm mesh, simulation 5

The results of the concrete mesh refinement study are presented in Figure 5-73, using residual missile velocity as the convergence criterion. Results are shown for concrete particle spacings of 2, 3, 4, 5, and 10 mm. The residual velocity for each simulation is presented in Table 5-30. The estimated rates of convergence and GCI are presented in Table 5-31; concrete particle spacings of 2, 3, and 4 mm (highlighted in Table 5-30) were used to make the calculations. The estimated value of the converged residual velocity, f_{21}^{*}, (=-15.4 m/s (-606 in/sec)) is in good agreement with the residual velocity predicted using the 2 mm mesh (=-15.2 m/s (-600 in/sec)).

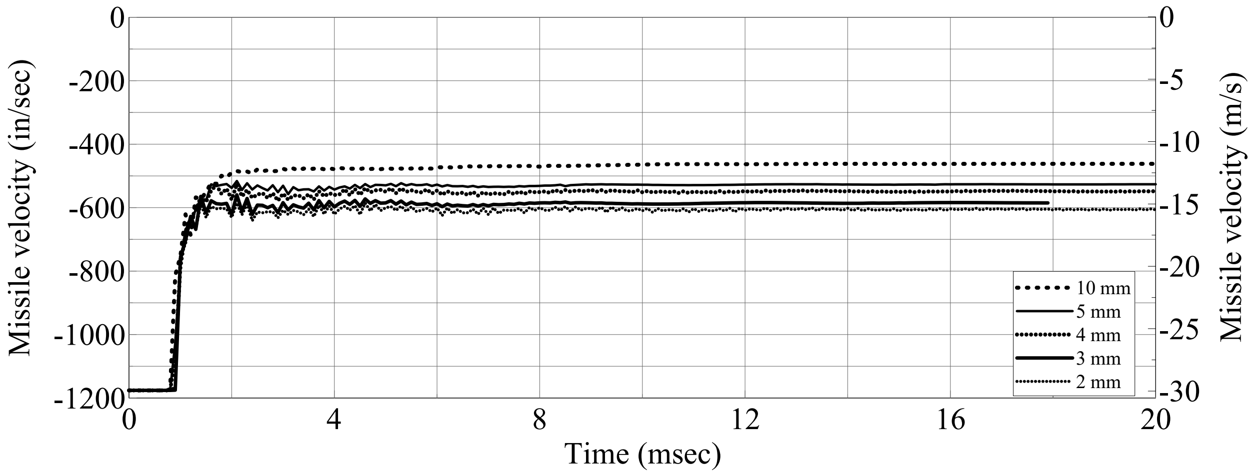

Figure 5-73: Velocity histories, solid missile, Test 11

Table 5-30: Residual velocities, solid missile, Test 11

Concrete mesh size, mm (in.)	2 (0.08)	3 (0.12)	4 (0.16)	5 (0.20)	10 (0.39)
Residual velocity, m/s (in/sec)	-15.2 (-600)	-14.8 (-584)	-13.9 (-548)	-13.4 (-526)	-11.7 (-462)

Table 5-31: Estimated rates of convergence and GCI, solid missile, Test 11

r_{21}	1.5	p	3.44
r_{32}	1.33	GCI_{21}	-0.011
e_{21}	-0.027	GCI_{32}	-0.046
e_{32}	-0.061	f_{21}^* m/s (in/sec)	-15.4 (-605)
F_s	1.25	AC	1.03
		CI_{95} m/s (in/sec)	[-15.4, -15.1] ([-606.6, -593.4])

The evolution of panel back-face lateral displacement is presented in Figure 5-74; significant local deformation at the midpoint of the panel is indicative of local damage and perforation.

The location of the SPH-axisymmetric solid element boundary is especially important in these impact simulations due to the possibility of instabilities at the interface between the axisymmetric solid elements and the SPH particles (i.e., distortion of the axisymmetric solid elements leading to negative volume errors and separation of the groups of SPH particles due to the distortion of the solid elements). Figure 5-75 shows the simulation results using the finest mesh (2 mm), where the panel consisted of 30 inches (762 mm) of axisymmetric solid elements and 60 inches (1524 mm) of SPH particles. Significant distortion of the axisymmetric solid elements and separation of the SPH particles was observed and these were eliminated by reducing the annular radius of the axisymmetric solid elements at the outer boundary of the panel to 15 inches (381 mm) (see Figure 5-71). The simulation results presented in this section utilized the model shown in Figure 5-71.

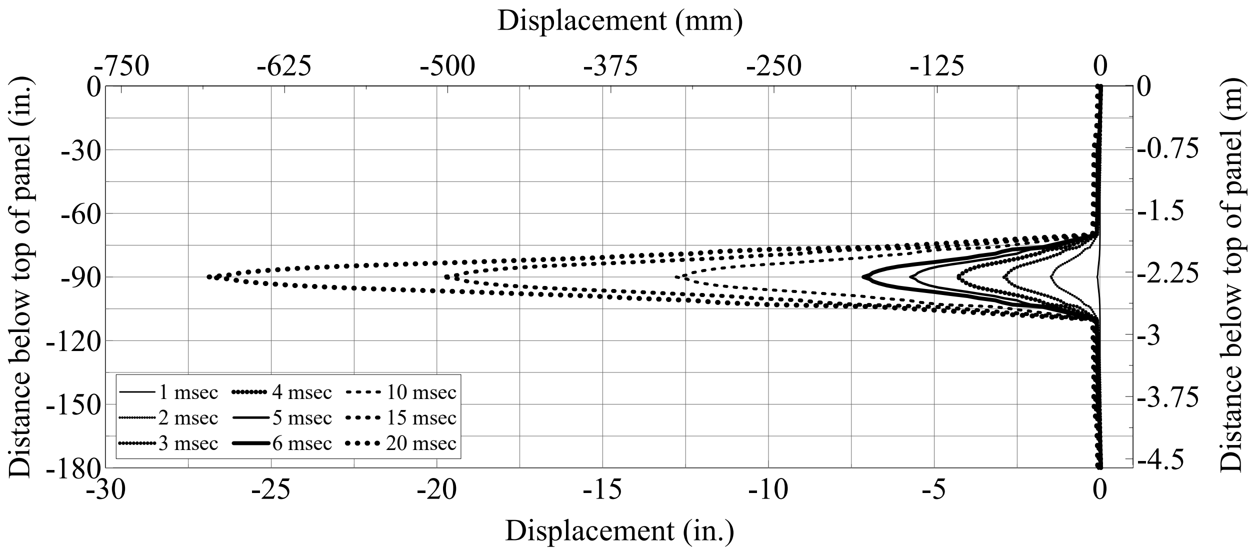

Figure 5-74: Panel back-face lateral displacement, solid missile, Test 11, 2 mm mesh, simulation 5

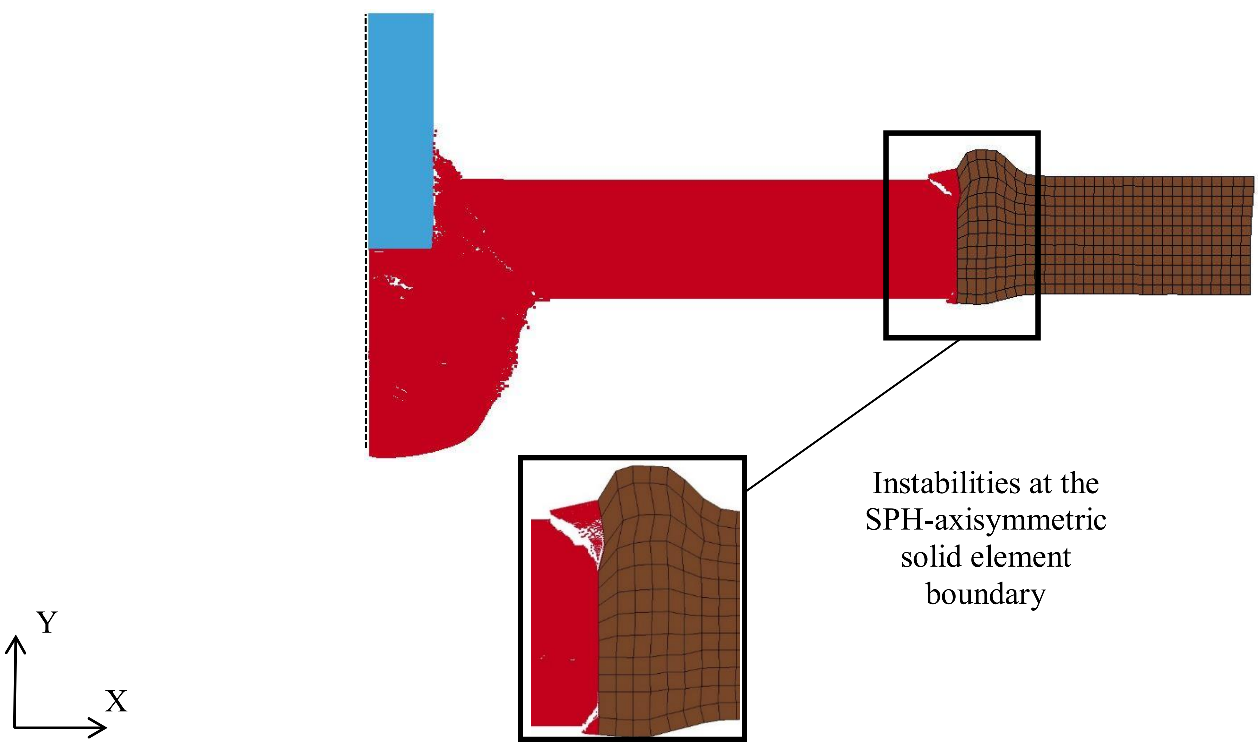

Figure 5-75: Instabilities at SPH-axisymmetric solid element boundary, Test 11, 2 mm mesh

5.10.3 Test 10 Data, Solid Missile

The response of a concrete panel impacted by a solid missile was investigated using data from EPRI Test 10 (see Table 5-1). The solid missile had the same mass and initial velocity (=143 fps (43.6 m/s)) as the Schedule 40 pipe in Test 10. The axisymmetric model used in the simulations is presented in Figure 5-76. The material models, strain rate effects, particle spacing requirements, and element formulations for the panel and the pipe are the same as those described in Section 5.10.2. Table 5-32 identifies the simulations performed for Test 10.

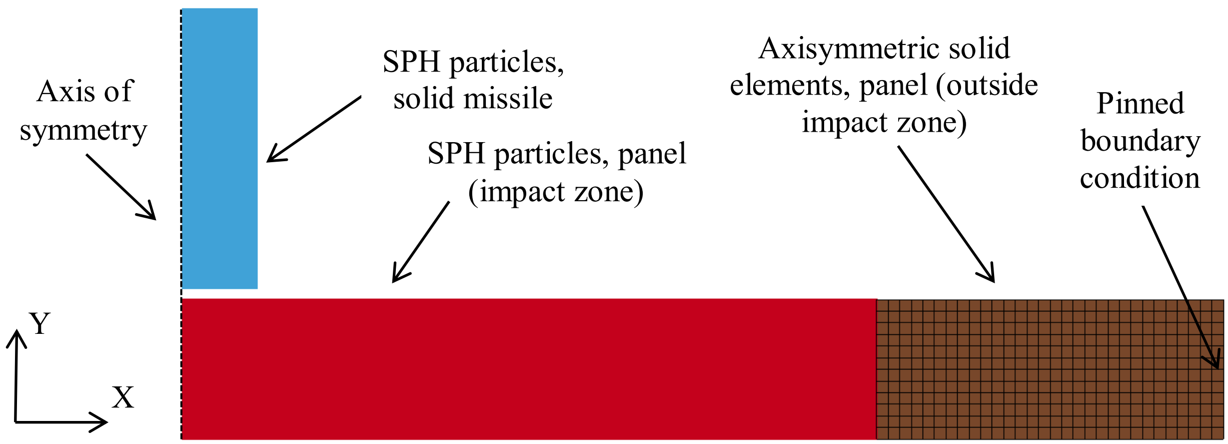

Figure 5-76: Axisymmetric model, 12 inch (305 mm) panel, solid missile, Test 10

Table 5-32: Numerical simulations, MAT072R3, solid missile, Test 10

Simulation	Concrete mesh mm (in.)	Solid missile mesh mm (in.)	f_c' MPa (psi)	f_t' MPa (psi)
1	10 (0.39)	5.35 (0.21)	25.5 (3700)	3.83 (555)
2	5 (0.20)	2.67 (0.11)	25.5 (3700)	3.83 (555)
3	4 (0.16)	2.14 (0.09)	25.5 (3700)	3.83 (555)
4	3 (0.12)	1.6 (0.06)	25.5 (3700)	3.83 (555)
5	2 (0.08)	1 (0.04)	25.5 (3700)	3.83 (555)

Figure 5-77 presents the results of the simulation using the finest mesh (2 mm), which corresponds to simulation 5 in Table 5-32. Perforation of the panel and ejection of the concrete on the back face are shown in Figure 5-77a and Figure 5-77b, respectively.

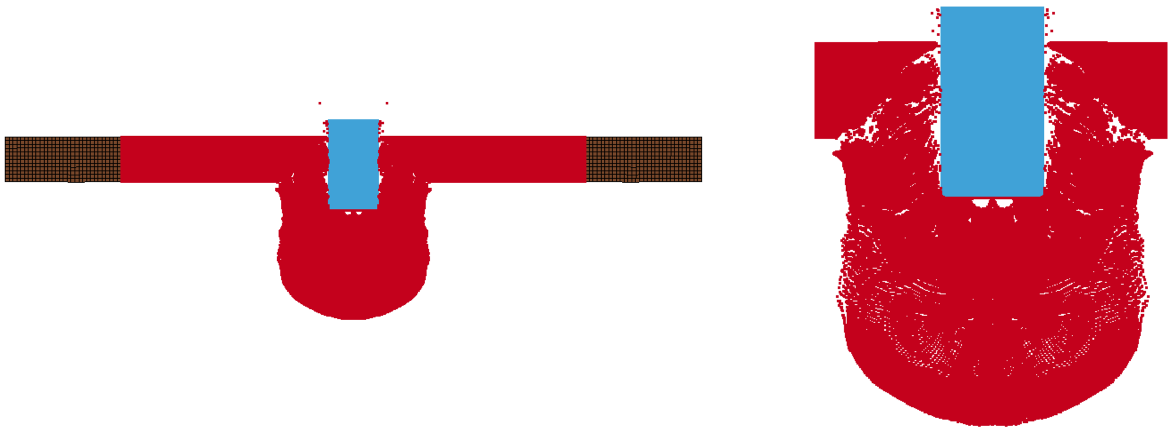

(a) Perforation of panel (b) Ejection of concrete on the back face

Figure 5-77: Simulation results, 20 msec, solid missile, Test 10, 2 mm mesh, simulation 5

Results of the mesh refinement study are presented in Figure 5-78, using the residual velocity of the solid missile as the convergence criterion. The residual velocities are summarized in Table 5-33. The estimated rates of convergence and GCI are presented in Table 5-34. The residual velocities of the solid missile for concrete particle spacings of 2, 3, and 4 mm (highlighted in Table 5-33) were used in the calculations. The estimated value of the converged residual velocity, f_{21}^*, (=-35.1 m/s (-1381 in/sec)) is significantly different from the residual missile velocity predicted using the 2 mm mesh (=-25.4 m/s (-1000 in/sec)). Since the parameter f_{21} (=-1.0 m/s (-41 in/sec)) is slightly greatly than f_{32} (=-0.7 m/s (-28 in/sec)), the GCI indicates that the solution has not converged numerically. However, the differences in the metrics used to establish the converged numerical solution (e.g., f_{21} and f_{32}) are tiny compared to that of the initial pipe velocity (=-43.6 m/s (-1716 in/sec)), indicating that the velocities are not likely to converge as the mesh is refined beyond 2 mm.

Table 5-33: Residual velocities, solid missile, Test 10

Concrete mesh size, mm (in.)	2 (0.08)	3 (0.12)	4 (0.16)	5 (0.20)	10 (0.39)
Residual velocity, m/s (in/sec)	-25.4 (-1000)	-24.4 (-959)	-23.6 (-931)	-23.1 (-908)	-21.4 (-844)

The evolution of panel back-face displacement is presented in Figure 5-79; significant deformation at the point of impact and displacements on the order of three times the panel thickness indicate perforation of the panel. Results are shown for the simulation using the finest mesh (2 mm).

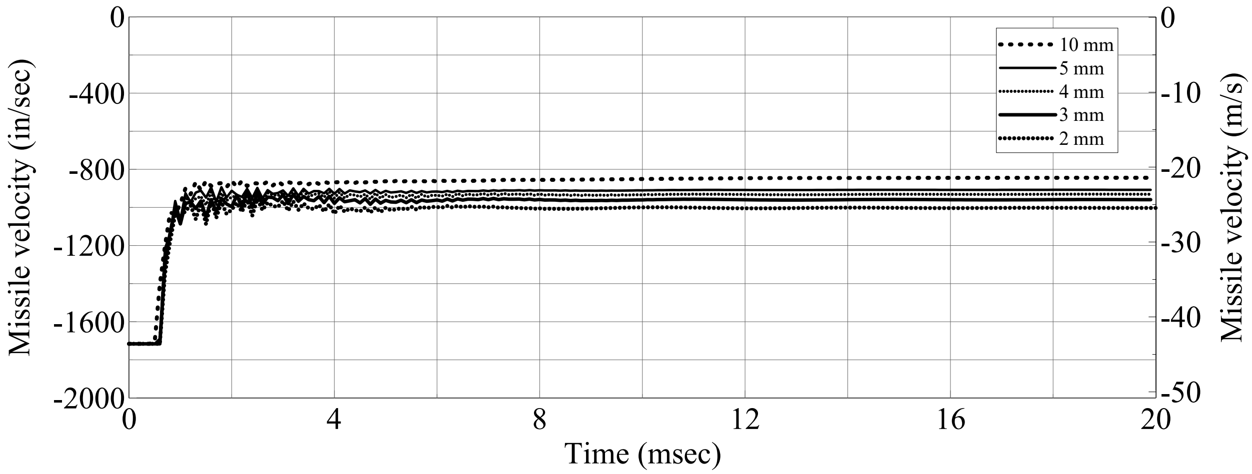

Figure 5-78: Velocity histories, solid missile, Test 10

Table 5-34: Estimated rates of convergence and GCI, solid missile, Test 10

r_{21}	1.33	p	0.22
r_{32}	1.25	GCI_{21}	-0.55
e_{21}	-0.03	GCI_{32}	-0.6
e_{32}	-0.024	f_{21}^{*} m/s (in/sec)	-35.1 (-1381)
F_s	1.25	AC	1.03
		CI_{95} m/s (in/sec)	[-53.3, -15.8], ([-2100, -622])

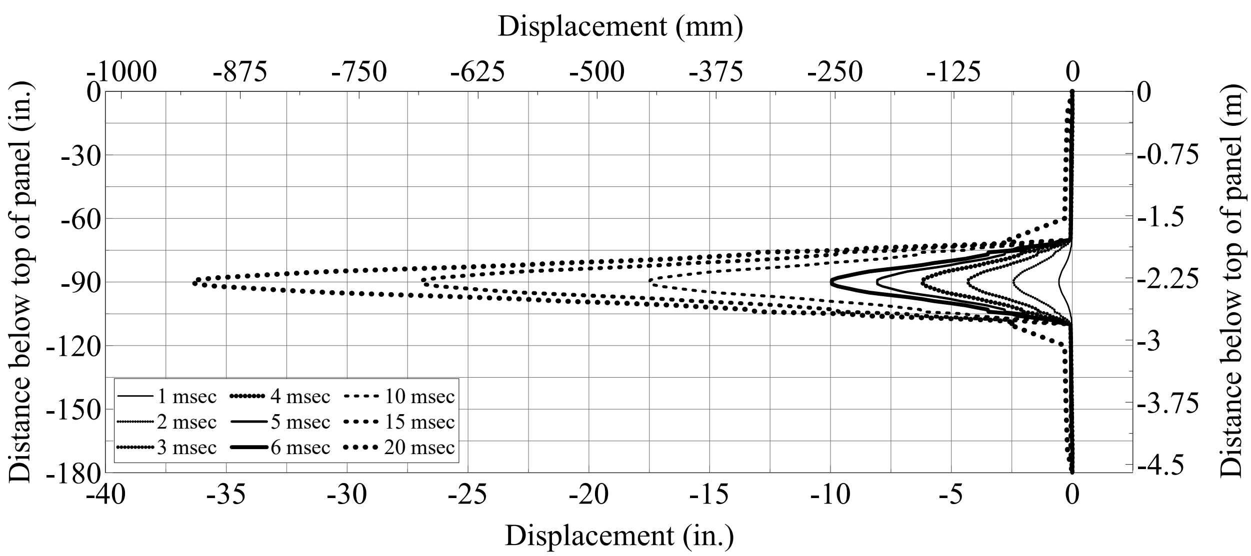

Figure 5-79: Panel back-face lateral displacement, solid missile, Test 10, 2 mm mesh, simulation 5

5.10.4 Test 3 Data, Solid Missile

The response of a concrete panel impacted by a solid missile is investigated here using data from EPRI Test 3 (see Table 5-1). The solid missile had the same mass and initial velocity (=202 fps (61.6 m/s)) as the Schedule 40 pipe in Test 3. The dimensions of the solid missile are described in Section 5.10.1. The axisymmetric model used for these simulations is presented in Figure 5-80. SPH particles are used for the panel and the solid missile. The material models, strain rate effects, particle spacing requirements, and element formulations for the SPH particles in the panel and the missile are those described in Section 5.3. Two columns of SPH particles constrained displacement in the Y-direction on the outer edge of the panel to simulate the pinned boundary condition imposed in the experiment. The location of the boundary is shown in Figure 5-80.

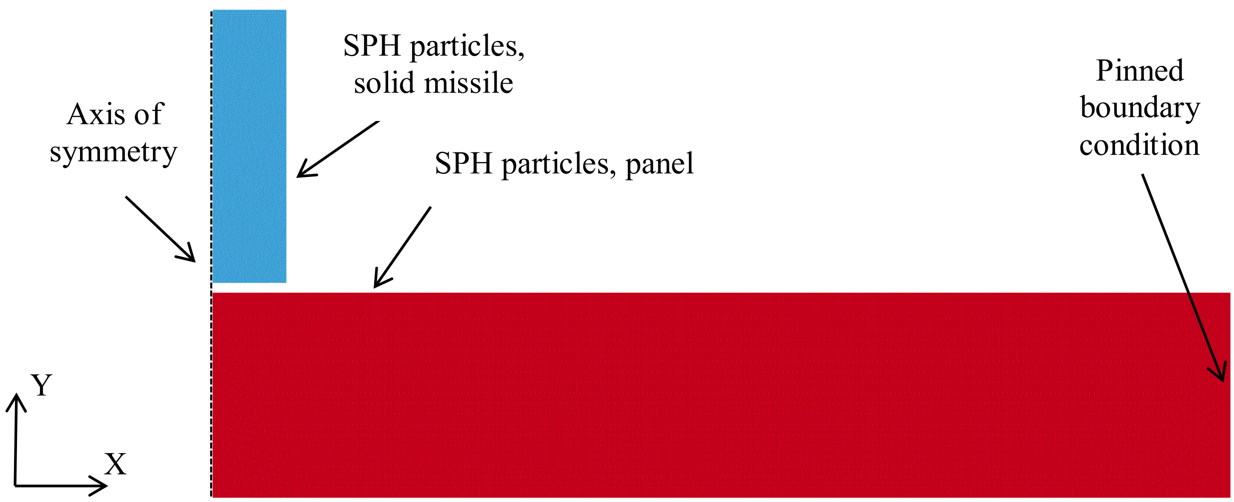

Figure 5-80: Axisymmetric model, 18-inch (457 mm) panel, solid missile, Test 3

The numerical simulations of Test 3 are listed in Table 5-35. Figure 5-81 presents results of the simulation using the finest mesh (3 mm), 20 msec after impact. Perforation of the panel and ejection of concrete on the back face are shown in Figure 5-81a and Figure 5-81b, respectively.

Table 5-35: Numerical simulations, MAT072R3, solid missile, Test 3

Simulation	Concrete mesh mm (in.)	Solid missile mesh mm (in.)	f_c' MPa (psi)	f_t' MPa (psi)
1	10 (0.39)	5.35 (0.21)	23.4 (3400)	3.45 (500)
2	5 (0.20)	2.67 (0.11)	23.4 (3400)	3.45 (500)
3	4 (0.16)	2.14 (0.09)	23.4 (3400)	3.45 (500)
4	3 (0.12)	1.6 (0.06)	23.4 (3400)	3.45 (500)

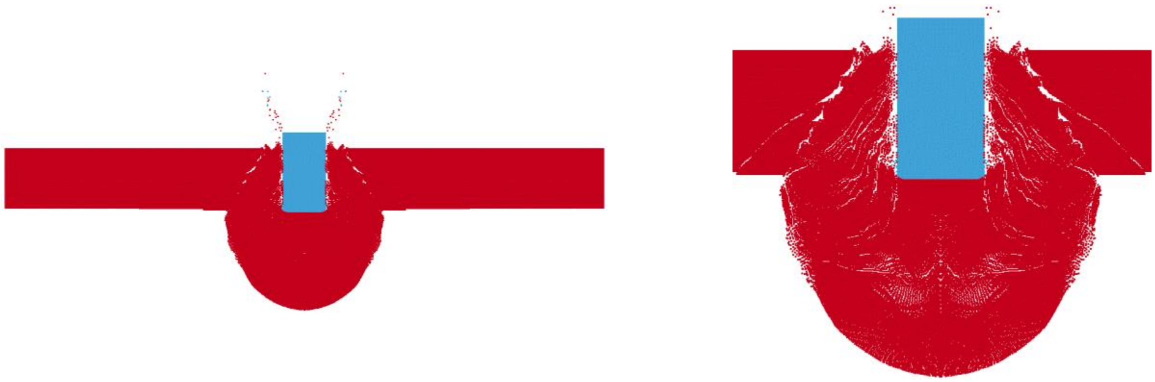

(a) Perforation of panel (b) Ejection of concrete on back face

Figure 5-81: Simulation results, 20 msec, solid missile, Test 3, 3 mm mesh, simulation 4

The missile velocity histories are presented in Figure 5-82. Predicted residual velocity is used as the convergence criterion; results are summarized in Table 5-36 for all particle spacings. The estimated rates of convergence and GCI are presented in Table 5-37. Concrete particle spacings of 3, 4, and 5 mm were used for the calculations (highlighted in Table 5-36). The estimated value of the converged residual velocity, f_{21}^{*}, (=-30.0 m/s (-1180 in/sec)) is significantly different from the residual missile velocity predicted using the 3 mm mesh (=-24.3 m/s (-955 in/sec)). Since the parameter f_{32} (=-0.66 m/s (-26 in/sec)) is slightly smaller than f_{21} (=-0.76 m/s (-30 in/sec)), the GCI indicates that the solution has not yet converged. The residual velocity is not likely to converge further as the mesh is refined below 3 mm because the difference in the residual velocities used to compute the converged numerical solution (e.g., f_{21} and f_{32}) are tiny compared to the initial missile velocity (=-61.6 m/s (-2424 in/sec)).

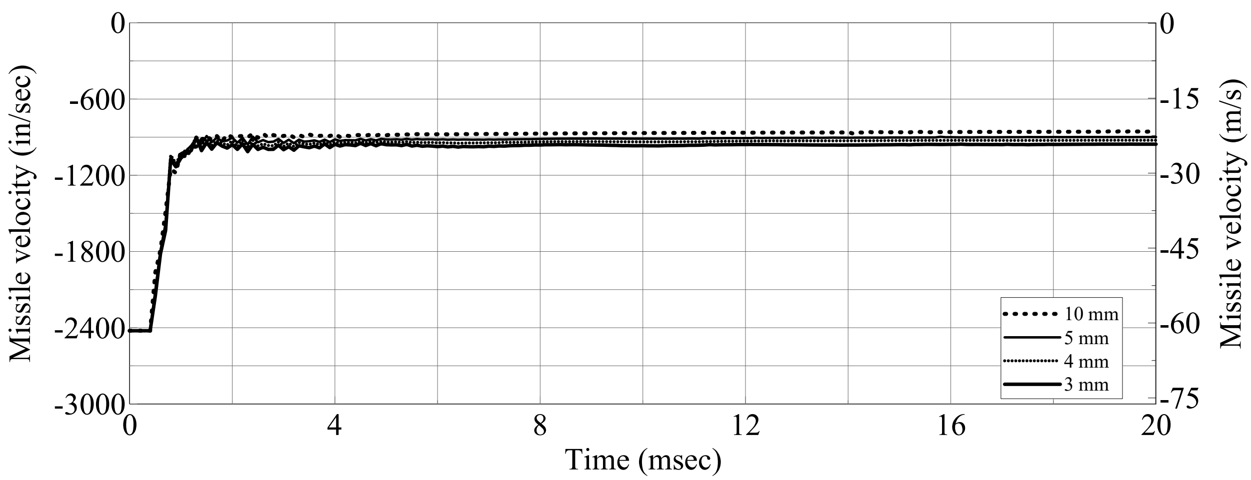

Figure 5-82: Velocity histories, solid missile, Test 3

Table 5-36: Residual velocities, solid missile, Test 3

Concrete mesh size, mm (in.)	3 (0.12)	4 (0.16)	5 (0.20)	10 (0.39)
Residual velocity, m/s (in/sec)	-24.3 (-955)	-23.5 (-925)	-22.8 (-899)	-21.7 (-854)

Table 5-37: Estimated rates of convergence and GCI, solid missile, Test 3

r_{21}	1.33	p	0.435
r_{32}	1.25	GCI_{21}	-0.29
e_{21}	-0.03	GCI_{32}	-0.34
e_{32}	-0.028	f_{21}^{*} m/s (in/sec)	-30 (-1180)
F_s	1.25	AC	1.03
		CI_{95} m/s (in/sec)	[-38.7, -21.3] ([-1522, -838])

The evolution of the panel back-face displacement is presented in Figure 5-83. The displacement profile indicates a purely local response.

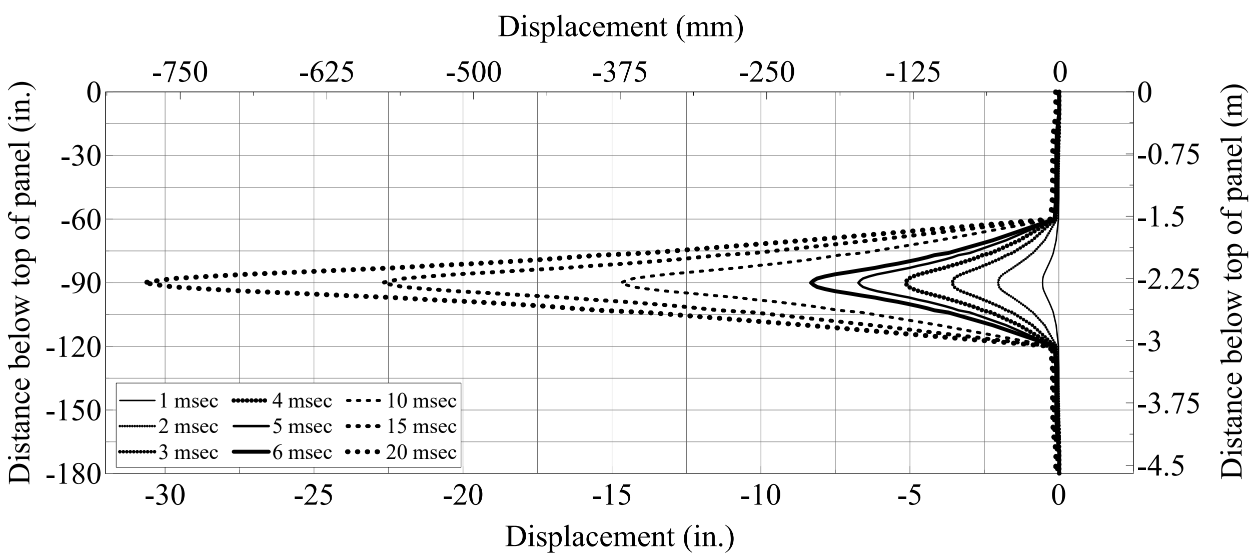

Figure 5-83: Panel back-face lateral displacement, solid missile, Test 3, 3 mm mesh, simulation 4

5.10.5 Test 8 Data, Solid Missile

EPRI Test 8 data (see Table 5-1) are used here to investigate the response of a concrete panel impacted by a solid missile. The axisymmetric model used in the simulations is presented in Figure 5-84; SPH particles are used for the solid missile and the concrete panel. The solid missile has the same mass and initial velocity (=202 fps (61.6 m/s)) as the Schedule 40 pipe. The dimensions of the solid missile are presented in Section 5.10.1. The material models, strain rate effects, particle spacing requirements, element formulations, and boundary conditions for the SPH particles in the missile and panel are those described in Section 5.3. The numerical simulations of Test 8 are listed in Table 5-38.

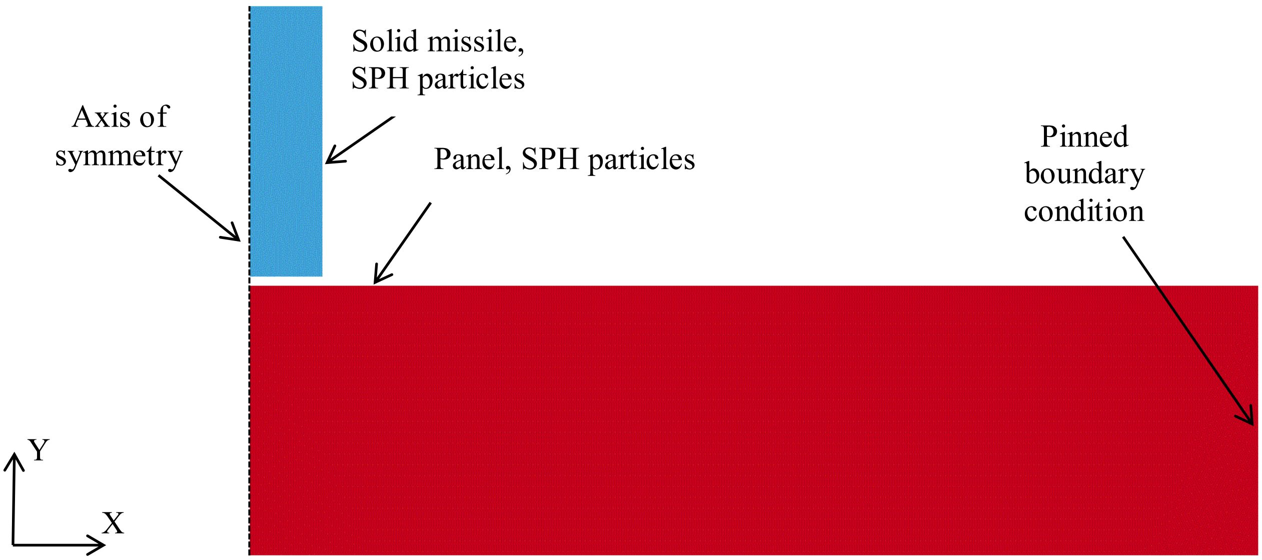

Figure 5-84: Axisymmetric model, 24-inch (610 mm) panel, solid missile, Test 8

Table 5-38: Numerical simulations, MAT072R3, solid missile, Test 8

Simulation	Concrete mesh mm (in.)	Solid missile mesh mm (in.)	f_c' MPa (psi)	f_t' MPa (psi)
1	10 (0.39)	5.35 (0.21)	26.2 (3800)	3.9 (570)
2	5 (0.20)	2.67 (0.11)	26.2 (3800)	3.9 (570)
3	4 (0.16)	2.14 (0.09)	26.2 (3800)	3.9 (570)
4	3 (0.12)	1.6 (0.06)	26.2 (3800)	3.9 (570)

Figure 5-85a and Figure 5-85b show perforation of the panel and ejection of the concrete on the back face, respectively, 20 msec after impact. Results are shown for the simulation using the finest mesh (3 mm). Figure 5-86 presents the missile velocity history for each particle spacing. A summary of the residual velocities is presented in Table 5-39.

Table 5-39: Residual velocities, solid missile, Test 8

Concrete mesh size, mm (in.)	3 (0.12)	4 (0.16)	5 (0.20)	10 (0.39)
Residual velocity, m/s (in/sec)	-11.8 (-463)	-10.5 (-415)	-9.4 (-369)	-7.3 (-288)

(g) Perforation of panel (h) Ejection of concrete on back face

Figure 5-85: Simulation results, 20 msec, solid missile, Test 8, 3 mm mesh, simulation 4

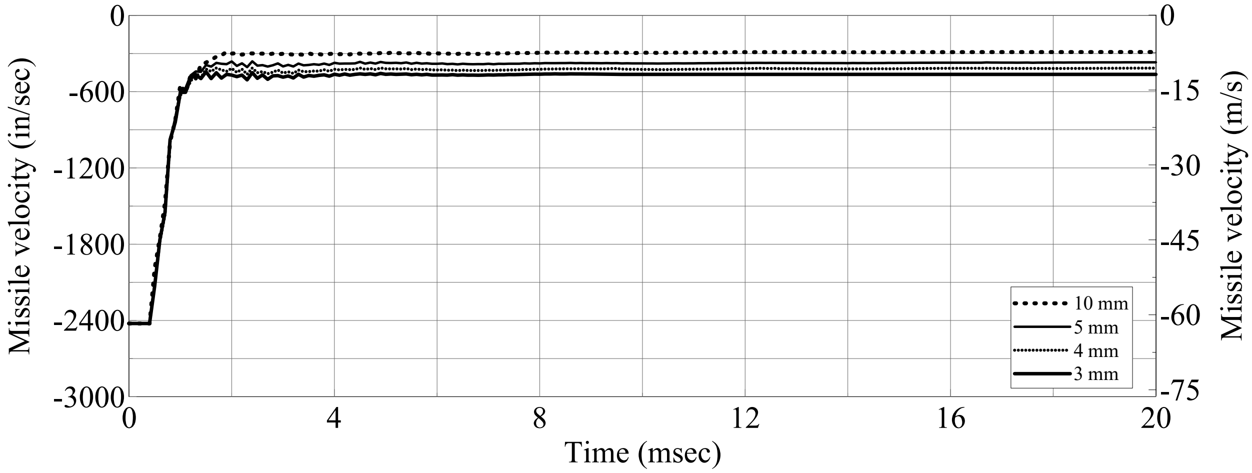

Figure 5-86: Velocity histories, solid missile, Test 8

The estimated rates of convergence and GCI are presented in Table 5-40. Concrete particle spacings of 3, 4, and 5 mm are used for the calculations (highlighted in Table 5-39). The estimated value of the converged residual velocity, f_{21}^{*}, (=-16.3 m/s (-641 in/sec)) is different from the residual velocity predicted using the finest mesh (3 mm) (=-11.8 m/s (-463 in/sec)). Since, the metric f_{32} (=-1.1 m/s (-46 in/sec)) is slightly smaller than f_{21} (=-1.2 m/s (-48 in/sec)), the GCI indicates that the analytical solution has not converged. However, f_{21} and f_{32}, are tiny compared to the initial velocity of the solid missile (=-61.6 m/s (-2424 in/sec)), indicating the numerical results are not likely to converge further as the mesh is refined below 3 mm. The evolution of the panel lateral displacement is shown in Figure 5-87 using results from the simulation using the finest mesh (3 mm). Significant local deformation at the midpoint of the panel is indicative of perforation.

Table 5-40: Estimated rates of convergence and GCI, solid missile, Test 8

r_{21}	1.33	p	0.832
r_{32}	1.25	GCI_{21}	-0.479
e_{21}	-0.10	GCI_{32}	-0.680
e_{32}	-0.11	f_{21}^* m/s (in/sec)	-16.3 (-641)
F_s	1.25	AC	1.1
		CI_{95} m/s (in/sec)	[-24.1, -8.5], ([-948, -334])

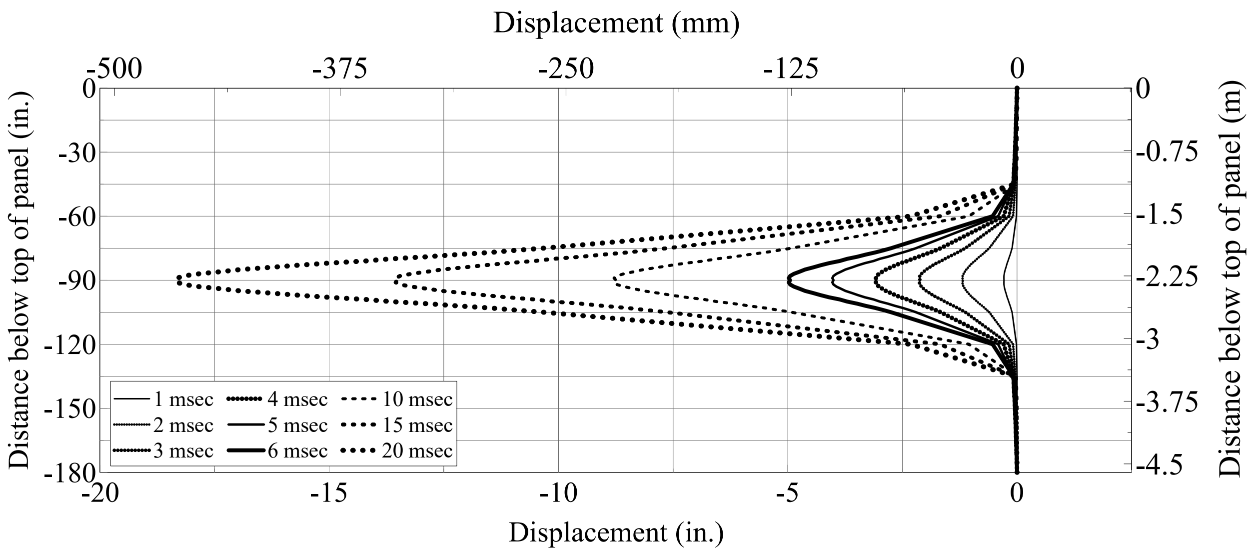

Figure 5-87: Panel back-face lateral displacement, solid missile, Test 8, 3 mm mesh, simulation 4

5.10.6 Rigid Missile Impact

Simulation 5 (see Table 5-32) and simulation 4 (see Table 5-35) from the solid missile impact studies of EPRI Tests 10 (see Section 5.10.3) and 3 (see Section 5.10.4), respectively, were repeated using a *rigid* missile. The elastic modulus of the solid cylindrical steel missile (=2.9×10^7 psi (2.0×10^5 MPa)) was increased by a factor a 10 to determine whether a *rigid* missile would cause more/less damage than a solid missile. The numerical models used for the simulations are shown in Figure 5-76 and Figure 5-80, for Tests 10 and 3, respectively. The two simulations used the finest concrete particle spacing determined from mesh convergence studies: 2 mm and 3 mm for Tests 10 and 3, respectively.

Figure 5-88 shows the velocity histories of the *rigid* missiles (RMs) for EPRI Tests 10 and 3. The velocity histories of the solid missiles (SMs) using the finest meshes are also shown in this figure to enable a comparison. The residual velocities for the solid missiles and *rigid* missiles are presented in Table 5-41. The results indicate that the panel response to the solid and rigid missiles are identical (i.e., equal exit velocities) for each test, and so the solid missiles used above are effectively rigid. The rigid missile impact simulations of EPRI Tests 10 and 3 were terminated at 3.2 and 6 msec, respectively.

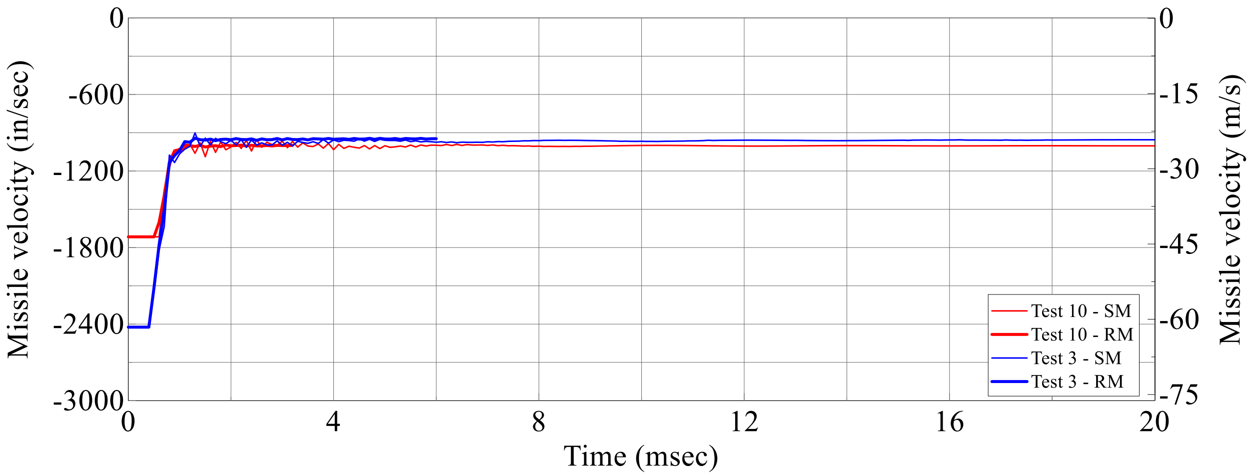

Figure 5-88: Velocity histories for SMs and RMs, Tests 10 and 3

Table 5-41: Residual velocities for SMs and RMs

	Test 10		Test 3	
	SM	RM	SM	RM
Residual velocity, m/s (in/sec)	-25.4 (-1000)	-25.4 (-1000)	-24.3 (-955)	-24.3 (-955)

5.10.7 Comparison of Solid and Annular Missile Impact Simulations

The response of a concrete panel impacted by a solid missile having the same mass as the Schedule 40 pipe was investigated using data from EPRI Tests 11, 10, 3, and 8 (see Table 5-1). These simulations involved 12-inch (305 mm) to 24-inch (610 mm) thick reinforced concrete panels normally impacted by a solid missile with impact velocities ranging from 98 fps (30 m/s) to 202 fps (62 m/s). In this section, the results of these simulations are compared to the impact simulations using the Schedule 40 pipe shown in Section 5.9.

Damage to the panel impacted by a solid missile is significantly different from that predicted using the Schedule 40 pipe, as shown in Figure 5-89. Results are presented for the Schedule 40 pipe (solid missile) in Figure 5-89a (b), Figure 5-89c (d), Figure 5-89e (f), and Figure 5-89g (h) for Tests 11, 10, 3, and 8, respectively, 20 msec after impact.

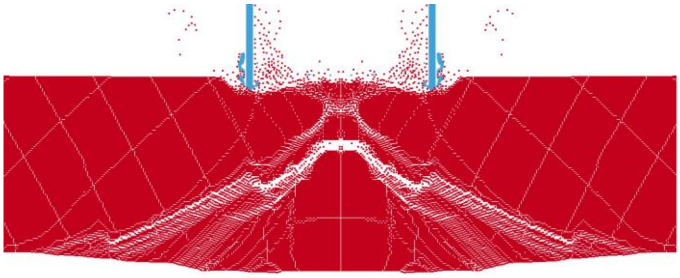
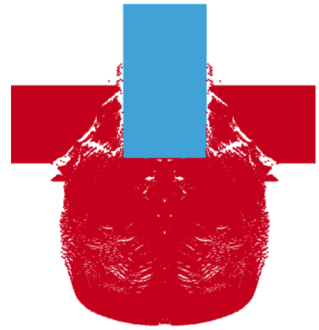

(a) Schedule 40 pipe, 3 mm mesh, Test 11 (b) Solid missile, 2mm mesh, Test 11


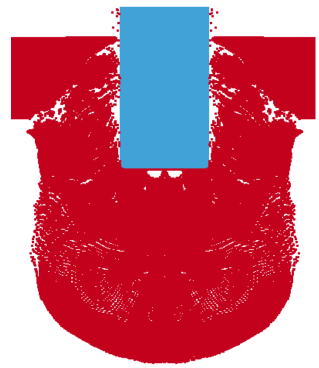

(c) Schedule 40 pipe, 2 mm mesh, Test 10 (d) Solid missile, 2mm mesh, Test 10

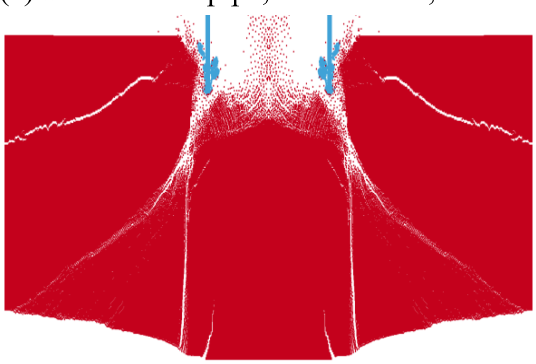
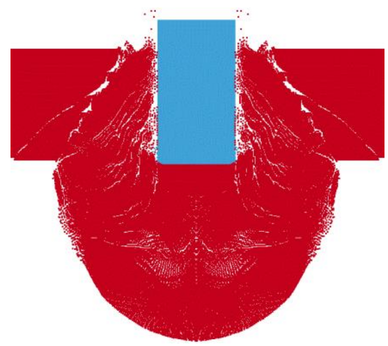

(e) Schedule 40 pipe, 2 mm mesh, Test 3 (f) Solid missile, 3 mm mesh, Test 3


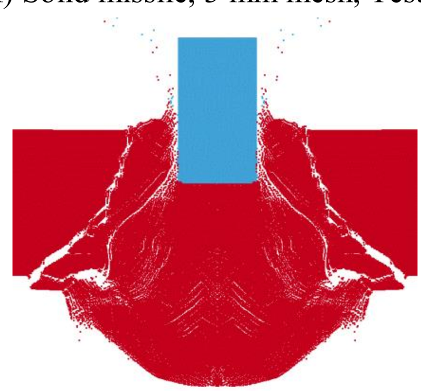

(g) Schedule 40 pipe, 3 mm mesh, Test 8 (h) Solid missile, 3 mm mesh, Test 8

Figure 5-89: Predicted damage to the panel from Schedule 40 pipe and solid missile, 20 msec

The finest (converged) mesh for each simulation is used for the comparison. Significant spalling of concrete on front face is observed for the pipe impact but not for the solid missile impact. The damage to the panel caused by pipe and solid missile impact varied significantly, with the likelihood of perforation greater with the solid missile.

5.11 Summary and Conclusions

The overarching goal of this chapter was to validate, in part, a numerical model, to be used in parametric studies for the development of design guidance for wind-borne missile impact. This chapter discussed the steps taken toward the partial validation of the numerical model. Data from the EPRI experiments (seen in Table 5-1) were used to aid in the validation process. The SPH formulation was used in this chapter to overcome the shortcomings associated with the Lagrangian formulation identified in Chapter 4. An axisymmetric formulation was used to reduce the high computational demand associated with the SPH formulation. Three concrete material models compatible with the SPH formulation in LS-DYNA (e.g., MAT016, MAT072R3, and MAT159) were used to explore the behavior of the panel during and after impact.

The quasi-static behavior of these three concrete material models was investigated using 3D models of a cylinder comprised of a) SPH particles, and b) Lagrangian elements. Mesh refinement studies were conducted for the SPH cylinder; the study highlighted the importance of mesh density in predicting compressive strength and elastic modulus. Using the finest mesh, the unconfined SPH cylinder reasonably recovered the elastic modulus and peak strength of the Lagrangian cylinder for MAT016, MAT072R3, and MAT159, but the post-peak softening using MAT072R3 and the elastic-plastic behavior at large strains using MAT016, both observed in the Lagrangian cylinder, were not predicted using the SPH cylinder. To further investigate the post-peak behavior of MAT072R3 and MAT016, confined cube simulations were conducted using the SPH and Lagrangian formulations. The results showed that for extremely low levels of confinement (on the order of 0.2% of the concrete compressive strength), the post-peak softening behavior of the SPH cube using MAT072R3 was recovered and was similar to that of the unconfined Lagrangian cube. Further, the elastic-plastic behavior at large strains using the MAT016 material model was recovered using a confinement pressure of 1 MPa (2% of the concrete compressive strength). Considering that the confining pressures at the interface between the pipe and the panel during impact are expected to be on the order of 150 MPa, as was observed in the simulations, the SPH formulation is fully capable of recovering the behavior of the Lagrangian formulation using all three concrete material models.

The wall panel behavior was investigated as a function of the three concrete material models available for SPH calculations. Data from EPRI Test 11 (see Table 5-1) were used for this study; the concrete compressive strength was increased (=4500 psi) from that specified in the physical test (=3600 psi) to accommodate the CSCM material model in the simulations. The input parameters for all three material models describing the elastic response and inelastic response including shear failure envelope, compressibility, and tensile failure were internally generated, using only the uniaxial concrete compressive strength as input. The shear failure surfaces of the three material models were generated and used to make predictions of panel resistance to perforation. The impact simulations using the three material models predicted significantly different results: MAT016 (MAT159) provided the least (greatest) resistance to panel perforation, results that were consistent with the predictions based on the generated shear failure surfaces. The confining pressures at the interface between the pipe and the panel were also investigated and were consistent with the order-of-magnitude pressures identified in Schwer (2008b) for impact simulations.

EPRI Test 11 (see Table 5-1) was simulated in LS-DYNA using MAT016 and MAT072R3; the reported uniaxial compressive strength (=3600 psi) was used for the simulations. The uniaxial concrete compressive strength was used to generate material model parameters; the estimated tensile strength was 10% of the uniaxial concrete compressive strength. The numerical simulations predicted perforation of the panel using both material models, which was not observed in the experiment. The poor correlation of predicted and observed damage prompted an investigation of the effects of concrete compressive and tensile strength on the impact resistance of reinforced concrete panels. The concrete material model MAT072R3 was used in the simulations as it is the only material model (of the three studied here) that allows the user to input tensile strength. The results show an increase in panel perforation resistance as the compressive and tensile strength are increased. Based on these findings, the Schedule 40 pipe impact simulations of Test 11, 10, 3, and 8 (see Table 5-1) were then repeated using MAT072R3 with a concrete tensile strength set equal to 15% of compressive strength (i.e., 5% greater than that generated internally by the material model codes). The numerical simulations reasonably reproduced the results of the experiments (i.e., front and back face crater diameters and perforation of the panel in Test 10, formation and size of the conical plug on the back face in Test 11, and the global response of the panel in Test 8). However, perforation was predicted in Test 3 but not observed in the experiment. In addition, the depth of penetration of the pipe was underestimated by a factor of three in Tests 8 and 11.

The reasonable agreement between the EPRI experiments and the numerical simulations using MAT072R3 and a tensile strength corresponding to 15% of the concrete compressive strength, provides a level of confidence in the robustness of the numerical model. However, the lack of information and metadata from the experiments poses a challenge to fully validate the numerical model for impact analysis. The partially validated numerical model is used in Chapter 6 to investigate the effects of panel thickness, Schedule 40 pipe diameter, impact velocity, and concrete compressive and tensile strength on impact resistance.

The response of reinforced concrete panels impacted by solid (and effectively rigid) cylindrical missiles having the same mass as the Schedule 40 pipe was studied. EPRI Tests 3, 8, 10, and 11 (see Table 5-1) provided much of the basis for these simulations. Results were compared with those of simulations using Schedule 40 annular pipes. A solid missile will generate more damage on the back face of a panel than an annular missile of the same mass.

SECTION 6
A PARAMETRIC STUDY OF WIND-BORNE MISSILE IMPACT

6.1 Introduction

The results of 153 finite element analyses of concrete panels are used to investigate the effects of panel thickness, Schedule 40 pipe size (mass and diameter), pipe velocity, and uniaxial concrete compressive and tensile strength on the response of reinforced concrete panels to normal impact by wind-borne missiles. The results are used to provide design guidance. The numerical model used in the simulations was validated to the degree possible in Section 5.9 using results of the EPRI experiments (see Table 5-1). The 6 in (152 mm) diameter Schedule 40 pipe is included in the set of missiles to be used for the design of exterior, above grade, walls and slabs specified by Regulatory Guides (RG) 1.76 (2007) and 1.221 (2011) for nuclear power plants. The Schedule 40 pipe is capable of penetrating concrete panels and scabbing concrete on the back face, and so it is the focus of this parametric study.

Section 6.2 describes the LS-DYNA models and the design parameters chosen for the parametric study. Analysis results and key findings are presented in Section 6.3. Results are used to provide guidance on the assessment of reinforced concrete panels impacted by wind-borne missiles in Section 6.4. The focus of Section 6.4 will be on the design requirements specified by RG 1.76 (2007) and RG 1.221 (2011) for Schedule 40 pipes.

6.2 Modeling of Reinforced Concrete Panels

The general-purpose finite element code LS-DYNA is used to simulate the response of 153 concrete panels to normal impact of wind-borne missiles.

6.2.1 Design Parameters

A significant number of parameters affect the impact resistance of reinforced concrete panels, including panel thickness, and uniaxial concrete compressive strength and tensile strength. The mass and diameter of the Schedule 40 pipe and the impact velocity also play a significant role in the response of the panel. Panel thicknesses of 12 in (305 mm), 15 in (381 mm), 18 in (460 mm), and 25.6 in (650 mm), typical of walls in nuclear power plants, were investigated. Table 6-1 identifies parameters and their magnitudes examined in this study. In this table, d is the outer diameter of the Schedule 40 pipe, v is the impact velocity of the pipe, and f_c' and f_t' are the concrete compressive and tensile strengths, respectively. Three magnitudes of each parameter were considered: low, medium, and high. Schedule 40 pipe diameters of 6 in. (152.4 mm), 8 in (203 mm), and 10 in (254 mm) were used in the study. Their masses, for a 15 ft. (4.58 m) length, are 0.74 lb-sec^2/in (130 kg), 1.11 lb-sec^2/in (195 kg), and 1.57 lb-sec^2/in (276 kg), respectively. (Fifteen feet (4.58 m) is the length of the 6-inch (152.4 mm) diameter Schedule 40 pipe identified in RG 1.76 (2007) and RG 1.221 (2011).) Schedule 40 pipes with diameters of 8 in (203.2 mm) and 10 in (254 mm) were included in this study to expand the dataset and the utility of the conclusions.

Table 6-1: Variables used in parametric study

	Low	Medium	High
d , in (mm)	6 (152)	8 (203)	10 (254)
v , in/sec (m/sec)	1575 (40)	2756 (70)	3937 (100)
f_c' , psi (MPa)	4351 (30)	5801 (40)	7251 (50)
f_t' , psi (MPa)	435 (3)	580 (4)	725 (5)

Three magnitudes of impact velocity were investigated: 1575 in/sec (40 m/s), 2756 in/sec (70 m/s), and 3937 in/sec (100 m/s). The chosen velocities envelope the maximum velocities recommended by RG 1.76 (=1620 in/sec (41 m/s)) and RG 1.221 (=3696 in/sec (94 m/s)) for the design of panels to resist impact by Schedule 40 pipes. Concrete compressive strengths of 4351 psi (30 MPa), 5801 psi (40 MPa), and 7251 psi (50 MPa) were examined: enveloping concrete strengths in nuclear power plant structures. Concrete tensile strength also has a significant effect on the impact resistance of reinforced concrete panels as seen in Section 5.8. Tensile strengths ranging from 435 psi (3 MPa) to 725 psi (5 MPa) were considered in this study and these are 10% of the compressive strengths for 4351 psi (30 MPa) and 7251 psi (50 MPa) concrete, respectively.

Figure 6-1 describes the simulations conducted for the 12-inch (305 mm) thick panel. Since a 12-inch (305 mm) thick panel is more vulnerable to concrete scabbing (e.g., ejection of concrete on the back face) and perforation (e.g., complete penetration of the panel) than the 15 in (381 mm), 18 in (460 mm), and 25.6 in (650 mm) thick panels, all 81 combinations of Schedule 40 pipe diameter, pipe velocity and compressive and tensile strength identified in Table 6-1 were simulated. These combinations are presented in Table 6-2 (rows 1 through 81).

Figure 6-2 identifies the simulations for the 15 in (381 mm), 18 in (460 mm), and 25.6 in (650 mm) thick panels. The red outline in Figure 6-2 shows the path used to identify the simulations considered in this part of the study. Simulations were conducted for each diameter of Schedule 40 pipe (e.g., 6 in (152 mm), 8 in (203 mm), and 10 in (254 mm)), for each panel thickness. Simulations were performed for the low and high values of projectile velocity and concrete compressive and tensile strength identified in Table 6-1 for each pipe diameter. Simulations for the 15 in (381 mm), 18 in (460 mm), and 25.6 in (650 mm) thick panels are presented in rows 82 through 105, 106 through 129, and 130 through 153 of Table 6-2, respectively.

Figure 6-1: Simulations for the 12 in (305 mm) thick panel

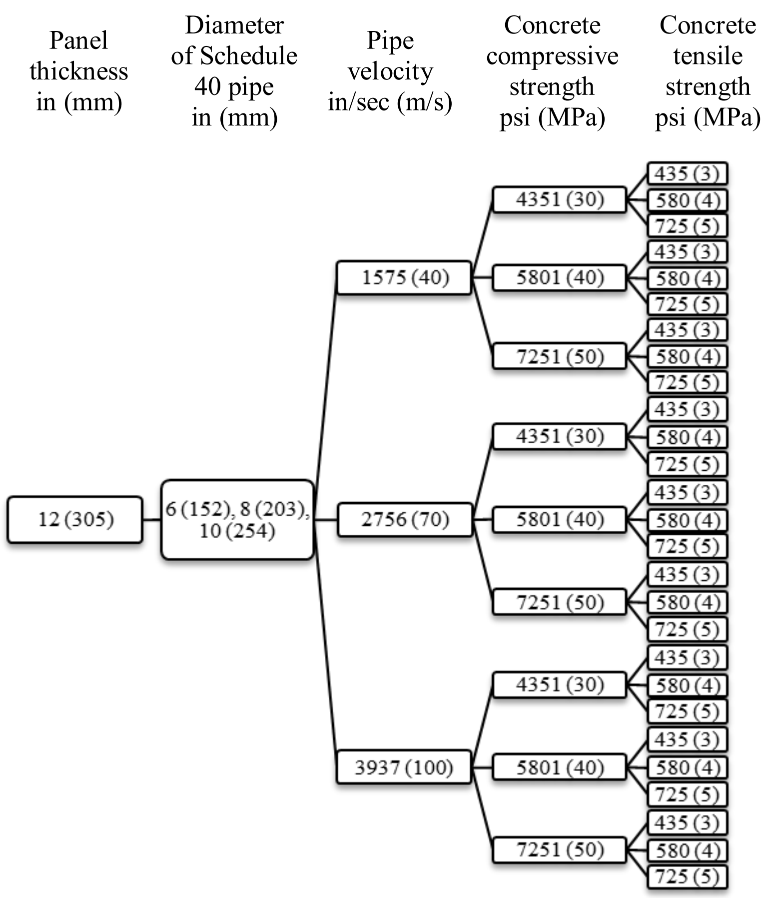

Figure 6-2: Simulations for the 15 in (381 mm), 18 in (480 mm) and 25.6 in (650 mm) thick panels

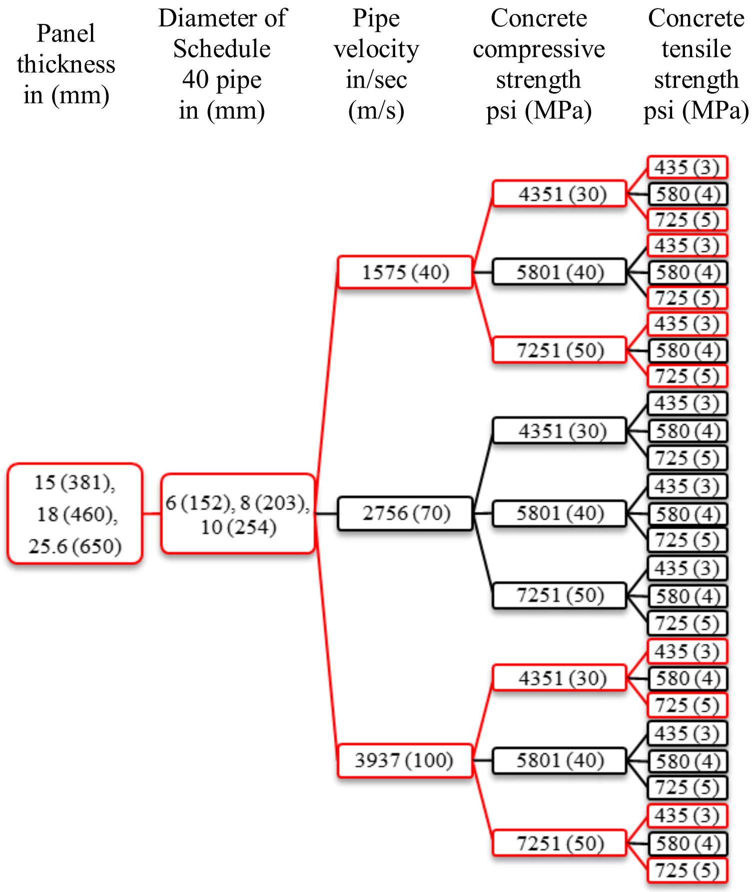

Table 6-2: Simulations conducted in parametric study

No.	Wall thickness t mm (in.)	Schedule 40 pipe diameter mm (in)	Pipe velocity v m/s (in/s)	f_c' MPa (psi)	f_t' MPa (psi)
1	305 mm (12 in)	152 (6)	40 (1575)	30 (4351)	3 (435)
2		152 (6)	40 (1575)	30 (4351)	4 (580)
3		152 (6)	40 (1575)	30 (4351)	5 (725)
4		152 (6)	40 (1575)	40 (5801)	3 (435)
5		152 (6)	40 (1575)	40 (5801)	4 (580)
6		152 (6)	40 (1575)	40 (5801)	5 (725)
7		152 (6)	40 (1575)	50 (7251)	3 (435)
8		152 (6)	40 (1575)	50 (7251)	4 (580)
9		152 (6)	40 (1575)	50 (7251)	5 (725)
10		152 (6)	70 (2756)	30 (4351)	3 (435)
11		152 (6)	70 (2756)	30 (4351)	4 (580)
12		152 (6)	70 (2756)	30 (4351)	5 (725)
13		152 (6)	70 (2756)	40 (5801)	3 (435)
14		152 (6)	70 (2756)	40 (5801)	4 (580)
15		152 (6)	70 (2756)	40 (5801)	5 (725)
16		152 (6)	70 (2756)	50 (7251)	3 (435)
17		152 (6)	70 (2756)	50 (7251)	4 (580)
18		152 (6)	70 (2756)	50 (7251)	5 (725)
19		152 (6)	100 (3937)	30 (4351)	3 (435)
20		152 (6)	100 (3937)	30 (4351)	4 (580)
21		152 (6)	100 (3937)	30 (4351)	5 (725)
22		152 (6)	100 (3937)	40 (5801)	3 (435)
23		152 (6)	100 (3937)	40 (5801)	4 (580)
24		152 (6)	100 (3937)	40 (5801)	5 (725)
25		152 (6)	100 (3937)	50 (7251)	3 (435)
26		152 (6)	100 (3937)	50 (7251)	4 (580)
27		152 (6)	100 (3937)	50 (7251)	5 (725)
28		203 (8)	40 (1575)	30 (4351)	3 (435)
29		203 (8)	40 (1575)	30 (4351)	4 (580)
30		203 (8)	40 (1575)	30 (4351)	5 (725)
31		203 (8)	40 (1575)	40 (5801)	3 (435)
32		203 (8)	40 (1575)	40 (5801)	4 (580)
33		203 (8)	40 (1575)	40 (5801)	5 (725)
34		203 (8)	40 (1575)	50 (7251)	3 (435)
35		203 (8)	40 (1575)	50 (7251)	4 (580)
36		203 (8)	40 (1575)	50 (7251)	5 (725)
37		203 (8)	70 (2756)	30 (4351)	3 (435)
38		203 (8)	70 (2756)	30 (4351)	4 (580)
39		203 (8)	70 (2756)	30 (4351)	5 (725)
40		203 (8)	70 (2756)	40 (5801)	3 (435)
41		203 (8)	70 (2756)	40 (5801)	4 (580)
42		203 (8)	70 (2756)	40 (5801)	5 (725)
43		203 (8)	70 (2756)	50 (7251)	3 (435)
44		203 (8)	70 (2756)	50 (7251)	4 (580)
45		203 (8)	70 (2756)	50 (7251)	5 (725)
46		203 (8)	100 (3937)	30 (4351)	3 (435)
47		203 (8)	100 (3937)	30 (4351)	4 (580)
48		203 (8)	100 (3937)	30 (4351)	5 (725)
49		203 (8)	100 (3937)	40 (5801)	3 (435)

Table 6-2: Simulations conducted in parametric study (contd.)

50		203 (8)	100 (3937)	40 (5801)	4 (580)
51		203 (8)	100 (3937)	40 (5801)	5 (725)
52		203 (8)	100 (3937)	50 (7251)	3 (435)
53		203 (8)	100 (3937)	50 (7251)	4 (580)
54		203 (8)	100 (3937)	50 (7251)	5 (725)
55		254 (10)	40 (1575)	30 (4351)	3 (435)
56		254 (10)	40 (1575)	30 (4351)	4 (580)
57		254 (10)	40 (1575)	30 (4351)	5 (725)
58		254 (10)	40 (1575)	40 (5801)	3 (435)
59		254 (10)	40 (1575)	40 (5801)	4 (580)
60		254 (10)	40 (1575)	40 (5801)	5 (725)
61		254 (10)	40 (1575)	50 (7251)	3 (435)
62		254 (10)	40 (1575)	50 (7251)	4 (580)
63		254 (10)	40 (1575)	50 (7251)	5 (725)
64		254 (10)	70 (2756)	30 (4351)	3 (435)
65		254 (10)	70 (2756)	30 (4351)	4 (580)
66		254 (10)	70 (2756)	30 (4351)	5 (725)
67		254 (10)	70 (2756)	40 (5801)	3 (435)
68		254 (10)	70 (2756)	40 (5801)	4 (580)
69		254 (10)	70 (2756)	40 (5801)	5 (725)
70		254 (10)	70 (2756)	50 (7251)	3 (435)
71		254 (10)	70 (2756)	50 (7251)	4 (580)
72		254 (10)	70 (2756)	50 (7251)	5 (725)
73		254 (10)	100 (3937)	30 (4351)	3 (435)
74		254 (10)	100 (3937)	30 (4351)	4 (580)
75		254 (10)	100 (3937)	30 (4351)	5 (725)
76		254 (10)	100 (3937)	40 (5801)	3 (435)
77		254 (10)	100 (3937)	40 (5801)	4 (580)
78		254 (10)	100 (3937)	40 (5801)	5 (725)
79		254 (10)	100 (3937)	50 (7251)	3 (435)
80		254 (10)	100 (3937)	50 (7251)	4 (580)
81		254 (10)	100 (3937)	50 (7251)	5 (725)
82	381 mm (15 in)	152 (6)	40 (1575)	30 (4351)	3 (435)
83		152 (6)	40 (1575)	30 (4351)	5 (725)
84		152 (6)	40 (1575)	50 (7251)	3 (435)
85		152 (6)	40 (1575)	50 (7251)	5 (725)
86		152 (6)	100 (3937)	30 (4351)	3 (435)
87		152 (6)	100 (3937)	30 (4351)	5 (725)
88		152 (6)	100 (3937)	50 (7251)	3 (435)
89		152 (6)	100 (3937)	50 (7251)	5 (725)
90		203 (8)	40 (1575)	30 (4351)	3 (435)
91		203 (8)	40 (1575)	30 (4351)	5 (725)
92		203 (8)	40 (1575)	50 (7251)	3 (435)
93		203 (8)	40 (1575)	50 (7251)	5 (725)
94		203 (8)	100 (3937)	30 (4351)	3 (435)
95		203 (8)	100 (3937)	30 (4351)	5 (725)
96		203 (8)	100 (3937)	50 (7251)	3 (435)
97		203 (8)	100 (3937)	50 (7251)	5 (725)
98		254 (10)	40 (1575)	30 (4351)	3 (435)
99		254 (10)	40 (1575)	30 (4351)	5 (725)
100		254 (10)	40 (1575)	50 (7251)	3 (435)
101		254 (10)	40 (1575)	50 (7251)	5 (725)

Table 6-2: Simulations conducted in parametric study (contd.)

102		254 (10)	100 (3937)	30 (4351)	3 (435)
103		254 (10)	100 (3937)	30 (4351)	5 (725)
104		254 (10)	100 (3937)	50 (7251)	3 (435)
105		254 (10)	100 (3937)	50 (7251)	5 (725)
106	460 mm (18 in)	152 (6)	40 (1575)	30 (4351)	3 (435)
107		152 (6)	40 (1575)	30 (4351)	5 (725)
108		152 (6)	40 (1575)	50 (7251)	3 (435)
109		152 (6)	40 (1575)	50 (7251)	5 (725)
110		152 (6)	100 (3937)	30 (4351)	3 (435)
111		152 (6)	100 (3937)	30 (4351)	5 (725)
112		152 (6)	100 (3937)	50 (7251)	3 (435)
113		152 (6)	100 (3937)	50 (7251)	5 (725)
114		203 (8)	40 (1575)	30 (4351)	3 (435)
115		203 (8)	40 (1575)	30 (4351)	5 (725)
116		203 (8)	40 (1575)	50 (7251)	3 (435)
117		203 (8)	40 (1575)	50 (7251)	5 (725)
118		203 (8)	100 (3937)	30 (4351)	3 (435)
119		203 (8)	100 (3937)	30 (4351)	5 (725)
120		203 (8)	100 (3937)	50 (7251)	3 (435)
121		203 (8)	100 (3937)	50 (7251)	5 (725)
122		254 (10)	40 (1575)	30 (4351)	3 (435)
123		254 (10)	40 (1575)	30 (4351)	5 (725)
124		254 (10)	40 (1575)	50 (7251)	3 (435)
125		254 (10)	40 (1575)	50 (7251)	5 (725)
126		254 (10)	100 (3937)	30 (4351)	3 (435)
127		254 (10)	100 (3937)	30 (4351)	5 (725)
128		254 (10)	100 (3937)	50 (7251)	3 (435)
129		254 (10)	100 (3937)	50 (7251)	5 (725)
130	650 mm (25.6 in)	152 (6)	40 (1575)	30 (4351)	3 (435)
131		152 (6)	40 (1575)	30 (4351)	5 (725)
132		152 (6)	40 (1575)	50 (7251)	3 (435)
133		152 (6)	40 (1575)	50 (7251)	5 (725)
134		152 (6)	100 (3937)	30 (4351)	3 (435)
135		152 (6)	100 (3937)	30 (4351)	5 (725)
136		152 (6)	100 (3937)	50 (7251)	3 (435)
137		152 (6)	100 (3937)	50 (7251)	5 (725)
138		203 (8)	40 (1575)	30 (4351)	3 (435)
139		203 (8)	40 (1575)	30 (4351)	5 (725)
140		203 (8)	40 (1575)	50 (7251)	3 (435)
141		203 (8)	40 (1575)	50 (7251)	5 (725)
142		203 (8)	100 (3937)	30 (4351)	3 (435)
143		203 (8)	100 (3937)	30 (4351)	5 (725)
144		203 (8)	100 (3937)	50 (7251)	3 (435)
145		203 (8)	100 (3937)	50 (7251)	5 (725)
146		254 (10)	40 (1575)	30 (4351)	3 (435)
147		254 (10)	40 (1575)	30 (4351)	5 (725)
148		254 (10)	40 (1575)	50 (7251)	3 (435)
149		254 (10)	40 (1575)	50 (7251)	5 (725)
150		254 (10)	100 (3937)	30 (4351)	3 (435)
151		254 (10)	100 (3937)	30 (4351)	5 (725)
152		254 (10)	100 (3937)	50 (7251)	3 (435)
153		254 (10)	100 (3937)	50 (7251)	5 (725)

6.2.2 Models used in the Parametric Study

The axisymmetric models of the 12 in (305 mm), 15 in (381 mm), 18 in (460 mm) and 25.6 in (650 mm) thick panels are presented in Figure 6-3a, Figure 6-3b, Figure 6-3c, and Figure 6-3d, respectively. Twelve models were used in the simulations; three pipe sizes for each panel thickness. SPH particles were used for the concrete panels and pipes. A concrete particle spacing of 0.08 in (2 mm) was used for the 12 in (305 mm), 15 in (381 mm), and 18 in (460 mm) thick panels. A 0.12 in (3 mm) spacing was adopted for the 25.6 in (650 mm) thick panel. The chosen mesh size for each panel thickness was based on mesh sensitivity studies presented in Section 5.9 for the 12 in (305 mm), 18 in (460 mm), and 24 in (610 mm) thick panels. The spacing of the pipe particles was set equal to one half that of the spacing of the concrete particles to ensure that each particle had the same mass.

The material model MAT072R3 in LS-DYNA was used for the concrete because it recovered the results of the EPRI experiments (see Table 5-1) with reasonable accuracy (see Section 5.9). The Dynamic Increase Factors for strain rate effects in concrete, were those described previously in Section 5.3.2. The Johnson-Cook (JC) material model (MAT015) was used for the Schedule 40 pipe; yield strength was set equal to 73 ksi (503 MPa). The Borvik et al. (2004) JC material parameters for 71 ksi (490 MPa) steel were used, as described in Section 5.3. The equation of state keyword EOS_LINEAR_POLYNOMIAL was activated for the JC material model by setting the variable C1 equal to the bulk modulus of steel (=2.3×10^7 psi (1.6×10^5 MPa)).

The default particle approximation theory (ELFORM=0 in LS-DYNA) was used for the SPH particles. Monaghan-type artificial viscosity was activated by setting the variable IAVIS to zero in the *CONTROL_SPH keyword, which is required for axisymmetric simulations. Variables Q1 and Q2 were set equal to one in the *CONTROL_BULK_VISCOSITY keyword per Liu et al. (2003). Two columns of SPH particles constrained displacement in the Y-direction on the outer edge of the panel to simulate a pinned boundary condition.

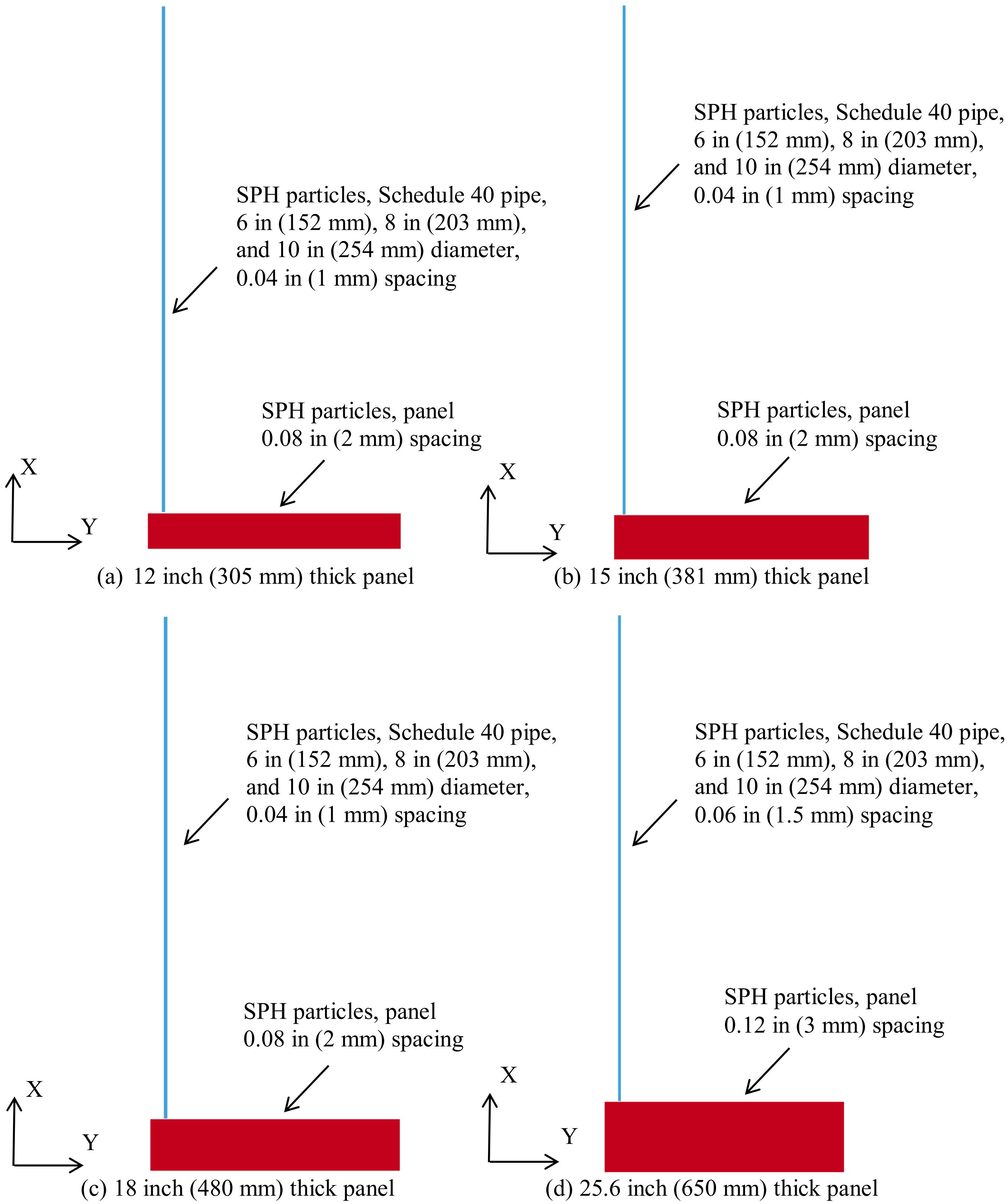

Figure 6-3: Axisymmetric models used in parametric study

6.3 Impact Simulation Results

6.3.1 Introduction

The effects on resistance to impact of panel thickness, concrete compressive and tensile strength, Schedule 40 pipe mass and diameter, and impact velocity are investigated in this section. Figure 6-4 presents the terminology used to evaluate the panels. The simulation results are categorized by non-perforation (Figure 6-4a and Figure 6-4b) and perforation (Figure 6-4c) tests. In the non-perforation tests, the pipe does not completely penetrate the panel (e.g., exit velocity of the pipe is zero). Two outcomes of importance are considered in the non-perforation tests: 1) no damage to the back (non-impact) face (Figure 6-4a), and 2) formation of a conical plug on the back face of the panel (Figure 6-4b). If the conical plug forms, scabbing (ejection of fragments from the back (non-impact) face) of concrete is assumed to occur. (Spalling of concrete from the front or impact face is not of concern because material will not be lost inside containment.) In the perforation tests, the pipe completely penetrates the panel (e.g., exit velocity is greater than zero) (see Figure 6-4c). The predicted conical plug diameter for non-perforation and perforation tests is defined in Figure 6-4b and Figure 6-4c, respectively.

Although the definition used herein to define conical plug diameter is the same as that used in the EPRI tests (Stephenson, 1977; Rotz, 1975), different conical plug shapes were observed in the simulations, particularly in those tests where perforation was predicted. Figure 6-5a and Figure 6-5b, show the formation of a conical plug for tests wherein the pipe had a low exit velocity (approximately 3% of impact velocity) and a high exit velocity (67% of the impact velocity), respectively. The results are significantly different from that shown in Figure 6-4c. All conical plug sizes measured in the simulations for perforation and non-perforation tests were described using the definition of Figure 6-4.

The predicted conical plug diameters and exit velocities for all 153 simulations were tabulated and the results are presented in Table D-1 of Appendix D. Simulations 12, 53, and 127 (highlighted in Table D-1) terminated prematurely and results cannot be reported. The following sections present plots of the exit velocity and conical plug diameter as a function of panel thickness, concrete compressive and tensile strength, pipe velocity, and Schedule 40 pipe mass and diameter, to investigate their influence on impact resistance. The effect of concrete compressive and tensile strength, and Schedule 40 pipe velocity and size on impact resistance are evaluated using results of the 12-inch (305 mm) thick panel (simulations 1 through 81 in Table 6-2) because thicker panels are less vulnerable to concrete scabbing and perforation. The effectiveness of a panel to resist pipe impact is based on its ability to prevent a) perforation, and b) scabbing of concrete on the back face.

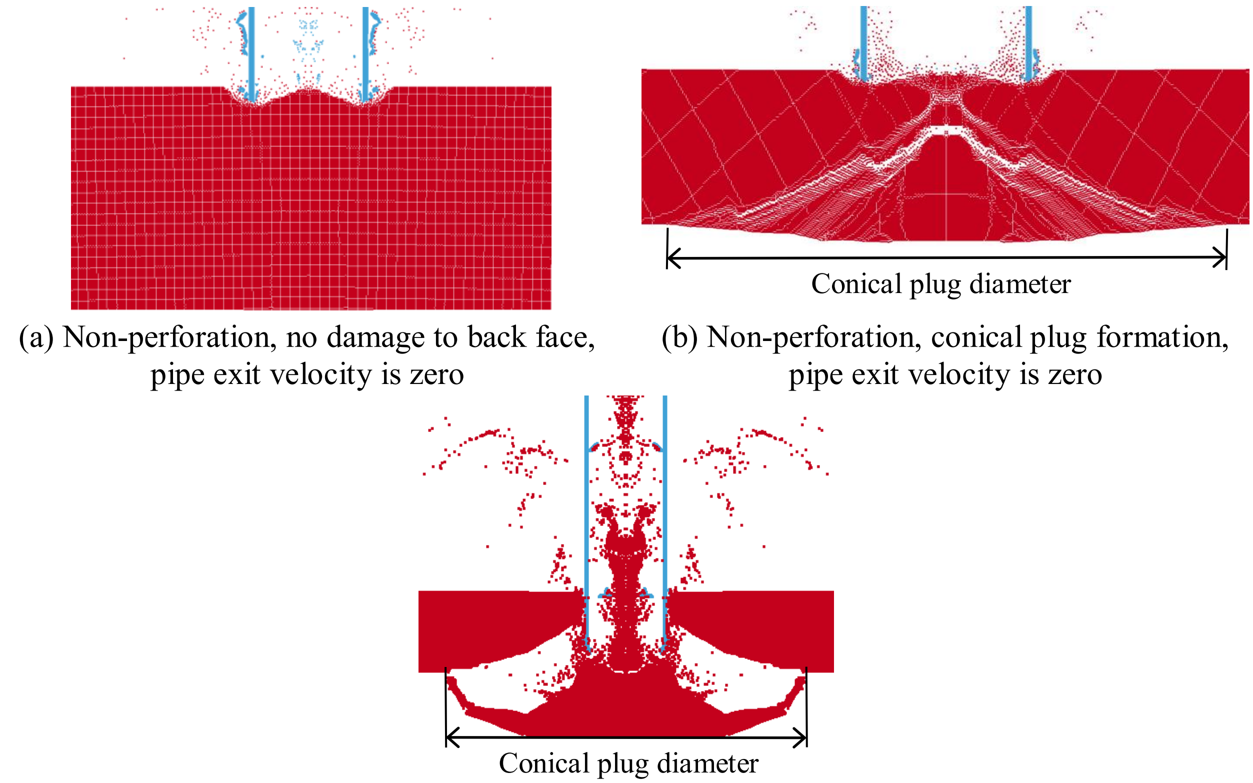

(a) Non-perforation, no damage to back face, pipe exit velocity is zero

(b) Non-perforation, conical plug formation, pipe exit velocity is zero

(c) Perforation, pipe exit velocity is nonzero

Figure 6-4: Terminology used to evaluate panel response

(a) Low exit velocity (approximately 3% of impact velocity)

(b) High exit velocity (approximately 67% of impact velocity)

Figure 6-5: Alternate conical plug formations in perforation tests

6.3.2 Concrete Panel Thickness

Figure 6-6 presents the exit velocity of the Schedule 40 pipe as a function of concrete panel thickness for 6 in (152 mm), 8 in (203 mm), and 10 in (254 mm) diameter pipes normally impacting panels at a velocity of 3937 in/sec (100 m/s). The masses of the 6 in. (152.4 mm), 8 in (203 mm), and 10 in (254 mm) diameter pipes are 0.74 lb-sec^2/in (130 kg), 1.11 lb-sec^2/in (195 kg), and 1.57 lb-sec^2/in (276 kg), respectively. Results are presented for concrete compressive strengths of 4351 psi (30 MPa) and 7251 psi (50 MPa) and tensile strengths of 435 psi (3 MPa) and 725 psi (5 MPa). The pipe exit velocity decreases as the panel thickness increases, which is an expected result. The 25.6 in (650 mm) thick panels were not perforated (e.g., exit velocity is zero) for all three diameters of pipe. Figure D-1 presents information for an impact velocity of 1575 in/sec (40 m/s); perforation was observed in only three of the 48 simulations.

The conical plug diameter as a function of concrete panel thickness, for an impact velocity of 3937 in/sec (100 m/s), is presented in Figure 6-7. Results are shown for the 6 in (152 mm), 8 in (203 mm), and 10 in (254 mm) diameter pipes, and concrete compressive and tensile strengths of 4351 psi (30 MPa) and 7251 psi (50 MPa), and 435 psi (3 MPa) and 725 psi (5 MPa). The conical plug diameter decreases as panel thickness increases for the 6 inch (152 mm) diameter Schedule 40 pipe, consistent with the decreasing likelihood of perforation and decreasing depth of penetration as a fraction of panel thickness. Information is presented in Figure D-2 for an impact velocity of 1575 in/sec (40 m/s).

6.3.3 Concrete Compressive Strength

The exit velocity of the Schedule 40 pipe as a function of concrete compressive strength is presented in Figure 6-8 for 6 in (152 mm), 8 in (203 mm), and 10 in (254 mm) diameter pipes normally impacting panels at a velocity of 3937 in/sec (100 m/s). Results are shown for concrete tensile strengths of 435 psi (3 MPa), 580 psi (4 MPa), and 725 psi (5 MPa). The results suggest that concrete compressive strength has a relatively small effect on impact resistance. Results are presented in Figures D-3 and D-4 for pipe impact velocities of 1575 in/sec (40 m/s) and 2756 in/sec (70 m/s), respectively.

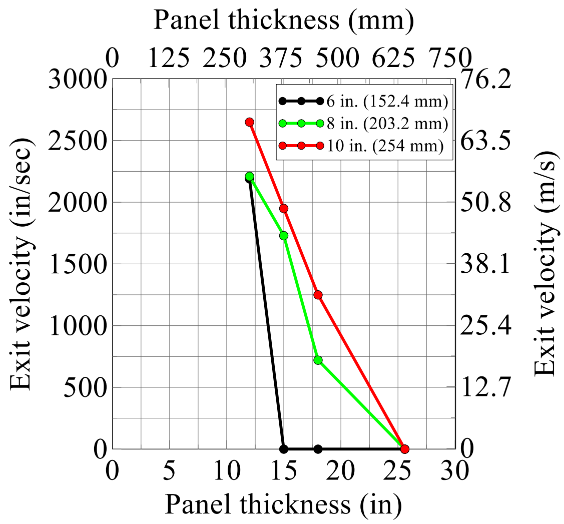

(a) f_c' =4351 psi (30 MPa), f_t' =435 psi (3 MPa)

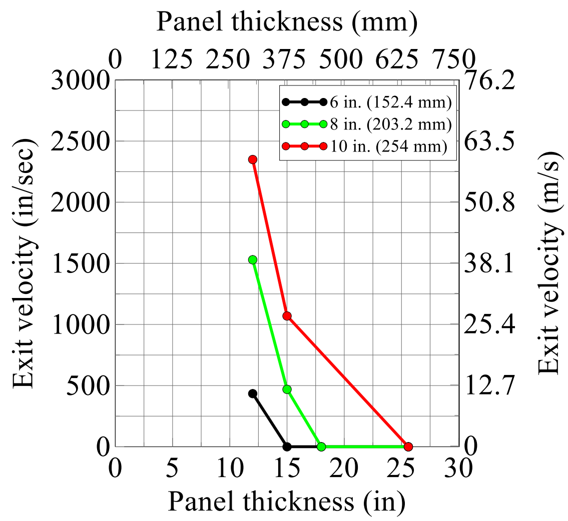

(b) f_c' =4351 psi (30 MPa), f_t' =725 psi (5 MPa)

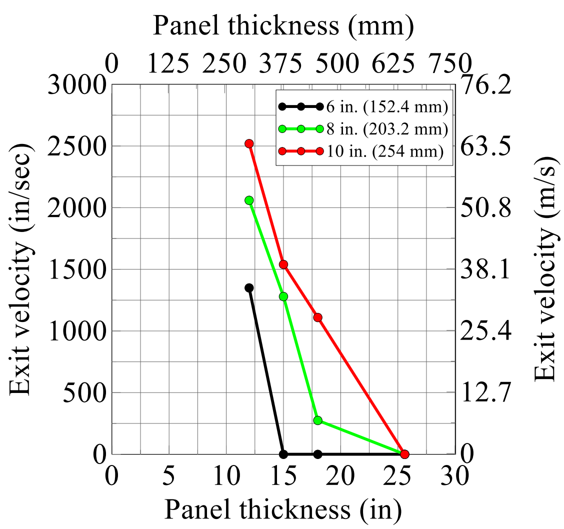

(c) f_c' =7251 psi (50 MPa), f_t' =435 psi (3 MPa)

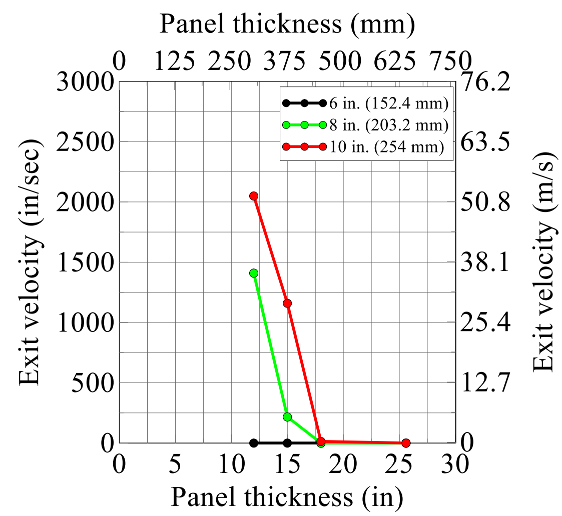

(d) f_c' =7251 psi (50 MPa), f_t' =725 psi (5 MPa)

Figure 6-6: Exit velocity of Schedule 40 pipe as a function of panel thickness, v =3937 in/sec (100 m/sec), MAT072R3

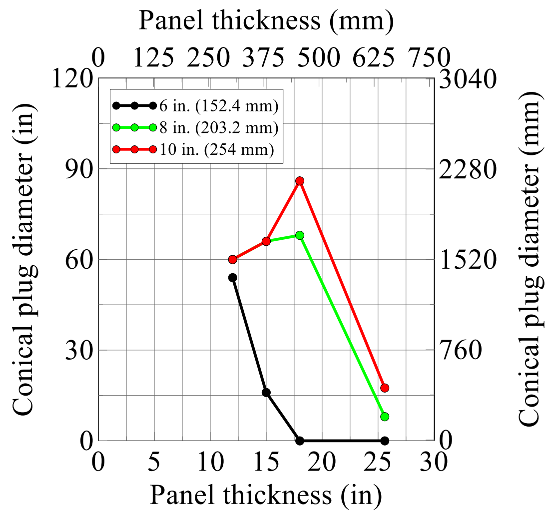

(a) f_c'=4351 psi (30 MPa), f_t'=435 psi (3 MPa)

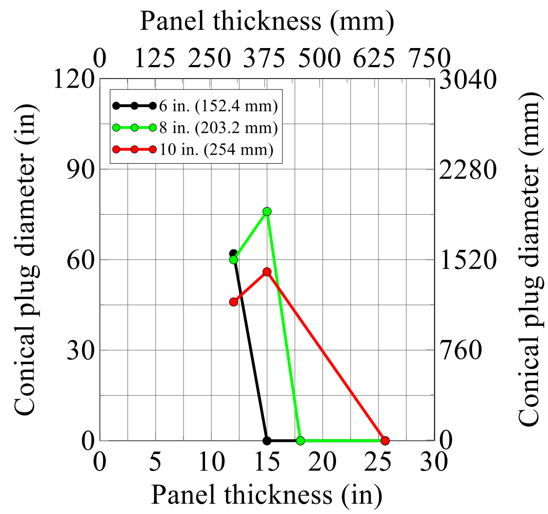

(b) f_c'=4351 psi (30 MPa), f_t'=725 psi (5 MPa)

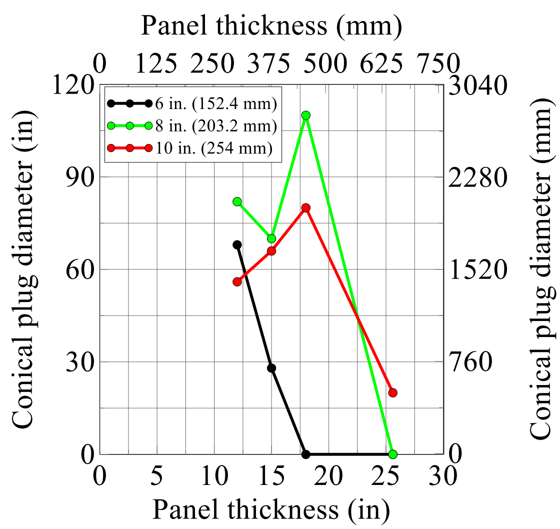

(c) f_c'=7251 psi (50 MPa), f_t'=435 psi (3 MPa)

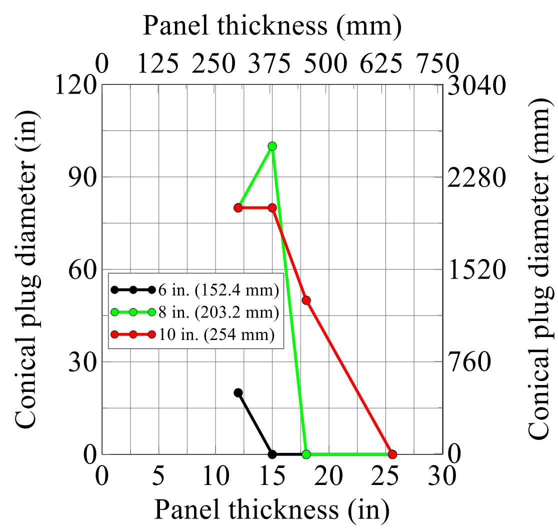

(d) f_c'=7251 psi (50 MPa), f_t'=725 psi (5 MPa)

Figure 6-7: Conical plug diameter as a function of panel thickness, v=3937 in/sec (100 m/sec), MAT072R3

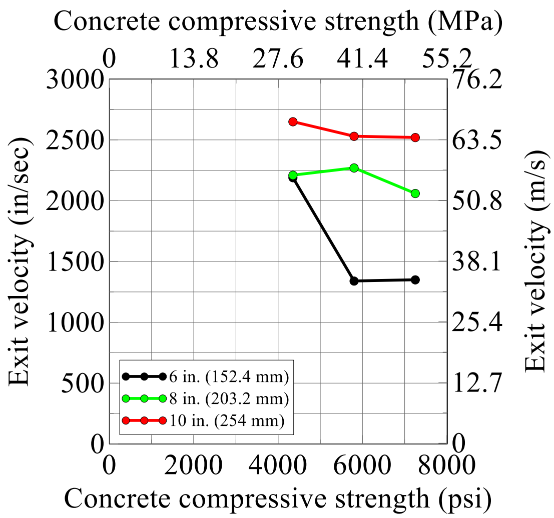

(a) f_t' =435 psi (3 MPa)

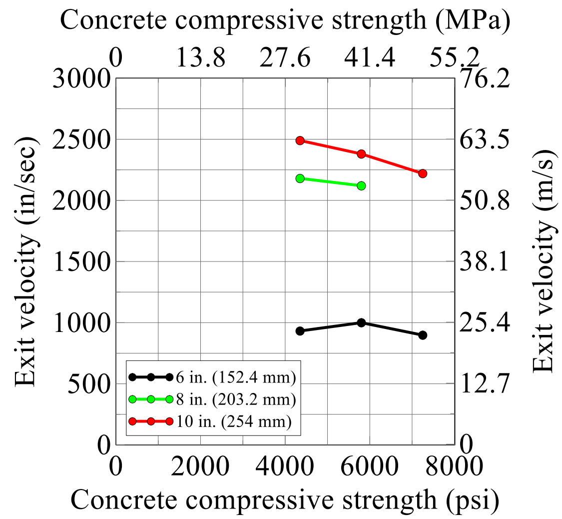

(b) f_t' =580 psi (4 MPa)

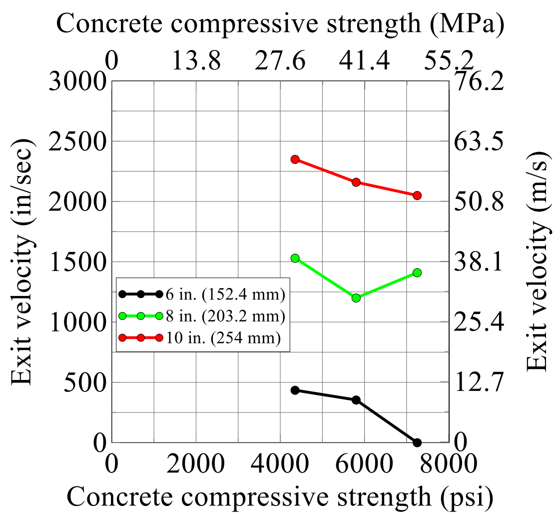

(c) f_t' =725 psi (5 MPa)

Figure 6-8: Exit velocity of Schedule 40 pipe as a function of concrete compressive strength, v =3937 in/sec (100 m/sec), 12-inch (305 mm) thick panel, MAT072R3

Figure 6-9 presents conical plug diameter as a function of concrete compressive strength for 6 in (152 mm), 8 in (203 mm), and 10 in (254 mm) diameter pipes normally impacting panels at an impact velocity of 3937 in/sec (100 m/s). For impact by the 8 in (203 mm) and 10 in (254 mm) diameter pipes, the plug diameter increases as the concrete compressive strength increases. Figures D-5 and D-6 present data for impact velocities of 1575 in/sec (40 m/s) and 2756 in/sec (70 m/s), respectively.

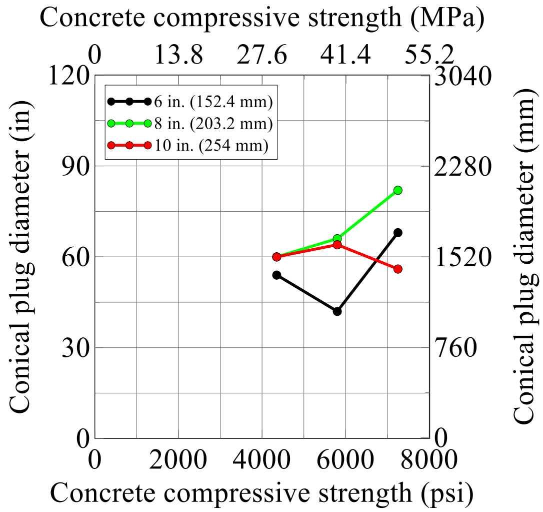

(a) f_t'=435 psi (3 MPa)

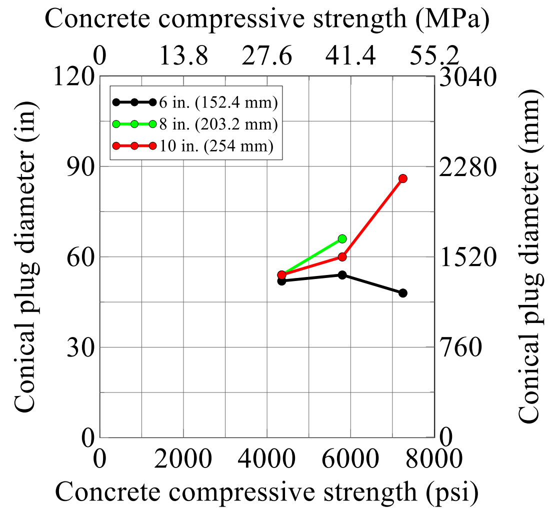

(b) f_t'=580 psi (4 MPa)

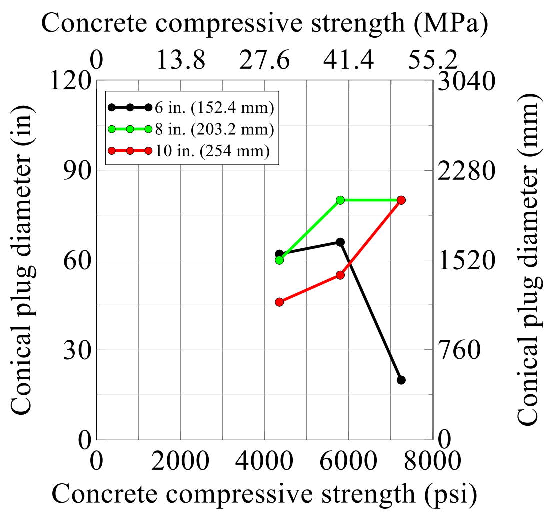

(c) f_t'=725 psi (5 MPa)

Figure 6-9: Conical plug diameter as a function of concrete compressive strength, v=3937 in/sec (100 m/sec), 12-inch (305 mm) thick panel, MAT072R3

6.3.4 Concrete Tensile Strength

The exit velocity of the Schedule 40 pipe as a function of concrete tensile strength is presented in Figure 6-10 for 6 in (152 mm), 8 in (203 mm), and 10 in (254 mm) diameter pipes normally impacting the 12-inch (305 mm) thick panel at a velocity of 3937 in/sec (100 m/s). Results are presented for concrete compressive strengths of 4351 psi (30 MPa), 5801 psi (40 MPa), and 7251 psi (50 MPa). The exit velocities decrease substantially as concrete tensile strength increases, indicating that this parameter has a very significant effect on the impact resistance of a panel.

Similar trends are observed for impact velocities of 1575 in/sec (40 m/s) and 2756 in/sec (70 m/s), shown in Figures D-7 and D-8, respectively.

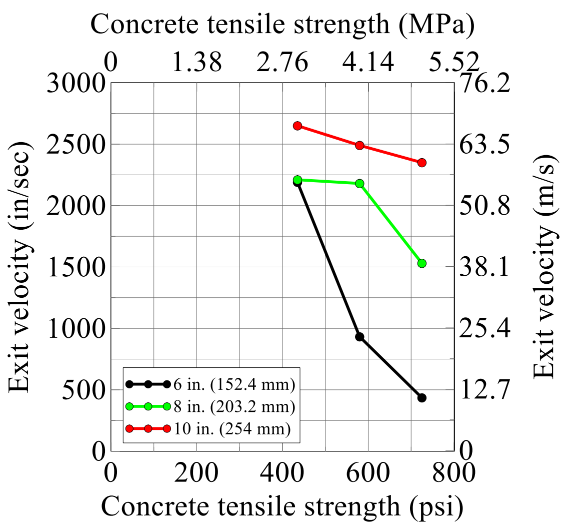

(a) f_c' =4351 psi (30 MPa)

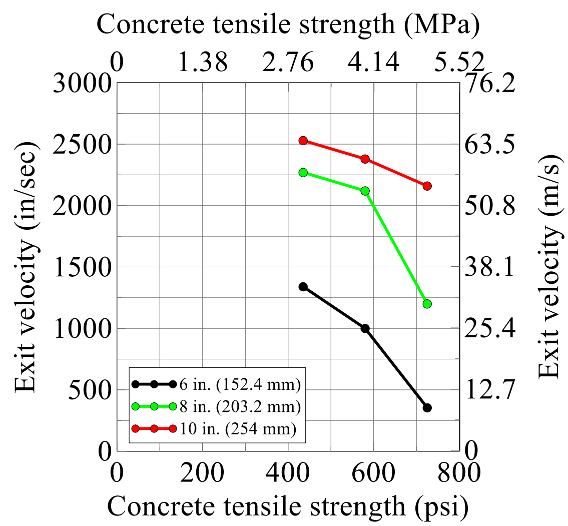

(b) f_c' =5801 psi (40 MPa)

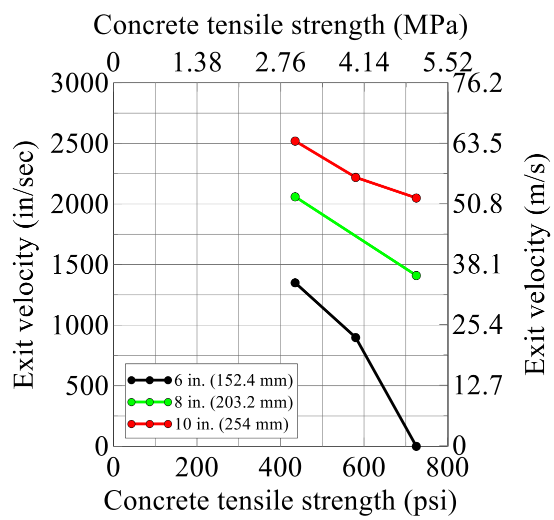

(c) f_c' =7251 psi (50 MPa)

Figure 6-10: Exit velocity of Schedule 40 pipe as a function of concrete tensile strength, v =3937 in/sec (100 m/sec), 12-inch (305 mm) thick panel, MAT072R3

Figure 6-11 presents conical plug diameter as a function of concrete tensile strength for an impact velocity of 3937 in/sec (100 m/s). Although concrete tensile strength has a significant effect on the impact resistance for a pipe impact velocity of 3937 in/sec (100 m/s), it has little effect on the diameter of the conical plug. Data for pipe impact velocities of 1575 in/sec (40 m/s) and 2756 in/sec (70 m/s), are presented in Figures D-9 and D-10, respectively.

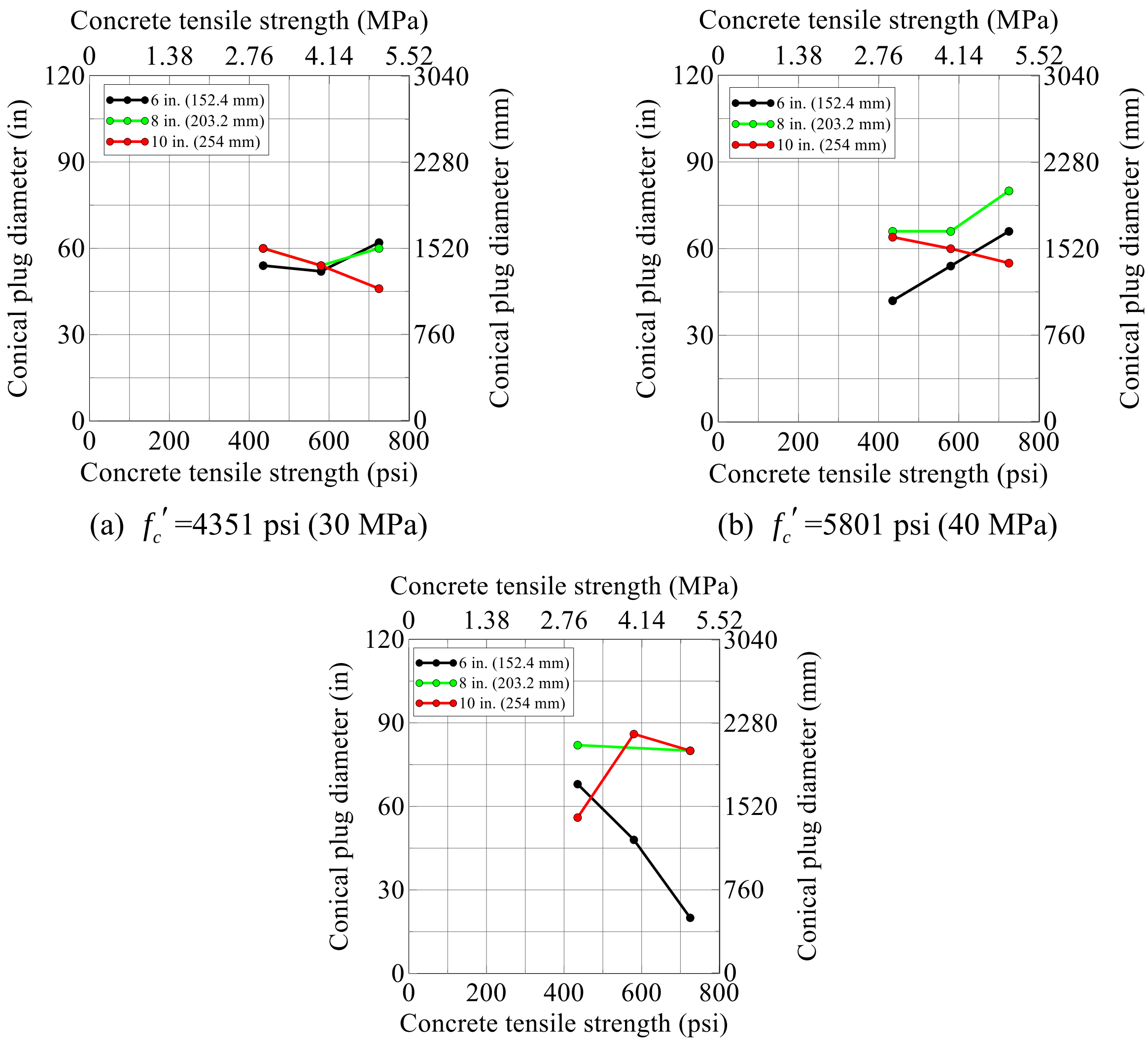

(a) f_c' =4351 psi (30 MPa)

(b) f_c' =5801 psi (40 MPa)

(c) f_c' =7251 psi (50 MPa)

Figure 6-11: Conical plug diameter as a function of concrete tensile strength, v=3937 in/sec (100 m/sec), 12-inch (305 mm) thick panel, MAT072R3

6.3.5 Schedule 40 Pipe Diameter and Varying Mass

The exit velocity of the Schedule 40 pipe as a function of pipe mass is presented in Figure 6-12 for a concrete compressive strength of 4351 psi (30 MPa). The results are shown for concrete tensile strengths of 435 psi (3 MPa), 580 psi (4 MPa), and 725 psi (5 MPa). The pipe exit velocities increase as the mass of the pipe increases, which is an expected result considering that the mass of the 10 in (254 mm) diameter Schedule 40 pipe is twice that of the 6 in (152 mm) diameter pipe, resulting in nearly twice the kinetic energy being transferred to the panel during impact. Similar trends are observed for concrete compressive strengths of 5801 psi (40 MPa) and 7251 psi (50 MPa), shown in Figures D-11 and D-12, respectively.

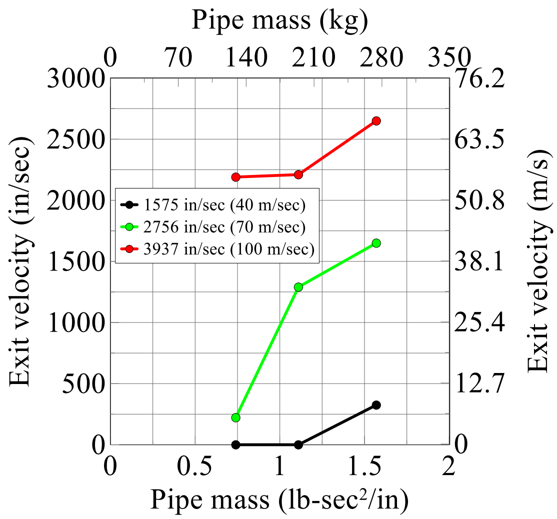

(a) f_t' =435 psi (3 MPa)

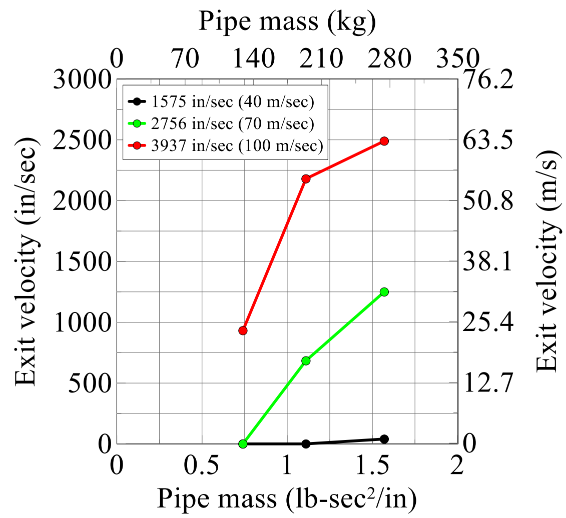

(b) f_t' =580 psi (4 MPa)

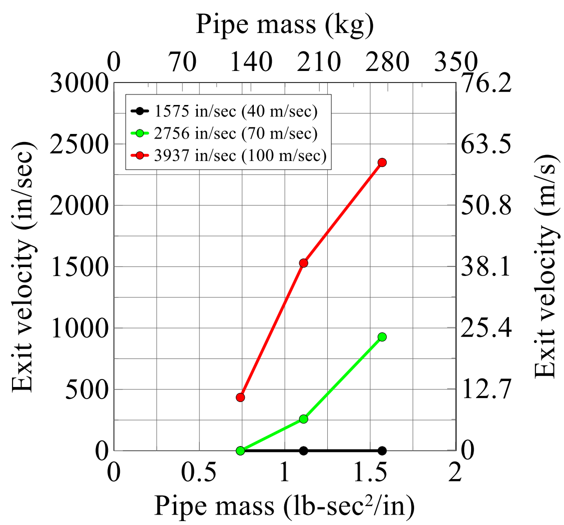

(c) f_t' =725 psi (5 MPa)

Figure 6-12: Pipe exit velocity as a function of Schedule 40 pipe mass, f_c' =4351 psi (30 MPa), 12-inch (305 mm) thick panel, MAT072R3

Figure 6-13 presents conical plug diameter as a function of pipe mass for a concrete compressive strength of 4351 psi (30 MPa). The diameter of the conical plug increases as the mass of the pipe increases, for impact velocities of 1575 in/sec (40 m/s) and 2756 in/sec (70 m/s). The plug diameter remains relatively constant with an increase in pipe mass for an impact velocity of 3937 in/sec (100 m/s). Figures D-13 and D-14 show data for concrete compressive strengths of 5801 psi (40 MPa) and 7251 psi (50 MPa), respectively. Similar outcomes to that presented for a concrete compressive strength of 4351 psi (30 MPa) are observed.

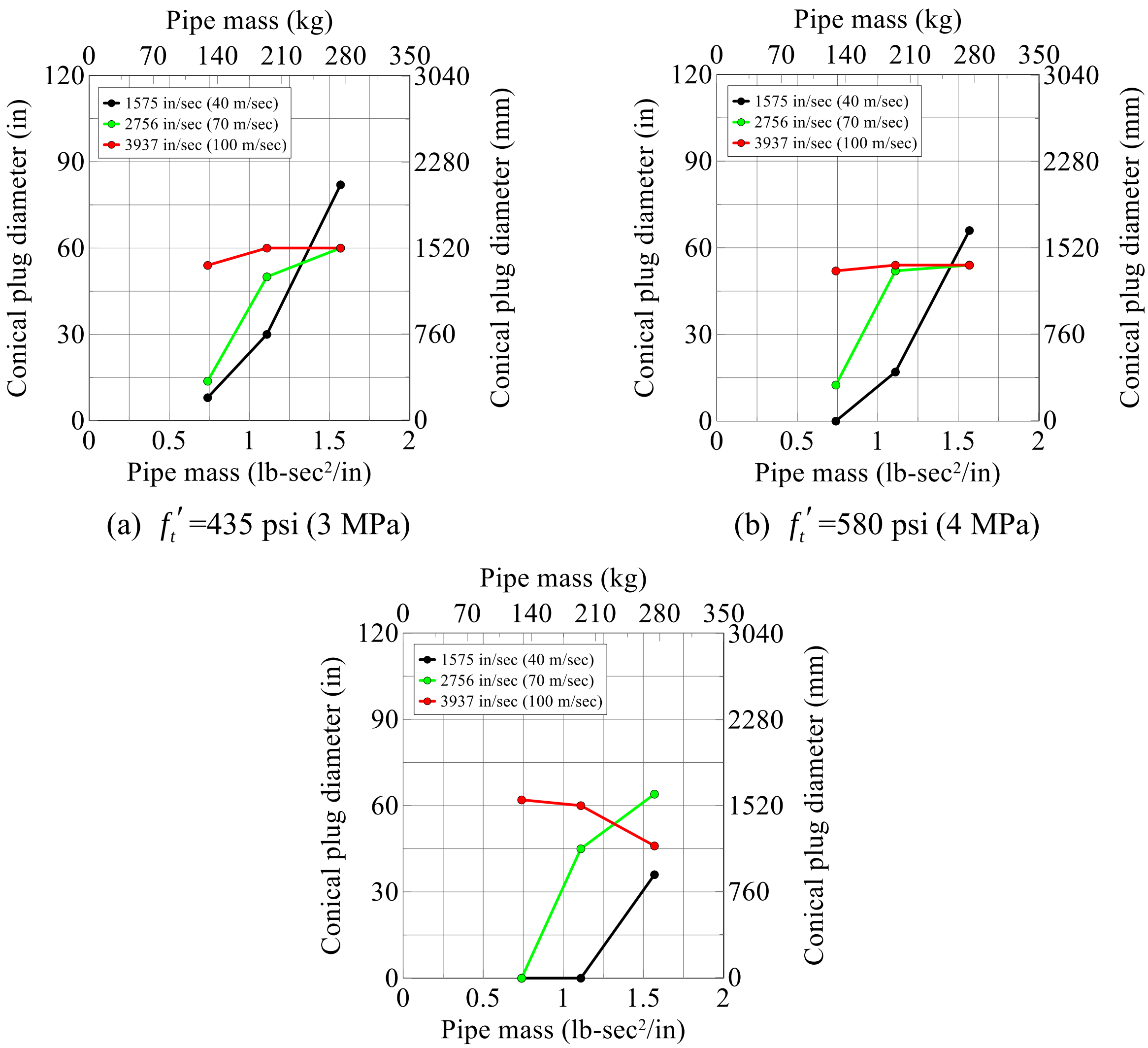

(a) f_t'=435 psi (3 MPa)

(b) f_t'=580 psi (4 MPa)

(c) f_t'=725 psi (5 MPa)

Figure 6-13: Conical plug diameter as a function of Schedule 40 pipe mass, f_c'=4351 psi (30 MPa), 12-inch (305 mm) thick panel, MAT072R3

The exit velocity of the Schedule 40 pipe as a function of diameter is presented in Figure 6-14 for a concrete compressive strength of 4351 psi (30 MPa). (The mass of the pipe increases with diameter.) The pipe exit velocity increases as the diameter of the pipe increases but the relative contributions of pipe diameter and mass to panel damage (i.e., perforation and scabbing) cannot be determined from these simulations alone. The effect of pipe diameter on impact resistance is investigated in Section 6.3.7 using a constant mass for all three diameter pipes; conclusions are drawn in that section. Companion data for concrete compressive strengths of 5801 psi (40 MPa) and 7251 psi (50 MPa) are presented in Figures D-15 and D-16, respectively.

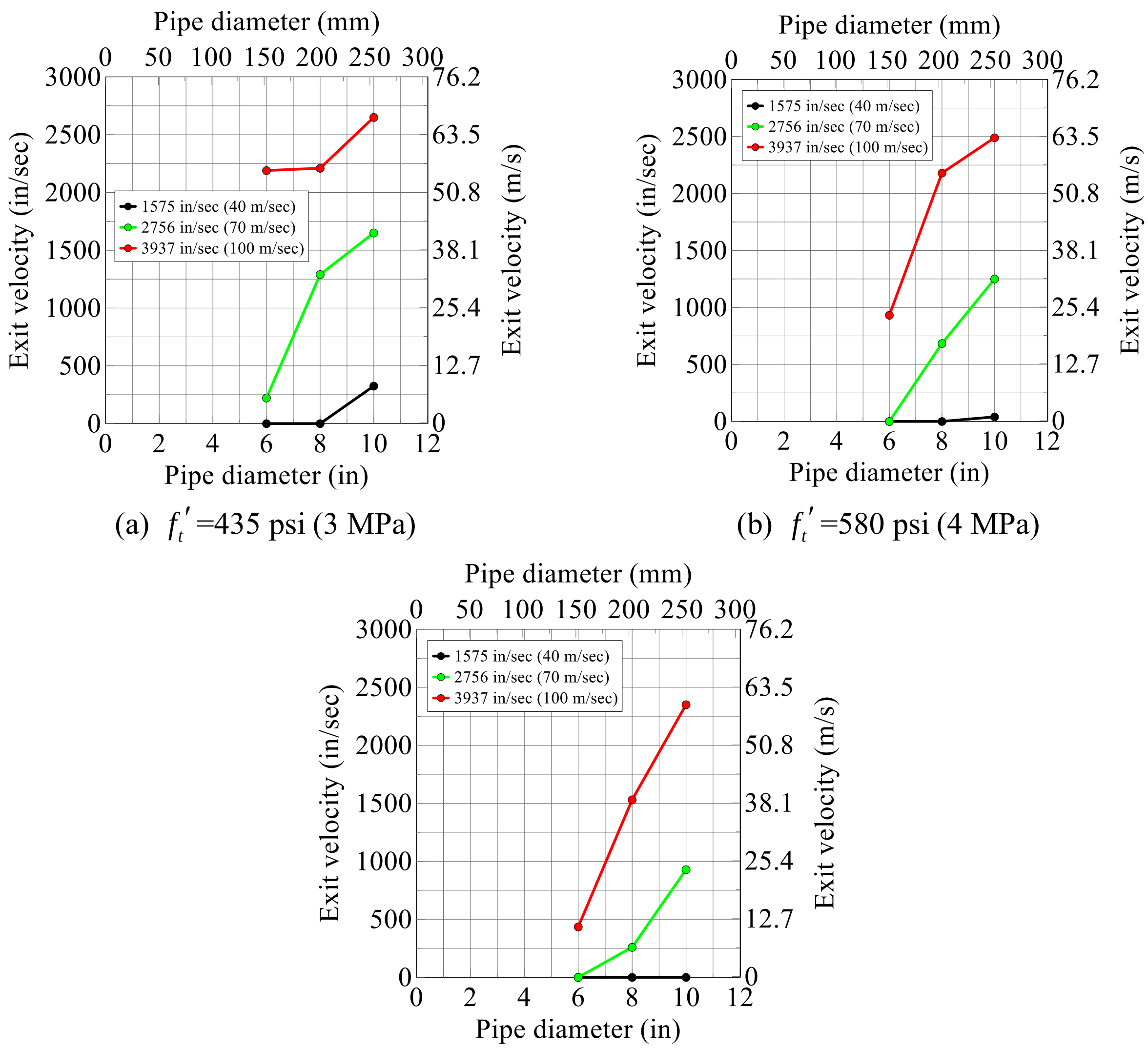

(a) f_t' =435 psi (3 MPa)

(b) f_t' =580 psi (4 MPa)

(c) f_t' =725 psi (5 MPa)

Figure 6-14: Pipe exit velocity as a function of Schedule 40 pipe diameter, f_c' =4351 psi (30 MPa), 12-inch (305 mm) thick panel, MAT072R3

Figure 6-15 presents conical plug diameter as a function of pipe diameter for a concrete compressive strength of 4351 psi (30 MPa). Similar to Figure 6-13, the diameter of the conical plug increases as the diameter of the pipe increases, for impact velocities of 1575 in/sec (40 m/s) and 2756 in/sec (70 m/s). Figures D-17 and D-18 present information for concrete compressive strengths of 5801 psi (40 MPa) and 7251 psi (50 MPa), respectively. Since the independent effect of pipe mass and diameter on conical plug diameter cannot be determined from these simulations, an additional study was performed and results are presented in Section 6.3.7: conical plug diameter as a function of pipe diameter with constant mass.

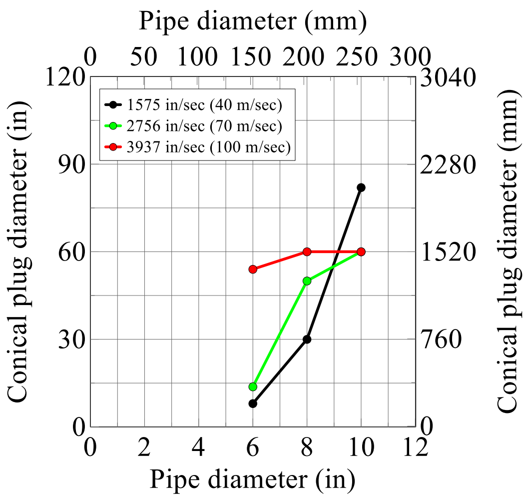

(a) f_t' =435 psi (3 MPa)

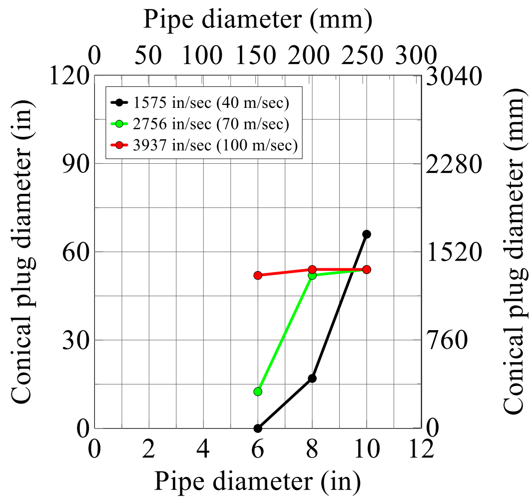

(b) f_t' =580 psi (4 MPa)

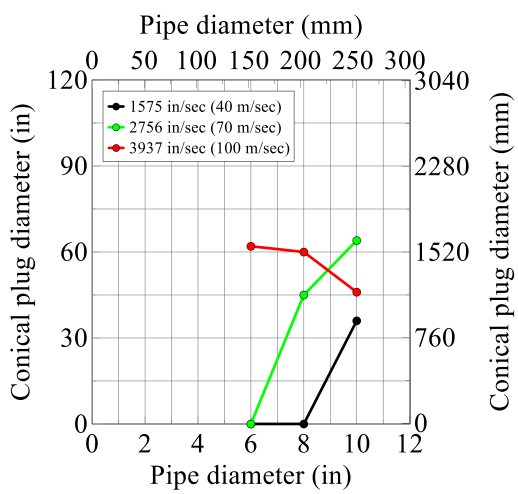

(c) f_t' =725 psi (5 MPa)

Figure 6-15: Conical plug diameter as a function of Schedule 40 pipe diameter, f_c' =4351 psi (30 MPa), 12-inch (305 mm) thick panel, MAT072R3

6.3.6 Schedule 40 Pipe Impact Velocity

The pipe exit velocity as a function of impact velocity is shown in Figure 6-16 for diameters of 6 in (152 mm), 8 in (203 mm), and 10 in (254 mm), and a concrete compressive strength of 4351 psi (30 MPa). Results are shown for concrete tensile strengths of 435 psi (3 MPa), 580 psi (4 MPa), and 725 psi (5 MPa). The open square in Figure 6-16c identifies a simulation that terminated prematurely; the exit velocity of 0 in/sec is based on judgement. Based on the data in these figures, the exit velocity increases as the impact velocity increases: an expected result. Similar trends are observed for concrete compressive strengths of 5801 psi (40 MPa) and 7251 psi (50 MPa), presented in Figures D-19 and D-20, respectively.

Figure 6-17 presents conical plug diameter as a function of pipe impact velocity for a concrete compressive strength of 4351 psi (30 MPa). The conical plug diameter for the simulation that terminated prematurely is shown in Figure 6-17c using an open square; the value plotted is based on conical plug diameters predicted for the same impact velocity and pipe diameter using concrete tensile strengths of 435 psi (3 MPa) and 580 psi (4 MPa). Figures D-21 and D-22 present companion data for concrete compressive strengths of 5801 psi (40 MPa) and 7251 psi (50 MPa), respectively. There is no clear relationship between conical plug diameter and pipe impact velocity.

Figure 6-18a, Figure 6-18b, and Figure 6-18c show simulation results of a 6-inch (152 mm) diameter Schedule 40 pipe impacting a 12-inch concrete panel at velocities of 1575 in/sec (40 m/s), 2756 in/sec (70 m/s), and 3937 in/sec (100 m/s), respectively, 20 msec after impact. The concrete panel has a concrete compressive and tensile strength of 4351 psi (30 MPa) and 435 psi (3 MPa), respectively. The results show that there are significant differences in the conical plug diameters as the impact velocity of the pipe increases. These differences are likely caused by rate effects in the concrete and is the focus of an ongoing study.

6.3.7 Schedule 40 Pipe Diameter with Constant Mass

The impact of pipes with constant mass but varying diameter on a 12-inch (305 mm) thick reinforced concrete panel was simulated to isolate the effect of pipe diameter. Fifteen feet (4572 mm) long Schedule 40 pipes with diameters of 6 in (152 mm), 8 in (203 mm), and 10 in (254 mm) were considered. The mass of each pipe was set equal to that of the 10 in (254 mm) diameter Schedule 40 pipe (=1.95 lb-sec^2/in (276 kg)). The density of the material in the 6 in (152 mm) and 8 in (203 mm) diameter Schedule 40 pipes was modified to achieve the target mass. The simulations are listed in Table 6-3. Impact velocities of 1575 in/sec (40 m/s), 2756 in/sec (70 m/s), and 3937 in/sec (100 m/s) were considered. The compressive and tensile strengths of the concrete in the panel were 4351 psi (30 MPa) and 725 psi (5 MPa), respectively. The axisymmetric model used for the simulations is presented in Section 5.3.2. A concrete particle spacing of 0.08 in (2 mm) was used for all simulations, based on the mesh convergence studies conducted in Chapter 5 for the Schedule 40 pipe impact simulations (see Section 5.9).

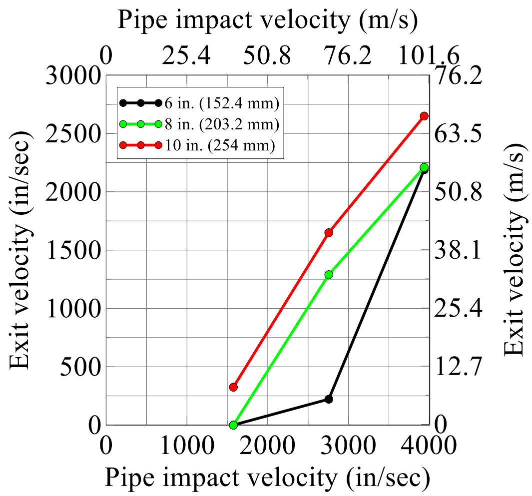

(a) f_t' =435 psi (3 MPa)

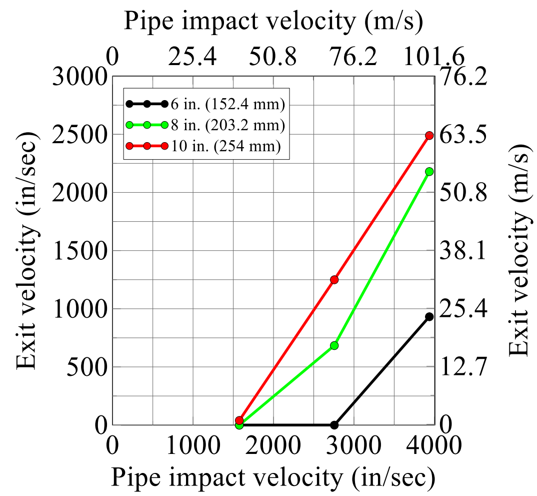

(b) f_t' =580 psi (4 MPa)

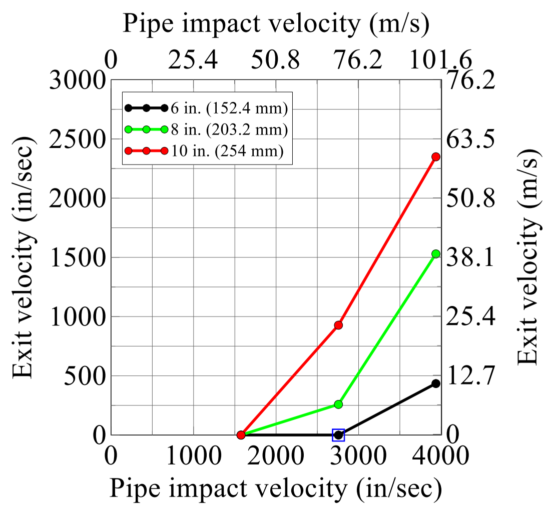

(c) f_t' =725 psi (5 MPa)

Figure 6-16: Pipe exit velocity as a function of pipe impact velocity, Schedule 40 pipe, f_c' =4351 psi (30 MPa), 12-inch (305 mm) thick panel, MAT072R3

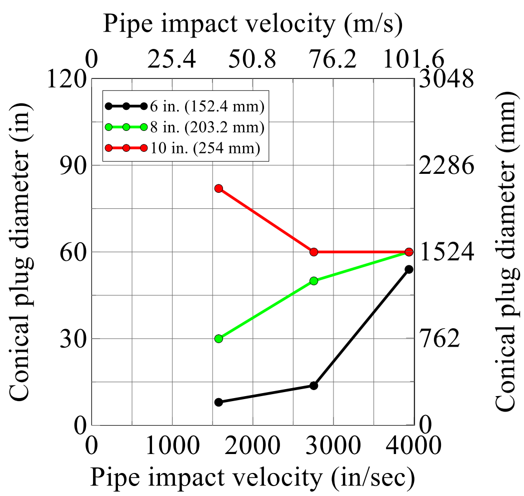

(a) f_t' =435 psi (3 MPa)

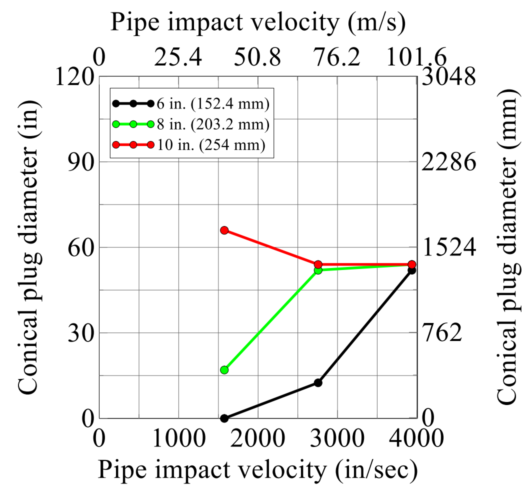

(b) f_t' =580 psi (4 MPa)

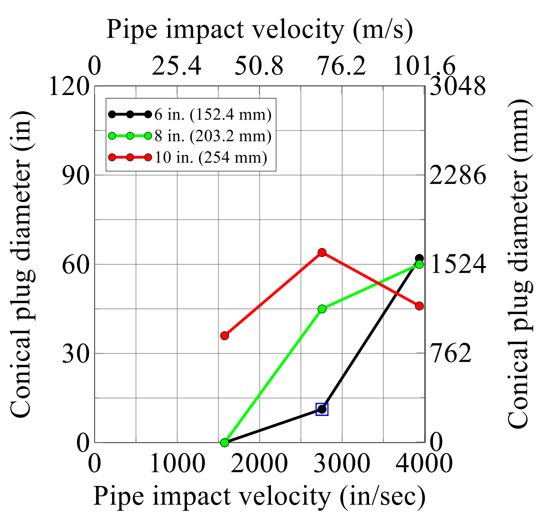

(c) f_t' =725 psi (5 MPa)

Figure 6-17: Conical plug diameter as a function of pipe impact velocity, Schedule 40 pipe, f_c' =4351 psi (30 MPa), 12-inch (305 mm) thick panel, MAT072R3

(a) v=1575 in/sec (40 m/s)

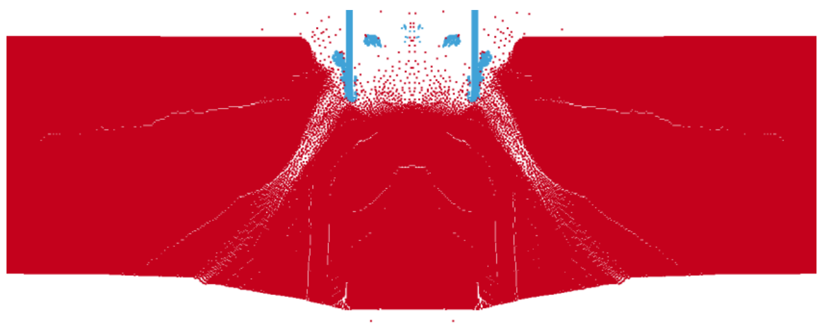

(b) v=2756 in/sec (70 m/s)

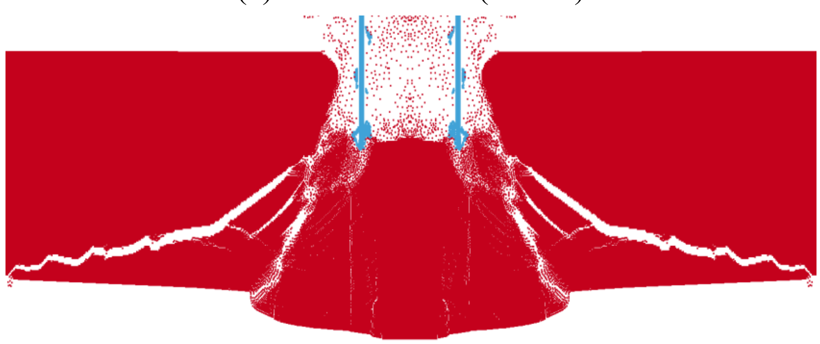

(c) v=3937 in/sec (100 m/s)

Figure 6-18:Simulation results, 20 msec after impact, 6 in (152 mm) diameter Schedule 40 pipe, 12 in (305 mm) thick panel, f_c'=4351 psi (30 MPa), f_t'=435 psi (3 MPa), MAT072R3

The exit velocities of the Schedule 40 pipe as a function of its diameter are presented in Figure 6-19. Perforation (i.e., exit velocity greater than zero) was predicted for all of the simulations with impact velocities of 2756 in/sec (70 m/s) and 3937 in/sec (100 m/s). For these simulations, the exit velocity decreased as the diameter of the pipe increased. The predicted conical plug diameters, as defined in Figure 6-4, are presented in Figure 6-20 as a function of pipe diameter. The predicted diameters of the conical plug increase as the pipe diameter increases, because a larger shear failure plane (through the thickness of the panel) is mobilized, resulting in greater resistance to perforation and lower exit velocities. The reduction in exit velocity associated with the increase in diameter (see Figure 6-19) is significantly less than the increases in exit velocity caused by the increase in pipe size (i.e., mass and diameter), indicating that pipe mass has a much greater effect on impact resistance than pipe diameter.

Table 6-3: Summary results, 12-in (305 mm) thick panel, varying pipe diameter, MAT072R3

Simulation	Diameter mm (in.)	Velocity m/s (in/sec)	f_c' MPa (psi)	f_t' MPa (psi)	Exit velocity m/s (in/sec)
1	152 (6)	40 (1575)	30 (4351)	5 (725)	0
2	203 (8)	40 (1575)	30 (4351)	5 (725)	0
3	254 (10)	40 (1575)	30 (4351)	5 (725)	0
4	152 (6)	70 (2756)	30 (4351)	5 (725)	30 (1180)
5	203 (8)	70 (2756)	30 (4351)	5 (725)	28.7 (1130)
6	254 (10)	70 (2756)	30 (4351)	5 (725)	23.6 (929)
7	152 (6)	100 (3937)	30 (4351)	5 (725)	62.5 (2460)
8	203 (8)	100 (3937)	30 (4351)	5 (725)	64.5 (2540)
9	254 (10)	100 (3937)	30 (4351)	5 (725)	59.7 (2350)

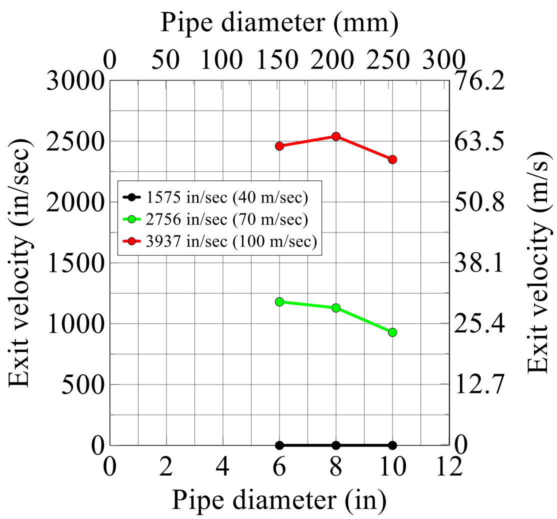

Figure 6-19: Exit velocity of Schedule 40 pipe as a function of pipe diameter with a constant mass, MAT072R3

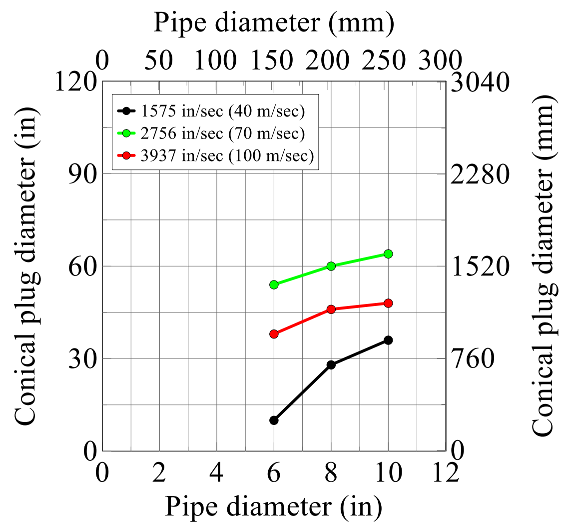

Figure 6-20: Conical plug diameter as a function of pipe diameter with a constant mass, MAT072R3

6.3.8 Schedule 40 Pipe Impact on Panels Thicker than 25.6 in (650 mm)

The 8 in (203 mm) and 10 in (254 mm) diameter Schedule 40 pipes scabbed concrete from the back face of the 25.6 in (650 mm) thick panel at an impact velocity of 3937 in/sec (100 m/s) (see simulations 142 and 150 in Table D-1); the compressive and tensile strength of the concrete in the panel was 4351 psi (30 MPa) and 435 psi (3 MPa), respectively. These two simulations were repeated, but using thicker panels, to determine the panel thickness required to prevent scabbing of concrete. Table 6-4 provides information on the simulations. The mass of the 8 in (203 mm) and 10 in (254 mm) diameter Schedule 40 pipes were 1.11 lb-sec^2/in (195 kg) and 1.57 lb-sec^2/in (276 kg), respectively: the same masses considered in the parametric study.

The modeling techniques are similar to those described in Section 5.3.3 for the 24 in (610 mm) thick panel. SPH particles and axisymmetric solid elements were used in the impact and non-impact zone of the panel, respectively. A concrete particle spacing of 0.12 in (3 mm) was used in the simulations, which was based on the mesh convergence study presented in Section 5.9.5.2. The material model MAT072R3 was used for the concrete in all simulations.

Table 6-4: Numerical simulations, panel thickness study, MAT072R3

Simulation	Panel thickness mm (in.)	Pipe diameter mm (in.)	Velocity m/s (in/sec)	f_c' MPa (psi)	f_t' MPa (psi)	Back face damage
1	762 (30)	203 (8)	100 (3937)	30 (4351)	3 (435)	Yes
2	838 (33)	203 (8)	100 (3937)	30 (4351)	3 (435)	No
3	1000 (39.4)	203 (8)	100 (3937)	30 (4351)	3 (435)	No
4	838 (33)	254 (10)	100 (3937)	30 (4351)	3 (435)	Yes
5	914 (36)	254 (10)	100 (3937)	50 (7251)	3 (435)	No
6	1000 (39.4)	254 (10)	100 (3937)	50 (7251)	3 (435)	No

The last column of Table 6-4 identifies if damage to the back face of the panel was predicted in a simulation. A 33 in (838 mm) and 36 in (914 mm) thick panel is required to prevent scabbing if impacted by an 8 in (203 mm) and 10 in (254 mm) diameter Schedule 40 pipe, respectively, at a velocity of 3937 in/sec (100 m/sec), for concrete compressive and tensile strengths greater than or equal to 4351 psi (30 MPa) and 435 psi (3 MPa), respectively.

6.4 Regulatory Guidance on Wind-borne Missile Impact

6.4.1 Introduction

United States Nuclear Regulatory Commission Regulatory Guide (RG) 1.76, *Design-Basis Tornado and Tornado Missiles for Nuclear Power Plants*, and RG 1.221, *Design-Basis Hurricane and Hurricane Missiles for Nuclear Power Plants*, identify the 6 in (152 mm) diameter Schedule 40 pipe as a missile capable of penetrating a concrete panel. The recommended design velocities of the 6 in (152 mm) diameter Schedule 40 pipe for RG 1.76 (2007) and RG 1.221 (2011) are 1614 in/sec (41 m/s) and 3701 in/sec (94 m/s), respectively. The specified impact velocities in the Regulatory Guides for wind-borne missile impact provided a basis for the impact velocities considered in the parametric study presented in this chapter ((1575 in/sec (40 m/s) to 3937 in/sec (100 m/s)) (see Table 6-1). Since the lower and upper bound impact velocities from the parametric study correspond to the maximum design velocities of RG 1.76 (=1614 in/sec (41 m/s)) and RG 1.221 (=3701 in/sec (94 m/s)), respectively, the results presented in Section 6.3 can be used to provide guidance on design of reinforced concrete panels impacted by a 6 in (152 mm) diameter Schedule 40 pipe, with a mass equal to 0.74 lb-sec^2/in (130 kg).

6.4.2 Tornado-borne missiles

Table 6-5 presents results of the 12 in (305 mm), 15 in (381 mm), 18 in (460 mm), and 25.6 in (650 mm) thick concrete panels impacted by a 6 in (152 mm) diameter Schedule 40 pipe at a velocity of 1575 in/sec (40 m/s). Concrete compressive strengths of 4351 psi (30 MPa), 5801 psi (40 MPa), and 7251 psi (50 MPa) and tensile strengths of 435 psi (3 MPa), 580 psi (4 MPa), and 725 psi (5 MPa) were considered. A conical plug formed on the back face of the 12 in (305 mm) thick panel for compressive strengths of 4351 psi (30 MPa), 5801 psi (40 MPa), and 7251 psi (50 MPa) and a tensile strength of 435 psi (3 MPa), which corresponds to 10%, 7.4%, and 6% of the concrete compressive strength. These simulations are highlighted in Table 6-5. Since a conical plug formed in the simulations, it is likely (and assumed here) that concrete will scab from the back face of the panel. The impact of a 6-inch diameter Schedule 40 pipe did not produce back face damage to the 15 in (381 mm), 18 in (460 mm), and 25.6 in (650 mm) thick panels for all combinations of concrete compressive and tensile strength considered. Based on these results, a concrete panel should be at least 15 in (381 mm) thick to prevent scabbing (and perforation) for the impact of a 6 in (152 mm) diameter Schedule 40 pipe at a velocity of 1575 in/sec (40 m/s). This conclusion applies for concrete compressive and tensile strengths greater than or equal to 4351 psi (30 MPa) and 435 psi (3 MPa), respectively.

6.4.3 Hurricane-borne Missiles

Results of simulations of 12 in (305 mm), 15 in (381 mm), 18 in (460 mm), and 25.6 mm (650 mm) thick concrete panels, impacted by a 6 in (152 mm) diameter Schedule 40 pipe at a velocity of 3937 in/sec (100 m/s), are presented in Table 6-6. Concrete compressive strengths of 4351 psi (30 MPa) and 7251 psi (50 MPa), and tensile strengths of 435 psi (3 MPa) and 725 psi (5 MPa)

Table 6-5: Summary results, tornado-borne missile impact, v=40 m/s (1575 in/sec), 152 mm (6 in) diameter Schedule 40 pipe

Wall thickness, t mm (in.)	f_c' MPa (psi)	f_t' MPa (psi)	Conical plug diameter, mm (in)	Exit velocity, m/s (in/sec)	Scabbing of concrete
305 mm (12 in)	30 (4351)	3 (435)	203 (8)	0	Yes
	30 (4351)	4 (580)	0	0	No
	30 (4351)	5 (725)	0	0	No
	40 (5801)	3 (435)	203 (8)	0	Yes
	40 (5801)	4 (580)	0	0	No
	40 (5801)	5 (725)	0	0	No
	50 (7251)	3 (435)	203 (8)	0	Yes
	50 (7251)	4 (580)	0	0	No
	50 (7251)	5 (725)	0	0	No
381 mm (15 in)	30 (4351)	3 (435)	0	0	No
	30 (4351)	5 (725)	0	0	No
	50 (7251)	3 (435)	0	0	No
	50 (7251)	5 (725)	0	0	No
460 mm (18 in)	30 (4351)	3 (435)	0	0	No
	30 (4351)	5 (725)	0	0	No
	50 (7251)	3 (435)	0	0	No
	50 (7251)	5 (725)	0	0	No
650 mm (25.6 in)	30 (4351)	3 (435)	0	0	No
	30 (4351)	5 (725)	0	0	No
	50 (7251)	3 (435)	0	0	No
	50 (7251)	5 (725)	0	0	No

were considered. Perforation was observed in all but one of the simulations involving the 12 in (305 mm) thick panel: concrete compressive and tensile strengths of 7251 psi (50 MPa) and 725 psi (5 MPa), respectively. Although perforation of the 12 in (305 mm) thick panel did not occur for this case, a conical plug formed on the back face of the panel and scabbing is considered likely. The conical plug formed for two of the simulations using the 15 in (381 mm) thick panel: concrete compressive strengths of 4351 psi (30 MPa) and 7251 psi (50 MPa), and a tensile strength of 435 psi (3 MPa). The simulations for which damage was predicted (perforation, formation of a conical plug, and scabbing) are highlighted in Table 6-6. No damage was predicted to the 18 in (460 mm) and 25.6 in (650 mm) thick panels. Based on these results, a concrete panel should be at least 18 in (460 mm) thick to prevent scabbing (and perforation) for the impact of a 6 in (152 mm) diameter Schedule 40 pipe at a velocity of 3937 in/sec (100 m/s). This conclusion assumes concrete compressive and tensile strengths greater than or equal to 4351 psi (30 MPa) and 435 psi (3 MPa), respectively.

Table 6-6: Summary results, hurricane-borne missile impact, v=100 m/s (3937 in/sec), 152 mm (6 in) diameter Schedule 40 pipe

Wall thickness, t mm (in.)	f_c' MPa (psi)	f_t' MPa (psi)	Conical plug diameter, mm (in)	Exit velocity, m/s (in/sec)	Scabbing of concrete
305 mm (12 in)	30 (4351)	3 (435)	1372 (54)	55.6 (2190)	Yes
	30 (4351)	4 (580)	1321 (52)	23.7 (932)	Yes
	30 (4351)	5 (725)	1575 (62)	11.0 (435)	Yes
	40 (5801)	3 (435)	1067 (42)	34.0 (1340)	Yes
	40 (5801)	4 (580)	1372 (54)	25.4 (1000)	Yes
	40 (5801)	5 (725)	1676 (66)	9.0 (354)	Yes
	50 (7251)	3 (435)	1727 (68)	34.3 (1350)	Yes
	50 (7251)	4 (580)	1219 (48)	22.8 (898)	Yes
	50 (7251)	5 (725)	508 (20)	0	Yes
381 mm (15 in)	30 (4351)	3 (435)	406 (16)	0	Yes
	30 (4351)	5 (725)	0	0	No
	50 (7251)	3 (435)	711 (28)	0	Yes
	50 (7251)	5 (725)	0	0	No
460 mm (18 in)	30 (4351)	3 (435)	0	0	No
	30 (4351)	5 (725)	0	0	No
	50 (7251)	3 (435)	0	0	No
	50 (7251)	5 (725)	0	0	No
650 mm (25.6 in)	30 (4351)	3 (435)	0	0	No
	30 (4351)	5 (725)	0	0	No
	50 (7251)	3 (435)	0	0	No
	50 (7251)	5 (725)	0	0	No

"This Page Intentionally Left Blank"

SECTION 7
SUMMARY, CONCLUSIONS, DESIGN GUIDANCE, AND RECOMMENDATIONS

7.1 Summary and Conclusions

The United States Nuclear Regulatory Commission Regulatory Guide (RG) 1.76, *Design-Basis Tornado and Tornado Missiles for Nuclear Power Plants*, and RG 1.221, *Design-Basis Hurricane and Hurricane Missiles for Nuclear Power Plants*, identify a set of missiles and impact velocities to be considered in the design of nuclear power plants. Empirical formulae are used to calculate local behavior (scabbing, penetration, perforation) of reinforced concrete walls and slabs impacted by tornado- and hurricane-borne missiles. Chapter 3 examined these empirical formulae and compared predictions of response with test data. The predictions were by-and-large poor, and not of the standard expected for the design of a nuclear structure. The shortcomings with the predictive equations, and a lack of knowledge regarding those parameters that most affect impact resistance against soft and hard missiles, prompted the authors to validate, to the degree possible, a numerical tool for impact analysis of reinforced concrete panels. Data from tests performed by EPRI in the 1970s were used for validation. The three-dimensional Lagrangian and axisymmetric Smooth Particle Hydrodynamics (SPH) algorithms in LS-DYNA (LSTC, 2012) were used for the numerical studies presented in this report.

Four EPRI tests were chosen for the validation exercise, which involved 12 in (305 mm), 18 in (460 mm) and 24 in (610 mm) thick reinforced concrete panels impacted by 12-inch (305 mm) diameter Schedule 40 pipes with impact velocities ranging from 98 fps (30 m/s) to 202 fps (62 m/s). The Lagrangian analysis of the 12 in (305 mm) thick panels reasonably reproduced the front- and back-face crater diameters in EPRI Tests 10 and 11, and the impact force of Test 11. Perforation was predicted for Test 10 but the depth of penetration was underestimated in Test 11. Shortcomings with the Lagrangian formulation for impact loading (e.g., significant deformation of elements in the impact zone leading to decreased time steps, and termination of analysis due to negative volume error) became apparent in the simulations of the response of the 18 in (460 mm) and 24 in (610 mm) thick panels, and this led to an exploration of the SPH method. Axisymmetric SPH models were adopted to reduce the computational effort, with no perceived loss of accuracy.

A series of numerical simulations were conducted to investigate the material models compatible with SPH in LS-DYNA (i.e., MAT016, MAT072R3, and MAT159) and to enable a comparison with the EPRI test data. Using the MAT072R3 material model and a tensile strength set equal to 15% of the concrete compressive strength, the numerical model reasonably reproduced results of the experiments (i.e., front and back face crater diameters and perforation of panel in Test 10, formation and size of the conical plug on the back face in Test 11, and the global response of the panel in Test 8). Perforation was predicted for Test 3 but not observed in the experiment. The depth of penetration of the pipe into the panels was underpredicted by a factor of three for the non-perforation tests. Although the numerical model predicted the results of the experiments with reasonable accuracy, the lack of detailed information and metadata from the EPRI experiments made it impossible to formally validate a numerical model for impact analysis.

The impact of reinforced concrete panels by solid (effectively rigid) cylindrical missiles having the same mass and velocity as the Schedule 40 pipe was simulated to identify the effects of missile geometry (i.e., solid versus annular). Results showed that solid missiles are more damaging than annular missiles, for a given mass and impact velocity.

A parametric study was conducted to investigate the effects of panel thickness, Schedule 40 pipe size (mass and diameter), impact velocity, and concrete compressive and tensile strength, on impact resistance. Results of the parametric study show that all of these parameters affect the impact resistance of reinforced concrete panels, and so should be considered in design and in future development of empirical formulae.

7.2 Guidance for the Analysis and Design of RC Panels Subjected to Impact by Wind-borne Missiles

One objective of this research project was to formulate guidance for the analysis and design of reinforced concrete panels impacted by Schedule 40 pipes at velocities identified in the Regulatory Guides (1.76, 1.221) for wind-borne missiles. The following guidance is offered for consideration to the U.S. Nuclear Regulatory Commission and is based on the results of the parametric study presented in Section 6.3 and Appendix D.

Table 7-1 presents the minimum panel thickness required to prevent scabbing and perforation if normally impacted by a 6 in (152 mm), 8 in (203 mm), and 10 in (254 mm) diameter Schedule

40 pipe. Concrete scabbing governs the design of the panel (i.e., the panel thickness required to prevent scabbing is greater than that required to prevent perforation). Results are shown for impact velocities of 1575 in/sec (40 m/s) and 3937 in/sec (100 m/s), which correspond to the maximum design velocities of RG 1.76 (=1614 in/sec (41 m/s)) and RG 1.221 (=3701 in/sec (94 m/s)), respectively. These conclusions are based on minimum values of concrete uniaxial compressive and tensile strengths of 4351 psi (30 MPa) and 435 psi (3 MPa), respectively.

Table 7-1: Minimum panel thickness, $f_c^{'} \geq$ 4351 psi (30 MPa), $f_t^{'} \geq$ 435 psi (3 MPa)

Impact velocity, m/s (in/sec)	Schedule 40 pipe diameter, mm (in)	Prevent perforation, mm (in)	Prevent scabbing, mm (in)
40 (1575)	152 (6)	305 (12)	381 (15)
	203 (8)	305 (12)	381 (15)
	254 (10)	381 (15)	460 (18)
100 (3937)	152 (6)	381 (15)	460 (18)
	203 (8)	650 (25.6)	838 (33)
	254 (10)	650 (25.6)	914 (36)

Table 7-2 presents values of minimum panel thickness for concrete compressive and tensile strengths greater than or equal to 7251 psi (50 MPa) and 725 psi (5 MPa), respectively. For the impact velocity of 3937 in/sec (100 m/s), the minimum panel thicknesses required to prevent scabbing due to the impact of an 8 in (203 mm) and 10 in (254 mm) diameter Schedule 40 pipe are substantially less than those presented in Table 7-1 because the increase in tensile strength significantly improves impact resistance.

Table 7-2: Minimum panel thickness, $f_c^{'} \geq$ 7251 psi (50 MPa), $f_t^{'} \geq$ 725 psi (5 MPa)

Impact velocity, m/s (in/sec)	Schedule 40 pipe diameter, mm (in)	Prevent perforation, mm (in)	Prevent scabbing, mm (in)
40 (1575)	152 (6)	305 (12)	305 (12)
	203 (8)	305 (12)	381 (15)
	254 (10)	305 (12)	381 (15)
100 (3937)	152 (6)	305 (12)	381 (15)
	203 (8)	460 (18)	460 (18)
	254 (10)	650 (25.6)	650 (25.6)

Design guidance specific to U.S. NRC Regulatory Guides 1.76 and 1.221 for tornado- and hurricane-borne missiles, respectively, is presented in Section 6.4. Charts were presented in Chapter 6 and Appendix D to establish relationships between input variables (e.g., panel thickness, concrete compressive and tensile strength, Schedule 40 pipe velocity and size) and panel response (e.g., exit velocity and conical plug diameter), to identify those parameters that most affect impact resistance. The guidance presented in Section 6.4 and the charts can be used for design of reinforced concrete panels for wind-borne missile impact.

A numerical model was developed in LS-DYNA to predict panel response and damage (e.g., perforation, front and back face crater diameters, and scabbing) caused by impact of a Schedule 40 pipe and solid missiles for a wide range of panel thickness, pipe diameter, and concrete compressive and tensile strengths.

7.3 Design of Experiments for Formal Model Validation

Although the axisymmetric SPH model presented in Chapter 5 reasonably predicts damage to reinforced concrete panels produced by *normal* impact of a Schedule 40 pipe, the lack of information, repeat experiments and metadata from the Sandia experiments made it impossible to formally validate numerical models for impact analysis. The tensile strength of the concrete, which significantly affects the impact resistance of concrete panels, was not documented in the experiments, and it is unclear whether the concrete (cylinders) used for compression testing was representative of that in the panels on the days of testing. Analysis by others of the Sandia test results indicated that flexural reinforcement does not prevent the formation of a conical plug and/or scabbing of back-face concrete for the rebar ratios of up to 0.6% (used in the experiments). Shear reinforcement was not included in the specimens tested at Sandia although it may influence the perforation resistance of a panel. Further, strain gage data for the panel reinforcement was sparse and transducers were not used to measure back-face displacement histories.

Additional experiments will be required to aid in the formal validation of a numerical model for impact analysis. The test plan should address the following:

1. The mix design of the concrete (i.e., water/cement ratio, aggregate size, and admixtures) should be properly documented. Concrete compressive strength should be measured using multiple cores cut from the panel to ensure the measured strength is representative of the specimen being tested. Tensile strength of concrete should also be measured by

testing cores (split-tension) taken from the panel and coupons cast and cured identically to the concrete in the specimen.

2. The mechanical properties of the rebar used for testing should be measured.

3. Impact tests should be conducted on concrete panels with 1) no reinforcement, 2) flexural reinforcement only, and 3) shear and flexural reinforcement. A range of reinforcement ratios should be considered.

4. Panels of thickness between 12 in (305 mm) to 39.4 in (1000 mm) should be tested.

5. Schedule 40 pipes and solid cylindrical missiles should be used for testing to evaluate the effects of missile geometry on panel response. Impact velocities should envelope those found in Regulatory Guides 1.76 (2007) and 1.221 (2011) for Schedule 40 pipes.

6. The solid missile study presented in Chapter 5 and the parametric study presented in Chapter 6 using Schedule 40 pipes can be used to create a test matrix. Each experiment should be repeated two or three times to evaluate repeatability of test results.

7. Strain gages should be installed on flexural and shear reinforcement to monitor behavior.

8. High-speed cameras should be used to monitor the acceleration of the missile and the displacement response of the panel. Load cells should be placed at the corners of the concrete panel to measure reaction histories.

9. Damage to the panel, including 3D imaging of front and back face craters, should be documented.

"This Page Intentionally Left Blank"

SECTION 8
REFERENCES

Alderson, M. A. H. G., Davis, I., Bartley, R., and O'Brien, T. P. (1977). "Reinforced concrete behavior due to missile impact," *Transactions, 4th International Conference on Structural Mechanics in Reactor Technology (SMiRT)*, San Francisco, USA, June.

American Concrete Institute (ACI). (2013). "Code requirements for nuclear safety-related concrete structures and commentary," *ACI 349-13*, Farmington Hills, MI.

American Society of Mechanical Engineers (ASME). (2006). "Guide for verification and validation in computational solid mechanics," *ASME V&V 10-2006*, New York, NY.

Banerjee, A., Dhar, S., Acharyya, S., Datta, D., Nayak, N. (1978). "Determination of Johnson-Cook material and failure model constants and numerical modeling of Charpy impact tests of armour steel," *Materials Science and Engineering A*, 640: 200-209.

Bathe, K. J. (1996). *Finite Element Procedures,* PHI Learning Private Limited, New Delhi, India.

Berriaud, C., Sokolovsky, A., Gueraud, R., Dulac, J., and Labrot, R. (1978). "Local behaviour of reinforced concrete walls under missile impact," *Nuclear Engineering and Design*, 45: 457-469.

Beth, R. A. (1946). "Final report on concrete penetration," *NDRC Report No. A-388*, National Defense Research Committee, Washington, DC.

Biggs, J. (1964). *Introduction to Structural Dynamics*, McGraw-Hill Inc, New York, NY.

Bischoff, P. H., and Perry, S.H. (1991). "Compressive behaviour of concrete at high strain rates," *Materials and Structures*, 24 (6): 425-450.

Borvik, T., Hopperstad, O. S., Dey, S., Pizzinato, E. V., Langseth, M., and Albertini, C. (2005). "Strength and ductility of Weldox 460 E steel at high strain rates, elevated temperatures and various stress triaxilities," *Engineering Fracture Mechanics*, 72: 1071-1087.

Broadhouse, B. J. and Attwood, G. J. (1993). "Finite element analysis of the impact response of reinforced concrete structures using DYNA 3D," *Transactions, 12th International Conference on Structural Mechanics in Reactor Technology (SMiRT)*, Stuttgart, Germany, August.

Bruhl, J. C., Varma, A. H., and Johnson, W. H. (2015). "Design of composite SC walls to prevent perforation from missile impact," *International Journal of Impact Engineering*, 75: 75-87.

Chang, W. S. (1981). "Impact of solid missiles on concrete barriers," *Journal of the Structural Division*, 107 (2): 257-271.

Comite Euro-international du Beton (CEB). (1993). "CEB-FIP model code 1990," Thomas Telford, London, England.

Dancygier, A. N., Yankelevsky, D. Z., and Jaegermann, C. (2007) "Response of high performance concrete plates to impact of non-deforming projectiles," *International Journal of Impact Engineering*, 34: 1768-1779.

Dassault Systèmes Simulia Corp (SIMULIA). (2012). *Abaqus analysis user's manual version 6.12*, Providence, RI.

Davidson, R. F., Rodriguez, E. A., and Walsh, M. L. (1996). "Epic hydrodynamic code modeling of Hanford Site HLW tank 241-SY-101 for bounding Hydrogen detonation," *LA-UR-96-1956*, Los Alamos National Laboratory, Los Alamos, NM.

Department of Energy (DOE). (2006). "Accident analysis for aircraft crash into hazardous facilities," *DOE-STD-3014-2006*, Washington, DC.

Doyle, J. F. (1997). *Wave Propagation in Structures,* Springer Science and Business Media, New York, NY.

Dusenberry, D. ed. (2010). *Handbook for Blast Resistant Design of Buildings*, John Wiley & Sons, Hoboken, NJ.

Gran, J. K., Florence, A. L., and Colton, J. D. (1989). "Dynamic triaxial tests of high-strength concrete," *Journal of Engineering Mechanics*, 115 (5): 891-904.

Grote, D. L., Park, S. W., and Zhou, M. (2001). "Dynamic behavior of concrete at high strain rates and pressures: I. experimental characterization," *International Journal of Impact Engineering*, 25 (9): 869-886.

Gupta, Y. M. and Seaman, L. (1975). "Dynamic behavior of reinforced concrete under missile impact loading," *Proceedings, 2nd ASCE Specialty Conference on Structural Design of Nuclear Plant Facilities*, New Orleans, USA, December.

Gwaltney, R. C. (1968). "Missile generation and protection in light-water-cooled power reactor plants," *ORNI-NSIC-22*, Oak Ridge National Laboratory, Oak Ridge, TN.

Hao, Y., Hao, H., and Li, Z. X. (2013). "Influence of end friction confinement on impact tests of concrete material at high strain rate," *International Journal of Impact Engineering*, 60 (2013): 82-106.

Hu, S., Wu, C. T., and Guo, Y. (2010). "Engine impeller sub-fragmentation simulation using EFG method," *Proceedings, 11th International LS-DYNA Users Conference*, Detroit, MI, June.

Kennedy, R. P. (1975). "A review of procedures for the analysis and design of concrete structures to resist missile impact effects," *Nuclear Engineering and Design*, 37: 183-203.

Lacome, J. L., (2000). “Smooth particle hydrodynamics (SPH): a new feature in LS-DYNA,” *Proceedings, 6th International LS-DYNA Users Conference*, Dearborn, MI, April.

Li, Q. M., and Meng, H. (2003). “About the dynamic strength enhancement of concrete-like materials in a split Hopkinson pressure bar test,” *International Journal of Solids and Structures*, 40: 343-360.

Liu, G. R., and Liu, M. B. (2003). *Smoothed Particle Hydrodynamics: A Meshfree Particle Method*, World Scientific, Singapore.

Livermore Software Technology Corporation (LSTC). (2012). *LS-DYNA keyword user's manual V971*, Livermore, CA.

Magallenes, J. M., Wu, J. Malvar, L. J., and Crawford, J. E. (2010). “Recent improvements to release III of the K&C concrete model,” *Proceedings*, *11th International LS-DYNA Users Conference*, Dearborn, MI, June.

Malvar, L. J., Crawford, J. E., Wesevich, J. W., and Simons, D. (1997). “A plasticity-based concrete material model for DYNA3D,” *International Journal of Impact Engineering*, 19 (9-10): 847-873.

Malvar, L. J., and Ross, C. A. (1998). “Review of static and dynamic properties of concrete in tension,” *ACI Materials Journal*, 95 (6): 735-739.

McDonald, J. R. (1999). “Rationale for wind-borne missile citeria for DOE facilities,” *UCRL-CR-135697*, Lawrence Livermore National Laboratory, Livermore, CA.

Mehra, V., CD, S., Mishra, V., and Chaturvedi, S. (2012). “Tensile instability and artificial stresses in impact problems in SPH,” *Journal of Physics*, 370 (2012): 1-4.

Mizuno, J., Koshika, N., Sawamoto, Y., Niwa, N., Yamashita, T., and Suzuki, A. (2005). “Investigation on impact resistance of steel plate reinforced concrete barriers against aircraft impact. Part 1: Test program and results,” *Transactions, 18th International Conference on Structural Mechanics in Reactor Technology (SMiRT)*, Beijing, China, August.

Morikawa, H., Mizuno, J., Momma, T., Fukuda, R., Takeuch, M., and Shikama, Y. (1999). “Scale model tests of multiple barriers against aircraft impact part 2: simulation analyses of scale model impact tests,” *Transactions, 15th International Conference on Structural Mechanics in Reactor Technology (SMiRT)*, Seoul, Korea, August.

Morris, C. J., (2014). Diablo Canyon Nuclear Power Plant. *Encyclopedia Britannica*, http://www.britannica.com/EBchecked/media/99753/The-Diablo-Canyon-nuclear-power-plant-in-San-Luis-Obispo, Accessed: September 10th.

Murray, Y. D., Abu-Odeh, A., and Bligh, R. (2007a). “Evaluation of the concrete material model 159,” *FHWA-HRT-05-063*, Federal Highway Administration, McLean, VA.

Murray, Y. D., Abu-Odeh, A., and Bligh, R. (2007b). “User's manual for LS-DYNA concrete material model 159,” *FHWA-HRT-05-062*, Federal Highway Administration, McLean, VA.

National Research Council Committee on Fortification Design (NRCCFD). (1944). “Final report,” National Academies, Washington, D.C.

Nuclear Energy Agency (NEA) and Committee on the Safety of Nuclear Installations (CSNI). (2011). “Improving robustness assessment methodologies for structures impacted by missiles (IRIS_2010),” Paris, France.

Nuclear Energy Institute (NEI). (2009). “Methodology for performing aircraft impact assessments for new plant designs,” *NEI 07-13 Revision 7*, Washington, DC.

Ohnuma, H., Ito, C., and Nomachi, C. G. (1985). “Dynamic response and local rupture of reinforced concrete beam and slab under impact loading,” *Transactions, 8th International Conference on Structural Mechanics in Reactor Technology (SMiRT)*, Brussels, Belgium, August.

Oliveira, D. A., Lee, N. H., and Elgohary, M. (2009). “Missile impact on reinforced concrete walls: simulation of experiments,” *Transactions, 20th International Conference on Structural Mechanics in Reactor Technology (SMiRT)*, Espoo, Finland, August.

O'Toole, B., Trabia, M., Hixson, R., Shawoon, K. R., Pena, M., Becker, S., Daykin, E., Machorro, E., Jennings, R., and Matthes, M. (2015). “Modeling plastic deformation of steel plates in hypervelocity impact experiments,” *Proceedings, 13th Hypervelocity Impact Symposium*, Boulder, CO, April.

Rabbat, B. G., and Russell, H. G. (1985). “Friction coefficient of steel on concrete or grout,” *Journal of Structural Engineering*, 111 (3): 505-515.

Rahman, I., Zaidi, A., and Latif, Q. (2010). “Review on empirical studies of local impact effects of hard missile on concrete structures,” *International Journal of Sustainable Construction Engineering & Technology*, 1: 1-97.

Rotz, J. V. (1975). “Results of missile impact tests on reinforced concrete panels,” *Proceedings, Second ASCE Specialty Conference on Structural Design of Nuclear Plant Facilities,* New Orleans, LA, December.

Russell, C. R. (1962). *Reactor Safeguards*, The Macmillan Company, New York, NY.

Sawamoto, Y., Tsubota, H., Kasai, Y., Koshika, N., and Morikawa, H. (1998). “Analytical studies on local damage to reinforced concrete structures under impact loading by discrete element method,” *Nuclear Engineering and Design*, 179: 157-177.

Schuler, H., Mayrhofer, C., and Thoma, K. (2006). “Spall experiments for the measurement of the tensile strength and fracture energy of concrete at high strain rates,” *International Journal of Impact Engineering*, 32 (10): 1635-1650.

Schwer, L. and Malvar, L. J. (2005). "Simplified concrete modeling with MAT CONCRETE DAMAGE REL3," *Proceedings, JRI LS-DYNA User Week 2005*, Nagoya, Japan, November.

Schwer, L. (2008a). "Is your mesh refined enough? Estimating discretization error using GCI," *Proceedings, 2008 German Forum*. Bamberg, Germany, September. https://www.dynamore.de/de/download/papers/forum08/dokumente/1-1-03

Schwer, L. (2008b). "Simple input concrete constitutive models: an illustration of brick wall & concrete cylinder perforation," *Proceedings, 10th International LS-DYNA Users Conference*, Dearborn, MI, June.

Schwer, L. (2009a). "Aluminum plate perforation: a comparative case study using Lagrange with erosion, multi-material ALE, and Smooth Particle Hydrodynamics," *Proceedings, 7th European LS-DYNA Conference*, Stuttgart, Germany, June.

Schwer, L. (2009b). "SPH, MM-ALE, & erosion simulation of concrete cylinder perforation," *Transactions, 20th International Conference on Structural Mechanics in Reactor Technology (SMiRT)*, Espoo, Finland, August.

Schwer, L. (2009c). "Strain rate induced strength enhancement in concrete: much ado about nothing?" *Proceedings, 7th European LS-DYNA Conference*. Stuttgart, Germany, June.

Schwer, L. (2015). Personal communication, July.

Shin, J., Whittaker, A. S., Aref, A. J., and Cormie, D. (2014). "Air-blast effects on civil structures," Technical Report MCEER-14-0006, The State University of New York at Buffalo, Buffalo, NY.

Shin, J., Whittaker, A. S., and Aref, A. J. (2015). "Near-field blast assessment of reinforced concrete components," *International Journal of Protective Structures*, 6 (3): 487-508.

Sliter, G. E. (1979). "Assessment of empirical concrete impact formulas," *ASCE Conference on Civil Engineering and Nuclear Power*, Boston, MA, April.

Stephenson, A. E. (1977). "Full-scale tornado-missile impact tests," *EPRI NP-440 Project 399*, Electric Power Research Institute, Sandia Laboratories, Albuquerque, NM.

Sugano, T. (1993a). "Full-scale aircraft impact test for evaluation of impact force," *Nuclear Engineering and Design*, 140 (3): 373-385.

Sugano, T. (1993b). "Local damage to reinforced concrete structures caused by impact of aircraft engine missiles part 1: test program, methods, and results," *Nuclear Engineering and Design*, 140 (3): 387-405.

Tabiei, A. (2014). *LSTC Seminar: Penetration in LS-DYNA*, Troy, MI, August.

Takeda, J., Tachikawa, H., and Fujimoto, K. (1974). "Mechanical behaviour of concrete under higher rate loading than in static tests," *Mechanical Behaviour of Materials*, 2: 479-486.

Tedesco, J. W., and Ross, C. A. (1998). "Strain-rate-dependent constitutive equations for concrete," *Journal of Pressure Vessel Technology*, 120 (4): 398-405.

Tsubota, H., Koshika, N., Mizuno, J., Sanai, M., Peterson, B., Saito, H., and Imamura, A. (1999). "Scale model tests of multiple barriers against aircraft impact part 1: experimental program and test results," *Transactions, 15th International Conference on Structural Mechanics in Reactor Technology (SMiRT)*, Seoul, Korea, August.

Tu, D. and Murray, R. (1977). "Numerical simulation of tornado-borne missile impact," *UCRL-52223*, Lawrence Livermore Laboratory, Livermore, CA.

U.S. Army Corps of Engineers (ACE). (2008). "Methodology manual for the single-degree-of-freedom blast effects design spreadsheets (SBEDS)," *PDC TR-06-01 Rev 1*, Protective Design Center, St. Louis, MO.

U.S. Nuclear Regulatory Commission (NRC). (2007). "Regulatory Guide 1.76: Design-basis tornado and tornado missiles for nuclear power plants," Washington, DC

U.S. Nuclear Regulatory Commission (NRC). (2011). "Regulatory Guide 1.221: Design-basis hurricane and hurricane missiles for nuclear power plants," Washington, DC

Vassallo, F. A. (1975). "Missile impact testing of reinforced concrete panels," *Calspan Report No. HC-5609-D-1*, Calspan Corporation, Buffalo, NY.

Whirley, R. G., Engellman, B. E., and Hallquist, J. O. (1993). "DYNA3D: A nonlinear explicit three-dimensional finite element code for solid and structural mechanics--user manual," *Report No. UCRL-MA-107254 Rev 1*, Lawrence Livermore National Laboratory, Livermore, CA.

Wu, Y., Crawford, J. E., and Magallanes, J. M. (2012). "Performance of LS-DYNA concrete constitutive models," *Proceedings, 12th International LS-DYNA Users Conference*, Detroit, MI, June.

Wu, Y., Magallanes, J. M., Hyung-Jin, C., and Crawford, J. E. (2013). "Evolutionarily coupled finite-element mesh-free formulation for modeling concrete behaviors under blast and impact loadings," *Journal of Engineering Mechanics*, 139 (4): 525-536.

Wu, Y., and Crawford, J. E. (2015). "Numerical modeling of concrete using a partially associative plasticity model," *Journal of Engineering Mechanics*, 141 (12).

Yamaguchi, H., Fujimoto, K., and Nomura, S. (1989). "Strain rate effect on stress-strain relationships of concrete," *Proceedings, 4th Symposium on the Interaction of Non-Nuclear Munitions with Structures*, Panama City, FL, April.

Yankelevsky, D. Z. (1997). "Local response of concrete slabs to low velocity missile impact," *International Journal of Impact Engineering*, 19 (4): 331-343.

Zhang, M., Wu, H. J., Li, Q. M., and Huang, F. L. (2009). "Further investigation on the dynamic compressive strength enhancement of concrete-like materials based on split Hopkinson pressure bar tests. Part 1: experiments," *International Journal of Impact Engineering*, 36 (12): 1327-1334.

Zhou, X. Q., and Hao, C. (2008). "Modelling of compressive behaviour of concrete-like materials at high strain rate," *International Journal of Solids and Structures*, 45 (17): 4648-4661.

Zineddin, M., and Krauthammer, T. (2007). "Dynamic response and behavior of reinforced concrete slabs under impact loading," *International Journal of Impact Engineering*, 34: 1517-1534.

"This Page Intentionally Left Blank"

APPENDIX A
EVALUATION OF THE JACOBIAN AND DEVELOPMENT OF STIFFNESS MATRICES FOR DISTORTED ELEMENTS

A.1 Introduction

The Jacobian and the stiffness matrix of the 2D solid elements presented in Figure 2-21a and Figure 2-21b are calculated in this appendix to highlight the shortcomings of the Lagrangian formulation once the element becomes severely distorted. The steps for calculating the Jacobian and stiffness matrix of a 2D solid element are presented in Section A.2. The Jacobians and stiffness matrices for the non-distorted and distorted elements shown in Figure 2-21a and Figure 2-21b respectively, are calculated in Sections A.3 and A.4, respectively. Conclusions are presented in Section A.5.

A.2 Jacobian and Stiffness Matrix of a 2D Solid Element

The stiffness matrix, $[K]$, of an element is constructed using equation (A-1) (Bathe, 1996).

$$[K] = \iiint_{V_e} [B]^T [C][B] dV = \iint_{A_e} [B]^T [C][B] t |J| drds \tag{A-1}$$

where $[B]$ is the strain-displacement matrix, $[C]$ is the constitutive matrix, V_e is the volume of the element, A_e is the area of the element, t is thickness of the element, and $|J|$ is the determinant of the Jacobian matrix. Numerical integration is used to evaluate the integral of equation (A-1) per Bathe (1996):

$$[K] = t\sum_{i=1}^{n} w_{r_i} w_{s_i} B_i^T C B_i |J| \tag{A-2}$$

where w_{r_i} and w_{s_i} are sampling weights for r and s, respectively and n is the number of Gauss points.

The relationship between the physical and iso-parametric space is presented in chain rule and matrix form in equations (A-3), (A-4), and (A-5), respectively. The Jacobian, $[J]$, is given by equation (A-6).

$$\frac{\partial}{\partial r}=\frac{\partial}{\partial X}\frac{\partial X}{\partial r}+\frac{\partial}{\partial Y}\frac{\partial Y}{\partial r} \tag{A-3}$$

$$\frac{\partial}{\partial s}=\frac{\partial}{\partial X}\frac{\partial X}{\partial s}+\frac{\partial}{\partial Y}\frac{\partial Y}{\partial s} \tag{A-4}$$

$$\begin{bmatrix}\dfrac{\partial}{\partial r}\\ \dfrac{\partial}{\partial s}\end{bmatrix}=\begin{bmatrix}\dfrac{\partial X}{\partial r} & \dfrac{\partial Y}{\partial r}\\ \dfrac{\partial X}{\partial s} & \dfrac{\partial Y}{\partial s}\end{bmatrix}\begin{bmatrix}\dfrac{\partial}{\partial X}\\ \dfrac{\partial}{\partial Y}\end{bmatrix}=\left[J\right]\begin{bmatrix}\dfrac{\partial}{\partial X}\\ \dfrac{\partial}{\partial Y}\end{bmatrix} \tag{A-5}$$

$$\left[J\right]=\begin{bmatrix}\dfrac{\partial X}{\partial r} & \dfrac{\partial Y}{\partial r}\\ \dfrac{\partial X}{\partial s} & \dfrac{\partial Y}{\partial s}\end{bmatrix} \tag{A-6}$$

where $\left(\frac{\partial}{\partial r},\frac{\partial}{\partial s}\right)$ and $\left(\frac{\partial}{\partial X},\frac{\partial}{\partial Y}\right)$ are partial derivatives of element displacements with respect to the iso-parametric and physical space, respectively. The variables X and Y are defined using equations (A-7) and (A-8), respectively.

$$X = X_1N_1 + X_2N_2 + X_3N_3 + X_4N_4 \tag{A-7}$$

$$Y = Y_1N_1 + Y_2N_2 + Y_3N_3 + Y_4N_4 \tag{A-8}$$

where (X_1 through X_4) and (Y_1 through Y_4) are nodal coordinates of the iso-parametric element defined in the physical space, as illustrated in Figure 2-21b. The shape functions of a four-noded solid element N_1, N_2, N_3, and N_4, defined in the iso-parametric space are (Bathe, 1996):

$$N_1=\frac{1}{4}(1+r)(1+s) \tag{A-9}$$

$$N_2=\frac{1}{4}(1-r)(1+s) \tag{A-10}$$

$$N_3=\frac{1}{4}(1-r)(1-s) \tag{A-11}$$

$$N_4=\frac{1}{4}(1+r)(1-s) \tag{A-12}$$

The nodal displacements of the element, U and V, in the physical space are shown in equations (A-13) and (A-14), respectively. The displacements are presented in matrix form in equation (A-15).

$$U = U_1N_1 + U_2N_2 + U_3N_3 + U_4N_4 \tag{A-13}$$

$$V = V_1N_1 + V_2N_2 + V_3N_3 + V_4N_4 \tag{A-14}$$

$$\begin{Bmatrix} U \\ V \end{Bmatrix} = \begin{bmatrix} N_1 & 0 & N_2 & 0 & N_3 & 0 & N_4 & 0 \\ 0 & N_1 & 0 & N_2 & 0 & N_3 & 0 & N_4 \end{bmatrix} \begin{Bmatrix} U_1 \\ V_1 \\ U_2 \\ V_2 \\ U_3 \\ V_3 \\ U_4 \\ V_4 \end{Bmatrix} = [N]\{U\} \tag{A-15}$$

Consider a plane-stress element. The strains can be written in matrix form (equation A-16) to develop the relationship between the strains and the displacements defined as the $[B]$ matrix (see equation A-16). The constitutive matrix, $[C]$, for a plane-stress element is shown in equation (A-17).

$$\{\varepsilon\} = \begin{Bmatrix} \varepsilon_x \\ \varepsilon_y \\ \gamma_{xy} \end{Bmatrix} = \begin{Bmatrix} \dfrac{\partial U}{\partial X} \\ \dfrac{\partial V}{\partial Y} \\ \dfrac{\partial U}{\partial Y} + \dfrac{\partial V}{\partial X} \end{Bmatrix} = [B]\{U\} \tag{A-16}$$

$$[C] = \frac{E}{1-v^2} \begin{bmatrix} 1 & v & 0 \\ v & 1 & 0 \\ 0 & 0 & \dfrac{1-v}{2} \end{bmatrix} \tag{A-17}$$

where ε_x and ε_y are strain components in the X and Y direction, respectively; γ_{xy} is the shear strain in the XY plane; E is the Young's modulus; and v is Poisson's ratio.

Substituting the nodal displacements of the element, U (equation (A-13)) and V (equation (A-14)), into equation (A-5), and solving for the partial derivatives in the physical space, gives the relationships shown in equations (A-18) and (A-19), respectively.

$$\begin{bmatrix} \dfrac{\partial U}{\partial X} \\ \dfrac{\partial U}{\partial Y} \end{bmatrix} = [J]^{-1} \begin{bmatrix} \dfrac{\partial U}{\partial r} \\ \dfrac{\partial U}{\partial s} \end{bmatrix} \tag{A-18}$$

$$\begin{bmatrix} \dfrac{\partial V}{\partial X} \\ \dfrac{\partial V}{\partial Y} \end{bmatrix} = [J]^{-1} \begin{bmatrix} \dfrac{\partial V}{\partial r} \\ \dfrac{\partial V}{\partial s} \end{bmatrix} \tag{A-19}$$

Substituting the partial derivatives of U (equation (A-13)) and V (equation (A-14)) into equations (A-18) and (A-19), respectively, gives equations (A-20) and (A-21), respectively.

$$\begin{bmatrix} \dfrac{\partial U}{\partial X} \\ \dfrac{\partial U}{\partial Y} \end{bmatrix} = [J]^{-1} \begin{bmatrix} \dfrac{\partial N_1}{\partial r} & 0 & \dfrac{\partial N_2}{\partial r} & 0 & \dfrac{\partial N_3}{\partial r} & 0 & \dfrac{\partial N_4}{\partial r} & 0 \\ \dfrac{\partial N_1}{\partial s} & 0 & \dfrac{\partial N_2}{\partial s} & 0 & \dfrac{\partial N_3}{\partial s} & 0 & \dfrac{\partial N_4}{\partial s} & 0 \end{bmatrix} \begin{Bmatrix} U_1 \\ V_1 \\ U_2 \\ V_2 \\ U_3 \\ V_3 \\ U_4 \\ V_4 \end{Bmatrix} \tag{A-20}$$

$$\begin{bmatrix} \dfrac{\partial V}{\partial X} \\ \dfrac{\partial V}{\partial Y} \end{bmatrix} = [J]^{-1} \begin{bmatrix} 0 & \dfrac{\partial N_1}{\partial r} & 0 & \dfrac{\partial N_2}{\partial r} & 0 & \dfrac{\partial N_3}{\partial r} & 0 & \dfrac{\partial N_4}{\partial r} \\ 0 & \dfrac{\partial N_1}{\partial s} & 0 & \dfrac{\partial N_2}{\partial s} & 0 & \dfrac{\partial N_3}{\partial s} & 0 & \dfrac{\partial N_4}{\partial s} \end{bmatrix} \begin{Bmatrix} U_1 \\ V_1 \\ U_2 \\ V_2 \\ U_3 \\ V_3 \\ U_4 \\ V_4 \end{Bmatrix} \tag{A-21}$$

Equations (A-20) and (A-21) are used to assemble $[B]$ as shown in equation (A-22).

$$[B] = \begin{Bmatrix} \dfrac{\partial U}{\partial X} \\ \dfrac{\partial V}{\partial Y} \\ \dfrac{\partial U}{\partial Y} + \dfrac{\partial V}{\partial X} \end{Bmatrix} = \begin{bmatrix} \dfrac{\partial N_1}{\partial r} & 0 & \dfrac{\partial N_2}{\partial r} & 0 & \dfrac{\partial N_3}{\partial r} & 0 & \dfrac{\partial N_4}{\partial r} & 0 \\ 0 & \dfrac{\partial N_1}{\partial s} & 0 & \dfrac{\partial N_2}{\partial s} & 0 & \dfrac{\partial N_3}{\partial s} & 0 & \dfrac{\partial N_4}{\partial s} \\ \dfrac{\partial N_1}{\partial s} & \dfrac{\partial N_1}{\partial r} & \dfrac{\partial N_2}{\partial s} & \dfrac{\partial N_2}{\partial r} & \dfrac{\partial N_3}{\partial s} & \dfrac{\partial N_3}{\partial r} & \dfrac{\partial N_4}{\partial s} & \dfrac{\partial N_4}{\partial r} \end{bmatrix} \begin{Bmatrix} U_1 \\ V_1 \\ U_2 \\ V_2 \\ U_3 \\ V_3 \\ U_4 \\ V_4 \end{Bmatrix} \tag{A-22}$$

The locations and weights of the Gauss points in the iso-parametric space are presented in Table A-1. These points are used to evaluate $[B]$ at the integration points.

Table A-1: Gauss point locations and weights

Gauss point	r	s	w_{r_i}	w_{s_i}
1	0.5774	0.5774	1	1
2	-0.5774	0.5774	1	1
3	-0.5774	-0.5774	1	1
4	0.5774	-0.5774	1	1

The matrix $[B]$ (equation (A-22)), matrix $[C]$ (equation A-17), determinant of the Jacobian, $|J|$ (Equation (A-6)), thickness of the element, t, and the Gauss point weights (Table A-1) are substituted into equation (A-2) to numerically evaluate the stiffness matrix of an element. The Jacobians and the stiffness matrices of the elements shown in Figure 2-21 are evaluated below.

A.3 Non-distorted Element

The nodal coordinates of the non-distorted element shown in Figure 2-21a in the physical space are presented in Table A-2.

Table A-2: Nodal coordinates of non-distorted element in physical space

X_1	10	Y_1	10
X_2	0	Y_2	10
X_3	0	Y_3	0
X_4	10	Y_4	0

The steps to compute the Jacobian of the element are:

$$X = X_1 N_1 + X_2 N_2 + X_3 N_3 + X_4 N_4$$

$$X = \frac{10}{4}(1+r)(1+s) + \frac{10}{4}(1+r)(1-s)$$

$$\frac{\partial X}{\partial r} = 5$$

$$\frac{\partial X}{\partial s} = 0$$

$$Y = Y_1 N_1 + Y_2 N_2 + Y_3 N_3 + Y_4 N_4$$

$$Y = \frac{10}{4}(1+r)(1+s) + \frac{10}{4}(1-r)(1+s)$$

$$\frac{\partial Y}{\partial r} = 0$$

$$\frac{\partial Y}{\partial s} = 5$$

$$J = \begin{vmatrix} \frac{\partial X}{\partial r} & \frac{\partial Y}{\partial r} \\ \frac{\partial X}{\partial s} & \frac{\partial Y}{\partial s} \end{vmatrix} = \begin{bmatrix} 5 & 0 \\ 0 & 5 \end{bmatrix}$$

The determinant of the Jacobian (computed below) is positive and constant at all locations within the element.

$$|J| = (5 \times 5) - (0 \times 0) = 25$$

Substituting $[J]^{-1}$ and the partial derivatives of U (equation (A-13)) and V (equation (A-14)) into equations (A-20) and (A-21), respectively, gives:

$$\begin{bmatrix} \dfrac{\partial U}{\partial X} \\ \dfrac{\partial U}{\partial Y} \end{bmatrix} = \frac{1}{25}\begin{bmatrix} 5 & 0 \\ 0 & 5 \end{bmatrix}\begin{bmatrix} \frac{1}{4}+\frac{1}{4}s & 0 & -\frac{1}{4}-\frac{1}{4}s & 0 & -\frac{1}{4}+\frac{1}{4}s & 0 & \frac{1}{4}-\frac{1}{4}s & 0 \\ \frac{1}{4}+\frac{1}{4}r & 0 & \frac{1}{4}-\frac{1}{4}r & 0 & -\frac{1}{4}+\frac{1}{4}r & 0 & -\frac{1}{4}-\frac{1}{4}r & 0 \end{bmatrix}\begin{Bmatrix} U_1 \\ V_1 \\ U_2 \\ V_2 \\ U_3 \\ V_3 \\ U_4 \\ V_4 \end{Bmatrix} \tag{A-23}$$

$$\begin{bmatrix} \dfrac{\partial V}{\partial X} \\ \dfrac{\partial V}{\partial Y} \end{bmatrix} = \frac{1}{25}\begin{bmatrix} 5 & 0 \\ 0 & 5 \end{bmatrix}\begin{bmatrix} 0 & \frac{1}{4}+\frac{1}{4}s & 0 & -\frac{1}{4}-\frac{1}{4}s & 0 & -\frac{1}{4}+\frac{1}{4}s & 0 & \frac{1}{4}-\frac{1}{4}s \\ 0 & \frac{1}{4}+\frac{1}{4}r & 0 & \frac{1}{4}-\frac{1}{4}r & 0 & -\frac{1}{4}+\frac{1}{4}r & 0 & -\frac{1}{4}-\frac{1}{4}r \end{bmatrix}\begin{Bmatrix} U_1 \\ V_1 \\ U_2 \\ V_2 \\ U_3 \\ V_3 \\ U_4 \\ V_4 \end{Bmatrix} \tag{A-24}$$

Equations (A-23) and (A-24) are used to assemble $[B]$ defined in equation (A-22). The matrix $[B]$ is evaluated at all four Gauss points shown in Table A-1 and substituted into equation (A-2) to compute the stiffness matrix of the element, $[K]$. The elastic modulus, E, and Poisson's ratio, v, are equal to 1 and 0.3, respectively, for the calculation of the constitutive matrix, $[C]$.

$$[K] = \begin{bmatrix} 0.65 & 0.26 & -0.46 & -0.05 & -0.25 & -0.14 & 0.05 & -0.07 \\ 0.26 & 0.55 & -0.01 & 0.00 & -0.15 & -0.25 & -0.10 & -0.30 \\ -0.46 & -0.01 & 0.65 & -0.20 & 0.05 & 0.01 & -0.25 & 0.20 \\ -0.05 & 0.00 & -0.20 & 0.55 & 0.04 & -0.30 & 0.21 & -0.25 \\ -0.25 & -0.15 & 0.05 & 0.04 & 0.34 & 0.16 & -0.14 & -0.04 \\ -0.14 & -0.25 & 0.01 & -0.30 & 0.16 & 0.44 & -0.02 & 0.11 \\ 0.05 & -0.10 & -0.25 & 0.21 & -0.14 & -0.02 & 0.34 & -0.10 \\ -0.07 & -0.30 & 0.20 & -0.25 & -0.04 & 0.11 & -0.10 & 0.44 \end{bmatrix}$$

A.4 Distorted Element

The nodal coordinates of the distorted element (Figure 2-21b) in the physical space are presented in Table A-3.

Table A-3: Nodal coordinates of distorted element in physical space

X_1	8	Y_1	9
X_2	12	Y_2	8
X_3	0	Y_3	0
X_4	10	Y_4	2

The steps to compute the Jacobian of the distorted element are:

$$X = X_1 N_1 + X_2 N_2 + X_3 N_3 + X_4 N_4$$

$$X = \frac{8}{4}(1+r)(1+s) + \frac{12}{4}(1-r)(1+s) + \frac{10}{4}(1+r)(1-s)$$

$$\frac{\partial X}{\partial r} = 1.5 - 3.5s$$

$$\frac{\partial X}{\partial s} = 2.5 - 3.5r$$

$$Y = Y_1 N_1 + Y_2 N_2 + Y_3 N_3 + Y_4 N_4$$

$$Y = \frac{9}{4}(1+r)(1+s) + \frac{8}{4}(1-r)(1+s) + \frac{2}{4}(1+r)(1-s)$$

$$\frac{\partial Y}{\partial r} = 0.75 - 0.25s$$

$$\frac{\partial Y}{\partial s} = 3.75 - 0.25r$$

$$J = \begin{vmatrix} \frac{\partial X}{\partial r} & \frac{\partial Y}{\partial r} \\ \frac{\partial X}{\partial s} & \frac{\partial Y}{\partial s} \end{vmatrix} = \begin{bmatrix} 1.5 - 3.5s & 0.75 - 0.25s \\ 2.5 - 3.5r & 3.75 - 0.25r \end{bmatrix}$$

The determinant of the Jacobian in the iso-parametric space is given by:

$$|J| = 3.75 + 2.25r - 12.5s$$

Table A-3 shows the determinant of the Jacobian, $|J|$, evaluated at all four nodes of the element (see Figure 2-21). The locations of the nodes in iso-parametric space are also shown in the table. Significant distortion of the element causes the determinant of the Jacobian to be negative at nodes 1 and 2 (highlighted in Table A-3): an expected result. In a finite element simulation, this behavior will cause a negative volume error and trigger termination of the analysis.

Table A-3: Jacobian determinants for a distorted element

Node	r	s	$\|J\|$
1	1	1	-6.5
2	-1	1	-11
3	-1	-1	14
4	1	-1	18.5

The substitution of $[J]^{-1}$ and the partial derivatives of U (equation (A-13)) and V (equation (A-14)) into equations (A-20) and (A-21), respectively, gives:

$$\begin{bmatrix} \dfrac{\partial U}{\partial X} \\ \dfrac{\partial U}{\partial Y} \end{bmatrix} = \frac{1}{3.75+2.25r-12.5s} \begin{bmatrix} 1.5-3.5s & 0.75-0.25s \\ 2.5-3.5r & 3.75-0.25r \end{bmatrix} \begin{bmatrix} \frac{1}{4}+\frac{1}{4}s & 0 & -\frac{1}{4}-\frac{1}{4}s & 0 & -\frac{1}{4}+\frac{1}{4}s & 0 & \frac{1}{4}-\frac{1}{4}s & 0 \\ \frac{1}{4}+\frac{1}{4}r & 0 & \frac{1}{4}-\frac{1}{4}r & 0 & -\frac{1}{4}+\frac{1}{4}r & 0 & -\frac{1}{4}-\frac{1}{4}r & 0 \end{bmatrix} \begin{Bmatrix} U_1 \\ V_1 \\ U_2 \\ V_2 \\ U_3 \\ V_3 \\ U_4 \\ V_4 \end{Bmatrix} \tag{A-25}$$

$$\begin{bmatrix} \dfrac{\partial V}{\partial X} \\ \dfrac{\partial V}{\partial Y} \end{bmatrix} = \frac{1}{3.75+2.25r-12.5s} \begin{bmatrix} 1.5-3.5s & 0.75-0.25s \\ 2.5-3.5r & 3.75-0.25r \end{bmatrix} \begin{bmatrix} 0 & \frac{1}{4}+\frac{1}{4}s & 0 & -\frac{1}{4}-\frac{1}{4}s & 0 & -\frac{1}{4}+\frac{1}{4}s & 0 & \frac{1}{4}-\frac{1}{4}s \\ 0 & \frac{1}{4}+\frac{1}{4}r & 0 & \frac{1}{4}-\frac{1}{4}r & 0 & -\frac{1}{4}+\frac{1}{4}r & 0 & -\frac{1}{4}-\frac{1}{4}r \end{bmatrix} \begin{Bmatrix} U_1 \\ V_1 \\ U_2 \\ V_2 \\ U_3 \\ V_3 \\ U_4 \\ V_4 \end{Bmatrix} \tag{A-26}$$

The information in equations (A-23) and (A-24) is used to assemble $[B]$ defined in equation (A-22). The matrix $[B]$ is evaluated at all four Gauss points shown in Table A-1 and substituted into equation (A-2) to compute the stiffness matrix of the element, $[K]$, shown below. The elastic modulus, E, and Poisson's ratio, v, are equal to 1 and 0.3, respectively, for this calculation.

$$[K]=\begin{bmatrix} 2.62 & -0.32 & -3.40 & 0.20 & -0.81 & 0.11 & 1.53 & 0.01 \\ -0.32 & 0.58 & 0.16 & -0.73 & 0.09 & -0.12 & 0.06 & 0.27 \\ -3.40 & 0.16 & 4.52 & 0.01 & 1.10 & -0.14 & -2.22 & -0.03 \\ 0.20 & -0.73 & 0.01 & 1.46 & -0.13 & 0.27 & -0.07 & -1.00 \\ -0.81 & 0.09 & 1.10 & -0.13 & 0.37 & -0.07 & -0.66 & 0.10 \\ 0.11 & -0.12 & -0.14 & 0.27 & -0.07 & 0.07 & 0.10 & -0.22 \\ 1.53 & 0.06 & -2.22 & -0.07 & -0.66 & 0.10 & 1.35 & -0.08 \\ 0.01 & 0.27 & -0.03 & -1.00 & 0.10 & -0.22 & -0.08 & 0.95 \end{bmatrix}$$

A.5 Conclusions

The Jacobians and stiffness matrices for the non-distorted and distorted elements presented in Figure 2-21a and Figure 2-21b, respectively, were calculated in this appendix. The determinant of the Jacobian of the non-distorted element was positive and constant at all locations within the element indicating that the unique relationship between the physical and iso-parametric space exists. The determinant of the Jacobian of the distorted element was evaluated at all four nodes and found to be negative in the top half of the element which is an expected result considering the element was severely distorted. In this case, a unique relationship between the physical and iso-parametric space no longer exists and the negative determinant triggers termination of the finite element simulation. This behavior highlights one of the significant shortcomings associated with the use of the Lagrangian formulation for impact and blast loading in which severe element distortion may occur.

“This Page Intentionally Left Blank”

APPENDIX B
CSCM CONCRETE MODEL INPUTS AND BEST-FIT STRAIN-RATE CURVES

Table B-1: CSCM concrete model inputs, EPRI Test 10

G (psi)	1.5E+06	D_1 (psi)	1.72E-06
K (psi)	1.65E+06	D_2 (psi^2)	1.66E-11
α (psi)	2005.4695	B_d	100
β (psi^{-1})	1.33E-04	D_b	0.1
λ (psi)	1522.8963	G_{FT} (psi-in)	0.4763
θ	2.82E-01	G_{FC} (psi-in)	47.63
α_1	0.74735	G_{FS} (psi-in)	0.4763
β_1 (psi^{-1})	5.14E-04	$PWRC$	5
λ_1	0.17	$PWRT$	1
θ_1 (psi^{-1})	8.95E-06	η_t	0.70
α_2	0.66	η_{ot}	1.6E-04
β_2 (psi^{-1})	5.21E-04	η_c	0.55
λ_2	0.16	η_{oc}	1.85E-04
θ_2 (psi^{-1})	1.05E-06	$Srate$	1
R	5	$Overc$ (psi)	2891.3
X_o (psi)	1.29E+04	$Overt$ (psi)	2891.3
W_p	0.05	$REPOW$	1

Table B-2: CSCM concrete model inputs, EPRI Test 3

G (psi)	1.43E+06	D_1 (psi)	1.72E-06
K (psi)	1.57E+06	D_2 (psi^2)	1.66E-11
α (psi)	1947.2083	B_d	100
β (psi^{-1})	1.33E-04	D_b	0.1
λ (psi)	1522.8963	G_{FT} (psi-in)	0.4452
θ	2.75E-01	G_{FC} (psi-in)	44.52
α_1	0.74735	G_{FS} (psi-in)	0.4452
β_1 (psi^{-1})	5.26E-04	$PWRC$	5
λ_1	0.17	$PWRT$	1
θ_1 (psi^{-1})	9.30E-06	η_t	0.70
α_2	0.66	η_{ot}	1.60E-04
β_2 (psi^{-1})	5.33E-04	η_c	0.55
λ_2	0.16	η_{oc}	1.85E-04
θ_2 (psi^{-1})	1.09E-05	$Srate$	1
R	5	$Overc$ (psi)	2809
X_o (psi)	1.27E+04	$Overt$ (psi)	2809
W_p	0.05	$REPOW$	1

Table B-2: CSCM concrete model inputs, EPRI Test 8

G (psi)	1.53E+06	D_1 (psi)	1.72E-06
K (psi)	1.67E+06	D_2 (psi^2)	1.66E-11
α (psi)	2022.4959	B_d	100
β (psi^{-1})	1.33E-04	D_b	0.1
λ (psi)	1522.8963	G_{FT} (psi-in)	0.4858
θ	2.85E-01	G_{FC} (psi-in)	48.58
α_1	0.74735	G_{FS} (psi-in)	0.4858
β_1 (psi^{-1})	5.10E-04	$PWRC$	5
λ_1	0.17	$PWRT$	1
θ_1 (psi^{-1})	8.84E-06	η_t	0.70
α_2	0.66	η_{ot}	1.6E-04
β_2 (psi^{-1})	5.17E-04	η_c	0.55
λ_2	0.16	η_{oc}	1.85E-04
θ_2 (psi^{-1})	1.03E-05	$Srate$	1
R	5	$Overc$ (psi)	2921
X_o (psi)	1.29E+04	$Overt$ (psi)	2921
W_p	0.05	$REPOW$	1

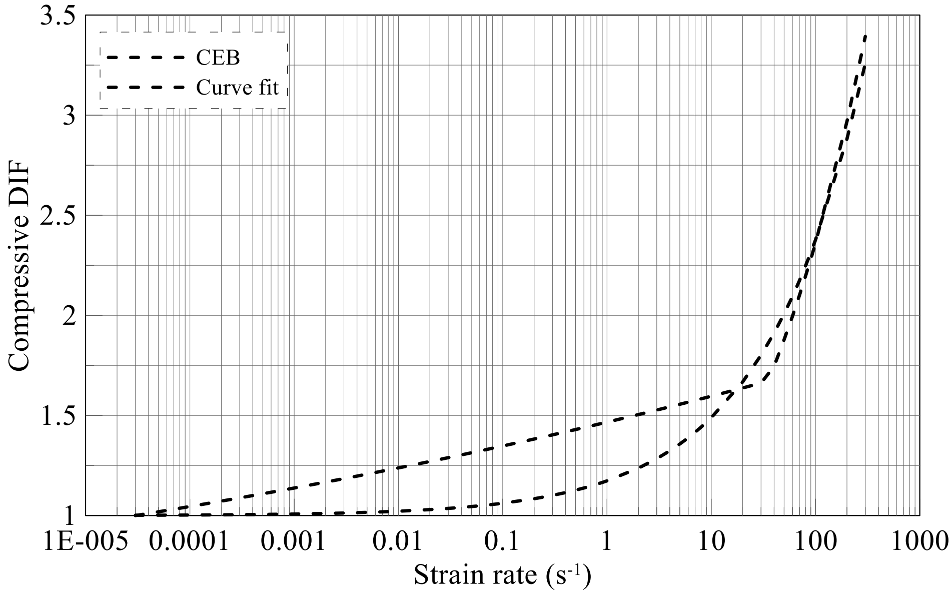

(a) CEB formulation in compression and best fit line

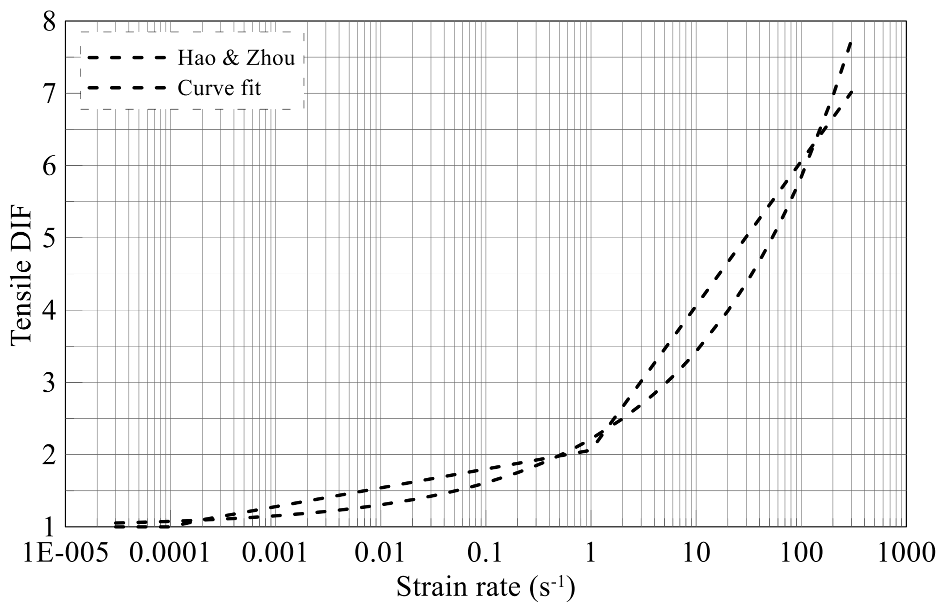

(b) Hao and Zhou formulation and best fit line

Figure B-1: Compressive and tensile DIFs, Test 10

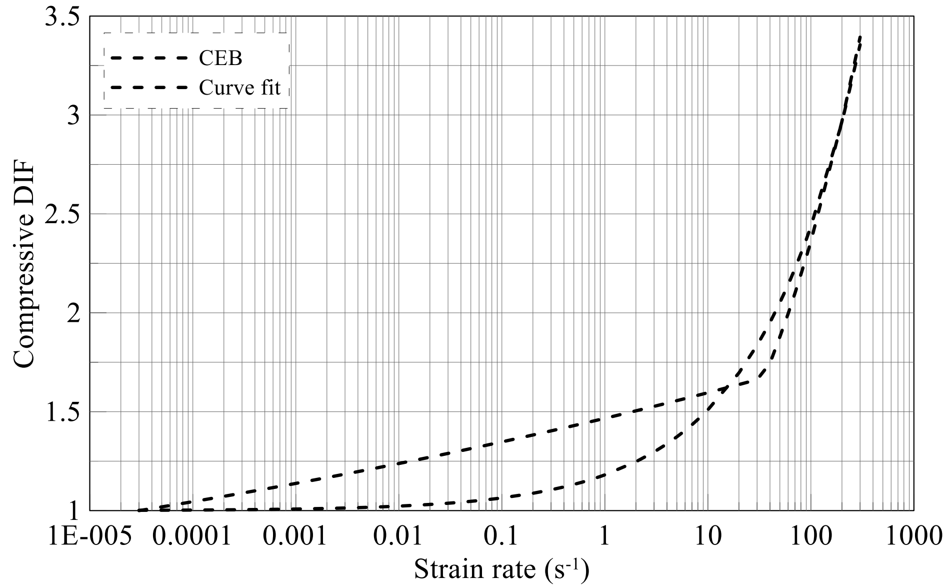

(a) CEB formulation in compression and best fit line

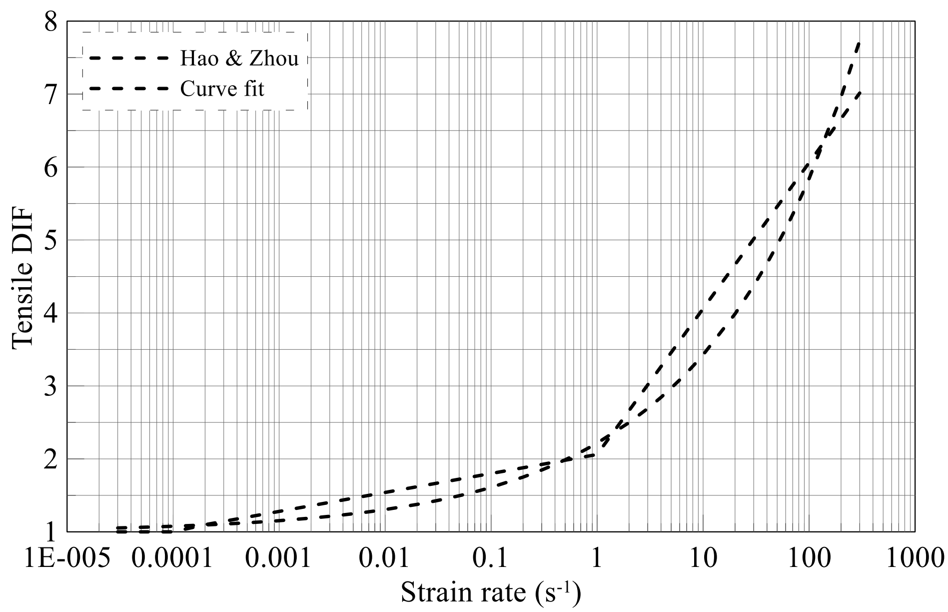

(b) Hao and Zhou formulation and best fit line

Figure B-2: Compressive and tensile DIFs, Test 3

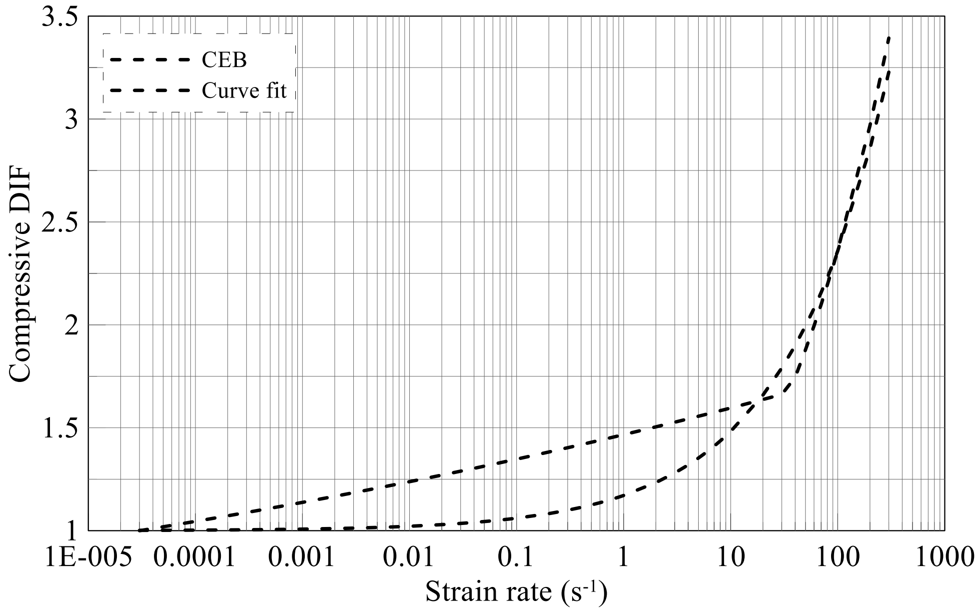

(a) CEB formulation in compression and best fit line

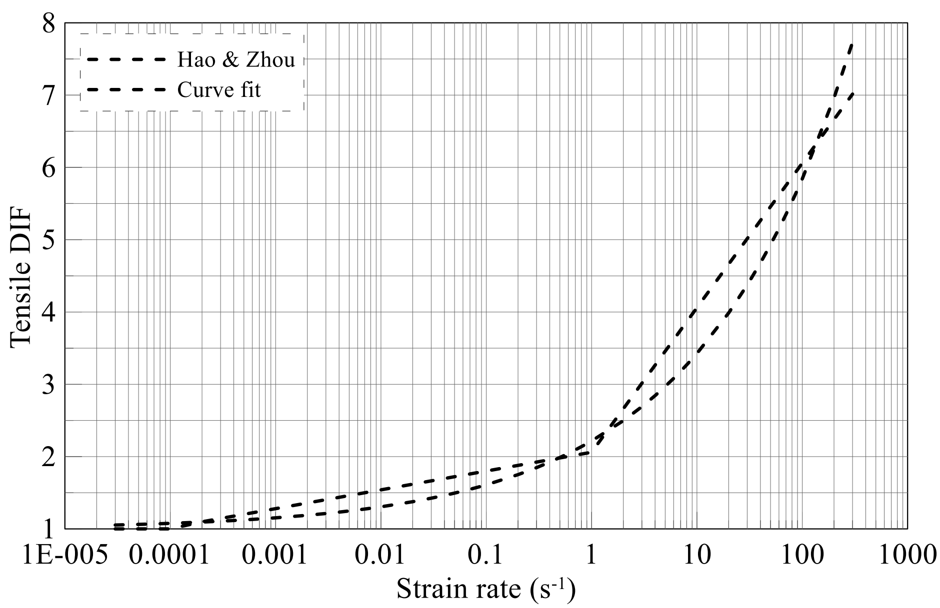

(b) Hao and Zhou formulation and best fit line

Figure B-3: Compressive and tensile DIFs, Test 8

APPENDIX C
SMOOTH PARTICLE HYDRODYNAMICS MESH-REFINEMENT STUDIES

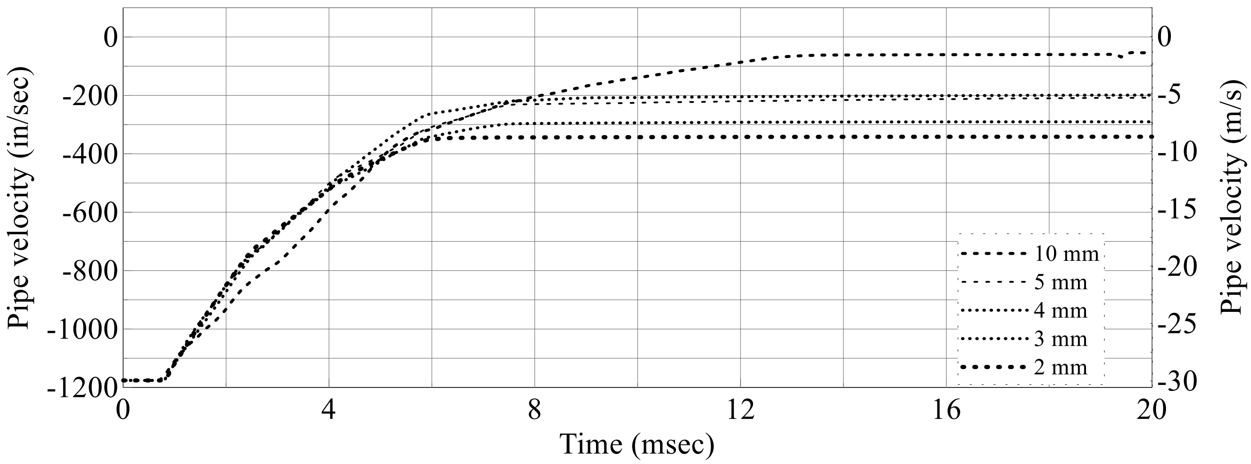

Figure C-1: Pipe velocity history, $f_c' = 2000$ psi (13.8 MPa)

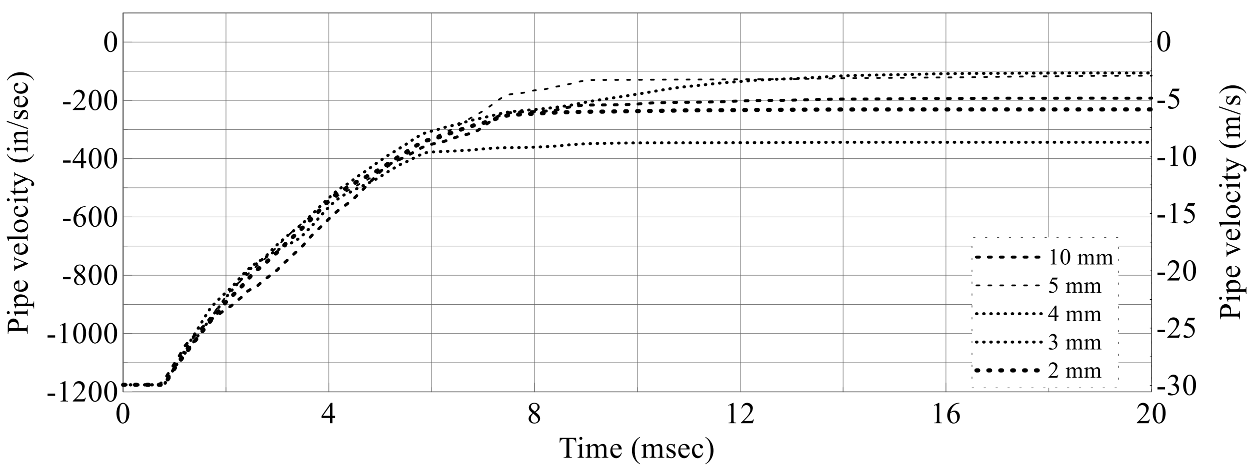

Figure C-2: Pipe velocity history, $f_c' = 3000$ psi (20.7 MPa)

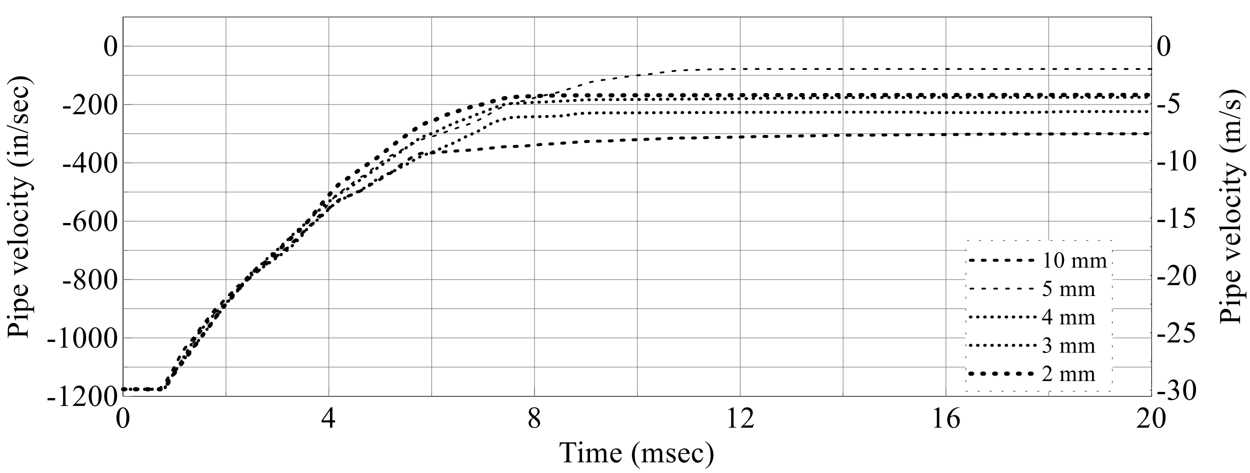

Figure C-3: Pipe velocity history, $f_c' = 3500$ psi (24.1 MPa)

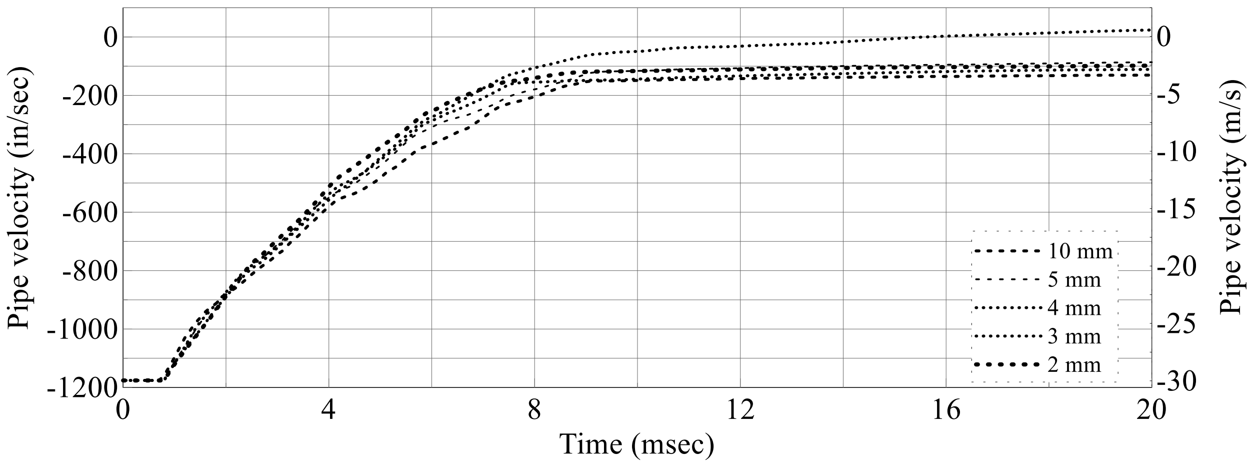

Figure C-4: Pipe velocity history, $f_c' = 4000$ psi (27.6 MPa)

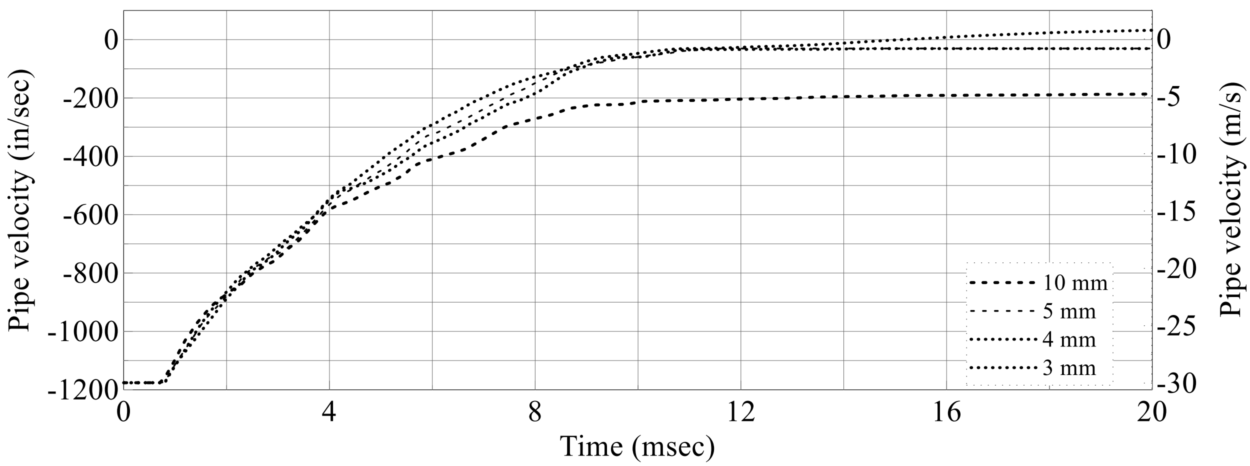

Figure C-5: Pipe velocity history, $f_c' = 4500$ psi (31.0 MPa)

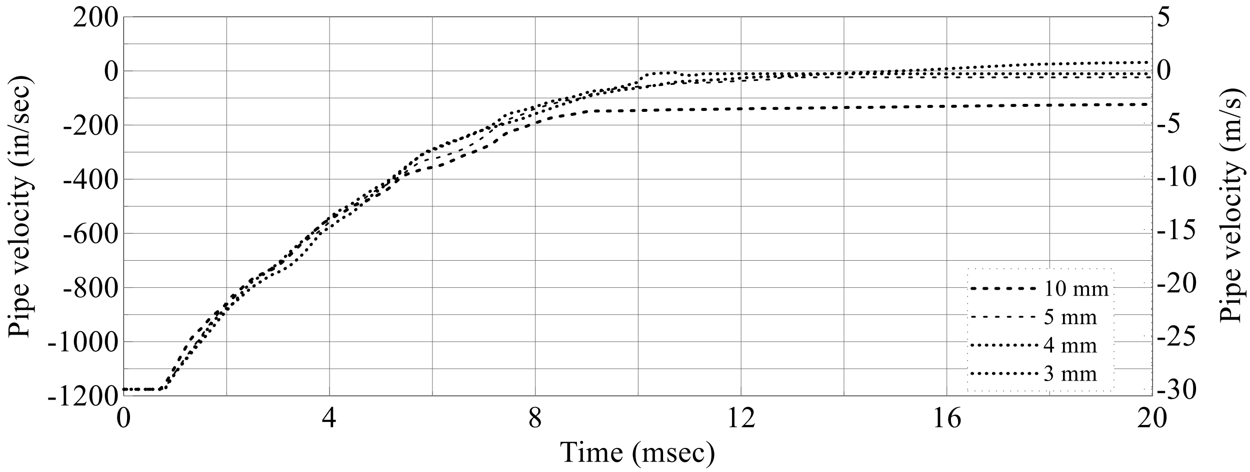

Figure C-6: Pipe velocity history, $f_c' = 6000$ psi (41.4 MPa)

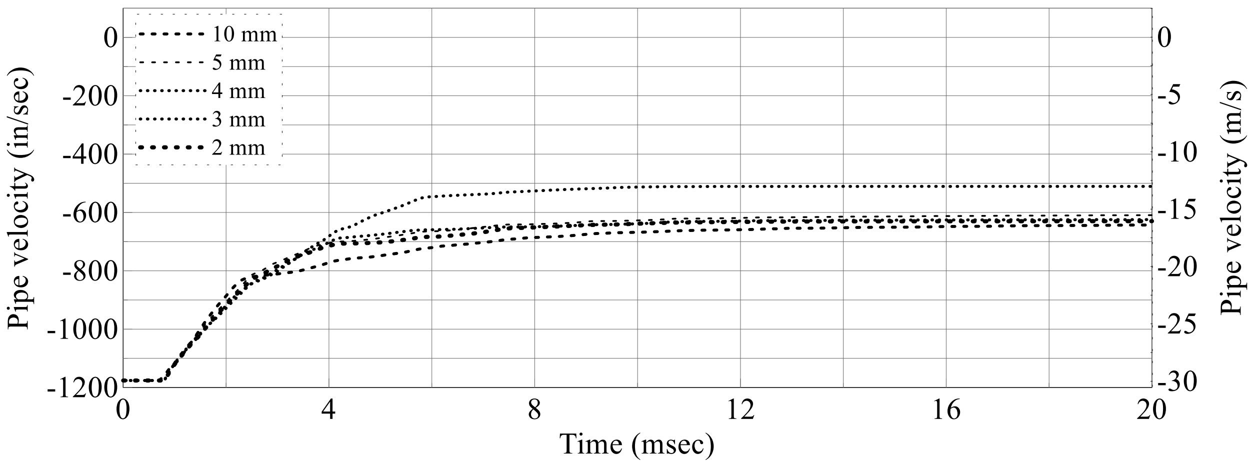

Figure C-7: Pipe velocity history, $f_t' = 180$ psi (1.24 MPa)

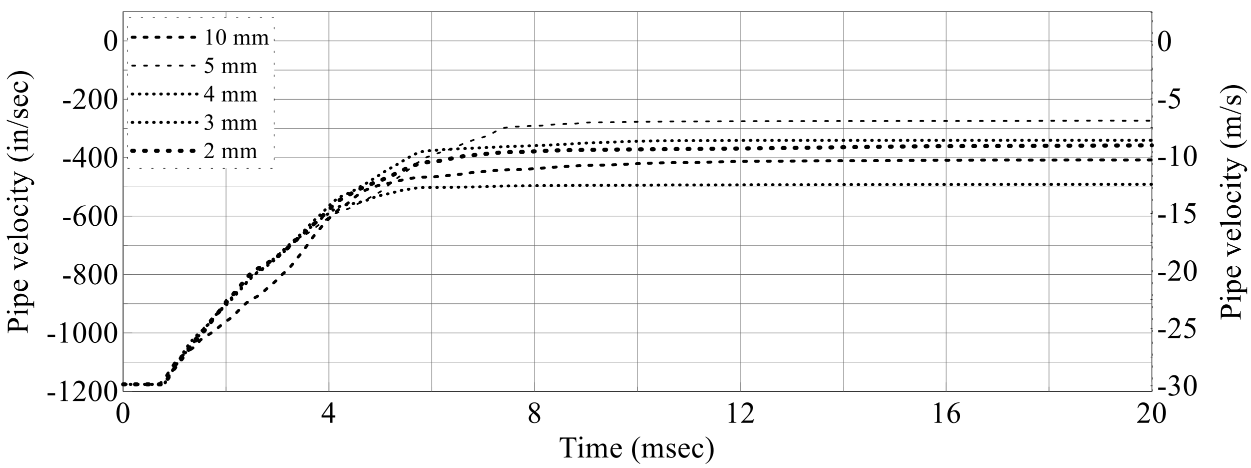

Figure C-8: Pipe velocity history, $f_t' = 360$ psi (2.48 MPa)

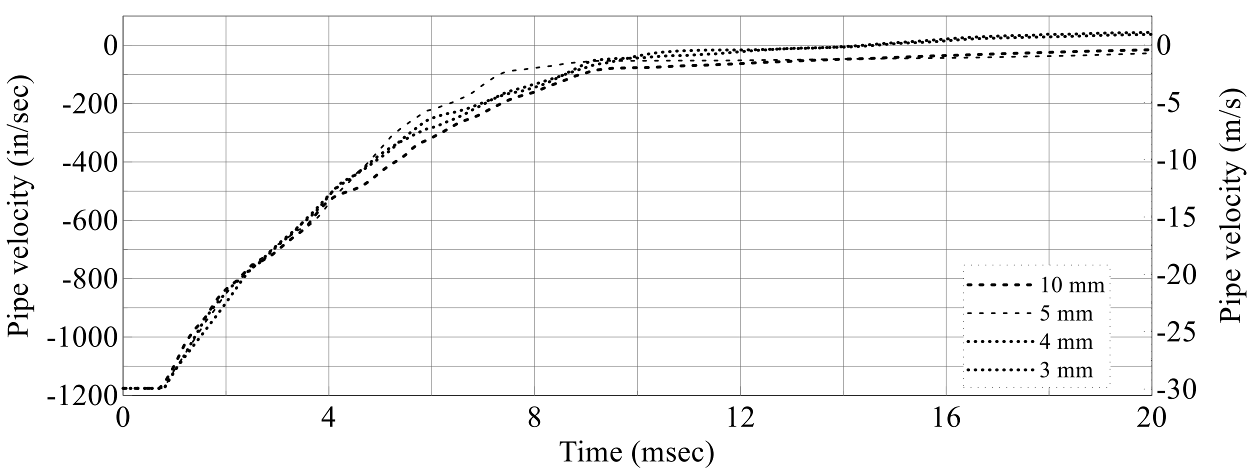

Figure C-9: Pipe velocity history, $f_t' = 540$ psi (3.72 MPa)

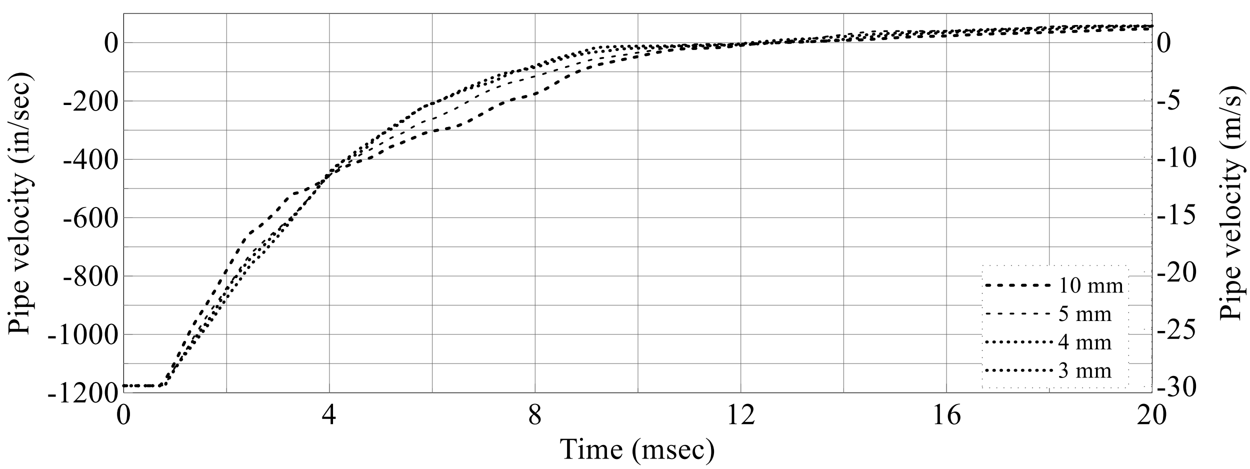

Figure C-10: Pipe velocity history, f_t' = 720 psi (4.96 MPa)

Table C-1: Estimated rates of convergence and GCI for different compressive strengths

<table>
<tr><th>Concrete particle spacing</th><th>Metric, f [1]</th><th>Compressive strength</th><th colspan="2">GCI values[2]</th></tr>
<tr><td rowspan="2">10 mm (0.39 in)</td><td rowspan="2">-1.8 m/s (-71 in/s)</td><td rowspan="10">f_c' = 13.8 MPa (2000 psi)</td><td>r_{21}</td><td>1.5</td></tr>
<tr><td>r_{32}</td><td>1.33</td></tr>
<tr><td rowspan="2">5 mm (0.2 in)</td><td rowspan="2">-5.0 m/s (-195 in/s)</td><td>e_{21}</td><td>-0.05</td></tr>
<tr><td>e_{32}</td><td>-0.36</td></tr>
<tr><td rowspan="2">4 mm (0.16 in)</td><td rowspan="2">-4.9 m/s (-192 in/s)</td><td>p</td><td>7.13</td></tr>
<tr><td>GCI_{21}</td><td>-0.003</td></tr>
<tr><td rowspan="2">3 mm (0.12 in)</td><td rowspan="2">-7.6 m/s (-300 in/s)</td><td>GCI_{32}</td><td>-0.066</td></tr>
<tr><td>f_{21}^* m/s (in/s)</td><td>-8.0 (-316)</td></tr>
<tr><td rowspan="2">2 mm (0.08 in)</td><td rowspan="2">-8.0 m/s (-315 in/s)</td><td>AC</td><td>1.05</td></tr>
<tr><td>CI_{95} m/s (in/s)</td><td>[-8.0, -7.9] ([-316, -314])</td></tr>
<tr><td>10 mm (0.39 in)</td><td>-5.1 m/s (-200 in/s)</td><td rowspan="5">f_c' = 20.7 MPa (3000 psi)</td><td colspan="2" rowspan="5">Not calculated[3]</td></tr>
<tr><td>5 mm (0.2 in)</td><td>-2.5 m/s (-100 in/s)</td></tr>
<tr><td>4 mm (0.16 in)</td><td>-8.9 m/s (-350 in/s)</td></tr>
<tr><td>3 mm (0.12 in)</td><td>-2.5 m/s (-100 in/s)</td></tr>
<tr><td>2 mm (0.08 in)</td><td>-5.1 m/s (-200 in/s)</td></tr>
<tr><td rowspan="2">10 mm (0.39 in)</td><td rowspan="2">-7.6 m/s (-301 in/s)</td><td rowspan="10">f_c' = 24.1 MPa (3500 psi)</td><td>r_{21}</td><td>1.5</td></tr>
<tr><td>r_{32}</td><td>1.33</td></tr>
<tr><td rowspan="2">5 mm (0.2 in)</td><td rowspan="2">-2.1 m/s (-82 in/s)</td><td>e_{21}</td><td>0.02</td></tr>
<tr><td>e_{32}</td><td>0.24</td></tr>
<tr><td rowspan="2">4 mm (0.16 in)</td><td rowspan="2">-4.6 m/s (-183 in/s)</td><td>p</td><td>8.73</td></tr>
<tr><td>GCI_{21}</td><td>0.001</td></tr>
<tr><td rowspan="2">3 mm (0.12 in)</td><td rowspan="2">-3.8 m/s (-148 in/s)</td><td>GCI_{32}</td><td>0.026</td></tr>
<tr><td>f_{21}^* m/s (in/s)</td><td>-3.7 (-145)</td></tr>
<tr><td rowspan="2">2 mm (0.08 in)</td><td rowspan="2">-3.7 m/s (-145 in/s)</td><td>AC</td><td>0.98</td></tr>
<tr><td>CI_{95} m/s (in/s)</td><td>[-3.69, -3.68] ([-145.1, -144.9])</td></tr>
</table>

1. Parameter used to describe damage or a response being estimated (e.g. residual velocity or penetration depth). The highlighted metrics for each compressive strength were used to make the GCI calculations.
2. All GCI parameters were defined in Section 5.4.
3. The results did not converge and the GCI was not calculated.

Table C-1: Estimated rates of convergence and GCI for different compressive strengths (contd.)

Concrete particle spacing	Metric, f	Compressive strength	GCI values	
10 mm (0.39 in)	-3.5 m/s (-136 in/s)	f_c' = 27.6 MPa (4000 psi)	Not calculated[5]	
5 mm (0.2 in)	-2.7 m/s (-105 in/s)			
4 mm (0.16 in)	-2.8 m/s (-110 in/s)			
3 mm (0.12 in)	0.6 m/s (24 in/s)[4]			
2 mm (0.08 in)	-2.8 m/s (-110 in/s)			
10 mm (0.39 in)	Perforation	f_c' = 31.0 MPa (4500 psi)	r_{21}	1.25
			r_{32}	1.33
5 mm (0.2 in)	33 mm (1.3 in)		e_{21}	-0.07
			e_{32}	-0.07
4 mm (0.16 in)	36 mm (1.4 in)		p	0.998
			GCI_{21}	-0.25
			GCI_{32}	-0.36
3 mm (0.12 in)	38 mm (1.5 in)		f_{21}^* mm (in)	46 (1.8)
			AC	1.07
			CI_{95} mm (in)	[48, 28] ([1.88, 1.1])
10 mm (0.39 in)	Perforation	f_c' = 41.4 MPa (6000 psi)	Not calculated[6]	
5 mm (0.2 in)	30 mm (1.2 in)			
4 mm (0.16 in)	30 mm (1.2 in)			
3 mm (0.12 in)	30 mm (1.2 in)			

4. The results predicted using the 3 mm mesh were discarded because the results were significantly different than those predicted using the other mesh sizes.
5. The values of GCI were not calculated because the residual velocity predicted using the 2 and 4 mm concrete particle spacings were identical, indicating a converged mesh.
6. The values of GCI were not calculated because the penetration depth predicted using the 3 and 4 mm meshes were identical, indicating a converged mesh.

Table C-2: Estimated rates of convergence and GCI for different tensile strengths

Concrete particle spacing	Metric, f	Compressive strength	GCI values	
10 mm (0.39 in)	-17.0 m/s (-671 in/s)	f_t' = 1.2 MPa (180 psi)	r_{21}	1.5
			r_{32}	1.33
5 mm (0.2 in)	-15.3 m/s (-603 in/s)		e_{21}	-0.01
			e_{32}	-0.17
4 mm (0.16 in)	-13.0 m/s (-510 in/s)		p	8.6
			GCI_{21}	-0.0006
3 mm (0.12 in)	-15.5 m/s (-611 in/s)		GCI_{32}	0.019
			f_{21}^* m/s (in/s)	-15.8 (-621)
2 mm (0.08 in)	-15.7 m/s (-620 in/s)		AC	1.02
			CI_{95} m/s (in/s)	[-15.8, -15.7] ([-620.3, -619.6])
10 mm (0.39 in)	-9.2 m/s (-363 in/s)	f_t' = 2.5 MPa (360 psi)	r_{21}	1.5
			r_{32}	1.33
5 mm (0.2 in)	-6.7 m/s (-264 in/s)		e_{21}	0.017
			e_{32}	0.331
4 mm (0.16 in)	-11.8 m/s (-466 in/s)		p	10.41
			GCI_{21}	0.0003
3 mm (0.12 in)	-8.9 m/s (-350 in/s)		GCI_{32}	0.0218
			f_{21}^* m/s (in/s)	-8.7 (-344)
2 mm (0.08 in)	-8.6 m/s (-344 in/s)		AC	0.986
			CI_{95} m/s (in/s)	[-8.74, -8.73] ([-344.1, -343.9])
10 mm (0.39 in)	Perforation	f_t' = 3.7 MPa (540 psi)	Not calculated[1]	
5 mm (0.2 in)	Perforation			
4 mm (0.16 in)	38 mm (1.5 in)			
3 mm (0.12 in)	38 mm (1.5 in)			

1. The values of GCI were not calculated because the penetration depths predicted using the 3 and 4 mm meshes were identical, indicating a converged mesh.

Table C-2: Estimated rates of convergence and GCI for different tensile strengths (contd.)

Concrete particle spacing	Metric, f	Compressive strength	GCI values
10 mm (0.39 in)	51 mm (2 in)	f_t' = 5.0 MPa (720 psi)	Not calculated[2]
5 mm (0.2 in)	51 mm (2 in)		
4 mm (0.16 in)	53 mm (2.1 in)		
3 mm (0.12 in)	53 mm (2.1 in)		

2. The values of GCI were not calculated because the penetration depths predicted using the 3 and 4 mm meshes were identical, indicating a converged mesh.

“This Page Intentionally Left Blank”

APPENDIX D
ADDITIONAL RESULTS OF A PARAMETRIC STUDY ON WIND-BORNE MISSILE IMPACT ON REINFORCED CONCRETE PANELS

Table D-1: Parametric study: simulations and results

No.	Wall thickness, t mm (in.)	Schedule 40 pipe, mm (in)	Pipe velocity, v m/s (in/s)	f_c', MPa (psi)	f_t', MPa (psi)	Conical plug diameter, mm (in)	Exit velocity, m/s (in/sec)	Scabbing of concrete
1	305 mm (12 in)	152 (6)	40 (1575)	30 (4351)	3 (435)	203 (8)	0	Yes
2		152 (6)	40 (1575)	30 (4351)	4 (580)	0	0	No
3		152 (6)	40 (1575)	30 (4351)	5 (725)	0	0	No
4		152 (6)	40 (1575)	40 (5801)	3 (435)	203 (8)	0	Yes
5		152 (6)	40 (1575)	40 (5801)	4 (580)	0	0	No
6		152 (6)	40 (1575)	40 (5801)	5 (725)	0	0	No
7		152 (6)	40 (1575)	50 (7251)	3 (435)	203 (8)	0	Yes
8		152 (6)	40 (1575)	50 (7251)	4 (580)	0	0	No
9		152 (6)	40 (1575)	50 (7251)	5 (725)	0	0	No
10		152 (6)	70 (2756)	30 (4351)	3 (435)	356 (14)	5.6 (222)	Yes
11		152 (6)	70 (2756)	30 (4351)	4 (580)	330 (13)	0	Yes
12		152 (6)	70 (2756)	30 (4351)	5 (725)	-	-	-
13		152 (6)	70 (2756)	40 (5801)	3 (435)	1829 (72)	2.1 (81)	Yes
14		152 (6)	70 (2756)	40 (5801)	4 (580)	508 (20)	0	Yes
15		152 (6)	70 (2756)	40 (5801)	5 (725)	305 (12)	0	Yes
16		152 (6)	70 (2756)	50 (7251)	3 (435)	1524 (60)	5.0 (195)	Yes
17		152 (6)	70 (2756)	50 (7251)	4 (580)	508 (20)	0	Yes
18		152 (6)	70 (2756)	50 (7251)	5 (725)	356 (14)	0	Yes
19		152 (6)	100 (3937)	30 (4351)	3 (435)	1372 (54)	55.6 (2190)	Yes
20		152 (6)	100 (3937)	30 (4351)	4 (580)	1321 (52)	23.7 (932)	Yes
21		152 (6)	100 (3937)	30 (4351)	5 (725)	1575 (62)	11.0 (435)	Yes
22		152 (6)	100 (3937)	40 (5801)	3 (435)	1067 (42)	34.0 (1340)	Yes
23		152 (6)	100 (3937)	40 (5801)	4 (580)	1372 (54)	25.4 (1000)	Yes
24		152 (6)	100 (3937)	40 (5801)	5 (725)	1676 (66)	9.0 (354)	Yes
25		152 (6)	100 (3937)	50 (7251)	3 (435)	1727 (68)	34.3 (1350)	Yes
26		152 (6)	100 (3937)	50 (7251)	4 (580)	1219 (48)	22.8 (898)	Yes
27		152 (6)	100 (3937)	50 (7251)	5 (725)	508 (20)	0	Yes
28		203 (8)	40 (1575)	30 (4351)	3 (435)	762 (30)	0	Yes
29		203 (8)	40 (1575)	30 (4351)	4 (580)	432 (17)	0	Yes
30		203 (8)	40 (1575)	30 (4351)	5 (725)	0	0	No
31		203 (8)	40 (1575)	40 (5801)	3 (435)	660 (26)	0	Yes
32		203 (8)	40 (1575)	40 (5801)	4 (580)	432 (17)	0	Yes
33		203 (8)	40 (1575)	40 (5801)	5 (725)	305 (12)	0	Yes
34		203 (8)	40 (1575)	50 (7251)	3 (435)	1321 (52)	0.17 (6.6)	Yes
35		203 (8)	40 (1575)	50 (7251)	4 (580)	460 (18)	0	Yes
36		203 (8)	40 (1575)	50 (7251)	5 (725)	356 (14)	0	Yes
37		203 (8)	70 (2756)	30 (4351)	3 (435)	1270 (50)	32.8 (1290)	Yes
38		203 (8)	70 (2756)	30 (4351)	4 (580)	1321 (52)	17.4 (684)	Yes
39		203 (8)	70 (2756)	30 (4351)	5 (725)	1143 (45)	6.6 (259)	Yes
40		203 (8)	70 (2756)	40 (5801)	3 (435)	2032 (80)	31.8 (1250)	Yes
41		203 (8)	70 (2756)	40 (5801)	4 (580)	1778 (70)	16.5 (651)	Yes
42		203 (8)	70 (2756)	40 (5801)	5 (725)	1880 (74)	6.1 (240)	Yes
43		203 (8)	70 (2756)	50 (7251)	3 (435)	2184 (86)	30.0 (1180)	Yes
44		203 (8)	70 (2756)	50 (7251)	4 (580)	1626 (64)	15.2 (600)	Yes
45		203 (8)	70 (2756)	50 (7251)	5 (725)	2032 (80)	9.0 (353)	Yes
46		203 (8)	100 (3937)	30 (4351)	3 (435)	1524 (60)	56.1 (2210)	Yes
47		203 (8)	100 (3937)	30 (4351)	4 (580)	1372 (54)	55.4 (2180)	Yes
48		203 (8)	100 (3937)	30 (4351)	5 (725)	1524 (60)	38.9 (1530)	Yes
49		203 (8)	100 (3937)	40 (5801)	3 (435)	1676 (66)	57.7 (2270)	Yes

Table D-1: Parametric study: simulations and results (contd.)

50		203 (8)	100 (3937)	40 (5801)	4 (580)	1676 (66)	53.8 (2120)	Yes
51		203 (8)	100 (3937)	40 (5801)	5 (725)	2032 (80)	30.5 (1200)	Yes
52		203 (8)	100 (3937)	50 (7251)	3 (435)	2083 (82)	52.3 (2060)	Yes
53		203 (8)	100 (3937)	50 (7251)	4 (580)	-	-	-
54		203 (8)	100 (3937)	50 (7251)	5 (725)	2032 (80)	35.8 (1410)	Yes
55		254 (10)	40 (1575)	30 (4351)	3 (435)	2083 (82)	8.3 (325)	Yes
56		254 (10)	40 (1575)	30 (4351)	4 (580)	1676 (66)	1.0 (40)	Yes
57		254 (10)	40 (1575)	30 (4351)	5 (725)	914 (36)	0	Yes
58		254 (10)	40 (1575)	40 (5801)	3 (435)	2083 (82)	6.2 (243)	Yes
59		254 (10)	40 (1575)	40 (5801)	4 (580)	-	0.34 (13.2)	Yes
60		254 (10)	40 (1575)	40 (5801)	5 (725)	889 (35)	0	Yes
61		254 (10)	40 (1575)	50 (7251)	3 (435)	1778 (70)	5.4 (212)	Yes
62		254 (10)	40 (1575)	50 (7251)	4 (580)	-	0.38 (15)	Yes
63		254 (10)	40 (1575)	50 (7251)	5 (725)	914 (36)	0	Yes
64		254 (10)	70 (2756)	30 (4351)	3 (435)	1524 (60)	41.9 (1650)	Yes
65		254 (10)	70 (2756)	30 (4351)	4 (580)	1372 (54)	31.8 (1250)	Yes
66		254 (10)	70 (2756)	30 (4351)	5 (725)	1626 (64)	23.6 (928)	Yes
67		254 (10)	70 (2756)	40 (5801)	3 (435)	2286 (90)	38.1 (1500)	Yes
68		254 (10)	70 (2756)	40 (5801)	4 (580)	2032 (80)	32.3 (1270)	Yes
69		254 (10)	70 (2756)	40 (5801)	5 (725)	1778 (70)	27.2 (1070)	Yes
70		254 (10)	70 (2756)	50 (7251)	3 (435)	2235 (88)	36.8 (1450)	Yes
71		254 (10)	70 (2756)	50 (7251)	4 (580)	2083 (82)	23.4 (920)	Yes
72		254 (10)	70 (2756)	50 (7251)	5 (725)	1880 (74)	20.5 (809)	Yes
73		254 (10)	100 (3937)	30 (4351)	3 (435)	1524 (60)	67.3 (2650)	Yes
74		254 (10)	100 (3937)	30 (4351)	4 (580)	1372 (54)	63.2 (2490)	Yes
75		254 (10)	100 (3937)	30 (4351)	5 (725)	1168 (46)	59.7 (2350)	Yes
76		254 (10)	100 (3937)	40 (5801)	3 (435)	1626 (64)	64.3 (2530)	Yes
77		254 (10)	100 (3937)	40 (5801)	4 (580)	1524 (60)	60.5 (2380)	Yes
78		254 (10)	100 (3937)	40 (5801)	5 (725)	1397 (55)	54.9 (2160)	Yes
79		254 (10)	100 (3937)	50 (7251)	3 (435)	1422 (56)	64.0 (2520)	Yes
80		254 (10)	100 (3937)	50 (7251)	4 (580)	2184 (86)	56.4 (2220)	Yes
81		254 (10)	100 (3937)	50 (7251)	5 (725)	2032 (80)	52.1 (2050)	Yes
82	381 mm (15 in)	152 (6)	40 (1575)	30 (4351)	3 (435)	0	0	No
83		152 (6)	40 (1575)	30 (4351)	5 (725)	0	0	No
84		152 (6)	40 (1575)	50 (7251)	3 (435)	0	0	No
85		152 (6)	40 (1575)	50 (7251)	5 (725)	0	0	No
86		152 (6)	100 (3937)	30 (4351)	3 (435)	406 (16)	0	Yes
87		152 (6)	100 (3937)	30 (4351)	5 (725)	0	0	No
88		152 (6)	100 (3937)	50 (7251)	3 (435)	711 (28)	0	Yes
89		152 (6)	100 (3937)	50 (7251)	5 (725)	0	0	No
90		203 (8)	40 (1575)	30 (4351)	3 (435)	0	0	No
91		203 (8)	40 (1575)	30 (4351)	5 (725)	0	0	No
92		203 (8)	40 (1575)	50 (7251)	3 (435)	0	0	No
93		203 (8)	40 (1575)	50 (7251)	5 (725)	0	0	No
94		203 (8)	100 (3937)	30 (4351)	3 (435)	1676 (66)	43.9 (1730)	Yes
95		203 (8)	100 (3937)	30 (4351)	5 (725)	1930 (76)	11.9 (470)	Yes
96		203 (8)	100 (3937)	50 (7251)	3 (435)	1778 (70)	32.5 (1280)	Yes
97		203 (8)	100 (3937)	50 (7251)	5 (725)	2540 (100)	5.5 (217)	Yes
98		254 (10)	40 (1575)	30 (4351)	3 (435)	762 (30)	0	Yes
99		254 (10)	40 (1575)	30 (4351)	5 (725)	0	0	No
100		254 (10)	40 (1575)	50 (7251)	3 (435)	762 (30)	0	Yes
101		254 (10)	40 (1575)	50 (7251)	5 (725)	0	0	No

Table D-1: Parametric study: simulations and results (contd.)

102		254 (10)	100 (3937)	30 (4351)	3 (435)	1676 (66)	49.5 (1950)	Yes
103		254 (10)	100 (3937)	30 (4351)	5 (725)	1422 (56)	27.2 (1070)	Yes
104		254 (10)	100 (3937)	50 (7251)	3 (435)	1676 (66)	39.1 (1540)	Yes
105		254 (10)	100 (3937)	50 (7251)	5 (725)	2032 (80)	29.5 (1160)	Yes
106	460 mm (18 in)	152 (6)	40 (1575)	30 (4351)	3 (435)	0	0	No
107		152 (6)	40 (1575)	30 (4351)	5 (725)	0	0	No
108		152 (6)	40 (1575)	50 (7251)	3 (435)	0	0	No
109		152 (6)	40 (1575)	50 (7251)	5 (725)	0	0	No
110		152 (6)	100 (3937)	30 (4351)	3 (435)	0	0	No
111		152 (6)	100 (3937)	30 (4351)	5 (725)	0	0	No
112		152 (6)	100 (3937)	50 (7251)	3 (435)	0	0	No
113		152 (6)	100 (3937)	50 (7251)	5 (725)	0	0	No
114		203 (8)	40 (1575)	30 (4351)	3 (435)	0	0	No
115		203 (8)	40 (1575)	30 (4351)	5 (725)	0	0	No
116		203 (8)	40 (1575)	50 (7251)	3 (435)	0	0	No
117		203 (8)	40 (1575)	50 (7251)	5 (725)	0	0	No
118		203 (8)	100 (3937)	30 (4351)	3 (435)	1727 (68)	18.3 (721)	Yes
119		203 (8)	100 (3937)	30 (4351)	5 (725)	0	0	No
120		203 (8)	100 (3937)	50 (7251)	3 (435)	2794 (110)	7.0 (275)	Yes
121		203 (8)	100 (3937)	50 (7251)	5 (725)	0	0	No
122		254 (10)	40 (1575)	30 (4351)	3 (435)	0	0	No
123		254 (10)	40 (1575)	30 (4351)	5 (725)	0	0	No
124		254 (10)	40 (1575)	50 (7251)	3 (435)	0	0	No
125		254 (10)	40 (1575)	50 (7251)	5 (725)	0	0	No
126		254 (10)	100 (3937)	30 (4351)	3 (435)	2184 (86)	31.8 (1250)	Yes
127		254 (10)	100 (3937)	30 (4351)	5 (725)	-	-	-
128		254 (10)	100 (3937)	50 (7251)	3 (435)	2032 (80)	28.2 (1110)	Yes
129		254 (10)	100 (3937)	50 (7251)	5 (725)	1270 (50)	0.34 (13.5)	Yes
130	650 mm (25.6 in)	152 (6)	40 (1575)	30 (4351)	3 (435)	0	0	No
131		152 (6)	40 (1575)	30 (4351)	5 (725)	0	0	No
132		152 (6)	40 (1575)	50 (7251)	3 (435)	0	0	No
133		152 (6)	40 (1575)	50 (7251)	5 (725)	0	0	No
134		152 (6)	100 (3937)	30 (4351)	3 (435)	0	0	No
135		152 (6)	100 (3937)	30 (4351)	5 (725)	0	0	No
136		152 (6)	100 (3937)	50 (7251)	3 (435)	0	0	No
137		152 (6)	100 (3937)	50 (7251)	5 (725)	0	0	No
138		203 (8)	40 (1575)	30 (4351)	3 (435)	0	0	No
139		203 (8)	40 (1575)	30 (4351)	5 (725)	0	0	No
140		203 (8)	40 (1575)	50 (7251)	3 (435)	0	0	No
141		203 (8)	40 (1575)	50 (7251)	5 (725)	0	0	No
142		203 (8)	100 (3937)	30 (4351)	3 (435)	203 (8)	0	Yes
143		203 (8)	100 (3937)	30 (4351)	5 (725)	0	0	No
144		203 (8)	100 (3937)	50 (7251)	3 (435)	0	0	No
145		203 (8)	100 (3937)	50 (7251)	5 (725)	0	0	No
146		254 (10)	40 (1575)	30 (4351)	3 (435)	0	0	No
147		254 (10)	40 (1575)	30 (4351)	5 (725)	0	0	No
148		254 (10)	40 (1575)	50 (7251)	3 (435)	0	0	No
149		254 (10)	40 (1575)	50 (7251)	5 (725)	0	0	No
150		254 (10)	100 (3937)	30 (4351)	3 (435)	445 (17.5)	0	Yes
151		254 (10)	100 (3937)	30 (4351)	5 (725)	0	0	No
152		254 (10)	100 (3937)	50 (7251)	3 (435)	508 (20)	0	Yes
153		254 (10)	100 (3937)	50 (7251)	5 (725)	0	0	No

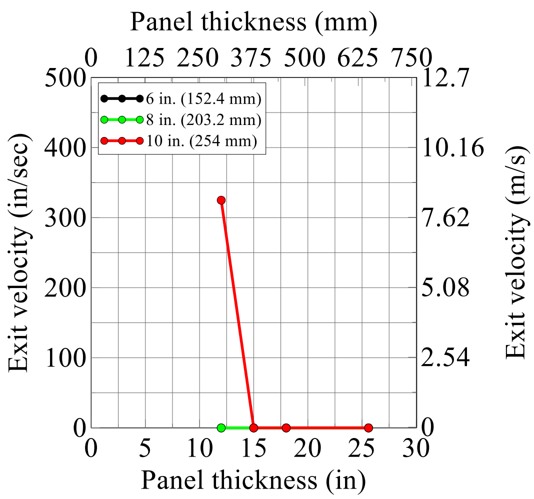

(a) f_c' =4351 psi (30 MPa), f_t' =435 psi (3 MPa)

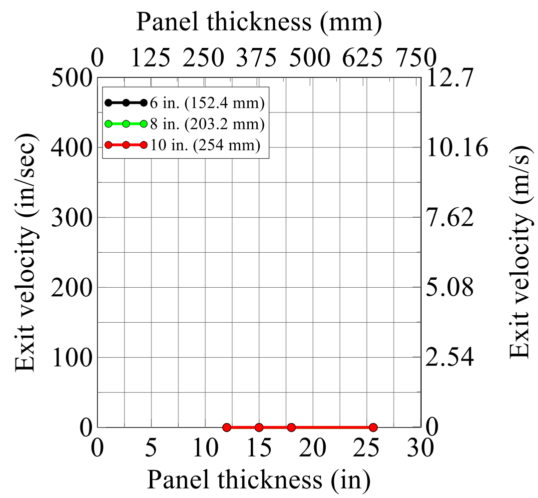

(b) f_c' =4351 psi (30 MPa), f_t' =725 psi (5 MPa)

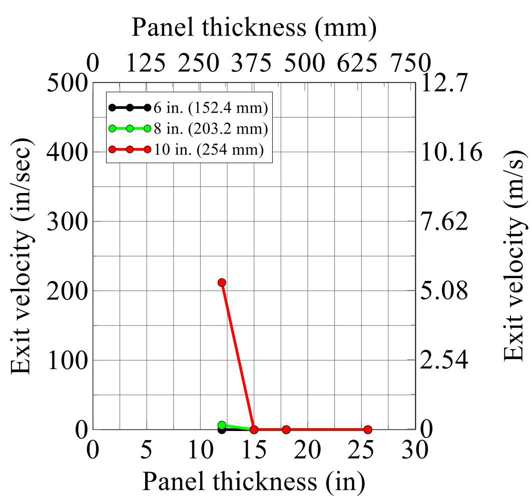

(c) f_c' =7251 psi (50 MPa), f_t' =435 psi (3 MPa)

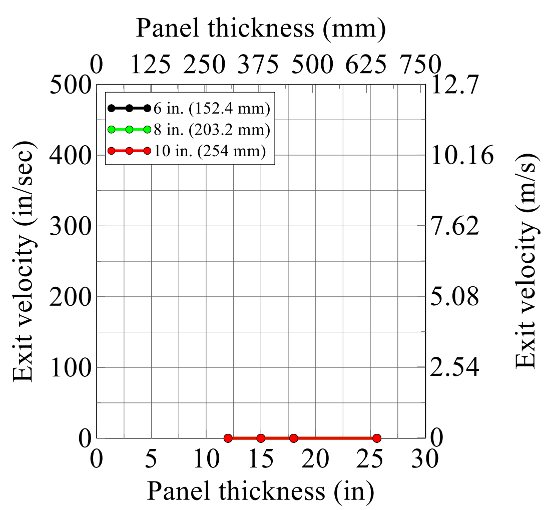

(d) f_c' =7251 psi (50 MPa), f_t' =725 psi (5 MPa)

Figure D-1: Exit velocity of Schedule 40 pipe as a function of panel thickness, v =1575 in/sec (40 m/sec), 12-inch (305 mm) thick panel, MAT072R3

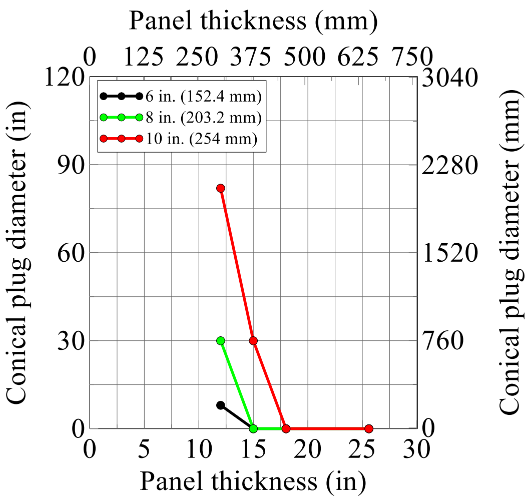

(a) f_c' =4351 psi (30 MPa), f_t' =435 psi (3 MPa)

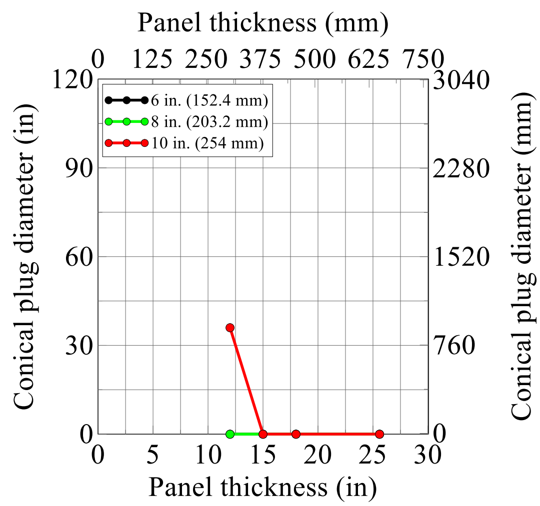

(b) f_c' =4351 psi (30 MPa), f_t' =725 psi (5 MPa)

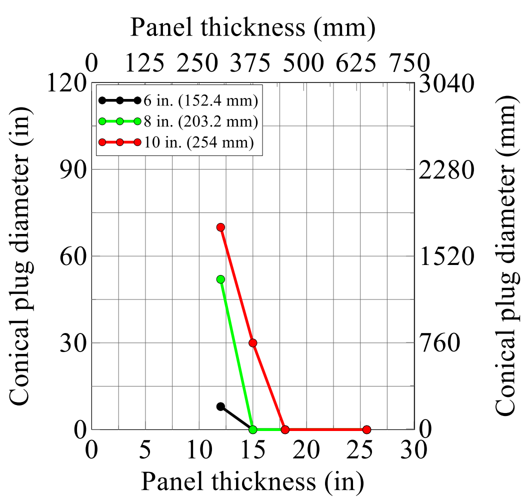

(c) f_c' =7251 psi (50 MPa), f_t' =435 psi (3 MPa)

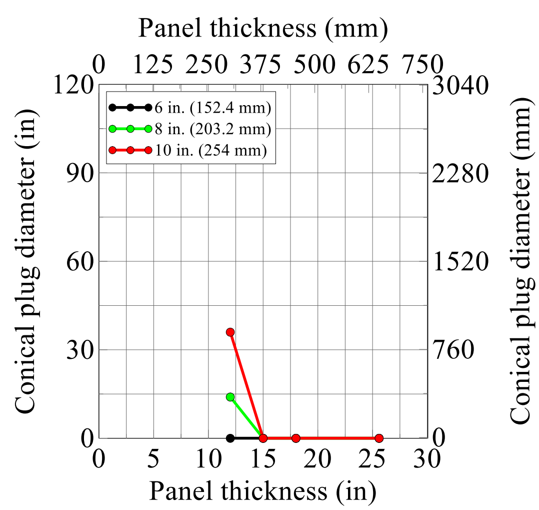

(d) f_c' =7251 psi (50 MPa), f_t' =725 psi (5 MPa)

Figure D-2: Conical plug diameter as a function of panel thickness, v=1575 in/sec (40 m/sec), 12-inch (305 mm) thick panel, MAT072R3

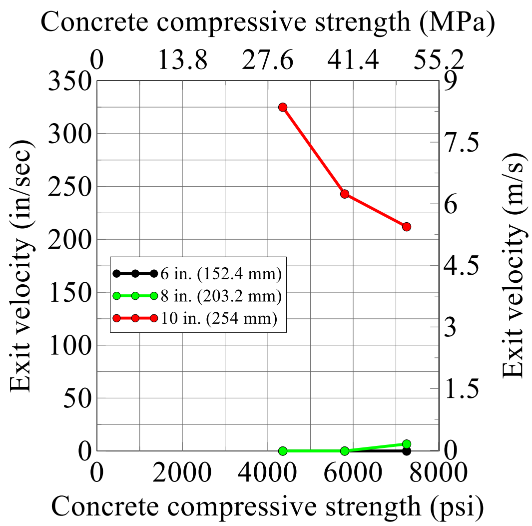

(a) f_t' =435 psi (3 MPa)

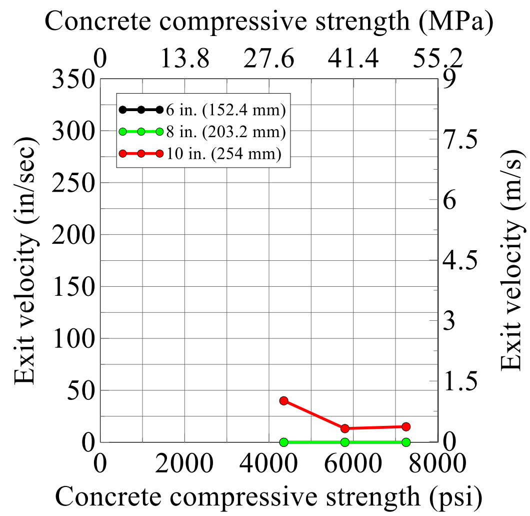

(b) f_t' =580 psi (4 MPa)

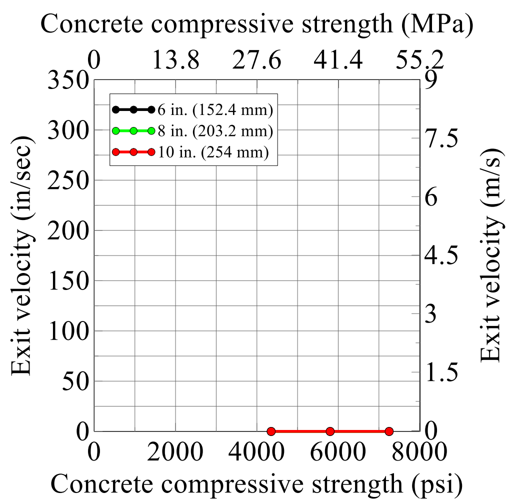

(c) f_t' =725 psi (5 MPa)

Figure D-3: Exit velocity of Schedule 40 pipe as a function of concrete compressive strength, v =1575 in/sec (40 m/sec), 12-inch (305 mm) thick panel, MAT072R3

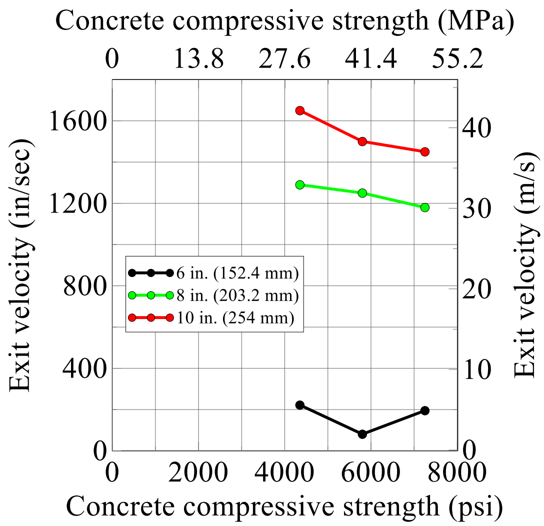

(a) f_t'=435 psi (3 MPa)

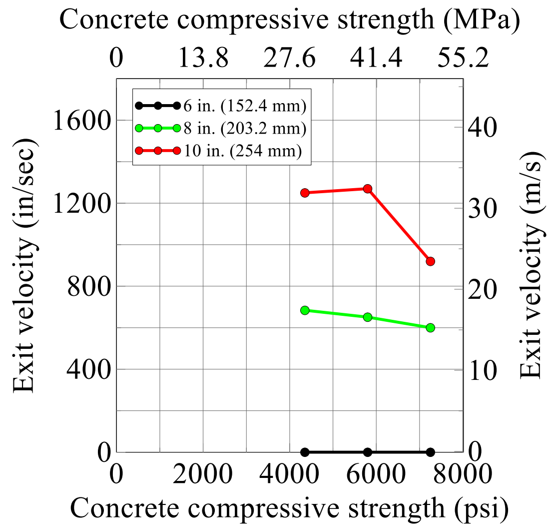

(b) f_t'=580 psi (4 MPa)

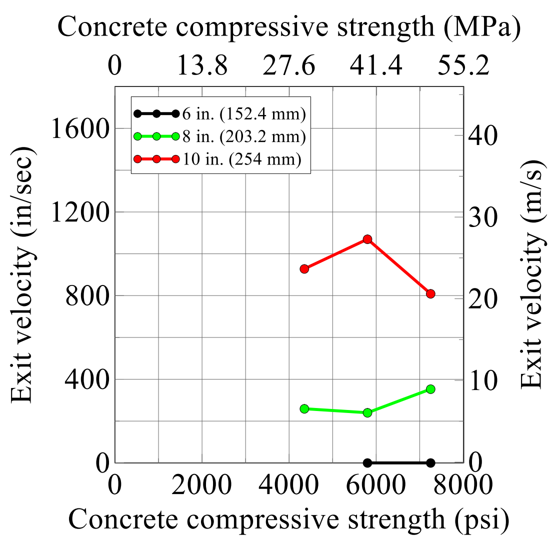

(c) f_t'=725 psi (5 MPa)

Figure D-4: Exit velocity of Schedule 40 pipe as a function of concrete compressive strength, v=2756 in/sec (70 m/sec), 12-inch (305 mm) thick panel, MAT072R3

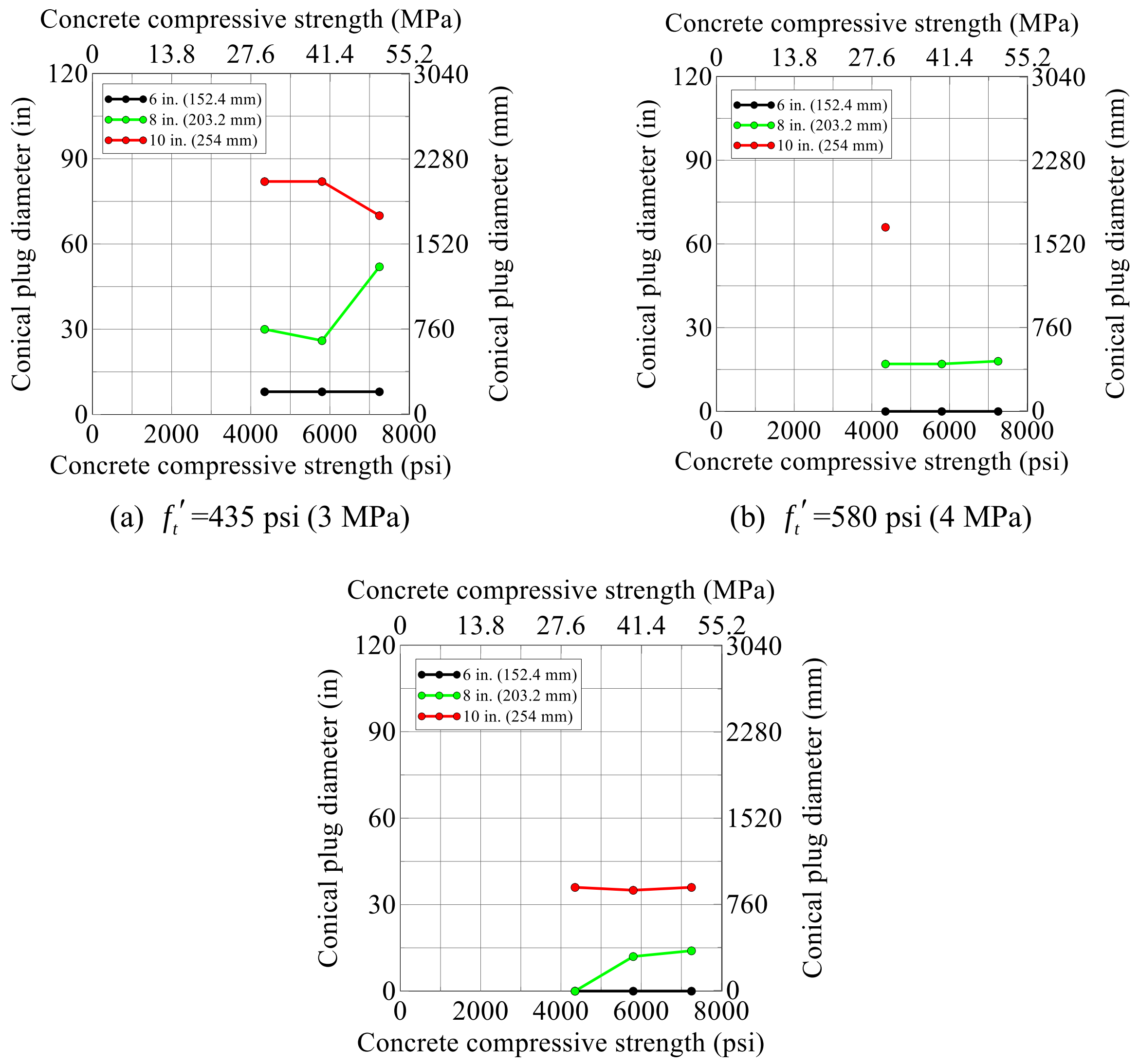

(a) f_t' =435 psi (3 MPa)

(b) f_t' =580 psi (4 MPa)

(c) f_t' =725 psi (5 MPa)

Figure D-5: Conical plug diameter as a function of concrete compressive strength, v =1575 in/sec (40 m/sec), 12-inch (305 mm) thick panel, MAT072R3

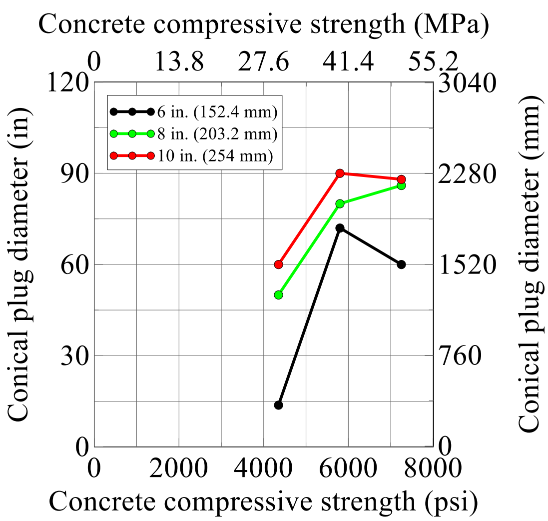

(a) f_t' =435 psi (3 MPa)

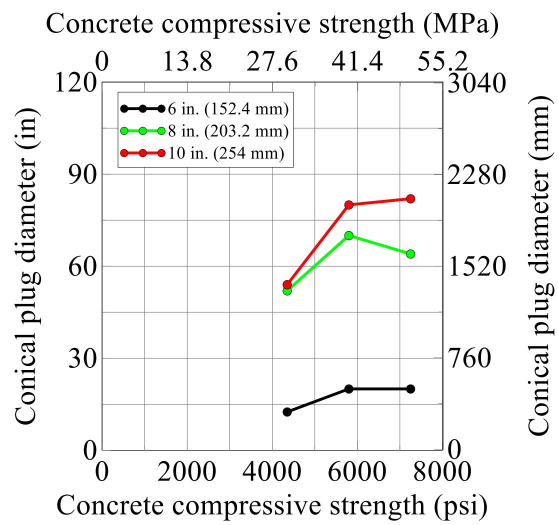

(b) f_t' =580 psi (4 MPa)

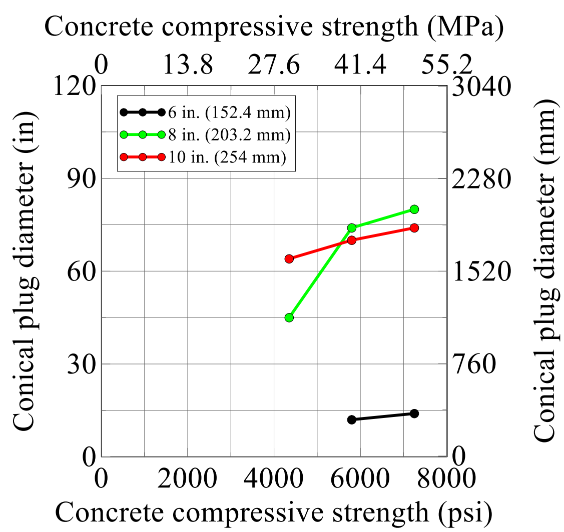

(c) f_t' =725 psi (5 MPa)

Figure D-6: Conical plug diameter as a function of concrete compressive strength, v =2756 in/sec (70 m/sec), 12-inch (305 mm) thick panel, MAT072R3

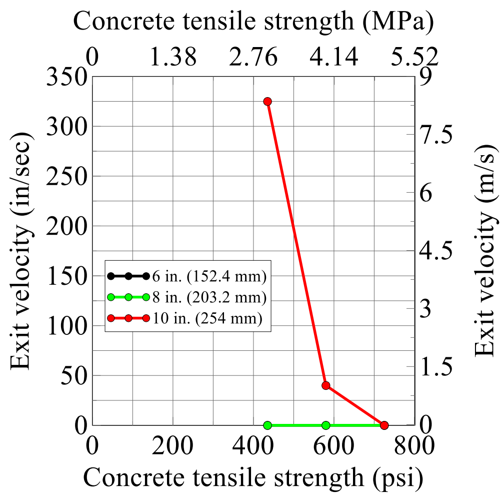

(a) f_c' =4351 psi (30 MPa)

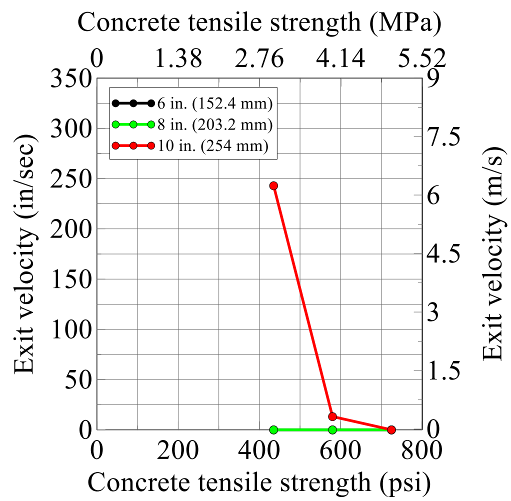

(b) f_c' =5801 psi (40 MPa)

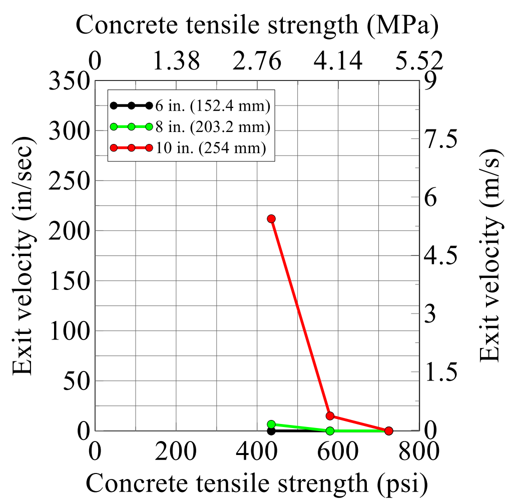

(c) f_c' =7251 psi (50 MPa)

Figure D-7: Exit velocity of Schedule 40 pipe as a function of concrete tensile strength, v =1575 in/sec (40 m/sec), 12-inch (305 mm) thick panel, MAT072R3

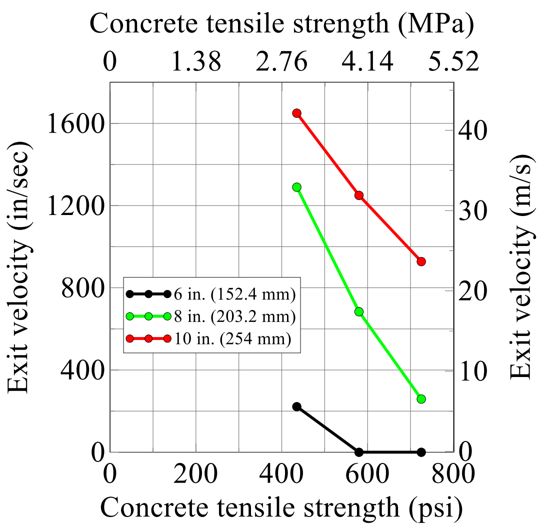

(a) f_c' =4351 psi (30 MPa)

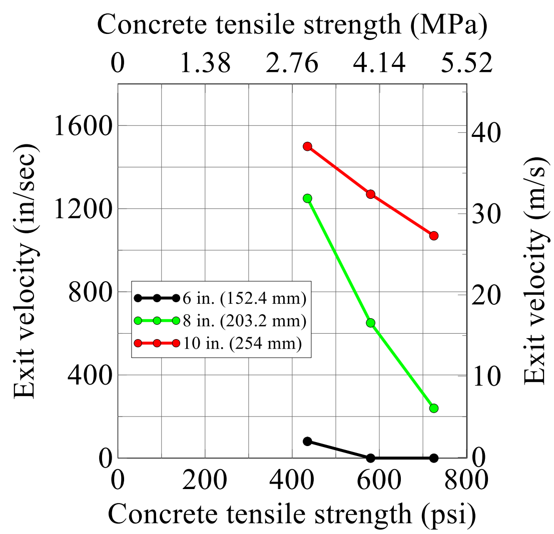

(b) f_c' =5801 psi (40 MPa)

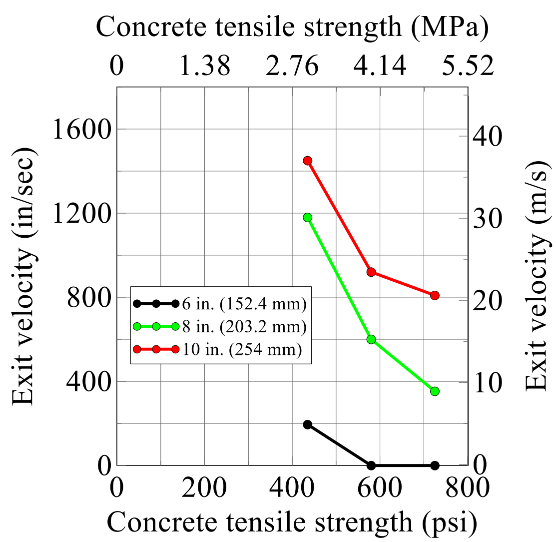

(c) f_c' =7251 psi (50 MPa)

Figure D-8: Exit velocity of Schedule 40 pipe as a function of concrete tensile strength, v =2756 in/sec (70 m/sec), 12-inch (305 mm) thick panel, MAT072R3

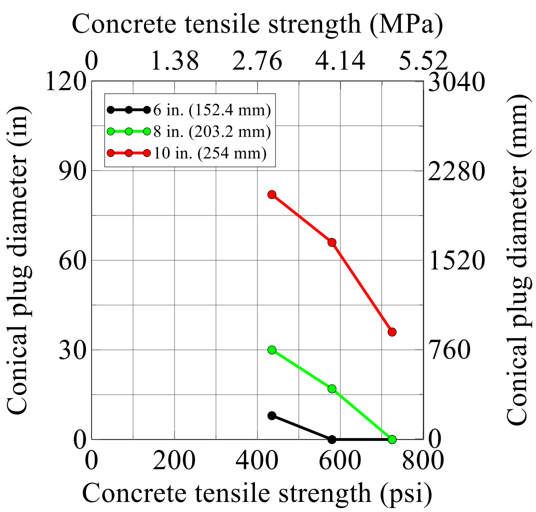

(a) f_c'=4351 psi (30 MPa)

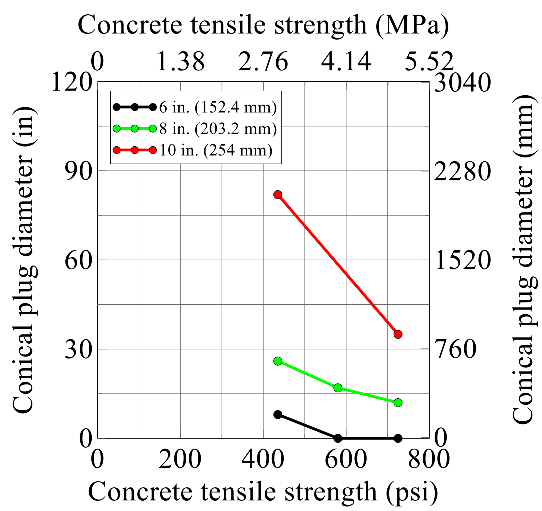

(b) f_c'=5801 psi (40 MPa)

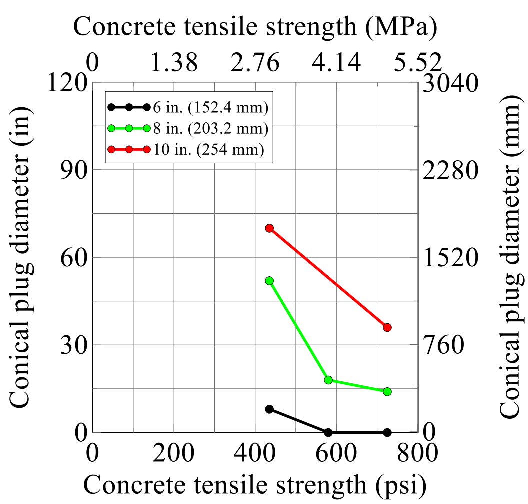

(c) f_c'=7251 psi (50 MPa)

Figure D-9: Conical plug diameter as a function of concrete tensile strength, v=1575 in/sec (40 m/sec), 12-inch (305 mm) thick panel, MAT072R3

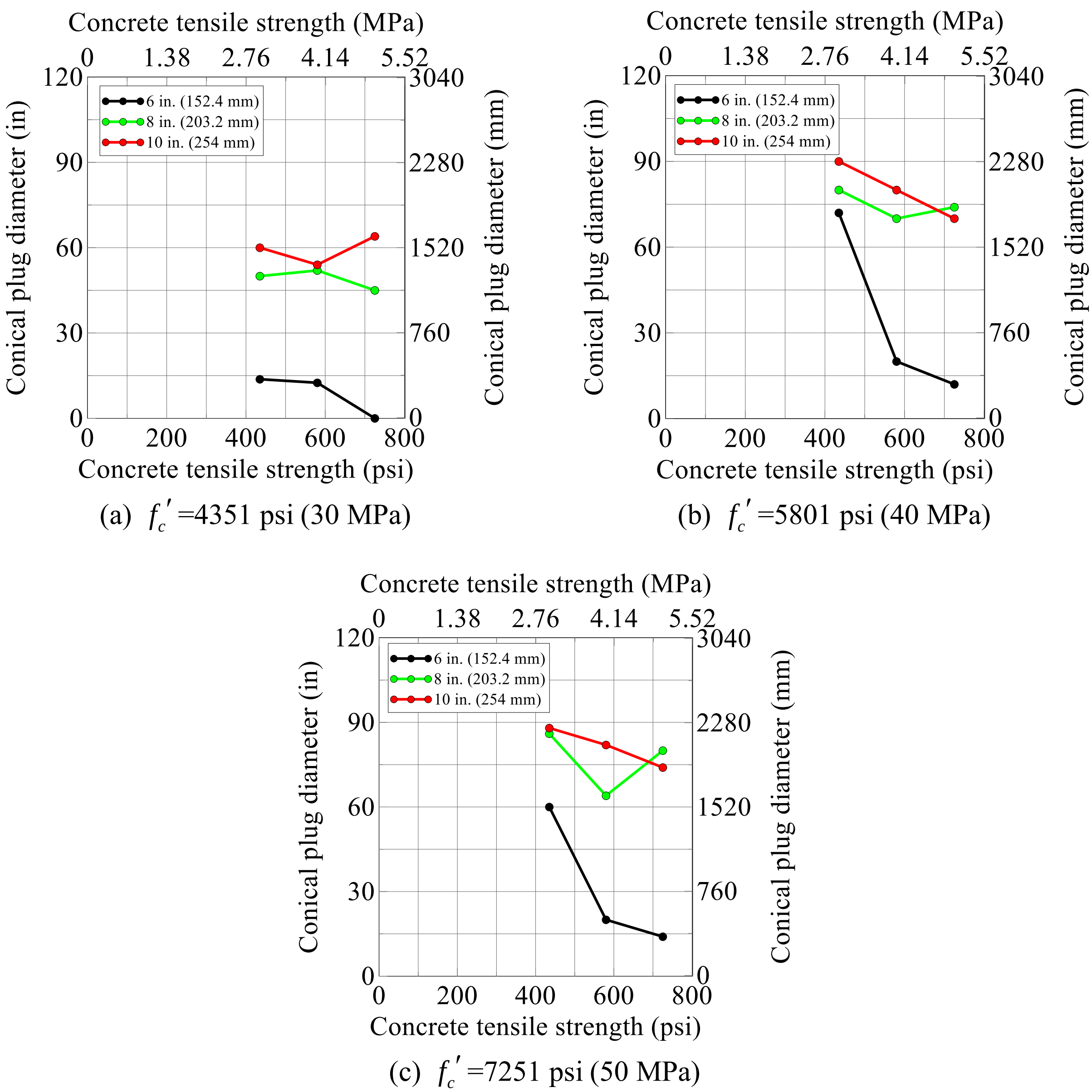

Figure D-10: Conical plug diameter as a function of concrete tensile strength, v=2756 in/sec (70 m/sec), 12-inch (305 mm) thick panel, MAT072R3

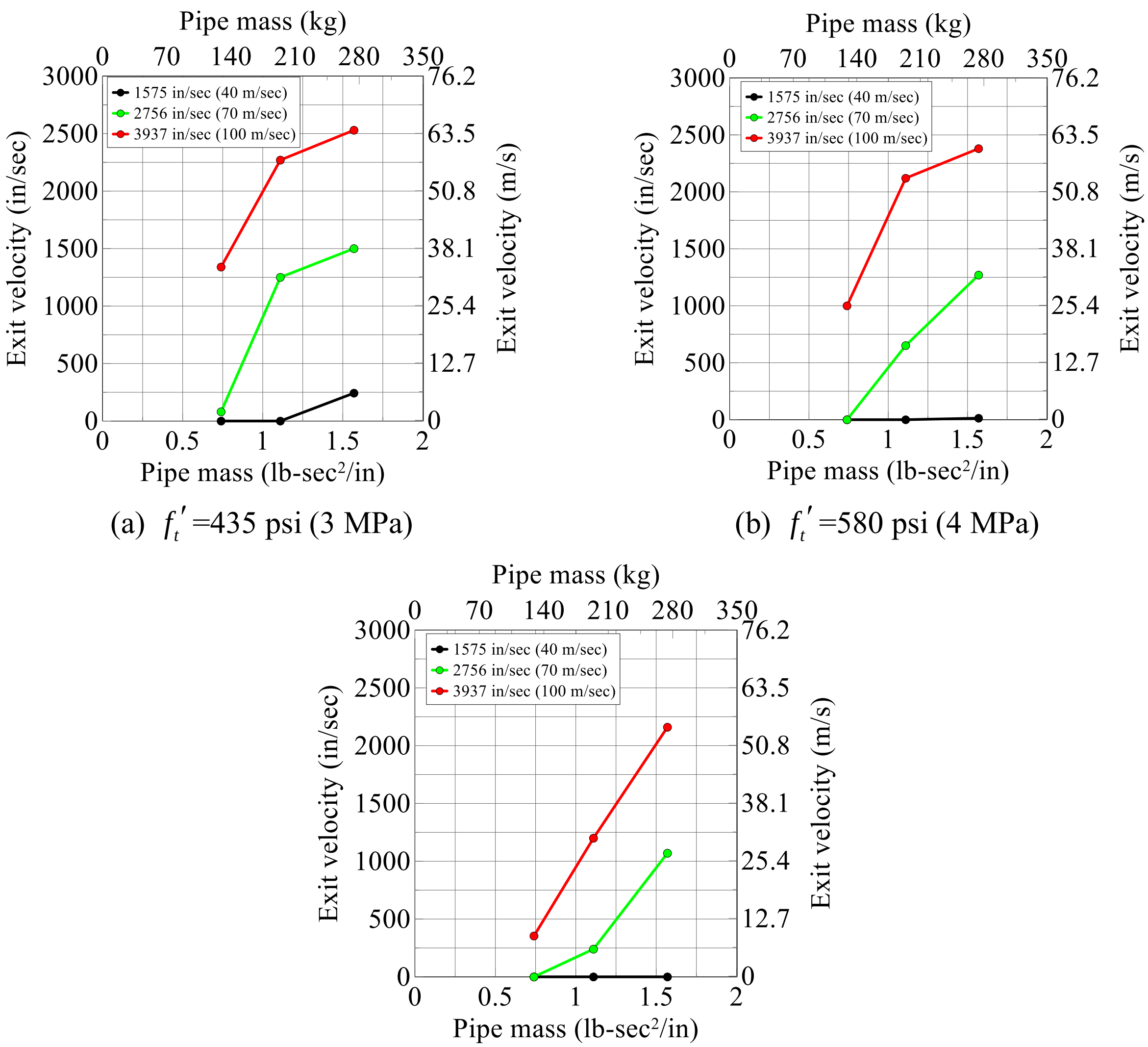

(a) f_t' =435 psi (3 MPa)

(b) f_t' =580 psi (4 MPa)

(c) f_t' =725 psi (5 MPa)

Figure D-11: Pipe exit velocity as a function of Schedule 40 pipe mass, f_c' =5801 psi (30 MPa), 12-inch (305 mm) thick panel, MAT072R3

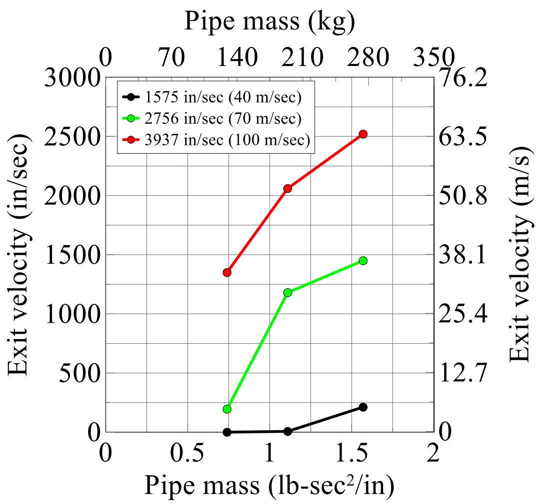

(a) f_t' =435 psi (3 MPa)

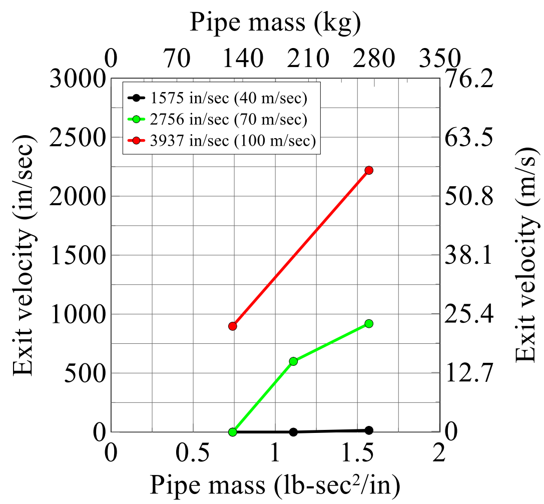

(b) f_t' =580 psi (4 MPa)

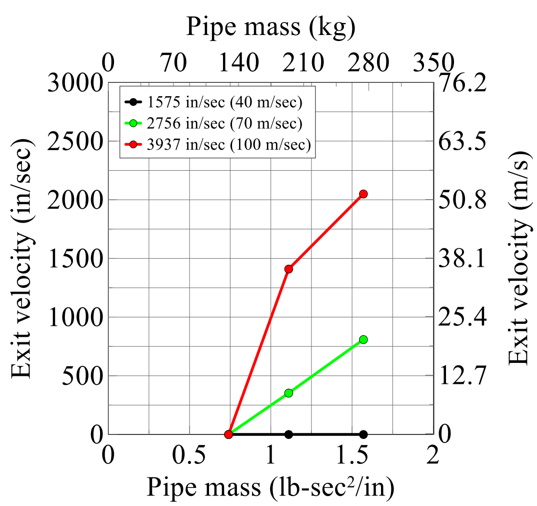

(c) f_t' =725 psi (5 MPa)

Figure D-12: Pipe exit velocity as a function of Schedule 40 pipe mass, f_c' =7251 psi (30 MPa), 12-inch (305 mm) thick panel, MAT072R3

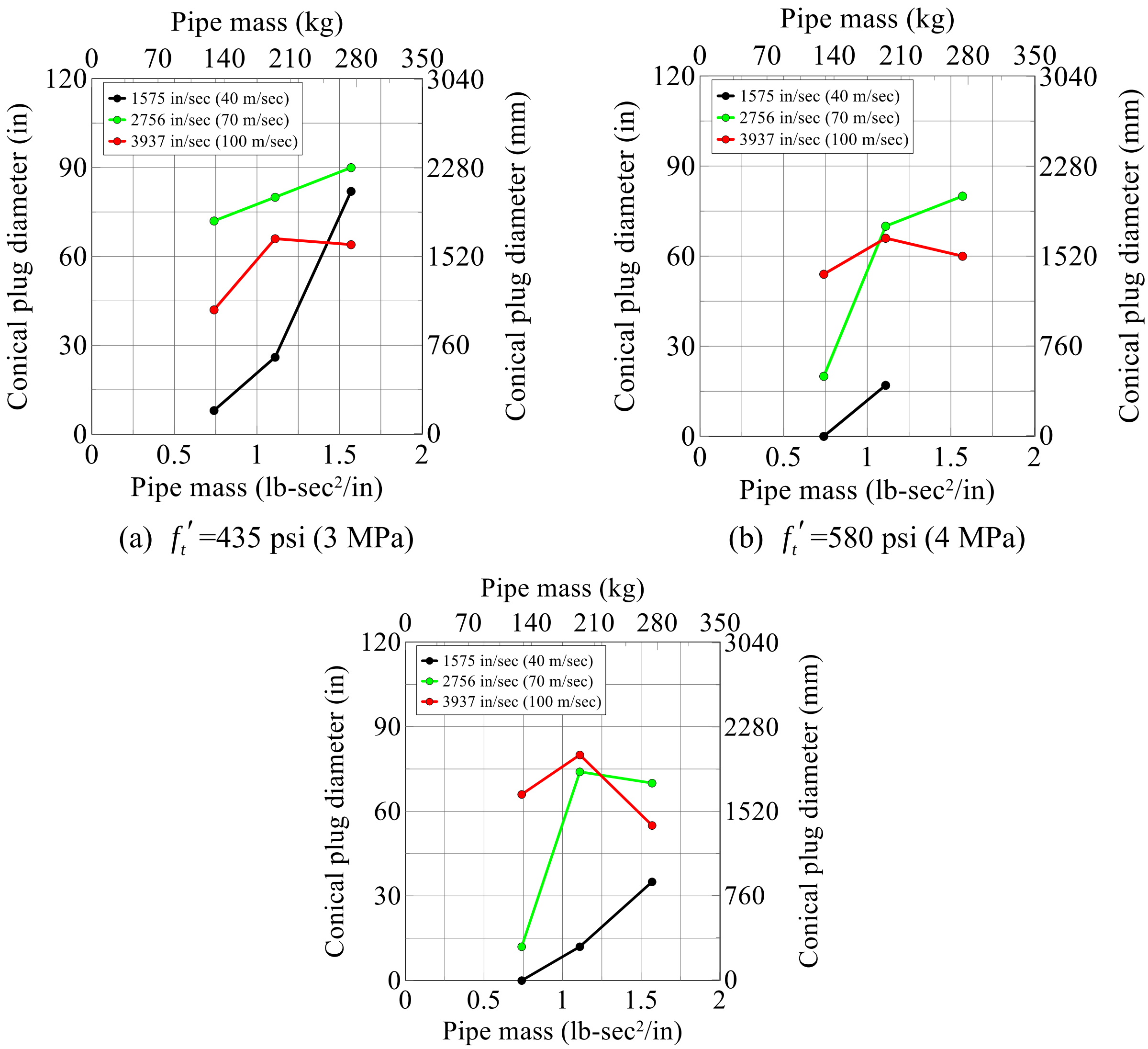

(a) f_t' =435 psi (3 MPa)

(b) f_t' =580 psi (4 MPa)

(c) f_t' =725 psi (5 MPa)

Figure D-13: Conical plug diameter as a function of Schedule 40 pipe mass, f_c' =5801 psi (30 MPa), 12-inch (305 mm) thick panel, MAT072R3

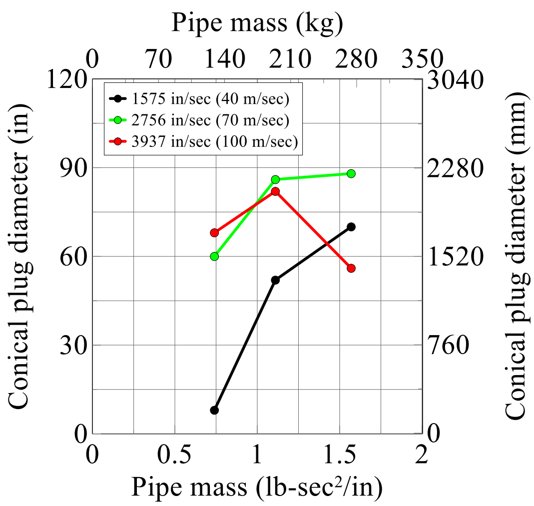

(a) f_t' =435 psi (3 MPa)

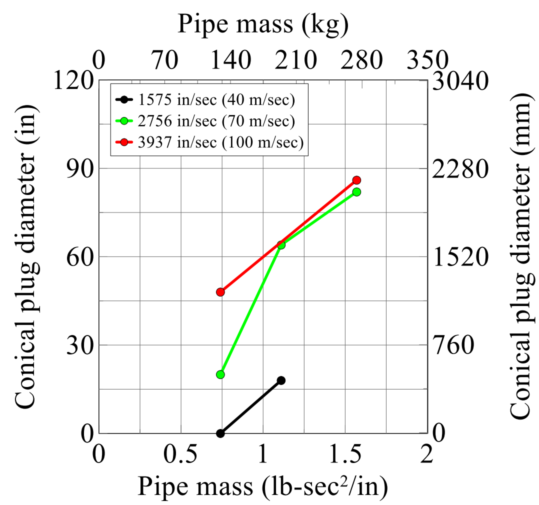

(b) f_t' =580 psi (4 MPa)

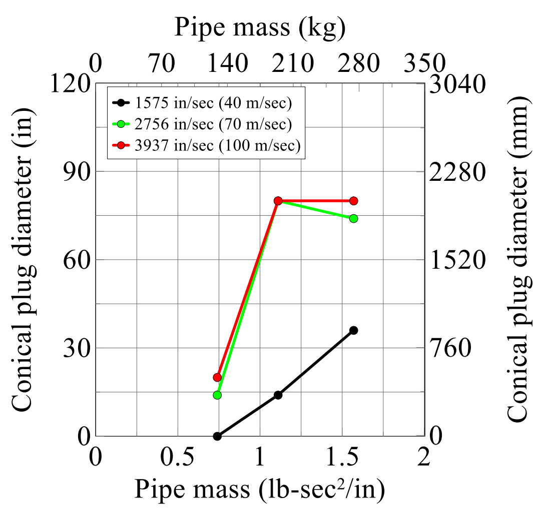

(c) f_t' =725 psi (5 MPa)

Figure D-14: Conical plug diameter as a function of Schedule 40 pipe mass, f_c' =7251 psi (30 MPa), 12-inch (305 mm) thick panel, MAT072R3

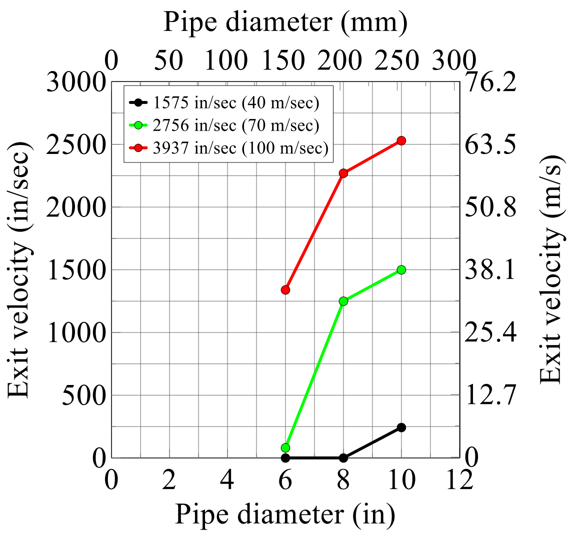

(a) f_t' =435 psi (3 MPa)

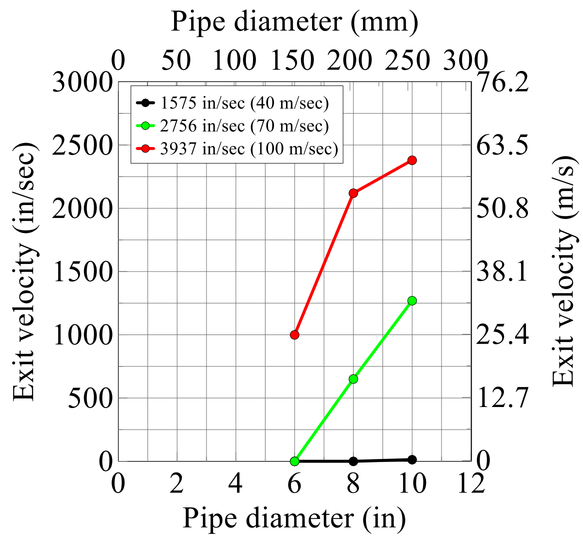

(b) f_t' =580 psi (4 MPa)

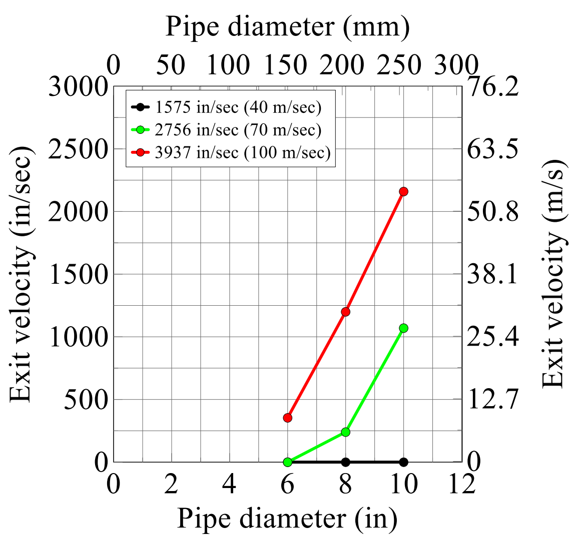

(c) f_t' =725 psi (5 MPa)

Figure D-15: Pipe exit velocity as a function of Schedule 40 pipe diameter, f_c' =5801 psi (40 MPa), 12-inch (305 mm) thick panel, MAT072R3

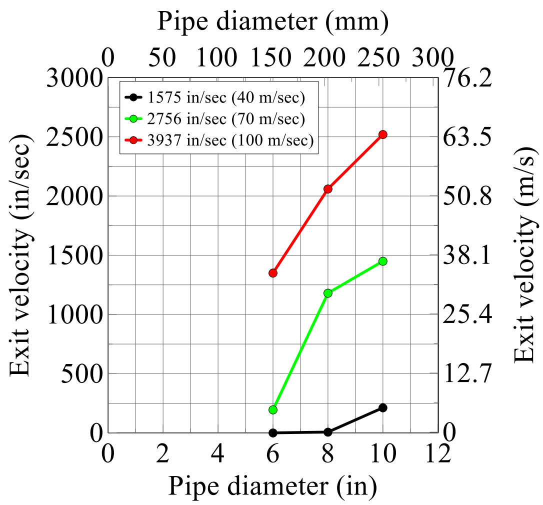

(a) f_t' =435 psi (3 MPa)

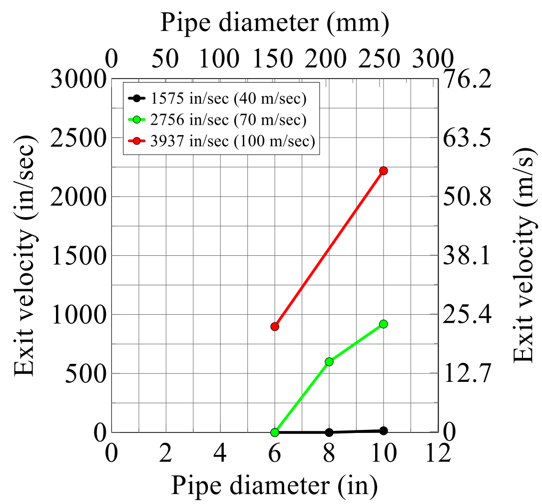

(b) f_t' =580 psi (4 MPa)

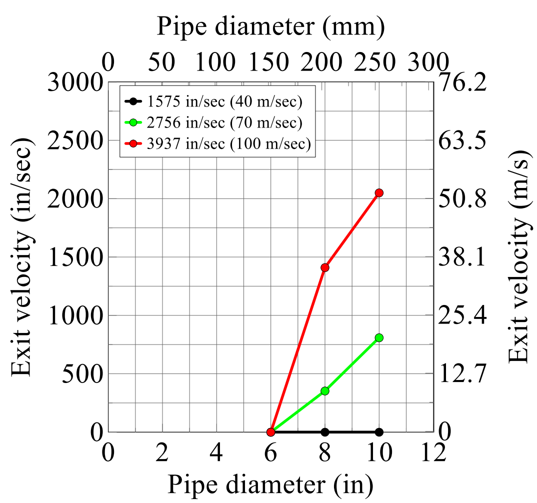

(c) f_t' =725 psi (5 MPa)

Figure D-16: Pipe exit velocity as a function of Schedule 40 pipe diameter, f_c' =7251 psi (50 MPa), 12-inch (305 mm) thick panel, MAT072R3

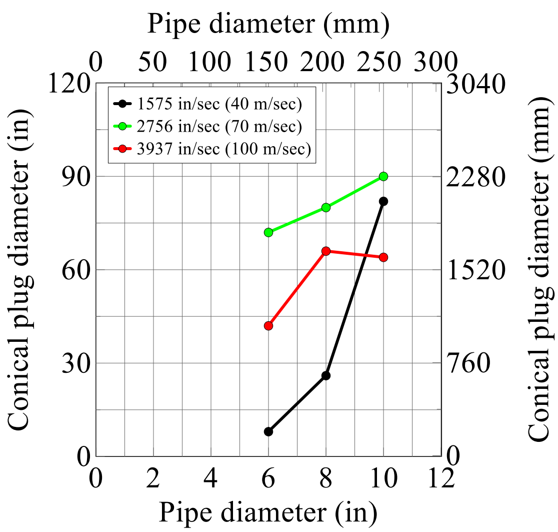

(a) f_t' =435 psi (3 MPa)

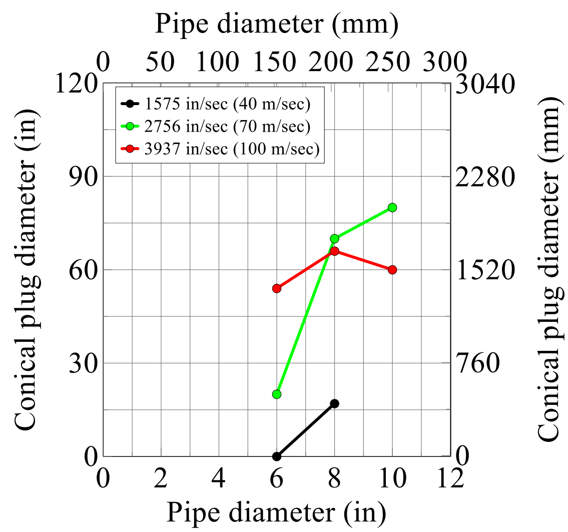

(b) f_t' =580 psi (4 MPa)

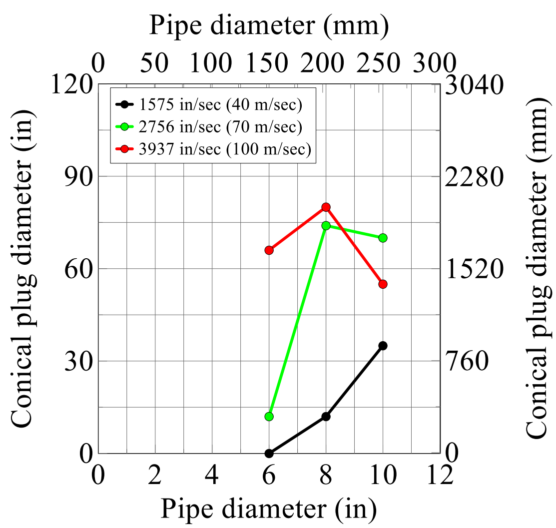

(c) f_t' =725 psi (5 MPa)

Figure D-17: Conical plug diameter as a function of Schedule 40 pipe diameter, f_c' =5801 psi (40 MPa), 12-inch (305 mm) thick panel, MAT072R3

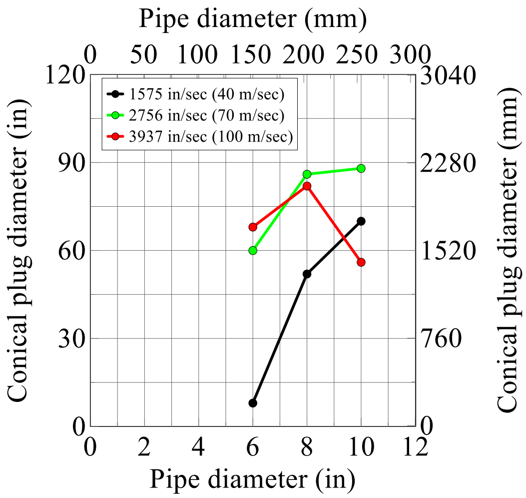

(a) f_t'=435 psi (3 MPa)

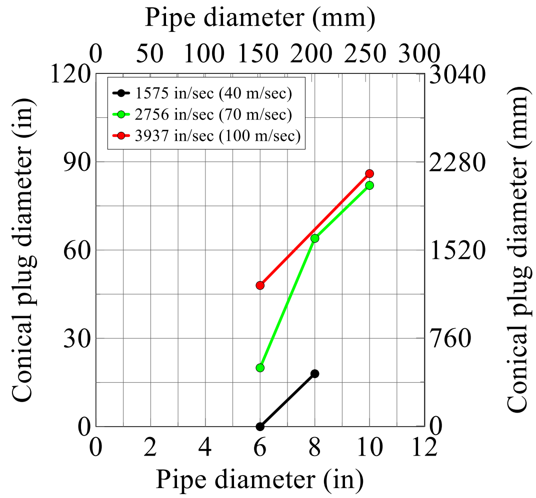

(b) f_t'=580 psi (4 MPa)

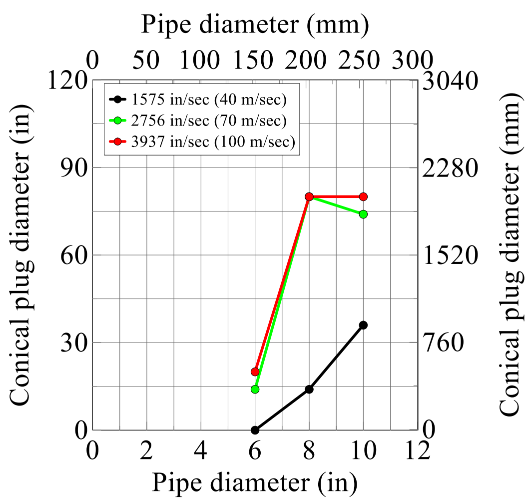

(c) f_t'=725 psi (5 MPa)

Figure D-18: Conical plug diameter as a function of Schedule 40 pipe diameter, f_c'=7251 psi (50 MPa), 12-inch (305 mm) thick panel, MAT072R3

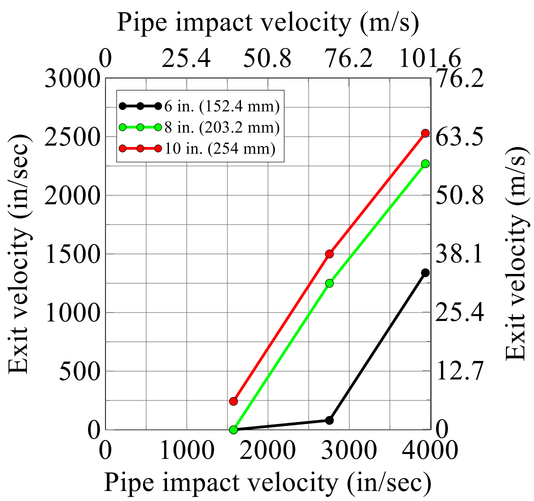

(a) f_t' =435 psi (3 MPa)

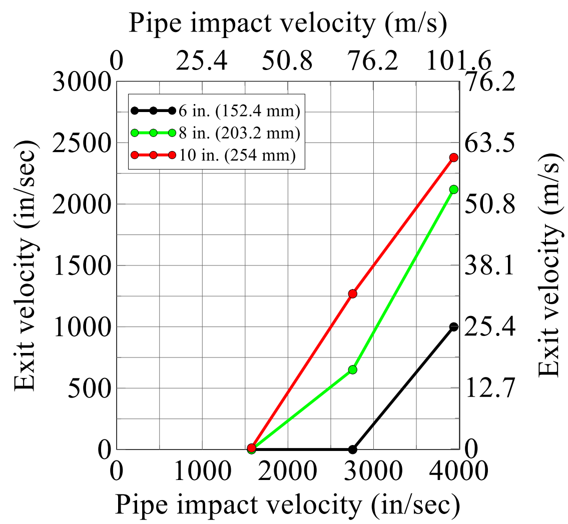

(b) f_t' =580 psi (4 MPa)

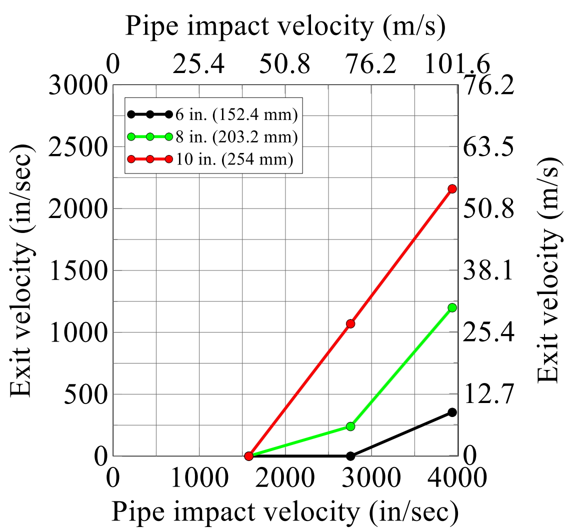

(c) f_t' =725 psi (5 MPa)

Figure D-19: Pipe exit velocity as a function of pipe impact velocity, Schedule 40 pipe, f_c' =5801 psi (40 MPa), 12-inch (305 mm) thick panel, MAT072R3

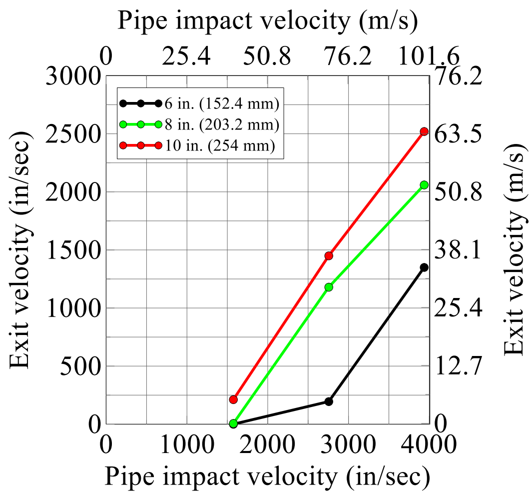

(a) f_t' =435 psi (3 MPa)

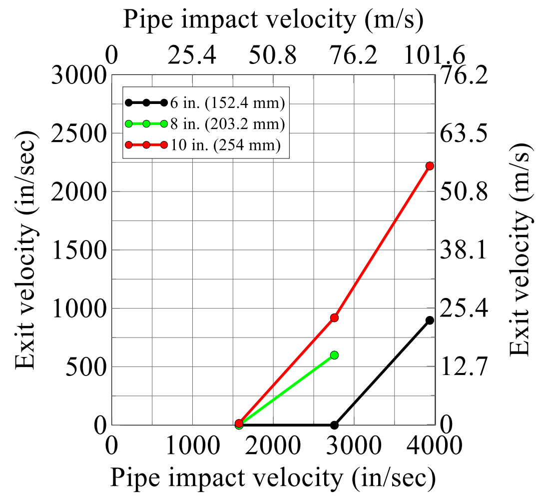

(b) f_t' =580 psi (4 MPa)

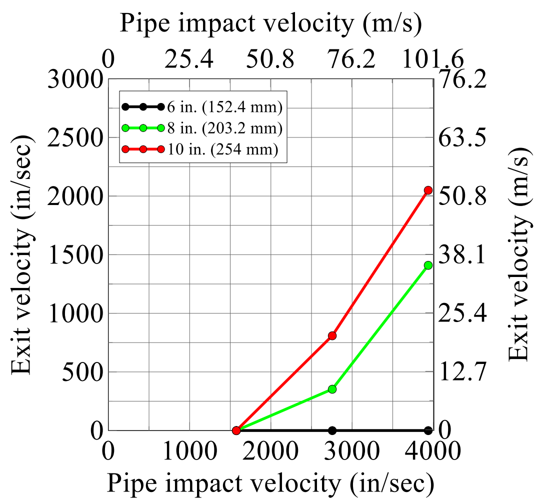

(c) f_t' =725 psi (5 MPa)

Figure D-20: Pipe exit velocity as a function of pipe impact velocity, Schedule 40 pipe, f_c' =7251 psi (50 MPa), 12-inch (305 mm) thick panel, MAT072R3

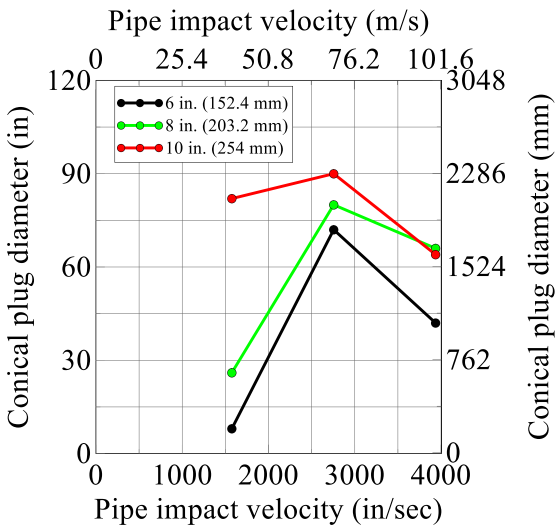

(a) f_t' =435 psi (3 MPa)

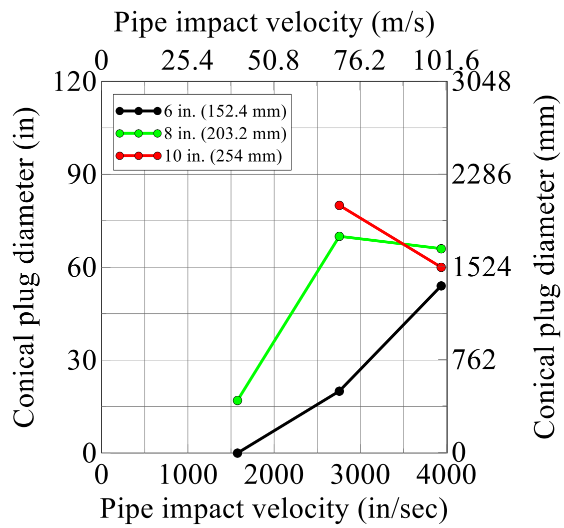

(b) f_t' =580 psi (4 MPa)

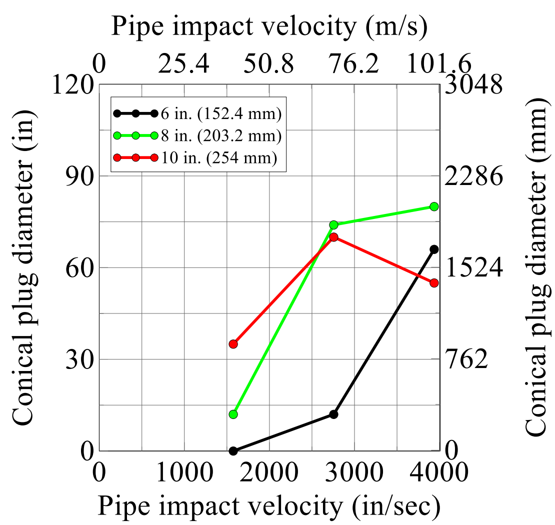

(c) f_t' =725 psi (5 MPa)

Figure D-21: Conical plug diameter as a function of pipe impact velocity, Schedule 40 pipe, f_c' =5801 psi (40 MPa), 12-inch (305 mm) thick panel, MAT072R3

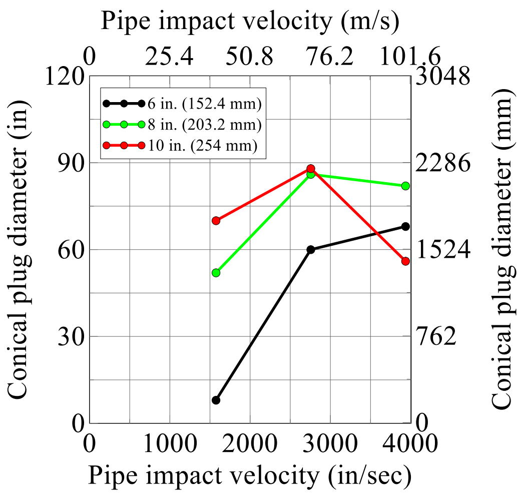

(a) f_t' =435 psi (3 MPa)

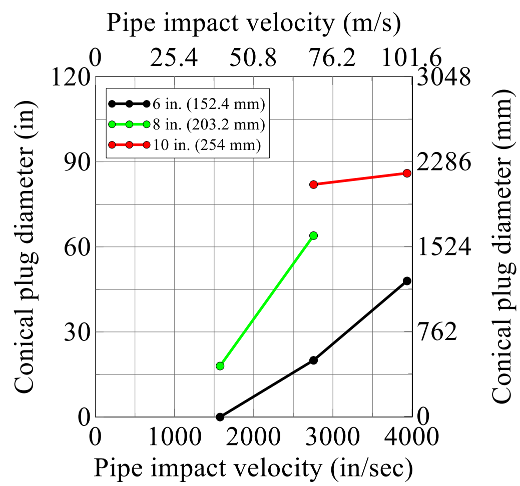

(b) f_t' =580 psi (4 MPa)

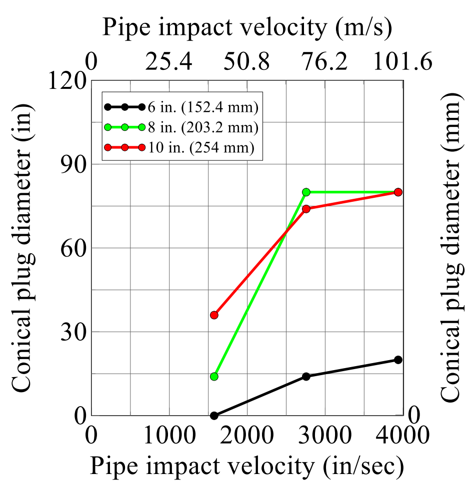

(c) f_t' =725 psi (5 MPa)

Figure D-22: Conical plug diameter as a function of pipe impact velocity, Schedule 40 pipe, f_c' =7251 psi (50 MPa), 12-inch (305 mm) thick panel, MAT072R3

MCEER Technical Reports

MCEER publishes technical reports on a variety of subjects written by authors funded through MCEER. These reports can be downloaded from the MCEER website at http://www.buffalo.edu/mceer. They can also be requested through NTIS, P.O. Box 1425, Springfield, Virginia 22151. NTIS accession numbers are shown in parenthesis, if available.

NCEER-87-0001 "First-Year Program in Research, Education and Technology Transfer," 3/5/87, (PB88-134275, A04, MF-A01).

NCEER-87-0002 "Experimental Evaluation of Instantaneous Optimal Algorithms for Structural Control," by R.C. Lin, T.T. Soong and A.M. Reinhorn, 4/20/87, (PB88-134341, A04, MF-A01).

NCEER-87-0003 "Experimentation Using the Earthquake Simulation Facilities at University at Buffalo," by A.M. Reinhorn and R.L. Ketter, not available.

NCEER-87-0004 "The System Characteristics and Performance of a Shaking Table," by J.S. Hwang, K.C. Chang and G.C. Lee, 6/1/87, (PB88-134259, A03, MF-A01). This report is available only through NTIS (see address given above).

NCEER-87-0005 "A Finite Element Formulation for Nonlinear Viscoplastic Material Using a Q Model," by O. Gyebi and G. Dasgupta, 11/2/87, (PB88-213764, A08, MF-A01).

NCEER-87-0006 "Symbolic Manipulation Program (SMP) - Algebraic Codes for Two and Three Dimensional Finite Element Formulations," by X. Lee and G. Dasgupta, 11/9/87, (PB88-218522, A05, MF-A01).

NCEER-87-0007 "Instantaneous Optimal Control Laws for Tall Buildings Under Seismic Excitations," by J.N. Yang, A. Akbarpour and P. Ghaemmaghami, 6/10/87, (PB88-134333, A06, MF-A01). This report is only available through NTIS (see address given above).

NCEER-87-0008 "IDARC: Inelastic Damage Analysis of Reinforced Concrete Frame - Shear-Wall Structures," by Y.J. Park, A.M. Reinhorn and S.K. Kunnath, 7/20/87, (PB88-134325, A09, MF-A01). This report is only available through NTIS (see address given above).

NCEER-87-0009 "Liquefaction Potential for New York State: A Preliminary Report on Sites in Manhattan and Buffalo," by M. Budhu, V. Vijayakumar, R.F. Giese and L. Baumgras, 8/31/87, (PB88-163704, A03, MF-A01). This report is available only through NTIS (see address given above).

NCEER-87-0010 "Vertical and Torsional Vibration of Foundations in Inhomogeneous Media," by A.S. Veletsos and K.W. Dotson, 6/1/87, (PB88-134291, A03, MF-A01). This report is only available through NTIS (see address given above).

NCEER-87-0011 "Seismic Probabilistic Risk Assessment and Seismic Margins Studies for Nuclear Power Plants," by Howard H.M. Hwang, 6/15/87, (PB88-134267, A03, MF-A01). This report is only available through NTIS (see address given above).

NCEER-87-0012 "Parametric Studies of Frequency Response of Secondary Systems Under Ground-Acceleration Excitations," by Y. Yong and Y.K. Lin, 6/10/87, (PB88-134309, A03, MF-A01). This report is only available through NTIS (see address given above).

NCEER-87-0013 "Frequency Response of Secondary Systems Under Seismic Excitation," by J.A. HoLung, J. Cai and Y.K. Lin, 7/31/87, (PB88-134317, A05, MF-A01). This report is only available through NTIS (see address given above).

NCEER-87-0014 "Modelling Earthquake Ground Motions in Seismically Active Regions Using Parametric Time Series Methods," by G.W. Ellis and A.S. Cakmak, 8/25/87, (PB88-134283, A08, MF-A01). This report is only available through NTIS (see address given above).

NCEER-87-0015 "Detection and Assessment of Seismic Structural Damage," by E. DiPasquale and A.S. Cakmak, 8/25/87, (PB88-163712, A05, MF-A01). This report is only available through NTIS (see address given above).

NCEER-87-0016 "Pipeline Experiment at Parkfield, California," by J. Isenberg and E. Richardson, 9/15/87, (PB88-163720, A03, MF-A01). This report is available only through NTIS (see address given above).

NCEER-87-0017 "Digital Simulation of Seismic Ground Motion," by M. Shinozuka, G. Deodatis and T. Harada, 8/31/87, (PB88-155197, A04, MF-A01). This report is available only through NTIS (see address given above).

NCEER-87-0018 "Practical Considerations for Structural Control: System Uncertainty, System Time Delay and Truncation of Small Control Forces," J.N. Yang and A. Akbarpour, 8/10/87, (PB88-163738, A08, MF-A01). This report is only available through NTIS (see address given above).

NCEER-87-0019 "Modal Analysis of Nonclassically Damped Structural Systems Using Canonical Transformation," by J.N. Yang, S. Sarkani and F.X. Long, 9/27/87, (PB88-187851, A04, MF-A01).

NCEER-87-0020 "A Nonstationary Solution in Random Vibration Theory," by J.R. Red-Horse and P.D. Spanos, 11/3/87, (PB88-163746, A03, MF-A01).

NCEER-87-0021 "Horizontal Impedances for Radially Inhomogeneous Viscoelastic Soil Layers," by A.S. Veletsos and K.W. Dotson, 10/15/87, (PB88-150859, A04, MF-A01).

NCEER-87-0022 "Seismic Damage Assessment of Reinforced Concrete Members," by Y.S. Chung, C. Meyer and M. Shinozuka, 10/9/87, (PB88-150867, A05, MF-A01). This report is available only through NTIS (see address given above).

NCEER-87-0023 "Active Structural Control in Civil Engineering," by T.T. Soong, 11/11/87, (PB88-187778, A03, MF-A01).

NCEER-87-0024 "Vertical and Torsional Impedances for Radially Inhomogeneous Viscoelastic Soil Layers," by K.W. Dotson and A.S. Veletsos, 12/87, (PB88-187786, A03, MF-A01).

NCEER-87-0025 "Proceedings from the Symposium on Seismic Hazards, Ground Motions, Soil-Liquefaction and Engineering Practice in Eastern North America," October 20-22, 1987, edited by K.H. Jacob, 12/87, (PB88-188115, A23, MF-A01). This report is available only through NTIS (see address given above).

NCEER-87-0026 "Report on the Whittier-Narrows, California, Earthquake of October 1, 1987," by J. Pantelic and A. Reinhorn, 11/87, (PB88-187752, A03, MF-A01). This report is available only through NTIS (see address given above).

NCEER-87-0027 "Design of a Modular Program for Transient Nonlinear Analysis of Large 3-D Building Structures," by S. Srivastav and J.F. Abel, 12/30/87, (PB88-187950, A05, MF-A01). This report is only available through NTIS (see address given above).

NCEER-87-0028 "Second-Year Program in Research, Education and Technology Transfer," 3/8/88, (PB88-219480, A04, MF-A01).

NCEER-88-0001 "Workshop on Seismic Computer Analysis and Design of Buildings With Interactive Graphics," by W. McGuire, J.F. Abel and C.H. Conley, 1/18/88, (PB88-187760, A03, MF-A01). This report is only available through NTIS (see address given above).

NCEER-88-0002 "Optimal Control of Nonlinear Flexible Structures," by J.N. Yang, F.X. Long and D. Wong, 1/22/88, (PB88-213772, A06, MF-A01).

NCEER-88-0003 "Substructuring Techniques in the Time Domain for Primary-Secondary Structural Systems," by G.D. Manolis and G. Juhn, 2/10/88, (PB88-213780, A04, MF-A01).

NCEER-88-0004 "Iterative Seismic Analysis of Primary-Secondary Systems," by A. Singhal, L.D. Lutes and P.D. Spanos, 2/23/88, (PB88-213798, A04, MF-A01).

NCEER-88-0005 "Stochastic Finite Element Expansion for Random Media," by P.D. Spanos and R. Ghanem, 3/14/88, (PB88-213806, A03, MF-A01).

NCEER-88-0006 "Combining Structural Optimization and Structural Control," by F.Y. Cheng and C.P. Pantelides, 1/10/88, (PB88-213814, A05, MF-A01).

NCEER-88-0007 "Seismic Performance Assessment of Code-Designed Structures," by H.H-M. Hwang, J-W. Jaw and H-J. Shau, 3/20/88, (PB88-219423, A04, MF-A01). This report is only available through NTIS (see address given above).

NCEER-88-0008 "Reliability Analysis of Code-Designed Structures Under Natural Hazards," by H.H-M. Hwang, H. Ushiba and M. Shinozuka, 2/29/88, (PB88-229471, A07, MF-A01). This report is only available through NTIS (see address given above).

NCEER-88-0009 "Seismic Fragility Analysis of Shear Wall Structures," by J-W Jaw and H.H-M. Hwang, 4/30/88, (PB89-102867, A04, MF-A01).

NCEER-88-0010 "Base Isolation of a Multi-Story Building Under a Harmonic Ground Motion - A Comparison of Performances of Various Systems," by F-G Fan, G. Ahmadi and I.G. Tadjbakhsh, 5/18/88, (PB89-122238, A06, MF-A01). This report is only available through NTIS (see address given above).

NCEER-88-0011 "Seismic Floor Response Spectra for a Combined System by Green's Functions," by F.M. Lavelle, L.A. Bergman and P.D. Spanos, 5/1/88, (PB89-102875, A03, MF-A01).

NCEER-88-0012 "A New Solution Technique for Randomly Excited Hysteretic Structures," by G.Q. Cai and Y.K. Lin, 5/16/88, (PB89-102883, A03, MF-A01).

NCEER-88-0013 "A Study of Radiation Damping and Soil-Structure Interaction Effects in the Centrifuge," by K. Weissman, supervised by J.H. Prevost, 5/24/88, (PB89-144703, A06, MF-A01).

NCEER-88-0014 "Parameter Identification and Implementation of a Kinematic Plasticity Model for Frictional Soils," by J.H. Prevost and D.V. Griffiths, not available.

NCEER-88-0015 "Two- and Three- Dimensional Dynamic Finite Element Analyses of the Long Valley Dam," by D.V. Griffiths and J.H. Prevost, 6/17/88, (PB89-144711, A04, MF-A01).

NCEER-88-0016 "Damage Assessment of Reinforced Concrete Structures in Eastern United States," by A.M. Reinhorn, M.J. Seidel, S.K. Kunnath and Y.J. Park, 6/15/88, (PB89-122220, A04, MF-A01). This report is only available through NTIS (see address given above).

NCEER-88-0017 "Dynamic Compliance of Vertically Loaded Strip Foundations in Multilayered Viscoelastic Soils," by S. Ahmad and A.S.M. Israil, 6/17/88, (PB89-102891, A04, MF-A01).

NCEER-88-0018 "An Experimental Study of Seismic Structural Response With Added Viscoelastic Dampers," by R.C. Lin, Z. Liang, T.T. Soong and R.H. Zhang, 6/30/88, (PB89-122212, A05, MF-A01). This report is available only through NTIS (see address given above).

NCEER-88-0019 "Experimental Investigation of Primary - Secondary System Interaction," by G.D. Manolis, G. Juhn and A.M. Reinhorn, 5/27/88, (PB89-122204, A04, MF-A01).

NCEER-88-0020 "A Response Spectrum Approach For Analysis of Nonclassically Damped Structures," by J.N. Yang, S. Sarkani and F.X. Long, 4/22/88, (PB89-102909, A04, MF-A01).

NCEER-88-0021 "Seismic Interaction of Structures and Soils: Stochastic Approach," by A.S. Veletsos and A.M. Prasad, 7/21/88, (PB89-122196, A04, MF-A01). This report is only available through NTIS (see address given above).

NCEER-88-0022 "Identification of the Serviceability Limit State and Detection of Seismic Structural Damage," by E. DiPasquale and A.S. Cakmak, 6/15/88, (PB89-122188, A05, MF-A01). This report is available only through NTIS (see address given above).

NCEER-88-0023 "Multi-Hazard Risk Analysis: Case of a Simple Offshore Structure," by B.K. Bhartia and E.H. Vanmarcke, 7/21/88, (PB89-145213, A05, MF-A01).

NCEER-88-0024 "Automated Seismic Design of Reinforced Concrete Buildings," by Y.S. Chung, C. Meyer and M. Shinozuka, 7/5/88, (PB89-122170, A06, MF-A01). This report is available only through NTIS (see address given above).

NCEER-88-0025 "Experimental Study of Active Control of MDOF Structures Under Seismic Excitations," by L.L. Chung, R.C. Lin, T.T. Soong and A.M. Reinhorn, 7/10/88, (PB89-122600, A04, MF-A01).

NCEER-88-0026 "Earthquake Simulation Tests of a Low-Rise Metal Structure," by J.S. Hwang, K.C. Chang, G.C. Lee and R.L. Ketter, 8/1/88, (PB89-102917, A04, MF-A01).

NCEER-88-0027 "Systems Study of Urban Response and Reconstruction Due to Catastrophic Earthquakes," by F. Kozin and H.K. Zhou, 9/22/88, (PB90-162348, A04, MF-A01).

NCEER-88-0028 "Seismic Fragility Analysis of Plane Frame Structures," by H.H-M. Hwang and Y.K. Low, 7/31/88, (PB89-131445, A06, MF-A01).

NCEER-88-0029 "Response Analysis of Stochastic Structures," by A. Kardara, C. Bucher and M. Shinozuka, 9/22/88, (PB89-174429, A04, MF-A01).

NCEER-88-0030 "Nonnormal Accelerations Due to Yielding in a Primary Structure," by D.C.K. Chen and L.D. Lutes, 9/19/88, (PB89-131437, A04, MF-A01).

NCEER-88-0031 "Design Approaches for Soil-Structure Interaction," by A.S. Veletsos, A.M. Prasad and Y. Tang, 12/30/88, (PB89-174437, A03, MF-A01). This report is available only through NTIS (see address given above).

NCEER-88-0032 "A Re-evaluation of Design Spectra for Seismic Damage Control," by C.J. Turkstra and A.G. Tallin, 11/7/88, (PB89-145221, A05, MF-A01).

NCEER-88-0033 "The Behavior and Design of Noncontact Lap Splices Subjected to Repeated Inelastic Tensile Loading," by V.E. Sagan, P. Gergely and R.N. White, 12/8/88, (PB89-163737, A08, MF-A01).

NCEER-88-0034 "Seismic Response of Pile Foundations," by S.M. Mamoon, P.K. Banerjee and S. Ahmad, 11/1/88, (PB89-145239, A04, MF-A01).

NCEER-88-0035 "Modeling of R/C Building Structures With Flexible Floor Diaphragms (IDARC2)," by A.M. Reinhorn, S.K. Kunnath and N. Panahshahi, 9/7/88, (PB89-207153, A07, MF-A01).

NCEER-88-0036 "Solution of the Dam-Reservoir Interaction Problem Using a Combination of FEM, BEM with Particular Integrals, Modal Analysis, and Substructuring," by C-S. Tsai, G.C. Lee and R.L. Ketter, 12/31/88, (PB89-207146, A04, MF-A01).

NCEER-88-0037 "Optimal Placement of Actuators for Structural Control," by F.Y. Cheng and C.P. Pantelides, 8/15/88, (PB89-162846, A05, MF-A01).

NCEER-88-0038 "Teflon Bearings in Aseismic Base Isolation: Experimental Studies and Mathematical Modeling," by A. Mokha, M.C. Constantinou and A.M. Reinhorn, 12/5/88, (PB89-218457, A10, MF-A01). This report is available only through NTIS (see address given above).

NCEER-88-0039 "Seismic Behavior of Flat Slab High-Rise Buildings in the New York City Area," by P. Weidlinger and M. Ettouney, 10/15/88, (PB90-145681, A04, MF-A01).

NCEER-88-0040 "Evaluation of the Earthquake Resistance of Existing Buildings in New York City," by P. Weidlinger and M. Ettouney, 10/15/88, not available.

NCEER-88-0041 "Small-Scale Modeling Techniques for Reinforced Concrete Structures Subjected to Seismic Loads," by W. Kim, A. El-Attar and R.N. White, 11/22/88, (PB89-189625, A05, MF-A01).

NCEER-88-0042 "Modeling Strong Ground Motion from Multiple Event Earthquakes," by G.W. Ellis and A.S. Cakmak, 10/15/88, (PB89-174445, A03, MF-A01).

NCEER-88-0043 "Nonstationary Models of Seismic Ground Acceleration," by M. Grigoriu, S.E. Ruiz and E. Rosenblueth, 7/15/88, (PB89-189617, A04, MF-A01).

NCEER-88-0044 "SARCF User's Guide: Seismic Analysis of Reinforced Concrete Frames," by Y.S. Chung, C. Meyer and M. Shinozuka, 11/9/88, (PB89-174452, A08, MF-A01).

NCEER-88-0045 "First Expert Panel Meeting on Disaster Research and Planning," edited by J. Pantelic and J. Stoyle, 9/15/88, (PB89-174460, A05, MF-A01).

NCEER-88-0046 "Preliminary Studies of the Effect of Degrading Infill Walls on the Nonlinear Seismic Response of Steel Frames," by C.Z. Chrysostomou, P. Gergely and J.F. Abel, 12/19/88, (PB89-208383, A05, MF-A01).

NCEER-88-0047 "Reinforced Concrete Frame Component Testing Facility - Design, Construction, Instrumentation and Operation," by S.P. Pessiki, C. Conley, T. Bond, P. Gergely and R.N. White, 12/16/88, (PB89-174478, A04, MF-A01).

NCEER-89-0001 "Effects of Protective Cushion and Soil Compliancy on the Response of Equipment Within a Seismically Excited Building," by J.A. HoLung, 2/16/89, (PB89-207179, A04, MF-A01).

NCEER-89-0002 "Statistical Evaluation of Response Modification Factors for Reinforced Concrete Structures," by H.H-M. Hwang and J-W. Jaw, 2/17/89, (PB89-207187, A05, MF-A01).

NCEER-89-0003 "Hysteretic Columns Under Random Excitation," by G-Q. Cai and Y.K. Lin, 1/9/89, (PB89-196513, A03, MF-A01).

NCEER-89-0004 "Experimental Study of `Elephant Foot Bulge' Instability of Thin-Walled Metal Tanks," by Z-H. Jia and R.L. Ketter, 2/22/89, (PB89-207195, A03, MF-A01).

NCEER-89-0005 "Experiment on Performance of Buried Pipelines Across San Andreas Fault," by J. Isenberg, E. Richardson and T.D. O'Rourke, 3/10/89, (PB89-218440, A04, MF-A01). This report is available only through NTIS (see address given above).

NCEER-89-0006 "A Knowledge-Based Approach to Structural Design of Earthquake-Resistant Buildings," by M. Subramani, P. Gergely, C.H. Conley, J.F. Abel and A.H. Zaghw, 1/15/89, (PB89-218465, A06, MF-A01).

NCEER-89-0007 "Liquefaction Hazards and Their Effects on Buried Pipelines," by T.D. O'Rourke and P.A. Lane, 2/1/89, (PB89-218481, A09, MF-A01).

NCEER-89-0008 "Fundamentals of System Identification in Structural Dynamics," by H. Imai, C-B. Yun, O. Maruyama and M. Shinozuka, 1/26/89, (PB89-207211, A04, MF-A01).

NCEER-89-0009 "Effects of the 1985 Michoacan Earthquake on Water Systems and Other Buried Lifelines in Mexico," by A.G. Ayala and M.J. O'Rourke, 3/8/89, (PB89-207229, A06, MF-A01).

NCEER-89-R010 "NCEER Bibliography of Earthquake Education Materials," by K.E.K. Ross, Second Revision, 9/1/89, (PB90-125352, A05, MF-A01). This report is replaced by NCEER-92-0018.

NCEER-89-0011 "Inelastic Three-Dimensional Response Analysis of Reinforced Concrete Building Structures (IDARC-3D), Part I - Modeling," by S.K. Kunnath and A.M. Reinhorn, 4/17/89, (PB90-114612, A07, MF-A01). This report is available only through NTIS (see address given above).

NCEER-89-0012 "Recommended Modifications to ATC-14," by C.D. Poland and J.O. Malley, 4/12/89, (PB90-108648, A15, MF-A01).

NCEER-89-0013 "Repair and Strengthening of Beam-to-Column Connections Subjected to Earthquake Loading," by M. Corazao and A.J. Durrani, 2/28/89, (PB90-109885, A06, MF-A01).

NCEER-89-0014 "Program EXKAL2 for Identification of Structural Dynamic Systems," by O. Maruyama, C-B. Yun, M. Hoshiya and M. Shinozuka, 5/19/89, (PB90-109877, A09, MF-A01).

NCEER-89-0015 "Response of Frames With Bolted Semi-Rigid Connections, Part I - Experimental Study and Analytical Predictions," by P.J. DiCorso, A.M. Reinhorn, J.R. Dickerson, J.B. Radziminski and W.L. Harper, 6/1/89, not available.

NCEER-89-0016 "ARMA Monte Carlo Simulation in Probabilistic Structural Analysis," by P.D. Spanos and M.P. Mignolet, 7/10/89, (PB90-109893, A03, MF-A01).

NCEER-89-P017 "Preliminary Proceedings from the Conference on Disaster Preparedness - The Place of Earthquake Education in Our Schools," Edited by K.E.K. Ross, 6/23/89, (PB90-108606, A03, MF-A01).

NCEER-89-0017 "Proceedings from the Conference on Disaster Preparedness - The Place of Earthquake Education in Our Schools," Edited by K.E.K. Ross, 12/31/89, (PB90-207895, A012, MF-A02). This report is available only through NTIS (see address given above).

NCEER-89-0018 "Multidimensional Models of Hysteretic Material Behavior for Vibration Analysis of Shape Memory Energy Absorbing Devices, by E.J. Graesser and F.A. Cozzarelli, 6/7/89, (PB90-164146, A04, MF-A01).

NCEER-89-0019 "Nonlinear Dynamic Analysis of Three-Dimensional Base Isolated Structures (3D-BASIS)," by S. Nagarajaiah, A.M. Reinhorn and M.C. Constantinou, 8/3/89, (PB90-161936, A06, MF-A01). This report has been replaced by NCEER-93-0011.

NCEER-89-0020 "Structural Control Considering Time-Rate of Control Forces and Control Rate Constraints," by F.Y. Cheng and C.P. Pantelides, 8/3/89, (PB90-120445, A04, MF-A01).

NCEER-89-0021 "Subsurface Conditions of Memphis and Shelby County," by K.W. Ng, T-S. Chang and H-H.M. Hwang, 7/26/89, (PB90-120437, A03, MF-A01).

NCEER-89-0022 "Seismic Wave Propagation Effects on Straight Jointed Buried Pipelines," by K. Elhmadi and M.J. O'Rourke, 8/24/89, (PB90-162322, A10, MF-A02).

NCEER-89-0023 "Workshop on Serviceability Analysis of Water Delivery Systems," edited by M. Grigoriu, 3/6/89, (PB90-127424, A03, MF-A01).

NCEER-89-0024 "Shaking Table Study of a 1/5 Scale Steel Frame Composed of Tapered Members," by K.C. Chang, J.S. Hwang and G.C. Lee, 9/18/89, (PB90-160169, A04, MF-A01).

NCEER-89-0025 "DYNA1D: A Computer Program for Nonlinear Seismic Site Response Analysis - Technical Documentation," by Jean H. Prevost, 9/14/89, (PB90-161944, A07, MF-A01). This report is available only through NTIS (see address given above).

NCEER-89-0026 "1:4 Scale Model Studies of Active Tendon Systems and Active Mass Dampers for Aseismic Protection," by A.M. Reinhorn, T.T. Soong, R.C. Lin, Y.P. Yang, Y. Fukao, H. Abe and M. Nakai, 9/15/89, (PB90-173246, A10, MF-A02). This report is available only through NTIS (see address given above).

NCEER-89-0027 "Scattering of Waves by Inclusions in a Nonhomogeneous Elastic Half Space Solved by Boundary Element Methods," by P.K. Hadley, A. Askar and A.S. Cakmak, 6/15/89, (PB90-145699, A07, MF-A01).

NCEER-89-0028 "Statistical Evaluation of Deflection Amplification Factors for Reinforced Concrete Structures," by H.H.M. Hwang, J-W. Jaw and A.L. Ch'ng, 8/31/89, (PB90-164633, A05, MF-A01).

NCEER-89-0029 "Bedrock Accelerations in Memphis Area Due to Large New Madrid Earthquakes," by H.H.M. Hwang, C.H.S. Chen and G. Yu, 11/7/89, (PB90-162330, A04, MF-A01).

NCEER-89-0030 "Seismic Behavior and Response Sensitivity of Secondary Structural Systems," by Y.Q. Chen and T.T. Soong, 10/23/89, (PB90-164658, A08, MF-A01).

NCEER-89-0031 "Random Vibration and Reliability Analysis of Primary-Secondary Structural Systems," by Y. Ibrahim, M. Grigoriu and T.T. Soong, 11/10/89, (PB90-161951, A04, MF-A01).

NCEER-89-0032 "Proceedings from the Second U.S. - Japan Workshop on Liquefaction, Large Ground Deformation and Their Effects on Lifelines, September 26-29, 1989," Edited by T.D. O'Rourke and M. Hamada, 12/1/89, (PB90-209388, A22, MF-A03).

NCEER-89-0033 "Deterministic Model for Seismic Damage Evaluation of Reinforced Concrete Structures," by J.M. Bracci, A.M. Reinhorn, J.B. Mander and S.K. Kunnath, 9/27/89, (PB91-108803, A06, MF-A01).

NCEER-89-0034 "On the Relation Between Local and Global Damage Indices," by E. DiPasquale and A.S. Cakmak, 8/15/89, (PB90-173865, A05, MF-A01).

NCEER-89-0035 "Cyclic Undrained Behavior of Nonplastic and Low Plasticity Silts," by A.J. Walker and H.E. Stewart, 7/26/89, (PB90-183518, A10, MF-A01).

NCEER-89-0036 "Liquefaction Potential of Surficial Deposits in the City of Buffalo, New York," by M. Budhu, R. Giese and L. Baumgrass, 1/17/89, (PB90-208455, A04, MF-A01).

NCEER-89-0037 "A Deterministic Assessment of Effects of Ground Motion Incoherence," by A.S. Veletsos and Y. Tang, 7/15/89, (PB90-164294, A03, MF-A01).

NCEER-89-0038 "Workshop on Ground Motion Parameters for Seismic Hazard Mapping," July 17-18, 1989, edited by R.V. Whitman, 12/1/89, (PB90-173923, A04, MF-A01).

NCEER-89-0039 "Seismic Effects on Elevated Transit Lines of the New York City Transit Authority," by C.J. Costantino, C.A. Miller and E. Heymsfield, 12/26/89, (PB90-207887, A06, MF-A01).

NCEER-89-0040 "Centrifugal Modeling of Dynamic Soil-Structure Interaction," by K. Weissman, Supervised by J.H. Prevost, 5/10/89, (PB90-207879, A07, MF-A01).

NCEER-89-0041 "Linearized Identification of Buildings With Cores for Seismic Vulnerability Assessment," by I-K. Ho and A.E. Aktan, 11/1/89, (PB90-251943, A07, MF-A01).

NCEER-90-0001 "Geotechnical and Lifeline Aspects of the October 17, 1989 Loma Prieta Earthquake in San Francisco," by T.D. O'Rourke, H.E. Stewart, F.T. Blackburn and T.S. Dickerman, 1/90, (PB90-208596, A05, MF-A01).

NCEER-90-0002 "Nonnormal Secondary Response Due to Yielding in a Primary Structure," by D.C.K. Chen and L.D. Lutes, 2/28/90, (PB90-251976, A07, MF-A01).

NCEER-90-0003 "Earthquake Education Materials for Grades K-12," by K.E.K. Ross, 4/16/90, (PB91-251984, A05, MF-A05). This report has been replaced by NCEER-92-0018.

NCEER-90-0004 "Catalog of Strong Motion Stations in Eastern North America," by R.W. Busby, 4/3/90, (PB90-251984, A05, MF-A01).

NCEER-90-0005 "NCEER Strong-Motion Data Base: A User Manual for the GeoBase Release (Version 1.0 for the Sun3)," by P. Friberg and K. Jacob, 3/31/90 (PB90-258062, A04, MF-A01).

NCEER-90-0006 "Seismic Hazard Along a Crude Oil Pipeline in the Event of an 1811-1812 Type New Madrid Earthquake," by H.H.M. Hwang and C-H.S. Chen, 4/16/90, (PB90-258054, A04, MF-A01).

NCEER-90-0007 "Site-Specific Response Spectra for Memphis Sheahan Pumping Station," by H.H.M. Hwang and C.S. Lee, 5/15/90, (PB91-108811, A05, MF-A01).

NCEER-90-0008 "Pilot Study on Seismic Vulnerability of Crude Oil Transmission Systems," by T. Ariman, R. Dobry, M. Grigoriu, F. Kozin, M. O'Rourke, T. O'Rourke and M. Shinozuka, 5/25/90, (PB91-108837, A06, MF-A01).

NCEER-90-0009 "A Program to Generate Site Dependent Time Histories: EQGEN," by G.W. Ellis, M. Srinivasan and A.S. Cakmak, 1/30/90, (PB91-108829, A04, MF-A01).

NCEER-90-0010 "Active Isolation for Seismic Protection of Operating Rooms," by M.E. Talbott, Supervised by M. Shinozuka, 6/8/9, (PB91-110205, A05, MF-A01).

NCEER-90-0011 "Program LINEARID for Identification of Linear Structural Dynamic Systems," by C-B. Yun and M. Shinozuka, 6/25/90, (PB91-110312, A08, MF-A01).

NCEER-90-0012 "Two-Dimensional Two-Phase Elasto-Plastic Seismic Response of Earth Dams," by A.N. Yiagos, Supervised by J.H. Prevost, 6/20/90, (PB91-110197, A13, MF-A02).

NCEER-90-0013 "Secondary Systems in Base-Isolated Structures: Experimental Investigation, Stochastic Response and Stochastic Sensitivity," by G.D. Manolis, G. Juhn, M.C. Constantinou and A.M. Reinhorn, 7/1/90, (PB91-110320, A08, MF-A01).

NCEER-90-0014 "Seismic Behavior of Lightly-Reinforced Concrete Column and Beam-Column Joint Details," by S.P. Pessiki, C.H. Conley, P. Gergely and R.N. White, 8/22/90, (PB91-108795, A11, MF-A02).

NCEER-90-0015 "Two Hybrid Control Systems for Building Structures Under Strong Earthquakes," by J.N. Yang and A. Danielians, 6/29/90, (PB91-125393, A04, MF-A01).

NCEER-90-0016 "Instantaneous Optimal Control with Acceleration and Velocity Feedback," by J.N. Yang and Z. Li, 6/29/90, (PB91-125401, A03, MF-A01).

NCEER-90-0017 "Reconnaissance Report on the Northern Iran Earthquake of June 21, 1990," by M. Mehrain, 10/4/90, (PB91-125377, A03, MF-A01).

NCEER-90-0018 "Evaluation of Liquefaction Potential in Memphis and Shelby County," by T.S. Chang, P.S. Tang, C.S. Lee and H. Hwang, 8/10/90, (PB91-125427, A09, MF-A01).

NCEER-90-0019 "Experimental and Analytical Study of a Combined Sliding Disc Bearing and Helical Steel Spring Isolation System," by M.C. Constantinou, A.S. Mokha and A.M. Reinhorn, 10/4/90, (PB91-125385, A06, MF-A01). This report is available only through NTIS (see address given above).

NCEER-90-0020 "Experimental Study and Analytical Prediction of Earthquake Response of a Sliding Isolation System with a Spherical Surface," by A.S. Mokha, M.C. Constantinou and A.M. Reinhorn, 10/11/90, (PB91-125419, A05, MF-A01).

NCEER-90-0021 "Dynamic Interaction Factors for Floating Pile Groups," by G. Gazetas, K. Fan, A. Kaynia and E. Kausel, 9/10/90, (PB91-170381, A05, MF-A01).

NCEER-90-0022 "Evaluation of Seismic Damage Indices for Reinforced Concrete Structures," by S. Rodriguez-Gomez and A.S. Cakmak, 9/30/90, PB91-171322, A06, MF-A01).

NCEER-90-0023 "Study of Site Response at a Selected Memphis Site," by H. Desai, S. Ahmad, E.S. Gazetas and M.R. Oh, 10/11/90, (PB91-196857, A03, MF-A01).

NCEER-90-0024 "A User's Guide to Strongmo: Version 1.0 of NCEER's Strong-Motion Data Access Tool for PCs and Terminals," by P.A. Friberg and C.A.T. Susch, 11/15/90, (PB91-171272, A03, MF-A01).

NCEER-90-0025 "A Three-Dimensional Analytical Study of Spatial Variability of Seismic Ground Motions," by L-L. Hong and A.H.-S. Ang, 10/30/90, (PB91-170399, A09, MF-A01).

NCEER-90-0026 "MUMOID User's Guide - A Program for the Identification of Modal Parameters," by S. Rodriguez-Gomez and E. DiPasquale, 9/30/90, (PB91-171298, A04, MF-A01).

NCEER-90-0027 "SARCF-II User's Guide - Seismic Analysis of Reinforced Concrete Frames," by S. Rodriguez-Gomez, Y.S. Chung and C. Meyer, 9/30/90, (PB91-171280, A05, MF-A01).

NCEER-90-0028 "Viscous Dampers: Testing, Modeling and Application in Vibration and Seismic Isolation," by N. Makris and M.C. Constantinou, 12/20/90 (PB91-190561, A06, MF-A01).

NCEER-90-0029 "Soil Effects on Earthquake Ground Motions in the Memphis Area," by H. Hwang, C.S. Lee, K.W. Ng and T.S. Chang, 8/2/90, (PB91-190751, A05, MF-A01).

NCEER-91-0001 "Proceedings from the Third Japan-U.S. Workshop on Earthquake Resistant Design of Lifeline Facilities and Countermeasures for Soil Liquefaction, December 17-19, 1990," edited by T.D. O'Rourke and M. Hamada, 2/1/91, (PB91-179259, A99, MF-A04).

NCEER-91-0002 "Physical Space Solutions of Non-Proportionally Damped Systems," by M. Tong, Z. Liang and G.C. Lee, 1/15/91, (PB91-179242, A04, MF-A01).

NCEER-91-0003 "Seismic Response of Single Piles and Pile Groups," by K. Fan and G. Gazetas, 1/10/91, (PB92-174994, A04, MF-A01).

NCEER-91-0004 "Damping of Structures: Part 1 - Theory of Complex Damping," by Z. Liang and G. Lee, 10/10/91, (PB92-197235, A12, MF-A03).

NCEER-91-0005 "3D-BASIS - Nonlinear Dynamic Analysis of Three Dimensional Base Isolated Structures: Part II," by S. Nagarajaiah, A.M. Reinhorn and M.C. Constantinou, 2/28/91, (PB91-190553, A07, MF-A01). This report has been replaced by NCEER-93-0011.

NCEER-91-0006 "A Multidimensional Hysteretic Model for Plasticity Deforming Metals in Energy Absorbing Devices," by E.J. Graesser and F.A. Cozzarelli, 4/9/91, (PB92-108364, A04, MF-A01).

NCEER-91-0007 "A Framework for Customizable Knowledge-Based Expert Systems with an Application to a KBES for Evaluating the Seismic Resistance of Existing Buildings," by E.G. Ibarra-Anaya and S.J. Fenves, 4/9/91, (PB91-210930, A08, MF-A01).

NCEER-91-0008 "Nonlinear Analysis of Steel Frames with Semi-Rigid Connections Using the Capacity Spectrum Method," by G.G. Deierlein, S-H. Hsieh, Y-J. Shen and J.F. Abel, 7/2/91, (PB92-113828, A05, MF-A01).

NCEER-91-0009 "Earthquake Education Materials for Grades K-12," by K.E.K. Ross, 4/30/91, (PB91-212142, A06, MF-A01). This report has been replaced by NCEER-92-0018.

NCEER-91-0010 "Phase Wave Velocities and Displacement Phase Differences in a Harmonically Oscillating Pile," by N. Makris and G. Gazetas, 7/8/91, (PB92-108356, A04, MF-A01).

NCEER-91-0011 "Dynamic Characteristics of a Full-Size Five-Story Steel Structure and a 2/5 Scale Model," by K.C. Chang, G.C. Yao, G.C. Lee, D.S. Hao and Y.C. Yeh," 7/2/91, (PB93-116648, A06, MF-A02).

NCEER-91-0012 "Seismic Response of a 2/5 Scale Steel Structure with Added Viscoelastic Dampers," by K.C. Chang, T.T. Soong, S-T. Oh and M.L. Lai, 5/17/91, (PB92-110816, A05, MF-A01).

NCEER-91-0013 "Earthquake Response of Retaining Walls; Full-Scale Testing and Computational Modeling," by S. Alampalli and A-W.M. Elgamal, 6/20/91, not available.

NCEER-91-0014 "3D-BASIS-M: Nonlinear Dynamic Analysis of Multiple Building Base Isolated Structures," by P.C. Tsopelas, S. Nagarajaiah, M.C. Constantinou and A.M. Reinhorn, 5/28/91, (PB92-113885, A09, MF-A02).

NCEER-91-0015 "Evaluation of SEAOC Design Requirements for Sliding Isolated Structures," by D. Theodossiou and M.C. Constantinou, 6/10/91, (PB92-114602, A11, MF-A03).

NCEER-91-0016 "Closed-Loop Modal Testing of a 27-Story Reinforced Concrete Flat Plate-Core Building," by H.R. Somaprasad, T. Toksoy, H. Yoshiyuki and A.E. Aktan, 7/15/91, (PB92-129980, A07, MF-A02).

NCEER-91-0017 "Shake Table Test of a 1/6 Scale Two-Story Lightly Reinforced Concrete Building," by A.G. El-Attar, R.N. White and P. Gergely, 2/28/91, (PB92-222447, A06, MF-A02).

NCEER-91-0018 "Shake Table Test of a 1/8 Scale Three-Story Lightly Reinforced Concrete Building," by A.G. El-Attar, R.N. White and P. Gergely, 2/28/91, (PB93-116630, A08, MF-A02).

NCEER-91-0019 "Transfer Functions for Rigid Rectangular Foundations," by A.S. Veletsos, A.M. Prasad and W.H. Wu, 7/31/91, not available.

NCEER-91-0020 "Hybrid Control of Seismic-Excited Nonlinear and Inelastic Structural Systems," by J.N. Yang, Z. Li and A. Danielians, 8/1/91, (PB92-143171, A06, MF-A02).

NCEER-91-0021 "The NCEER-91 Earthquake Catalog: Improved Intensity-Based Magnitudes and Recurrence Relations for U.S. Earthquakes East of New Madrid," by L. Seeber and J.G. Armbruster, 8/28/91, (PB92-176742, A06, MF-A02).

NCEER-91-0022 "Proceedings from the Implementation of Earthquake Planning and Education in Schools: The Need for Change - The Roles of the Changemakers," by K.E.K. Ross and F. Winslow, 7/23/91, (PB92-129998, A12, MF-A03).

NCEER-91-0023 "A Study of Reliability-Based Criteria for Seismic Design of Reinforced Concrete Frame Buildings," by H.H.M. Hwang and H-M. Hsu, 8/10/91, (PB92-140235, A09, MF-A02).

NCEER-91-0024 "Experimental Verification of a Number of Structural System Identification Algorithms," by R.G. Ghanem, H. Gavin and M. Shinozuka, 9/18/91, (PB92-176577, A18, MF-A04).

NCEER-91-0025 "Probabilistic Evaluation of Liquefaction Potential," by H.H.M. Hwang and C.S. Lee," 11/25/91, (PB92-143429, A05, MF-A01).

NCEER-91-0026 "Instantaneous Optimal Control for Linear, Nonlinear and Hysteretic Structures - Stable Controllers," by J.N. Yang and Z. Li, 11/15/91, (PB92-163807, A04, MF-A01).

NCEER-91-0027 "Experimental and Theoretical Study of a Sliding Isolation System for Bridges," by M.C. Constantinou, A. Kartoum, A.M. Reinhorn and P. Bradford, 11/15/91, (PB92-176973, A10, MF-A03).

NCEER-92-0001 "Case Studies of Liquefaction and Lifeline Performance During Past Earthquakes, Volume 1: Japanese Case Studies," Edited by M. Hamada and T. O'Rourke, 2/17/92, (PB92-197243, A18, MF-A04).

NCEER-92-0002 "Case Studies of Liquefaction and Lifeline Performance During Past Earthquakes, Volume 2: United States Case Studies," Edited by T. O'Rourke and M. Hamada, 2/17/92, (PB92-197250, A20, MF-A04).

NCEER-92-0003 "Issues in Earthquake Education," Edited by K. Ross, 2/3/92, (PB92-222389, A07, MF-A02).

NCEER-92-0004 "Proceedings from the First U.S. - Japan Workshop on Earthquake Protective Systems for Bridges," Edited by I.G. Buckle, 2/4/92, (PB94-142239, A99, MF-A06).

NCEER-92-0005 "Seismic Ground Motion from a Haskell-Type Source in a Multiple-Layered Half-Space," A.P. Theoharis, G. Deodatis and M. Shinozuka, 1/2/92, not available.

NCEER-92-0006 "Proceedings from the Site Effects Workshop," Edited by R. Whitman, 2/29/92, (PB92-197201, A04, MF-A01).

NCEER-92-0007 "Engineering Evaluation of Permanent Ground Deformations Due to Seismically-Induced Liquefaction," by M.H. Baziar, R. Dobry and A-W.M. Elgamal, 3/24/92, (PB92-222421, A13, MF-A03).

NCEER-92-0008 "A Procedure for the Seismic Evaluation of Buildings in the Central and Eastern United States," by C.D. Poland and J.O. Malley, 4/2/92, (PB92-222439, A20, MF-A04).

NCEER-92-0009 "Experimental and Analytical Study of a Hybrid Isolation System Using Friction Controllable Sliding Bearings," by M.Q. Feng, S. Fujii and M. Shinozuka, 5/15/92, (PB93-150282, A06, MF-A02).

NCEER-92-0010 "Seismic Resistance of Slab-Column Connections in Existing Non-Ductile Flat-Plate Buildings," by A.J. Durrani and Y. Du, 5/18/92, (PB93-116812, A06, MF-A02).

NCEER-92-0011 "The Hysteretic and Dynamic Behavior of Brick Masonry Walls Upgraded by Ferrocement Coatings Under Cyclic Loading and Strong Simulated Ground Motion," by H. Lee and S.P. Prawel, 5/11/92, not available.

NCEER-92-0012 "Study of Wire Rope Systems for Seismic Protection of Equipment in Buildings," by G.F. Demetriades, M.C. Constantinou and A.M. Reinhorn, 5/20/92, (PB93-116655, A08, MF-A02).

NCEER-92-0013 "Shape Memory Structural Dampers: Material Properties, Design and Seismic Testing," by P.R. Witting and F.A. Cozzarelli, 5/26/92, (PB93-116663, A05, MF-A01).

NCEER-92-0014 "Longitudinal Permanent Ground Deformation Effects on Buried Continuous Pipelines," by M.J. O'Rourke, and C. Nordberg, 6/15/92, (PB93-116671, A08, MF-A02).

NCEER-92-0015 "A Simulation Method for Stationary Gaussian Random Functions Based on the Sampling Theorem," by M. Grigoriu and S. Balopoulou, 6/11/92, (PB93-127496, A05, MF-A01).

NCEER-92-0016 "Gravity-Load-Designed Reinforced Concrete Buildings: Seismic Evaluation of Existing Construction and Detailing Strategies for Improved Seismic Resistance," by G.W. Hoffmann, S.K. Kunnath, A.M. Reinhorn and J.B. Mander, 7/15/92, (PB94-142007, A08, MF-A02).

NCEER-92-0017 "Observations on Water System and Pipeline Performance in the Limón Area of Costa Rica Due to the April 22, 1991 Earthquake," by M. O'Rourke and D. Ballantyne, 6/30/92, (PB93-126811, A06, MF-A02).

NCEER-92-0018 "Fourth Edition of Earthquake Education Materials for Grades K-12," Edited by K.E.K. Ross, 8/10/92, (PB93-114023, A07, MF-A02).

NCEER-92-0019 "Proceedings from the Fourth Japan-U.S. Workshop on Earthquake Resistant Design of Lifeline Facilities and Countermeasures for Soil Liquefaction," Edited by M. Hamada and T.D. O'Rourke, 8/12/92, (PB93-163939, A99, MF-E11).

NCEER-92-0020 "Active Bracing System: A Full Scale Implementation of Active Control," by A.M. Reinhorn, T.T. Soong, R.C. Lin, M.A. Riley, Y.P. Wang, S. Aizawa and M. Higashino, 8/14/92, (PB93-127512, A06, MF-A02).

NCEER-92-0021 "Empirical Analysis of Horizontal Ground Displacement Generated by Liquefaction-Induced Lateral Spreads," by S.F. Bartlett and T.L. Youd, 8/17/92, (PB93-188241, A06, MF-A02).

NCEER-92-0022 "IDARC Version 3.0: Inelastic Damage Analysis of Reinforced Concrete Structures," by S.K. Kunnath, A.M. Reinhorn and R.F. Lobo, 8/31/92, (PB93-227502, A07, MF-A02).

NCEER-92-0023 "A Semi-Empirical Analysis of Strong-Motion Peaks in Terms of Seismic Source, Propagation Path and Local Site Conditions, by M. Kamiyama, M.J. O'Rourke and R. Flores-Berrones, 9/9/92, (PB93-150266, A08, MF-A02).

NCEER-92-0024 "Seismic Behavior of Reinforced Concrete Frame Structures with Nonductile Details, Part I: Summary of Experimental Findings of Full Scale Beam-Column Joint Tests," by A. Beres, R.N. White and P. Gergely, 9/30/92, (PB93-227783, A05, MF-A01).

NCEER-92-0025 "Experimental Results of Repaired and Retrofitted Beam-Column Joint Tests in Lightly Reinforced Concrete Frame Buildings," by A. Beres, S. El-Borgi, R.N. White and P. Gergely, 10/29/92, (PB93-227791, A05, MF-A01).

NCEER-92-0026 "A Generalization of Optimal Control Theory: Linear and Nonlinear Structures," by J.N. Yang, Z. Li and S. Vongchavalitkul, 11/2/92, (PB93-188621, A05, MF-A01).

NCEER-92-0027 "Seismic Resistance of Reinforced Concrete Frame Structures Designed Only for Gravity Loads: Part I - Design and Properties of a One-Third Scale Model Structure," by J.M. Bracci, A.M. Reinhorn and J.B. Mander, 12/1/92, (PB94-104502, A08, MF-A02).

NCEER-92-0028 "Seismic Resistance of Reinforced Concrete Frame Structures Designed Only for Gravity Loads: Part II - Experimental Performance of Subassemblages," by L.E. Aycardi, J.B. Mander and A.M. Reinhorn, 12/1/92, (PB94-104510, A08, MF-A02).

NCEER-92-0029 "Seismic Resistance of Reinforced Concrete Frame Structures Designed Only for Gravity Loads: Part III - Experimental Performance and Analytical Study of a Structural Model," by J.M. Bracci, A.M. Reinhorn and J.B. Mander, 12/1/92, (PB93-227528, A09, MF-A01).

NCEER-92-0030 "Evaluation of Seismic Retrofit of Reinforced Concrete Frame Structures: Part I - Experimental Performance of Retrofitted Subassemblages," by D. Choudhuri, J.B. Mander and A.M. Reinhorn, 12/8/92, (PB93-198307, A07, MF-A02).

NCEER-92-0031 "Evaluation of Seismic Retrofit of Reinforced Concrete Frame Structures: Part II - Experimental Performance and Analytical Study of a Retrofitted Structural Model," by J.M. Bracci, A.M. Reinhorn and J.B. Mander, 12/8/92, (PB93-198315, A09, MF-A03).

NCEER-92-0032 "Experimental and Analytical Investigation of Seismic Response of Structures with Supplemental Fluid Viscous Dampers," by M.C. Constantinou and M.D. Symans, 12/21/92, (PB93-191435, A10, MF-A03). This report is available only through NTIS (see address given above).

NCEER-92-0033 "Reconnaissance Report on the Cairo, Egypt Earthquake of October 12, 1992," by M. Khater, 12/23/92, (PB93-188621, A03, MF-A01).

NCEER-92-0034 "Low-Level Dynamic Characteristics of Four Tall Flat-Plate Buildings in New York City," by H. Gavin, S. Yuan, J. Grossman, E. Pekelis and K. Jacob, 12/28/92, (PB93-188217, A07, MF-A02).

NCEER-93-0001 "An Experimental Study on the Seismic Performance of Brick-Infilled Steel Frames With and Without Retrofit," by J.B. Mander, B. Nair, K. Wojtkowski and J. Ma, 1/29/93, (PB93-227510, A07, MF-A02).

NCEER-93-0002 "Social Accounting for Disaster Preparedness and Recovery Planning," by S. Cole, E. Pantoja and V. Razak, 2/22/93, (PB94-142114, A12, MF-A03).

NCEER-93-0003 "Assessment of 1991 NEHRP Provisions for Nonstructural Components and Recommended Revisions," by T.T. Soong, G. Chen, Z. Wu, R-H. Zhang and M. Grigoriu, 3/1/93, (PB93-188639, A06, MF-A02).

NCEER-93-0004 "Evaluation of Static and Response Spectrum Analysis Procedures of SEAOC/UBC for Seismic Isolated Structures," by C.W. Winters and M.C. Constantinou, 3/23/93, (PB93-198299, A10, MF-A03).

NCEER-93-0005 "Earthquakes in the Northeast - Are We Ignoring the Hazard? A Workshop on Earthquake Science and Safety for Educators," edited by K.E.K. Ross, 4/2/93, (PB94-103066, A09, MF-A02).

NCEER-93-0006 "Inelastic Response of Reinforced Concrete Structures with Viscoelastic Braces," by R.F. Lobo, J.M. Bracci, K.L. Shen, A.M. Reinhorn and T.T. Soong, 4/5/93, (PB93-227486, A05, MF-A02).

NCEER-93-0007 "Seismic Testing of Installation Methods for Computers and Data Processing Equipment," by K. Kosar, T.T. Soong, K.L. Shen, J.A. HoLung and Y.K. Lin, 4/12/93, (PB93-198299, A07, MF-A02).

NCEER-93-0008 "Retrofit of Reinforced Concrete Frames Using Added Dampers," by A. Reinhorn, M. Constantinou and C. Li, not available.

NCEER-93-0009 "Seismic Behavior and Design Guidelines for Steel Frame Structures with Added Viscoelastic Dampers," by K.C. Chang, M.L. Lai, T.T. Soong, D.S. Hao and Y.C. Yeh, 5/1/93, (PB94-141959, A07, MF-A02).

NCEER-93-0010 "Seismic Performance of Shear-Critical Reinforced Concrete Bridge Piers," by J.B. Mander, S.M. Waheed, M.T.A. Chaudhary and S.S. Chen, 5/12/93, (PB93-227494, A08, MF-A02).

NCEER-93-0011 "3D-BASIS-TABS: Computer Program for Nonlinear Dynamic Analysis of Three Dimensional Base Isolated Structures," by S. Nagarajaiah, C. Li, A.M. Reinhorn and M.C. Constantinou, 8/2/93, (PB94-141819, A09, MF-A02).

NCEER-93-0012 "Effects of Hydrocarbon Spills from an Oil Pipeline Break on Ground Water," by O.J. Helweg and H.H.M. Hwang, 8/3/93, (PB94-141942, A06, MF-A02).

NCEER-93-0013 "Simplified Procedures for Seismic Design of Nonstructural Components and Assessment of Current Code Provisions," by M.P. Singh, L.E. Suarez, E.E. Matheu and G.O. Maldonado, 8/4/93, (PB94-141827, A09, MF-A02).

NCEER-93-0014 "An Energy Approach to Seismic Analysis and Design of Secondary Systems," by G. Chen and T.T. Soong, 8/6/93, (PB94-142767, A11, MF-A03).

NCEER-93-0015 "Proceedings from School Sites: Becoming Prepared for Earthquakes - Commemorating the Third Anniversary of the Loma Prieta Earthquake," Edited by F.E. Winslow and K.E.K. Ross, 8/16/93, (PB94-154275, A16, MF-A02).

NCEER-93-0016 "Reconnaissance Report of Damage to Historic Monuments in Cairo, Egypt Following the October 12, 1992 Dahshur Earthquake," by D. Sykora, D. Look, G. Croci, E. Karaesmen and E. Karaesmen, 8/19/93, (PB94-142221, A08, MF-A02).

NCEER-93-0017 "The Island of Guam Earthquake of August 8, 1993," by S.W. Swan and S.K. Harris, 9/30/93, (PB94-141843, A04, MF-A01).

NCEER-93-0018 "Engineering Aspects of the October 12, 1992 Egyptian Earthquake," by A.W. Elgamal, M. Amer, K. Adalier and A. Abul-Fadl, 10/7/93, (PB94-141983, A05, MF-A01).

NCEER-93-0019 "Development of an Earthquake Motion Simulator and its Application in Dynamic Centrifuge Testing," by I. Krstelj, Supervised by J.H. Prevost, 10/23/93, (PB94-181773, A-10, MF-A03).

NCEER-93-0020 "NCEER-Taisei Corporation Research Program on Sliding Seismic Isolation Systems for Bridges: Experimental and Analytical Study of a Friction Pendulum System (FPS)," by M.C. Constantinou, P. Tsopelas, Y-S. Kim and S. Okamoto, 11/1/93, (PB94-142775, A08, MF-A02).

NCEER-93-0021 "Finite Element Modeling of Elastomeric Seismic Isolation Bearings," by L.J. Billings, Supervised by R. Shepherd, 11/8/93, not available.

NCEER-93-0022 "Seismic Vulnerability of Equipment in Critical Facilities: Life-Safety and Operational Consequences," by K. Porter, G.S. Johnson, M.M. Zadeh, C. Scawthorn and S. Eder, 11/24/93, (PB94-181765, A16, MF-A03).

NCEER-93-0023 "Hokkaido Nansei-oki, Japan Earthquake of July 12, 1993, by P.I. Yanev and C.R. Scawthorn, 12/23/93, (PB94-181500, A07, MF-A01).

NCEER-94-0001 "An Evaluation of Seismic Serviceability of Water Supply Networks with Application to the San Francisco Auxiliary Water Supply System," by I. Markov, Supervised by M. Grigoriu and T. O'Rourke, 1/21/94, (PB94-204013, A07, MF-A02).

NCEER-94-0002 "NCEER-Taisei Corporation Research Program on Sliding Seismic Isolation Systems for Bridges: Experimental and Analytical Study of Systems Consisting of Sliding Bearings, Rubber Restoring Force Devices and Fluid Dampers," Volumes I and II, by P. Tsopelas, S. Okamoto, M.C. Constantinou, D. Ozaki and S. Fujii, 2/4/94, (PB94-181740, A09, MF-A02 and PB94-181757, A12, MF-A03).

NCEER-94-0003 "A Markov Model for Local and Global Damage Indices in Seismic Analysis," by S. Rahman and M. Grigoriu, 2/18/94, (PB94-206000, A12, MF-A03).

NCEER-94-0004 "Proceedings from the NCEER Workshop on Seismic Response of Masonry Infills," edited by D.P. Abrams, 3/1/94, (PB94-180783, A07, MF-A02).

NCEER-94-0005 "The Northridge, California Earthquake of January 17, 1994: General Reconnaissance Report," edited by J.D. Goltz, 3/11/94, (PB94-193943, A10, MF-A03).

NCEER-94-0006 "Seismic Energy Based Fatigue Damage Analysis of Bridge Columns: Part I - Evaluation of Seismic Capacity," by G.A. Chang and J.B. Mander, 3/14/94, (PB94-219185, A11, MF-A03).

NCEER-94-0007 "Seismic Isolation of Multi-Story Frame Structures Using Spherical Sliding Isolation Systems," by T.M. Al-Hussaini, V.A. Zayas and M.C. Constantinou, 3/17/94, (PB94-193745, A09, MF-A02).

NCEER-94-0008 "The Northridge, California Earthquake of January 17, 1994: Performance of Highway Bridges," edited by I.G. Buckle, 3/24/94, (PB94-193851, A06, MF-A02).

NCEER-94-0009 "Proceedings of the Third U.S.-Japan Workshop on Earthquake Protective Systems for Bridges," edited by I.G. Buckle and I. Friedland, 3/31/94, (PB94-195815, A99, MF-A06).

NCEER-94-0010 "3D-BASIS-ME: Computer Program for Nonlinear Dynamic Analysis of Seismically Isolated Single and Multiple Structures and Liquid Storage Tanks," by P.C. Tsopelas, M.C. Constantinou and A.M. Reinhorn, 4/12/94, (PB94-204922, A09, MF-A02).

NCEER-94-0011 "The Northridge, California Earthquake of January 17, 1994: Performance of Gas Transmission Pipelines," by T.D. O'Rourke and M.C. Palmer, 5/16/94, (PB94-204989, A05, MF-A01).

NCEER-94-0012 "Feasibility Study of Replacement Procedures and Earthquake Performance Related to Gas Transmission Pipelines," by T.D. O'Rourke and M.C. Palmer, 5/25/94, (PB94-206638, A09, MF-A02).

NCEER-94-0013 "Seismic Energy Based Fatigue Damage Analysis of Bridge Columns: Part II - Evaluation of Seismic Demand," by G.A. Chang and J.B. Mander, 6/1/94, (PB95-18106, A08, MF-A02).

NCEER-94-0014 "NCEER-Taisei Corporation Research Program on Sliding Seismic Isolation Systems for Bridges: Experimental and Analytical Study of a System Consisting of Sliding Bearings and Fluid Restoring Force/Damping Devices," by P. Tsopelas and M.C. Constantinou, 6/13/94, (PB94-219144, A10, MF-A03).

NCEER-94-0015 "Generation of Hazard-Consistent Fragility Curves for Seismic Loss Estimation Studies," by H. Hwang and J-R. Huo, 6/14/94, (PB95-181996, A09, MF-A02).

NCEER-94-0016 "Seismic Study of Building Frames with Added Energy-Absorbing Devices," by W.S. Pong, C.S. Tsai and G.C. Lee, 6/20/94, (PB94-219136, A10, A03).

NCEER-94-0017 "Sliding Mode Control for Seismic-Excited Linear and Nonlinear Civil Engineering Structures," by J. Yang, J. Wu, A. Agrawal and Z. Li, 6/21/94, (PB95-138483, A06, MF-A02).

NCEER-94-0018 "3D-BASIS-TABS Version 2.0: Computer Program for Nonlinear Dynamic Analysis of Three Dimensional Base Isolated Structures," by A.M. Reinhorn, S. Nagarajaiah, M.C. Constantinou, P. Tsopelas and R. Li, 6/22/94, (PB95-182176, A08, MF-A02).

NCEER-94-0019 "Proceedings of the International Workshop on Civil Infrastructure Systems: Application of Intelligent Systems and Advanced Materials on Bridge Systems," Edited by G.C. Lee and K.C. Chang, 7/18/94, (PB95-252474, A20, MF-A04).

NCEER-94-0020 "Study of Seismic Isolation Systems for Computer Floors," by V. Lambrou and M.C. Constantinou, 7/19/94, (PB95-138533, A10, MF-A03).

NCEER-94-0021 "Proceedings of the U.S.-Italian Workshop on Guidelines for Seismic Evaluation and Rehabilitation of Unreinforced Masonry Buildings," Edited by D.P. Abrams and G.M. Calvi, 7/20/94, (PB95-138749, A13, MF-A03).

NCEER-94-0022 "NCEER-Taisei Corporation Research Program on Sliding Seismic Isolation Systems for Bridges: Experimental and Analytical Study of a System Consisting of Lubricated PTFE Sliding Bearings and Mild Steel Dampers," by P. Tsopelas and M.C. Constantinou, 7/22/94, (PB95-182184, A08, MF-A02).

NCEER-94-0023 “Development of Reliability-Based Design Criteria for Buildings Under Seismic Load,” by Y.K. Wen, H. Hwang and M. Shinozuka, 8/1/94, (PB95-211934, A08, MF-A02).

NCEER-94-0024 “Experimental Verification of Acceleration Feedback Control Strategies for an Active Tendon System,” by S.J. Dyke, B.F. Spencer, Jr., P. Quast, M.K. Sain, D.C. Kaspari, Jr. and T.T. Soong, 8/29/94, (PB95-212320, A05, MF-A01).

NCEER-94-0025 “Seismic Retrofitting Manual for Highway Bridges,” Edited by I.G. Buckle and I.F. Friedland, published by the Federal Highway Administration (PB95-212676, A15, MF-A03).

NCEER-94-0026 “Proceedings from the Fifth U.S.-Japan Workshop on Earthquake Resistant Design of Lifeline Facilities and Countermeasures Against Soil Liquefaction,” Edited by T.D. O’Rourke and M. Hamada, 11/7/94, (PB95-220802, A99, MF-E08).

NCEER-95-0001 "Experimental and Analytical Investigation of Seismic Retrofit of Structures with Supplemental Damping: Part 1 - Fluid Viscous Damping Devices," by A.M. Reinhorn, C. Li and M.C. Constantinou, 1/3/95, (PB95-266599, A09, MF-A02).

NCEER-95-0002 "Experimental and Analytical Study of Low-Cycle Fatigue Behavior of Semi-Rigid Top-And-Seat Angle Connections," by G. Pekcan, J.B. Mander and S.S. Chen, 1/5/95, (PB95-220042, A07, MF-A02).

NCEER-95-0003 "NCEER-ATC Joint Study on Fragility of Buildings," by T. Anagnos, C. Rojahn and A.S. Kiremidjian, 1/20/95, (PB95-220026, A06, MF-A02).

NCEER-95-0004 "Nonlinear Control Algorithms for Peak Response Reduction," by Z. Wu, T.T. Soong, V. Gattulli and R.C. Lin, 2/16/95, (PB95-220349, A05, MF-A01).

NCEER-95-0005 "Pipeline Replacement Feasibility Study: A Methodology for Minimizing Seismic and Corrosion Risks to Underground Natural Gas Pipelines," by R.T. Eguchi, H.A. Seligson and D.G. Honegger, 3/2/95, (PB95-252326, A06, MF-A02).

NCEER-95-0006 "Evaluation of Seismic Performance of an 11-Story Frame Building During the 1994 Northridge Earthquake," by F. Naeim, R. DiSulio, K. Benuska, A. Reinhorn and C. Li, not available.

NCEER-95-0007 "Prioritization of Bridges for Seismic Retrofitting," by N. Basöz and A.S. Kiremidjian, 4/24/95, (PB95-252300, A08, MF-A02).

NCEER-95-0008 "Method for Developing Motion Damage Relationships for Reinforced Concrete Frames," by A. Singhal and A.S. Kiremidjian, 5/11/95, (PB95-266607, A06, MF-A02).

NCEER-95-0009 "Experimental and Analytical Investigation of Seismic Retrofit of Structures with Supplemental Damping: Part II - Friction Devices," by C. Li and A.M. Reinhorn, 7/6/95, (PB96-128087, A11, MF-A03).

NCEER-95-0010 "Experimental Performance and Analytical Study of a Non-Ductile Reinforced Concrete Frame Structure Retrofitted with Elastomeric Spring Dampers," by G. Pekcan, J.B. Mander and S.S. Chen, 7/14/95, (PB96-137161, A08, MF-A02).

NCEER-95-0011 "Development and Experimental Study of Semi-Active Fluid Damping Devices for Seismic Protection of Structures," by M.D. Symans and M.C. Constantinou, 8/3/95, (PB96-136940, A23, MF-A04).

NCEER-95-0012 "Real-Time Structural Parameter Modification (RSPM): Development of Innervated Structures," by Z. Liang, M. Tong and G.C. Lee, 4/11/95, (PB96-137153, A06, MF-A01).

NCEER-95-0013 "Experimental and Analytical Investigation of Seismic Retrofit of Structures with Supplemental Damping: Part III - Viscous Damping Walls," by A.M. Reinhorn and C. Li, 10/1/95, (PB96-176409, A11, MF-A03).

NCEER-95-0014 "Seismic Fragility Analysis of Equipment and Structures in a Memphis Electric Substation," by J-R. Huo and H.H.M. Hwang, 8/10/95, (PB96-128087, A09, MF-A02).

NCEER-95-0015 "The Hanshin-Awaji Earthquake of January 17, 1995: Performance of Lifelines," Edited by M. Shinozuka, 11/3/95, (PB96-176383, A15, MF-A03).

NCEER-95-0016 "Highway Culvert Performance During Earthquakes," by T.L. Youd and C.J. Beckman, available as NCEER-96-0015.

NCEER-95-0017 "The Hanshin-Awaji Earthquake of January 17, 1995: Performance of Highway Bridges," Edited by I.G. Buckle, 12/1/95, not available.

NCEER-95-0018 "Modeling of Masonry Infill Panels for Structural Analysis," by A.M. Reinhorn, A. Madan, R.E. Valles, Y. Reichmann and J.B. Mander, 12/8/95, (PB97-110886, MF-A01, A06).

NCEER-95-0019 "Optimal Polynomial Control for Linear and Nonlinear Structures," by A.K. Agrawal and J.N. Yang, 12/11/95, (PB96-168737, A07, MF-A02).

NCEER-95-0020 "Retrofit of Non-Ductile Reinforced Concrete Frames Using Friction Dampers," by R.S. Rao, P. Gergely and R.N. White, 12/22/95, (PB97-133508, A10, MF-A02).

NCEER-95-0021 "Parametric Results for Seismic Response of Pile-Supported Bridge Bents," by G. Mylonakis, A. Nikolaou and G. Gazetas, 12/22/95, (PB97-100242, A12, MF-A03).

NCEER-95-0022 "Kinematic Bending Moments in Seismically Stressed Piles," by A. Nikolaou, G. Mylonakis and G. Gazetas, 12/23/95, (PB97-113914, MF-A03, A13).

NCEER-96-0001 "Dynamic Response of Unreinforced Masonry Buildings with Flexible Diaphragms," by A.C. Costley and D.P. Abrams," 10/10/96, (PB97-133573, MF-A03, A15).

NCEER-96-0002 "State of the Art Review: Foundations and Retaining Structures," by I. Po Lam, not available.

NCEER-96-0003 "Ductility of Rectangular Reinforced Concrete Bridge Columns with Moderate Confinement," by N. Wehbe, M. Saiidi, D. Sanders and B. Douglas, 11/7/96, (PB97-133557, A06, MF-A02).

NCEER-96-0004 "Proceedings of the Long-Span Bridge Seismic Research Workshop," edited by I.G. Buckle and I.M. Friedland, not available.

NCEER-96-0005 "Establish Representative Pier Types for Comprehensive Study: Eastern United States," by J. Kulicki and Z. Prucz, 5/28/96, (PB98-119217, A07, MF-A02).

NCEER-96-0006 "Establish Representative Pier Types for Comprehensive Study: Western United States," by R. Imbsen, R.A. Schamber and T.A. Osterkamp, 5/28/96, (PB98-118607, A07, MF-A02).

NCEER-96-0007 "Nonlinear Control Techniques for Dynamical Systems with Uncertain Parameters," by R.G. Ghanem and M.I. Bujakov, 5/27/96, (PB97-100259, A17, MF-A03).

NCEER-96-0008 "Seismic Evaluation of a 30-Year Old Non-Ductile Highway Bridge Pier and Its Retrofit," by J.B. Mander, B. Mahmoodzadegan, S. Bhadra and S.S. Chen, 5/31/96, (PB97-110902, MF-A03, A10).

NCEER-96-0009 "Seismic Performance of a Model Reinforced Concrete Bridge Pier Before and After Retrofit," by J.B. Mander, J.H. Kim and C.A. Ligozio, 5/31/96, (PB97-110910, MF-A02, A10).

NCEER-96-0010 "IDARC2D Version 4.0: A Computer Program for the Inelastic Damage Analysis of Buildings," by R.E. Valles, A.M. Reinhorn, S.K. Kunnath, C. Li and A. Madan, 6/3/96, (PB97-100234, A17, MF-A03).

NCEER-96-0011 "Estimation of the Economic Impact of Multiple Lifeline Disruption: Memphis Light, Gas and Water Division Case Study," by S.E. Chang, H.A. Seligson and R.T. Eguchi, 8/16/96, (PB97-133490, A11, MF-A03).

NCEER-96-0012 "Proceedings from the Sixth Japan-U.S. Workshop on Earthquake Resistant Design of Lifeline Facilities and Countermeasures Against Soil Liquefaction, Edited by M. Hamada and T. O'Rourke, 9/11/96, (PB97-133581, A99, MF-A06).

NCEER-96-0013 "Chemical Hazards, Mitigation and Preparedness in Areas of High Seismic Risk: A Methodology for Estimating the Risk of Post-Earthquake Hazardous Materials Release," by H.A. Seligson, R.T. Eguchi, K.J. Tierney and K. Richmond, 11/7/96, (PB97-133565, MF-A02, A08).

NCEER-96-0014 "Response of Steel Bridge Bearings to Reversed Cyclic Loading," by J.B. Mander, D-K. Kim, S.S. Chen and G.J. Premus, 11/13/96, (PB97-140735, A12, MF-A03).

NCEER-96-0015 "Highway Culvert Performance During Past Earthquakes," by T.L. Youd and C.J. Beckman, 11/25/96, (PB97-133532, A06, MF-A01).

NCEER-97-0001 "Evaluation, Prevention and Mitigation of Pounding Effects in Building Structures," by R.E. Valles and A.M. Reinhorn, 2/20/97, (PB97-159552, A14, MF-A03).

NCEER-97-0002 "Seismic Design Criteria for Bridges and Other Highway Structures," by C. Rojahn, R. Mayes, D.G. Anderson, J. Clark, J.H. Hom, R.V. Nutt and M.J. O'Rourke, 4/30/97, (PB97-194658, A06, MF-A03).

NCEER-97-0003 "Proceedings of the U.S.-Italian Workshop on Seismic Evaluation and Retrofit," Edited by D.P. Abrams and G.M. Calvi, 3/19/97, (PB97-194666, A13, MF-A03).

NCEER-97-0004 "Investigation of Seismic Response of Buildings with Linear and Nonlinear Fluid Viscous Dampers," by A.A. Seleemah and M.C. Constantinou, 5/21/97, (PB98-109002, A15, MF-A03).

NCEER-97-0005 "Proceedings of the Workshop on Earthquake Engineering Frontiers in Transportation Facilities," edited by G.C. Lee and I.M. Friedland, 8/29/97, (PB98-128911, A25, MR-A04).

NCEER-97-0006 "Cumulative Seismic Damage of Reinforced Concrete Bridge Piers," by S.K. Kunnath, A. El-Bahy, A. Taylor and W. Stone, 9/2/97, (PB98-108814, A11, MF-A03).

NCEER-97-0007 "Structural Details to Accommodate Seismic Movements of Highway Bridges and Retaining Walls," by R.A. Imbsen, R.A. Schamber, E. Thorkildsen, A. Kartoum, B.T. Martin, T.N. Rosser and J.M. Kulicki, 9/3/97, (PB98-108996, A09, MF-A02).

NCEER-97-0008 "A Method for Earthquake Motion-Damage Relationships with Application to Reinforced Concrete Frames," by A. Singhal and A.S. Kiremidjian, 9/10/97, (PB98-108988, A13, MF-A03).

NCEER-97-0009 "Seismic Analysis and Design of Bridge Abutments Considering Sliding and Rotation," by K. Fishman and R. Richards, Jr., 9/15/97, (PB98-108897, A06, MF-A02).

NCEER-97-0010 "Proceedings of the FHWA/NCEER Workshop on the National Representation of Seismic Ground Motion for New and Existing Highway Facilities," edited by I.M. Friedland, M.S. Power and R.L. Mayes, 9/22/97, (PB98-128903, A21, MF-A04).

NCEER-97-0011 "Seismic Analysis for Design or Retrofit of Gravity Bridge Abutments," by K.L. Fishman, R. Richards, Jr. and R.C. Divito, 10/2/97, (PB98-128937, A08, MF-A02).

NCEER-97-0012 "Evaluation of Simplified Methods of Analysis for Yielding Structures," by P. Tsopelas, M.C. Constantinou, C.A. Kircher and A.S. Whittaker, 10/31/97, (PB98-128929, A10, MF-A03).

NCEER-97-0013 "Seismic Design of Bridge Columns Based on Control and Repairability of Damage," by C-T. Cheng and J.B. Mander, 12/8/97, (PB98-144249, A11, MF-A03).

NCEER-97-0014 "Seismic Resistance of Bridge Piers Based on Damage Avoidance Design," by J.B. Mander and C-T. Cheng, 12/10/97, (PB98-144223, A09, MF-A02).

NCEER-97-0015 "Seismic Response of Nominally Symmetric Systems with Strength Uncertainty," by S. Balopoulou and M. Grigoriu, 12/23/97, (PB98-153422, A11, MF-A03).

NCEER-97-0016 "Evaluation of Seismic Retrofit Methods for Reinforced Concrete Bridge Columns," by T.J. Wipf, F.W. Klaiber and F.M. Russo, 12/28/97, (PB98-144215, A12, MF-A03).

NCEER-97-0017 "Seismic Fragility of Existing Conventional Reinforced Concrete Highway Bridges," by C.L. Mullen and A.S. Cakmak, 12/30/97, (PB98-153406, A08, MF-A02).

NCEER-97-0018 "Loss Asssessment of Memphis Buildings," edited by D.P. Abrams and M. Shinozuka, 12/31/97, (PB98-144231, A13, MF-A03).

NCEER-97-0019 "Seismic Evaluation of Frames with Infill Walls Using Quasi-static Experiments," by K.M. Mosalam, R.N. White and P. Gergely, 12/31/97, (PB98-153455, A07, MF-A02).

NCEER-97-0020 "Seismic Evaluation of Frames with Infill Walls Using Pseudo-dynamic Experiments," by K.M. Mosalam, R.N. White and P. Gergely, 12/31/97, (PB98-153430, A07, MF-A02).

NCEER-97-0021 "Computational Strategies for Frames with Infill Walls: Discrete and Smeared Crack Analyses and Seismic Fragility," by K.M. Mosalam, R.N. White and P. Gergely, 12/31/97, (PB98-153414, A10, MF-A02).

NCEER-97-0022 "Proceedings of the NCEER Workshop on Evaluation of Liquefaction Resistance of Soils," edited by T.L. Youd and I.M. Idriss, 12/31/97, (PB98-155617, A15, MF-A03).

MCEER-98-0001 "Extraction of Nonlinear Hysteretic Properties of Seismically Isolated Bridges from Quick-Release Field Tests," by Q. Chen, B.M. Douglas, E.M. Maragakis and I.G. Buckle, 5/26/98, (PB99-118838, A06, MF-A01).

MCEER-98-0002 "Methodologies for Evaluating the Importance of Highway Bridges," by A. Thomas, S. Eshenaur and J. Kulicki, 5/29/98, (PB99-118846, A10, MF-A02).

MCEER-98-0003 "Capacity Design of Bridge Piers and the Analysis of Overstrength," by J.B. Mander, A. Dutta and P. Goel, 6/1/98, (PB99-118853, A09, MF-A02).

MCEER-98-0004 "Evaluation of Bridge Damage Data from the Loma Prieta and Northridge, California Earthquakes," by N. Basoz and A. Kiremidjian, 6/2/98, (PB99-118861, A15, MF-A03).

MCEER-98-0005 "Screening Guide for Rapid Assessment of Liquefaction Hazard at Highway Bridge Sites," by T. L. Youd, 6/16/98, (PB99-118879, A06, not available on microfiche).

MCEER-98-0006 "Structural Steel and Steel/Concrete Interface Details for Bridges," by P. Ritchie, N. Kauhl and J. Kulicki, 7/13/98, (PB99-118945, A06, MF-A01).

MCEER-98-0007 "Capacity Design and Fatigue Analysis of Confined Concrete Columns," by A. Dutta and J.B. Mander, 7/14/98, (PB99-118960, A14, MF-A03).

MCEER-98-0008 "Proceedings of the Workshop on Performance Criteria for Telecommunication Services Under Earthquake Conditions," edited by A.J. Schiff, 7/15/98, (PB99-118952, A08, MF-A02).

MCEER-98-0009 "Fatigue Analysis of Unconfined Concrete Columns," by J.B. Mander, A. Dutta and J.H. Kim, 9/12/98, (PB99-123655, A10, MF-A02).

MCEER-98-0010 "Centrifuge Modeling of Cyclic Lateral Response of Pile-Cap Systems and Seat-Type Abutments in Dry Sands," by A.D. Gadre and R. Dobry, 10/2/98, (PB99-123606, A13, MF-A03).

MCEER-98-0011 "IDARC-BRIDGE: A Computational Platform for Seismic Damage Assessment of Bridge Structures," by A.M. Reinhorn, V. Simeonov, G. Mylonakis and Y. Reichman, 10/2/98, (PB99-162919, A15, MF-A03).

MCEER-98-0012 "Experimental Investigation of the Dynamic Response of Two Bridges Before and After Retrofitting with Elastomeric Bearings," by D.A. Wendichansky, S.S. Chen and J.B. Mander, 10/2/98, (PB99-162927, A15, MF-A03).

MCEER-98-0013 "Design Procedures for Hinge Restrainers and Hinge Sear Width for Multiple-Frame Bridges," by R. Des Roches and G.L. Fenves, 11/3/98, (PB99-140477, A13, MF-A03).

MCEER-98-0014 "Response Modification Factors for Seismically Isolated Bridges," by M.C. Constantinou and J.K. Quarshie, 11/3/98, (PB99-140485, A14, MF-A03).

MCEER-98-0015 "Proceedings of the U.S.-Italy Workshop on Seismic Protective Systems for Bridges," edited by I.M. Friedland and M.C. Constantinou, 11/3/98, (PB2000-101711, A22, MF-A04).

MCEER-98-0016 "Appropriate Seismic Reliability for Critical Equipment Systems: Recommendations Based on Regional Analysis of Financial and Life Loss," by K. Porter, C. Scawthorn, C. Taylor and N. Blais, 11/10/98, (PB99-157265, A08, MF-A02).

MCEER-98-0017 "Proceedings of the U.S. Japan Joint Seminar on Civil Infrastructure Systems Research," edited by M. Shinozuka and A. Rose, 11/12/98, (PB99-156713, A16, MF-A03).

MCEER-98-0018 "Modeling of Pile Footings and Drilled Shafts for Seismic Design," by I. PoLam, M. Kapuskar and D. Chaudhuri, 12/21/98, (PB99-157257, A09, MF-A02).

MCEER-99-0001 "Seismic Evaluation of a Masonry Infilled Reinforced Concrete Frame by Pseudodynamic Testing," by S.G. Buonopane and R.N. White, 2/16/99, (PB99-162851, A09, MF-A02).

MCEER-99-0002 "Response History Analysis of Structures with Seismic Isolation and Energy Dissipation Systems: Verification Examples for Program SAP2000," by J. Scheller and M.C. Constantinou, 2/22/99, (PB99-162869, A08, MF-A02).

MCEER-99-0003 "Experimental Study on the Seismic Design and Retrofit of Bridge Columns Including Axial Load Effects," by A. Dutta, T. Kokorina and J.B. Mander, 2/22/99, (PB99-162877, A09, MF-A02).

MCEER-99-0004 "Experimental Study of Bridge Elastomeric and Other Isolation and Energy Dissipation Systems with Emphasis on Uplift Prevention and High Velocity Near-source Seismic Excitation," by A. Kasalanati and M. C. Constantinou, 2/26/99, (PB99-162885, A12, MF-A03).

MCEER-99-0005 "Truss Modeling of Reinforced Concrete Shear-flexure Behavior," by J.H. Kim and J.B. Mander, 3/8/99, (PB99-163693, A12, MF-A03).

MCEER-99-0006 "Experimental Investigation and Computational Modeling of Seismic Response of a 1:4 Scale Model Steel Structure with a Load Balancing Supplemental Damping System," by G. Pekcan, J.B. Mander and S.S. Chen, 4/2/99, (PB99-162893, A11, MF-A03).

MCEER-99-0007 "Effect of Vertical Ground Motions on the Structural Response of Highway Bridges," by M.R. Button, C.J. Cronin and R.L. Mayes, 4/10/99, (PB2000-101411, A10, MF-A03).

MCEER-99-0008 "Seismic Reliability Assessment of Critical Facilities: A Handbook, Supporting Documentation, and Model Code Provisions," by G.S. Johnson, R.E. Sheppard, M.D. Quilici, S.J. Eder and C.R. Scawthorn, 4/12/99, (PB2000-101701, A18, MF-A04).

MCEER-99-0009 "Impact Assessment of Selected MCEER Highway Project Research on the Seismic Design of Highway Structures," by C. Rojahn, R. Mayes, D.G. Anderson, J.H. Clark, D'Appolonia Engineering, S. Gloyd and R.V. Nutt, 4/14/99, (PB99-162901, A10, MF-A02).

MCEER-99-0010 "Site Factors and Site Categories in Seismic Codes," by R. Dobry, R. Ramos and M.S. Power, 7/19/99, (PB2000-101705, A08, MF-A02).

MCEER-99-0011 "Restrainer Design Procedures for Multi-Span Simply-Supported Bridges," by M.J. Randall, M. Saiidi, E. Maragakis and T. Isakovic, 7/20/99, (PB2000-101702, A10, MF-A02).

MCEER-99-0012 "Property Modification Factors for Seismic Isolation Bearings," by M.C. Constantinou, P. Tsopelas, A. Kasalanati and E. Wolff, 7/20/99, (PB2000-103387, A11, MF-A03).

MCEER-99-0013 "Critical Seismic Issues for Existing Steel Bridges," by P. Ritchie, N. Kauhl and J. Kulicki, 7/20/99, (PB2000-101697, A09, MF-A02).

MCEER-99-0014 "Nonstructural Damage Database," by A. Kao, T.T. Soong and A. Vender, 7/24/99, (PB2000-101407, A06, MF-A01).

MCEER-99-0015 "Guide to Remedial Measures for Liquefaction Mitigation at Existing Highway Bridge Sites," by H.G. Cooke and J. K. Mitchell, 7/26/99, (PB2000-101703, A11, MF-A03).

MCEER-99-0016 "Proceedings of the MCEER Workshop on Ground Motion Methodologies for the Eastern United States," edited by N. Abrahamson and A. Becker, 8/11/99, (PB2000-103385, A07, MF-A02).

MCEER-99-0017 "Quindío, Colombia Earthquake of January 25, 1999: Reconnaissance Report," by A.P. Asfura and P.J. Flores, 10/4/99, (PB2000-106893, A06, MF-A01).

MCEER-99-0018 "Hysteretic Models for Cyclic Behavior of Deteriorating Inelastic Structures," by M.V. Sivaselvan and A.M. Reinhorn, 11/5/99, (PB2000-103386, A08, MF-A02).

MCEER-99-0019 "Proceedings of the 7th U.S.- Japan Workshop on Earthquake Resistant Design of Lifeline Facilities and Countermeasures Against Soil Liquefaction," edited by T.D. O'Rourke, J.P. Bardet and M. Hamada, 11/19/99, (PB2000-103354, A99, MF-A06).

MCEER-99-0020 "Development of Measurement Capability for Micro-Vibration Evaluations with Application to Chip Fabrication Facilities," by G.C. Lee, Z. Liang, J.W. Song, J.D. Shen and W.C. Liu, 12/1/99, (PB2000-105993, A08, MF-A02).

MCEER-99-0021 "Design and Retrofit Methodology for Building Structures with Supplemental Energy Dissipating Systems," by G. Pekcan, J.B. Mander and S.S. Chen, 12/31/99, (PB2000-105994, A11, MF-A03).

MCEER-00-0001 "The Marmara, Turkey Earthquake of August 17, 1999: Reconnaissance Report," edited by C. Scawthorn; with major contributions by M. Bruneau, R. Eguchi, T. Holzer, G. Johnson, J. Mander, J. Mitchell, W. Mitchell, A. Papageorgiou, C. Scaethorn, and G. Webb, 3/23/00, (PB2000-106200, A11, MF-A03).

MCEER-00-0002 "Proceedings of the MCEER Workshop for Seismic Hazard Mitigation of Health Care Facilities," edited by G.C. Lee, M. Ettouney, M. Grigoriu, J. Hauer and J. Nigg, 3/29/00, (PB2000-106892, A08, MF-A02).

MCEER-00-0003 "The Chi-Chi, Taiwan Earthquake of September 21, 1999: Reconnaissance Report," edited by G.C. Lee and C.H. Loh, with major contributions by G.C. Lee, M. Bruneau, I.G. Buckle, S.E. Chang, P.J. Flores, T.D. O'Rourke, M. Shinozuka, T.T. Soong, C-H. Loh, K-C. Chang, Z-J. Chen, J-S. Hwang, M-L. Lin, G-Y. Liu, K-C. Tsai, G.C. Yao and C-L. Yen, 4/30/00, (PB2001-100980, A10, MF-A02).

MCEER-00-0004 "Seismic Retrofit of End-Sway Frames of Steel Deck-Truss Bridges with a Supplemental Tendon System: Experimental and Analytical Investigation," by G. Pekcan, J.B. Mander and S.S. Chen, 7/1/00, (PB2001-100982, A10, MF-A02).

MCEER-00-0005 "Sliding Fragility of Unrestrained Equipment in Critical Facilities," by W.H. Chong and T.T. Soong, 7/5/00, (PB2001-100983, A08, MF-A02).

MCEER-00-0006 "Seismic Response of Reinforced Concrete Bridge Pier Walls in the Weak Direction," by N. Abo-Shadi, M. Saiidi and D. Sanders, 7/17/00, (PB2001-100981, A17, MF-A03).

MCEER-00-0007 "Low-Cycle Fatigue Behavior of Longitudinal Reinforcement in Reinforced Concrete Bridge Columns," by J. Brown and S.K. Kunnath, 7/23/00, (PB2001-104392, A08, MF-A02).

MCEER-00-0008 "Soil Structure Interaction of Bridges for Seismic Analysis," I. PoLam and H. Law, 9/25/00, (PB2001-105397, A08, MF-A02).

MCEER-00-0009 "Proceedings of the First MCEER Workshop on Mitigation of Earthquake Disaster by Advanced Technologies (MEDAT-1), edited by M. Shinozuka, D.J. Inman and T.D. O'Rourke, 11/10/00, (PB2001-105399, A14, MF-A03).

MCEER-00-0010 "Development and Evaluation of Simplified Procedures for Analysis and Design of Buildings with Passive Energy Dissipation Systems, Revision 01," by O.M. Ramirez, M.C. Constantinou, C.A. Kircher, A.S. Whittaker, M.W. Johnson, J.D. Gomez and C. Chrysostomou, 11/16/01, (PB2001-105523, A23, MF-A04).

MCEER-00-0011 "Dynamic Soil-Foundation-Structure Interaction Analyses of Large Caissons," by C-Y. Chang, C-M. Mok, Z-L. Wang, R. Settgast, F. Waggoner, M.A. Ketchum, H.M. Gonnermann and C-C. Chin, 12/30/00, (PB2001-104373, A07, MF-A02).

MCEER-00-0012 "Experimental Evaluation of Seismic Performance of Bridge Restrainers," by A.G. Vlassis, E.M. Maragakis and M. Saiid Saiidi, 12/30/00, (PB2001-104354, A09, MF-A02).

MCEER-00-0013 "Effect of Spatial Variation of Ground Motion on Highway Structures," by M. Shinozuka, V. Saxena and G. Deodatis, 12/31/00, (PB2001-108755, A13, MF-A03).

MCEER-00-0014 "A Risk-Based Methodology for Assessing the Seismic Performance of Highway Systems," by S.D. Werner, C.E. Taylor, J.E. Moore, II, J.S. Walton and S. Cho, 12/31/00, (PB2001-108756, A14, MF-A03).

MCEER-01-0001 "Experimental Investigation of P-Delta Effects to Collapse During Earthquakes," by D. Vian and M. Bruneau, 6/25/01, (PB2002-100534, A17, MF-A03).

MCEER-01-0002 "Proceedings of the Second MCEER Workshop on Mitigation of Earthquake Disaster by Advanced Technologies (MEDAT-2)," edited by M. Bruneau and D.J. Inman, 7/23/01, (PB2002-100434, A16, MF-A03).

MCEER-01-0003 "Sensitivity Analysis of Dynamic Systems Subjected to Seismic Loads," by C. Roth and M. Grigoriu, 9/18/01, (PB2003-100884, A12, MF-A03).

MCEER-01-0004 "Overcoming Obstacles to Implementing Earthquake Hazard Mitigation Policies: Stage 1 Report," by D.J. Alesch and W.J. Petak, 12/17/01, (PB2002-107949, A07, MF-A02).

MCEER-01-0005 "Updating Real-Time Earthquake Loss Estimates: Methods, Problems and Insights," by C.E. Taylor, S.E. Chang and R.T. Eguchi, 12/17/01, (PB2002-107948, A05, MF-A01).

MCEER-01-0006 "Experimental Investigation and Retrofit of Steel Pile Foundations and Pile Bents Under Cyclic Lateral Loadings," by A. Shama, J. Mander, B. Blabac and S. Chen, 12/31/01, (PB2002-107950, A13, MF-A03).

MCEER-02-0001 "Assessment of Performance of Bolu Viaduct in the 1999 Duzce Earthquake in Turkey" by P.C. Roussis, M.C. Constantinou, M. Erdik, E. Durukal and M. Dicleli, 5/8/02, (PB2003-100883, A08, MF-A02).

MCEER-02-0002 "Seismic Behavior of Rail Counterweight Systems of Elevators in Buildings," by M.P. Singh, Rildova and L.E. Suarez, 5/27/02. (PB2003-100882, A11, MF-A03).

MCEER-02-0003 "Development of Analysis and Design Procedures for Spread Footings," by G. Mylonakis, G. Gazetas, S. Nikolaou and A. Chauncey, 10/02/02, (PB2004-101636, A13, MF-A03, CD-A13).

MCEER-02-0004 "Bare-Earth Algorithms for Use with SAR and LIDAR Digital Elevation Models," by C.K. Huyck, R.T. Eguchi and B. Houshmand, 10/16/02, (PB2004-101637, A07, CD-A07).

MCEER-02-0005 "Review of Energy Dissipation of Compression Members in Concentrically Braced Frames," by K.Lee and M. Bruneau, 10/18/02, (PB2004-101638, A10, CD-A10).

MCEER-03-0001 "Experimental Investigation of Light-Gauge Steel Plate Shear Walls for the Seismic Retrofit of Buildings" by J. Berman and M. Bruneau, 5/2/03, (PB2004-101622, A10, MF-A03, CD-A10).

MCEER-03-0002 "Statistical Analysis of Fragility Curves," by M. Shinozuka, M.Q. Feng, H. Kim, T. Uzawa and T. Ueda, 6/16/03, (PB2004-101849, A09, CD-A09).

MCEER-03-0003 "Proceedings of the Eighth U.S.-Japan Workshop on Earthquake Resistant Design f Lifeline Facilities and Countermeasures Against Liquefaction," edited by M. Hamada, J.P. Bardet and T.D. O'Rourke, 6/30/03, (PB2004-104386, A99, CD-A99).

MCEER-03-0004 "Proceedings of the PRC-US Workshop on Seismic Analysis and Design of Special Bridges," edited by L.C. Fan and G.C. Lee, 7/15/03, (PB2004-104387, A14, CD-A14).

MCEER-03-0005 "Urban Disaster Recovery: A Framework and Simulation Model," by S.B. Miles and S.E. Chang, 7/25/03, (PB2004-104388, A07, CD-A07).

MCEER-03-0006 "Behavior of Underground Piping Joints Due to Static and Dynamic Loading," by R.D. Meis, M. Maragakis and R. Siddharthan, 11/17/03, (PB2005-102194, A13, MF-A03, CD-A00).

MCEER-04-0001 "Experimental Study of Seismic Isolation Systems with Emphasis on Secondary System Response and Verification of Accuracy of Dynamic Response History Analysis Methods," by E. Wolff and M. Constantinou, 1/16/04 (PB2005-102195, A99, MF-E08, CD-A00).

MCEER-04-0002 "Tension, Compression and Cyclic Testing of Engineered Cementitious Composite Materials," by K. Kesner and S.L. Billington, 3/1/04, (PB2005-102196, A08, CD-A08).

MCEER-04-0003 "Cyclic Testing of Braces Laterally Restrained by Steel Studs to Enhance Performance During Earthquakes," by O.C. Celik, J.W. Berman and M. Bruneau, 3/16/04, (PB2005-102197, A13, MF-A03, CD-A00).

MCEER-04-0004 "Methodologies for Post Earthquake Building Damage Detection Using SAR and Optical Remote Sensing: Application to the August 17, 1999 Marmara, Turkey Earthquake," by C.K. Huyck, B.J. Adams, S. Cho, R.T. Eguchi, B. Mansouri and B. Houshmand, 6/15/04, (PB2005-104888, A10, CD-A00).

MCEER-04-0005 "Nonlinear Structural Analysis Towards Collapse Simulation: A Dynamical Systems Approach," by M.V. Sivaselvan and A.M. Reinhorn, 6/16/04, (PB2005-104889, A11, MF-A03, CD-A00).

MCEER-04-0006 "Proceedings of the Second PRC-US Workshop on Seismic Analysis and Design of Special Bridges," edited by G.C. Lee and L.C. Fan, 6/25/04, (PB2005-104890, A16, CD-A00).

MCEER-04-0007 "Seismic Vulnerability Evaluation of Axially Loaded Steel Built-up Laced Members," by K. Lee and M. Bruneau, 6/30/04, (PB2005-104891, A16, CD-A00).

MCEER-04-0008 "Evaluation of Accuracy of Simplified Methods of Analysis and Design of Buildings with Damping Systems for Near-Fault and for Soft-Soil Seismic Motions," by E.A. Pavlou and M.C. Constantinou, 8/16/04, (PB2005-104892, A08, MF-A02, CD-A00).

MCEER-04-0009 "Assessment of Geotechnical Issues in Acute Care Facilities in California," by M. Lew, T.D. O'Rourke, R. Dobry and M. Koch, 9/15/04, (PB2005-104893, A08, CD-A00).

MCEER-04-0010 "Scissor-Jack-Damper Energy Dissipation System," by A.N. Sigaher-Boyle and M.C. Constantinou, 12/1/04 (PB2005-108221).

MCEER-04-0011 "Seismic Retrofit of Bridge Steel Truss Piers Using a Controlled Rocking Approach," by M. Pollino and M. Bruneau, 12/20/04 (PB2006-105795).

MCEER-05-0001 "Experimental and Analytical Studies of Structures Seismically Isolated with an Uplift-Restraint Isolation System," by P.C. Roussis and M.C. Constantinou, 1/10/05 (PB2005-108222).

MCEER-05-0002 "A Versatile Experimentation Model for Study of Structures Near Collapse Applied to Seismic Evaluation of Irregular Structures," by D. Kusumastuti, A.M. Reinhorn and A. Rutenberg, 3/31/05 (PB2006-101523).

MCEER-05-0003 "Proceedings of the Third PRC-US Workshop on Seismic Analysis and Design of Special Bridges," edited by L.C. Fan and G.C. Lee, 4/20/05, (PB2006-105796).

MCEER-05-0004 "Approaches for the Seismic Retrofit of Braced Steel Bridge Piers and Proof-of-Concept Testing of an Eccentrically Braced Frame with Tubular Link," by J.W. Berman and M. Bruneau, 4/21/05 (PB2006-101524).

MCEER-05-0005 "Simulation of Strong Ground Motions for Seismic Fragility Evaluation of Nonstructural Components in Hospitals," by A. Wanitkorkul and A. Filiatrault, 5/26/05 (PB2006-500027).

MCEER-05-0006 "Seismic Safety in California Hospitals: Assessing an Attempt to Accelerate the Replacement or Seismic Retrofit of Older Hospital Facilities," by D.J. Alesch, L.A. Arendt and W.J. Petak, 6/6/05 (PB2006-105794).

MCEER-05-0007 "Development of Seismic Strengthening and Retrofit Strategies for Critical Facilities Using Engineered Cementitious Composite Materials," by K. Kesner and S.L. Billington, 8/29/05 (PB2006-111701).

MCEER-05-0008 "Experimental and Analytical Studies of Base Isolation Systems for Seismic Protection of Power Transformers," by N. Murota, M.Q. Feng and G-Y. Liu, 9/30/05 (PB2006-111702).

MCEER-05-0009 "3D-BASIS-ME-MB: Computer Program for Nonlinear Dynamic Analysis of Seismically Isolated Structures," by P.C. Tsopelas, P.C. Roussis, M.C. Constantinou, R. Buchanan and A.M. Reinhorn, 10/3/05 (PB2006-111703).

MCEER-05-0010 "Steel Plate Shear Walls for Seismic Design and Retrofit of Building Structures," by D. Vian and M. Bruneau, 12/15/05 (PB2006-111704).

MCEER-05-0011 "The Performance-Based Design Paradigm," by M.J. Astrella and A. Whittaker, 12/15/05 (PB2006-111705).

MCEER-06-0001 "Seismic Fragility of Suspended Ceiling Systems," H. Badillo-Almaraz, A.S. Whittaker, A.M. Reinhorn and G.P. Cimellaro, 2/4/06 (PB2006-111706).

MCEER-06-0002 "Multi-Dimensional Fragility of Structures," by G.P. Cimellaro, A.M. Reinhorn and M. Bruneau, 3/1/06 (PB2007-106974, A09, MF-A02, CD A00).

MCEER-06-0003 "Built-Up Shear Links as Energy Dissipators for Seismic Protection of Bridges," by P. Dusicka, A.M. Itani and I.G. Buckle, 3/15/06 (PB2006-111708).

MCEER-06-0004 "Analytical Investigation of the Structural Fuse Concept," by R.E. Vargas and M. Bruneau, 3/16/06 (PB2006-111709).

MCEER-06-0005 "Experimental Investigation of the Structural Fuse Concept," by R.E. Vargas and M. Bruneau, 3/17/06 (PB2006-111710).

MCEER-06-0006 "Further Development of Tubular Eccentrically Braced Frame Links for the Seismic Retrofit of Braced Steel Truss Bridge Piers," by J.W. Berman and M. Bruneau, 3/27/06 (PB2007-105147).

MCEER-06-0007 "REDARS Validation Report," by S. Cho, C.K. Huyck, S. Ghosh and R.T. Eguchi, 8/8/06 (PB2007-106983).

MCEER-06-0008 "Review of Current NDE Technologies for Post-Earthquake Assessment of Retrofitted Bridge Columns," by J.W. Song, Z. Liang and G.C. Lee, 8/21/06 (PB2007-106984).

MCEER-06-0009 "Liquefaction Remediation in Silty Soils Using Dynamic Compaction and Stone Columns," by S. Thevanayagam, G.R. Martin, R. Nashed, T. Shenthan, T. Kanagalingam and N. Ecemis, 8/28/06 (PB2007-106985).

MCEER-06-0010 "Conceptual Design and Experimental Investigation of Polymer Matrix Composite Infill Panels for Seismic Retrofitting," by W. Jung, M. Chiewanichakorn and A.J. Aref, 9/21/06 (PB2007-106986).

MCEER-06-0011 "A Study of the Coupled Horizontal-Vertical Behavior of Elastomeric and Lead-Rubber Seismic Isolation Bearings," by G.P. Warn and A.S. Whittaker, 9/22/06 (PB2007-108679).

MCEER-06-0012 "Proceedings of the Fourth PRC-US Workshop on Seismic Analysis and Design of Special Bridges: Advancing Bridge Technologies in Research, Design, Construction and Preservation," Edited by L.C. Fan, G.C. Lee and L. Ziang, 10/12/06 (PB2007-109042).

MCEER-06-0013 "Cyclic Response and Low Cycle Fatigue Characteristics of Plate Steels," by P. Dusicka, A.M. Itani and I.G. Buckle, 11/1/06 06 (PB2007-106987).

MCEER-06-0014 "Proceedings of the Second US-Taiwan Bridge Engineering Workshop," edited by W.P. Yen, J. Shen, J-Y. Chen and M. Wang, 11/15/06 (PB2008-500041).

MCEER-06-0015 "User Manual and Technical Documentation for the REDARS^{TM} Import Wizard," by S. Cho, S. Ghosh, C.K. Huyck and S.D. Werner, 11/30/06 (PB2007-114766).

MCEER-06-0016 "Hazard Mitigation Strategy and Monitoring Technologies for Urban and Infrastructure Public Buildings: Proceedings of the China-US Workshops," edited by X.Y. Zhou, A.L. Zhang, G.C. Lee and M. Tong, 12/12/06 (PB2008-500018).

MCEER-07-0001 "Static and Kinetic Coefficients of Friction for Rigid Blocks," by C. Kafali, S. Fathali, M. Grigoriu and A.S. Whittaker, 3/20/07 (PB2007-114767).

MCEER-07-0002 "Hazard Mitigation Investment Decision Making: Organizational Response to Legislative Mandate," by L.A. Arendt, D.J. Alesch and W.J. Petak, 4/9/07 (PB2007-114768).

MCEER-07-0003 "Seismic Behavior of Bidirectional-Resistant Ductile End Diaphragms with Unbonded Braces in Straight or Skewed Steel Bridges," by O. Celik and M. Bruneau, 4/11/07 (PB2008-105141).

MCEER-07-0004 "Modeling Pile Behavior in Large Pile Groups Under Lateral Loading," by A.M. Dodds and G.R. Martin, 4/16/07(PB2008-105142).

MCEER-07-0005 "Experimental Investigation of Blast Performance of Seismically Resistant Concrete-Filled Steel Tube Bridge Piers," by S. Fujikura, M. Bruneau and D. Lopez-Garcia, 4/20/07 (PB2008-105143).

MCEER-07-0006 "Seismic Analysis of Conventional and Isolated Liquefied Natural Gas Tanks Using Mechanical Analogs," by I.P. Christovasilis and A.S. Whittaker, 5/1/07, not available.

MCEER-07-0007 "Experimental Seismic Performance Evaluation of Isolation/Restraint Systems for Mechanical Equipment – Part 1: Heavy Equipment Study," by S. Fathali and A. Filiatrault, 6/6/07 (PB2008-105144).

MCEER-07-0008 "Seismic Vulnerability of Timber Bridges and Timber Substructures," by A.A. Sharma, J.B. Mander, I.M. Friedland and D.R. Allicock, 6/7/07 (PB2008-105145).

MCEER-07-0009 "Experimental and Analytical Study of the XY-Friction Pendulum (XY-FP) Bearing for Bridge Applications," by C.C. Marin-Artieda, A.S. Whittaker and M.C. Constantinou, 6/7/07 (PB2008-105191).

MCEER-07-0010 "Proceedings of the PRC-US Earthquake Engineering Forum for Young Researchers," Edited by G.C. Lee and X.Z. Qi, 6/8/07 (PB2008-500058).

MCEER-07-0011 "Design Recommendations for Perforated Steel Plate Shear Walls," by R. Purba and M. Bruneau, 6/18/07, (PB2008-105192).

MCEER-07-0012 "Performance of Seismic Isolation Hardware Under Service and Seismic Loading," by M.C. Constantinou, A.S. Whittaker, Y. Kalpakidis, D.M. Fenz and G.P. Warn, 8/27/07, (PB2008-105193).

MCEER-07-0013 "Experimental Evaluation of the Seismic Performance of Hospital Piping Subassemblies," by E.R. Goodwin, E. Maragakis and A.M. Itani, 9/4/07, (PB2008-105194).

MCEER-07-0014 "A Simulation Model of Urban Disaster Recovery and Resilience: Implementation for the 1994 Northridge Earthquake," by S. Miles and S.E. Chang, 9/7/07, (PB2008-106426).

MCEER-07-0015 "Statistical and Mechanistic Fragility Analysis of Concrete Bridges," by M. Shinozuka, S. Banerjee and S-H. Kim, 9/10/07, (PB2008-106427).

MCEER-07-0016 "Three-Dimensional Modeling of Inelastic Buckling in Frame Structures," by M. Schachter and AM. Reinhorn, 9/13/07, (PB2008-108125).

MCEER-07-0017 "Modeling of Seismic Wave Scattering on Pile Groups and Caissons," by I. Po Lam, H. Law and C.T. Yang, 9/17/07 (PB2008-108150).

MCEER-07-0018 "Bridge Foundations: Modeling Large Pile Groups and Caissons for Seismic Design," by I. Po Lam, H. Law and G.R. Martin (Coordinating Author), 12/1/07 (PB2008-111190).

MCEER-07-0019 "Principles and Performance of Roller Seismic Isolation Bearings for Highway Bridges," by G.C. Lee, Y.C. Ou, Z. Liang, T.C. Niu and J. Song, 12/10/07 (PB2009-110466).

MCEER-07-0020 "Centrifuge Modeling of Permeability and Pinning Reinforcement Effects on Pile Response to Lateral Spreading," by L.L Gonzalez-Lagos, T. Abdoun and R. Dobry, 12/10/07 (PB2008-111191).

MCEER-07-0021 "Damage to the Highway System from the Pisco, Perú Earthquake of August 15, 2007," by J.S. O'Connor, L. Mesa and M. Nykamp, 12/10/07, (PB2008-108126).

MCEER-07-0022 "Experimental Seismic Performance Evaluation of Isolation/Restraint Systems for Mechanical Equipment – Part 2: Light Equipment Study," by S. Fathali and A. Filiatrault, 12/13/07 (PB2008-111192).

MCEER-07-0023 "Fragility Considerations in Highway Bridge Design," by M. Shinozuka, S. Banerjee and S.H. Kim, 12/14/07 (PB2008-111193).

MCEER-07-0024 "Performance Estimates for Seismically Isolated Bridges," by G.P. Warn and A.S. Whittaker, 12/30/07 (PB2008-112230).

MCEER-08-0001 "Seismic Performance of Steel Girder Bridge Superstructures with Conventional Cross Frames," by L.P. Carden, A.M. Itani and I.G. Buckle, 1/7/08, (PB2008-112231).

MCEER-08-0002 "Seismic Performance of Steel Girder Bridge Superstructures with Ductile End Cross Frames with Seismic Isolators," by L.P. Carden, A.M. Itani and I.G. Buckle, 1/7/08 (PB2008-112232).

MCEER-08-0003 "Analytical and Experimental Investigation of a Controlled Rocking Approach for Seismic Protection of Bridge Steel Truss Piers," by M. Pollino and M. Bruneau, 1/21/08 (PB2008-112233).

MCEER-08-0004 "Linking Lifeline Infrastructure Performance and Community Disaster Resilience: Models and Multi-Stakeholder Processes," by S.E. Chang, C. Pasion, K. Tatebe and R. Ahmad, 3/3/08 (PB2008-112234).

MCEER-08-0005 "Modal Analysis of Generally Damped Linear Structures Subjected to Seismic Excitations," by J. Song, Y-L. Chu, Z. Liang and G.C. Lee, 3/4/08 (PB2009-102311).

MCEER-08-0006 "System Performance Under Multi-Hazard Environments," by C. Kafali and M. Grigoriu, 3/4/08 (PB2008-112235).

MCEER-08-0007 "Mechanical Behavior of Multi-Spherical Sliding Bearings," by D.M. Fenz and M.C. Constantinou, 3/6/08 (PB2008-112236).

MCEER-08-0008 "Post-Earthquake Restoration of the Los Angeles Water Supply System," by T.H.P. Tabucchi and R.A. Davidson, 3/7/08 (PB2008-112237).

MCEER-08-0009 "Fragility Analysis of Water Supply Systems," by A. Jacobson and M. Grigoriu, 3/10/08 (PB2009-105545).

MCEER-08-0010 "Experimental Investigation of Full-Scale Two-Story Steel Plate Shear Walls with Reduced Beam Section Connections," by B. Qu, M. Bruneau, C-H. Lin and K-C. Tsai, 3/17/08 (PB2009-106368).

MCEER-08-0011 "Seismic Evaluation and Rehabilitation of Critical Components of Electrical Power Systems," S. Ersoy, B. Feizi, A. Ashrafi and M. Ala Saadeghvaziri, 3/17/08 (PB2009-105546).

MCEER-08-0012 "Seismic Behavior and Design of Boundary Frame Members of Steel Plate Shear Walls," by B. Qu and M. Bruneau, 4/26/08 . (PB2009-106744).

MCEER-08-0013 "Development and Appraisal of a Numerical Cyclic Loading Protocol for Quantifying Building System Performance," by A. Filiatrault, A. Wanitkorkul and M. Constantinou, 4/27/08 (PB2009-107906).

MCEER-08-0014 "Structural and Nonstructural Earthquake Design: The Challenge of Integrating Specialty Areas in Designing Complex, Critical Facilities," by W.J. Petak and D.J. Alesch, 4/30/08 (PB2009-107907).

MCEER-08-0015 "Seismic Performance Evaluation of Water Systems," by Y. Wang and T.D. O'Rourke, 5/5/08 (PB2009-107908).

MCEER-08-0016 "Seismic Response Modeling of Water Supply Systems," by P. Shi and T.D. O'Rourke, 5/5/08 (PB2009-107910).

MCEER-08-0017 "Numerical and Experimental Studies of Self-Centering Post-Tensioned Steel Frames," by D. Wang and A. Filiatrault, 5/12/08 (PB2009-110479).

MCEER-08-0018 "Development, Implementation and Verification of Dynamic Analysis Models for Multi-Spherical Sliding Bearings," by D.M. Fenz and M.C. Constantinou, 8/15/08 (PB2009-107911).

MCEER-08-0019 "Performance Assessment of Conventional and Base Isolated Nuclear Power Plants for Earthquake Blast Loadings," by Y.N. Huang, A.S. Whittaker and N. Luco, 10/28/08 (PB2009-107912).

MCEER-08-0020 "Remote Sensing for Resilient Multi-Hazard Disaster Response – Volume I: Introduction to Damage Assessment Methodologies," by B.J. Adams and R.T. Eguchi, 11/17/08 (PB2010-102695).

MCEER-08-0021 "Remote Sensing for Resilient Multi-Hazard Disaster Response – Volume II: Counting the Number of Collapsed Buildings Using an Object-Oriented Analysis: Case Study of the 2003 Bam Earthquake," by L. Gusella, C.K. Huyck and B.J. Adams, 11/17/08 (PB2010-100925).

MCEER-08-0022 "Remote Sensing for Resilient Multi-Hazard Disaster Response – Volume III: Multi-Sensor Image Fusion Techniques for Robust Neighborhood-Scale Urban Damage Assessment," by B.J. Adams and A. McMillan, 11/17/08 (PB2010-100926).

MCEER-08-0023 "Remote Sensing for Resilient Multi-Hazard Disaster Response – Volume IV: A Study of Multi-Temporal and Multi-Resolution SAR Imagery for Post-Katrina Flood Monitoring in New Orleans," by A. McMillan, J.G. Morley, B.J. Adams and S. Chesworth, 11/17/08 (PB2010-100927).

MCEER-08-0024 "Remote Sensing for Resilient Multi-Hazard Disaster Response – Volume V: Integration of Remote Sensing Imagery and VIEWS^{TM} Field Data for Post-Hurricane Charley Building Damage Assessment," by J.A. Womble, K. Mehta and B.J. Adams, 11/17/08 (PB2009-115532).

MCEER-08-0025 "Building Inventory Compilation for Disaster Management: Application of Remote Sensing and Statistical Modeling," by P. Sarabandi, A.S. Kiremidjian, R.T. Eguchi and B. J. Adams, 11/20/08 (PB2009-110484).

MCEER-08-0026 "New Experimental Capabilities and Loading Protocols for Seismic Qualification and Fragility Assessment of Nonstructural Systems," by R. Retamales, G. Mosqueda, A. Filiatrault and A. Reinhorn, 11/24/08 (PB2009-110485).

MCEER-08-0027 "Effects of Heating and Load History on the Behavior of Lead-Rubber Bearings," by I.V. Kalpakidis and M.C. Constantinou, 12/1/08 (PB2009-115533).

MCEER-08-0028 "Experimental and Analytical Investigation of Blast Performance of Seismically Resistant Bridge Piers," by S.Fujikura and M. Bruneau, 12/8/08 (PB2009-115534).

MCEER-08-0029 "Evolutionary Methodology for Aseismic Decision Support," by Y. Hu and G. Dargush, 12/15/08.

MCEER-08-0030 "Development of a Steel Plate Shear Wall Bridge Pier System Conceived from a Multi-Hazard Perspective," by D. Keller and M. Bruneau, 12/19/08 (PB2010-102696).

MCEER-09-0001 "Modal Analysis of Arbitrarily Damped Three-Dimensional Linear Structures Subjected to Seismic Excitations," by Y.L. Chu, J. Song and G.C. Lee, 1/31/09 (PB2010-100922).

MCEER-09-0002 "Air-Blast Effects on Structural Shapes," by G. Ballantyne, A.S. Whittaker, A.J. Aref and G.F. Dargush, 2/2/09 (PB2010-102697).

MCEER-09-0003 "Water Supply Performance During Earthquakes and Extreme Events," by A.L. Bonneau and T.D. O'Rourke, 2/16/09 (PB2010-100923).

MCEER-09-0004 "Generalized Linear (Mixed) Models of Post-Earthquake Ignitions," by R.A. Davidson, 7/20/09 (PB2010-102698).

MCEER-09-0005 "Seismic Testing of a Full-Scale Two-Story Light-Frame Wood Building: NEESWood Benchmark Test," by I.P. Christovasilis, A. Filiatrault and A. Wanitkorkul, 7/22/09 (PB2012-102401).

MCEER-09-0006 "IDARC2D Version 7.0: A Program for the Inelastic Damage Analysis of Structures," by A.M. Reinhorn, H. Roh, M. Sivaselvan, S.K. Kunnath, R.E. Valles, A. Madan, C. Li, R. Lobo and Y.J. Park, 7/28/09 (PB2010-103199).

MCEER-09-0007 "Enhancements to Hospital Resiliency: Improving Emergency Planning for and Response to Hurricanes," by D.B. Hess and L.A. Arendt, 7/30/09 (PB2010-100924).

MCEER-09-0008 "Assessment of Base-Isolated Nuclear Structures for Design and Beyond-Design Basis Earthquake Shaking," by Y.N. Huang, A.S. Whittaker, R.P. Kennedy and R.L. Mayes, 8/20/09 (PB2010-102699).

MCEER-09-0009 "Quantification of Disaster Resilience of Health Care Facilities," by G.P. Cimellaro, C. Fumo, A.M Reinhorn and M. Bruneau, 9/14/09 (PB2010-105384).

MCEER-09-0010 "Performance-Based Assessment and Design of Squat Reinforced Concrete Shear Walls," by C.K. Gulec and A.S. Whittaker, 9/15/09 (PB2010-102700).

MCEER-09-0011 "Proceedings of the Fourth US-Taiwan Bridge Engineering Workshop," edited by W.P. Yen, J.J. Shen, T.M. Lee and R.B. Zheng, 10/27/09 (PB2010-500009).

MCEER-09-0012 "Proceedings of the Special International Workshop on Seismic Connection Details for Segmental Bridge Construction," edited by W. Phillip Yen and George C. Lee, 12/21/09 (PB2012-102402).

MCEER-10-0001 "Direct Displacement Procedure for Performance-Based Seismic Design of Multistory Woodframe Structures," by W. Pang and D. Rosowsky, 4/26/10 (PB2012-102403).

MCEER-10-0002 "Simplified Direct Displacement Design of Six-Story NEESWood Capstone Building and Pre-Test Seismic Performance Assessment," by W. Pang, D. Rosowsky, J. van de Lindt and S. Pei, 5/28/10 (PB2012-102404).

MCEER-10-0003 "Integration of Seismic Protection Systems in Performance-Based Seismic Design of Woodframed Structures," by J.K. Shinde and M.D. Symans, 6/18/10 (PB2012-102405).

MCEER-10-0004 "Modeling and Seismic Evaluation of Nonstructural Components: Testing Frame for Experimental Evaluation of Suspended Ceiling Systems," by A.M. Reinhorn, K.P. Ryu and G. Maddaloni, 6/30/10 (PB2012-102406).

MCEER-10-0005 "Analytical Development and Experimental Validation of a Structural-Fuse Bridge Pier Concept," by S. El-Bahey and M. Bruneau, 10/1/10 (PB2012-102407).

MCEER-10-0006 "A Framework for Defining and Measuring Resilience at the Community Scale: The PEOPLES Resilience Framework," by C.S. Renschler, A.E. Frazier, L.A. Arendt, G.P. Cimellaro, A.M. Reinhorn and M. Bruneau, 10/8/10 (PB2012-102408).

MCEER-10-0007 "Impact of Horizontal Boundary Elements Design on Seismic Behavior of Steel Plate Shear Walls," by R. Purba and M. Bruneau, 11/14/10 (PB2012-102409).

MCEER-10-0008 "Seismic Testing of a Full-Scale Mid-Rise Building: The NEESWood Capstone Test," by S. Pei, J.W. van de Lindt, S.E. Pryor, H. Shimizu, H. Isoda and D.R. Rammer, 12/1/10 (PB2012-102410).

MCEER-10-0009 "Modeling the Effects of Detonations of High Explosives to Inform Blast-Resistant Design," by P. Sherkar, A.S. Whittaker and A.J. Aref, 12/1/10 (PB2012-102411).

MCEER-10-0010 "L'Aquila Earthquake of April 6, 2009 in Italy: Rebuilding a Resilient City to Withstand Multiple Hazards," by G.P. Cimellaro, I.P. Christovasilis, A.M. Reinhorn, A. De Stefano and T. Kirova, 12/29/10.

MCEER-11-0001 "Numerical and Experimental Investigation of the Seismic Response of Light-Frame Wood Structures," by I.P. Christovasilis and A. Filiatrault, 8/8/11 (PB2012-102412).

MCEER-11-0002 "Seismic Design and Analysis of a Precast Segmental Concrete Bridge Model," by M. Anagnostopoulou, A. Filiatrault and A. Aref, 9/15/11.

MCEER-11-0003 'Proceedings of the Workshop on Improving Earthquake Response of Substation Equipment," Edited by A.M. Reinhorn, 9/19/11 (PB2012-102413).

MCEER-11-0004 "LRFD-Based Analysis and Design Procedures for Bridge Bearings and Seismic Isolators," by M.C. Constantinou, I. Kalpakidis, A. Filiatrault and R.A. Ecker Lay, 9/26/11.

MCEER-11-0005 "Experimental Seismic Evaluation, Model Parameterization, and Effects of Cold-Formed Steel-Framed Gypsum Partition Walls on the Seismic Performance of an Essential Facility," by R. Davies, R. Retamales, G. Mosqueda and A. Filiatrault, 10/12/11.

MCEER-11-0006 "Modeling and Seismic Performance Evaluation of High Voltage Transformers and Bushings," by A.M. Reinhorn, K. Oikonomou, H. Roh, A. Schiff and L. Kempner, Jr., 10/3/11.

MCEER-11-0007 "Extreme Load Combinations: A Survey of State Bridge Engineers," by G.C. Lee, Z. Liang, J.J. Shen and J.S. O'Connor, 10/14/11.

MCEER-12-0001 "Simplified Analysis Procedures in Support of Performance Based Seismic Design," by Y.N. Huang and A.S. Whittaker.

MCEER-12-0002 "Seismic Protection of Electrical Transformer Bushing Systems by Stiffening Techniques," by M. Koliou, A. Filiatrault, A.M. Reinhorn and N. Oliveto, 6/1/12.

MCEER-12-0003 "Post-Earthquake Bridge Inspection Guidelines," by J.S. O'Connor and S. Alampalli, 6/8/12.

MCEER-12-0004 "Integrated Design Methodology for Isolated Floor Systems in Single-Degree-of-Freedom Structural Fuse Systems," by S. Cui, M. Bruneau and M.C. Constantinou, 6/13/12.

MCEER-12-0005 "Characterizing the Rotational Components of Earthquake Ground Motion," by D. Basu, A.S. Whittaker and M.C. Constantinou, 6/15/12.

MCEER-12-0006 "Bayesian Fragility for Nonstructural Systems," by C.H. Lee and M.D. Grigoriu, 9/12/12.

MCEER-12-0007 "A Numerical Model for Capturing the In-Plane Seismic Response of Interior Metal Stud Partition Walls," by R.L. Wood and T.C. Hutchinson, 9/12/12.

MCEER-12-0008 "Assessment of Floor Accelerations in Yielding Buildings," by J.D. Wieser, G. Pekcan, A.E. Zaghi, A.M. Itani and E. Maragakis, 10/5/12.

MCEER-13-0001 "Experimental Seismic Study of Pressurized Fire Sprinkler Piping Systems," by Y. Tian, A. Filiatrault and G. Mosqueda, 4/8/13.

MCEER-13-0002 "Enhancing Resource Coordination for Multi-Modal Evacuation Planning," by D.B. Hess, B.W. Conley and C.M. Farrell, 2/8/13.

MCEER-13-0003 "Seismic Response of Base Isolated Buildings Considering Pounding to Moat Walls," by A. Masroor and G. Mosqueda, 2/26/13.

MCEER-13-0004 "Seismic Response Control of Structures Using a Novel Adaptive Passive Negative Stiffness Device," by D.T.R. Pasala, A.A. Sarlis, S. Nagarajaiah, A.M. Reinhorn, M.C. Constantinou and D.P. Taylor, 6/10/13.

MCEER-13-0005 "Negative Stiffness Device for Seismic Protection of Structures," by A.A. Sarlis, D.T.R. Pasala, M.C. Constantinou, A.M. Reinhorn, S. Nagarajaiah and D.P. Taylor, 6/12/13.

MCEER-13-0006 "Emilia Earthquake of May 20, 2012 in Northern Italy: Rebuilding a Resilient Community to Withstand Multiple Hazards," by G.P. Cimellaro, M. Chiriatti, A.M. Reinhorn and L. Tirca, June 30, 2013.

MCEER-13-0007 "Precast Concrete Segmental Components and Systems for Accelerated Bridge Construction in Seismic Regions," by A.J. Aref, G.C. Lee, Y.C. Ou and P. Sideris, with contributions from K.C. Chang, S. Chen, A. Filiatrault and Y. Zhou, June 13, 2013.

MCEER-13-0008 "A Study of U.S. Bridge Failures (1980-2012)," by G.C. Lee, S.B. Mohan, C. Huang and B.N. Fard, June 15, 2013.

MCEER-13-0009 "Development of a Database Framework for Modeling Damaged Bridges," by G.C. Lee, J.C. Qi and C. Huang, June 16, 2013.

MCEER-13-0010 "Model of Triple Friction Pendulum Bearing for General Geometric and Frictional Parameters and for Uplift Conditions," by A.A. Sarlis and M.C. Constantinou, July 1, 2013.

MCEER-13-0011 "Shake Table Testing of Triple Friction Pendulum Isolators under Extreme Conditions," by A.A. Sarlis, M.C. Constantinou and A.M. Reinhorn, July 2, 2013.

MCEER-13-0012 "Theoretical Framework for the Development of MH-LRFD," by G.C. Lee (coordinating author), H.A Capers, Jr., C. Huang, J.M. Kulicki, Z. Liang, T. Murphy, J.J.D. Shen, M. Shinozuka and P.W.H. Yen, July 31, 2013.

MCEER-13-0013 "Seismic Protection of Highway Bridges with Negative Stiffness Devices," by N.K.A. Attary, M.D. Symans, S. Nagarajaiah, A.M. Reinhorn, M.C. Constantinou, A.A. Sarlis, D.T.R. Pasala, and D.P. Taylor, September 3, 2014.

MCEER-14-0001 "Simplified Seismic Collapse Capacity-Based Evaluation and Design of Frame Buildings with and without Supplemental Damping Systems," by M. Hamidia, A. Filiatrault, and A. Aref, May 19, 2014.

MCEER-14-0002 "Comprehensive Analytical Seismic Fragility of Fire Sprinkler Piping Systems," by Siavash Soroushian, Emmanuel "Manos" Maragakis, Arash E. Zaghi, Alicia Echevarria, Yuan Tian and Andre Filiatrault, August 26, 2014.

MCEER-14-0003 "Hybrid Simulation of the Seismic Response of a Steel Moment Frame Building Structure through Collapse," by M. Del Carpio Ramos, G. Mosqueda and D.G. Lignos, October 30, 2014.

MCEER-14-0004 "Blast and Seismic Resistant Concrete-Filled Double Skin Tubes and Modified Steel Jacketed Bridge Columns," by P.P. Fouche and M. Bruneau, June 30, 2015.

MCEER-14-0005 "Seismic Performance of Steel Plate Shear Walls Considering Various Design Approaches," by R. Purba and M. Bruneau, October 31, 2014.

MCEER-14-0006 "Air-Blast Effects on Civil Structures," by Jinwon Shin, Andrew S. Whittaker, Amjad J. Aref and David Cormie, October 30, 2014.

MCEER-14-0007 "Seismic Performance Evaluation of Precast Girders with Field-Cast Ultra High Performance Concrete (UHPC) Connections," by G.C. Lee, C. Huang, J. Song, and J. S. O'Connor, July 31, 2014.

MCEER-14-0008 "Post-Earthquake Fire Resistance of Ductile Concrete-Filled Double-Skin Tube Columns," by Reza Imani, Gilberto Mosqueda and Michel Bruneau, December 1, 2014.

MCEER-14-0009 "Cyclic Inelastic Behavior of Concrete Filled Sandwich Panel Walls Subjected to In-Plane Flexure," by Y. Alzeni and M. Bruneau, December 19, 2014.

MCEER-14-0010 "Analytical and Experimental Investigation of Self-Centering Steel Plate Shear Walls," by D.M. Dowden and M. Bruneau, December 19, 2014.

MCEER-15-0001 "Seismic Analysis of Multi-story Unreinforced Masonry Buildings with Flexible Diaphragms," by J. Aleman, G. Mosqueda and A.S. Whittaker, June 12, 2015.

MCEER-15-0002 "Site Response, Soil-Structure Interaction and Structure-Soil-Structure Interaction for Performance Assessment of Buildings and Nuclear Structures," by C. Bolisetti and A.S. Whittaker, June 15, 2015.

MCEER-15-0003 "Stress Wave Attenuation in Solids for Mitigating Impulsive Loadings," by R. Rafiee-Dehkharghani, A.J. Aref and G. Dargush, August 15, 2015.

MCEER-15-0004 "Computational, Analytical, and Experimental Modeling of Masonry Structures," by K.M. Dolatshahi and A.J. Aref, November 16, 2015.

MCEER-15-0005 "Property Modification Factors for Seismic Isolators: Design Guidance for Buildings," by W.J. McVitty and M.C. Constantinou, June 30, 2015.

MCEER-15-0006 "Seismic Isolation of Nuclear Power Plants using Sliding Bearings," by Manish Kumar, Andrew S. Whittaker and Michael C. Constantinou, December 27, 2015.

MCEER-15-0007 "Quintuple Friction Pendulum Isolator Behavior, Modeling and Validation," by Donghun Lee and Michael C. Constantinou, December 28, 2015.

MCEER-15-0008 "Seismic Isolation of Nuclear Power Plants using Elastomeric Bearings," by Manish Kumar, Andrew S. Whittaker and Michael C. Constantinou, December 29, 2015.

MCEER-16-0001 "Experimental, Numerical and Analytical Studies on the Seismic Response of Steel-Plate Concrete (SC) Composite Shear Walls," by Siamak Epackachi and Andrew S. Whittaker, June 15, 2016.

MCEER-16-0002 "Seismic Demand in Columns of Steel Frames," by Lisa Shrestha and Michel Bruneau, June 17, 2016.

MCEER-16-0003 "Development and Evaluation of Procedures for Analysis and Design of Buildings with Fluidic Self-Centering Systems" by Shoma Kitayama and Michael C. Constantinou, July 21, 2016.

MCEER-16-0004 "Real Time Control of Shake Tables for Nonlinear Hysteretic Systems," by Ki Pung Ryu and Andrei M. Reinhorn, October 22, 2016.

MCEER-16-0006 "Seismic Isolation of High Voltage Electrical Power Transformers," by Kostis Oikonomou, Michael C. Constantinou, Andrei M. Reinhorn and Leon Kemper, Jr., November 2, 2016.

MCEER-16-0007 "Open Space Damping System Theory and Experimental Validation," by Erkan Polat and Michael C. Constantinou, December 13, 2016.

MCEER-16-0008 "Seismic Response of Low Aspect Ratio Reinforced Concrete Walls for Buildings and Safety-Related Nuclear Applications," by Bismarck N. Luna and Andrew S. Whittaker.

MCEER-16-0009 "Buckling Restrained Braces Applications for Superstructure and Substructure Protection in Bridges," by Xiaone Wei and Michel Bruneau, December 28, 2016.

MCEER-16-0010 "Procedures and Results of Assessment of Seismic Performance of Seismically Isolated Electrical Transformers with Due Consideration for Vertical Isolation and Vertical Ground Motion Effects," by Shoma Kitayama, Michael C. Constantinou and Donghun Lee, December 31, 2016.

MCEER-17-0001 "Diagonal Tension Field Inclination Angle in Steel Plate Shear Walls," by Yushan Fu, Fangbo Wang and Michel Bruneau, February 10, 2017.

MCEER-17-0002 "Behavior of Steel Plate Shear Walls Subjected to Long Duration Earthquakes," by Ramla Qureshi and Michel Bruneau, September 1, 2017.

MCEER-17-0003 "Response of Steel-plate Concrete (SC) Wall Piers to Combined In-plane and Out-of-plane Seismic Loadings," by Brian Terranova, Andrew S. Whittaker, Siamak Epackachi and Nebojsa Orbovic, July 17, 2017.

MCEER-17-0004 "Design of Reinforced Concrete Panels for Wind-borne Missile Impact," by Brian Terranova, Andrew S. Whittaker and Len Schwer, July 18, 2017.

MCEER
EARTHQUAKE ENGINEERING TO EXTREME EVENTS
University at Buffalo, The State University of New York
133A Ketter Hall ▪ Buffalo, New York 14260-4300
Phone: (716) 645-3391 ▪ Fax: (716) 645-3399
Email: *mceer@buffalo.edu* ▪ Web: *http://mceer.buffalo.edu*
University at Buffalo *The State University of New York*

ISSN 1520-295X